Technische Universität München
TUM School of Natural Sciences

Neutral atomic hydrogen shells in the local Milky Way

Daniel Kröll

Vollständiger Abdruck der von der TUM School of Natural Sciences der Teschnichen Universität München zur Erlangung eines

Doktors der Naturwissenschaften (Dr. rer. nat)

genehmigten Dissertation.

Vorsitz: Prof. Dr. Lothar Oberauer

Prüfer
der Dissertation: 1. apl. Prof. Dr. Roland Diehl
2. Prof. Dr. Alejandro Ibarra

Die Dissertation wurde am 19.05.2023 bei der Technischen Universität München eingereicht und durch die TUM School of Natural Sciences am 15.11.2023 angenommen.

Abstract

In this thesis expanding shells in the local Galactic interstellar medium have been investigated using the newest and highest resolution all-sky neutral hydrogen survey. New algorithms to identify the pattern of shells in sequences of images along the measured frequency space have been developed and connected to an automated search algorithm for expanding H I shells. This results in a new catalog of H I shells in the local Milky Way, which has been evaluated to derive the physical properties of the shells, statistics about the distribution of shell sizes, their locations and their connections to spiral arm segments. By using the volume of shells, the three dimensional porosity of the shells has been determined and compared to other observations. Using two approaches to determine the initial density of the interstellar medium, before the shell was produced, the expected total energy output, predicted by analytical models, has been compared to the measured kinetic shell energies. Further, the interstellar medium near the Scorpius-Centaurus OB association and the connection to its three stellar groups have been analyzed. The parameters of the surrounding H I shells have been refined by using visual as well as automated approaches. The distances have been determined using Na I absorption line measurements as well as stellar extinction maps. An idealized spherical shell model considering background emission for this region has been fitted to the H I data to determine the shell masses. The initial stellar content of the three stellar groups has been determined to predict the expected time stamps, where supernovae appeared by using a stellar synthesis code. The results have been connected to the kinetic age estimation derived from the shell parameters. Based on the connection of the new results, a proposal for the evolution of this region is presented.

Abstrakt

In dieser Dissertation wurden expandierende Schalen im lokalen galaktischen interstellaren Medium anhand neuester, hochauflösender Himmelskarten des neutralen Wasserstoffs untersucht. Es wurden neue Algorithmen zur Identifikation von Eigenschaften der Schalen in Bildsequenzen entlang der gemessenen Frequenz entwickelt. Die Algorithmen wurden zu einem automatisierten Suchalgorithmus für expandierende Schalen des neutralen Wasserstoffs kombiniert. Das Ergebnis der Anwendung ist ein neuer Katalog mit Schalen der lokalen Milchstraße. Dieser wurde ausgewertet um physikalische Eigenschaften der Schalen und Statistiken über deren Größen, Verteilungen, Lokalitäten und Dichteschwankungen in lokalen Segmenten der Galaxie zu ermitteln. Astrophysikalische Eigenschaften der Schalen konnten durch Berechnung ihrer Volumina, ihrer kinetischen Energien sowie des, durch analytische Modelle vorhergesagten, theoretischen Energieausstoßes der Stern bestimmt werden. Weiter wurde das interstellare Medium um die Scorpius-Centaurus OB Assoziation und dessen Verbindung mit den drei zugehörigen Sternengruppen analysiert. Die Parameter der umgebenden Wasserstoff-Schalen wurden durch Nutzung visueller und automatisierter Methoden neu ermittelt. Ihre Distanzen wurden mit Hilfe von Natrium Absorptionslinien und Karten von Interstellarer Extinktion des Sternenlichts bestimmt. Durch das Fitten eines idealisierten sphärischen Schalenmodells an die Daten des neutralen Wasserstoffs unter Anwendung eines, für die Region entwickelten, Hintergrund Modells, konnten die Schalenmassen bestimmt werden. Der ursprüngliche Sterneninhalt der drei Sternengruppen wurde bestimmt, um durch die Anwendung eines stellaren Synthese Codes die Zeitpunkte der Supernovae zu bestimmen und mit dem bestimmten Alter aus den Schalen Parametern zu vergleichen. Basierend auf der Verbindung aller neuen Ergebnisse wurde ein Szenario für die vorangegangene Entwicklung der Region um Scorpius-Centaurus abgeleitet.

Danksagung

An dieser Stelle möchte ich all jenen danken, die durch ihre fachliche und persönliche Unterstützung zum Gelingen dieser Dissertation beigetragen haben. Mein Dank gilt vor allem Herrn Prof. Dr. rer. nat. Roland Diehl für die Aufnahme in die Arbeitsgruppe und die sehr gute Betreuung über den gesamten Zeitraum meiner Dissertation.
Besonderer Dank gilt auch Privatdozent Dr. Jürgen Kerp, der mir stets mit seiner Expertise zur Seite stand und in Bonn einen zusätzlichen Arbeitsplatz zur Forschung zur Verfügung stellte. Außerdem bedanke ich mich bei Dr. rer. nat. Martin Klein, Dr. rer. nat Thomas Siegert und meinem Freund Dr. rer. nat Lotfi Benabderrahmane für die vielen konstruktiven Diskussionen.
Darüber hinaus danke ich meiner Frau Christina Pack für ihr Vertrauen, ihre Geduld und den Freiraum, den sie mir während der Forschung und Erstellung der Arbeit, insbesondere in meiner Freizeit und an Wochenenden ermöglichte.
Zuletzt möchte ich meiner verstorbenen Mutter Helga Kröll danken. Ihr Vorbild und ihre Erziehung haben mich stets motiviert diese Arbeit auch nach dem Eintritt in das Berufsleben abzuschließen.

Contents

List of Figures

List of Tables

List of Abbrevations

CA	Canny Algorithm
CAR	Platte Carée
CNM	Cold neutral medium
EBHIS	Effelsberg-Bonn HI Survey
EHSS	Expanding homogeneous spherical shell
EROSITA	Extended ROentgen Survey with an Imaging Telescope Array
FAST	Five Hundred meter Aperture Spherical Telescope
FIR	Far Infrared
FITS	Flexible Image Transport System
FWHM	Full width half maximum
GAIA	Globale Astronometrische Interferometer fuer die Astrophysik
GASS	Galactic All-Sky Survey
GPS	Global Positional System
HEALpix	Hierarchical Equal Area iso-Latitude pixelization
HIPASS	Hydrogen Parkes All-sky Survey
HIPPARCOS	High precision parallax collecting satellite
IGIMF	Integrated Galactic Initial Mass Function
IMF	Initial mass function
INTEGRAL	International Gamma-Ray Astrophysics Laboratory
IR	Infrared
ISM	Interstellar medium
LAB	Leiden Argentine Bonn
LB	Local bubble
LCC	Lower Centaurus Crux
LoS	Line of sight
LSR	Local Standard of Rest
MCMC	Markov Chain Monte Carlo
PDMF	Present day mass function
PPV	Position- position velocity
PV	Position Velocity
RFI	Radio frequency interference
RMS	root mean square
ROSAT	A Roenthgen SATellit
Sco-Cen	Scorpius Centaurus OB association
SFL	Sanson-Flamsteed
SFR	star formation rate

SN	supernova
SNR	supernova remnant
UCL	Upper Centaurus Lupus
UV	Ultra Violet
WIM	Warm ionized medium
WNM	Warm neutral medium

CHAPTER 1

Introduction

Stars are shaped out of the interstellar medium and in turn eject matter as well as energy back into the interstellar medium, which leads to turbulent and complex structures that can be observed. Especially the feedback of stars that are massive enough to end their lives in a supernova explosion leads to the production of shells, not only by the supernovae, but also by their stellar winds during their lifetimes. High mass clusters contain multiple massive stars that can form merged shells, which reach sizes up to kilo parsec scales (Ferrière 2001; Draine 2011).

The produced shells can be traced by the 21 cm emission line of neutral atomic hydrogen, H I (Ewen & Purcell 1951), which can be detected by radio telescopes. Steerable single dish telescopes are able to cover large fractions of the sky. The combination of telescopes at different locations led to the first ever full-sky survey in H I, called the Leiden-Argentine-Bonn survey (Kalberla et al. 2005). More recently, the data of the newer Galactic full-sky survey McClure-Griffiths et al. (2009) and the Effelsberg-Bonn H I survey Winkel et al. (2016) covering the southern-, and northern hemisphere respectively, have been released. The combination of both led to the highest resolution full-sky survey, the HI4PI survey (HI4PI Collaboration et al. 2016) with an effective four times higher resolution compared to its predecessor. The HI4PI survey is the main data source used in the analyzes of the interstellar medium, presented in this work.

Due to its wavelength, H I is not absorbed by dust. It also is the most abundant element and almost omnipresent in the interstellar medium. Hence the interstellar medium structures throughout the Milky Way can be traced by H I observation revealing the kinematics of the spiral arms and the rotation curve. On smaller scales, H I shells can often be connected to nearby stellar groups. While distant shells can have angular radii as small as the resolution limit, some shells in the local interstellar medium fill large angular parts of the sky and can be identified visually in full-sky maps. The first investigations of these H I shells have been carried out visually and one of the first compiled H I shell catalogs was produced by Heiles (1979) identifying 23 objects. Partly automated algorithms have been developed with pioneer works of mainly Ehlerová & Palouš (2005) and Ehlerová & Palouš (2013), who detected hundreds of objects in the local Galaxy, using the data of the Leiden-Argentine-Bonn survey. However, no search for H I shells has been performed on the above introduced HI4PI data with four times higher resolution. Also, the known search methods focus on density gradient searches and do not include pattern recognition, which might reveal additional objects.

Milestones for theoretical analytical descriptions of wind- and supernova driven shells are the studies of e.g. Taylor (1950a), Taylor (1950b), Sedov (1958), Chevalier (1974) and Weaver et al. (1977).

Newer models of bubbles driven by stellar winds and supernovae aim to reproduce realistic scenarios, where multiple stellar explosions shape the interstellar medium in their vicinity and sometimes expand into a non homogeneous ISM (e.g. (Breitschwerdt et al. 2012; Krause et al. 2013)). These models predict properties of H I shells, which on the other hand can be tested by observation.

One of the major focuses of this thesis is the investigation of the general properties and distribution of H I shells in the Galaxy. By developing new methods to objectively investigate the structures of the interstellar medium, the aim is to detect new H I shells and also to determine their parameters. Inspired by the pattern, visible in the ISM near the well known OB associations Scorpius Centaurus and Orion, also to overcome the systematic limitations introduced by the biased search for structures by eye, a new partly automated search algorithm for Galactic H I shells has been developed. HI4PI is the state of the art digital database, allowing such an approach, because of its full-sky sampling. The product is a new catalog of H I shells. Analyzing and testing the developed detection methods on H I test- and then on real H I data, connecting the different methods, measuring and analyzing the results are major parts of this work. To draw conclusions of the properties of Galactic H I shells, the physical parameters as well as the spatial distribution of the shells have been derived using kinematic distance estimations. Using the shell parameters, the kinetic energy as well as an estimation of the age of the shells have been derived. These have been connected to the total energy, predicted by analytical models. The results have been compared to Galactic and extragalactic results from other H I shell observation studies as well as state of the art hydrodynamic models.

Supplementary to the general investigations of H I shells in the interstellar medium, young stellar clusters and their surrounding interstellar medium have been analyzed to connect the H I structures to the stellar history. One of the most prominent regions to analyze is the above mentioned Scorpius Centaurus OB-association, which is the nearest site of recent massive star formation (de Zeeuw et al. 1999). In addition to properties of the stellar content, investigations of the turbulent interstellar medium structure in the vicinity of Scorpius Centaurus have been carried out in the past (Blaauw 1964b; Weaver 1979; Cappa de Nicolau & Poeppel 1986; de Geus 1992; Egger & Aschenbach 1995; Ortega et al. 2009; Poeppel et al. 2010).

This work received funding via a multi wavelength research proposal[1] on multiple open questions of which the one: ”What is the kinetic energy, mass distribution and structure of the ISM in the vicinity of Scorpius Centaurus?” initiated the second main topic of this work.

The hydrogen shells in the vicinity of the Scorpius Centaurus OB association have been investigated by using methods that have been fine tuned towards the properties of the ISM in this region. Also a geometric parameterization of H I shells has been used to fit the H I data to determine the parameters of the shells in detail. Background emissions of the Galactic disk in this region have also been considered. In addition, the H I data have been connected to data of interstellar reddening induced by dust (Schlafly et al. 2014; Green et al. 2015). To limit the distance towards the analyzed H I clouds, sodium absorption line data from Welsh et al. (2010) have been fitted to the H I data. Distances and kinematics of the stellar sub-groups of Scorpius Centaurus from Preibisch & Mamajek (2008) as well as the newer ones from the GAIA-satellite (Lindegren et al. 2016) have been used to redefine the distances to the shells. By using a stellar synthesis code (Voss et al. 2009) and by deriving the initial mass distribution of the stars of Scorpius Centaurus, the theoretical energy output as well as the supernova time stamps have been determined to compare it to the measured kinetic ages of the shells.

[1] “Deciphering the interstellar medium around the Scorpius Centaurus OB association”, Deutsche Forschungsgesellschaft Priority Programme 1573

Finally, the interpretation of the results has led to a proposal of the evolution of the OB association and its interstellar medium.

This thesis is structured as follows. Chapter 2 covers the introduction to properties, components and physics of the interstellar medium, a summary of researches of the local interstellar medium in multi wavelengths, the evolution of supernova remnants, the interaction between OB associations and super shells and the state of research of the Scorpius Centaurus OB association.

In chapter 3, radio telescopes and sampling strategies, the relevant telescopes and H I surveys are introduced. The data format and its properties, as well as the explanation of the visualization of H I structures, especially the characteristics of expanding H I shells in the data are presented.

In chapter 4, approaches to H I data analyses are presented. The evaluation and tests of methods to detect H I structures are described. This includes pattern recognition in images as well as the geometric description of an expanding homogeneous spherical shell in the three dimensional data structure. The tests of the developed methods on artificial– as well as real H I data are described. The connection of the methods to a search algorithm for Galactic H I shells and its application to H I data to produce an H I shell catalog are presented. Finally, specific methods to determine the distances towards local H I clouds and expanding shells are introduced.

In chapter 5, the resulting shell catalog of the search algorithm for Galactic H I shells from chapter 4 is presented. The analysis of the statistical distribution of the shells in the H I data and the comparison to the ones of existing catalogs of H I shells are presented. After that the derivation of the distance towards the shells, their physical properties, the analysis of their distribution in the local Milky Way as well as the derived kinetic shell energies and ages are described. Finally, in this chapter astrophysical properties like the fraction of the Milky Way volume that is covered by the shells as well as the ratio between kinetic energies and calculated theoretical energy inputs induced by analytical models are discussed.

The analysis of the H I in the vicinity of the Scorpius Centaurus OB association is presented in chapter 6. The derivation of the distance towards specific H I clouds, using multiple wavelength data sources and combining them with H I measurements, is presented. A combination of visual analyses and the application of algorithms to determine the shell parameters are presented in this chapter.

Subsequently, the fits of the idealized spherical shell model from chapter 4 to the H I data to determine the shell masses are presented. The derivation of the initial stellar content of the three stellar groups, the derivation of the expected supernova time stamps by using a stellar synthesis code and the connection of the results to the kinetic age estimation, derived from the shell parameters, are presented. Based on the connection of the new results, a proposal for the evolution of this region is presented. The results are summarized for each H I shell and proposals for the geometries of the ISM structures and a scenario of the history of this region are made.

Finally a conclusion is provided in chapter 7.

CHAPTER 2

Stellar feedback and interstellar medium structures

The content of this chapter is a general introduction to the properties and physics of the interstellar medium (ISM), expanding shells in the Milky Way in both, observation and simulations. The connection between the ISM and the feedback of massive stars and the current research status in this field are presented.

The structure of this chapter is as follows. First the general components and different phases of the ISM are introduced in section 2.1. The geometries and kinematics of the local ISM, its measurement in different wavelengths and its concrete structures are explored in section 2.2. An introduction to relevant parts of stellar evolution as well as the evolution of single supernova remnants (SNR) and their different phases is done in section 2.3. The transition from single objects to groups of stars is made in section 2.4. There the current understanding gained by using and connecting theoretical analytical as well as hydrodynamic simulation models of multiple massive stars producing shells and supershells are introduced. Therein also the observational results of Galactic- and extragalactic shells are discussed.

Since the ambient ISM of the OB association Scorpius Centaurus is one of the main research topics in this thesis, the current research status regarding its stellar evolution and the ISM structures in its vicinity are reviewed in section 2.5. Finally this chapter is summarized in section 2.6.

2.1 The interstellar medium in the Milky Way

The ISM is a complex and highly dynamic system with varying properties like velocities, abundance, composition and phase between different regions. The turbulence of the ISM is driven by different sources like stellar winds, supernovae and the Galactic magnetic field (Elmegreen 1999; Burkhart et al. 2013; Krumholz & Burkhart 2016). This leads to a highly structured ISM that is observed in the visible wavelength regime indirectly due to absorption- and extinction of stellar light as well as directly due to de-excitation of gas that is ionized by stellar radiation or spontaneous emission. But it is also directly observed in the far infrared (FIR), due to radiation emission of dust. In radio wavelengths, the emission from gas is mainly in the form of atomic hydrogen (H I) that is observed directly. Molecular hydrogen (H_2), is mainly traced by the molecule carbon monoxide (CO), with high uncertainties because conversion factors vary between different regions (Hammer et al. 2009; Kennicutt & Evans 2012; Bolatto et al. 2013)).

The ISM is an important component of galaxies because it is the fuel for star formation and accounts for about 10-15 % of the total mass of the Galactic disk in the Milky Way. The H I disks of spiral galaxies extent three times larger than the stellar one (Kalberla & Kerp 2009). The average number density of the Galactic ISM in general is one atom per cubic centimeter (1 per cm^{-3} but falls off exponentially starting at a Galactic radius of 5 kpc down to 0.001 per cm^3 at a radius of 35 kpc (e.g. Kalberla & Kerp (2009)). This is 20 orders of magnitude lower than the density of the earth's atmosphere and hence difficult to reproduce in laboratories. But the ISM is highly structured and 50 % of the ISM consists of clouds which only take an interstellar volume of 1–2 % from the total volume (Ferrière 2001). Except from e.g. the Hα line, which traces the ISM in the visible regime, it can primarily be observed by absorption-, emission- and continuum lines, which are connected to different temperatures and physical processes. Observation of the ISM in different environments and stages of evolution is important because the large volumes needed and the long time scales between particle interactions that are given in space are additional challenges for the setup of experiments in laboratories. Hence observation and simulations of the ISM are key to understand processes like cloud formation, star formation and the physics of shells driven by the stellar feedback. The relevant components of the ISM for this work are introduced in the following.

2.1.1 Hydrogen in the Galactic interstellar medium

Hydrogen is by far the most abundant element in the ISM. The ISM constitutes to about 75 % by mass and 90% by numbers of hydrogen (e.g. Morton et al. (1973), Rogerson et al. (1973)). The hydrogen component of the ISM consists of three different subgroups, the very cold neutral hydrogen (CNM) in the form of cold molecular hydrogen (see section 2.1.1), and cold atomic hydrogen (section 2.1.1), the warm component which is also divided into warm neutral medium (WNM) and the warm ionized medium (WIM) and finally the hot ionized gas (Ferrière 2001; Kalberla & Kerp 2009). In this thesis, the atomic part of the CNM and the WNM are the most important phases and hence are introduced in more detail.

Cold and warm atomic hydrogen

The cold neutral hydrogen component of the interstellar medium has a temperature of about 100 K and is found in the Galactic disk spreading out radially up to 30 kpc with a scale height of $|z| \approx 150$ pc

above the Galactic plane at the location of the sun (Ferrière 2001; Kalberla & Kerp 2009). The WNM can be considered as a gas layer, which has no distinct cloud structure and scales of multiple 100 pc, with a local scale height of 400 pc and increasing scale height with galactocentric radius (Kalberla 2003; Kalberla & Kerp 2009). Atomic hydrogen is generally heated by electron emission of dust (Field et al. 1969; Wolfire et al. 1995), but also near stars by stellar radiation. Its primary cooling mechanism is the radiative de-excitation of collisionally excited fine structure lines of metals (Goldsmith et al. 1969). Lyman-alpha cooling is the most efficient cooling mechanism for WNM with temperatures of T= 6000 – 10000 K (Dickey et al. 1978). Dust influences the cooling and heating mechanisms of the ISM (sec. 2.1.2). The interstellar medium has a velocity dispersion of roughly 7 km/s (Belfort & Crovisier 1984) but is also not constant throughout the Galaxy as described below. It becomes important for the investigation of old hydrogen shells produced by winds and supernovae of massive stars at their evolutionary latest stages, short from merging into the ambient ISM. Observed expansion velocities of these shells are often in the range of 10-20 km/s (Heiles 1984; McClure-Griffiths et al. 2002; Ehlerová & Palouš 2005), which is close to the velocity dispersion. This is why the velocity dispersion becomes important for the detection of expanding H I shells in this work and is used as a lower limit for detectable expansion velocities in chapters 4, 5 and 6 and is discussed in more detail below.

The 21 cm line The 21 cm line of hydrogen penetrates deep through the ISM compared to e.g. visible wavelengths. Additionally, atomic hydrogen is almost omnipresent in the ISM and therefore is detectable throughout the whole Galaxy. The line was predicted in 1945 (van de Hulst 1945) and was discovered six years later by Ewen & Purcell (1951). Through an interaction between the magnetic moment of the atomic core with the magnetic field induced by the shell (electron) at the location of the core, the ground state of the hydrogen atom is split into two hyperfine levels. As shown schematically in figure 2.1, the first energy level corresponds to the state where the spin of the electron and the one of the proton are parallel and the total spin adds up to $F = 1$ (left hand side of the figure). Through a hyperfine level transition, the spin of the electron flips and the atom reaches the energetic more favorable state with a total spin of $F = 0$ (e.g. Griffiths (1982), Demtröeder (2005)). A photon of the frequency 1420.4 MHz (in wavelength 21.1 cm) is emitted through this transition. This transition is a forbidden one, meaning it has a very low transition probability of

$$A_{10} = 2.85 \cdot 10^{-15}\,\mathrm{s}^{-1}, \tag{2.1}$$

which corresponds to a lifetime of $\tau_{1/2} = 11$ Myr of the state where the spins of the proton and electron are parallel. The derivation of eq. 2.1 can be found in the appendix.

This is the reason why this spontaneous transition is very difficult to produce in a laboratory. Due to the need of comparable densities of one particle per cm^3 to minimize the amount of particle collisions and to compensate for the low transition rate, large volumes are needed to increase the probability to observe such a transition.

In space, these conditions are fulfilled in general and hence observation of the 21 cm line traces the CNM very well.

Line broadening and -dispersion The long lifetime of the higher energy state ($F = 1$) of H I results in a very small natural line width, due to the Heisenberg uncertainty principle $\Delta E \cdot \Delta t \geq \frac{\hbar}{2}$. Hence its line broadening is dominated by Doppler broadening induced by motion of the particles,

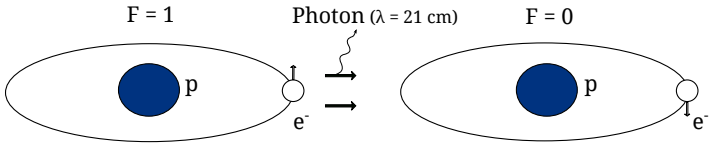

Figure 2.1: Illustration showing the transition from the hyperfine structure state $F = 1$ to $F = 0$ of the hydrogen atom, resulting in the emission of the 21 cm line. For more information see text.

which is a composition of thermal line broadening (thermal Doppler velocity dispersion) and line broadening due to turbulence in the ISM. As both are approximated by Gaussians[1], the term "velocity dispersion", which introduced above, sometimes denotes the standard deviation ($\sigma_{\mathrm{H\,I}}$) or the full width half maximum V_{FWHM} of the maximum value of the Gaussian in the literature. One value can be converted into another by $\Delta V_{\mathrm{FWHM}} = 2\sqrt{2\ln 2} \cdot \sigma_{\mathrm{H\,I}}$. In this thesis if not mentioned explicitly, when the **velocity dispersion** is discussed, the **standard deviation** is meant.

Studies of external edge-on galaxies [2] showed consistent results of $\sigma_{\mathrm{H\,I}} = 69\,\mathrm{km/s}$ dispersion velocities for their outer discs and $\sigma_{\mathrm{H\,I}} = 10 - 15\,\mathrm{km/s}$ for the inner part where active star formation takes place (van der Kruit & Shostak 1984; Dickey et al. 1990; Rownd et al. 1994). Using the Millenium Arecibo 21 cm Absorption-line Survey. The velocity dispersion of the ISM in the Milky Way was determined to be 7.1 km/s for the CNM and 11.4 km/s for the WNM (Heiles & Troland 2003). General trends in the Milky Way were independently investigated using the Leiden Argentine Bonn survey (see section 3.2.3 and table 3.1 therein.) with a lower resulting velocity dispersion of $\sigma_{\mathrm{H\,I}} = 1.3\,\mathrm{km/s}$ for the CNM and $\sigma_{\mathrm{H\,I}} = 10.1\,\mathrm{km/s}$ for the WNM (Haud & Kalberla 2007). In summary, the dispersion of the ISM is different for different regions and hence comes with uncertainties when assuming a general velocity dispersion as will become important in chapter 5 and 6.

Column densities The column density for different atoms or molecules is determined in this work. Since this term is already needed here, the general definition is provided. The integration of all particles of species x across a distance R on the line of sight (LoS) is the **column density**:

$$\mathrm{N_x} = \int_0^R n_x(r)\,\mathrm{d}r, \tag{2.2}$$

where $n_x(r)$ is the number of particles in the line segment $\mathrm{d}r$. $\mathrm{N_x}$ has the units cm^{-2} and for presentation often $\log \mathrm{N_x}$ is chosen because of its high magnitude[3]. H I data measurements are generally often expressed in units of jansky or as is done in this work in K km/s (brightness temperature). In section 3.5, it is explained how to determine the hydrogen column density $\mathrm{N_{H\,I}}$ from H I measurements directly.

[1] More precisely thermal velocity follows the Maxwell distribution but the projection on to the LoS is a gaussian in the first order approximation

[2] Edge-on means that the inclination of the Galactic disk in respect to the line of sight is smaller than 20°, which is needed in order to determine the velocity of the gas correctly (Rownd et al. 1994).

[3] log always denotes the logarithm with base 10 in this work

Ionized Hydrogen

The WNM component of the general ISM is embedded into a layer of WIM with a scale height of $1.83^{+0.12}_{-0.23}$ kpc (Gaensler et al. 2008) and temperatures of 10^4K. The outer layer has extensions up to the Galactic halo and consists of the hot interstellar medium, which has the highest of all temperatures of all components, higher than 10^5 K (York 1974), and a scale height of at least 2.7 kpc (Savage et al. 2000). It is traced by UV observation of strongly ionized oxygen O VI or sodium Na V.

Molecular hydrogen and carbon monoxide

If hydrogen column densities $N_{H\,I}$ reach values of about $4 \cdot 10^{20}$ cm^{-2}, the transition from atomic- to molecular hydrogen (H_2) is possible (e.g. Heithausen et al. (2001)). H_2 can also be found towards lower densities but not in a stable phase (Richter et al. 2003). This is because the binding energy of molecules in general is overcome by cosmic rays and low ionizing radiation fields. Hence, dense and cold clouds ($T \approx 10-20$ K) are needed to form H_2 (Snow & McCall 2006). The general understanding is that this is possible by the recombination of hydrogen atoms on the surface of interstellar dust grains (Hollenbach & Salpeter 1971).

The H_2 molecule has no electric dipole moment in its lowest electronic state and hence a radiation field is needed to detect H_2 directly. If excited by radiation, H_2 can be detected in the UV spectrum (Carruthers 1970) e.g. in the Lyman alpha band where it has been detected first in solar spectra (Jordan et al. 1977; Bartoe et al. 1979).

But for star forming regions, the Carbon Monoxide (^{12}CO) molecule can be used as an indirect tracer for molecular gas (e.g. Scoville & Sanders (1987)). The integrated observed ^{12}CO line emission from the transition of the excited state $J = 1$ to the ground state $J = 0$ can be converted into a molecular hydrogen column density N_{H_2} with the general conversion factor $X_{CO} = 2{\cdot}10^{20}\mathrm{K}^{-1}\,\mathrm{km}^{-1}\,\mathrm{s}$ (Bolatto et al. 2013). The ratio can change significantly for different regions, given different local conditions. There are known regions where H_2 exists but no CO (Shetty et al. 2011; Feldmann et al. 2012) and hence uncertainties that arise using this conversion should to be considered.

2.1.2 Additional relevant components of the interstellar medium

Measurements of sodium absorption lines and extinction due to dust are used in this work to trace the distance of H I clouds of the region around the Scorpius Centaurus OB association (Sco-Cen) region using the kinematics.

Sodium Sodium (Na) belongs to the most abundant elements in the ISM and was used to map the spatial distribution of the local ISM by Welsh et al. (2010). Sodium needs way less ionization energy than hydrogen and hence absorption of stellar radiation of more distant stars in the ISM is possible. The ionization and the following recombination of Na produces the famous Na D-line doublet, which lies in the visible part of the spectrum at 589 nm. The sodium line is in the following referred to as Na I. Similar to the CO to H_2 correlation factor, an observational correlations between $N_{H\,I}$ and the sodium absorption line column density ($N_{Na\,I}$) in the ISM was derived (Hobbs 1974):

$$X_{Na\,I} = 10^{-9}\frac{N_{Na\,I}}{N_{H\,I}} \tag{2.3}$$

This factor varies also for different environments and should be determined for the respective investigated region. Observations of these absorption lines induced by stellar radiation are used to limit the distance towards the cloud by using the known distance to the star as will be explained in more detail in section 4.7.3.

Dust Dust is important for the formation of molecules, like H_2. It radiates in different wavelengths than atomic- or molecular hydrogen since it consists of more complex molecular chains. In general the dust column densities follow the presence of interstellar gas quite well (e.g. Bohlin (1975)) but also here the ratio can also vary for different regions. Extinction maps towards a high number of stars revealed a general ratio of 1/150 (Jenkins & Savage 1974). The origin of Dust is not completely understood yet, but parts are believed to be produced in the cool outer atmosphere of red giants and supergiants (Woolf & Ney 1969). It mainly consists of graphite particles, polycyclic aromatic hydrocarbons and silicates (Gilra 1972; Duley & Williams 1981). Lower abundant types are amorphous carbon and organic refractory material (Tielens & Allamandola 1987). Dusts thermal emission is observable in the infrared (IR) coming from amorphous silicates (9.7 μm and 18 μm (Knacke & Thomson 1973) and polycyclic aromatic hydrocarbons (3.3 μm–11.3 μm (Duley & Williams 1981)). The UV radiation of dust is produced by graphite particles.

Stellar extinction is observed if the stellar radiation penetrates dust clouds (Trumpler 1930). Since stars have an intrinsic color index that is reddened by extinction through dust, the difference between the color index and the intrinsic one can be measured and is called "color excess" (e.g. Schultz & Wiemer (1975)). The more stars and the more details about its parameters are known, the more accurate the distance can be measured towards ISM clouds. The method will be described in section 4.7). In this thesis, three dimensional maps of the ISM by (Green et al. 2015) and (Lallement et al. 2014) are used as additional distance indicators for the H I clouds in the local ISM near Sco-Cen.

Properties and structures of the local ISM are introduced in the following.

2.2 The local interstellar medium

In the following, the distribution of the local ISM is presented and relevant ISM structures for the analyses of this work are introduced.

2.2.1 Mappings of the local interstellar medium

One method that reveals the distribution of the local ISM are studies of interstellar (IS) lines, e.g. (Frisch 1995). The local ISM was mapped using the above introduced Na I, H I and Ca II lines (Sfeir et al. 1999; Vergely et al. 2001; Lallement et al. 2003; Welsh et al. 2010), extinction due to dust (Lallement et al. 2014) and reddening (Green et al. 2015) as described in the following. Even newer maps are available Lallement et al. (2022) but have been published after the analyses of this thesis have already been completed. This is also the case for latest mappings of star, dust and gas in the solar neighborhood due to the latest GAIA releases (Gaia Collaboration et al. 2018; Zucker et al. 2021, 2022).

Measurements of the ISM in the solar neighborhood revealed that the Sun is embedded in a region of low density, a cavity called local cavity or the term that is also used in this work, Local Bubble (LB), which is delimited by interstellar clouds to other neighboring bubbles (Cox & Reynolds 1987). Lately the three dimensional structure of the local hot bubble, which is the portion of the LB filled with hot gas (e.g. Cox & Snowden (1986)), was revealed by cleaned X-ray maps of the ROSAT (abbreviation for Röntgensatellit) R12 band (Liu et al. 2016). The LB is likely to be formed by multiple supernovae (SNe) but the estimated number of SNe differs, depending on the assumed scenario (Maíz-Apellániz 2001; Berghöfer & Breitschwerdt 2002) and it is still debated to which stellar cluster the SNe actually belong. Maíz-Apellániz (2001a) even concludes as one possible scenario that the LB is partly the result of SNe that have gone off in the Scorpius Centaurus OB association itself, about 10 Myrs ago and that the association was closer to the Sun, back then.

Absorption line maps

The three dimensional distribution of the neutral and partly ionized ISM was mapped using over 50,000 Na I doublet (482 nearby sight-lines) and Ca II (807 nearby sight lines) interstellar lines within 300 pc from the Sun (Welsh et al. 2010). Using an inversion method (Vergely et al. 2001) as well as the equations 4.39 and 4.40, individual maps for both interstellar lines were derived. Representatively a Galactic plane cut of the resulting map that was extracted from the paper of Welsh et al. (2010) is shown in figure 2.2. The corresponding figure B.0.1 for Ca II can be found in the appendix. These maps reveal a three dimensional picture of the local ISM but since the number of stars that can be used for this method is limited, other methods which use information from much more stars were devised and raised the accuracy on the three dimensional distribution as described in the following sections. But nevertheless the absorption line data for individual line of sights from Welsh et al. (2010) are used directly in this work to fit the sodium lines to the H I spectra for the analysis of the ISM near Sco-Cen in chapter 6.

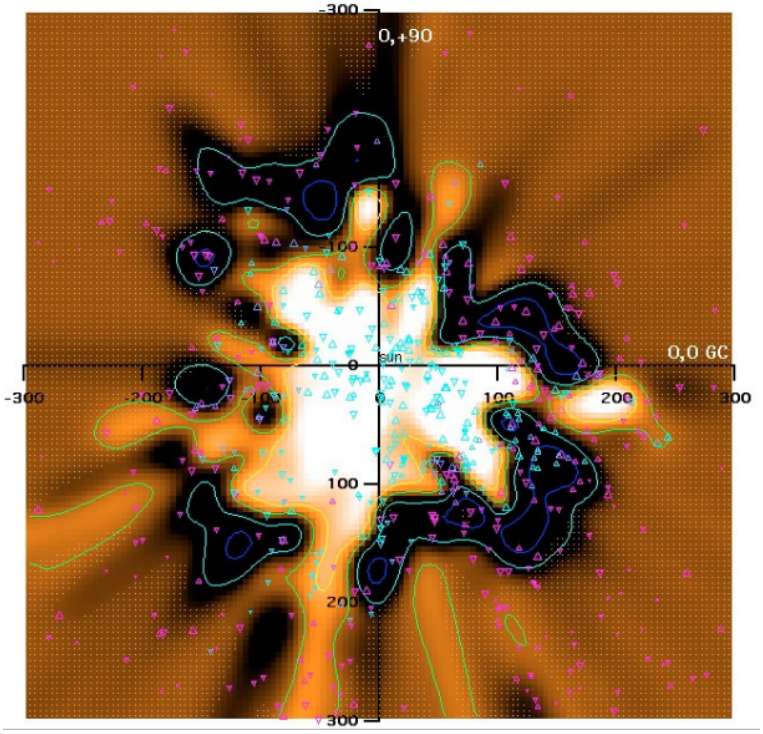

Figure 2.2: Galactic plane view of the ISM revealed by the interstellar Na I absorption (Figure from Welsh et al. (2010)). The position of the Sun is at 0,0 and the ISM is traced to distances of 300 pc.

Three dimensional interstellar reddening maps

If stellar radiation penetrates the ISM, dust grains therein absorb or scatter radiation of wavelength in the blue.. The extinction measured in the V-band is the difference in magnitude of stellar light and is connected to the reddening by $A_v = 3.2 \cdot E(B-V)$, where $E(B-V)$ is the degree of reddening, e.g. (Gottlieb & Upson 1969). Similar to the technique for the interstellar absorption, the distance of the star serves as an estimate for the distance to the ISM (see section 4.7.3). The success of this technique is based on the number of stellar colors and distances available. The large data bases from the Panoramic Survey Telescope And Rapid Response System (Pan-STARRS 1, Chambers et al. (2016), Flewelling et al. (2016)[4]) and the Two Micron All Sky Survey (2MASS, Skrutskie et al. (2006)) of more than 800 million stars were used to create 3D maps of interstellar reddening due to dust for three-quarters of the sky up to distances of 2 kpc (Green et al. 2015). For the line of sight (LoS) towards each star a probabilistically inferred distance and reddening is available within individual distance bins. The distances are binned into equally spaced distance moduli μ_i, using

$$\mu_i = 5 \log d_i \tag{2.4}$$

where d_i is the distance to the star in units of 10 pc (Schlafly et al. 2014). These data were published and are used in this work in section 6.2.4 for the distance analysis of the H I structures.

[4] The data used by Green et al. (2015) were from an earlier data release

Color excess maps

The compilation of multiple individual distance-limited ISM measurements to three dimensional maps by using the inversion method was also applied to measurements of stellar color excess in the optical (Lallement et al. 2014). Together with the parallax and photometric distances 23,000 sight lines towards stars within 2.5 kpc were used resulting in a 3D dust distribution in the vicinity of the Sun. In the resulting color–excess maps, the extinction is color coded and the highest extinction (purple) represents the highest density regions while the lowest extinction (red) denotes a low density regions and in some cases cavities. The size of spatial fluctuations than can be resolved depends on the smoothing kernel. For the chosen kernel in the studies of Lallement et al. (2014), the resolution is about 10 pc close to the Sun and ≈ 100 pc beyond 1 kpc. Since no other information on the accuracy were provided in the paper, it is assumed here that increase is linear between those two distance values.

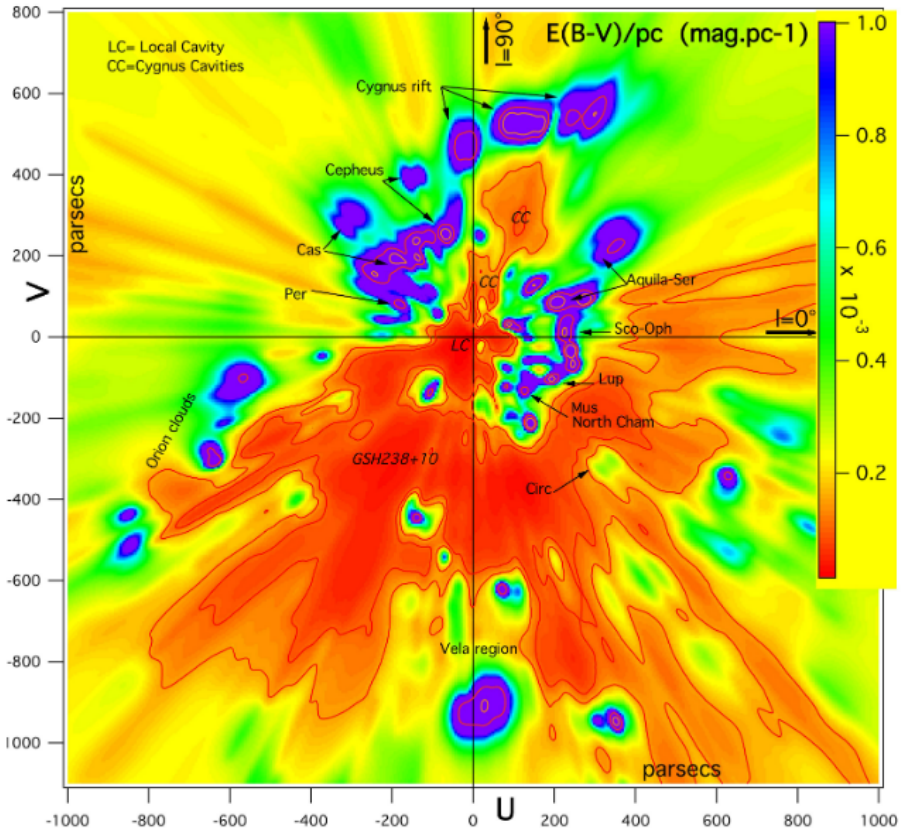

Figure 2.3: Map of the local ISM in the Galactic plane view from Lallement et al. (2014) showing the inverted differential opacity distribution of dust. The Sun is located in the center, while the Galactic center is in the direction of $l = 0^{\circ}$. The color highlights the opacity, increasing from red to violet. Individual regions that were identified by the author are labelled like the Local Bubble (LC in the plot) and parts of Sco-Cen (Sco-Oph)

Representatively, the Galactic plane view of slices of the resulting 3D-maps is shown in figure 2.3, adopted from Lallement et al. (2014)[5]. This map reveals the local cavity spreading over 80-100 pc

[5] The other maps that are used later on to determine the distance to the center of the clumps and voids are also appended and shown in figure B.0.6, B.0.35 and B.0.36.

in the direction of the Galactic center. The highest density clouds and star forming regions, which have the highest opacities can be clearly identified as high opacity regions (violet clumps). In the direction of Sco-Cen (mainly $l = 290^\circ$–360° at about 150 pc distance from the Sun), many regions of low extinction surrounded by clumps can be seen. The cavities can be even better seen in the vertical plane slices e.g. in fig. B.0.6 in appendix B. If these clumps belong to shells identified in H I is part of the analysis of chapter 6.

2.2.2 Relevant structures in the local interstellar medium

In the following it is focussed on the local structures of the ISM like spiral arm segments but also features in the direction of the Scorpius Centaurus OB association.

The Gould Belt The Gould Belt is a ring of H I, inclined compared to the Galactic plane (Lindblad 1967) that contains multiple regions of recent- and ongoing star formation and is still a topic of many investigations (e.g. Lesh (1968), Pöppel (2001), Palouš & Ehlerová (2014), Bobylev (2014), Bobylev (2016), Ortiz-León et al. (2017)). The origin of this ring is investigated intensively. One proposed scenario is that it is a remnant of the impact of a giant molecular cloud that hit the gas in the Galactic disk (e.g. Poppel et al. (1996)). Recent studies suggest that the Glould Belt belongs to a 2.7 kpc-long coherent, thin wave consisting of chains of clouds Alves et al. (2020) and that the perturbation might be caused e.g. by a passage of a Dwarf galaxy (Li & Chen 2022). The very high rate of SN events of 20–27 events per million years during the last couple of millions years is much higher than the average local SN-rate of the Milky Way (Grenier 2000) and might also have its origin in the ring. Comeron & Torra (1994) stated that about 40-50% of the young and massive stars within 450 pc distance of the Sun belong to the Gould Belt and it was suggested that the Sco-Cen Association is also part of it (e.g. Perrot & Grenier (2003),Poeppel et al. (2010)). The relation of the gas of Sco-Cen to the Gould Belt is not discussed further in this thesis as it is not important for the determination of the parameters of the H I shells of Sco-Cen itself.

The North Polar Spur The North Polar Spur is a structure with extensions up to the Galactic north pole in projection and covers almost one Galactic quadrant, see e.g. fig. 3.7 in chapter 3.3 that shows an all-sky image in H I. It was previously proposed to have a distance of 100±20 pc (Bingham 1967) that fits the distance of loop I. Its size and high latitude suggests that the North Polar Spur belongs to a very local event and hence may be connected to a supernova remnant from (Davelaar et al. 1980). But more recently analyses of soft X-ray data at 0.89 keV from the Roenthgen Satellit (ROSAT) archive suggest that the feature is much further away than previously thought, has a distance of 1.01±0.25 kpc and is suggested to be a halo object (Sofue 2015). Also, a combination of X-ray data and dust extinction ruled out a distance closer than 300 pc for the North Polar Spur (Lallement et al. 2016). The results of the recent allsky survey in X-ray using the **e**xtended **RO**entgen **S**urvey with an **I**maging **T**elescope **A**rray (eROSITA), suggest that the North Polar Spur belongs to an outflow on Galactic scales of two super bubbles emerging in the center of the Galaxy perpendicular to the Galactic plane, with each of them having radii up to but 7 kpc Predehl et al. (2020).

Loop I The Loop I feature is a radio loop with a radius of $(58\pm4)^\circ$, centered at $l = (329 \pm 1)^\circ$ and $b = (17.5 \pm 3)^\circ$ (Berkhuijsen et al. 1971) and was previously assumed to be part of the North Polar

Spur because of its similar centers and the previously assumed closeness of the North Polar Spur to the Sun (D = 100±20 pc (Bingham 1967)) that was later refined. The newer distance results suggest that loop I does not belong to the North Polar Spur. Numerous investigations mapped the interface between the LB and the Loop I bubble in multiple wavelengths (Egger & Aschenbach 1995; Reis & Corradi 2008; Sallmen et al. 2008; Wolleben 2007; Reis et al. 2011; Santos et al. 2011). In the ROSAT All Sky Survey, a soft X-ray shadow has been discovered on the periphery of the loop I supershell being surrounded by dense H I gas that interacts with the LB at a distance of 70 pc and is observed in H I due to the rise in column density from 10^{20} to $7 \cdot 10^{20}$ cm^{-2} at this distance (Egger & Aschenbach 1995). Other authors aimed to reproduce the detected ring, using photometric data (Reis & Corradi 2008). The results showed that if the structure forms a ring it would be very fragmented and that the western part would have a distance of $D = 110 \pm 20$ pc, while the eastern part would be more far away, with $D = 280 \pm 50$ pc (Reis & Corradi 2008; Santos et al. 2011). The interaction zone was also investigated using the Far Ultraviolet Spectroscopic Explorer (FUSE) satellite to observe O VI emission Sallmen et al. (2008) and the results were consistent with the H I column densities. Models of loop I suggest that it consists of two shells, one with the center at the Galactic plane and another one at the same distance but at higher latitudes (Wolleben 2007; Reis et al. 2011). For this thesis the eastern part of the loop is of relevance since it is proposed to lie at a distance of 70-110 pc in the literature and could potentially be connected to the largest shells of Sco-Cen.

The Serpens-Aquila Rift The Serpens-Aquila rift (Aquila Rift) is a region of dark molecular clouds, covering several degrees on the sky (Loinard 2013). Different distances of 250 to 650 pc have been suggested for this molecular cloud complex (Eiroa et al. 2008; Dzib et al. 2010) where the widely accepted distance is the one of Straižys et al. (1996) that is (259±35) pc. The angular extent ranges from $l = 16^\circ$–40° to $b = 01^\circ$–20° and it is oriented from the south-west to the north-east compared to the direction of the Galactic plane in the Galactic coordinate system with the point of view in the location of the Sun (Dame et al. 1987, 2001). This complex is present in velocity channels from +5–+10 km/s and hence is considered to be an external source, overlapping with the kinematics and positions of the Upper Scorpius subgroup of Sco-Cen (see introduction below in sec. 2.5).

The Gum Nebula The Gum nebula was initially discovered in Hα photographs of the southern Milky Way (Gum 1951). Within the boundary of the GUM nebula lies the Vela shell that is a SNR of the same name nearby stellar group (Sushch et al. 2011). The distance estimates of the Vela shell suffer from high uncertainties and it is approximately 250 pc (Cha et al. 1999) to 350 pc (Dubner et al. 1998) away from the Sun. The Gum nebula is described as a 36° diameter sphere centered at $l = 258^\circ$, $b = -2^\circ$ (Chanot & Sivan 1983) with distance estimations from 300–800 pc from Hα (Reynoso & Dubner (1997) and references therein). The H I counterpart has a distance of 500 ± 300 pc and is visible at velocities between -5 km/s to +20 km/s with an expansion velocity of 6–8 km/s (Dubner et al. 1992; Woermann et al. 2001).

Ophiuchus The Ophiuchus molecular cloud complex (MCC) consists of multiple dark molecular clouds in the direction $l = (50 - 370)^\circ$ and $b = (6 - 24)^\circ$ at velocities of -1 km/s to +6 km/s with a velocity dispersion in the region of 3.4 km/s (de Geus et al. 1990). Ophiuchus has a mean distance of 125 ± 25 pc, a near site of 80 ± 20 pc and a far site of 170 ± 35 pc (de Geus et al. 1989). The USco

stellar group and the Ophiuchus MCC either penetrate each other or the Ophiuchus complex might even be part of the Upper Scorpius stellar subgroup of Sco-Cen.

Lupus I Similar to the Ophiuchus MCC, the Lupus I MCC is located near the stellar group Upper Scorpius at Galactic coordinates $l = (335 - 350)^\circ$ and $b = +5^\circ$ to $+25^\circ$ and velocities -4.5 to +10 km/s (de Geus & Burton 1991). It is located at the edge of the UScо-loop and might be produced by a collision of the loop and some gas of the UCL stellar group (Gaczkowski et al. 2015).

Local segments of Galactic spiral arms The Milky Way has spiral arm structures where most star formation takes place (e.g. Elmegreen (2011)). The spiral arm pattern is logarithmic (Seigar & James 1998) and each arm has a certain pitch angle (Davis et al. 2012). A schematic visualization of the spiral arms, in an on-plane view of the Galactic disk, can be found e.g. in figure 5.8. The mean width of a spiral arm is roughly 0.25 kpc (Hou & Han 2014), varying between different locations on the respective arm and between different arms. The nearest such structure in the direction of the Galactic center is the Sagittarius Arm with a distance of $0.6 - 1.2$ kpc (Hou & Han 2014). The Sun itself is placed at the inner edge of the Orion Arm. Distances towards the densest regions of the arm are 0.6-1.2 kpc in the anti center direction. Towards the same direction, the Perseus Arm in the longitude range $l = 180 - 270^\circ$ is in the mean 2 kpc (Xu et al. 2006) away with ranges of 1.5-2.2 kpc (Griv et al. 2017). More distant, is a segment of the outer Arm in this direction with a distance of 6 kpc (Hachisuka et al. 2009).

2.3 Evolution of massive stars and supernova remnants

All stars eject mass, momentum and energy into the ISM. But the feedback of the most massive stars of stellar clusters have the dominating impact on the ambient ISM and hence on the formation of shells and supershells. This is why in the following section 2.3.1, the focus lies on the evolution of massive stars ($M \leq 8\,\mathrm{M}_\odot$). The theoretical evolution of supernova remnants induced by single stars is covered in section 2.3.2.

2.3.1 Evolution of massive stars

Star formation and young stellar objects

When the ISM reaches low temperatures, i.e. if the column density reaches values of about $4 \cdot 10^{20}\,\mathrm{cm}^{-2}$ (Heithausen et al. 2001)) molecular hydrogen and hence molecular clouds can be formed (section 2.1.1). During the last decades, progress in understanding the formation of stars out of molecular clouds led to at least four different theories for star formation. These are the competitive accretion scenario (Bonnell et al. 1998, 2004), the single core collapse model (Krumholz & McKee 2008), the collisional mergers (Moeckel & Clarke 2011) and the fragmentation-induced starvation model (Peters et al. 2011) for star formation. Star formation can also be triggered by stellar feedback or cloud collisions and is amongst others observed at the edges of H I shells (e.g. Gaczkowski et al. (2015)). This means that regions on H I shells of low H I density might still contain high molecular density and hence is a source of uncertainties for the calculation of the mass of the shell using H I data only. The mass is a parameter needed to calculate the kinetic energy, which is an estimate for the total energy input by stars (see section 2.4). While dense molecular clouds can be generally traced by CO (see section 2.1.1), clouds containing protostars or young stellar objects can be observed in the infrared because of the ionization of the gas by the strong UV radiation of O- and B–stars.

The lifetime of stars on the main sequence

The higher the initial stellar mass, the stronger its radiation. This is induced by the empirically determined mass-luminosity relation (Kippenhahn & Weigert 1990):

$$L \propto M^{\eta} \tag{2.5}$$

where L is the luminosity and M is the mass with the average value of $\eta = 3.88$ for stellar masses between 1–10 $\mathrm{M}_\odot$. This is because the more massive a star, the faster it consumes its fuel resulting in a shorter lifetime. The relation flattens for higher mass ranges because the ratio between radiation- and gravitation pressure is higher and for stellar masses between $10\,\mathrm{M}_\odot \leq M \leq 50\,\mathrm{M}_\odot$, η is 2.76 (Vitrichenko et al. 2007) leading to an overall mean value for the range 1–40 $\mathrm{M}_\odot$ of $\eta = 3.35$.

This relation holds for zero age main sequence stars, which is the longest stage of its evolution and the lifetime can be determined from it as follows. The main sequence lifetime τ_H of a star in the Hertzsprung-Russell diagram, where the star is in the hydrogen burning phase, depends on the luminosity L and the energy reservoir E_H that is available for hydrogen burning. The approximation,

$E_{\mathrm{H}}/10^7$ yrs is about equal to the hydrogen mass a star contains, together with equation 2.5 yields

$$\tau_H(M) \approx 10^{10}\,\mathrm{yrs} \cdot \frac{M}{L} = 10^{10}\,\mathrm{yrs} \cdot M^{\gamma} \tag{2.6}$$

with γ being equal to $1-\eta$ (Kippenhahn & Weigert 1990). Following this equation, a star of one solar mass has a lifetime on the main sequence of approximately 10 Gyr and a star of 8 $\mathrm{M}_\odot$ and 50 $\mathrm{M}_\odot$ would just have one of 25 Myr and 10 Myr respectively. In table A.0.1 in the appendix, this calculation is presented for stellar masses in the range of 1–85 $\mathrm{M}_\odot$ and is used later in chapter 6 for analyses. The results show that the lifetime of the most massive stars of a star cluster can be as low as several Myrs, which is short compared to the evolution time of the stellar cluster. Since the most massive stars have the highest impact on the surrounding ISM, this means that most of the feedback is provided during that time frame. After the hydrogen burning phase, massive stars experience high mass losses as discussed in the following.

Mass loss of massive stars

It is important to discuss the mass loss rate of massive stars since the emerging stellar winds are the main drivers to shape shells out of the surrounding ISM besides the supernova event taking place at the end of the lifetime of a massive star. The winds that create shells are from O and B stars and are driven by radiation pressure on the resonance absorption lines of heavy elements such as carbon and nitrogen (Castor et al. 1975). The winds result in mass loss rates for massive O stars, up to masses of $M \leq 60\,\mathrm{M}_\odot$, of about 10^{-7}–10^{-5} $\mathrm{M}_\odot$/yr (De Loore et al. 1977). The wind velocities reach values of 1000–2000 km/s. The post-main sequence stars of masses between 0.1–10 $M_\odot$ have mass loss rate of about $3 \cdot 10^{-7}$ $\mathrm{M}_\odot$/yr and its wind velocity is 10 km/s for giants, supergiants and active giant branch stars (Knapp et al. 1998). These winds are driven by radiation pressure from the stars, e.g. on dust condensing in the upper atmosphere of the stars and generally on the atoms and molecules of the surrounding ISM (Mattsson & Höfner 2011; Lamers & Cassinelli 1999). Stars with a higher initial mass ($25\,M_\odot \leq M \leq 80\,M_\odot$) evolve into a Wolf-Rayet (WR) phase. They spend about 10% out of their approximately 5 Myr lifetime in this phase and produce wind velocities comparable to O-stars during the main sequence lifetime ranging from 1000 –2500 km/s (Puls et al. 2008) and mass loss rates from $10^{-5.5}$–10^{-4} $M_\odot$/yr depending on the individual mass and metallicity Crowther (2007). Star formation generally takes place in clusters, meaning massive stars are often close to each other. Additionally, the fraction of binaries for massive stars is 45% to 75% (Mason et al. 2009; Langer 2012), this means that massive stars can influence each other's evolution, which can lead to different final evolution stages (Cappellaro & Turatto 2001). These are not included into relations like eq. 2.6 and lead to uncertainties that are difficult to account for.

Last evolutionary stages of massive stars

At the end of their life, massive stars explode in a supernova (SN), where massive amounts of energy and momentum are released in a short amount of time. Observationally, SNe are divided into two main types. The first one are type II SNe, which show hydrogen lines in their spectra and are divided into multiple subtypes[6]. The other one are type I SNe that are divided into at least three subgroups

[6] Type II SNe are divided into two main types depending on the form of the light curve when the luminosity is plotted against time. In general the decay rate of the luminosity curve of type II SNe is much lower than the one of type I.

namely type I-a, type I-b and type I-c (Cappellaro & Turatto 2001; Turatto 2003)[7]. The spectra of these SNe show no sign of hydrogen. Type I-a SNe stem from thermonuclear SNe and its progenitors are white Dwarf stars in binary systems. The other ones are core collapse SNe. The progenitors of type I-b- and type I-c SNe are Wolf-Rayet stars[8], while the type II SNe stem from supergiants (Smartt 2009; Eldridge et al. 2013) of stars with initial masses of 8–50 $M_\odot$ (Gilmore 2004).

For this work, the most relevant quantity is the energy output of SNe. While the main energy is contained in the expelled neutrinos, they do not contribute to the formation of bubbles and shells because they don't interact with the ISM. But also kinetic energies of shells with magnitudes of over 10^{51} ergs (1 erg = 10^{-7} J) are produced depending on the progenitor/SN type. The focus here is on core collapse SNe that produce kinetic energies in the magnitude of 10^{51} ergs (e.g. (Janka 2012))[9]. Pair instability SNe can produce kinetic energies of $(1-100)\cdot 10^{51}$ergs and are only observed in galaxies with high star formation rates (SFR), since the progenitor stars are believed to have masses of 100–150 $M_\odot$ (Kasen et al. 2011). But in general, the approximation that one supernova produces output energies of 10^{51} ergs is used for theoretical and statistical studies and widely accepted in the literature (e.g. de Geus (1992), Poeppel et al. (2010), Ehlerová & Palouš (2013)).

2.3.2 Theoretical evolution of single supernova remnants

In the following the long term evolution of supernova remnants (SNR) is described. Since it is focused on the analysis of colder gas, the very early stages of a supernova remnant, where the visible light curve reaches its peak and the evolution is visible in units of days, are not described here. The later stages of SNR-evolution are more important here, where the surrounding gas has cooled down and is mainly driven by momentum pressure (Reynolds 2008). The different evolutionary phases are schematically presented in the following and can be seen in figure 2.4 that is an adoption of Parmanabhan (2001).

The free expansion phase Approximately in the first 200 yrs after the explosion, the SN-ejecta expand freely, behaving like a blast wave with $r \propto t$. When the ejected mass $M_{\rm ej}$ equals the swept up mass $M_{\rm sw}$, the radius r_f of the freely expanding blast wave is $r_f \propto M_{\rm ej}^{1/3} n_0$ (Parmanabhan 2001), where n_0 is the initial density of the ISM around the SNR. The free expansion time is then $t_f \simeq \frac{r_f}{v_{\rm ej}}$, which can also be expressed in terms of energy input by the supernova E_{51} as $t_f \propto M_{\rm ej} E_{51}^{5/6} n_0^{-1/3}$. The surrounding ISM has no effect on the expansion of the shock wave in this stage. The blast wave sweeps up ambient ISM and creates a bubble of high density compared to the initial ISM, which leads to the end of the free expansion phase. After that a reverse shock travels inwards and the remaining ISM in the bubble is heated leading to the Sedov-Taylor phase.

Type II-L SNe show a linear decline after the the peak luminosity, while type II-P has a plateau phase after the maximum luminosity is reached. There are also type II-n SNe and type II-b, where the former one contains narrow hydrogen lines in their spectrum and the latter ones contain weak hydrogen lines in their initial spectrum but almost no hydrogen line presence as it evolves.

[7] There are more subdivisions of type I SNe but the distinction is not important for this work

[8] There are WN-type stars that show helium emission lines and ionized nitrogen lines and WC-type stars that show oxygen emission lines and lines of ionized carbonate.

[9] Type I-a SNe eject also kinetic energies of $(1.3-1.4)\cdot 10^{51}$ ergs (Iwamoto & Kunugise 2006) but are not likely to be the progenitor processes of the shells investigated in this work.

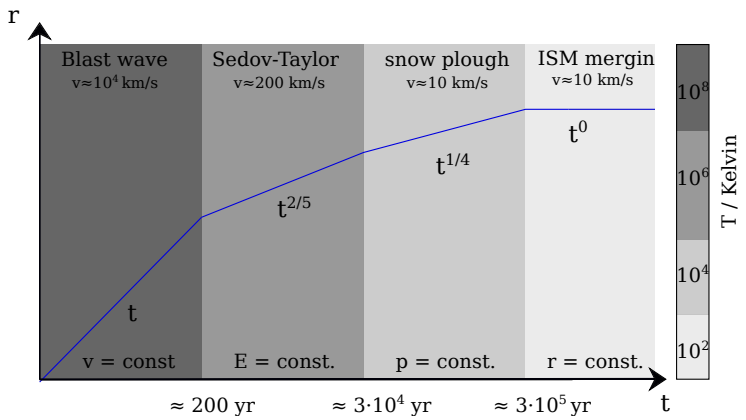

Figure 2.4: Illustration of the analytical model of the evolution of a SNR in terms of expansion velocity (v), temperature T, time t and the radius r. Figure made along the lines of figure 4.6 of Parmanabhan (2001)

The Sedov-Taylor phase The ISM inside the bubble is heated and the atoms are ionized, which keeps the energy losses by radiation low, i.e. in approximation E = constant. In this adiabatic phase, the gas is cooled during its expansion. The radius scales with time, energy input and density like $r \propto t^{2/5} E_{51}^{1/5} n_0^{-1/5}$ (Parmanabhan 2001). The temperature at the end of this phase is 10^6 K at timescales of 10^4 yrs and the expansion velocity has decreased to about 200 km/s (Taylor 1950a,b; Sedov 1958) [10]. At the end of this phase, the SNR has a temperature of roughly $3{\cdot}10^6$ K and radiates strongly in x-rays. This phase ends when the energy loss due to radiative cooling becomes significant, which leads to the snow plough phase.

The snow plough phase When the energy loss leads to temperatures lower than 10^6 K, ions can capture free electrons and lose energy by photo radiation. The shell of the SNR is in the cooling phase, the deceleration first takes place at the outer edge of the shell. From the inside hot thin gas pressures the colder thick gas of the layer, letting the shell expand further but can also lead to Rayleigh-Taylor or Vishniac instabilities, which are described below in the sections 2.4.2. The material is swept up in analogy to a snow plough, and the shell can be observed by the 21 cm line of H I in the later stage of this phase. After approximately 10^5 yrs, the expansion velocity drops down to 100–10 km/s and the temperature of the shell has cooled down to orders of magnitude of 10^2 K at the end of this phase.

Break up and clumping After roughly 0.5 Myr the expansion decreases down to about 10 km/s. The interior pressure slowly vanishes and the shell is beginning to decay into clumps and then merges with the ISM (Sutherland et al. 2003).

[10] This phase of the evolution of SNRs is named after Taylor (1950a), Taylor (1950b) who found the "similarity solution" for flows after the explosion the nuclear bombs in 1945 in the second world war were released and Sedov (1958) who amongst others independently discovered this solution

The last two phases are the most important ones for this thesis, since most H I observations will most likely trace shells in the snow plough phase or in the Break up phase. Hence the relations of shells in these phases are covered in more detail in the following sections. The above explained theoretical stages are an oversimplification and distinct phases may be short, may not occur at all, or may occur simultaneously in different regions of the same SNR (Dubner & Giacani 2015).

Radio continuum emission In SNRs electrons are accelerated by different processes, e.g. due to diffusive shocks, where electrons gain energies by multiple crossings through the shock wave (Bell 1978a,b; Blandford & Ostriker 1978). The accelerated electrons emit synchrotron radiation (Moffet 1975), and the superposition of the spectra of all electrons in a pitch angle, can be observed as non thermal radio continuum emission (e.g. Dubner & Giacani (2015)). Catalogs of SNR observed in radio continuum have been produced (Green & Gull 1984; Green 1988, 1991; Stephenson & Green 2002; Green 2004a, 2009, 2014) resulting in the here used update Green (2019). There are various types of radio continuum SNRs in the catalog of Green (2019). The relevant types for this work are ones, where H I shells have already formed (shell-type) and where the synchrotron radiation happens in shock fronts. At the later stages, like the snow-plough phase, when the acceleration slows down and the temperature decreases, the shell is larger and the magnetic field is weaker, it can mainly be observed in H I. This is why most of the shells analyzed here do not have a counterpart in radio continuum surveys.

Relation for the Energy of a single SNR

If a massive star explodes in a SN, if spherical symmetry is assumed, it produces a shell with the energy $E_c(t)$:

$$E_c(t) = 5.3 \cdot 10^{43} n_0^{1.12} \cdot r_s^{3.12} \cdot v_{exp}^{1.4} \tag{2.7}$$

where n_0 is the initial density of the ambient ISM of the star, r_s is the radius of the shell and v_{exp} is its expansion velocity (Chevalier 1974). $E_c(t)$ is expressed in units of ergs. Chevalier (1974) used the relation $R \propto t^{0.31}$ and $v \propto t^{-0.69}$ to derive a time independent solution.

This equation is used in section 5.4 to determine the total energy input of the catalog shells. In reality many shells are driven by multiple winds and SNe, which can lead to older and larger shells than what can be explained by single SNR models. This leads to new relations, which is the topic of the next section.

2.4 OB associations and supershells

Stars are usually not formed in isolation but in groups or clusters (e.g. Lada & Lada (2003)). The mass distribution in clusters follows the initial mass function (IMF) (Salpeter 1955; Scalo 1986a,b; Kroupa 2002). In massive clusters of ages of magnitudes of 10^1Myr, the most massive stars have already exploded and the stellar distribution follows the present day mass function (PDMF). From the PDMF again, the IMF can be calculated if the age of the star cluster is known.

The initial mass function The **I**nitial **m**ass **f**unction (IMF) describes the distribution of stellar masses that form together. The IMF was first introduced by Salpeter Salpeter (1955) as a power law with the form:

$$\xi_{\mathrm{S}} = k \cdot m^{-\alpha} \ , \quad \alpha = 2.35 \ , \quad 0.4\,M_{\odot} \leq m \leq 10\,M_{\odot} \tag{2.8}$$

where k is a scaling factor. After further investigations, the canonical IMF was introduced (Kroupa et al. 1993), describing the distribution of stellar masses from 0.08 to 150 $M_{\odot}$ in a two part power law. It also contributes a separate third part with a power-law for brown dwarfs with mass ranges of 0.01-0.08 $M_{\odot}$. The parameters of the canonical IMF are:

$$\xi_{\star}(m) = k \cdot m^{-\alpha} \tag{2.9}$$

with the normalization constant k and

$$\alpha = \begin{cases} 1.3 \ , \ 0.08\,M_{\odot} < m \leq 0.5\,M_{\odot} \\ 2.3 \ , \ 0.5\,M_{\odot} < m \leq 150\,M_{\odot}. \end{cases} \tag{2.10}$$

Using the fact that stars are born in clusters and assuming each cluster has its own initial mass function with an m_{max}-to-M_{ecl} relation, the integrated Galactic initial mass function (IGIMF) is defined as (Kroupa & Weidner 2003; Weidner & Kroupa 2005a,b)

$$\xi_{\mathrm{IGIMF}}(m;t) = \int_{M_{\mathrm{ecl,min}}}^{M_{\mathrm{ecl,max}}(\mathrm{SFR}(t))} \xi(m \leq m_{\mathrm{max}}(M_{\mathrm{ecl}}))\xi_{\mathrm{ecl}}(M_{\mathrm{ecl}})\,\mathrm{d}M_{\mathrm{ecl}}. \tag{2.11}$$

This means the IGIMF is an integral over all star formation events between t and $t + \delta t$. The normalization conditions for this equation are

$$M_{\mathrm{ecl}} - m_{\mathrm{max}}(M_{\mathrm{ecl}}) = \int_{m_{\mathrm{max}}(0.07\,M_{\odot})}^{m_{\mathrm{max}}(M_{\mathrm{ecl}})} \xi(m')\,\mathrm{d}m' \tag{2.12}$$

and

$$1 = \int_{m_{\mathrm{max}}(M_{\mathrm{ecl}})}^{m_{\mathrm{max}}} \xi(m')\,\mathrm{d}m' \tag{2.13}$$

with the cluster mass M_{ecl} and the stellar IMF, contributed by ξ_{ecl}, collective star formation events with stellar masses in the interval $\left[M_{\mathrm{ecl}}, M_{\mathrm{ecl}} + \mathrm{d}M_{\mathrm{ecl}}\right]$ are given by $\xi(m \leq m_{\mathrm{max}}(M_{\mathrm{ecl}}))\,\xi(M_{\mathrm{ecl}})\,\mathrm{d}M_{\mathrm{ecl}}$.

2.4.1 Interaction of OB associations with the interstellar medium

Single stars and SNe produce shells and turbulence in the ISM. But collective winds and following supernovae of multiple stars in OB associations, which usually contains a few but sometimes up to thousands of massive stars (McCray & Kafatos 1987) form super-bubbles, or hereafter called super-shells that have radii up to kpc scale (Rand & Stone 1996; de Blok & Walter 2000; Tenorio-Tagle et al. 2003). They influence the ISM on Galactic scale, leading to the observable turbulent ISM because of the continuous shaping by wind and SNe (Breitschwerdt et al. 2012). While the interior of the shells contains hot gas ($T \approx 10^6$ K) observable in the X-rays (Silich et al. 2005), the surrounding swept up gas is cold and observed in H I (see also sec. 2.3.2).

In the first few million years, the ISM of a star forming region is shaped by the winds of the most massive stars with masses $M \geq 8\,M_\odot$ and after a few Myr, depending on the mass of the most massive stars, the first SNe go off (Massey 1999). The shell is then driven by these energetic events increasing the radius further (McCray & Kafatos 1987). The descriptions of the total energy output E_s as well as the radius of the shell R_s and its expansion velocity V_s for young associations are combinations of the wind energies $L_{38,sw}$ and supernova energies $L_{38,sn}$ constituted by the following equations (de Geus 1992). For a young association or shell where just the winds contribute to the bubble, the equations for the shell radius R_s, the expansion velocity V_s and the kinetic energy of the shell E_s are:

$$R_{s,theo} = 269\,\mathrm{pc}\,\left[L_{38}/n_0\right]^{1/5}\,t_7^{3/5} \tag{2.14}$$

$$V_{s,theo} = 15.8\,\mathrm{km/s}\,\left[L_{38}/n_0\right]^{1/5}\,t_7^{-2/5} \tag{2.15}$$

$$E_{s,theo} = 3.8\cdot 10^8\,(\mathrm{km/s})^2 L_{38}\,t_7 \tag{2.16}$$

with L_{38} being the total wind flux in 10^{38} ergs and t_7 being the age of the association in units of 10^7yrs. For older associations where almost all massive stars have ejected their energy, L_{38} is replaced by $L_{38,sw} + L_{38,sn}$ in these equations (McCray & Kafatos 1987; de Geus 1992). Here $L_{38,sn} = f\,N_{sn}E_{51}\,t_{gr}^{-1}$ where N_{sn} is the number of supernova events, t_{gr} is the age of the stellar group and f is the fraction of the SN energy that is contributed to the kinetic energy of the shell with a value of $f = 0.2$ (Weaver et al. 1977) used here.

These analytical models assume spherical expansion and a homogeneous ambient ISM. Below the consequences of shells expanding into non homogeneous ISM are discussed.

2.4.2 Enhanced descriptions of shells and supershells

Supershells in a stratified interstellar medium

For supershells, the ISM of a Milky-Way type galaxy is described by a symmetric exponential atmosphere perpendicular to the Galactic plane (Lockman 1984) with the density

$$\rho(z) = \rho_0\,\exp - \frac{|z - z_0|}{H} \tag{2.17}$$

where ρ_0 is the density in the Galactic disk, z_0 is the coordinate of the center of the explosion and H is the scale height, which is $H = 500$ pc for the WNM and $H = 100$ pc for the CNM (H I of shells) of the disk (Baumgartner & Breitschwerdt 2013). The Kompaneets approximation (Kompaneets 1960),

describing a point explosion in an inhomogeneous atmosphere is used (Maciejewski & Cox 1999; Baumgartner & Breitschwerdt 2013). The resulting shells of such models are elongated perpendicular to the Galactic Plane as can be seen in figure 2.5 on the left hand side. In this plot, the energy source is located in the Galactic plane with $z_0 = 0$ and a symmetric expansion of the shell above- and below the Galactic plane. The asymmetric shape is caused by the density gradient (eq. 2.17). On the right hand side of the figure, the source that forms the shell is set off plane ($z_0 > 0$). In this case the bubble expands asymmetrically as the bottom part has to travel through the dense disk of the Galaxy and is barely able to plow through the Galactic plane, while the upper part of the bubble expands into a thinner medium due to eq 2.17 and hence can expand more freely with potential break- or blow-outs. It results in the more elongated shapes for each initial density, compared to the case with $z_0 = 0$. In both cases the bubble can blow out into the Galactic halo if the shell reaches sizes of 1–3 scale heights (e.g. Veilleux et al. (2005), Ferrara & Tolstoy (2000)). Bubbles that are able to blow out may be the source of Galactic fountains that shot H I into the halo in the past, where the ISM falls back into the Galaxy when the pressure decreases and the gravitational energy dominates the motion (Shapiro & Field 1976; de Avillez 2000). This is mentioned because the fall back or the general impact of hydrogen clouds might be an additional source for the formation of super-shells or -rings of gas but could also be the source of impacts of the extragalactic H I clouds with the Galactic disk as discussed further below (sec. 2.4.3).

The asymmetries of shells that arise due to inhomogeneities of the ISM are observed in almost every shell and not only supershells. This is further introduced and discussed below in section 2.4.3.

The most established analytical models from above that describe the evolution of supershells by continuous wind and SN input to a homogeneous ISM are good approximations if the size of a shell is small compared to the scale height of the ISM since the Milky Way, or spiral galaxies in general, have a stratified atmosphere. These models are however less accurate for the latest evolutionary stages of shells (Baumgartner & Breitschwerdt 2013).

Instability effects on shells

The density distribution on shells is not homogeneous and shells do not always have sharp edges since the ISM in the cavity as well as the radiation from origin stars are constantly interacting with the shell-ISM, which leads to instability effects. The main instability drivers that lead to effects that can be observed for shells are the following. **Kelvin-Helmholtz Instabilities** (KHI) appear when two fluids of different temperatures collide as it is the case e.g. when two bubbles of two different stars merge. Water-wave-like structures are then formed at the edges of the clouds. This effect can also be observed in atmospheres of planets.

If two fluids of different densities are accelerated against each other, a two-phase-instability occurs, which is called **Rayleigh-Taylor Instability** (e.g. Sharp (1984)). It appears at the interface between the inner edges of the ISM shell and the hot shocked bubble interior. Finger-like structures in shape can emerge as the perturbation grows at the interface. Due to shearing, the vorticity[11] of the flow increases until the two gas layers mix turbulently. The timescale on which this happens is 1–80 Myr depending on the position of the SNe compared to the Galactic plane and also where it is located in the bubble (Baumgartner & Breitschwerdt 2013).

When a blast wave expands into a sufficiently compressible medium as it is the case for the expansion

[11] The vorticity is a pseudo vector field describing the tendency of a fluid to rotate

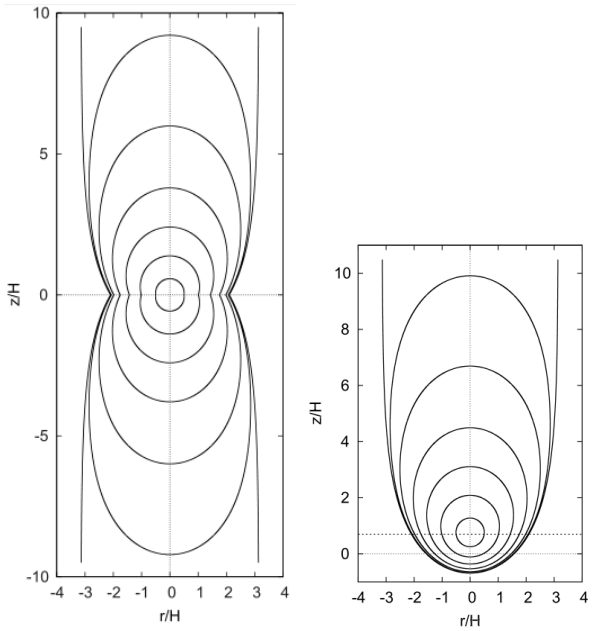

Figure 2.5: Shape and size of super bubbles in a stratified ISM environment. On the left hand side, the positions of the shock front in a symmetric model at certain values of a dimensionless time variable y= .5, 1.0, 1.4, 1.7, 1.9, 1.98 and 2.0 with the explosion center in the Galactic plane are shown. On the right hand side a similar plot is shown, but the SN source is located at $z_0 = 0.7\,H$ above the Galactic plane. In both plots the vertical height is marked by a dotted line. For an explanation see text in section 2.4.2 (Figure adopted from figure 1 and 2 from Baumgartner & Breitschwerdt (2013)).

of winds and SNe driven ISM, the medium is subject to a linear overstability that leads to filamentary structures. While the Rayleigh-Taylor instability is strongly connected to the acceleration phases, by shocks of SNe towards the inner part of the shell, this instability appears when the shell decelerates and the outer edges collide further with the ambient ISM. This instability is called **Vishniac Instability** (Vishniac 1983). The differences in densities causes the gas to flow from the high density regions of the shell into regions of smaller density. This leads to a situation where the initially higher density region now has a lower density, leading to cycles of density exchange and to possible increasing peak densities (Vishniac & Ryu 1989). This is why Vishniac instabilities are believed to explain the filamentary structures that are observed on the shells as shown below along the hydrodynamic simulations of Krause et al. (2013) but is also the suggestion by Minière et al. (2018) and Michaut et al. (2012).

Numerical simulations of super-shells

The energy input of massive stars into the ISM was modeled using hydrodynamic simulations in different studies. 2D hydrodynamic simulations for the energy input of isolated massive stars that include the effect of photo-ionization showed that the gas dynamical effects are dominated by the mechanical energy input (Freyer et al. 2003; Freyer et al. 2006). They show that 38% and 9% of the total energy input has been added to the ISM during the whole stellar lifetime in the simulations for a $35\,M_\odot$ and $60\,M_\odot$ star respectively. The effect of multiple stellar wind inputs were also modeled (van

Marle, A. J. et al. 2012), showing that the bubbles produced by two stars with 16.2 pc distance merge quickly and that the colliding wind parts of the two separate bubbles are swept into the smaller bubble due to pressure differences. The resulting superbubble is, during the merging process, not symmetric but reaches isotropy after a few Myr. The effects of multiple stellar wind and SN energy input into the ISM were analyzed in three dimensional hydrodynamic simulations in a homogeneous ambient ISM (Krause et al. 2013, 2014). The stellar masses of the group are 25, 32 and 60 $M_\odot$.

The results of the hydrodynamic simulations are shown in figure 2.6 and figure B.0.2 in appendix B. The bubble evolutions are plotted there for different snapshots in time. The most massive star (60 $M_\odot$) is in the center of the coordinate frame and it can be seen that it dominates the bubble expansion at 1.95 Myr (first row of plots). The bubbles of the smaller stars collide with the larger one and start merging. The surrounding gas of the bubbles have already cooled and the gas is compressed into thin shells for each bubble, which is visible as the high column density regions at the edges of the bubbles (orange). As in the 2D simulations from above, the large bubble expands into the smaller ones, ejecting material and merges into a superbubble that has an asymmetrical shape (time = 4.05 Myr). At the inner edges of the shells Vishniac instabilities lead to the filamentary structures that can be seen in the plots. The interface between the three bubbles undergoes Kelvin Helmholtz instabilities, since the cold fluid of the larger bubbles meets the hotter fluid of the smaller bubbles. At 4.05 Myr, the first SN goes off and the shock waves leads to the above introduced Rayleigh-Taylor instabilities. The effects of the winds in this phase can hardly be noticed and filamentary gas is found inside the bubbles. In these simulations the highest densities on the shell reaches 180 times the ambient ISM density Krause et al. (2013) and appears at 1 Myr after each SN, which can be compared to observation. For this see e.g. the measured intensities in the cavities, shells and of the ambient ISM in section 3.4.3.

The shells reach thicknesses of 10–20 % of its total radius depending on the initial parameters (see fig. B.0.3), which is thicker than assumed for analytical models but on the lower edge compared to observation, where relative thicknesses of 20–40 % are common (Churchwell et al. 2006).

Also some 3D simulations of SNe in inhomogeneous ISM were carried out, visualizing the turbulence Breitschwerdt et al. (2012). From simulations, different properties of shells can be predicted that can be compared to measurements from observation of the H I shells.

Physical and statistical properties of expanding shells

The radial distribution, the volume filling factor and the ratio of kinetic energy to theoretic predicted total energy input of shells and supershells are introduced in the following.

Volume filling factor The partial volume of space that is filled by bubbles or shells is called porosity[12] in general or as is called hereafter shell-volume-fraction (or filling factor). It is defined by $f_{3D} = \sum_i^n V_i / V_{ref}$, where n is the number of shells, V_i is the volume of the i-th shell and V_{ref} is the reference volume. V_{ref} can e.g. be the volume where it was searched for shells or the volume of a galaxy.

From the results of numerical 3D hydrodynamic simulations, the shell-volume-fraction compared to the total volume of ISM was analysed for different scale heights Krause et al. (2015). For a total limit of $\approx 3H$, the determined volume fraction for ambient ISM densities of 0.1–10 cm^{-3} is between

[12] porosity is the relationship between cavities and total volume of any material. In the sense of the ISM it means the lower density regions, namely the cavities of the shells.

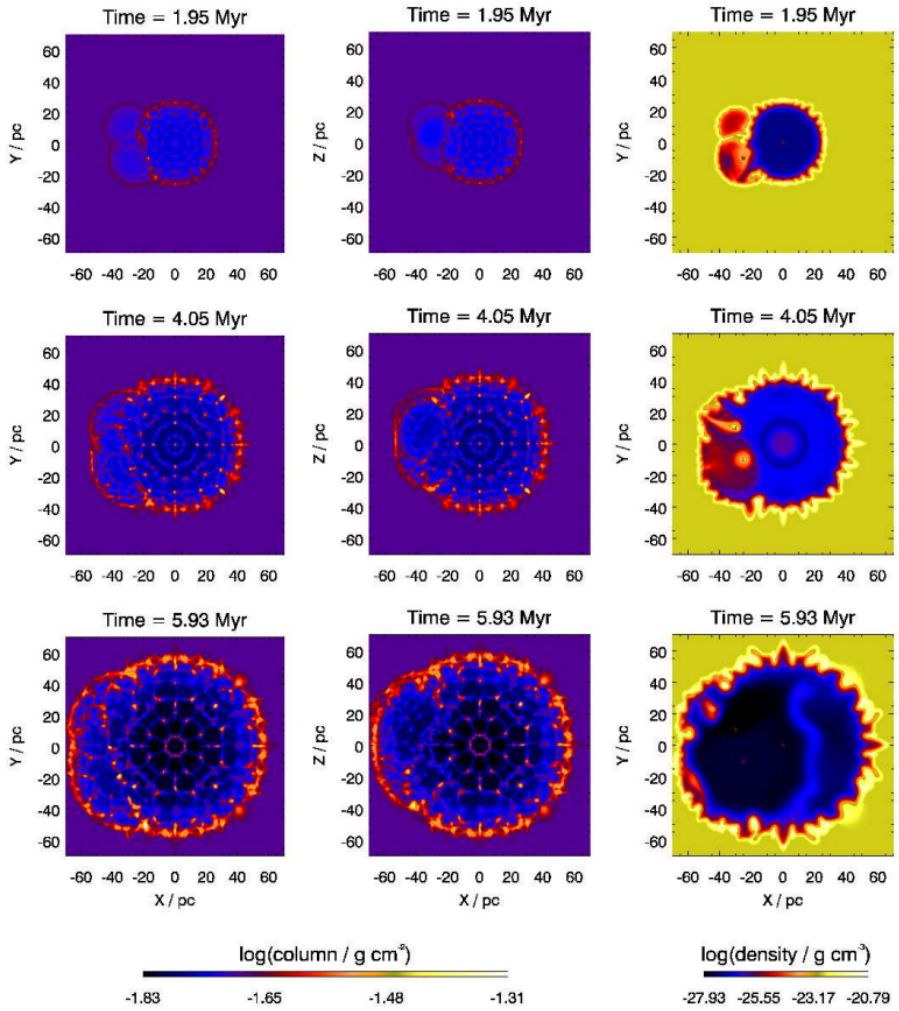

Figure 2.6: Hydrodynamic simulation of the evolution of merging bubbles produced by three stars (M = 60, 32, 25 $M_\odot$) are shown for three different time snapshots (from the top to the bottom) and different slices through the bubbles. The column density is integrated over z-direction (left), y-direction (middle) and the x-y plane (right). Projected positions of stars indicated by three red stars in the right panel. The figure stems from Krause & Diehl (2014), figure 3 therein.

3.1-115 (Baumgartner & Breitschwerdt 2013). These values do not match observation (see sec. 2.4.3 below). But as was described above and is visible in figure B.0.3 (Krause & Diehl 2014), the 3D hydrodynamic simulations showed time efficient bubble merging and could explain that most observed bubbles are a result of merging processes. From the self regulated star formation rate (SFR) via SN feedback using the SFR and the macroscopic gas density in galactic disks lead to a model where "the filling factor of SFR-suppressed supernova bubbles self-regulates to a constant $f \approx 0.5$" (Sarkar et al. 2019). This is demonstrated in cosmological and isolated-galaxy simulations. This value is closer to the previously observed ones. Supershells can reach radii up to the kpc scale (e.g. Breitschwerdt & de Avillez (2006)). The size distribution of superbubbles in a uniform ISM was predicted by Oey & Clarke (1997) using the standard adiabatic shell evolution as a power law of

$$\mathrm{d}N(r_{\mathrm{sh}}) \propto r_{\mathrm{sh}}^{-\alpha}\mathrm{d}r_{\mathrm{sh}} \tag{2.18}$$

where $\mathrm{d}N$ is the number of shells in the range or shell radii of r_{sh} to $r_{\mathrm{sh}}+\mathrm{d}r_{\mathrm{sh}}$.

Age If the radius and the expansion velocity of a shell is known, an upper limit for the age τ_s can be calculated using

$$\tau_s = \alpha\frac{R}{V_{\mathrm{exp}}}. \tag{2.19}$$

where α is between 0.2–1 (Koo et al. (2020)).

Energy A relation for the radius determined by Weaver et al. (1977) is

$$r(t) = \alpha(L/\rho_0)^{1/5}t^{3/5} \tag{2.20}$$

with $\alpha = 0.76$ (snow-plough phase) and $\alpha = 0.83$. By using $E = L \cdot t$ and rearranging the total energy $E_{t,\mathrm{w}}$ can be expressed in terms of the radius $r(t)$ in units of pc and τ in units of 10^7yr:

$$E_{t,\mathrm{w}} = \frac{r(\tau)^5\rho_0}{\alpha^5}\tau^{-2}\cdot 10^{38}. \tag{2.21}$$

This equation can also be written in terms of expansion velocities, which gives:

$$E_{t,\mathrm{w}} = \frac{r(\tau)^3\rho_0}{\alpha^5}v_{\mathrm{exp}}^2\cdot 10^{38}. \tag{2.22}$$

The kinetic energy can be derived if the mass M and the expansion velocity v_{exp} of a shell are known by:

$$E_{\mathrm{kin}} = \frac{1}{2}M_{\mathrm{s}}v_{\mathrm{exp}}^2. \tag{2.23}$$

For identified H I shells, these values can be determined if the distance towards the shell is known and

can be compared to the theoretical values of e.g. eq. 2.16. Then the kinetic energy fraction

$$\epsilon = E_{\mathrm{kin}}(t)/E(t) \tag{2.24}$$

can then be derived. The remaining fraction of the total energy is thermal energy $E_t(t)$. These values have been tracked for hydrodynamic simulations (Krause & Diehl 2014). While this value varies over the evolution time of a bubble, it is generally described well by the thin shell approximation of eq. 2.20 with a power law of $t^{3/5}$ for most phases. According to the simulation results, ϵ should then vary between 0.2–1, with values of 0.3 for constant luminosity wind and 0.4 for single SNRs. Shortly after a SN explosion, thermal energies dominate the energy output. In between and especially after the last SN, E_{kin} starts to dominate the equation (Krause & Diehl 2014). The relation and time dependence of ϵ is shown in figure B.0.4 in the appendix.

2.4.3 Observation of shells and supershells in H I

In the ISM of the Milky Way cavities, delimited by arcs and shells, are observed (e.g. Churchwell et al. (2006), Paladini et al. (2012)) that are mostly connected to stellar groups (e.g. Blaauw (1964b), Cash et al. (1980),Maciejewski et al. (1996), Jaskot et al. (2011)) and sometimes by individual stars or SNe (e.g. Gruendl et al. (2000), Green (2004b)). There are also different sources e.g. high-velocity clouds that blast into the disk of a galaxy and produces expanding shells (Kulkarni & Heiles 1987; Tenorio-Tagle & Bodenheimer 1988; Rand & Stone 1996; Santillan et al. 1999; Braun & Burton 1999). More recently Westmeier (2018) produced an all-sky map of high-velocity clouds, based on the HI4PI dataset[13].

Observation of Supershells in nearby galaxies

ISM holes and shells were first observed in satellite galaxies of the MW, like the LMC (Westerlund & Mathewson 1966) and the SMC (Hindman 1967) and later in external galaxies as M31 (Brinks & Bajaja 1986) and M33 (Deul & den Hartog 1990). More research for shells in other spiral galaxies was carried out in the works of e.g. Thilker et al. (1998), Thilker (1999) or Daigle et al. (2007)). Later, the H I Nearby Galaxy Survey (THINGS, Walter et al. (2008)) has been carried out with the Very Large Array (VLA) and provided H I observation for 34 galaxies at distances from 3–15 Mpc. The aim was to investigate the small-scale and three-dimensional structure of the ISM and the processes leading to star formation. Using this survey, the properties of holes (supershells) were analysed by Bagetakos et al. (2010). In their work, 20 galaxies were analysed and more than 1000 supershells with diameters of 0.1–2 kpc and expansion velocities of 4–36 km/s and ages of 3–150 Myr were detected. The kinetic energies of the supershells, based on the expansion velocity measures, are in the range of 10^{50}–10^{54} erg (e.g. Bagetakos et al. (2010)). In some cases the energy needed to produce these structures exceeds the expected amount that can be produced by star clusters. More powerful events are needed to explain this and one possible explanation is the infalling of high-velocity clouds into the disk of the respective galaxy (Tenorio-Tagle & Bodenheimer 1988; Rand & Stone 1996; Santillan et al. 1999). For each of the 20 galaxies the observed shell-volume-fraction (filling-factor) f_{o} (Cox & Smith 1974) has been determined. The result between different galaxies are in the range of 0.1–19.3% (Bagetakos et al. 2010).

[13] This map serves as a comparison if shells are detected at regions, where no stellar feedback is expected in this work.

The distribution of the holes show differences between dwarf galaxies, where in general they appear rounder, and spiral galaxies, where they seem to be limited by the shear. In spiral galaxies, holes outside of R_{25}[14] seem to be larger and older, which can also be explained by the shear that is particularly strong in the inner part of spiral galaxies. It was found that the general size distribution of holes falls of with a power law of $A_\nu \approx -2,9$ (Bagetakos et al. 2010). Further, considering the H I holes to be connected to SNR, an average lifetime per H I hole of 60 Myr was used to convert the supernova history into a supernova rate per century (SN-rate$_{100}$) with rates of 10^{-5} to 15.8 per 100 yr (see Bagetakos et al. (2010) and table 6 therein).

H I Shells in the Milky Way

Due to the observer being located in the Galactic disk, where observations suffer from the mixed H I emissions from different sources in the disk, especially into the direction of the Galactic center, observation of Galactic shells is challenging. On top of that, compared to extra Galactic face on galaxies, the shells in the Milky Way all have different distances towards the observer and the Galactic distance estimations for H I generally suffer from high uncertainties (sec. 3.5). And finally, the observer has to cover, optimally, the whole sky for a survey of shells in the MW. However, analyses of H I shells on a statistical basis are needed to derive general properties of the MW shells and can on the other hand be done in higher detail compared to observation of the ISM in external galaxies.

One of the first researches in collecting detected H I shells and creating a catalog is the work of Heiles (1979), who included 68 H I shells and updated it later (Heiles 1984). Additional 19 new visually detected shells were added by (McClure-Griffiths et al. 2002).

The ISM contains complex structure and in H I overlapping emissions of different sources at similar positions are common. Also the data are measured in position-position-velocity space and hence human intuition when visually inspecting the data can lead to a high number of missed detections. Especially when not focussing on specific regions, visualizing not the correct density gradient or zoom levels are the reason for this.

This is where automated algorithms have an advantage and can be used to objectively analyze the data. In the last decades, research in this area has started with great success by the first pioneers. With the new data available for this work and the usage of different methods it is built up on the following research. The main driver in this field is the work of Ehlerová & Palouš (2005), who used partly automated methods to detect the pattern of H I shells in latitude-longitude maps (sec. 3.3.3) as well as in the spectral dimension. Daigle et al. (2007) used an automatic method using neural networks to recognize the dynamical signature of a bubble but focussed on detecting shells in or near the Galactic plane in a region of $9^\circ \times 49^\circ$ and focussed only on shells of arcminute size and used H I data of the Galactic plane survey. This survey has a high resolution due to the use of interferometry of the telescopes of the very large array (VLA) and they detected 7000 objects. Detecting similar objects is out of scope of this work due to resolution limits of the single dish telescope H I data used here.

The catalog of Ehlerová & Palouš (2005) was refined by the team in follow up works (Ehlerová & Palouš 2013), leading to a total number of 333 detected H I shells, partly overlapping with the ones of (Heiles 1979; McClure-Griffiths et al. 2002). Additionally, focussing on visual inspections, Sallmen et al. (2015) focussed on specific angular regions to detect H I shells. From their samples, the distribution of shells in the MW was determined to follow an exponential radial profile in the Galactic

[14] R_{25} is the standard 25 mag/arcsec2 isophotal ratio taken from primary and secondary galaxy catalogs.

plane with an index. The size distribution of shells is fitted by the power law of eq. 2.18 with the coefficient 2.6 and the index 1.8. The surface density in the $z-$direction decreases also exponentially with a scale height of 2.8 kpc. But for the determination of this value, the largest shells were excluded, which is why this is more biased towards a lower limit. Generally, the shells are connected to the Galactic disk with a half width at half maximum (HWHM) of 500 pc but there are more shells observed at higher coordinates than a gaussian profile would allow, meaning there are expanding wings to higher scales Ehlerová & Palouš (2005). A general lower limit for the volume filling factor of $f_{3D} = 0.05$ was derived, probably since they excluded the largest objects of their catalog of sizes above 1 kpc and stated themselves that this value is more of a lower limit. The lower limit for the general surface density is $f_{2D} = 0.4$, which was refined to $f_{2D} = 0.7$ in Ehlerová & Palouš (2013). However for the solar vicinity of up to 100 pc they found a surface density of $4/$ kpc, which is in consensus with the high number of OB associations of shells near the Sun. Independently the filling factor was also determined for the MW with a value of $f_{3D} = 0.2$ by (de Avillez & Breitschwerdt 2005). These values are in general lower than the ones induced by hydrodynamic simulations, introduced in section 2.4.2.

2.5 Scorpius Centaurus and the ambient interstellar medium

The Scorpius Centaurus OB association (Sco-Cen) is the nearest site of recent star formation. As introduced in section 1, it consists of three gravitational independent subgroups (Blaauw 1964b), the Upper Scorpius (USco), Upper Centaurus Lupus (UCL) and Lower Centaurus Crux (LCC). Figure 2.7 shows the distribution of the three subgroups in Galactic coordinates as well as the proper motion of the stars (de Zeeuw et al. 1999; Preibisch & Mamajek 2008). The proper motions, or the mean radial velocity component, of the cluster is important for the analysis of the surrounding ISM because it is expected that the surrounding gas that is not blown away or expanding should have matching velocities compared to the one of the subgroups. The H I shells near Sco-Cen, are all in the snow-plough or the break-up phase. Hence they just show small velocity deviations of 10–15 km/s compared to the moving velocities of the respective subgroup and the center velocities should be comparable. Deviations have to be considered due to the group drifting away with a determined velocity shift of approximately 5 km/s, e.g. (de Zeeuw et al. 1999; Perryman et al. 2001). The mean distance to the association is 140 pc (de Zeeuw et al. 1999). The full stellar content of the association was investigated and the stellar masses were determined in numerous surveys (e.g. Blaauw (1964a),de Zeeuw et al. (1999), Preibisch et al. (2002), Preibisch & Mamajek (2008)). Their results are summarized in sections 2.5.1 to 2.5.3.

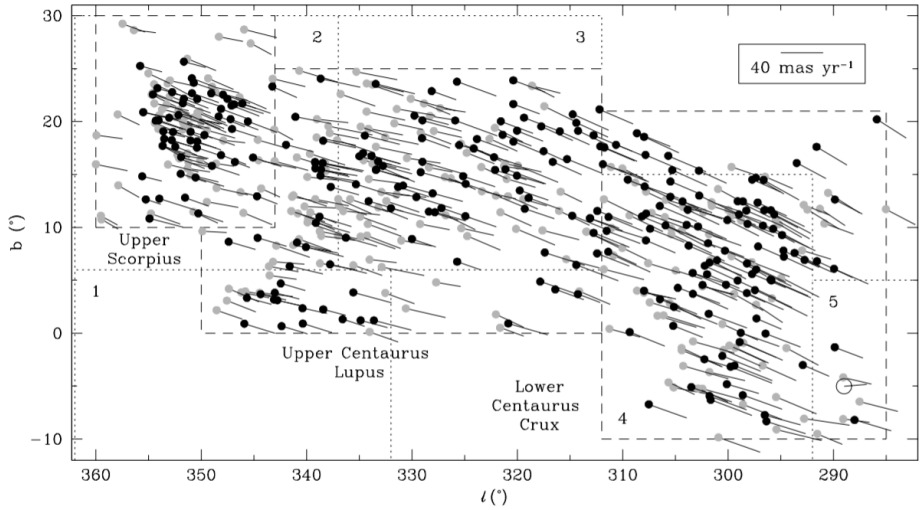

Figure 2.7: Locations of the three stellar subgroups of Sco-Cen. These are USco (top left), UCL (middle) and LCC (bottom right). The stars and their proper motions from the HIPPARCOS catalog are shown in a latitude-longitude plot covering the whole region. Figure credit: de Zeeuw et al. (1999) and Preibisch & Mamajek (2008)

Energy output by stellar groups The IMF was fitted to the present day mass function for each stellar subgroup using the parameters of Miller & Scalo (1979) and a separate scaling factor for each stellar subgroup of Sco-Cen (de Geus 1992)[15]. Then the authors determined the theoretical value for the output energy that determines the kinetic energy of a shell, $E_{\mathrm{kin,t}}$, by using equation 2.16. The

[15] These are older parameters and in this work more recent descriptions of the IMF from section 2.4 are used.

number of estimated SNe that contributed to the kinetic energy were estimated in three independent investigations (Blaauw 1991; Maíz-Apellániz 2001b; de Geus 1992). This was done for all three subgroups of Sco-Cen (de Geus 1992) and the results can be compared to the kinetic energies E_{kin}, which itself is derived from the shell properties that are introduced below for each shell. The presented values are listed in table A.0.4 in the appendix (adopted from de Geus (1992)).

The interstellar medium The ISM belonging to Sco-Cen spreads over almost one fourth of the sky in Galactic longitude, revealing large scale filaments and shells in H I[16]. The turbulent structure of the ISM around Sco-Cen was deciphered (Blaauw 1964b; Weaver 1979; Cappa de Nicolau & Poeppel 1986; de Geus 1992; Egger & Aschenbach 1995; Ortega et al. 2009; Poeppel et al. 2010). The spread of the large scale structures are schematically shown in figure 2.8 (de Geus 1992). The largest ring-like

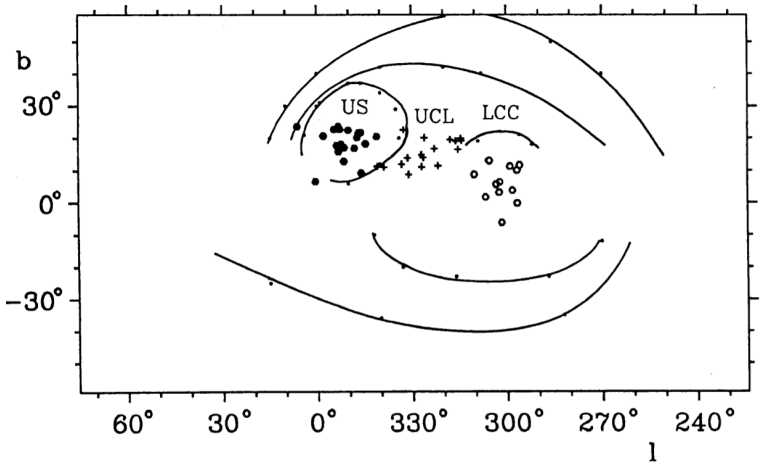

Figure 2.8: Illustration of arcs and shell-like structures in the vicinity of Sco-Cen. The black filled dots, the crosses and the circles denote the positions of the massive stars of USco (here denoted as US), UCL and LCC. The positions of the largest loops are drawn schematically. Figure credit de Geus (1992).

structure with an angular "radius" of about 40° is believed to be formed by the UCL–subgroup (Poeppel et al. 2010). The LCC–subgroup is surrounded by a semi loop and it was suggested that the second largest feature in the figure was also formed by LCC group or is a merger of shells belonging to the LCC- and UCL groups (de Geus 1992).

Regarding the USco group and its shells, two names are used— the USco-loop and the USco-shell (Cappa de Nicolau & Poeppel 1986; de Geus 1992; Poeppel et al. 2010). But the naming is inconsistent because in the study of de Geus (1992) the loop like structure around the USco–subgroup was called "Upper Scorpius shell", while in a later investigation (Poeppel et al. 2010) it was called "Upper Scorpius loop" and it was suggested that it is enclosed by a larger H I shell that they called "Upper Scorpius shell". The naming of Poeppel et al. (2010) is adopted in this thesis and the structure found by de Geus (1992) is also renamed into USco-loop here.

These shells are not completely spherical structures, nor do they have homogeneous density but consist of many substructures and are turbulently disturbed by other H I filaments. Analyses of each large scale feature were made, limiting its distance using interstellar absorption lines, for a total

[16] For a visualization of the region in H I using the Galactic Allsky Survey data, see figures 6.1, 6.2 and 6.3 in chapter 6

number of 29 features in the region around Sco-Cen in the velocity interval -40 to 20 km/s, mainly by Poeppel et al. (2010) and table 2 therein[17].

Masses of the shells In the literature rough mass estimations were made for each shell (listed on the right hand side of table A.0.4 adopted from de Geus (1992)). For the adopted masses no equations were provided in the paper and no background considerations were made, implying high uncertainties. On the left hand side of table A.0.4, the integrated masses in the listed velocity range were calculated by using equation C.14 in appendix masspoppelA (Poeppel et al. 2010)[18]. Poeppel et al. (2010) used the data of the LAB survey and did not take into account the pixel size change with latitude[19]. H I features that were assumed to be background sources that are not connected to the H I reservoir of Sco-Cen, like the Aquila rift and the GUM nebula (section 2.2.2), were subtracted in advance and the H I masses were interpolated in general for regions with $|b| \leq 10$. Their results are listed in column 4 and 5 of table A.0.4 in the appendix and is adopted from Poeppel et al. (2010), table 5. Any emission below 10° is either neglected or extrapolated in Poeppel et al. (2010).

Since all main shells belonging to Sco-Cen are at the latest stages of their SNR evolution and also probably mergers of single SNRs, where the expansion velocity has dropped down to about 10 km/s, for some shells fragmentation and clumping has already begun. As described in section 2.3.2, the decrease of the expansion velocity with time is not linear and changes over multiple magnitudes over the span of the first 10^6 years. Using the observed expansion velocity v_{exp} of a shell and the radius R, the upper limit for the age is calculated using eq. 2.19. This equation is used with a value of $\alpha = 1$ to estimate the ages of the shells in chapter 6 as well as the cited literature (de Geus 1992; Poeppel et al. 2010). This approximation is viable since the SNR are all old and expand with velocities of this magnitude for the longest part of their existence. These are also listed in table A.0.5. The parameters for each subgroup and the ISM are presented in the following.

2.5.1 Upper Scorpius

Upper Scorpius (USco) is the youngest of the three subgroups of Sco-Cen and historically the one, which is studied best, probably due to its high latitude, which results in less background emission from the Galactic disk compared to the other subgroups. Additionally the striking Usco-loop, surrounding the stellar group is even visual on allsky-H I maps. The stellar group contains regions of ongoing star formation, e.g. Lupus I (Gaczkowski et al. 2015, 2017) at the inner edge of a shell or the Ophiuchus region, implying possibility of sequential star formation (Preibisch & Zinnecker 2001). The parameters of USco that are introduced here can also be found in table A.0.2 and A.0.3 in the appendix. USco produced two main shells, which is arguably one shell that contains some smaller loops (Poeppel et al. 2010).

Stellar group From the main sequence turn-off in the Hertzsprung-Russell diagram, ages of the B- type stars were derived and the age of the Usco–subgroup was estimated to be 5–6 Myr (de Geus

[17] Since the results of this paper serve as a comparison to this work, their results are listed in appendix A in table A.0.17 and in appendix B in figure B.0.31 to B.0.34.

[18] A similar description is used in this thesis as described later by equation 3.19

[19] In this thesis equation 3.20 in section 6.3 is used that considers the latitude for each pixel, taking the varying pixel size into account.

et al. 1989). Independently the age for the low mass stars, determined from the Hertzsprung-Russell diagram of USco also resulted in 5 Myr with an absence of age spread (Preibisch et al. 2002) in agreement with other studies (Allen et al. 2003; Slesnick 2007). A newer investigation suggests an age of 11 Myr for this cluster (Pecaut et al. 2012). The discrepancy of 6 Myr is problematic because it leads to different predictions for the IMF, which results in a different number of massive stars and hence a different estimation of energy input per star. This can also influence the conclusion when comparing it to the independently determined parameters of the surrounding ISM. But age estimations calculated from various sets of modern models that reproduce Lithium depletion boundary ages of the β Pictoris Moving Group that is close to USco, also imply an age of ≈ 4 Myr for the low mass members of USco Herczeg & Hillenbrand (2015), which is again consistent with the common picture of a young USco–subgroup[20].

However, the cluster moves away from the Sun with an average radial velocity of $v = +5.5$ km/s at a mean distance of 145±2 pc (de Zeeuw et al. 1999) and has a depth of 50–60 pc (de Bruijne 1999). It contains numerous massive stars. These are 49 B-stars and 15 stars with a spectral type earlier than B2.5, i.e. $M \geq 8\,M_\odot$ (de Geus 1992; de Bruijne 1999). Overall USco consists of roughly 3300 stars and has a total stellar mass of $2350\,M_\odot$ (see table A.0.2).

The energy output of the stars by winds today is approximated to be 10^{47} ergs but according to the IMF, the association should have had at least one more massive member. The most massive star that exploded about 1.5 Myr ago is assumed to be a $50\,M_\odot$ O5–O6 star (Preibisch & Mamajek 2008). The trajectory of the runaway star ζ Oph suggests that the star was once located near the center of the stellar group and might be ejected by the already vanished O-star (Hoogerwerf et al. 2001).

This is consistent with the estimated number of SNe that should have gone off (Blaauw 1991; Maíz-Apellániz 2001b; de Geus 1992), considering a second one within the uncertainties. For the USco–subgroup this yields an estimated theoretical output energy of $E(t) = (3 \pm 2) \cdot 10^{50}$ erg (de Geus 1992). As will be shown in the following, the initial position of the runaway star is in agreement with the center of the H I shells and might have been one of its main sources.

USco loop The loop-like feature (USco-loop) around the USco–subgroup is present at velocities between 2–14 km/s is shown e.g. fig 3.12 or 6.3 . It is part of an expanding shell with an expansion velocity that was initially identified to be 6 km/s (Cappa de Nicolau & Poeppel 1986) and was later refined to be a higher with v_{exp} = 8–10 km/s (de Geus 1992; Poeppel et al. 2010) and a center velocity v_0 of 0–3 km/s [21]. For the loop, the center coordinates were estimated to be $l = 347°, b = 21°$ (Blaauw 1964a; de Geus 1992). This value was later suggested to be $l = 346, b = 25$ (Poeppel et al. 2010). The angular radius of this shell was estimated to be about 14° and the distance to the center of the USco-loop was estimated to be 130 pc, which is closer than the stellar group (145 pc (de Zeeuw et al. 1999)). This yields a radius of 32 pc.

Different investigations, each using their own background considerations, led to similar results. The mass of the USco-loop was estimated to be $0.8 \cdot 10^5\,M_\odot$ (de Geus 1992). A rough mass estimation of the total ISM around USco by integrating over the whole area and velocity range of the region yielded $1.65 \cdot 10^5\,M_\odot$ (Poeppel et al. 2010), which is an overestimation or upper limit because it also contains

[20] This topic will be discussed further, when the parameters of the shells determined in this thesis are summarised and discussed (see sec. 6.5)

[21] In this work v_0 is always the velocity of each point of the shell if the shell would not expand. This is true for the center coordinate even if the shell expands and hence v_0 is called center velocity.

the mass of the USco shell and background ISM (see section 2.5.1). The mass of the most striking single clouds, belonging to the USco-loop were estimated to be $0.2{\cdot}10^5\,M_\odot$ (Poeppel et al. 2010). These masses all contain uncertainties of up to 50 %, which is induced by the distance uncertainties of the shells.

Using equation 2.19 with $\alpha = 1$, the age of the USco-loop was estimated to be 1–4 Myrs (de Geus (1992) and Poeppel et al. (2010) respectively). These age estimations of the shells agree with the stellar age estimation of 5 Myr introduced above, but are not consistent with an age of 11 Myr that was suggested by the studies of Pecaut et al. (2012).

The determined kinetic energy of the USco-loop is $E_{\mathrm{kin}} = (1.7 \pm 0.8) \cdot 10^{50}$ ergs and is in agreement with the theoretical output value of $E(t) = (3 \pm 2) \cdot 10^{50}$ erg, determined using the properties of the stellar group (de Geus 1992).

USco shell In the investigation of de Geus (1992), the USco–loop was the only identified shell around the USco–subgroup. Poeppel et al. (2010) discussed that a larger feature, the USco-shell is embedding the USco-loop and is believed to be the main shell of the USco group. It has an angular radius of $23^\circ \pm 3^\circ$ and the center coordinates are $l = 350^\circ$ and $b = 21^\circ$. Because of the lack of distance information about the H I features, the center was estimated to lie at the distance of the center of the USco–subgroup, i.e. at 145 pc, which results in a radius of 61 pc of the shell. The center velocity is $v_0 \approx 3$ km/s and the shell expands with $v_{\mathrm{exp}} = 10$–12 km/s (Poeppel et al. 2010).

The shell has a larger radius and the center is estimated to lie at higher distances than the one of the USco-loop and since it embeds the Usco-loop, the calculated mass of the USco-shell is higher. In the literature, the total mass of the USco-shell was calculated using the LAB data (see equation C.14 of appendix C.2). It was determined to be $M = 1.65 \cdot 10^5 M_\odot$.

With equation 2.19, the age of the USco-shell was estimated to be in the range of 4.8–5.7 Myr (Poeppel et al. 2010), which is again consistent with the age estimation from the stellar group of 5 Myr (Preibisch et al. 2002; Allen et al. 2003; Slesnick 2007; Herczeg & Hillenbrand 2015).

Using the known mass and expansion velocity as well as using eq. 2.23, the present kinetic energy yields $1.6\text{-}2.5{\cdot}10^{50}$ ergs.

2.5.2 Upper Centaurus Lupus

UCL is the oldest subgroup of Sco-Cen and produced a supershell, the UCL-shell, which is the largest H I structure in this region and is in angular size, the largest observed in H I shell overall.

Stellar group UCL is located between the USco and LCC–subgroups, not only in angular projection with center coordinates of $l = 327^\circ$, $b = 12^\circ$, but also in radial distance from the Sun, with a mean distance value of 140 pc to the Sun (de Zeeuw et al. 1999). It is also the oldest subgroup of Sco-Cen with an age of 14–17 Myrs (Mamajek et al. 2002) and hence the most massive stars have already vanished. The total stellar mass of the cluster is 2190 $M_\odot$, including 17 stars with spectral type earlier than B2.5 and 66 B stars. Its mean radial moving velocity is v_0=+7 km/s. The age and mass of the UCL stellar group induces that multiple SN events should have happened.

The estimated numbers of SNe differ between different investigations and range between 3–13 SNe (Blaauw 1991; de Geus 1992; Maíz-Apellániz 2001b). The total estimated energy output by stars today is $(2.7 \pm 0.8) \cdot 10^{50}$ ergs and the contribution of previous SNe is $E_{\mathrm{SN,tot}} = (6 \pm 2) \cdot 10^{50}$ ergs (de

Geus 1992) resulting in an overall input energy to the surrounding ISM of $E(t) = (9 \pm 3) \cdot 10^{50}$ ergs (see table A.0.3).

UCL-shell The center of the UCL-shell is at $l = 320^\circ$ and $b = 10^\circ$ and has angular radius of at least 50° (de Geus 1992) up to probably 65° (Poeppel et al. 2010). The application of a visual "fit" of an ellipse in position-velocity-space (Cappa de Nicolau & Poeppel 1986) to the H I features and clumps that are believed to belong to the shell resulted in an expansion velocity of 8–12 km/s and a center velocity of 3 km/s[22]. A distance range of 110–140 pc for the center of the shell, where the upper limit was chosen according to the center coordinates of the stellar group, was proposed by de Geus (1992) and Poeppel et al. (2010). The radius has been determined to lie between 110–127 pc. The determined age range of the shell is 10–15.6 Myrs and hence is consistent with the age of the stellar group of 13–17 Myr (de Geus 1992; Poeppel et al. 2010).

The integration of the mass in the velocity range -42 km/s–20 km/s for longitudes between $l = 240^\circ$ and +40° and $\|b\| \leq 50^\circ$, subtracting the modelled background emission, is $0.6 \cdot 10^5\,M_\odot$ (tab. A.0.4,col. 5). The total mass of the UCL-shell was estimated to be $(3 \pm 1) \cdot 10^5 M_\odot$ (tab. A.0.4, col. 7 de Geus (1992)). The kinetic energy of the UCL shell, derived using equation 2.23 yields $(6 \pm 2) \cdot 10^{50}$ erg (table A.0.4, de Geus (1992), which is consistent with the theoretical value derived from the output energy of the subgroup from table A.0.3.

2.5.3 Lower Centaurus Crux

Even though the LCC stellar group is the closest subgroup of Sco-Cen, it is the least studied one, probably due to its position close to the Galactic plane (de Geus 1992). It is suggested to have formed two shells, one being the LCC-loop and an older one that has already merged with the ISM of the UCL-shell de Geus (1992).

Stellar group The center of this stellar group lies at $l = 299^\circ$ and $b = 5^\circ$, i.e. near the Galactic plane, ranging from Galactic latitude $b = -10\circ$ to $b = +20^\circ$. The northern part of the group is older ($\approx$ 17 Myr) and more distant (120 pc) than the southern part which has an age of 12 Myr and a distance of 110 pc Preibisch & Mamajek (2008). From the turn-off point of the Hertzsprung-Russell diagram, the general age of the LCC–subgroup was estimated to be 11–12 Myr (de Zeeuw et al. 1999). An independent investigation estimated that the stellar group is older and has an age of 16 Myr Mamajek et al. (2002). The stellar mass is $1300\,M_\odot$ and the distance to the center of the stellar group is 118 pc (de Zeeuw et al. 1999) and it has a depth of 30-40 pc (de Bruijne 1999). It has a mean radial moving velocity of 4.2 km/s (de Zeeuw et al. 1999). Since LCC is not studied well, there is a high variation in the estimation of SNe compared to the other Sco-Cen subgroups, ranging from 1.3 to 6 (Poeppel et al. 2010). The total output energy that contributes to the kinetic energy of the shells is $E(t) = (4 \pm 2) \cdot 10^{50}$ erg.

The LCC loop The LCC-group is surrounded by a semi loop-like structure called the LCC-loop that is centered at $l = 300^\circ$ and $b = 8^\circ$ (Poeppel et al. 2010)[23]. The position indicates a connection

[22] The shell has an ellipsoid-like shape and all three axes of the UCL-shell have to be considered separately, meaning one principal axis for each coordinate-direction of the shell will be determined in this work (ch. 6)

[23] It is visualized in H I in this work for example in figure 3.9 in two sub-plots of different intensity ranges.

between the LCC-loop and the stellar group (de Geus 1992). It was stated that this structure shows no sign of expansion (de Geus 1992; Poeppel et al. 2010) and hence is not defined to be an "expanding" shell. From the curvature of the semi loop an angular radius of 12.5° was derived by the authors. The estimated distance to this loop is 159 pc, which yields a radius of 35±10 degree. Since the LCC-loop is close to the Galactic plane, the density of the loop is higher compared to the ones of the UCL-shell, the USco-loop and -shell, but so is the Galactic disk background emission.

A mass for the LCC-loop of 100,000±50,000 $M_\odot$ was estimated by de Geus (1992). A a consistent result within these uncertainties of 50% was derived by Poeppel et al. (2010) by integrating column densities in the angular surroundings of the LCC cluster in the velocity range -50 km/s to -20 km/s and yielded a mass of 60, 000 $M_\odot$.

The LCC loop is estimated to be at least 10 Myrs old but since no signs of expansion could be derived in previous investigations (de Geus 1992; Poeppel et al. 2010), the independent estimation from H I and the kinematics are not determined.

The LCC shell The age and mass of the LCC–subgroup suggest that it should already have formed a larger structure than the LCC-loop. Using the geometric description of Cappa de Nicolau & Poeppel (1986)[24], the expansion velocity of a shell was fitted to several H I clumps in position-velocity maps and the detected shell was named LCC-shell (Poeppel et al. 2010) with center coordinates of ($l = 300°, b = 10°$) and an angular radius of 45° (see Poeppel et al. (2010) and table A.0.5) . Since no direct distance determination to the shell was possible and the center in Galactic coordinates coincides with the one of the LCC–subgroup, this distance was estimated to be the shells center at 118 pc. The fitted expansion velocities lie in the range of 6–12 km/s. Using equation 2.19 an age of 6–9 Myr for the shell is suggested by Poeppel et al. (2010)[25].

2.5.4 The history of Scorpius Centaurus

Recent star formation in USco may have been triggered by the older UCL–subgroup by the transition of the H I gas (Preibisch et al. 2002). This scenario was proposed to be consistent with the age and size of the UCL- and the USco-shells (de Geus 1992). The UCL shell has passed the USco–subgroup. Poeppel et al. (2010) stated that the subgroup might have emerged before the UCL-shell traversed the USco stellar group. Ortega et al. (2009) proposed a scenario where the UCL- and the LCC-shell merged into one larger shell and that between those subgroups some unbound groups composed of several young stellar associations like the one around the pre-main sequence star β Pictoris (Barrado y Navascués et al. 1999; Zuckerman et al. 2001) or the association around TW Hydrae (Kastner et al. 1997; Webb et al. 1999) emerged.

Investigations of molecular clouds in the vicinity of Usco and UCL gave rise to the suggestion that the USco-subgroup itself triggered star formation. One candidate is the Ophiuchus molecular cloud (de Geus & Burton 1991; de Geus 1992) Another one is the Lupus I cloud that may have emerged from a collision of the USco- loop and some expanding gas of a subregion of UCL as proposed by Gaczkowski et al. (2015).

[24] For an explanation of the geometric description see chapter 4.2, where a similar method is used to determine the expansion velocity for the EHSS-model that is also introduced in this section.

[25] Note that this age is younger than the one of the LCC-loop, which should not be the case. It can be argued that it is still correct within the uncertainties but due to these results, in the investigation of this thesis in the sections 6.2 to 6.5, the age of the LCC-loop will be revisited.

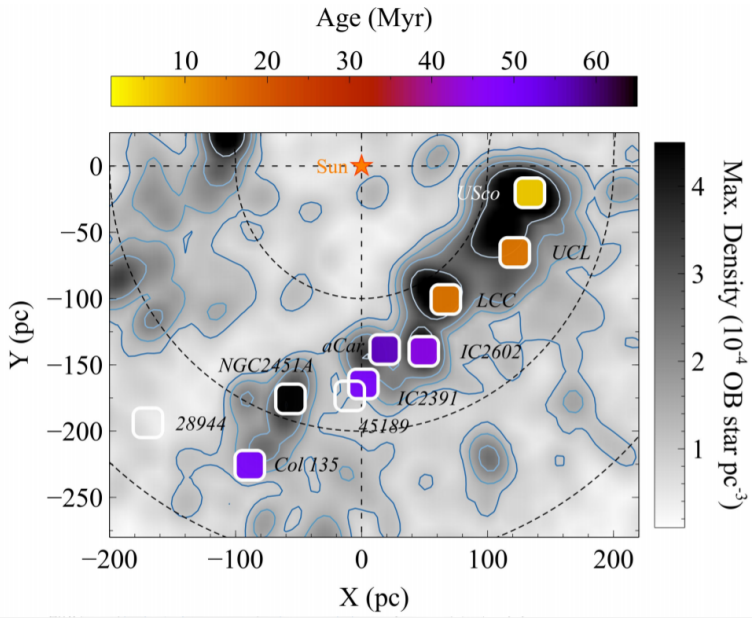

Figure 2.9: Illustration of nearby OB associations of the Sco-Cma stream and their ages shown in a Galactic plane view. The density of OB-stars is coded in grayscale. The position of known OB associations are marked by squares. The age of the cluster is color coded if available and transparent otherwise. The location of the Sun is indicated by the orange star and is the zero point of the coordinate system that is presented in units of parsec. Figure credit Bouy & Alves (2015)

Poeppel et al. (2010) suggested that the initial gas that formed Sco-Cen belongs to the Gould Belt (Lindblad 1967; Olano 1982; Perrot & Grenier 2003) (section 2.2.2). Assuming that the initial gas is the Gould belt gas, the ages of the shells were fitted in terms of the expansion velocities of the structures by Poeppel et al. (2010). The age, shape and size of the UCL-shell (11–16 Myr), the closeness of the UCL– and the LCC stellar subgroups, the age of the LCC–subgroup and the absence of an LCC shell due to their analysis, suggest that the UCL shell is a merger of a previously known LCC-shell and the initial UCL-shell as was concluded by (Poeppel et al. 2010). Even though a single LCC-shell was fitted (Poeppel et al. 2010), it might already be a part of the UCL shell but is still left for further investigations.

The distance between the USco- and UCL-stellar groups is about 70 pc, which together with the size of the UCL-shell supports the suggestion that star formation in USco was triggered by the UCL-shell. Independent newer investigations of multiple stellar groups, including Sco-Cen, show that the whole Sco-Cen OB association is part of a sequence of star formation events as can be seen in figure 2.9 where the age of the stellar groups increases from top right to the bottom left, with USco being the youngest stellar group (Bouy & Alves 2015).

2.6 Summary

A general introduction to the ISM and its components of previous research about the local ISM have been introduced in section 2.1 and 2.2. The absorption-, sodium-, extinction- and dust data of the introduced literature are used in this work to enhance the H I data analysis. This is especially useful for determining the distance towards local H I features and is applied for the analysis of Sco-Cen in chapter 6. It has been shown, which local ISM features have to be taken into account for the analysis of Sco-Cen, how they are connected to the region and which ones are close but do not directly influence the analysis in H I.

The evolution of massive stars, single supernova remnants and the interaction of OB associations have been introduced in section 2.3 and 2.4. The current research status of analytical descriptions as well as hydrodynamic simulations of shells have been provided. The introduced relations for describing the volume filling factor of shells, the energy deposition of feedback into the ISM and the evolution of shells will be used for connecting the observational results of the detected H I shells to theoretical stellar energy input and hydrodynamic simulations.

The status of observation of shells in H I has been described and it has been shown that there is still room for large scale survey attempts for H I shells in general and especially there is no large scale investigation carried out for the newer H I survey data yet.

The properties of the stellar groups as well as the features and shells of the Usco-, UCL- and the LCC-subgroup of Sco-Cen have been introduced in section 2.5 and the current picture of the star formation history has been provided there. It was shown that the Sco-Cen region is part of a larger region undergoing a sequence of star forming events. But it has also been described that there are open questions about a possible relation between the UCL-shell and the LB. Therefore the three dimensional structure of the ambient ISM of Sco-Cen has to be understood in more detail to derive the geometries of the surrounding shells and to determine the full picture about its history

H I data is the main source used in this work since it is the main tracer for shells in the snow-plot phase. The instruments used to detect H I, the general properties of the data as well as the properties of H I shells in the data are topic of the next chapter as a preparation for the analyses of H I in later chapters.

CHAPTER 3

Radio telescopes, H I surveys and data

The main data sources for this thesis are the ones of the Galactic All-sky Survey (GASS, (McClure-Griffiths et al. (2009), Kalberla et al. (2010), Kalberla & Haud (2015))) and the Effelsberg Bonn H I survey (EBHIS, (Winkel et al. 2016)), which are the latest large-scale surveys of the 21 cm emission line of neutral hydrogen. While GASS covers the southern hemisphere, EBHIS covers the northern one. Both surveys have an overlap region and the data are arranged in such a way, so that it is possible to produce one H I survey covering 4π (HI4PI), i.e. the whole sky. The HI4PI survey is the highest resolution all-sky survey and the successor of the Leiden Argentine Bonn survey (LAB) (Kalberla et al. 2005). The data of LAB, GASS, EBHIS and HI4PI are fully available for this thesis. The focus is on the latter three in this chapter, which is structured as follows.

Section 3.1 starts with an introduction of the general description of radio telescopes, the most important components of the telescopes, measures and general sampling strategies. Then in section 3.2, H I surveys and its specific configuration are described. The resulting data structure and -properties like projection effects, binning effects as well as properties of the ISM in datacubes are described in section 3.3. Building up on this foundation, in section 3.4, the properties of expanding shells in H I datacubes are introduced. The derivations of physical quantities of objects, detected in H I data, are explained in section 3.5.

3.1 Radio telescopes and general relations

A radio telescope consists of a parabolic main mirror (figures 3.2 and 3.4), which collects the incoming radiation and focuses it onto a receiver. State of the art single dish radio telescopes with movable mirrors reach sizes of 100 m diameter, e.g. the Green Bank- and the Effelsberg telescope. The stationary Arecibo Observatory has a diameter of 305 m and the recently constructed Five hundred meter Aperture Spherical Telescope (FAST) in china is the largest telescope constructed ever (Nan et al. 2011) operating at 10 cm–4.3 m wavelength. Radio telescopes have to be large because of the dependence of the angular resolution Ω on the wavelength λ (21 cm for the H I line), which is the Rayleigh criterion[1]:

$$\Omega = 1.22 \cdot \frac{\lambda}{D} \tag{3.1}$$

where D is the diameter of the antenna. The problem of a need for large diameters was overcome by using interferometry, where arrays of smaller radio telescope antennas work together as one single telescope. But these usually just trace smaller regions of the sky and hence, data produced with them, have not been used in this work. In the following, the main components of radio telescopes are described.

3.1.1 The receiver and relations

The receiver consists of multiple components. A conic wave guide directs the incoming radio waves to the decoupling pins. The horn enlightens the mirror uniformly to minimize the reception of unwanted radiation components. The arrangement of the decoupling pins sets the polarization of the signal. The systems contains arrangements of multiple horns, which reduces the measurement time for large scale surveys because multiple regions of the sky can be observed simultaneously (section 3.1.3). The radiometer processes the received signal and is described in the following.

Radiometers A general illustration for a radiometer is shown in figure 3.1. The radio waves received from the antenna denoted as (1) in the figure are amplified (2) and then filtered by a bandpass filter (3) where frequencies in the range $\Delta\nu$ pass. Next, the signal passes a quadratic multiplier (4) where the negative signals are squared in order to reach an output voltage, which is proportional to the power input. Lastly, the signal is processed by a low pass filter which integrates the signal over time τ (5). Finally the resulting signal is digitized (6) for further data reduction.

The system temperature The integrated voltage that is measured by the receiver is called system temperature T_{sys}. The main components are the following:

$$T_{\mathrm{sys}} = T_{\mathrm{R}} + T_{\mathrm{b}} + T_{\mathrm{atm}} + T_{\mathrm{CMB}} \tag{3.2}$$

where T_{R} is the receiver temperature, T_{b} is the radiation (brightness) temperature of the observed source, the temperature of the atmosphere of the earth is T_{atm} and T_{CMB} denotes the temperature of the

[1] The real resolution of radio telescopes is less accurate compared to unblocked circular apertures (Airy-Disks). Tapering of radio telescopes reduces the resolution to lower the side lobes which gives a factor of 1.02 instead of 1.22 (e.g.Wilson et al. (2012))

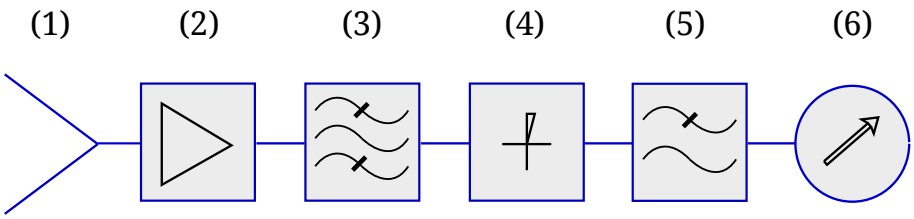

Figure 3.1: Schematic description of a radiometer including the antenna (1), the amplifier (2), the bandpass filter (3), the cubic multiplier (4), the integrator (5, low pass i.e. capacitor + resistor) and the digitizer (6).

cosmic microwave background. Normally $T_{\rm sys} >> T_{\rm b}$ because the telescope components have a much higher temperature than the observed source.

Radio telescopes receive an antenna temperature T_A, which depends on the beam pattern P and the true **brightness temperature** distribution T. The equation is, for simplicity, shown in Cartesian coordinates and the antenna diagram is split into the main beam area (mba) and the stray pattern (sp), which results in

$$T_{\rm A}(x,y) = \int_{\rm mba} P(x-x',y-y')T(x',y')\,{\rm d}x'\,{\rm d}y' + \int_{\rm sp} P(x-x',y-y')T(x',y')\,{\rm d}x'\,{\rm d}y' \qquad (3.3)$$

where P is normalized to 1. This equation can be rewritten by defining the main beam efficiency of the telescope

$$\eta_{\rm mba} \equiv \int_{\rm mba} P(x,y)\,{\rm d}x\,{\rm d}y \qquad (3.4)$$

and describing the brightness temperature $T_{\rm b}(x,y)$ by

$$T_{\rm b}(x,y) = \frac{T_{\rm A}(x,y)}{\eta_{\rm mba}} - \frac{1}{\eta_{\rm mba}} \int_{\rm sp} P(x-x',y-y')T(x',y')\,{\rm d}x'{\rm d}y'. \qquad (3.5)$$

The brightness temperature is the used measure for the intensity of the incoming signal. The brightness temperature and its connection to the column density are further described in appendix C.

The radiometer equation The threshold sensitivity of the receiver is described by the radiometer equation:

$$\sigma_{\rm rms} = \frac{KT_{\rm sys}}{\sqrt{\Delta\nu\tau}} \qquad (3.6)$$

where $\sigma_{\rm rms}$ is the standard deviation of the squared mean receiver output, depending on the integration time τ and the frequency width of the bandpass $\Delta\nu$. K describes the goodness of the noise with the restriction $1 < K < \sqrt{2}$. The values of $\sigma_{\rm rms}$ are discussed for different H I surveys in section 3.2.

3.1.2 Sampling and correction strategies

There are different sampling strategies between surveys and there are also different developed correction strategies. Here an overview is presented. Detailed data reduction steps for the surveys EBHIS and GASS are presented in more detail in appendix C.1.

Nyquist sampling The Nyquist Theorem (Shannon 1949) implies that a signal has to be sampled at a rate of at least two times its maximum frequency to be fully sampled. For radio telescopes this means that the spacing between two samples should be lower than $\lambda/2 \cdot D$. While the LAB survey did not fulfill the Nyquist criterion, GASS and EBHIS are fully Nyquist sampled leading to an additional increased effective resolution.

Baseline fitting The baseline is the telescope's response of points that do not contain emission lines. Usually, in radio astronomy a polynomial fit is used to describe the spectral continuum with possible artificial variations that are combinations of variations of the properties of the telescope itself and external variations like atmospheric ones. To determine the function of the baseline, the true height of emission lines has to be determined and background emission has to be identified.

Stray radiation correction The Galactic plane contributes the largest part of H I emission in the sky. If the Antenna side lobes point towards regions in or near the Galactic plane, a significant amount of background emission called stray radiation is produced that has no correlation with the targeted source. It is not a constant quantity and changes with time and with seasons (van Woerden et al. 1962). High latitude objects often have faint H I emission and hence the effect of side lobe emission reception is high, sometimes even higher than the signal from the actual source. The structure of the side lobes is different for each telescope because it depends on the antenna type and also its shape. It was found that the stray radiation produced by a parabolic reflectors are mainly from its support legs, which are needed to install the receiver in front of the mirror (Kalberla et al. 1980). These side lobes are called stray cones. Additional stray radiation is produced by the regions outside of the rim of the reflector, which is called the spillover region and also from other reflections within the aperture. Newer telescopes have minimized the effect of stray radiation by minimizing the number of scattering surfaces within the telescope, e.g. the Green Bank telescope (Prestage et al. 2009). This can raise the main beam efficiency up to 90% (Winkel et al. 2016). But the remaining stray radiation has to be minimized because its contribution to the emission is still large. After the first successful attempts for stray radiation correction(van Woerden et al. 1962), the methods were refined and still have to be defined individually for each telescope (e.g. Kalberla et al. (1980),Kalberla et al. (2010),Winkel et al. (2016)).

3.1.3 Telescopes

In the following, the Effelsberg- and the Parkes telescope and its properties are described since they are the instruments with which the surveys EBHIS and the GASS have been produced (sec. 3.2).

The Effelsberg telescope

The Effelsberg 100 m diameter telescope (see fig. 3.2) is the second largest steerable radio telescope. It has been in service since 1972 and continuous improvements of the instruments have been made. The EBHIS survey is one of the latest larger achievements.
Values resulting from the properties of the receiver and data reduction are explained in the following.

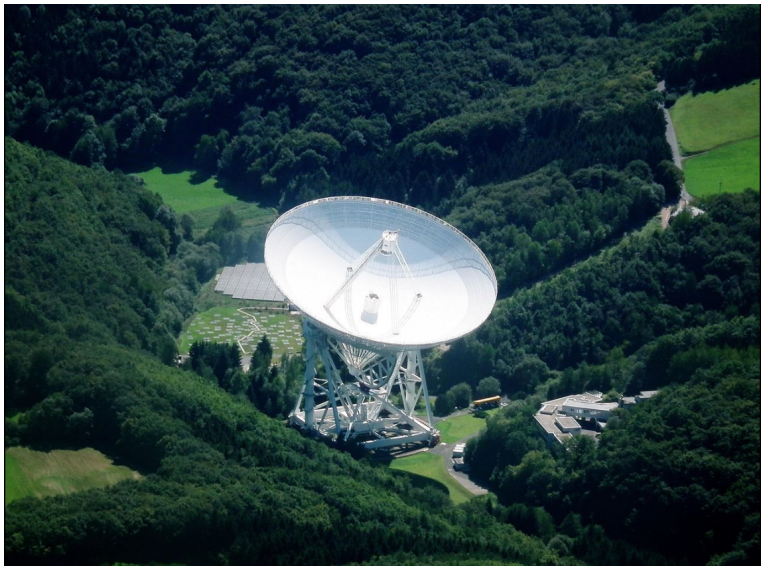

Figure 3.2: Aerial image of the Effelsberg, Germany 100 m diameter radio telescope, credit: Dr. G. Schmitz

With a diameter of 100 m and equation 3.1, the angular resolution of the telescope is 9.4′. The final resolution, after the application of interpolation methods during the data reduction, is 10.5′. EBHIS uses an L-band seven feed array consisting of 6 horns that are arranged hexagonally and the seventh one located in the middle. The arrangement of the horns is illustrated schematically in figure 3.3. 1024-channel spectrometers, based on a field programmable gate array, using flexible fast Fourier transformation are used. EBHIS needs one for each of the 7 feeds and additional 7 spectrometers for the polarization. The bandwidth is 100 MHz, hence EBHIS can cover the Galactic- and the extragalactic hydrogen in parallel. Each back-end has 16384 channels resulting in a channel width of 6.1 kHz. Using equation 3.7 introduced below, yields a velocity resolution of 1.25 km/s. The values described here are also summed up in table 3.1.

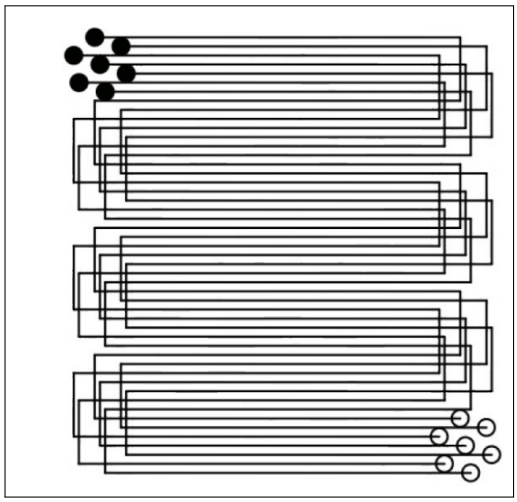

Figure 3.3: Illustration of the 7 feed array of the receiver of the Effelsberg telescope and the observation pattern (Peek & Heiles 2008). For more information see text.

The Parkes telescope

The GASS survey has been carried out using the CSIRO's Parkes radio telescope in Australia. The telescope has a diameter of 64 m and is also steerable. It has been taken in operation at 1961 and has also been used for many other researches e.g. the H I Parkes All-Sky Survey (HIPASS) for extragalactic astronomy as well as radio continuum surveys.

Figure 3.4: CSIRO´s Parkes, 64 m diameter, radio telescope. Credit: David McClenaghan, CSIRO

The survey parameters, described in the following can be derived by the quantities introduced in section 3.1.1 and are additionally listed in table 3.1. The receiver of GASS consists of 13 hexagonal horn-shaped wave guides, arranged circle-like, as shown schematically in the appendix in figure C.1.2 in the top panel. This multi-feed system lies in the focus plane of the main mirror. The signal is divided into 2048 channels with a channel width of 3,9 kHz and a total spectral range of 8 MHz. The effective channel width is $\Delta\nu = 4.7$ kHz, which is equivalent to an effective velocity width of

$$\Delta v = \frac{c\Delta\nu}{\nu_{10}} = 1.0\,\text{km/s}. \tag{3.7}$$

where ν_{10} is the transition between the hyperfine levels of spin F= 1 to F= 0 (sec. 2.1.1). This velocity resolution is 25% higher than the one of EBHIS.

Using equation 3.6 and knowing the required parameters $T_{\text{sys}} \approx 22$ K and $K = 1$ of the survey, the noise can be calculated and is

$$\sigma_{\text{RMS}} = \frac{1 \cdot 22\,\text{K}}{\sqrt{4700\,\text{Hz} \cdot 30\,\text{s}}} = 0.05859\,\text{K} \approx 59\,\text{mK}, \tag{3.8}$$

which is lower than the one of EBHIS.

3.2 H I Surveys

In the following, the properties of the three H I surveys of which the data have been used in this thesis are described. The survey parameters are listed in table 3.1. For comparison, the table also lists the properties of the successor of the HI4PI survey– the LAB survey, in column 1. In column 2, 3 and 4 the GASS, the EBHIS and the HI4PI survey properties are listed respectively. The coverage of the respective survey is listed in row 1 of the table. This is either up to a certain declination angle δ or a full sky coverage, marked by "full". The angular resolution Ω_{FWHM} is listed in row 2, the absolute velocity range $|v_{\mathrm{LSR}}|$ is listed in column 3, the spectral bin width Δv is listed in row 4, the spectral resolution δv is listed in row 5 and the temperature noise level σ_{rms} is listed in row 6. The parameters of the respective surveys are introduced in the following.

name	LAB	GASS	EBHIS	HI4PI	unit
coverage	full	$\delta \leq 1^\circ$	$\delta \geq -5^\circ$	full	
Ω_{FWHM}	$36'$	$16.2'$	$10'$	$16.2'$	
$\lvert v_{\mathrm{LSR}}\rvert$	≤ 460	≤ 470	600	≤ 600	km/s
Δv	1.03	0.8	1.25	1.25	km/s
δv	1.25	1.0	1.49	1.49	km/s
σ_{rms}	80	55	90	43	mK

Table 3.1: Table listing the parameters of the LAB survey, GASS (Kalberla et al. 2010; HI4PI Collaboration et al. 2016), EBHIS (Kalberla et al. 2010; Winkel et al. 2016) and the HI4PI survey HI4PI Collaboration et al. (2016). Row 1 contains sky coverage of the survey, either with the label "full" for full sky coverage or with the declination angle (δ) limit. The angular resolution Ω_{FWHM}, the velocity interval $|v_{\mathrm{LSR}}|$, the channel width Δv, the spectral resolution δv and the temperature noise level σ_{rms} are listed in the rows 2, 3, 4, 5 and 6 respectively. Table adopted from HI4PI Collaboration et al. (2016).

3.2.1 The Effelsberg Bonn H I Survey

The first data release of the Bonn Effelsberg H I survey (EBHIS) was made in January 2016 Winkel et al. (2016). If not mentioned otherwise, information provided in this section have been extracted from this data release as well as from Kerp (2009), Winkel et al. (2010a) and Winkel et al. (2010b). Also a second release is planned with a sensitivity improvement of about 30 %. This has been the latest larger single dish H I survey and may be the last one due to the rise of interferometry in radio astronomy.

Observation The survey covers the northern sky with declinations $\delta > -5^\circ$. The fraction of the sky is further divided into 915 individual maps, each having a size of 25 deg^2. The observations are made in an on-the-fly mapping mode. It is scanned in right ascension, α, while the declination δ is held constant. The seven-feed array is rotating according to the change of the parallactic angle during each scan line (Winkel et al. (2016)). This ensures a regular scan pattern of the offset feeds. This pattern is shown in figure 3.3 for one individual field with the mentioned size of 5° x 5°. There are three different time constraints that are applied for each observation field due to local, global and extra terrestrial given conditions. A mobile-communication broadcast tower in the vicinity of the telescope (at Az $\approx 290^\circ$) causes the southeastern quadrant to be preferred in azimuth to maximize the angular distance.

The rotation speed of the receiver box at the dish is limited. This means that large differential changes of the parallactic angle during each scan line have to be avoided. The largest extra terrestrial source of noise is the Sun (solar ripples). Hence observations have to be made in a direction as far away from it as possible. The full spectrum is stored each 500 ms with the flexible fast Fourier transformation. For a reasonably fast completion of the full sky coverage, a scan speed of 240 ″/s was chosen. The data produced with these observations have median noise levels of 90 mK, but vary between different fields. The data contains unwanted emission effects like radio frequency interferences (RFI) or stray radiation (see sec 3.1.1 and sec. C.1 in the appendix for details). Also the seasonal change of the ambient temperature affects the measurements and has to be taken into account. These effects and how they are reduced is explained in appendix C.1.

The final parameters of the survey after the different data reduction steps are shown in table 3.1. Some parameters and its derivation were already mentioned above. They are summarized here. EBHIS has an effective spectral resolution of 1.44 km/s and the channels are spaced at 1.25 km/s. The spatial resolution is 10.5′ and the maximum noise is 90 mK. The noise consists of three main sources that are pure thermal noise, calibration uncertainties and errors in the baseline. From emission line-free regions, typically at high latitudes and high velocities, the brightness temperature root mean square (RMS) can be determined assuming normal distributed noise. More details about observation and data reduction steps can be found in appendix C.1.

3.2.2 The Galactic All Sky Survey

The GASS maps the H I sky for declinations lower than 1°, meaning it overlaps over 4° with EBHIS. After the first data release (McClure-Griffiths et al. 2009), the data have been corrected for stray radiation and radio frequency interactions (RFI) which has led to the second data release (GASS II) (Kalberla et al. 2010). Some RFI remained, leading to stripes along the observation axis, see e.g. figure B.0.7 in appendix B. The RFI correction has been improved further removing these artifacts resulting in a third data release (GASS III, Kalberla & Haud (2015))[2]. Everything explained in this section is based on these three papers if not mentioned otherwise explicitly.

The observations have been made in eight sessions, two weeks for each, between January 2005 and November 2006. The goal for the GASS survey, which has been achieved, was to match the sensitivity of LAB but with a higher angular resolution. The survey covers the sky with full Nyquist sampling (sec. 3.1.1). In one scan, the telescope scans 8° of R.A. or declination in 8 min, which results in a spacing of 5′. For the observation, in-band frequency switching, explained below, was used to gain a higher efficiency while being sensitive to broader emission at the same time. To match the LAB sensitivity, the integration time was chosen so that the brightness temperature noise is smaller than 70 mK. The methods used for effective observations for this survey is frequency switching. Frequency switching is an observing mode where the local oscillator is shifted several times a second by some MHz. The frequencies are shifted to 1418.8435 and 1421.9685 MHz for the GASS. The variation is low enough so that the signal is also present in these reference frequencies. In the resulting spectrum, the same line appears in absorption and emission. If these spectra are folded, the signal to noise ratio improves by a factor of $\sqrt{2}$. The GASS uses ”in-band” frequency shifting. This increases the integration time available during observation and no emission free reference regions are needed to remove the continuum signal.

[2] The 3rd data release has been made during the creation of this thesis. That is why for some analysis, the GASS II version is used and for later ones, GASS III is used. The effects on the large scale features, investigated for Sco-Cen are negligible.

The resulting parameters of the survey, which were partially calculated above, are listed in table 3.1 (Kalberla et al. 2010; Winkel et al. 2016). The GASS survey has an effective spectral resolution of 1 km/s, while covering a velocity range of $|v_{\mathrm{LSR}}| = 468$ km/s. The effective spatial resolution is 16.1′, which is comparable to the one of EBHIS but a little bit lower. The noise level is $\sigma_{\mathrm{rms}} = 0.57$ mK.

Since the GASS covers most of the parts of the ISM around Sco-Cen and it has a higher velocity resolution than EBHIS, it is preferred to be used for the H I analysis of this region in chapter 6.

3.2.3 The HI4PI survey

The EBHIS and GASS data are arranged in a similar way and the resolutions are comparable. Both surveys have been connected to one all-sky survey, the above-mentioned HI4PI survey HI4PI Collaboration et al. (2016). The parameters of the HI4PI survey are listed in table 3.1. While GASS has a higher velocity resolution, the angular resolution of EBHIS is higher. In general, the parameters are limited by the lower limit of the respective parameters of EBHIS and GASS. Hence the angular resolution of HI4PI is 16.2′, the channel width is 1.29 km/s and its velocity resolution is 1.49 km/s. EBHIS has a 30–40% higher σ_{rms} than GASS. But smoothing EBHIS to the angular resolution of GASS and decreasing the spectral resolution of the latter one to match the one of EBHIS yields a lower noise level of ≈ 43 mK independently for both products used for the HI4PI. HI4PI covers velocities with $\left|v_{\mathrm{LSR}}\right| \leq 600$ km/s for the northern part and $\left|v_{\mathrm{LSR}}\right| \leq 470$ km/s for the southern part because of the GASS velocity range limits, since it focussed on higher velocity resolution). The resulting data of this survey are used for detecting expanding H I shells in the local Milky Way in chapter 5 and its parameters become important for the specification of search parameters for the algorithms developed in this work in chapter 4.

The HEALPix grid The requirements for the data are to use a mathematical structure which supports a suitable discretization of functions on a sphere at sufficiently high resolution, and to assure fast and accurate statistical and astrophysical analysis of massive full-sky data sets. That is why the data are gridded into the Hierarchical Equal Area iso-Latitude Pixelization (HEALPix)[3]. This produces a subdivision of a spherical surface in which each pixel covers the same surface area as every other pixel, as suggested in the name[4]. From this basis, the data can be re-gridded into different projections that can be presented in two dimensional maps. The most important projections that are relevant for this thesis are described in section 3.3.1.

[3] HEALpix was originally devised in early 1997 by Krzysztof M.Górski

[4] http://healpix.sourceforge.net

3.3 H I data

In this section the data, data structures and its properties are introduced. In this thesis large scale structures have been investigated and H I data up to high Galactic latitudes have been used (see figures 3.6 and 3.7), where effects due to angular projections are relevant. This is why the relevant coordinate projections and the respective properties are also introduced in section 3.3.1. After that, the general properties like the angular- and spectral intensity distributions of the H I dataset are introduced in section 3.3.2. In section 3.3.3, two dimensional slices of the three dimensional datacubes are presented.

3.3.1 Structure of H I data

In this work, the Galactic coordinate system has been used exclusively. By convention, the Galactic center lies at $l = 0, b = 0$ and the longitude increases from right to the left. The convention 0° to 360° has been used as well as sometimes the one from -180° to $+180^\circ$. On Galactic scales, pixels along the Galactic equator and at velocities of $|v_{\mathrm{lsr}}| \leq 20\,\mathrm{km/s}$ generally contain brightness temperatures in the range of $T_\mathrm{b} = 50 - 200\,\mathrm{K\,km/s}$, with some smaller pixel regions of high absorption, where the brightness temperature can be lower.

The data structure is called **datacube** because it is a three dimensional array of pixels used to describe longitude-latitude maps along the spectral (velocity) dimension and hence is in a cube-like shape. The channel width Δv, i.e. the spacing in which the data are stored was chosen to be smaller than the actual velocity resolution δv[5]. Each pixel contains an H I intensity (or brightness temperature) T_b for a certain channel width. a map containing arrays of pixels with values of T_b along longitudes and latitudes in one velocity bin are called **channel maps** here after and are described in more detail below. If values of T_b of multiple channels are integrated along pixels on a line of sight, i.e. pixels with the same $l - b$ coordinates in a specified velocity range, these maps are called moment0- or integrated maps (sec. 3.3.3). **Spectral maps** are datacube slices where one map contains the angular dimension along one axis and the spectral- or velocity-dimension along the second axis. These maps are perpendicular slices compared to the channel maps.

The data are stored in the Flexible Image Transport System (FITS) format. This is a standard format in astronomy for the interchange of images or other digital arrays. It provides an n-dimensional array, containing the data and the header that describes the structure and coordinate systems of the data array and can contain additional parameters and text in a specified format (Wells et al. 1981).

Coordinate Projections From the variety of projections, the plate carrée (CAR) projection is the one mainly used in this thesis. The **CAR projection** is a rectangular projection. It projects $x = \lambda, y = \phi$ and is equidistant in longitude. Along the equator (see figure 3.5, left hand side), the pixel size is also equidistant in latitude but the pixel size is not constant with rising latitude and has to be corrected by

$$f_{\mathrm{CAR}} = \cos(b) \tag{3.9}$$

where b is the Galactic latitude, to determine the correct area. This can just be done, when $\cos(b)$ is not changing significantly through one pixel, otherwise the full integral has to be calculated.

[5] For the concrete values see also table 3.1 in sec. 3.2.3.

This leads to the effect that for high latitudes near the poles objects are stretched, i.e. distributed to all pixels that are needed to maintain the rectangular shape of the map. One well known example that illustrates this effect is a CAR projection of the earth, where the continents Antarctic and the Arctic stretches along the whole longitude displaying a large area on the map, while in reality being smaller.

There exist other projections and each has advantages and disadvantages in different areas and have to be chosen depending on the task. For example, the **Mollweide** projection (see the all-sky maps of H I in figures 3.6 and 3.7) is an equal-area projection which projects the entire field of view onto an ellipse. The **SFL projection** maintains equal sized pixels over the whole map as can be seen in figure 3.5 on the right hand side. It uses the projection $x = (\lambda - \lambda_0)\cos\phi$, $y = \phi$. Here eq. 3.9 does not have to be applied, since the pixel size is constant. But depending on longitude, the circles are distorted along the equator and hence it is not useful for most cases of this study, since most shells are close to the equator and not close to the poles where the effects of pixel distortion become higher.

The plots and images in all chapters of this thesis are always shown in the CAR projection, if not mentioned otherwise. Equation 3.9 has always been considered when calculating quantities depending on the pixel intensities.

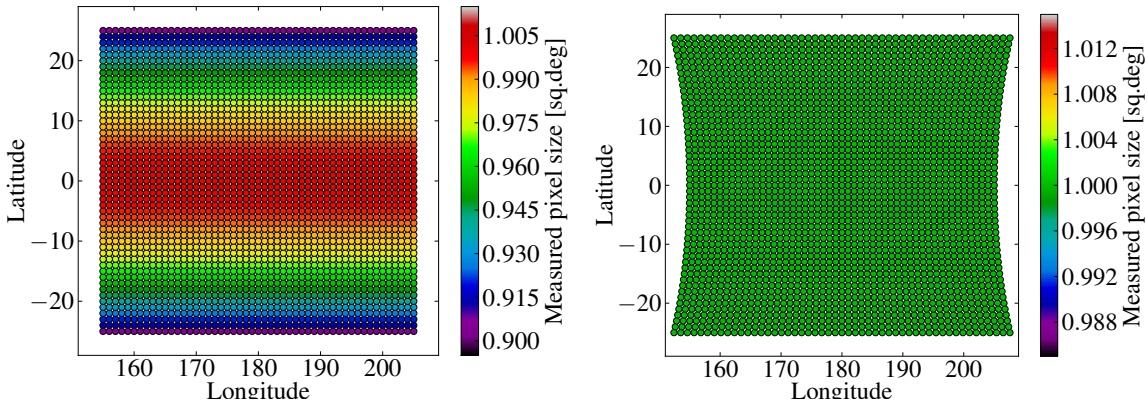

Figure 3.5: Illustration of the change of pixel size per latitude in two different projections. On the left hand side the CAR projection is shown and it can be seen that the pixel size changes with $\cos(b)$. On the right hand side where the SFL projection is used, all pixels have the same size. Credits to Dr. rer. nat. Benjamin Winkel who provided the basic python code to produce these images.

Splits of the full dataset Since the required computational resources to run the algorithms on the whole dataset is more than available, the data is subdivided into four sub datacubes. These cubes overlap by 30° in longitude to ensure that no border effect at the image edge affect analyses and detection of structures. The overlap of 30° was chosen so that each shell with a maximum radius of 20° (sec. 4.5) is detectable in at least one of the neighboring sub-cubes. Each of these sub-cubes has a size of 120°x100°, corresponding to (1440x1200) pixel. Dividing the whole dataset into sub-cubes also reduces the complexity of the data, e.g. the general H I density in the 1st and 4th datacube are much higher than in the 2nd or 3rd cube since the latter ones point away from the Galactic center. The properties of the sub-cubes are listed in table 3.2.

Cube	l_{min} °	l_{max} °	b_{min} °	b_{max} °	V_{min} km/s	V_{max} km/s
1	300	60	-50	50	-150	150
2	30	150	-50	50	-150	150
3	120	240	-50	50	-150	150
4	210	330	-50	50	-150	150

Table 3.2: Minimum- and maximum coordinates l_{min}, l_{max}, b_{min}, b_{max} as well as the minimum- and maximum velocities v_{min} and v_{max} of the four sub-datacubes from the HI4PI survey. For desciption of the usage see text here and section 4.5.

3.3.2 Global properties of Galactic H I in datacubes

As a first inside, two all-sky maps from the HI4PI survey are shown in figures 3.6 and 3.7. In the first figure, the total H I column density is plotted on a logarithmic scale in a Mollweide projection with color coded intensities. In this plot, global H I distributions such as the warp and flaring (Henderson et al. 1982; Levine et al. 2008; Kalberla & Kerp 2009) of the MW-disk can be seen but also smaller structures. Especially at higher latitudes, where the general column density is much lower compared to the disk, filaments and loops can be seen. These are also present at low latitudes but not visible in these integrated maps. When looking at single channel maps, or smaller integration intervals, more structures are revealed and filaments can also be seen in the Galactic disk. Since it is integrated over the full surveyed velocity range, not only MW objects can be seen but also halo objects as well as extragalactic objects like the Small Magellanic Cloud ($l = 302.8^\circ, b = -44.3^\circ$), the Large Margellanic Cloud ($l = 280.365^\circ, b = -32, 84^\circ$), Andromeda (M31, $l = 121.2^\circ, b = -21.57^\circ$) and M33 ($l = 133.6^\circ, b = -31.3^\circ$). When working with Galactic H I data, especially in the full velocity range these background sources should be considered. This is however not the case for this study, since the velocity range of interest is -150 to +150 km/s as described below. Some of the mentioned sources are more visual on a similar plot in figure 3.7, which shows the velocity distribution together with the H I column density. In this plot, the main difference is an additional dimension in the colorbar, including the velocity information. This weighting visualizes the spiral arms in colors and shows which structures are approaching the Sun and which ones are moving away.

Relevant regions and spectral ranges On top of what has been shown above, not only global features like spiral arms and the Galactic disk in general, also local large scale features dominate the H I column densities, especially at velocities $|V_{LoS}| < 10$ km/s (e.g. ScoCen- or Orion H I features). Intensive Galactic features are mainly found at $v_{LoS} \leq |150|$ km/s.

The general intensity distribution along the latitude axis is presented in the following. The mean intensities of each velocity bin in the range of $-150 \leq v_{Rad} \leq +150$ km/s are shown in the left panel of figure 3.8, with arrows highlighting the maximum intensities of each velocity bin. The mean intensity of each velocity bin is plotted for the full longitude range at fixed latitudes between $-50^\circ \leq b \leq +50^\circ$ in the right panel of the figure. The mean intensity for the whole $l - b$ angular range, ranges from $I_{mean,0} = 20.681$ K km/s at zero velocity down to $I_{mean,150} = 0.024$ K km/s at velocities of 150 km/s, which is the sensitivity level of the survey. There is an asymmetry between intensities at positive and negative velocities. The mean intensity at negative velocity channels is higher than the one of positive velocity channels.

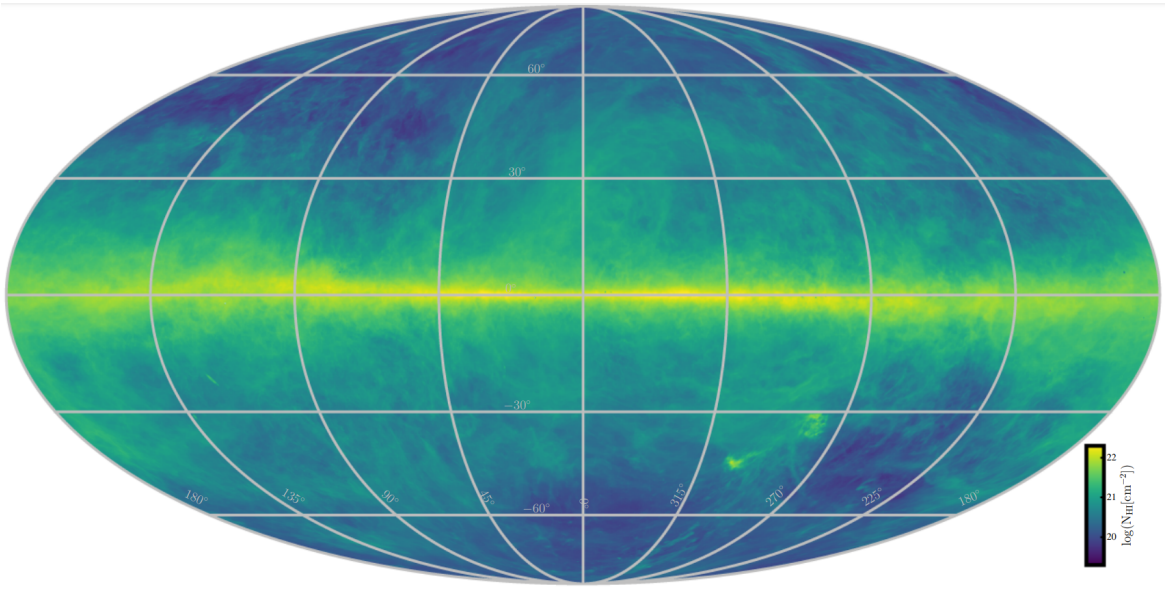

Figure 3.6: All-sky map of H I in the Mollweide projection. Figure adopted from HI4PI Collaboration et al. (2016)

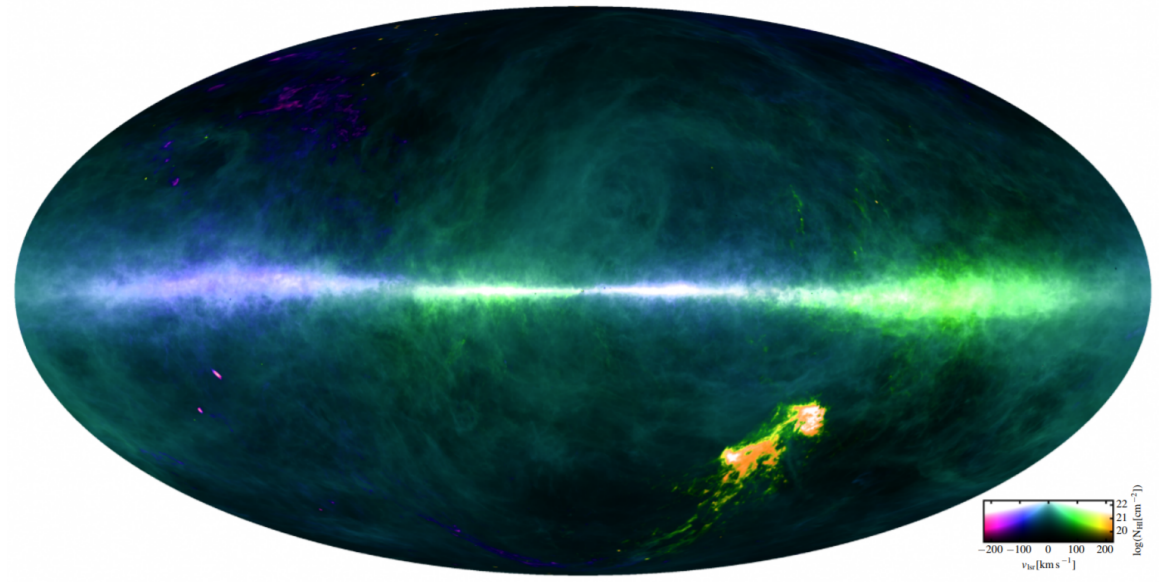

Figure 3.7: All-sky composite map of the H I column density and the intensity-weighted radial velocities in the Mollweide projection. On the bottom right of the plot, the color pattern for the radial velocities and column densities are shown. In general, low intensities are darker hues and negative velocities are in the range of blue to violet, while positive velocities are green to red. For more information see text. Figure adopted from HI4PI Collaboration et al. (2016)

The intensity along the latitude and longitude per channel follows the Galactic disk and the spiral arms. High intensities at high latitudes are observed at low velocities, corresponding to local large scale features and overlapping emissions from the Galactic plane. Extragalactic sources like the Andromeda galaxy ($V_{0,\,\mathrm{mean}} \approx 300 \pm 4$ km/s) and the LMC ($V_{0,\,\mathrm{mean}} \approx 278 \pm 2$ km/s) are present in higher velocity channels and hence are outside of the range of relevant velocity channels for this thesis. The SMC however is located at ($V_{\mathrm{Rad}} \approx 158 \pm 4$ km/s) and can potentially be a background source.

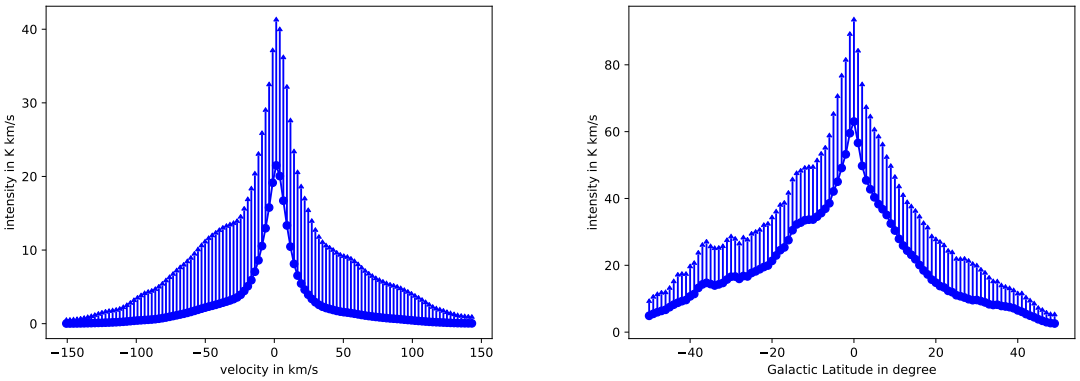

Figure 3.8: Two plots of distributions along different axes. On the left hand side, the mean intensity in each channel map from -150 km/s to +150 km/s is shown. The minimum mean channel intensities lie at the highest abstract velocity bins and the highest mean intensities are at velocities near 0 km/s. On the left hand side, the mean intensities along the longitude for different latitudes between -50° to +50° are plotted for the 0 km/s velocity channel, exemplary for all channels. The intensities increase towards the Galactic disk, i.e. $b = 0°$ and decrease towards the Galactic poles. For an interpretation see text.

Since most of the features are visible at low latitudes, the CAR-projection, introduced above (sec 3.3.1, is a good choice for the data analysis. The distortion of objects becomes higher with rising $|b|$. At higher latitudes, the signal to noise ratio is also lower as shown in figure 3.8 on the right panel, plus the expected presence for SNR is low since they are the outcome of young massive stars, exploding in dense star forming regions in the spiral arms.

3.3.3 Two dimensional slices of H I

Many investigated regions contain three dimensional complex structures in a turbulent background environment. But in the H I datacubes, the third dimension (velocity / frequency) is not a spatial dimension. Hence the visualization of shells in H I datacubes is not intuitive. Analyses are often reduced to one- or two dimensional slices through a datacube to trace the properties of the ISM. In the following it is explained how commonly two dimensional slices of datacubes are used to analyse H I data.

General H I properties in longitude and latitude

As introduced in section 3.2.3, the bin width of one channel map in the HI4PI survey is 1.25 km/s. Hence in a channel map, the received emission lines from hydrogen atoms of this velocity intervals are stored. On Galactic scales, due to the rotation of the Milky Way gas, these structures often also

denote the same spatial distance. However, this is not generally the case, since structures of all regions can have overlapping velocities and be potentially present in the same bin. This is why in the direction of the Galactic center, the emission is so high in each channel map. How to determine the distance towards H I is discussed further below in section 3.5. In case of an almost uniformly moving structure, the structure should be visible in a small number of channel maps. If a structure is expanding, the number of channels (velocity bins), where it is present is proportional to the expansion velocity of the object. It is often useful to investigate individual velocity slices maps to trace the kinematics or single channel maps to investigate two dimensional structures. One example of a channel map is shown in figure 3.9 in the right panel. In this plot, one part of the Galactic disk is seen as well as some higher latitude structures. one specific ellipse-like feature, containing also sub-structures itself, can be seen with the center at approximately $l = 308^\circ$, $b = 4^\circ$, and an extent of $l = 320 - 395^\circ$ and $b = -5 - 12^\circ$ in this image[6]. This feature is an ISM structure of the region around the Scorpius Centaurus OB association and belongs to the LCC-loop. The LCC-loop is special, since almost no expansion was observed in the literature, giving it its partial name "loop". This feature is analyzed in detail in chapter 6. As can be seen, the high latitude structures are less intense, barely visible and contain lower brightness temperatures compared to the features in or near the Galactic disk.

This is due to the choice of the colorbar range. In the left panel of figure 3.9, the same channel map is shown in a different colorbar range. If compared to the right panel, now the structures at the edges and outside the Galactic disk at high latitudes are clearly visible (e.g. the cloud at approximately $b_{\mathrm{mean}} = 55^\circ$ and $l_{\mathrm{mean}} = 285^\circ$). On the other hand, the inner structures in the Galactic disk cannot be seen anymore and if viewing this channel map, the loop might be missed. This shows how deceiving visual investigations of H I data can be and highlights the importance of a detailed analysis and the application of objective methods.

To derive the physical quantity, the column density, from the measured brightness temperature T_{B} that are given in H I datacubes and also to highlight features from the background that extend over multiple velocity channels, the above mentioned integrated maps are useful and hence its compilation is explained in the following.

Integrated maps Given multiple channel maps, the intensities of the pixels along one LoS in the defined velocity range are summed up to derive the zero moment maps, or as it will be called in this thesis, **integrated maps**:

$$M_0 = \Delta v \sum_i I_{\mathrm{b}}(v) \tag{3.10}$$

where $I_{\mathrm{b}}(v)$ is the intensity at the velocity v. This integration is useful because the total column density along a spectral axis is calculated for each pixel of the resulting integrated map, which directly gives access to the mass of the H I cloud.

Whether investigating integrated maps is useful, depends on the use case. When having observing low intensity features with high velocity dispersion, higher signal to noise ratios can be achieved by producing integrated maps but on the other hand sub-features of smaller velocity intervals could vanish (visually) or different clouds could be merged and cannot be distinguished from another since

[6] The visualization depends on the choice of the colorbar range. Hence, depending on the region, the colorbar range needs to be adjusted to ensure high visibility of the structure. This is also the case for detection algorithms, where the parameters need to be adjusted, depending on the region, which will be a topic in section 4.5

the velocity information is lost.

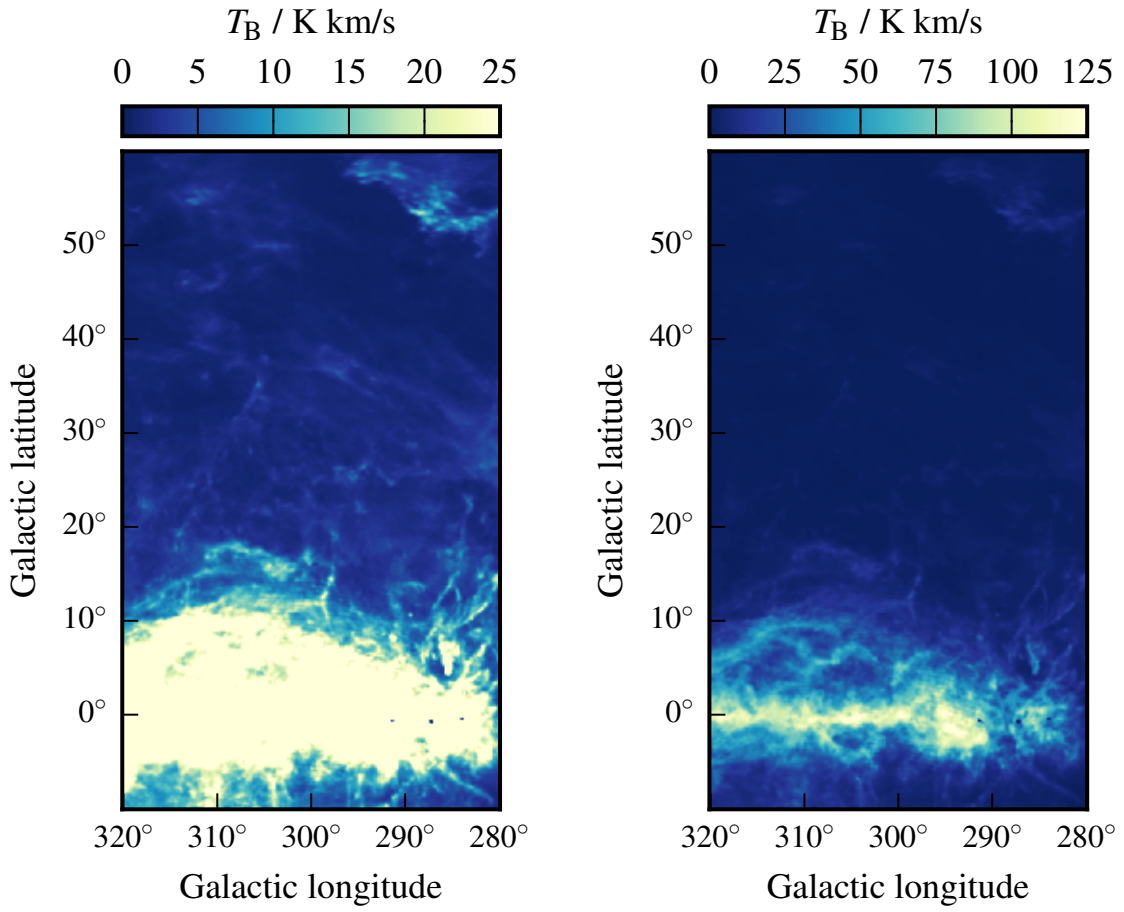

Figure 3.9: Two plots of the same segment of the GASS H I data in two different color ranges. On the left hand side, the region is shown in the color range of 0 to 25 K km/s and on the right hand plot, the color range is 0 to 125 K km/s. For more information, see text.

General H I properties in position–velocity slices

The perpendicular slice, compared to a channel map, in a datacube contains one Galactic coordinate axis as well as the spectral axis and is called **spectral map** or **position-velocity map** or pv-map hereafter. Exemplary, one pv–map is shown in figure 3.10. It shows a slice at $b = 25^\circ$ in the range of approximately 325°–8° in longitude. Since the spectral axis contains much less pixels than both angular axes, the pixel width along the spectral is chosen wider for visualization.

The main emission is located at velocities around 5 ± 5 km/s. Patterns can be seen especially at negative velocities. For example at $l = 330^\circ$ an H I cloud at -5 km/s can be seen that is separated from the main emission. In general, it is less intuitive to connect structures in pv-maps with three dimensional structures than it is for channel maps. This is why in the following, the visualization of expanding shells in datacubes are discussed in more detail.

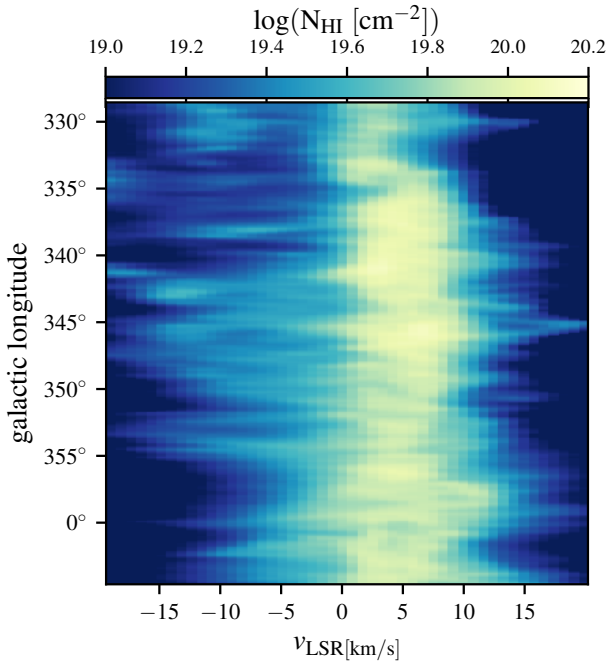

Figure 3.10: Position-velocity plot of a region in the Sco-Cen OB Association, where the longitude is plotted against the LSR velocity (v_{LSR}) for a slice at $b = 25^{\circ}$. The pixel size along the spectral axis is chosen to be larger compared to the one in angular direction for better visualization. The color bar denotes the logarithm of the column density $\log(N_{\mathrm{H\,I}})$ (sec. 3.5.2).

3.4 Properties of expanding shells in H I datacubes

Building up on the general introduction of SNRs from section 2.4 and the the general properties of H I from above, the visualization of expanding shells and their properties in H I data structures are described. For this again, the datacube is sliced into two dimensional maps and the properties and visualization of SNRs in channel- and spectral-maps are explained here.

3.4.1 Properties of expanding shells in channel maps

Analytical models suggest that the expanding shells in the ISM, that are formed by OB stars, are approximately spherical (sec. 2.4). Numerical simulations also show that even for multiple stars exploding in a wind driven bubble, after merging of the sub-bubbles of each star, the general shape is still sphere-like (Krause et al. 2013). Also according to simulations of van Marle, A. J. et al. (2012) and Van Marle et al. (2015), if two bubbles are separated and they merge into each other, the resulting bubble is aspherical but reaches an approximative isotropy after a few Myr. Hence from a theoretical view, it is expected to observe mostly spherical shell-like SNRs, as long as the decay at the latest stages of their evolution did not begin.

On the other hand most observed H I shells, especially older shells, are not spherical but show ellipsoid-like or arc-like structures and contain density gradients towards higher distances from the Galactic plane (e.g. Orion Eridanus Bubble, UCL). Therefore it has always to be considered that the shape of a supernova remnant may deviate from a perfect spherical structure and in many cases also not be fully engulfed by a fully closed shell.

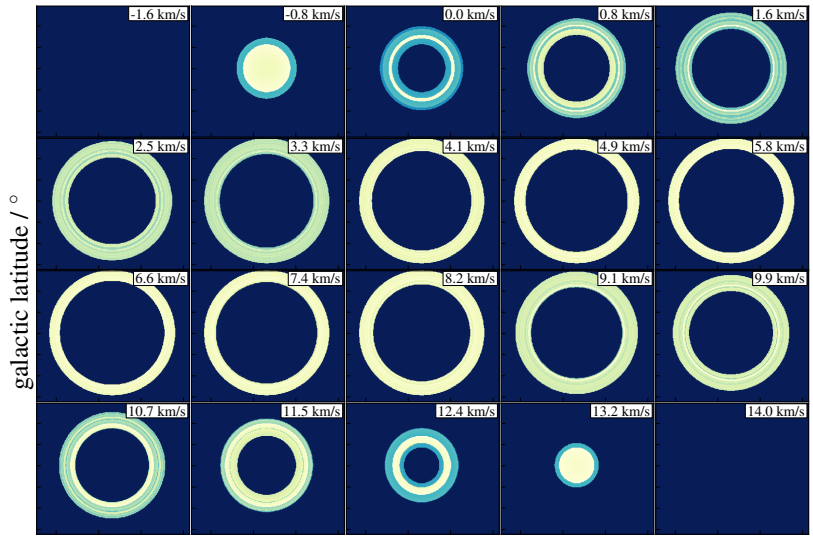

Figure 3.11: Modelled H I emission of an ideal and symmetric SNR with a center velocity $v_0 = 6$ km/s and an expansion velocity $v_{exp} = 7$ km/s. The different images show the H I emission in individual velocity channels as given at the top right of each of the 20 subplots. For a more detailed description see text.

According to theoretical models (e.g. Weaver et al. (1977), Kafatos et al. (1980)), an expanding shell in a simplified environment without background intensities, would have the properties as shown

in figure 3.11. The figure consists of 20 subplots, one for each velocity channel of the sequence in the chosen velocity range from -1.6 km/s to +14 km/s. The velocity channels are binned to 0.8 km/s in consensus with the resolution of GASS. The shell has an arbitrary angular size (no axes) at a chosen center velocity v_0 = 6 km/s and a thickness of 20% relative to the radius of the outer edge of the shell. This shell is visible in the channels from -0.8 to 13.2 km/s, which is due to its expansion velocity of 7 km/s. At the velocity channel -0.8 km/s, the disk-like cap (the front) of the approaching part of the shell can be seen. In the subsequent channels there are rings of increasing angular sizes where the largest one is at the center point, where the expansion of the shell is perpendicular to the line of sight. In the subsequent channel maps, the size of the rings of the receding parts decreases until, just the cap of the receding side can be seen as a disk-like structure at +13.2 km/s. Due to the chosen isotropic expansion velocity of the shell, the distribution would be fully symmetric in a high resolution datacube. But velocity binning effects make the shell appear not fully symmetric. The intensities belonging to certain velocities are binned into the nearest channel and this causes visual effects for some edge cases. Here the caps of the approaching side have a different size appearance than the one from the receding side as can be seen in figure 3.11 in the channel maps of lowest and highest velocity where the shell is seen[7].

The change of the radius of the rings in consecutive channel maps only depends on the expansion velocity. The maximum change of the radius per velocity bin is discussed in section 4.5.2.

In addition to the already mentioned reasons, projection effects depending on the projection choice (sec. 3.3.1) can also distort the shape of structures of large angular size. This is why famous objects at high latitude, like the upper part of the UCL-shell and the North Polar Spur (sec. 2.2.2) appear elongated. For the analysis of the UCL-shell in chapter 6, these effects will be taken into account.

The USco-loop (sec. 2.5 and chapter 6), which is one of the most prominent circular structures in H I highlights multiple properties of observed SNRs and is presented in figure 3.12. In the figure, 9 consecutive channel-maps, where the USco-loop is present are shown[8].

At channel maps of $v_{\mathrm{rad}} > 2.5$ km/s, a ring-like (or loop-like, like the name suggests) structure can be seen. At lower positive- and higher negative velocities the structure nearly vanishes and the plots are dominated by a mixture of shell fragments and overlapping emissions from other sources. Some are likely to stem from the H I reservoirs of the Aquila rift (Dame et al. 2001), the Gum nebula (Reynoso & Dubner 1997) and other nearby sources. Also a column density gradient of the loop towards higher latitudes, i.e. away from the Galactic disk, is clearly visible. The thickness of the loop is about 20% of its total radius, at the channel map where the loop has the largest radius. The Usco-loop also seems to be asymmetric in the spectral dimension since it shows almost no emission and especially no receding cap at more positive velocities. There is also a smaller loop contained in the Usco-loop. To conclude, it can be seen that real SNRs are complex structures, partly symmetric but do not have to be closed, nor homogeneous and can consist of embedded features.

[7] The uncertainties due to binning, set the minimum possible uncertainties for the velocity.

[8] Here the GASS-data were used, since it has a higher spectral resolution (1 km/s compared to 1.25 km/s) than the HI4PI survey

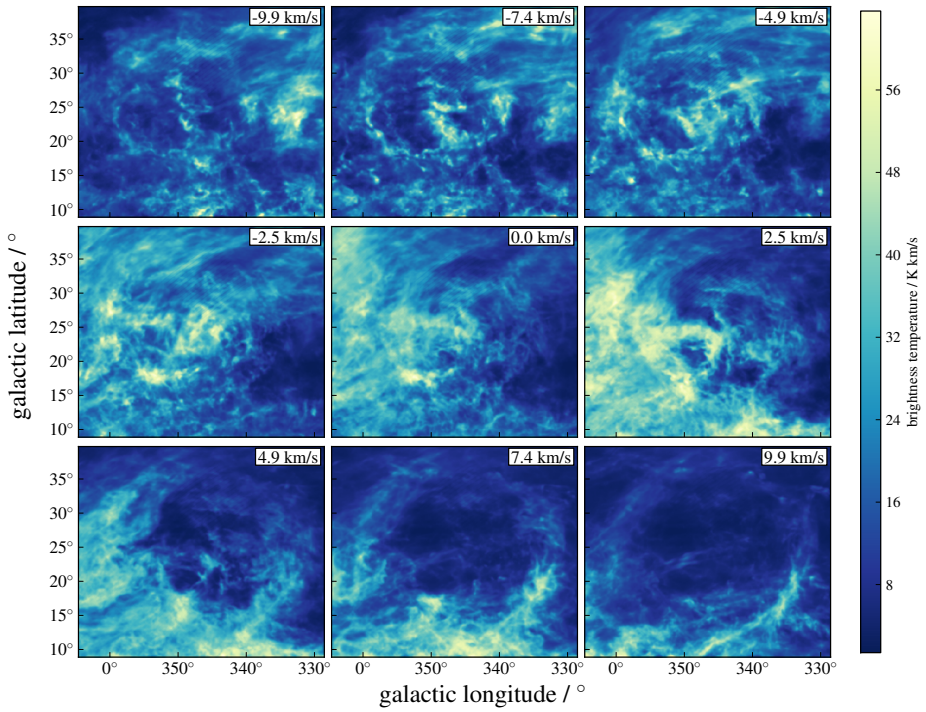

Figure 3.12: The ISM in the vicinity of the Upper Scorpius stellar cluster. The color marks the H I column density. The subplots are consecutive velocity channel maps with rising velocities from the top left to the bottom right.

3.4.2 Properties of expanding shells in the spectral slices

After understanding the properties of SNRs in channel maps, the perpendicular slice of a SNR in spectral-maps (sec. 3.3.3) is introduced. The visualization of the idealized description from above is taken up again and shown in figure 3.13, where 21 longitude-velocity slices for rising Galactic latitudes from the top left to the bottom right of the figure are shown. In general, the shells appear as ellipses, except for the slices of maximum- and minimum longitude where the velocity differences are too small to be resolved and all information is contained in one velocity bin. These features are the approaching- and the receding caps of the shell that are visible as disks in the representative channel maps (see figure 3.12). For an ideal spherical shell that is expanding homogeneously, the shapes in $l - v$ and $b - v$ are identical. If this symmetry cannot be assumed, both slices should be considered when investigating the data. The elliptical shape appears to be truncated at the lowest and highest longitudes. This is due to the binning along the longitude. Each pixel has a bin width of 0.08° , similar to the one observed for spectral binning of the channel maps that was explained above. Since the number of pixels along the spectral axis is much lower than the angular one, due to the small expansion velocities, the binning effects are visible along the radial velocity axes of the plots. In extreme cases, where the expansion velocity is not resolvable, the expanding shell would appear as a line, perpendicular towards the Galactic longitude in one of the slices of figure 3.12. And it would appear as a disk in a single channel map and hence in this case it is not possible to distinguish three dimensional shells from disks in H I.

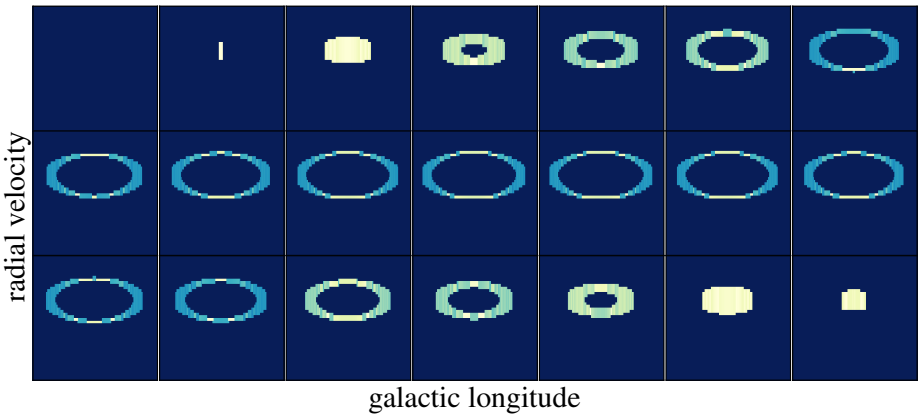

Figure 3.13: Sequence of spectral-maps (position-velocity maps) of an expanding shell of arbitrary angular radius and density in a datacube. Each plot shows an individual latitude slice with increasing latitude from the top left to the bottom right, covering the full latitude range of the SNR.

Spectral lines through the center of expanding supernova remnants

Properties of expanding shells can also be determined in 1D−slices (spectral-lines). An expanding shell embedded into the ISM shows peaks that are often distinguishable from the general ISM structures and can be determined e.g. by fitting multiple Gaussians line profiles to the data. Exemplary, an homogeneous idealized shell is placed into a real environment and the shell is put into this datacube[9]. There are four subplots showing spectral lines though the center longitude, l_0, of the expanding shell for four different latitudes, b, between the center latitude of the shell, b_0, and the latitude of the inner edge of the shell, $b_0 - r_{\rm in}$. It can be seen that the general ISM has broad lines and that there are distinct peaks, where the shell occurs in the center LoS through the center l_0, b_0. For latitudes more far away from the center, the two peaks become broader and merge finally together as visualized in the bottom right panel. This is the one dimensional counterpart to the two dimensional visualization in the channel maps of figure 3.11 and explanations therein. Examples of spectra through the centers of observed H I shells can also be found in figure 4.22.

The actual H I datacubes provide spectral lines, with an effective resolution of 1–1.25 km/s (see section 3.2.3). Gaussian decompositions of H I are standard methods used to analyse the spectrum along one or multiple summarized pixels (e.g. Haud & Kalberla (2007)). One method used in this thesis is the one adopted from Lenz et al. (2014). This method of Multi-component gaussian fitting is described in the following and applied in section 4.7.3 with a combination of sodium observation to determine distances towards the H I features.

Multi-component gaussian fit In order to derive the position of the peak intensities for the H I lines, the H I profiles are approximated by multi Gaussian decompositions. Each Gaussian is defined by three parameters. These are the peak coordinate μ, the standard deviation σ and the amplitude A for

[9] the geometrical EHSS-model that will later be introduced in section 4.2 is used for this.

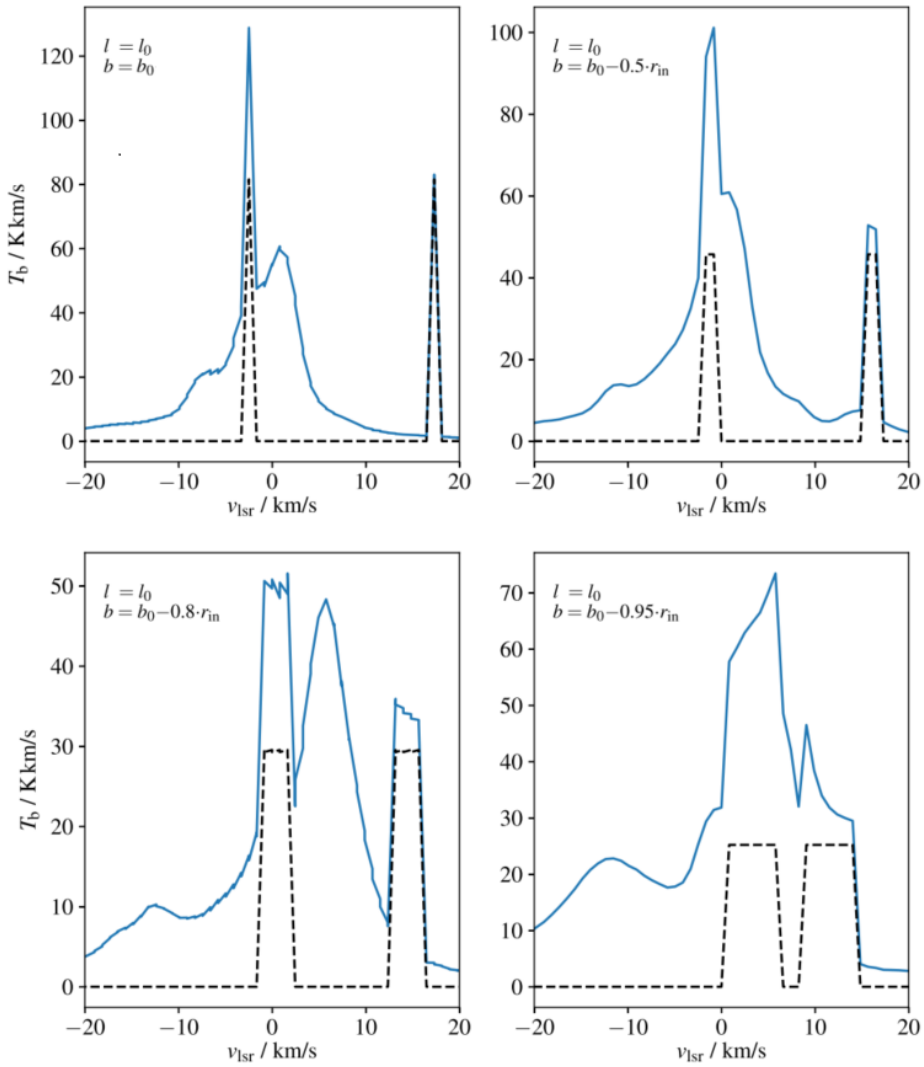

Figure 3.14: Each of the four plots shows one line profile of an expanding shell (produced using the EHSS-model from section 4.2) in real GASS background at center longitude, l_0, and with different latitudes, b, in the range b_0 to 95% of the inner radius r_{in} of the shell (see plot legend). In the plots, the line profile of each modeled shell is marked by the black-dashed line and the shell with background is marked by the blue solid line. For more information about the EHSS-shell parameters see text.

each Gaussian. The total fitted profile $P(x)$, for a given dataset x, is the sum of all Gaussian equations:

$$P(x) = \sum_{i=1}^{n} A_i \cdot (2\pi\sigma_i^2)^{-1/2} \cdot \exp\left(-\frac{x-\mu_i}{2\sigma_i^2}\right). \tag{3.11}$$

In the context of H I, usually one thick gaussian component denotes the Galactic background, other thicker components are the general distribution of the gas of the spiral arms and thinner Gaussian components often denote peaks of smaller-scale features. When analyzing the Sco-Cen region, this composition is determined and presented in section 6.1 and discussed further there.

Basic Peak detection Another, more basic, but also high performance method to derive the local maxima (peaks) and -minima (dips) along the profile has been used for the evaluation of the automated shell search in chapter 5 in section 4.6.3. It searches for values that are surrounded by lower or higher values for maxima and minima respectively. The parameters are the look-ahead-value, which defines the distance to look ahead from a peak candidate to determine if it is an actual peak or not and δ, which defines a minimum difference between a peak (or dip) and the following points. There are no general optimal parameters and the parameters have to be adjusted depending on the data sets. The larger the look-ahead-value is chosen, the higher the duration for the calculation. But if the look-ahead-value is chosen too small, then fluctuations in the ISM might be mismatched with a peak and lead to false positives. On the other hand, if it is chosen too high, local peaks/dips might be overseen. In case of expanding shells in the ISM, the lowest expansion velocities distinguishable from the dispersion of the ISM is about 4 km/s (e.g. Ehlerová & Palouš (2005), Kerp (2009)), meaning that in a sequence of 8 velocity channels (in GASS) two peaks and one dip could be found, the maximum look-ahead-value should not be higher than 2 pixel[10].

3.4.3 Assessment criteria and measurements of H I shell properties

For a first intuition or for checking or validating results of some methods, visually inspecting the H I structures in the datacube using visualization tools is efficient. This is subjective and can lead to misinterpretation or missing detections of features, like explained along the example above in section 3.3.3. Hence in the following, criteria are specified that have to be fulfilled to maintain a certain quality for visual investigations. The following criteria focus on the detection of cavities, which is used as a quality estimator for the results of the automated shell search in section 4.6.3[11].

1.) In one channel map, a region of low density must be surrounded by multiple high density arcs or in the best case a ring- or ellipse-like structure

2.) Visibility of a cavity candidate in multiple subsequent velocity channels (7 for the Sco-Cen region)

[10] This assumption was also tested on known supernova remnants and the value with the minimum false negative rate was chosen, while maintaining also a low false positive rate, which yielded also 2 pixel.

[11] Another method or an addition to these criteria would be to let different people try to detect the shells. This was tested with different persons, but the outcome was that it takes too much prior knowledge and experience with the data to reliably "evaluate" the results by hand. The human error for non specialists in this field was quite high for false detections, as well as missing detections. So larger tests using this approach were avoided.

3.) Comparison between the kinematics of the cavity candidate and the general trend of the ISM in the respective region

4.) Confirmation that the observed visual cavity is not a structure due to random projection effect, e.g. induced by the presence of other nearby clouds

5.) In the special case of Sco-Cen, the cavities have to be close to the coordinates of the Sco-Cen stellar subgroups, or in the best case, are centered near the center coordinates of the subgroups

For these analyses, open source interactive visualization tools like `KVIS` from the `KARMA` toolkit[12] (Gooch 1995) and also SAOImageDS9[13] (Joye & Mandel 2003) are the preferred tools here. The numerous functionalities are not introduced here but detailed descriptions can be found in the references.

[12] The open source KARMA toolkit is available at http://www.atnf.csiro.au/computing/software/karma. (date: 01.10.2016)
[13] The toolkit is available at https://sites.google.com/cfa.harvard.edu/saoimageds9, (date. 31.11.2018)

3.5 Determination of physical quantities from H I data

If the parameters towards an H I cloud, like the position, angular extent and velocity extent are known, physical quantities can be derived either directly from H I data itself or with a combination of H I and other data sources (see sec 4.7.3 for the latter case). The most important quantity to derive is the distance, because the derivation of most other physical quantities is dependent on the distance. But it is also the most challenging task that often comes with high uncertainties as will be one of the major points in chapter 5 and 6.

In the following, first the kinematic distance estimation is introduced in section 3.15. Then an equation to determine the H I column density from H I data is presented in section 3.5.2. If the column density and the distance are known, the mass can be determined, which is described in section 3.5.2.

3.5.1 Kinematic distance estimation

Knowing the rotation curve of the Galaxy, the distance towards H I clouds can be calculated for $R < R_0$, where R is the galactocentric radius of the cloud, and R_0 is the galactocentric radius of the Sun (Roman-Duval et al. 2009). This method is depicted in figure 3.15 and application of basic geometric relations yields:

$$R = R_0 \cdot \sin(l) \cdot \frac{V(r)}{V_r + V_0 \sin(l)} \tag{3.12}$$

where l is the Galactic longitude, $V(r)$ is the radial velocity in respect to the local standard of rest (LSR) and V_0 is the rotation velocity. Then the distance of the cloud in respect to the Sun can be calculated:

$$d = R_0 \cos(l) \pm \sqrt{R^2 - R_0^2 \sin^2(l)}. \tag{3.13}$$

This equation has two solutions, as can also be seen in figure 3.15. One for a cloud more far away than the tangential point and another one for a cloud being closer. These clouds have different velocities but the projected radial velocity is the same, meaning the solution is ambiguous for $R < R_0$, which will become important in section 5.3.

Another geometric approach to determine the rotation curve is adopted from (Brand & Blitz 1993) and their eq. 2:

$$V_r = \left(\frac{\Theta R_0}{R} - \Theta_0 \right) \tag{3.14}$$

where V_r is the observed radial velocity, Θ_0 the velocity of the Sun, R_0 the galactocentric radius of the Sun, R the galactocentric radius of the observed object and Θ its velocity. Θ can be replaced by:

$$\frac{\Theta}{\Theta_0} = a_1 \left(\frac{R}{R_0} \right)^{a_2} + a_3 \tag{3.15}$$

with $a_1 = 1.00767, a_2 = 0.0394, a_3 = 0.00712$ (Brand & Blitz 1993). R can also be expressed by the

distance of the object towards the Sun d:

$$R = \sqrt{d^2 \cos^2 b + R_0^2 - 2R_0 d \cos b \cos l} \tag{3.16}$$

This kinematic distance estimation is applied in section 5.3 to estimate the distance of the objects in the H I shell catalog. While equation 3.12 is applied to shells with $R < R_0$, equation 3.16 is used in the directions of +90° to 270°, where $R > R_0$ is always the case, in consensus with investigations of the literature (Ehlerová & Palouš 2005, 2013).

Local velocity perturbations make the tangential point method inaccurate but it is still the most efficient method for distance estimation without any other indicators in the Milky Way. The uncertainties increase further for higher Galactic latitudes, because at higher latitudes the rotation speed of an object is different. It is also just applicable for distant objects, because for local objects the radial velocity changes due to orbital motion around the Galactic center is equal or smaller than local velocity variations. It should also only be used for objects with a distance towards the Galactic center between 5 kpc$\leq R \leq$ 27.5 kpc since the rotation velocity is, in approximation, the same for objects in this range (e.g. Kalberla & Kerp (2009) and figure 2 therein). Hence the tangential point method is a good estimator on Galactic scale but cannot be applied for arbitrary regions. To achieve more accurate distance estimations and especially to determine the distance to local objects, additional different data sources are needed. The application of additional methods can be helpful in specific cases as will be described later in section 4.7.3.

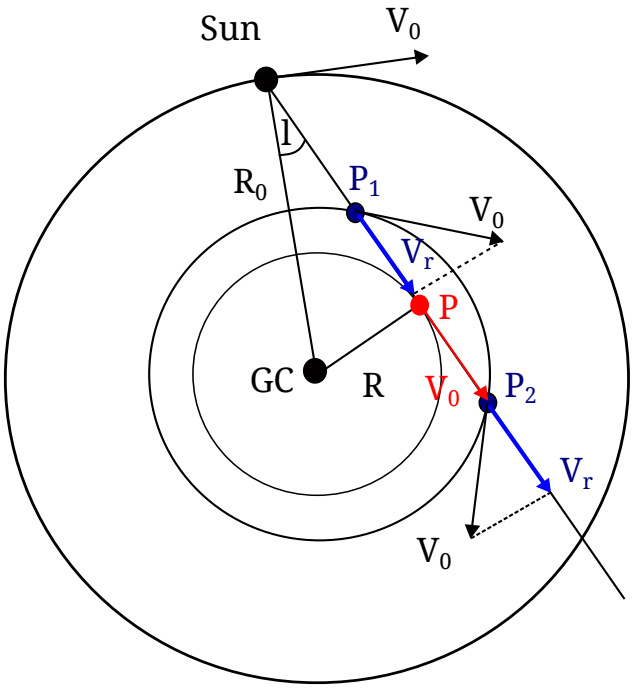

Figure 3.15: Schematic galactocentric plot showing the orbit of the Sun and the one of two clouds at points P_1 and P_2 around the Galactic center (GC). Using the geometric relations in this figure, equations 3.12 and 3.13 can be derived.

3.5.2 Mass determination from H I

When measuring the brightness temperatures T_b in H I, column densities can be derived and hence the mass can be calculated as follows.

H I Column density

With the general definition of the column density of eq 2.2, $N_{\mathrm{H\,I}}$ can be written as

$$N_{\mathrm{H\,I}}[\mathrm{cm^{-2}}] = 1.823 \cdot 10^{18} \int T_{\mathrm{B}} \mathrm{d}v \; [\mathrm{K\,km\,s^{-1}}]. \tag{3.17}$$

The full derivation of the column density is presented in appendix C. Equation 3.17 requires small optical depth, i.e. the opacity has to be much smaller than one, which is generally the case if $N_{\mathrm{H\,I}} < 10^{21}\,\mathrm{cm^{-2}}$ (e.g. Wilson et al. (2012)). If $N_{\mathrm{H\,I}}$ reaches values of $10^{21}\mathrm{cm^{-2}}$, the optical thickness becomes relevant (Braun 2012) and measured column densities are underestimated due to self absorption. .

General H I mass determination

If the distance to a cloud of known angular size is available, the mass can be calculated by integrating the measured column densities over the angular size of the source:

$$M_{\mathrm{H\,I}} = m_{\mathrm{H}} \int_{\mathrm{source}} d^2 N_{\mathrm{H\,I}}(\Theta, \phi) d\Omega \tag{3.18}$$

where m_{H} is the mass of one hydrogen atom, i.e. the mass of one proton in kg. Since the intensities or column densities are binned in the spectral axis of a datacube, a pixel in channel i, contains the column density of channel i, $N_{\mathrm{H\,I},i}$. With $d^2 \tan^2 \alpha$ being the area of a pixel and α being its angular size, the mass is calculated by summing up the $N_{\mathrm{H\,I},i}$ of each spectral bin:

$$M_{\mathrm{H\,I}} = m_{\mathrm{H}} \cdot d^2 \tan^2 \alpha \sum_i N_{\mathrm{H\,I},i} \, \mathrm{d}v. \tag{3.19}$$

This equation is used to determine the masses of the H I clouds and shells in multiple sections of chapter 5 and 6.

Concrete H I mass determination

Based on equation 3.19 from section 3.5.2 and by inserting the parameters of the GASS, the equation

$$M_{\mathrm{H\,I}} = c \left[\frac{\mathrm{cm^2\,M_\odot}}{\mathrm{K\,km\,s^{-1}\,pc^2\,cm^2}} \right] \cdot d^2[\mathrm{pc^2}] \cdot \tan^2 \left(0.08^\circ \cdot \frac{\pi}{180^\circ} \right) \cdot \sum_{\mathrm{i=1}}^{n} T_{\mathrm{b,i}} \, \mathrm{d}v[\mathrm{K\ km/s}] \cdot \cos(b_i) \tag{3.20}$$

is derived, where n is the number of pixels of which the brightness temperatures $T_{b,i}$ are summed up, 0.08° is the length and width of a pixel in a GASS datacube and $\cos(b)$ is the correction for varying pixel size with latitude in the Plate-carée (equirectangular) projection that is used here[14], d is the

[14] Note that this is only valid when b is not changing significantly in the range of one pixel as described in section 3.3.1.

distance towards the H I structure, $T_{\mathrm{b,pix}}$ is the brightness temperature of one pixel and the constant factor c is

$$\begin{aligned} c &= (3.0856 \cdot 10^{18}\,\mathrm{cm\,pc^{-1}})^2 \cdot 1.823 \cdot 10^{18}\mathrm{cm^{-2}\,K^{-1}\,(km/s)^{-1}} \\ &\quad \cdot\ 1.67 \cdot 10^{-27}\mathrm{kg\,M_\odot} \cdot (1.98 \cdot 10^{30}\mathrm{kg})^{-1} \\ &= 0.01467\ \frac{\mathrm{cm^2\,M_\odot}}{\mathrm{K\,km\,s^{-1}\,pc^2\,cm^2}}. \end{aligned} \tag{3.21}$$

This will only yield the H I mass and it is not accounted for the helium- nor molecular hydrogen mass, which are also highly abundant in the ISM and contain large fractions of the total mass. In the following when it is talked about "shell-mass" it is referred to the H I mass of the shell and if the term "total shell-mass" is used when the other components are included if not specifically mentioned differently.

In the literature of H I shell investigations in the vicinity of Sco-Cen, it is assumed that the H_2 mass is equal to the H I mass. The molecular hydrogen mass of the shells is not measured in this work and has to be approximated. Hence the total hydrogen mass of the shell will be estimated to be $2{\cdot}M_{\mathrm{H\,I}}$ for this region to be consistent with the literature and for the sake of comparison (de Geus 1992; Poeppel et al. 2010). The fraction of molecular to atomic hydrogen mass however changes between regions and this ratio has to be considered carefully for global Galactic H I investigations. It will be discussed in the mass determination of detected H I shells and is, apart from the distance uncertainties, a major contributing source of uncertainties for the total shell mass. Also the helium mass, which is generally 25% (see section 2.1) of the total mass of the ISM has to be taken into account. By using $M_{\mathrm{H,tot}} = M_{\mathrm{H_2}} + M_{\mathrm{H\,I}}$ this yields the helium mass

$$M_{\mathrm{He}} = \frac{M_{\mathrm{H,tot}}}{0.75} - M_{\mathrm{H,tot}}. \tag{3.22}$$

Given the masses of all components, the total mass then can be estimated by

$$M_{\mathrm{tot}} = M_{\mathrm{H,tot}} + M_{\mathrm{He}}. \tag{3.23}$$

3.6 Summary

In this chapter the fundamental understanding of the H I data has been built up. The survey properties that define the resolution of the H I data, used in this thesis, have been introduced. These parameters are important for the analysis of H I structures. The three dimensional structure of H I datacubes and their properties have been explained. The general properties of the ISM in datacubes have been introduced and subsequently, the properties of expanding H I shells therein have been explained along idealized theoretical visualizations and real examples. Investigation strategies for visually analyzing datacubes have been discussed. Finally the derivation of physical quantities from H I data have been described.

The methods developed and described in the following chapter build up on the learned properties of the H I data of this chapter.

CHAPTER 4

Approaches to H I data analysis

In this chapter it is presented how algorithms, methods and models have been developed, tested and applied to H I data to detect shells and to determine their properties. This has been achieved by using the gained knowledge from the previous chapters about the properties of expanding shells in general as well as their characteristics in H I measurements. This chapter is the longest read in this work since it is the backbone for both, the analysis of expanding shells in the local Milky Way of chapter 5 as well as for the analysis of Scorpius-Centaurus in chapter 6.

Pattern recognition methods and relations to detect structures in datacubes are introduced (sec. 4.1). A geometric model has been developed (sec. 4.2) and has been fitted to synthetic test data as well as well-constrained cases in H I data (sec. 4.3), also addressing the background treatment (sec. 4.4).

An algorithm to detect H I shells has been developed by combining the pattern recognition methods to a search algorithm for expanding H I shells along the Galactic plane up to absolute latitudes of 50° (sec. 4.5). The application of the algorithm to the data of the HI4PI survey is presented in section 4.6. With a combination of visual confirmation and automated methods, a ranking of the detected shells has been derived.

Since the distance determination is a mandatory part to determine the physical parameters of the shells, methods to determine the distance towards local H I shells are introduced in section 4.7. Finally the chapter is summarized in section 4.8.

4.1 Pattern recognition in two dimensions

A spherical expanding shell is represented by rings in the majority of the channel maps in H I datacubes where it is present (sec. 3.4). A thick ring can be described by five parameters which are the following:

1. the x-coordinate x_0 of the center pixel of the ring in units of pixels
2. the y-coordinate y_0 of the center pixel of the ring in units of pixels
3. the radius to the inner edge of the ring $r_{\rm in}$ in units of pixels
4. the thickness of the ring Δr in units of pixels
5. the brightness temperature in units of km/s of the shell $I_{\rm shell}$

This parameterization is called the Ring-model hereafter. The values in each pixel are intensities (H I brightness temperatures) for each pixel, $I(\mathrm{pix}_i)$, of a channel map. $I(\mathrm{pix}_i)$, with $i = 1, ..., n$ and n is the total number of pixels, is then described by the following equation:

$$I(\mathrm{pix}_i(x,y)) = \begin{cases} I_{\rm ring} & \text{if } r_{\rm in} \leq \sqrt{(x_i - x_0)^2 + (y_i - y_0)^2} \leq (r_{\rm in} + \Delta r) \\ 0 & \text{otherwise} \end{cases} \tag{4.1}$$

4.1.1 Edge detection methods

The approach of this work to detect shells is to first detect its cavities. To detect these, first the inner edges of the shell have to be detected. This is achieved e.g. by searching for high density gradients in local regions.

Two edge detection methods have been used. These are the "Canny algorithm" (CA) or Canny edge detection (Canny 1986) and a specialized combination of parts of the CA and Otsu's method (Otsu (1979)). In the first step data preprocessing has to be considered.

Preprocessing for detection methods

Edges in the context of H I are considered brightness temperature variations. Smaller variations in brightness temperature can also be produced by noise and potentially lead to false edge detection and hence as another preprocessing step, a Gaussian filter is applied to the data to reduce the noise[1]. Since an image or, in the case of H I a channel- or spectral map (section 3.3) is two dimensional, this filter is the product of two Gaussian functions, one is smoothing in the x- and another one in y-direction

$$h(x,y) = \frac{1}{2\pi\sigma_{\rm sm}^2} \, \mathrm{e}^{-\frac{x^2+y^2}{2\sigma_{\rm sm}^2}} \tag{4.2}$$

with the standard deviation $\sigma_{\rm sm}$. H I data contain noise values of 0.05–0.07 K km/s (sec. 3.2) and maximum intensities of up to 150 K km/s in single channel maps. For these data, the parameters of the Gaussian filter have to be determined, often empirically, in order to not remove thin and small edges.

[1] For edge detection algorithms it is necessary that the images are in grayscale. This is already the case for H I datacubes. But for other formats like RGB-images a conversion is necessary.

This is why, when no a priori knowledge about an region to analyze is given, it can be better to not use a gaussian filter at all. Hence whenever an edge detection is applied in this work, it is explained which preprocessing is applied.

Canny edge detection

The Canny edge detection uses the partial derivations in x- and y-direction of an image to calculate the intensity gradient of one pixel. To achieve this for the whole image, the Sobel operator (Sobel 2014) is applied. It consists of two operators of odd kernel sizes that calculate the gradients of a pixel in x- and y-direction separately and convolves the results to determine the absolute magnitude:

$$S = \sqrt{S_x^2 + S_y^2} \tag{4.3}$$

and gives the angular direction of the gradient by

$$\Theta = \text{atan2}\left(\frac{S_y}{S_x}\right). \tag{4.4}$$

The result is rounded to the vertical, horizontal and the two diagonal values of 0 °,45 °, 90° and 135° since one pixel has eight neighboring pixels. The resulting edge candidates are thinned afterwards by a non-maximum suppression where the strength T_i of an edge pixel i is compared to the strengths of the edge pixels in positive and negative gradient directions. If the strength of the current pixel is the largest, it is preserved as an edge pixel, otherwise suppressed. The results of S_x and S_y with the kernel sizes of 3, 5 and 7 have been applied to a dataset and are shown in figure B.0.21 in the appendix.

Hysteresis In the final step of the Canny edge detection, a double threshold is applied to the edge image. With the lower threshold T_{low} and the upper threshold T_{up}, the following three cases are possible for the edge strength T_i of a pixel i:

$$T_i \geq T_{\text{up}} \tag{4.5}$$

$$T_{\text{up}} > T_i \geq T_{\text{low}} \tag{4.6}$$

$$T_{\text{low}} > T_i \tag{4.7}$$

If relation 4.5 is fulfilled, the pixel is accepted as an edge pixel. In the case of relation 4.6, the pixel is accepted if it is connected to another pixel that fulfills case 4.5 and rejected otherwise. For the third relation 4.7, the pixel is always rejected.

Otsu's method

One well established method to automatically determine the edge thresholds in images is the one by Otsu (1979). The core algorithm computes the histogram, containing of N bins, of an image and separates it into two clusters with a threshold $t \in [0, 255]$ (grayscale-values) that is determined by minimization of the weighted variance

$$\sigma_\omega^2(t) = \omega_1(t)\sigma_1^2(t) + \omega_2(t)\sigma_2^2(t) \tag{4.8}$$

where $\omega_1(t)$ and $\omega_2(t)$ are the probabilities of the two classes and σ_1 and σ_2 are the respective variances. From the N bins and the probability of occurrence $p(i)$, the $\omega_1(t)$ and $\omega_2(t)$ can be computed as follows:

$$\omega_1(t) = \sum_{i=0}^{t-1} p(i) \tag{4.9}$$

$$\omega_2(t) = \sum_{i=t}^{N} p(i). \tag{4.10}$$

Minimizing the intra-class variance is equivalent to maximizing the inter-class variance and with $\omega_1\mu_1 + \omega_2\mu_2 = \mu_{\text{tot}}$, where μ_{tot} is the total mean value and $\mu_1(t)$ and $\mu_2(t)$ are the mean values of the two separation classes and with $\omega_1 + \omega_2 = 1$ this yields:

$$\sigma_b^2(t) = \omega_1(\mu_1 - \mu_{\text{tot}})^2 + \omega_2(\mu_2 - \mu_{\text{tot}})^2 = \omega_1(t)\omega_2(t)\left(\mu_1(t) - \mu_2(t)\right)^2 \tag{4.11}$$

Practically this is realized by starting with the initial values $\omega_i(0), \mu_i(0)$ and by iterating over all possible thresholds $t = 0, \ldots, t = I_{\text{max}}$ where I_{max} is the maximum intensity. In each step ω_i and μ_i are updated and the between-class variance value $\omega_b^2(t)$ is calculated until the maximum value is found. The complete derivation can be found in Otsu (1979) and further testing e.g. in Lee et al. (1990).

Customized edge detection algorithm

It is taken advantage of the strengths of the above introduced methods by combining them. No Gaussian smoothing is applied to the data in advance for this method. In the first step as for the Canny edge detection of section 4.1.1, the Sobel-Operators S_x and S_y are applied to the H I data but using a kernel size of 5 as derived by testing (see e.g. figure B.0.21 in appendix) and also commonly used as an improvement of the standard 3×3 Sobel operator to reduce noise as has been derived here but also published by Ye et al. (2011).

This results in two gradient images G_x and G_y on which a combined threshold of Otsu- and a simple binary-thresholding are applied respectively, which results again in two binary images B_x and B_y, which are combined by using the maximum values of both results and hence leaving out non-maximum suppression. This approach is the result of multiple tests of combinations of methods. By not using the non-maximum suppression a high number of edge-pixels at similar locations can be found, which is often not wanted in classic images with well defined edges but is actually the case in observed H I environments, i.e. gradients are distributed along, sometimes, hundreds of pixel. After doing additional research, it turned out that a similar approach has also been used by Ofir et al. (2017). In the following section 4.1.1, some exemplary results of the testing of the edge detection methods are presented and the importance of parameter choice for a low false detection rate and a low false negative rate of edge pixels is highlighted.

Testing the edge detection methods

The performance of edge detection methods is more robust if the intensity gradients at the edge pixel of objects can be limited in advance. This can be achieved by visually investigating the properties of an investigated region of an image in advance. To make the algorithm applicable on any images

without detailed prior knowledge about the intensity variations, automated thresholding methods like the above introduced method Otsu-thresholding should be used. The most basic automated method that is well established in classic thresholding is to use values around the mean intensity of the image as lower and higher threshold to separate objects from background noise (Umbaugh 2017), which is always a compromise between losing edge pixel and detecting false positives as edge pixels for regions in an image that don't represent the general intensity spread. Also the choice of the Gaussian smoothing kernel σ is crucial for the outcome of the edge detection as was mentioned above and will be shown in the following.

From the tests, two example test sets are presented here as shown in figure 4.1. On the left hand side a channel map of a synthetic dataset is plotted, which has been produced by using the EHSS-model that will be introduced in section 4.2. In this image 6 rings of different radii, thicknesses, center coordinates and brightness temperatures can be seen. These are just two dimensional slices of the full shells produced by the EHSS-model. The rings are embedded into a random noise environment between $0 - 1$ K km/s. The shells, i.e. the rings in the channel maps don't contain random noise, but noise due to the rounding that is done when binning the data. Since they are important for the parameter choice, the concrete brightness temperatures of the rings are listed, which are 6.7–8.2 K km/s for the top left ring, $3.8 - 4.06$ K km/s for the bottom left ring, 2.78 K km/s for the bottom right ring, $9 - 10.4$ K km/s for the top right ring, $7.8 - 8.0$ K km/s for the center left one and $9.3 - 8.86$ K km/s for the center right one. On the right hand side, a channel map of a real expanding shell, the USco-loop (see chapter 6), is shown. On these two datasets, the Canny-edge detection is tested.

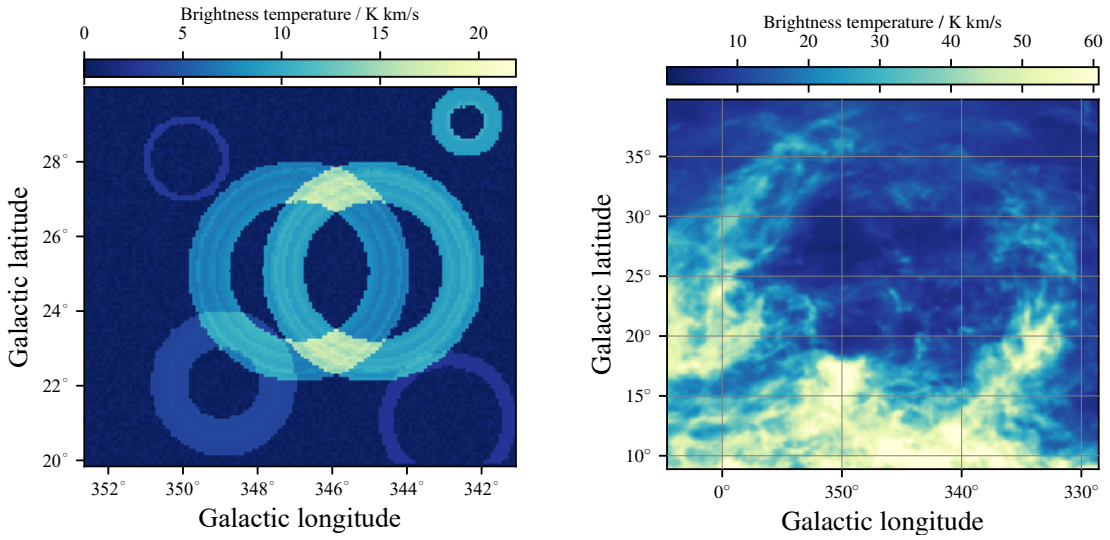

Figure 4.1: Two plots of test-data used for testing the edge detection algorithms. On the left hand side, synthetic data including 6 rings on a grid of 368x449 pixels is shown. The brightness temperature is color-coded and the rings are embedded into a random noise environment of 0-1 K,km/s. On the right hand side of the figure, a channel map at the radial velocity $v_{\mathrm{rad}} = 9.07$ km/s is shown and the fragments of the Upper Scorpius-loop (sec. 2.5) can be seen. For more information about the application of the canny edge detection see text and figures 4.2 and 4.3.

Canny thresholds The Canny edge detection has been applied for different configurations to the synthetic test dataset that is shown in the left panel of figure 4.1. By looping over the three parameters of the Canny edge detection with $\sigma \in \{0, 1, ..., 7\}$, $T_l \in \{0, 1, ..., 10\}$ K km/s, $T_h \in \{0, 1, ..., 15\}$ K km/s and the restriction that the lower threshold T_l is smaller or equal to the higher threshold T_h the results have been produced. 9 exemplary results are shown in figure 4.2 to highlight the importance of the correct parameter specifications.

In the top row there are three panels where, $\sigma = 0$, hence no smoothing was applied and T_l has been increased from 0 to 1 and T_h has been increased from 2 to 3 from left to right. It can be seen that on the upper left panel, the thresholds are too low and the noise pixels are recognized as edges. The circles can still be distinguished from the random edges since they have sharp borders, meaning the thickness of the edges is 1 pixel but for the application of further shape detection algorithms the noise would lead to a slow performance and to many false detections.

In the top right panel, the increase of $T_l = 1$ and $T_h = 3$ already eliminated fractions of the noise. The Best results have been achieved with the setup of $\sigma = 0$, $T_l = 2$ and $T_h = 5$, which can be seen in the left panel in the middle row of the figure. Here all circles but no noise are detected as edge pixels. Even the intensity gradients on the two largest rings in the middle are detected. Further, in the middle panel and the right panel of the middle row of figure 4.2, σ is increased. While at $\sigma = 1$, the circles are still detected and it can arguably be said that it leads to the cleanest detection of the raw circles, for $\sigma = 2$, detections are missed as seen in the right middle panel where the edges of the circles in the bottom left and top left on the image are not detected as edges.

Finally it is shown that even with small smoothing of $\sigma = 1$, which showed good results for $T_l = 2$ and $T_h = 5$, if the thresholds are set too high, also features can be missed, which can be seen in the bottom row. Here the choice of $T_h = 10$ shows that in the bottom left panel, the top left ring, the bottom right ring as well as the outer edges of the lower left ring are not detected anymore. Increasing T_l towards T_h leads to further false negatives. In this example, by setting up the concrete intensities for the circles and the noise it could be shown how important the prior knowledge about the intensities and noise in an investigated image is. Further for real world data, there might not be the one optimal choice of a parameter combination or at least it cannot be determined in advance and often depends on the use case as will be shown in the following.

Similar to the tests on the synthetic dataset, the Canny edge detection has been applied to the H I test-dataset shown in the right panel of figure 4.1. Again it has been looped over $\sigma \in \{0, 1\}$, $T_l \in \{0, 1, ..., 20\}$ K km/s and $T_h \in \{2, 3, ..., 25\}$ K km/s. In figure 4.3, 9 exemplary results are shown. From the top left to the bottom right, σ, T_l and T_h are increased. It can be seen that without Gaussian-smoothing and too low thresholds, the distribution of edges looks almost like random noise as shown in the top left panel. Increasing the thresholds to $T_l = 3$ and $T_h = 5$ separates the lowest intensity regions as shown in the top middle panel. With the same thresholds and $\sigma = 1$, the edges thin out as shown in the top right panel. When increasing T_l and T_h further, just the edges of the ring are still recognized and not the background fluctuations but also the low intensities of the upper right part of the ring are not detected anymore as can be seen in the series of images in the middle panel. In the lower panel, the thresholds T_l and T_h are set so that just the highest gradients are detected. Some fractions of the edges of the Usco-loop are still detected in the bottom left and the bottom middle panels, while in the bottom right panel just some random edges remain. From these results it can be seen that the "best parameter" set should lie at $\sigma = 1$ and between $T_l = 3 - 8$ K km/s and $T_h = 5 - 10$ K km/s, depending on the further use case. Since false positives are eliminated in follow up algorithms, it is acceptable to produce false edge detections if this reduces missed edges and features.

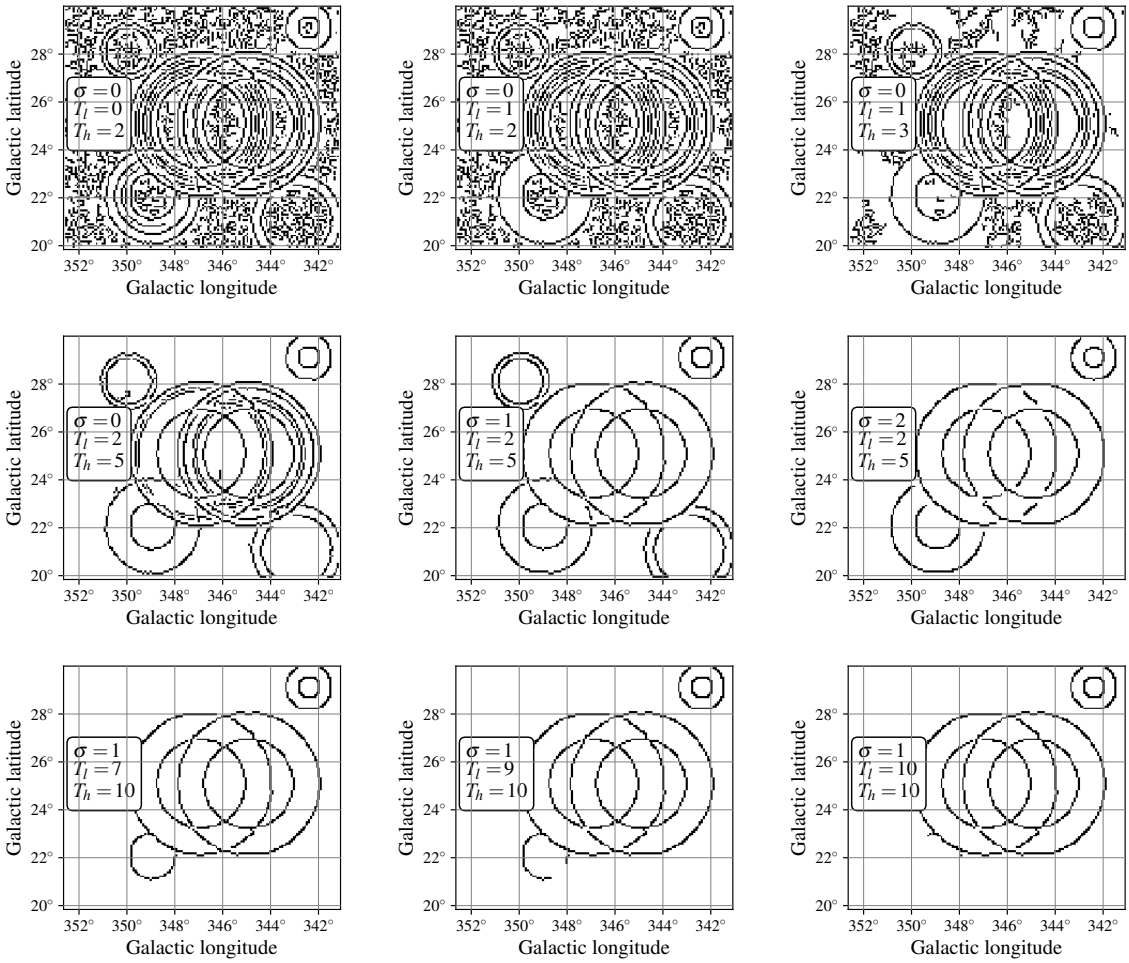

Figure 4.2: Nine edge maps, each containing the result of the Canny edge detection for one setup of the parameters σ, T_l and T_h on the same synthetic test dataset shown in figure 4.1 in the left panel. For more information see text

The thresholding and application of the CA and results will be discussed further in chapter 6, where this method is used together with the Hough-Transformation for circles to determine the parameters of the H I shells in the Sco-Cen region.

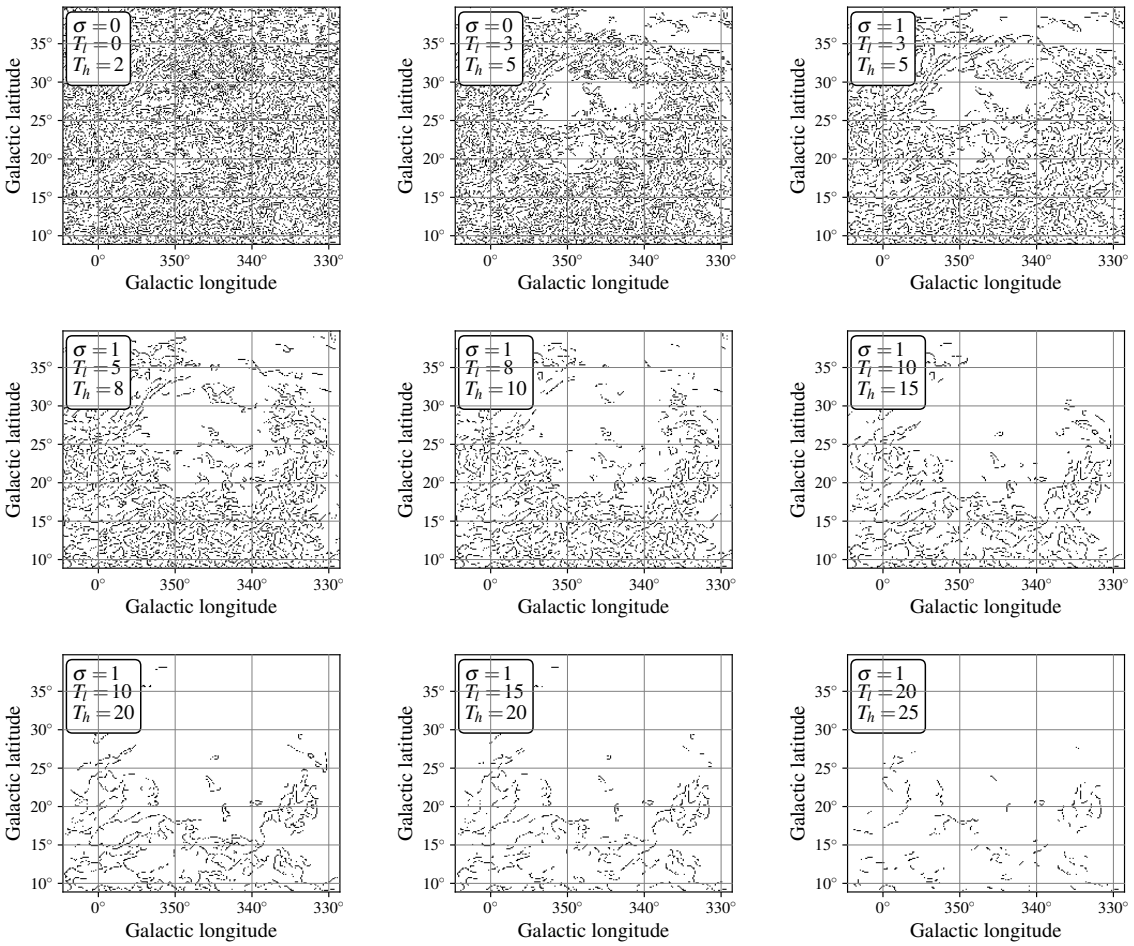

Figure 4.3: Nine edge maps, each containing the result of the canny edge detection for one setup of the parameters σ, T_l and T_h on the same H I dataset (see figure 4.1 right panel)

Testing the customized edge detection method on H I data sets Above it has been shown how the thresholding depends on the specific image or in this case the region that is investigated. Thresholding for specific regions of H I, like the Usco-loop has been tested. When looking at the global H I distribution as has been analyzed in section 3.3.2 and presented in figure 3.8 therein, the mean intensity range in latitude and also in the spectral (velocity) dimension varies by multiple magnitudes and hence it is not possible to specify one set of parameters for the whole dataset. The strength of the customized edge detection method is that it is applicable without manually specifying threshold parameters. This method is not as accurate as the CA-detection, when there is prior knowledge about the intensity gradient in specific regions but as shown exemplary in figure 4.4 is generally successful for the automated investigation of larger regions and large intensity ranges and can be applied for the full velocity range from -150 km/s to +150 km/s and the latitude range of $b = -50^\circ$ to $b = +50^\circ$[2]. In figure 4.4 in the top row, a channel map of approaching H I gas towards the Sun can be seen at $v_{\mathrm{rad}} = -85.5$ km/s with brightness temperatures between 85-0 K km/s (Top left panel). In comparison, the same intensity range for the same region is shown in the left-panel in the second row, which contains more high intensity features. The algorithm detects all main features, while reducing the noise. There are many connected edge pixels, visually "thicker appearing" edges. This is the result of not applying a non-maximum suppression. While this leads to numerous edge candidates in the same region, it also enables following algorithms to detect multiple similar fitting- and hence also the best fitting structures.

The results of the edge detection algorithms are binary images where edge pixels contain the value 1 and the other pixels contain the value 0. The next step is to apply structure detection algorithms on these binary images as explained in the following.

[2] It has been also tested to run the algorithm on smaller subregions to derive local parameter that lead to increased edge maps. But this procedure did not increase the quality.

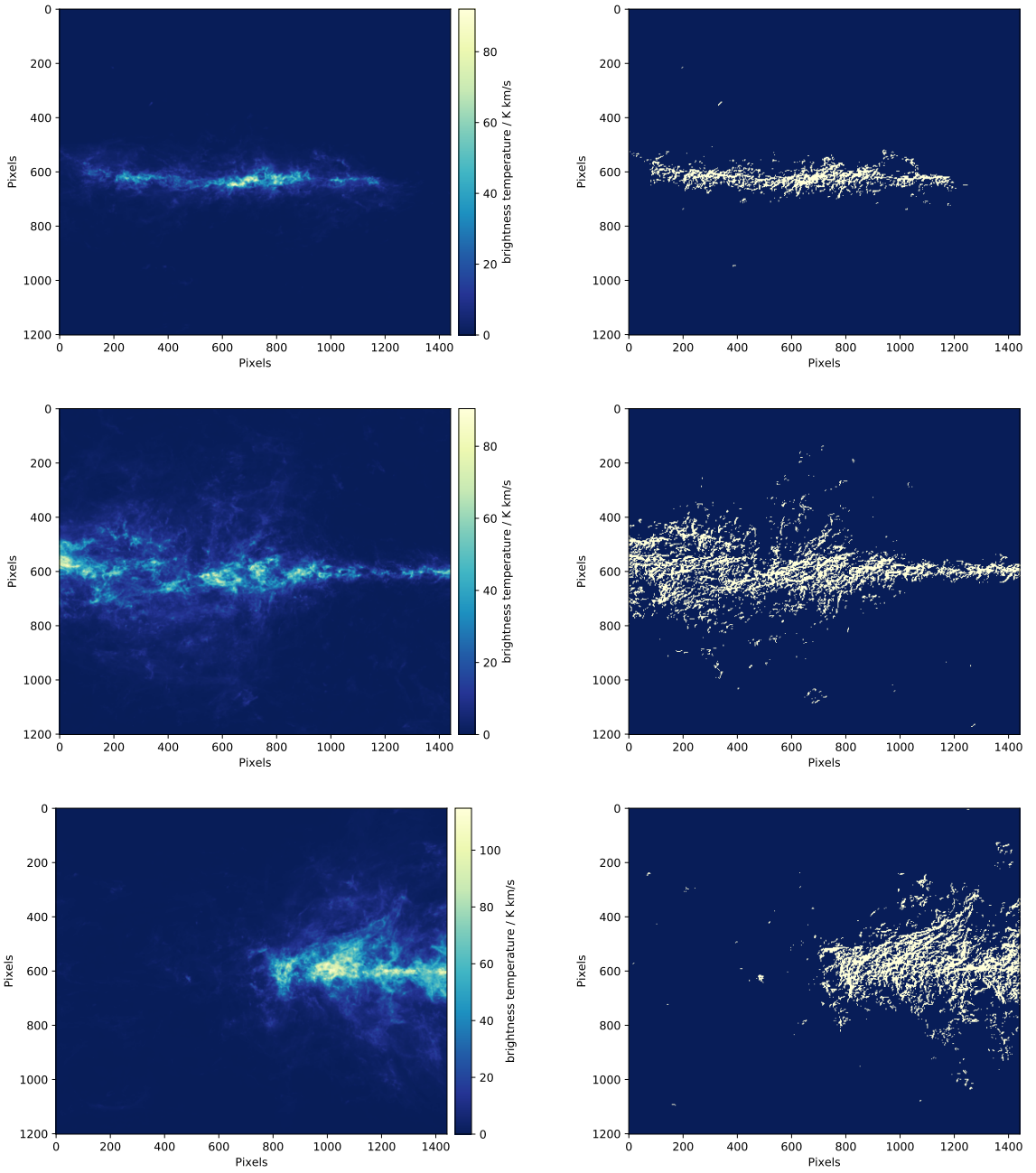

Figure 4.4: Resulting images produced by the customized edge detection method for three H I datasets. On the left hand side, three channel maps of the same region at the velocities -85.5 km/s, -21.3 km/s and 17.4 km/s are shown from top left to bottom left. On the right hand side of the figure in the three panels, the results of the customized automated edge detection method applied on the respective channel map on the left hand side are presented. The brightness temperature is color coded. For the three datasets, the color bar range is different, while for the edge-maps white denotes edge pixels while the color blue represents the background. For a discussion see text.

4.1.2 Detection of circles in edge maps

On the derived edge maps from above, pattern recognition algorithms can be applied to detect the inner edges of the shells, i.e. circles and parts of circles in this case. One method to achieve this is the Hough transformation, which was initially developed and applied to successfully detect bubbles in bubble chamber experiments (Hough 1959) and has been later generalized for other applications (e.g. Duda & Hart (1972)). Here the Hough transformation for circles has been used but the method can also be used for different geometrical shapes that can be parameterized in a binary image. The more complex the shape, meaning the more parameters it consists of, the less efficient this method is. In order to detect circles, each edge-pixel in a binary image is considered to be a point on a circle of radius r. An accumulation matrix is generated, containing all pixels and setting the starting value of each pixel to 0. Then for each edge pixel for a given r, the value of each potential center pixel that could lead to the edge pixel is raised by one. This is done for all radii sizes that are specified. Hence if a point represents a center point of a circle, it is a maximum in the accumulation matrix because the maximum number of points on a circle will have the exact distance r to this point, while even for the surrounding pixels of the center, most edge circles have a different distance.

This can be illustrated as shown in figure 4.5, where exemplary edge points are arranged on a circle. Circles of different radii, as specified below, are applied to each of these points and on the left hand side it can be seen, that the circles of low radii do not overlap, but with rising radius, the number of overlapping circles also increases. On the right hand side of figure 4.5 it can be seen, that for the idealized case all circles overlap in the center of the real circle and hence this point has the highest value in the accumulation matrix for this region.

The dimension of the Hough space directly depends on the number of parameters needed to describe the object, which are the two coordinates of the center pixel and one dimension for $r = \sqrt{\mathrm{pix}_x^2 + \mathrm{pix}_y^2}$ in the case of a circle. This highlights again that for each additional parameter needed, the processing gets more time expensive. Since the number of resulting circles of the Hough transformation only depends on the three radius parameters, the number of Hough circles is directly proportional to the number of radii steps between $R_{\mathrm{H,min}}$ and $R_{\mathrm{H,max}}$ for a fixed image size. The quality of the Hough circle, meaning how many edge pixels are on the respective Hough circle, are stored in an accumulator matrix (Acc). Since the result contains circles of all qualities, most algorithms have an additional parameter of a minimum quality value that can be set. Since this value varies for different regions, it is not applied in this thesis during the Hough transformation. The accumulator value is used in follow-up steps to sort out false positives. Additionally, most algorithms apply a non maximum suppression on the detected Hough circles of same radii in similar regions. For this the value ΔP_{c} is set in units of pixels and decides how close center points of circles of the same radii are allowed to be. The influence on the results are further discussed when testing the algorithm below.

Since the possible radii have to be specified in advance, a minimum- ($R_{\mathrm{H,min}}$), a maximum radius $R_{\mathrm{H,max}}$ and a step size ΔR_{H} have to be specified for each image that is investigated. For the H I data, to be able to detect all possible detectable circles, $R_{\mathrm{H,min}}$ is dependant on the angular resolution as well as ΔR_{H} and hence have been chosen as three- and one beam width, respectively. The $R_{\mathrm{H,max}}$ is the maximum detectable radius, which is one half of the range of the longest axis in the data. For the application in this thesis, the radii do not come close to these values. There is just one known supernova remnant that reaches this angular size, which is the UCL-shell, which is investigated in chapter 6. The specified Hough parameters for the automated search algorithm that is introduced in section 4.5 are specified and discussed in this section.

For each channel map in H I, where the Hough transformation is applied, the parameters of all circle-candidates are stored. The threshold of the accumulator value decides if a circle-candidate is considered a circle or not and has to be tuned for the use case of detecting expanding H I shells. The shells are not always fully closed circles and can also deviate from the shape of a circle as presented in section 3.4 and hence too high thresholds might lead to missing detections. But not any arbitrary low accumulation value should be allowed, because the false positive rate also increases rapidly with decreasing accumulator value[3]. The minimum limit that is allowed in this work is an accumulator value of 0.2 of the maximum accumulator value of the respective image. This value has been determined empirically and gives the best trade off between false positives and not missing detection, again with a tendency to allow more false positives than false negatives.

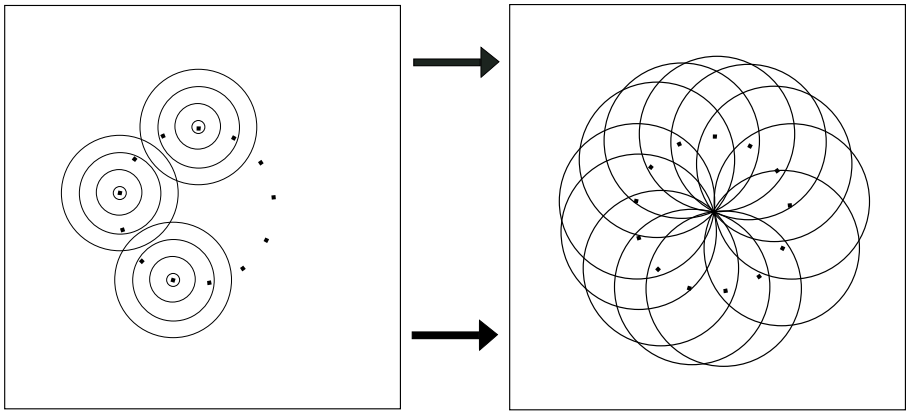

Figure 4.5: Schematics, illustrating the procedure of the Hough transformation. On the left hand side, edge-pixels (black dots) that are in a circular pattern are plotted. Each edge-pixel is considered the center point of multiple circles. These circles are specified by the minimum radius $R_{\mathrm{H,min}}$, the step width ΔR_{H} and the maximum radius $R_{\mathrm{H,max}}$. In this case, the circles of larger radii overlap at some points, but on the right hand side it is shown that all circles of these edge pixels overlap in one point if they have the radius r that is the real center of the circle, where the edge pixels are located. For a detailed explanation see text.

Testing the Hough transformation

The Hough transformation is tested on the edge-maps of the same test data that have been already used for the edge detection. Since in the data, two ring-like structures can be seen, a large one with center coordinates in the center of the image and a radius of roughly 10–14° and another one with a smaller radius of about 3–5°, with center coordinates at roughly $l = 345^{\circ}$ and $b = 20^{\circ}$, the radii are varied in these ranges. The minimum allowed radius is $R_{\mathrm{H,min}} = 2^{\circ}$, the step size is $\Delta R = 0.24^{\circ}$ (1 pixel) and the maximum radius is $R_{\mathrm{H,h}} = 14^{\circ}$. If no maximum suppression is applied, i.e. $\Delta P_c = 0$, this results in a total number of 398525 Hough circles. For $\Delta P_c = 3$ and 6 pixels, the results are thinned out to 131418 and 48740 Hough circles. The Hough circles are ranked by the accumulator value resulting from the Hough transformation. To discuss the results, in figure 4.6, some examples of the Hough transformation are plotted. The pixel map in the background is the middle left result of the above

[3] The theoretical maximum number of Hough circles is defined by the specification of the parameters for the minimum-, and maximum circles size as well as the step size between the radii

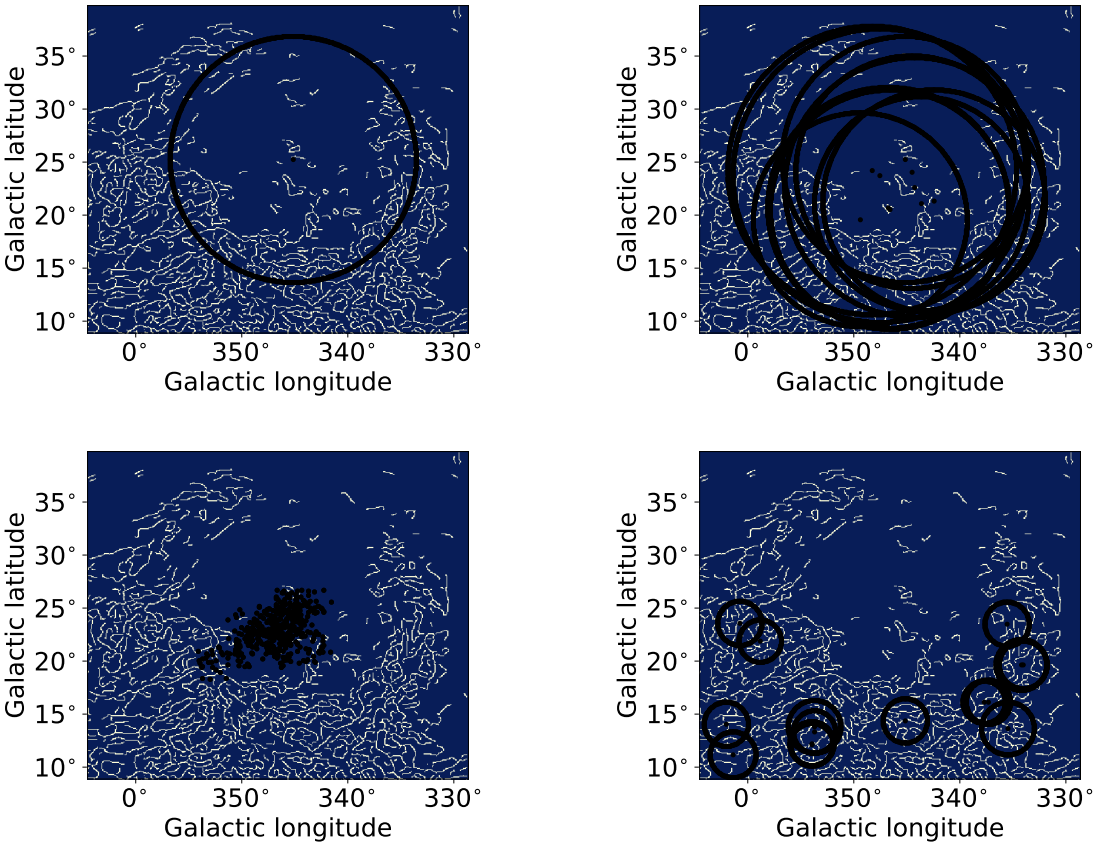

Figure 4.6: Four plots containing exemplary results of one Hough transformation run that is described in section 4.1.2. The plot in the top left panel shows the Hough circle in the radius range of $10 - 14^{\circ}$ with the highest accumulator value, i.e. the highest number of edge pixels. On The top right hand side, the top 10 accumulator value circles with radii between $10 - 14^{\circ}$ are plotted. Due to visibility for the top 500 Hough circles in the same range, just the center points are plotted in the bottom left panel while in the bottom right, the top 15 Hough circles with radii in the range of $2 - 8^{\circ}$ are presented.

discussed figure 4.3 of the Canny edge detection, with the parameters $\sigma = 1$, $T_l = 5$ and $T_h = 8$. On the top left side of figure 4.6, the highest accumulator value of circle radii in the range of 9–14° is plotted and it can be seen that it fits the inner edges of the ring-like structure. In the top right panel, the top 10 results in this range are plotted. For this range, the top 500 circle center points are plotted in the bottom left panel. Most of these scatter around the center coordinates of the larger ring-like feature with a small deviation from an ideal ring-like structure. These results, which are also forced due to the specified size range for radii and due to the center of the shell being also centered in the image. This is why one takeaway for the application in the later sections, the crops of the images will overlap, with an overlap larger than the largest radius, so that border regions do not affect the results.

The number of false positives is high for smaller radii even at high accumulator values compared to the one of larger radius. In the bottom right panel, the top 15 circles[4] are plotted for the range 2–5°. Most of them are located in regions with random edge pixels. There are methods that can be applied afterwards to sort out these false detections. One is using the definition of a cavity in channel maps, which is introduced in the following.

4.1.3 Cavities in two dimensions

For each detected edge-circle, it is determined if it traces an outer edge of a 2D-blob or an inner edge of a 2D-hole or as called hereafter a **cavitiy**. One way to achieve this is to sum up the intensities on a thin ring with the width Δr_{out} with a radius slightly larger than the radius of the edge-circle and normalizing it by the number of pixels that contribute:

$$I_{\mathrm{out}} = \frac{\sum_i^k I_{i,\mathrm{out}}}{k} \tag{4.12}$$

where k is the total number of pixels on that ring and compare it to the summed up intensities on a disk I_{in} with a radius $r_{\mathrm{in,max}}$ that has to be specified and has the restriction that it has to be smaller than the edge-circle radius:

$$I_{\mathrm{in}} = \frac{\sum_j^m I_{j,\mathrm{in}}}{m} \tag{4.13}$$

with the restriction $r_{j,\mathrm{in}} \leq r_{\mathrm{in,max}}$ and it is normalized by the total number of pixels m belonging to the disk. If $I_{\mathrm{out}} \geq I_{\mathrm{in}}$, it is unlikely that the edge-circle is a blob. The smaller this value, the more likely it is to detect a cavity. Hence the threshold value c_{cav} is determined:

$$c_{\mathrm{cav}} \geq \frac{I_{\mathrm{in}}}{I_{\mathrm{out}}}. \tag{4.14}$$

c_{cav} will also be measured amongst other properties, for 17 shells known from other studies of expanding shells, below in section 4.5.1.

Another method could be to calculate the mean intensities on the whole inner disk with a radius lower than R_{H}. But in the tests this led to false negatives. The interpretation is that circles that lie in, or around the Galactic disk suffer from this calculation, since the cavity of the shell contains overlapping emissions from different regions or emission inside the cavity from the region itself. Since the highest

[4] some overlaps occur, which is why just 12 circles are visible.

amount of H I emission can be found at low latitudes and the majority of the SNRs are close to the Galactic disk, this method would suffer from these emissions (see e.g. McClure-Griffiths et al. (2002), Ehlerová & Palouš (2013) or Sallmen et al. (2015)). This is why the above proposed method, to derive c_{cav} automatically, has been chosen for this work. Since the limit of this value is important for the search algorithm to sort out potential non-cavities, it will be again discussed further in section 4.5, where the application to the Galactic H I data is described.

4.2 Model of an expanding homogeneous spherical shell

In this section a model of an uniformly **e**xpanding **h**omogeneous **s**pherical **s**hell, EHSS- model hereafter, is introduced. This model describes the idealized view of an expanding H I shell.

Its parametrization and the conversion of this model from Cartesian coordinates into the longitude-latitude-velocity spaces of H I data-cubes are explained. This includes the projection of expansion velocities onto the line of sight and calculating the column densities for the respective bins in the H I datacubes.

The parameters of the EHSS-model are

- the Galactic longitude of the center of the shell l_0 in degree
- the Galactic latitude of the center of the shell b_0 in degree
- the radius of the inner edge of the shell r_{in} in degree
- the thickness of the shell Δr in degree
- the particle density of the shell n_{shell} in H I atoms per cm^3
- the expansion velocity of the shell V_{exp} in km/s
- the center velocity of the shell V_0 in km/s
- the distance to the center of the shell D_0 in pc

These parameters can be fitted to H I data. Here it is assumed that D_0 is known in advance and will not be fitted. For now the distance parameter is included in the model as a fixed value. The EHSS-model predicts column densities $N_{\mathrm{H\,I},i}$ for each pixel of a datacube with the pixel index i.

Since the EHSS-model contains multiple functions and coordinate transformations, an overview of the main functions is provided here. The model contains the eight enumerated parameters from above. The center of the shell l_0, b_0 and the angular radius r_{in} and thickness Δr are detectable in the channel maps where the inner edge has the largest radius, i.e. at the channel map with velocity $v_{\mathrm{lsr}} = V_0$, according to sec. 3.4. With the fixed value D_0 and the parameters l_0 and b_0 the Galactic coordinates of the center of the shell can be transformed into Cartesian coordinates. By also transforming r_{in} as well as Δr into Cartesian lengths, the complete shell can be reconstructed in Cartesian coordinates.

l–b coordinate pairs along the velocity axis of the H I datacube can also be seen as a line of sight (LoS) in this particular angular direction. To determine the theoretical observed column density on this LoS, it is calculated if the LoS penetrates the shell. If so, the intersection points $P_{\mathrm{IC},i/j}, i, j \in \{1, 2\}$ of the LoS with the edges of the shell are calculated. Knowing the intersection points of the outer- and inner edge of the front- and also the back of the shell, the total hydrogen density n_{shell} along the LoS in this width is calculated. With the expansion velocity V_{exp} of the shell, the radial velocity components that are visible in the datacubes can be calculated for the intersection points. Together with the center velocity of the shell V_0, the observed velocity interval, i.e. the number of channels where the shell contributes, between the intersection points, $P_{\mathrm{IC},i}$ are calculated. Then the shell can be re transformed into ppv-space and be included into a datacube because for each l–b coordinate pair, the calculated density n_{shell} as well as the calculated radial velocity interval are used to get a value for the column density $N_{\mathrm{H\,I},i}$ in each pixel of the datacube.

In the following, the complete dependencies of all functions are provided.

Theoretical description and dependencies

The equation for the column density in one pixel $N_{\mathrm{H\,I},i}$ with its dependencies on sub-functions is shown to give a mathematical connection between the equations describing a geometric shell. The concrete meaning behind the equations is presented further below. The column density for one pixel i is in a channel with the width Δv_{ch}:

$$N_{\mathrm{H\,I},i}(l_0, b_0, D_0, V_{\mathrm{exp}}, r_{\mathrm{in}}, \Delta r, n_{\mathrm{H\,I,shell}}) = \sum_{k=q}^{n_{\mathrm{p}}} n_{\mathrm{H\,I,shell}} \cdot w_k(P_k, P_{k+1}) + Re_{\mathrm{lo},i} + Re_{\mathrm{hi},i} \tag{4.15}$$

with the restriction that $v_{\mathrm{LoS}}(P_{n_{\mathrm{p}}-1}) - v_{\mathrm{LoS}}(P_0) \leq \Delta v_{\mathrm{ch}}$ and the remaining column density fraction for the lower limit of the channel width is $Re_{\mathrm{lo},i} = \frac{v(P_0)-v_{j-1}}{v(P_0)-v(P_{q-1})}$, which is 0 for $q = 0$ where P_0 equals either $P_{\mathrm{IC},1}$ or $P_{\mathrm{IC},2}$, depending on the case introduced below. The second remaining column density fraction for the upper limit of the channel width is $Re_{\mathrm{hi},i} = \frac{\Delta v_{\mathrm{ch}}-v(P_{n_{\mathrm{p}}-1})}{v(P_{n_{\mathrm{p}}})-v(P_{n_{\mathrm{p}}-1})}$, which again is 0 if $P_{n_{\mathrm{p}}-1}$ equals $P_{\mathrm{IC},2}$, $P_{\mathrm{IC},3}$ or $P_{\mathrm{IC},4}$, depending again on the respective case introduced below.

$N_{\mathrm{H\,I,tot},1/2}$ are the total column densities along the respective penetrated parts of the shell, which again depend on

$$P_{\mathrm{IC},1/2}(G_{\mathrm{LoS,i}}, F_{\mathrm{sph},1}),\ P_{\mathrm{IC},3/4}(G_{\mathrm{LoS,i}}, F_{\mathrm{sph},2}),$$

which are the calculated intersection points and in turn depend on two other functions each. The first one is $G_{\mathrm{LoS,i}}(l_i, b_i, P_0)$, the equation for a line segment describing the LoS, where P_0 is its origin that is also the observers location (0,0,0), and l_i, b_i are here angular position l_i, b_i of the pixels within an H I datacube. The second function is $F_{\mathrm{sph},1/2}$, the equation for a thick spherical shell can be described by two spheres of different radii:

$$F_{\mathrm{sph},1}\left(P_c(x(l_0, b_0, D_0), y(l_0, b_0, D_0), z(l_0, b_0, D_0)), R_{\mathrm{in}}(r_{\mathrm{in}}, D_0)\right), \tag{4.16}$$

$$F_{\mathrm{sph},2}\left(P_c(x(l_0, b_0, D_0), y(l_0, b_0, D_0), z(l_0, b_0, D_0)), R_{\mathrm{out}}(r_{\mathrm{in}} + \Delta r, D_0)\right) \tag{4.17}$$

where the point P_c is a Cartesian point, depending on the Cartesian coordinates x, y, z, which are connected to the parameters l_0, b_0 and D_0 by the transformation from spherical to Cartesian coordinates. R_{in} and R_{out} are the variables for the inner and outer radius of the shell in Cartesian coordinates, depending on the parameters $r_{\mathrm{in}}, \Delta r$ and D_0. In the denominator of eq. 4.15, $n_{\mathrm{ch},i,1/2}$ is the number of channels to which $N_{\mathrm{H\,I,tot},1/2}$ has to be allocated and it depends on the LoS-velocity ranges:

$$\vec{V}_{\mathrm{LoS},1/2}\left(P_{\mathrm{IC},1/2}, \vec{V}_{\mathrm{exp}}, b, D_0, r_{\mathrm{in}}\right),$$
$$\vec{V}_{\mathrm{LoS},3/4}\left(P_{\mathrm{IC},3/4}, \vec{V}_{\mathrm{exp}}, b, D_0, r_{\mathrm{in}}\right)$$

where $P_{\mathrm{IC},i/j}$ are the intersection points.

In the following, first the transformation from Galactic to Cartesian coordinates and then the calculation of $N_{\mathrm{H\,I,tot},1/2}$ from eq. 4.15 are explained in the following section 4.2

The shell in Cartesian coordinates

With the known distance to the center of the shell D_0, the Cartesian center point $P_c(l_0, b_0, D_0)$ can be calculated using the transformation from spherical- to Cartesian coordinates with the Galactic coordinates of the center l_0 and b_0. The physical radius of the shell R and its thickness ΔR can be calculated using the trigonometric relationship:

$$R = D_0 \cdot \tan r. \tag{4.18}$$

where r is the angular radius. The thickness ΔR can be obtained by replacing r with $r + \Delta r$ and subtracting R from the result. With the parameters P_c, R and ΔR two spheres are defined:

$$R_{1/2} = (x - x_0)^2 + (y - y_0)^2 + (z - z_0)^2 \tag{4.19}$$

where R_1 and R_2 are the inner and outer edge of the shell and the three coordinates x_0, y_0, z_0 define the center point P_0 for both spheres. These two equations represent $F_{\mathrm{sph},1/2}$ in relation 4.17 and are needed to calculate the column density between two Cartesian points.

The H I column densities along sight lines through the shell

The column density $N_{\mathrm{H\,I}}$ is the total amount of atomic hydrogen nuclei between two points on the LoS. To determine the column density for each pixel of the grid, the respective penetration width (fig. 4.7) through the sphere has to be known. In order to do this, the equation for a line segment for the LoS is needed, which is

$$G_i = \vec{P}_{\mathrm{Obs}} + u \cdot \left(\vec{P}_i - \vec{P}_{\mathrm{Obs}}\right), \tag{4.20}$$

where $\vec{P}_{\mathrm{Obs}} = (0, 0, 0)$ is the location of the observer, which is defined as the origin of the Cartesian coordinate system here. Then the equation simplifies to

$$G_i = u \cdot \vec{P}_i \tag{4.21}$$

where $\vec{P}_{\mathrm{i}} = (x_{2,i}, y_{2,i}, z_{2,i})$ is a point on the LoS at arbitrary higher distance than the shell and $G_i = (x, y, z)$ is the intersection point. The factor u is a dimensionless quantity between 0 and 1, defining how close the respective point is to $\vec{P}_{\mathrm{i}}$. To obtain the penetration width, the intersection points between the LoS and the sphere needs to be calculated. This is achieved by substituting eq. 4.21 into eq. 4.19. The result is a quadratic equation for the intersection points[5]:

$$P_{\mathrm{IC},1/2} = \frac{-b \pm \sqrt{b^2 - 4ac_{\mathrm{in/out}}}}{2a} \tag{4.22}$$

with $a = (x_{2,i} + y_{2,i} + z_{2,i})^2$, $b = -2 \cdot \left(x_{2,i}x_0 + y_{2,i}y_0 + z_{2,i}z_0\right)$ and $c = x_0^2 + y_0^2 + z_0^2 - R_{1/2}$. This equation has 0, 1 or 2 possible solutions for $P_{\mathrm{IC},1/2}$. For a shell, the intersection is calculated for the inner- and outer edge. This results in 9 possible solutions from which the physical irrelevant cases are excluded. For example if the sphere with smaller radius has two or one intersection point, the only

[5] The whole calculation can be seen in appendix C.3.

physically possible solution is that the outer, larger sphere must have two intersection points because it has to be penetrated to reach the smaller sphere. It is also assumed that the observer is not located on the edge of the sphere and neither in the sphere, which leaves 4 possible scenarios that are illustrated in figure 4.7. With the calculated penetration widths and the parameter n_{shell}, the column densities $N_{\mathrm{H\,I}}$ from eq. 4.15 are obtained:

$$N_{\mathrm{H\,I},i} = w\ [\mathrm{pc}] \cdot n_{\mathrm{H\,I,shell}}\ [\mathrm{H\,I\ atoms/pc^2}] \tag{4.23}$$

In order to determine what fraction of the total H I column density contributes to individual radial velocity channels of the H I data, V_{exp} has to be projected onto the LoS for the intersection points $P_{1/2}$ and $P_{3/4}$.

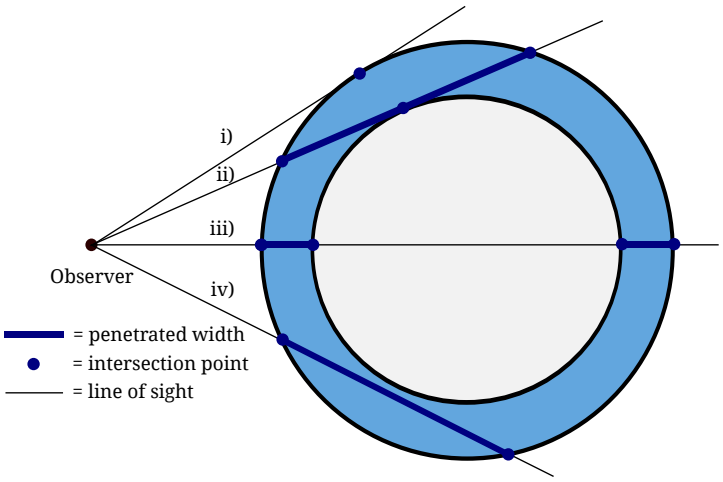

Figure 4.7: Schematics of the four relevant intersection patterns of the LoS (black line) with a spherical shell (cyan-blue). The intersection points are denoted as blue dots and the penetration widths are blue thick line segments. For more information see text.

Column densities in each pixel

To obtain the column density for one pixel $N_{\mathrm{H\,I},i}$, the total column density, eq. 4.23, can be homogeneously divided between all velocity channels between $\left[V_{\mathrm{LoS},1/2}, V_{\mathrm{LoS},3/4}\right]$. This approximation is always true for case iii) if the shell thickness is not larger than 50% of the outer radius and if V_{exp} is not larger than 20 km/s. This limit is never reached for the shells of Sco-Cen and maximum deviation of the linear approximation to the real value is 0.5 km/s for case ii), which is still smaller than the channel width of EBHIS (0.8 km/s) or GASS (1 km/s). On top of that, the bin sizes are already lower than the respective velocity resolutions of the surveys (table 3.1). But since this is a biased assumption and potentially the shells could have larger expansion velocities, the real function[6] is approximated by calculating the exact velocities for 15 points between the two calculated $P_{i/j,IC}$ on the LoS in the width of the respective case and approximate the function linearly between each of those total 17 points (including the outer points), as is shown in figure B.0.20 (blue-dotted line) exemplary. Adding 15 extra points are higher than the needed limit and result in a deviation of the linear approximation from the real value of 0.15 km/s for a shell with angular radius to the inner edge of 4° and a thickness of 9.5°[7] and V_{exp} = 50 km/s and the deviation. The deviation is overshadowed by the binning process and does not affect the shell. Again, this is an extreme case. For typical observable shells in H I, values as e.g. r_{in} = 11.9, Δr = 3 and V_{exp} = 10 km/s[8], the deviation is just $2.3 \cdot 10^{-4}$ km/s, which is negligible. This is done for each pixel and finally yields equation 4.15 from above.

The line of sight velocities of an expanding spherical shell

The determination of the LoS velocity, i.e. the radial velocity component of the expansion velocity that is observed, is explained here.

Given $P_{1/2}$, $P_{3/4}$, V_{exp} and V_0, the LoS velocity $\vec{V}_{\mathrm{LoS}}$ for each pixel of the shell in an H I datacube can be calculated using geometric relations that are illustrated in figure 4.8. To calculate the projection, the angle γ is needed. It is given by

$$\gamma_{1/2} = \arcsin\left(\sin\alpha_{1/2} \cdot \frac{D_0}{R}\right), \tag{4.24}$$

where α is the angle between the LoS (black line segment) in figure 4.8 and the line through the center of the sphere. Then $\vec{V}_{\mathrm{LoS},1/2}$ are

$$\vec{V}_{\mathrm{LoS},1/2} = \vec{V}_0 + \cos\left(\gamma_{1/2}\right) \cdot \vec{V}_{\mathrm{exp}}. \tag{4.25}$$

With the calculated intersection points $P_{\mathrm{IC},1/2}$ and $P_{\mathrm{IC},3/4}$, their respective radial velocities $V_{\mathrm{LoS},1/2}$ and $V_{\mathrm{LoS},3/4}$ as well as the total column density $N_{\mathrm{H\,I},i}$ on the LoS, equation 4.15 can be derived.

[6] The approximation is chosen, since it is fast to implement. In principle, the function, depending on one extra angle, is a generalization of the equations 4.24 and 4.25, but not needed to be determined, since the linear approximation is processed faster and the deviation is some orders of magnitude lower than the binning width in velocity.

[7] This is a thickness of 70% of the total radius and higher than observed thicknesses (Pittard 2013)

[8] These are the values of the USco-shell of section 6.5

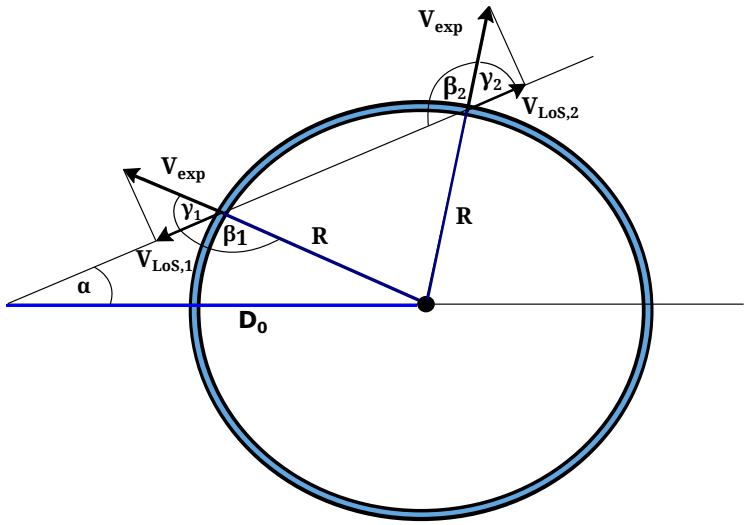

Figure 4.8: Illustration, showing the geometry for the calculation of the LoS velocities for given intersection points, between an expanding spherical shell and the LoS segment. The blue/cyan ring is a slice through a shell, the black dot in the middle is the center. V_{exp} is the expansion velocity of the shell. $V_{\mathrm{LoS},i}$ are the projected components of V_{exp}, the observer would see, R_{sph} is the radius of the shell and D_0 is the distance to the shell.

4.3 Fitting models to test datasets

A parameterization of a ring as well as the EHSS-model have been fitted to test datasets that consist of synthetic- as well as real H I data. The tests are described in the following.

4.3.1 Fit methods and metrics

When calculating χ^2, each modeled point is subtracted from each corresponding data-point, divided by the uncertainty and it is summed over all points:

$$\chi^2 = \sum_{i=0}^{n} \frac{(\text{data}_i - \text{model}_i)^2}{\sigma_i^2} \tag{4.26}$$

where in this context data_i is an intensity in a pixel of the datacube, model_i is the predicted intensity of same pixel of the datacube by a model and σ_i^2 is the uncertainty of the intensity in the pixel. It is summed over all pixels, i.e. n is the total number of pixels in the datacube. To determine the best model parameters, this equation is minimized. If not mentioned explicitly, the standard deviation of the data is used as a guess for the uncertainty for the variable x_i:

$$\sigma_x = \sqrt{\frac{1}{n-1}\sum_{i=1}^{n}(x_i - \overline{x})^2}; \quad \overline{x} = \frac{1}{n}\sum_{i=1}^{n} x_i \tag{4.27}$$

where $\overline{x}$ is, in this context, the mean brightness temperature or column density of the dataset. In this work χ^2 has been derived using multiple different minimization methods.

χ^2 can be minimized on a grid, which is the brute force method and is computational not very efficient but on the other hand is the most robust method and its accuracy only depends on how small the parameter steps are chosen. This method can be used when the parameter space is small[9]. For multiple parameter spaces, fitting by gradient searching algorithms or by Bayesian methods is preferred.

Levenberg-Marquardt-Algorithm The **L**evenberg-**M**arquardt-**A**lgorithm (LMA) is one of the standard methods to solve non linear fit problems. This method combines the Gauß-Newton-algorithm with another method that forces the algorithm to result in smaller values (Levenberg (1944) and Marquardt (1963)). The mathematical description of this method can be found in appendix C.4.

As any fit algorithm, depending on the choice of starting parameters, but also due to the specific gradient calculation, the algorithm can get stuck at local minima and not be able to find the global minimum.

Bayesian methods allow, due to its probability based sampling, to ”jump“ out of local minima, if the number of samples is high enough and hence are more robust to local minima, but their runs are also more time consuming because their sampling is not as efficient as gradient descent.

Markov Chain Monte Carlo In Bayesian approaches, the parameters are sampled and not calculated. Each parameter has its own sample distribution from which the mean and uncertainties can be

[9] e.g. for the EHSS-model, having 8 parameters it is used if two parameters are varied and the others are held fixed.

determined.

One of the most popular Bayesian approaches to implement the sampling is the **M**arkov **C**hain using **M**onte Carlo (MCMC) algorithm (e.g. Dynkin (1989), Press et al. (2007)) and it works as follows. For a given dataset D, the probability of the dataset given the parameters x is $P(D|x)$. The distributions of the parameters are called priors $p(x)$. The aim is to get information about the posterior distribution of the model, which is proportional to the not normalized distribution $\pi(D|X)$ that is defined by

$$\pi(D|x) = \frac{P(D|x)P(x)}{c}. \tag{4.28}$$

where x is the vector containing all parameters x_i. This distribution is not normalized but if sampled from it, quantities like the mean and standard deviation can be obtained. Due to the marginalization rule, the distribution of each parameter can also be sampled separately. Sampling parameters at certain intervals Δx_i yields the normalized distribution. This approach can in theory sample each parameter combination but is more efficient than a grid search, since the probability for sampling regions with higher $P(x)$ is higher. This is especially important if evaluating $P(x)$ is expensive. The advantage also comes in hand for data with a high number of parameters since the number of possible combinations are the product of all parameter points and if the whole space is sampled, this is slower by many orders of magnitude than using an MCMC method[10].

The Monte Carlo algorithm is implemented using a **Markov chain**, which is a chain of sampled points where the probability $P(x_i)$ of point x_i only depends on the previous point x_{i-1} of the chain, mathematically $p(x|x_{i-1})$. The distribution $\pi(x)$ is sampled ergodically if $p(x_i|x_{i-1})$ is chosen to satisfy

$$\pi(x_1)p(x_2|x_1) = \pi(x_2)p(x_1|x_2), \tag{4.29}$$

which when integrated yields

$$\int p(x_2|x_1)\,\pi(x_1)\,\mathrm{d}x_1 = \pi(x_2)\int p(x_1|x_2)\,\mathrm{d}x_1 = \pi(x_2). \tag{4.30}$$

This relation is called the detailed balance equation. This equation will be used in the following step method, which determines the transition between x_i and x_{i+1}.

Metropolis- Hasting Algorithm To create a Markov-Chain, the transition probability $p(x_1|x_2)$ of eq. 4.30 needs to be determined. A candidate point x_{2c} is drawn from a proposal distribution, $q(x_{2c}|x_1)$, and the acceptance rate

$$\alpha(x_1, x_{2c}) = \min\left(1, \frac{\pi(x_{2c})q(x_1|x_{2c})}{\pi(x_{1c})q(x_{2c}|x_1)}\right) \tag{4.31}$$

is calculated. If the acceptance rate exceeds a defined threshold, x_{2c} is accepted and is further used as x_2. Otherwise the point is rejected and $x_2 = x_1$ (Metropolis et al. 1953; Hastings 1970). The net result

[10] For example the run for the EHSS-model reaches the convergence region after about 5000 iterations, while rastering the whole grid of parameters in sufficient accurate steps would take about 10^10 iterations

is a transition probability $p(x_2|x_1) = q(x_2|x_1)\alpha(x_1, x_2)$ with $(x_2 \neq x_1)$. The proposal distribution is usually a Normal distribution but can in principle be any distribution. In the case of a model where no prior information about the parameters is available, a uniform proposal distribution can be chosen to ensure that the likelihood for each point in the parameters space is equal. The price is an increase in the conversion time. To construct a chain, a step method is needed. This is done as follows in the metropolis algorithm. The number of iterations is set in advance. The more steps are done, the more complete the representation of the posterior distribution. The first iterations of the chain are normally rejected, because a larger fraction of the parameter space is drawn due to a high logP. This so-called burn-in phase does not represent the distribution of the parameter because the chain has not converged yet. The amount of iterations necessary for the convergence of the chain is not known in advance. Using fractions of the data to reduce computational time is a possible approach to find the number of steps belonging to the burn-in phase. Additionally, the data may be thinned out by neglecting every n-th point of the shell to ensure that the sample is independent because data points next to each other are not independent. n has to be also determined empirically or is estimated. The number of iterations should exceed the burn-in phase in a way that the length of the chain consists of enough points for statistical analysis. Then, after drawing the distribution, the mean x_m of the posterior distribution of the drawn sample represents the parameters. The uncertainties of a parameter can be estimated from the standard deviation σ from x_m.

Even if the Markov Chain converges and reaches a stationary phase, for testing the robustness and variation, multiple runs with deviating start parameters are made below to test if the statistical fluctuations due to sampling, results in the same minimum or maybe different local minima. But if the parameters are roughly known in advance, it is also possible to draw them uniformly randomly between specified lower- and upper limits. Therefore four runs with different start parameters for the same problem are made. If all chains converge towards the same values, it is suggestive that these are the optimal values. It has to be ensured to set this variation high enough, so that the runs don't end in the same local minimum but either in the global one or multiple local minima if existent. But as for any minimization problem, the start parameters cannot be arbitrarily far away from its optimum values, because otherwise the problem might not converge. The range is different for each minimization problem.

4.3.2 Test datasets

The models from above and its applicability to be fitted to H I data have been tested. This problem differs from usual one dimensional functions that are fitted to a distribution of data. Here each point has a weight that is the intensity and this value lies in the three dimensional longitude-latitude-velocity space, which can consist of 10^4 up to 10^8 data points here.

In the following, the analyses of the two problems that are fitting a ring to channel maps of H I data (sec. 4.1) and fitting the EHSS-model to H I data (section 4.2) are presented. Special test datasets have been used to simplify the problem compared to the complexity of real H I data.

Ring test data

A ring has been set up within an area of 126×126 pixels ($(10^\circ \times 10^\circ)$) area. The ring has been included into the center of the image. Its parameters are listed in table 4.1. This ring has been set into three different environments. The three cases can be seen in figure 4.9 that is explained in more detail

	x_0	y_0	I_b	r_{in}	Δr
Unit:	pix	pix	K km/s	pix	pix
	65	63	5	30	15

Table 4.1: The parameter values of the modeled test ring in a channel map of a datacube. x_0 and y_0 are the pixel coordinates of the center of the ring, r_{in} and Δr are the radius and thickness in pixels and I_{shell} is the brightness temperature on the ring.

below. First the raw ring is put into an environment with the same brightness temperature T_b in each pixel (top left panel). Then the ring is put into a background environment with random noise as shown in the bottom right panel. In the remaining test case, a ring within a real H I background environment, also taken from the GASS is created.

Shell test data

Similar to the ring, the shell has been included into different environments. The parameter values for the modeled shell are listed in table 4.2. The shell has been included into a datacube of $126 \times 126 \times 63$ pixels ($10^\circ \times 10^\circ \times 50$ km/s), the velocity resolution has been binned to 0.8 km/s and the spatial resolution is $16.1'$, both to be consistent with the GASS data. A smaller datacube has been used than

	v_0	v_{exp}	l_0	b_0	n_{shell}	$r_{in}/^\circ$	$\Delta r/^\circ$	D_0/pc
Unit:	km/s	km/s	$^\circ$	$^\circ$	H I/cm^3	$^\circ$	$^\circ$	pc
	2	6	330	15	5	3	1	100

Table 4.2: Specified parameters of the shell used to test the fit of the EHSS-model to data. The parameters are the center velocity v_0, the expansion velocity $\vec{V}_{exp}$, the center coordinates l_0 and b_0, the density n_{shell}, the angular radius to the inner edge of the shell r_{in} and the thickness Δr

needed for the analysis of most of the shells around the Scorpius Centaurus OB association. This reduced the processing time but the reduction in data points did not have an impact on the results as tested for the pure shell in an empty environment. For large shells in real datasets, e.g. the USco-loop or the UCL-shell, data-cubes have sizes of $449 \times 386 \times 48$ and $2001 \times 1375 \times 111$ pixels respectively. In the following, the four different modeled datasets are listed. The values of the EHSS-model are always the ones of table 4.2. The first one is the **pure shell dataset**. The second one is a dataset where the EHSS-model has been inserted into a datacube with zero background intensity, the next one is a **shell in a random noise background environment**. Here a random noise value in a specified range has been added to the intensity in each pixel of the datacube where the shell does not contribute. This has been done for three different noise levels. Then **emission has been added to the shell**, which means that real H I emission of the GASS has been added to the sphere's intensity. The background pixels have zero intensity. The final dataset contains a **shell that is included into a real H I environment**. Here the shell without noise is embedded into a real background environment containing H I data from GASS. This means that the intensities of the pixels where the shell contributes are replaced by the shell's intensity values.

In figure 4.9, channel maps at the velocity $v = v_0$ are plotted for the four above described test datasets. As mentioned before for the rings, the plot on the top-left-hand side shows the channel map

of the pure shell test data, top-right for shell model in a real H I environment from the GASS-data, the bottom-left contains GASS-data on the shell and the bottom-right shows the shell model in a random noise background.

In the following, the tests are performed in the specific order of the datasets, from simple to complex, starting with the simplest test data set of an idealized object in an empty background environment.

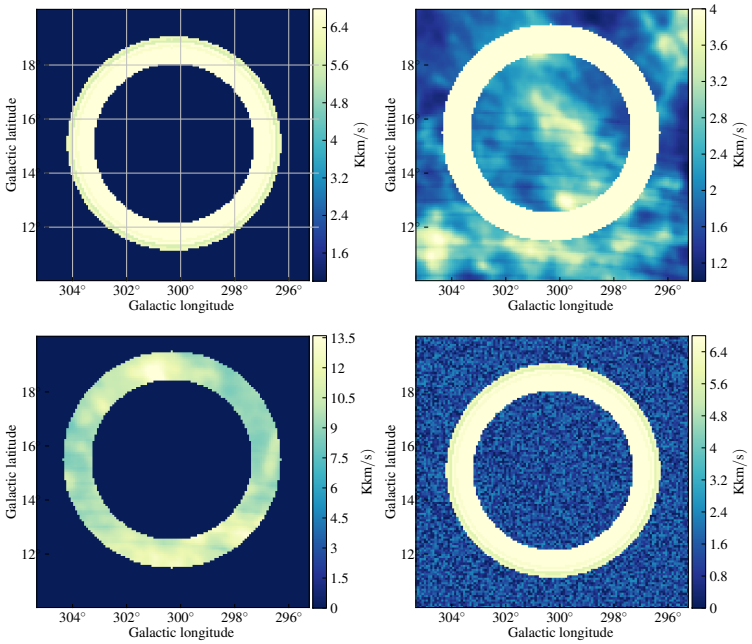

Figure 4.9: Figure showing the four created H I test datasets. The colorbar in each subplot denotes the respective brightness temperature. In each of the four panels a two dimensional slice of EHSS-model in different environments is shown. For a detailed explanation see text.

4.3.3 Fit of the ring to test datasets

The ring-model has been fitted to the different types of test datasets as described in the following. Beforehand, one parameter at a time was varied on a grid, while the others were held constant at its optimal values of table 4.1 to trace the change of χ^2 around the optimal values.

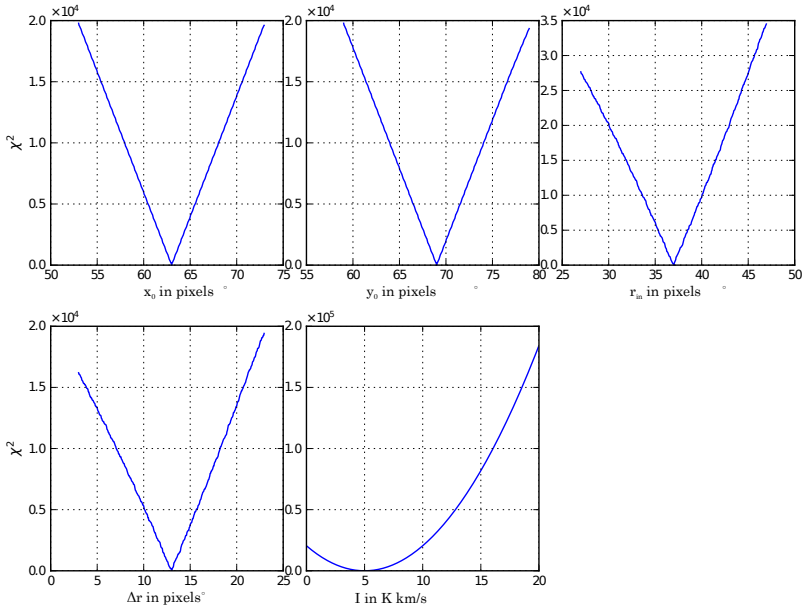

Figure 4.10: In each of the 5 plots, one parameter is varied around its optimum value, while the others are fixed at their optimum values. χ^2 is then plotted against the parameter value of the varied parameter in the respective plot. It is varied for 1000 steps in the respective ranges of each parameter.

Variation of one parameter on a grid As can be seen in figure 4.10, the variation of a single parameter of the ring leads to a monotonous downfall in χ^2 towards the minimum if the other parameters are held constant at their optimal values. Except for the density, χ^2 behaves linear around the minimum. Also χ^2 rises in at least 4 orders of magnitude when varying around the minimum, which could cause problems in the fitting process as is discussed below, where the model is fitted by using the MCMC method.

The MCMC approach The fit has been performed for 10^5 iterations and four times for different randomly sampled start parameters[11]. To test the robustness of the MCMC method for this problem, four runs with different start parameters have been performed. For the illustration, the burn-in phase is set to zero, as well as the thinning. The learning rate α has been tuned in such a way that the

[11] While it is more time efficient to use established MCMC routines because they are optimized in efficiency, a self coded MCMC sampler is used here for fitting the ring to the test datasets. At the cost of efficiency this grants access to each step of the code to track each processing step. And since the fit of the ring-model is 10^3 times faster than the one of the EHSS-model and the self written algorithm is just 10 times slower than the one of the PyMC package that will be used for the fit or the EHSS-model, as has been tested, the inefficiency can be neglected for the ring-model.

acceptance rate is about 30% for sufficient efficiency of the algorithm. This gives $\alpha = 0.02$ for each parameter.

Pure ring model The runs are presented in figure 4.11 that includes 5 subplots for the histograms as well as 5 subplots for the parameter progression during the fit process. In each plot, the results for 4 different runs, using randomly sampled start parameters are shown. The Markov Chain already converged after about 2000 iterations towards the optimal values, i.e. the values of table 4.1. The posterior distribution, in the best case following a Gaussian distribution if zoomed in, is just a bar in many cases in this unzoomed figure. But as is illustrated exemplary, below in figure 4.16, it is just distributed sharply around the optimal value. And as can be seen for each parameter, the fit of the ring-model is successful for this simplified dataset.

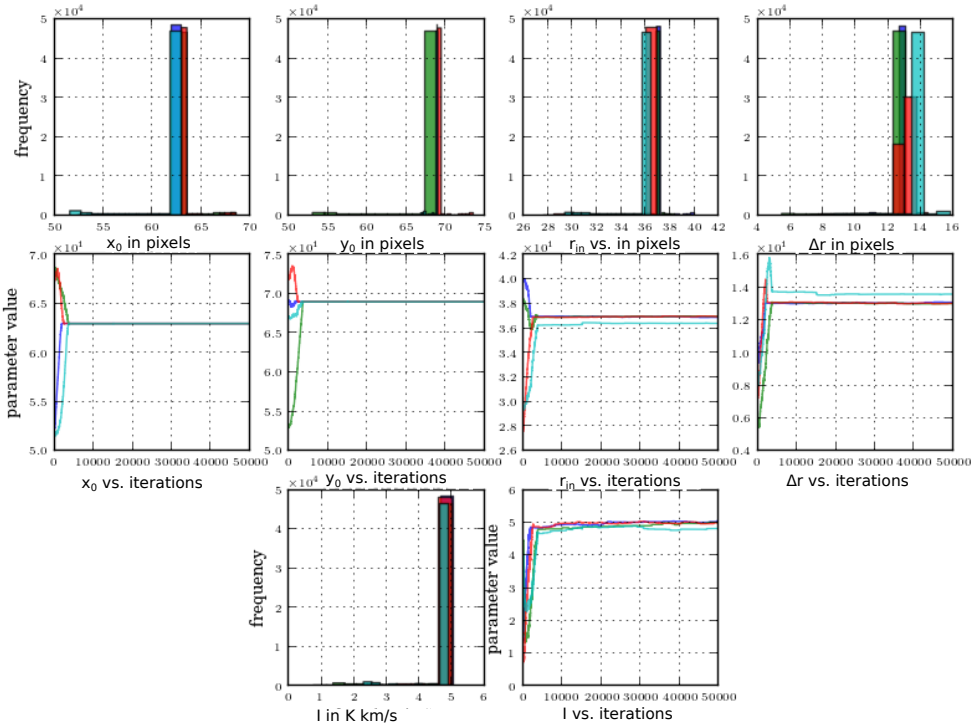

Figure 4.11: Results of the fit of the pure ring-model to test datasets with the parameters of table 4.1. There are two plots for each parameter. One showing the sampled distribution of the parameter and another one showing the progress of the sampled values for four 4 runs with different start parameters each. Counting the plots from the top left to the bottom right, the first 4 plots show the distributions of the parameters l_0, b_0, r and Δr respectively. Plots 5 to 8 show the parameter progression of l_0, b_0, r and Δr respectively. In the bottom row, plots 9 and 10 show the distribution and parameter variation of the density respectively. For a discussion see text.

Ring in a random noise background The modeled dataset contains a ring with a homogeneous brightness temperature of 5 K km/s and a noise background at the pixels where the ring does not contribute. Datasets have been made for three different noise levels. The noise was drawn from random brightness temperatures between 0–1 K km/s, 0–3 K km/s and 0–5 K km/s respectively. In figure B.0.8, the results for test data with 0–1 K km/s random noise are shown. The figure is arranged as figure 4.11. It can be seen that each parameter still converges towards its optimal values, but after a longer period of iterations as for the pure-ring test dataset.

If the noise level is raised to match the intensities of the ring, the results are ambiguous for different start parameter sets. The most striking value is r_{in}, because most Markov Chains converge towards a value close to a radius of 0 pixel, which would imply that the result is the best without the model, or at least with a model that contributes in a small portion of the whole pixel array. This is an unrealistic example, since in general, above the Galactic plane, the general intensity fluctuations are not as high as the intensity on the shell and if so, at least the cavity that the shell embeds should have a clearly lower density (sec. 4.1.3). Otherwise the shell would not be detectable. But even though this is an extreme scenario, the shape of the model is still idealized and the challenge for real H I shells would be even bigger.

Ring in a real H I background In this scenario, the ring has been fitted to a test ring in a real H I background environment taken from the GASS as introduced in section 4.3.2. Again four fits for uniformly randomly drawn start parameters have been applied using the MCMC algorithm with 10^5 iterations each. The results are appended in appendix B in fig.B.0.11.

A background model has been added by smoothing the original test dataset by applying a Gaussian filter to the pixel intensities (section 4.1.1). The resolution has been smoothed to the value of the estimated start parameter of the radius of the ring. The resulting datacube for this background has been added to the datacube of the ring model where the ring does not contribute, i.e. where T_{b}=0. The resulting model has been fitted to the data with the same specifications as for the fit without applying a background model. The results are shown in figure 4.12 where, similar to the plots above, results for four fits for uniformly randomly drawn start parameters are shown in a subplot for each parameter. For all parameters the four fits do not converge towards the same parameter values. For the fit, which is marked by the blue line in the subplots, the start parameters have been set too far away from the optimal values and it cannot converge. The other runs converge for Δr (dr in the plot), b_0 and are similar for r_{in}. But as can also be seen for the iterations of the thickness of the ring dr, in the center panel of the third row of figure 4.12, the burn-in phase would have to be set longer to avoid an over representation of outliers in the distribution.

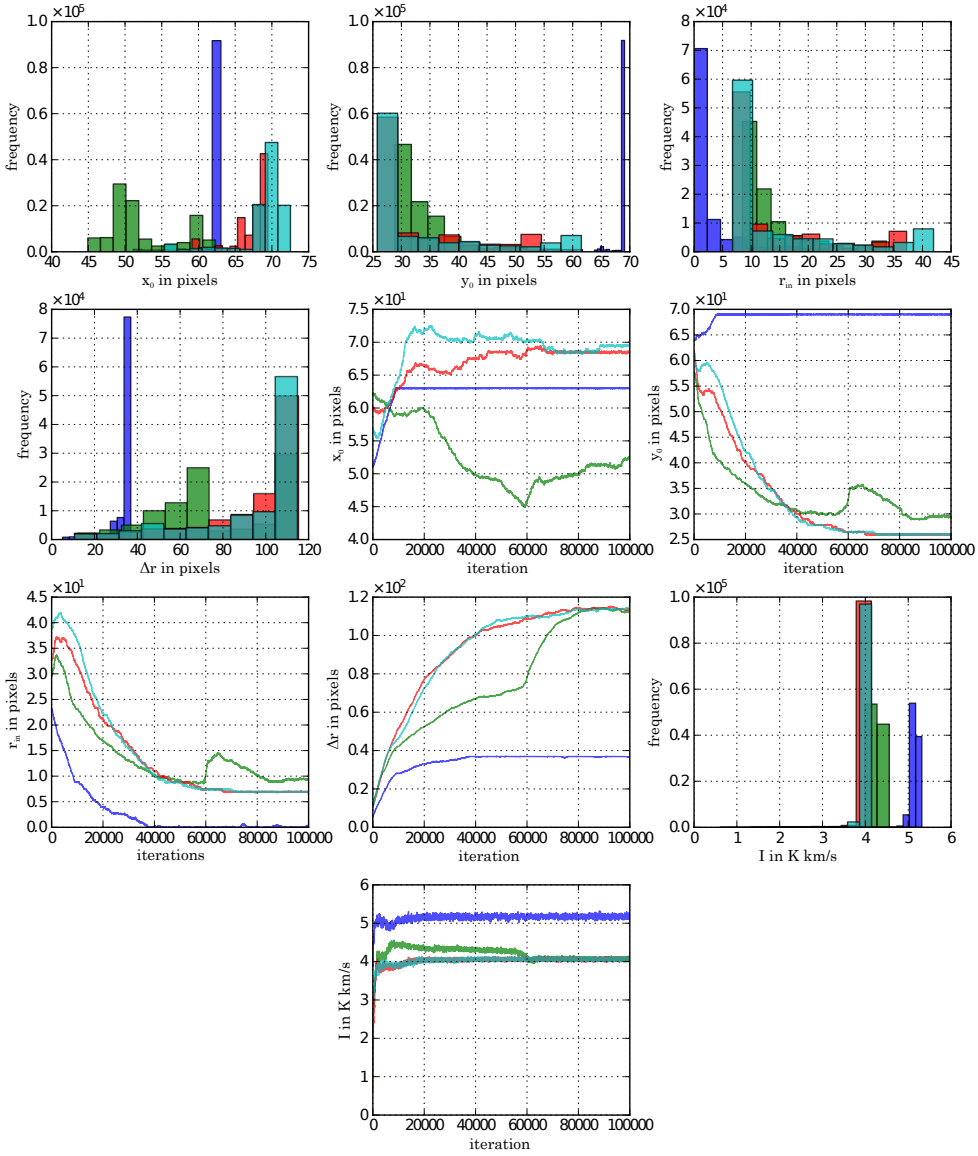

Figure 4.12: Similar figure to figure 4.11 with the same plot order but this time the fit is performed for a ring model in a real H I background environment. Fit results for four runs are shown and 5 panels show the distribution of the 5 parameters and the other 5 panels show the progression of the respective parameter.

4.3.4 Fitting the shell model to test data

For this problem, the MCMC fit method has been applied to fit the EHHS-shell model from section 4.2 to the test datasets from above[12]. The tests have been performed using a Gaussian distribution for the priors, i.e. the parameters as well as a uniform distribution. For the uniform distribution, each value in a specified range has the same a priori probability. The results are similar but the focus is on the results for the uniform distribution here, while the ones for Gaussian priors can be found in appendix B. For the uniform distribution, similar to the ring fit, upper- and lower boundaries and start parameters have been set for the priors. The Metropolis-Hastings sampler from section 4.3.1, has been used. The empirically determined number of iterations is 10000, because tests showed that, after 5000 iterations, the Markov chain is stationary, which can be seen e.g. in fig. 4.14. The thinning and the burn-in phase have been set to 0 to also trace the properties at the early phase.

Variation of one parameter on a grid Like for the ring-model, one parameter is varied manually in 500 steps around the minimum to learn how χ^2 changes. The other parameters have been kept fixed at the optimal values, which are the ones from table 4.2. The results for each parameter are shown in figure 4.13 and are represented by the green lines or -curves. While variation of the density and the thickness resulted in an expected change of χ^2, this is not the case for the other parameters. The variation of l_0 and b_0 show a very steep and linear change in χ^2, similar to that of the ring-model for values close to the optimum. For the variation of $\vec{V}_{\mathrm{exp}}$ and $\vec{V}_0$, χ^2 also increases steeply and linearly around the minimum but non linear if the parameter is more far away from the optimum than 1 km/s. Also the plots for V_{exp} and the inner radius show many rifles (small local minima).

In the following, it is focussed on the cyan colored curve that represents a variation of one parameter while all other parameters are offset. χ^2 is multiple magnitudes higher than for the other curves. For the parameters thickness (Δr) and expansion velocity (for V_{exp}, the curve cannot be seen in the plots as χ^2 is too high. For l_0 and b_0, the small offset of the other parameters leads to a maximum of χ^2 around the value that normally would result in the lowest χ^2. This is a potential trap for automated minimization, since certain parameters can be pushed away from its optimal values, if other values are too far away from their respective optimal values.

The sensitivity towards small parameter changes shows that the model is sharply defined and does not leave much space for offset start parameters. The high number of local minima made the application of the probabilistic ansatz of MCMC the preferred choice[13].

Fit to pure shell test data

The fit runs of the EHSS-model to the pure shell test dataset have been applied for 10^4 iterations without burn-in phase or thinning to track the complete path of the parameters here. For this particular dataset, the dominator in χ^2 according to eq. 4.27 is $\sigma_x = 1.50\,\mathrm{K\,km/s}$. The results are listed in

[12] In contrast to the ring-model, the fit is made using the open source python package PyMC (Patil et al. 2010), which provides an MCMC routine with integrated options to use different samplers like e.g. a Gibbs sampler or a Metropolis-Hastings sampler. This algorithm is optimized and faster than the self written code. This is important for testing since fitting this model is much more time expensive than the ring-model. 10000 iterations take approximately 5 hours to complete and four runs have been made to verify each fit.

[13] It has been tested how the ML algorithm performed on these data. The MCMC algorithm is stronger in getting out of local minima with the price of computational inefficiency. The ML algorithm is worse than the Bayesian approaches in determining the global minimum, especially when the start parameters are not close enough to the desired final parameters.

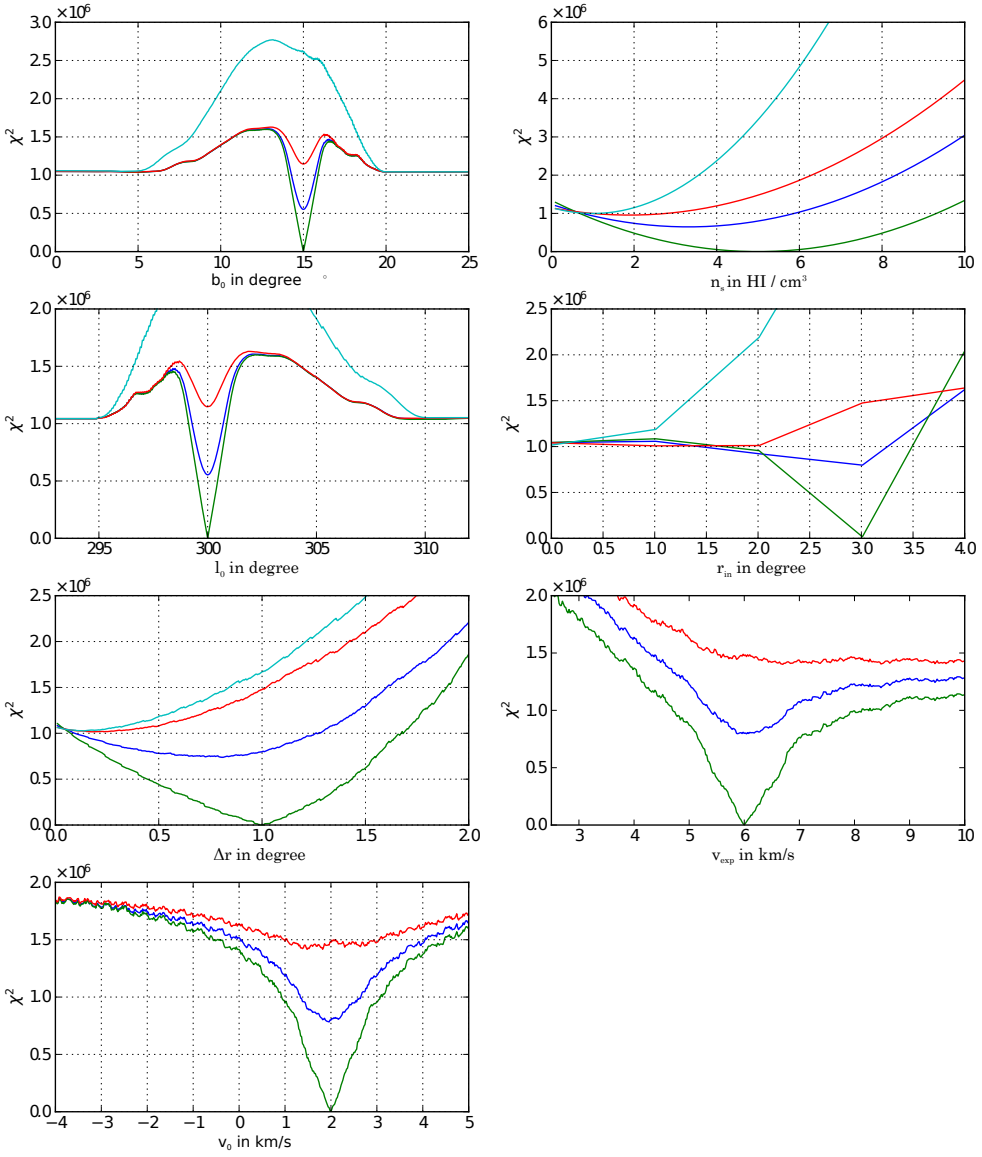

Figure 4.13: In each of the seven subplots, one parameter of the EHSS-model is varied while the other parameters are fixed. χ^2 is plotted against the respective parameter. The green solid line marks the variation where the fixed parameters have the values of table 4.2, i.e. the exact same parameters as the shell in the test data. The blue solid line represents the variation for one parameter while l_0 is shifted by 0.5°, except for the subplot on the top left where the center latitude (b_0) is shifted by that value since the center longitude (l_0) is varied here. For the red line, the shift in l_0 is 1°. The cyan solid line represents the variation where all fixed parameters are shifted by 1 for the respective units of the parameters l_0, the expansion velocity, the center velocity $\vec{V}_0$ and dens while for r_{in} and Δr the shift is 0.5°. For more information see text

table 4.3 as well as the specified lower and upper limits of the parameters and the randomly drawn start parameters $P_{\mathrm{st},i}$, where $i = 1, 2, 3, 4$ are the markers for the respective run and start parameter drawing. For the calculation of these values, a burn-in phase of 5000 iterations has been chosen to ensure that the chain is in the stationary state. It can be seen in the table that parameters like l_0, b_0, r_{in} and Δr have similar mean values between the four different runs. The highest differences between different runs for the same parameter occur for V_0 with a range of 6.0–7.6 km/s and V_{exp} that lies between 0.1–2.0 km/s as can be seen table 4.3.

In figure 4.14, in subplots for each parameter, the value of a parameter at its iteration step have been plotted to track the progress. This has been done along the line as it had been done for the fit of the ring described above. It can be identified that for each run, the chain converges after about 5000 iterations. For the center coordinates l_0 and b_0 all chains converge towards the same value but for the other parameters the fit results differentiate. In figure 4.15, the corresponding density distributions are plotted for each parameter.

Decreasing the range for start parameter limits The range in which the start parameters can be drawn uniformly was decreased to test if this increases the robustness of the fit results. Hence, the procedure from above has been repeated for this smaller range of start parameter variation and for 10^4 iterations. The resulting distributions of these four fits and for each parameter can be seen in figure B.0.17 in the appendix and the progression of the parameters are shown in figure B.0.18 therein. With the start parameters being closer towards the optimal values, a convergence towards the same values for all four runs is given as is shown in the figures.

The shape of the posterior distributions In both figures 4.15 and B.0.17, the distributions for all parameters show a thin peak-like distribution without significant flanks or tails. This is somewhat expected from the variation of one parameter from above since χ^2 increases by many orders of magnitudes even for a small variation. This means once the minimum is roughly found, values away from the minimum are almost always rejected according to eq. 4.31 and the variation of the stationary state of the chain is very small[14]. In figure 4.16m it is zoomed in and the bin size is adjusted and it can be seen that there is indeed a sampling around the optimal values and it is not just the same value that is always sampled.

[14] For this case the equation will always reject the proposed drawn parameter because a random drawn value will most likely have a higher value than the quotient

row	parameter units	l_0 °	b_0 °	r_{in} °	Δr °	nH I H I/cm^3	V_0 km/s	V_{exp} km/s
1	lower limit	299	14	1	0.5	1	0	1
2	upper limit	301	16	3	2	100	4	10
3	range: $\Delta P_{\text{st},i}$	±0.7	±0.7	±1	±.5	±4	±2	± 2
4	drawn $P_{\text{st},1}$	300.7	14.4	39.8	5.9	8.0	1.7	0.8
5	Results:							
6	$P_{\text{mean},1}$	300.04	15.0	2.94	1.15	0.3	7.64	0.47
7	$\sigma_{P_{\text{mean},1}}$	0.13	0.02	0.04	0.08	0.2	0.0	0.02
8	$P_{\text{mean},2}$	299.99	15.0	3.06	1.02	0.31	8.0	0.1
9	$\sigma_{P_{\text{mean},2}}$	0.03	0.02	0.06	0.14	0.22	0.0	0.01
10	$P_{\text{mean},3}$	299.97	15.0	2.99	1.02	0.4	5.99	1.98
11	$\sigma_{P_{\text{mean},3}}$	0.11	0.01	0.06	0.12	0.32	0.0	0.01
12	$P_{\text{mean},4}$	300.01	15.0	3.07	0.96	0.43	5.99	2.04
13	$\sigma_{P_{\text{mean},4}}$	0.06	0.0	0.02	0.04	0.23	0.0	0.07

Table 4.3: Lower- and upper limits of each start parameter in the rows 1 and 2. Row 3 contains the respective possible ranges $\Delta P_{\text{st},i}$ from which the start parameters $P_{\text{st},i}$ have been drawn uniformly. The drawn $P_{\text{st},i}$ are listed in row 4. The resulting fitted parameters of the EHSS-model using MCMC are listed in the rows 6–13. These are the mean values of the density distribution of each parameter $P_{\text{mean},i}$, as well as the standard deviation of the mean $\sigma_{P_{\text{mean},i}}$, which are listed in paired-rows for each start parameter set.

Fit to test data with background emission

Subsequently, the case of a shell in a noisy background and a real H I background environment, introduced above, have been tested. The shell in the test data has intensity values ranging from 7–14 K km/s as produced by the EHSS-model itself, while the random noise has been drawn uniformly between 0–2.5 K km/s[15]. This means the random noise has a maximum brightness temperature of 35% of the shell's intensity. Hence the shell is still "bright" compared to the background, which was identified to be necessary also for the simpler fit of the ring-model to noisy data from above. Again, the start parameters have been sampled randomly uniformly for four different runs. The resulting density distributions of each parameter are shown in the subplots of figure B.0.19 in the appendix.

Like for the case of the shell in an empty background, the results of different MCMC runs for the parameters $\vec{V}_{\text{exp}}$ and $\vec{V}_0$ are ambiguous. But even when choosing a small parameter range for random sampling, this problem remains. Similar results have been obtained for a real background environment. The results are not further discussed here but shown in the figures B.0.15 and B.0.14 in the appendix. The takeaways from all tests are discussed in the following.

[15] When setting up the EHSS-model, a particle density of 5 H I/cm^3 is chosen but this translates into an inhomogeneous intensity distribution in each channel map because the change of the projected expansion velocity is not homogeneous. Hence in different channel maps and on different radii, the intensities can vary.

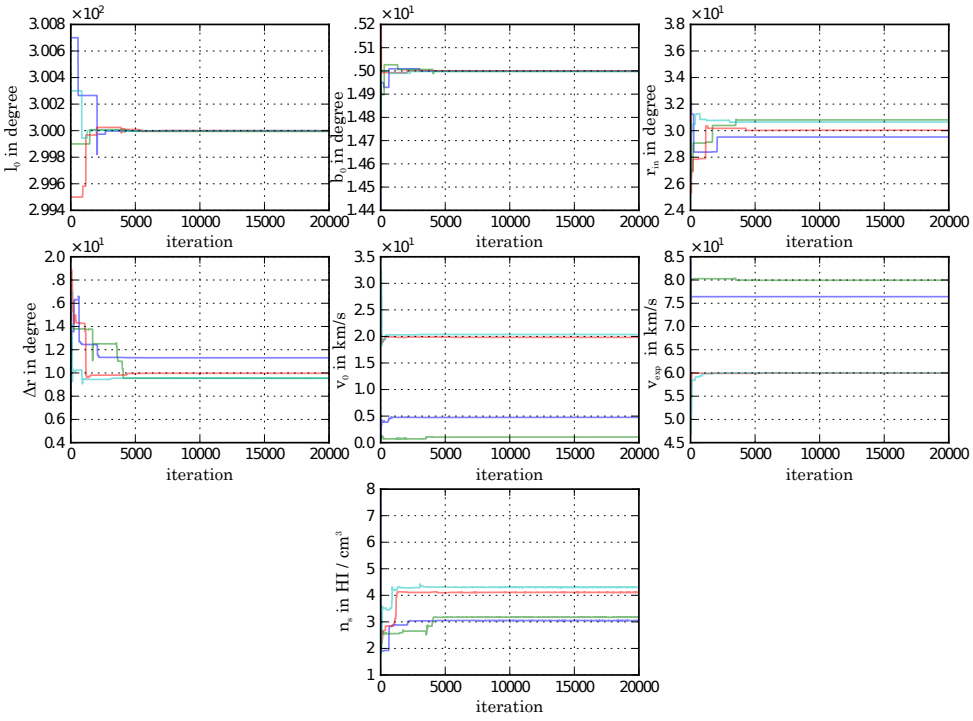

Figure 4.14: The progression of each parameter with each iteration of MCMC is shown. In each subplot, the results for one parameter for four MCMC fits of the EHSS-model to the pure shell test dataset, with different start values for the parameters, are plotted. For more information see text

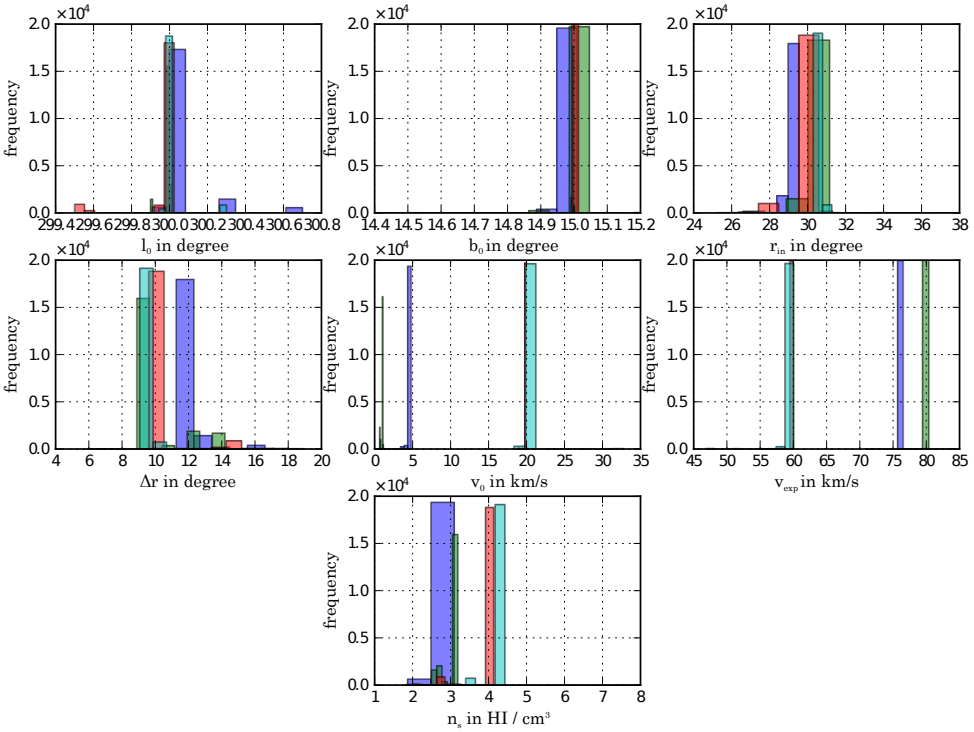

Figure 4.15: Histograms of the sampled density distributions using the MCMC algorithm to fit the EHSS-model to a pure shell dataset. The number of iterations is 20000 without burn-in phase. In each subplot, four MCMC runs have been performed for a respective uniformly drawn start parameter. For more information see text.

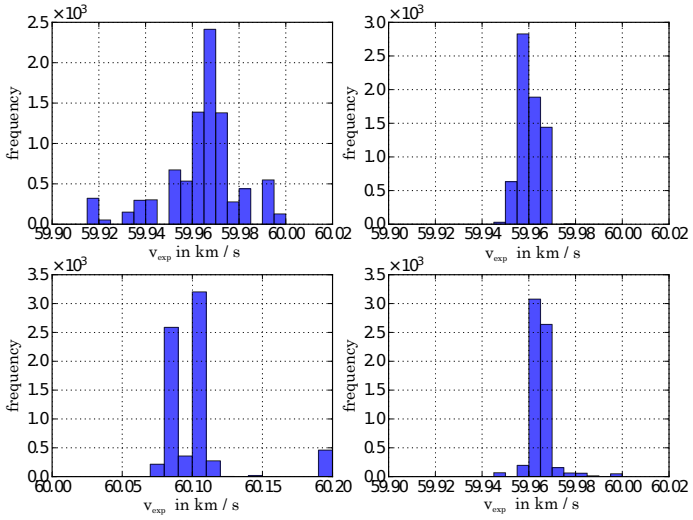

Figure 4.16: Exemplary, a zoom-in of figure B.0.17 with adjusted bin size and for one plot for each run, showing the sampled distribution of the expansion velocity. For more information see text.

4.3.5 Dicussion of the tests

For idealized cases, where a shell is put into an empty datacube, when the start parameters are not close to their optimum, the fit mainly converges towards the global minimum if the start parameter range is not too high. The MCMC approach is more robust than the classic ML approach but also fails in some examples. When adding noise to the shell with a level of about 20-40% of the shell's intensity, even with a small start parameter range around the optimal value, the four different runs do not converge towards the same values. The problem of this approach is that only the intensity difference in the respective pixels, where the model is present matter. If they are not in the range of the uncertainties for each parameter, χ^2 will instantly rise by a factor of 10^4 due to the background pixels that have wrong intensities. This magnitude depends on the number of data points, i.e. pixels in an image. If for example just the position of the shell or the ring is offset, χ^2 won't change until the position is near the one of the data as visualized in figure 4.13 for the variation on a grid. This is why the start parameters have to be close to the minimum values, which is just possible if prior knowledge about the shell is given, e.g. by prior visual investigations. Additionally, this method is sensitive to background emission. This is because the residuals of the intensities of each pixel are calculated and that also includes all background pixels. If for example the EHSS-shell or ring has the exact same parameters as the ring in the test datasets but the background intensities differ, this will dominate χ^2, depending on the amount of pixels the shell- and the background contributes. In general, the background volume is larger than the shell volume and hence if the background is not modeled nearly accurately, the fit won't find the minimum consistently.

It is possible to ignore pixels outside the modeled object and normalize χ^2 to the number of pixels of the shell/ring to the object. But this approach would be biased because it would perform better for smaller objects with less data points to be fitted than larger ones.

One reason for the deviation might be due to the amount of data points. The modeled shell contains 45541 data points where the shell contributes. For example even a deviation of one pixel for the center coordinates causes to increase the logarithm probability, i.e. χ^2, by four orders of magnitudes. The velocities are the most challenging parameters to fit. This can be seen as follows, if e.g. just the expansion velocity is off, each ring in each velocity channel is shifted and the increase in χ^2 is very high and might not change until a value close to the optimal one is drawn.

However, while it has not been possible to fit all parameters of the model reliably, this model is still a good description of an idealized spherical shell and can help to determine remaining parameters of a shell if most parameters of the shell have already been measured. This also reduces the dimension of the space and leads to higher performance. This approach is used below in section 4.4.2 to determine the masses of the shells.

4.4 Fitting the model to H I data

Here the derivation of an H I background model for the emission near the Sco-Cen region from the H I data of the GASS that is needed to determine shell masses in section 6.3.1 is presented.

4.4.1 Modeling the H I background emission

The main source of background emission that does not come from the Sco-Cen region at latitudes lower than about 10°, is the overlapping emission of the Galactic disk. When calculating the masses of the shells, this emission should be considered. Cappa de Nicolau & Poeppel (1986), de Geus (1992) and Poeppel et al. (2010) made a cut at 10° and the affected pixels were ejected or intensity values were extrapolated for these regions to avoid modeling the background directly, which is an efficient approach. But for the Sco-Cen region, in this thesis, a different approximation has been made by taking into account the exponential nature of the Milky Way disk, where the density and hence the emission decreases with increasing latitude. Equation 2.17 describes the general latitude dependence of the intensity. Since the complete H I data are available for this region and above, it has been tested if a region based background model can be derived.

In order to do that, first the mean brightness temperature $T_{\mathrm{b,mean}}$ at a fixed latitude ($b \pm 0.1^\circ$) along longitudes from 240°–20° of 5 consecutive velocity channels has been calculated. This has been done for 20 latitudes in the range of 0–20°. Due to the number of results, an excerpt of the full table A.0.15 from the appendix is shown here in table 4.4. This table shows the results of the channel range 50–55. For each range, this is done for multiple latitudes between $[0 - 20]^\circ$ as can be seen in columns 1. The standard deviation, denoted as $\sigma_{T_{\mathrm{b,mean}}}$, has also been calculated for each $T_{\mathrm{b,mean}}$. These points and their uncertainties are plotted in figure 4.17 as visualized by the blue dots and the blue error bars.

Then it was tested, which analytical function fits these values best. It can be seen that the distribution of one channel interval has a sigmoid-like shape. This shape is observed for each channel, but with different steepnesses. The first approach was to fit[16] an exponential function to the data, but it was not able to cover this sigmoid-like shape for all channels and has high uncertainties as can be seen by the red curve in figure 4.17. A different function that is well suited to fit sigmoid like shapes is needed, which leads to the introduction of the Hill function.

Approximation of the background emission by the Hill function

The best fitting function to the data that could be determined, is the Hill-function, or -equation (Hill 1910; Gesztelyi et al. 2012), which can be seen as the black line in figure 4.17. The Hill function is a sigmoid-like function that allows asymmetries between the upper and the lower tale of the function. Here the negative of the Hill function $HF(x)$ has been used, adding one fixed parameter that is the value of $T_{\mathrm{b,mean}}$ at zero latitude ($b = 0$):

$$HF(x) = -1 \cdot \frac{A \cdot x^N}{K^N + x^N} + T_{0,\mathrm{mean}} \tag{4.32}$$

where A, N and K are the parameters that have to be fitted, see also table 4.5.

[16] Here, fits have been performed using the Marquardt-Levenberg algorithm from section 4.3.1.

b / °	$T_{\mathrm{b,mean}}$ K km/s	$\sigma_{T_{\mathrm{b,mean}}}$ K km/s	$\mathrm{ch_{up}}$ -	$\mathrm{ch_{low}}$ -
0.0	76.0	36.2	55	50
0.2	75.2	35.4	55	50
0.3	74.2	34.3	55	50
0.5	69.9	32.1	55	50
0.6	67.9	31.5	55	50
0.8	63.3	30.3	55	50
1.0	59.7	29.4	55	50
1.5	53.4	27.5	55	50
2.0	48.7	25.7	55	50
3.0	42.0	22.0	55	50
4.0	36.8	18.6	55	50
6.0	29.5	14.0	55	50
7.0	27.3	12.2	55	50
9.0	26.3	9.6	55	50
10.0	24.0	8.6	55	50
12.0	25.4	9.7	55	50
13.0	26.1	10.2	55	50
14.0	25.7	10.5	55	50
17.0	22.5	12.8	55	50
20.0	19.8	10.6	55	50

Table 4.4: For 20 different latitudes b, listed in column 1, mean brightness temperatures $T_{\mathrm{b,mean}}$ (column 2) with standard deviations $\sigma_{T_{\mathrm{b,mean}}}$ (column 3) along the longitude range 240°–380° are averaged from velocity channel 55 (column 4) to velocity channel 50 (column 5). This table is an excerpt of table A.0.15 that shows the full relevant channel range of 0–110

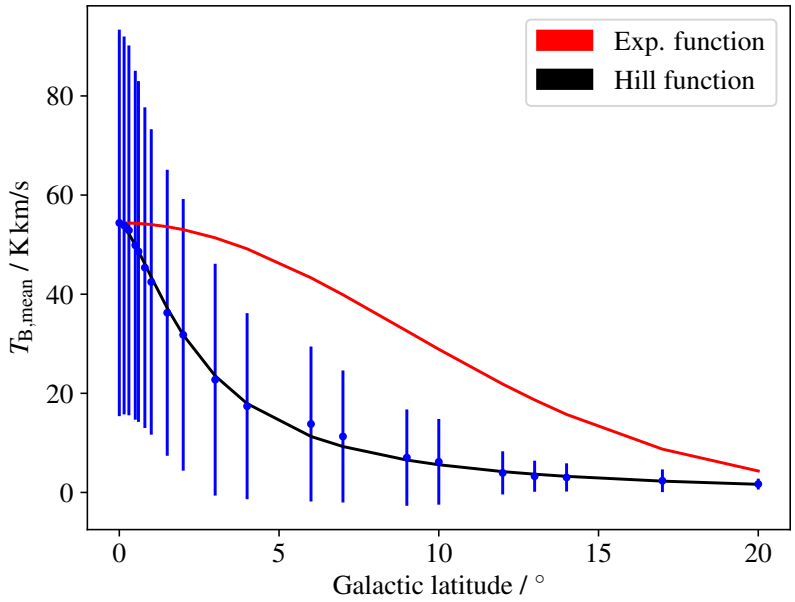

Figure 4.17: Exemplary plot of the fit results of an exponential function (red) and of the Hill function (black) using the data from table 4.4 for the channel range 30–35. The measured mean brightness temperatures are marked by blue dots and its standard deviations are marked by the blue vertical lines at the respective latitude.

Fit of the Hill function to H I data

To each channel range of the full table A.0.15, the Hill function has been fitted using the Marquardt-Levenberg algorithm from section 4.3.1. The fit results are listed in table 4.5, where the channel range is now expressed in velocity values, in columns 1 and 2, χ^2 is listed in column 3. Columns 4, 5 and 6 contain the fitted parameters of the Hill function and column 7 shows the respective mean brightness temperature value at zero latitude. The resulting shape for the channel range 50–55 is presented in figure 4.17 (blue line) and it can be seen that the Hill function fits the data well as is also induced by the low value of χ^2 in the table[17]. The Hill functions with its determined parameters for different channel ranges can be used as background models for the general Galactic disk emission in the regions of Sco-Cen for different channel maps.

ch_{low}	ch_{high}	χ^2	A	N	K	$T_{b,mean}(0^\circ)$
80	110	0.12	39.2	1.63	1.23	39.1
75	80	0.18	66.8	1.15	2.08	64.0
70	75	0.25	72.4	1.04	2.48	67.8
65	70	0.12	81.8	0.84	4.12	70.8
60	65	0.19	100.0	0.64	21.06	65.3
55	60	0.11	71.7	0.82	5.95	77.1
50	55	0.21	55.9	1.41	2.04	76.0
45	50	0.08	54.8	1.41	1.68	67.6
40	45	0.17	55.3	1.27	1.59	62.2
35	40	0.10	58.1	1.18	2.05	59.7
30	35	0.07	58.4	1.30	2.66	57.2
25	30	0.09	55.2	1.49	2.56	54.4
0	25	0.03	35.7	2.26	2.47	35.7

Table 4.5: Fit results for different channel ranges from channel 0–110 (row 1 and 2) corresponding to a velocity range of -45 to +45 km/s with a channel width of 0.8 km/s. The resulting χ^2 is listed in row 3 and the rows 4, 5 and 6 contain the best fit parameters of the Hill function. The mean brightness temperature at zero latitude is shown in row 7 in units of K km/s.

4.4.2 Mass determination of H I Shells by fitting the EHSS-model

For the analysis of the shells in the ISM in the vicinity of Sco-Cen that is presented in section 6.3.1, the EHSS-model from section 4.2 has been fitted to the GASS H I data of this region.

In this case, the shell parameters are known by different analyses of this work (ch. 6) and just the mass of the shell has been fitted. This means from the 8 parameters of the EHSS-model, just the density was varied. Using the knowledge derived from fitting this model to test data from section 4.3.4, the parameter was varied on a grid instead of fitting it. This can be done since the searching space is reduced to a one–dimensional problem and hence performance is not an issue compared to multidimensional search problems. For some shells of Sco-Cen, a density gradient towards higher distances (from the front, to the back of the shell) is observed. Therefore instead of fitting one shell to the data, two semi-shells have been fitted, having one density parameter each, ρ_{front} and ρ_{back}, leading to a two dimensional parameter space.

[17] In this plot it can also be seen that the standard deviation is an overestimation of the uncertainties. Dividing the uncertainties by 4 gives the same fit results and would result in a χ^2 of 1 that is often desired. But since this is a tuning of the value and does not change the results, the standard deviation is still chosen as the representative uncertainty.

Here exemplary, the grid search results for the USco-loop are presented. First, the variation has been done with large step sizes in the range of 0–100 H I cm^{-2} as this is a quite common range[18] to enclose the region of the minimum. Then a smaller step size was chosen to vary the density in the region around the minimum. The background model from section 4.4.1 is used to correct the model for the emission of the Galactic disk. The calculation of χ^2 then is:

$$\chi^2 = \sum_i^n \frac{\left(I_{\mathrm{data,i}} - (I_{\mathrm{model,i}} + I_{\mathrm{BG,i}})\right)^2}{\sigma_i^2} \tag{4.33}$$

where n is the total number of pixels, $I_{\mathrm{data,i}}$, $I_{\mathrm{model,i}}$ and $I_{\mathrm{BG,i}}$ are the intensities (brightness temperatures in units of K km/s) of the i-th pixel of the data, the model and the background model, respectively.

The grid search for ρ_{front} and ρ_{back} is shown in figure 4.18. On the left hand side, the dependence of χ^2 on both parameters is presented. It can be seen that the best fit values are reached at a number density of $\rho_{\mathrm{front}} = 4.8$ H I atoms per cm^2 and $\rho_{\mathrm{back}} = 0.48\,cm^{-2}$ (see also table 6.7). On the right hand side of the figure, the one dimensional change of ρ_{back} is shown for all variations on the grid. The lowest curve for the smallest χ^2 is the one, where ρ_{front} has the optimal value. The plots for the other parameters and shells are shown in appendix B in figure B.0.44.

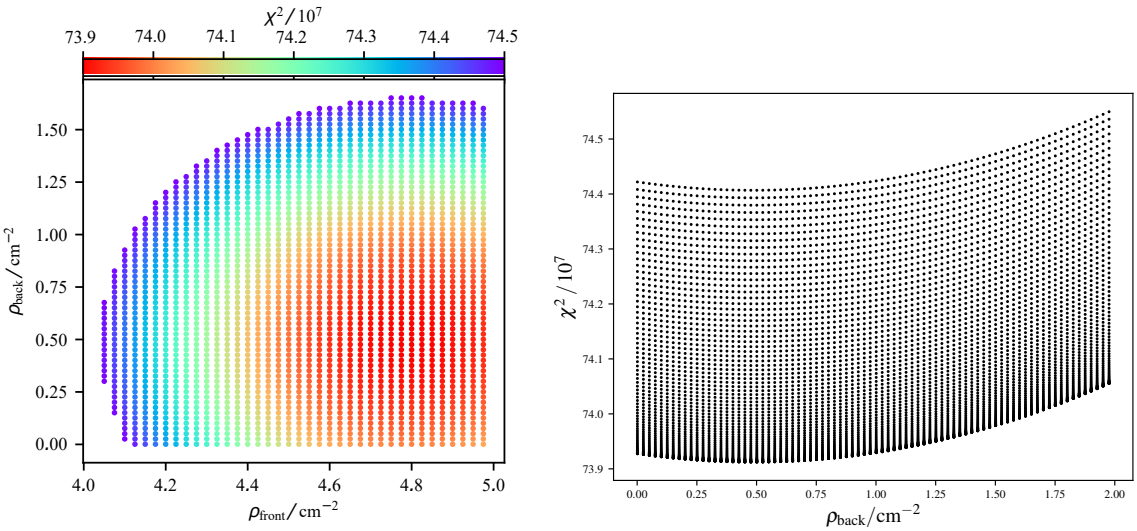

Figure 4.18: Two plots showing the results of the fit of the EHSS-model to the GASS data for the USco-loop. On the left hand side, ρ_{front} and ρ_{back} are plotted against each other for each variation on the grid. The color denotes the respective χ^2 at each point on the grid, where red denotes the lowest values of χ^2 and blue represents the highest values. In the right panel, χ^2 is plotted against ρ_{front} for each variation of ρ_{front} and ρ_{back}, illustrating the variation of χ^2 near the minimum in one dimension.

[18] It has been measured that 100 H I cm^{-2} is one order of magnitude too high

Mass calculation With the derived density parameters, the mass ($M_{\rm mod}$) on a spherical shell can be calculated as follows:

$$M_{\rm mod} = \frac{1}{2} \cdot (\rho_{\rm front} + \rho_{\rm back}) \cdot \frac{4}{3} \pi \, (R_{\rm out}^3 - R_{\rm in}^3) \tag{4.34}$$

where $R_{\rm min}$ and $R_{\rm max}$ are the radii of the inner- and outer edge of a shell. This equation is used as one of several methods for the mass calculation of the shells of Sco-Cen in section 4.18.

4.5 H I shell search algorithm for Galactic H I data

To analyze the Galactic H I data is a more complex task than to investigate specific regions due to complex structures and high intensity-, as well as velocity ranges and because these properties are not a priori known for all regions. To do this visually by hand is not an option. On the one hand because of the amount of data to investigate and on the other since this is also prone to missing detections of shells and biases. Automated shell detection algorithms aim to detect new shells. In the past, some pioneer works using partly automated surveys like (Ehlerová & Palouš 2005, 2013; Suad et al. 2014) or exclusive visual inspections like the ones from McClure-Griffiths et al. (2002) or Sallmen et al. (2015) have been applied to H I datasets like the ones of LAB (see also sec. 2.4.3). Some of these investigations used higher resolution data but for smaller fractions of the sky. For this work, the effective 4 times higher resolution of the HI4PI is available that also covers the full sky (sec. 3.2). In this thesis, the aim is to apply an automated **S**earch **A**lgorithm for **G**alactic **H I S**hells, (**SAGHIS** hereafter). This naming is to distinguish it from search algorithms from other studies and the EHSS-model from section 4.2. The algorithm uses a different approach compared to other known studies. The results have been post processed by a visual analysis to eliminate false positives and quality measures to rank the shell as will be done in section 4.6.3.

Gained knowledge about properties of H I in general as well as the characteristics of expanding H I shells in these data has been used (sec. 3.3) . The complexity of H I structures in the Galaxy implies that a detection algorithm needs to be robust to high intensity variations in latitude, longitude as well as in the spectral dimension (velocity). Many classic image feature detection algorithms focus on the most prominent features or strong, well defined edges and disregard lesser prominent features, which is not sufficient enough for the detection of expanding shells in H I.

Based on this knowledge, pattern recognition algorithms have been introduced and tested in section 4.1 to detect these characteristics in two-dimensional slices of the data. The region adaptive method of section 4.1.1 is key to reliably detect features in a large angular range in the HI4PI data. The SAGHIS, described in the following is a connection of these methods. Each step of the algorithm contains various parameters. These parameters and their specifications are introduced and specified. To derive some parameter values, properties of known shells in ISM environments of different intensities, at different moving velocities, latitudes and of different expansion velocities have been measured as follows.

4.5.1 Measuring properties of different H I shells

Some observed Galactic shells from other studies (McClure-Griffiths et al. 2002; Ehlerová & Palouš 2013; Sallmen et al. 2015) have been inspected visually, following the assessment criteria from section 3.4.3 as described here. The shells have been chosen to cover a high variety in l, b and v as well as different angular sizes in the range of 1–20°. The main properties of different objects of different studies have been converted to be in the same measures to make the objects comparable. These are the center longitude l_0 , the center latitude b_0, the latitude spread Δl, the longitude spread Δb, the expansion velocity v_{exp} and the moving velocity v_0. These are listed in table A.0.16 in the appendix. The 17 shells have then been inspected using the HI4PI data. The velocity extent, which is in approximation $2v_{\mathrm{exp}}$ (column 7) has been remeasured for some cases and is listed in columns 9 and 10 of the table. The aim was to gather insights on the intensity ranges in the cavity of the shell, compared to the ones on the shell and of the ambient ISM around the shell. The values have been

stored in table 4.6 and are explained in the following.

For each shell $i \in \{1, 2, ..., 17\}$, intensities (brightness temperatures) $I_{\mathrm{cav},i,j}$ with j being one of 20–30 random points in the cavity (cav) of the shell i are measured. The mean intensity in the cavity of each shell $\overline{I}_{\mathrm{cav},i}$ has then been calculated and stored in column 3 of table 4.6. The corresponding standard deviation $\Delta\overline{I}_{\mathrm{cav},i}$ is listed in column 4. $I_{\mathrm{cav},i}$ range from 0.3–20.5 K km/s for the different shells. Similarly the mean brightness temperatures on the shells $\overline{I}_{s,i}$ have been measured. These values are between 3.2–48.8 K km/s. Having these values for each shell, the ratio $c_{\mathrm{cav},i} = \overline{I}_{\mathrm{cav},i}/\overline{I}_{s,i}$ can be determined, which is listed in column 1. This value ranges from 0.09–0.71. Intuitively, the value is expected to be smaller than one since in the cavity less material should be left compared to regions on the shells, which contain compressed ISM due to stellar winds and SNe (section 2.3).

The ranges of the values show how different the shell properties are. Some shells contain severe background material at the velocity channels in its cavities and the mean difference between the intensities of the cavities and the ones of the shell is small (e.g. GSH 052+10-087 or GSH 040+04+048), while for others, the shell is much denser than the cavity with GSH 134-43-062 being the most extreme example with $c_{\mathrm{cav}} = 0.09$ (see also section 4.1.3). The difference between the center points of the shell in two neighboring channel maps is measured and the mean value $\overline{\delta p_{ij}}$ and its uncertainties $\Delta\overline{\delta p_{ij}}$ have been calculated and are listed in Columns 10 and 11 of the table. This is used in the following.

4.5.2 Description of the algorithm

In the first step, each channel map of the H I datacube is analyzed separately. Here it has been searched for the inner edges of the ring using the pattern recognition algorithms from section 4.1.

Edge detection As explained in section 4.1.1, usually the data have been preprocessed for edge detection methods by Gaussian smoothing to delete noise, which could lead to false edge detections. But due to the test results therein, no smoothing has been applied to the HI4PI data here. The benefit is that no information are lost in the first step. It has been focussed on the elimination of false positives in later steps. It is important that the edge detection performs adaptively, depending on the intensity distributions of the region. This is why the customized edge detection method has been applied instead of the Canny edge detection, since tests in this section also showed that this method leads to the most accurate edge maps, if a priori the thresholds are not known specifically.

Hough Transformation for circles On the resulting binary images produced by the edge detection algorithm, the Hough transformation for circles from section 4.1.2 has been applied. The choice of the starting radius $R_{\mathrm{H,min}}$, increment steps in radius size ΔR_{H} as well as the maximum radius, $R_{\mathrm{H,\,max}}$, are decisive for the limitations of the shell survey. To detect the smallest circle-like structure that can be resolved, $R_{\mathrm{H,min}}$ should be higher than 0.27° (3 pixels), which is the resolution of HI4PI. ΔR_{H} is also set to 0.27°[19].

The maximum allowed circle radius $R_{\mathrm{H,\,max}}$ can in theory be set to the maximum known size of a supernova remnant in angular radius, which is the UCL-shell with an elliptical shape and a major-half axis of 140°, i.e. $R_{\mathrm{H,\,max}} = 70^\circ$. The largest SNRs in angular size are local ones and the total number of known Galactic SNRs, above an angular radius of 20°, in other previous studies are less than 10

[19] It has been tested to set the increase to 1 pixel (0.08°) instead but this resulted in a much higher number of clustered false positives in the later steps of the algorithm.

1	2	3	4	5	6	7	8	9	10	11
shellname	c_{cav}	Δc_{cav}	$\overline{I}_{\mathrm{cav}}$	$\Delta\overline{I}_{\mathrm{cav}}$	$\overline{I}_{\mathrm{s}}$	$\Delta\overline{I}_{\mathrm{s}}$	$\overline{I}_{\mathrm{a}}$	$\Delta\overline{I}_{\mathrm{a}}$	$\overline{\delta p}$	$\Delta\overline{\delta p}$
GSH 263+00+47	0.19	0.068	6.7	1.7	35	8.8	5	1.3		
GSH 267-01+77	0.51	0.179	8.6	2.2	17	4.3	17.9	4.5		
GSH 327+04-25	0.6	0.213	20.5	5.1	34	8.5	38.5	9.6		
GSH 319-01+13	0.19	0.068	5.5	1.4	28.5	7.1	29.3	7.3		
GSH 255-00+52	0.19	0.137	9.6	5.5	51	22.7	19.7	23.1	2.4	0.5
GSH 292-01+55	0.27	0.118	6	1.1	22.3	9	16.1	20.5	0.3	0.5
GSH 179-24+012	0.33	0.182	16.3	7.4	48.8	14.6	38.3	27.8	3.5	1.0
GSH 052+10-087	0.71	0.178	4.7	0.7	6.7	1.4	3	1.3		
GSH 040+04+048	0.62	0.17	18.5	0.4	30	8.2	33.8	18.7		
GSH 052-05+023	0.49	0.201	19.9	6.2	40.7	11.1	38.9	23.6	0.9	0.5
GSH 062+03-102	0.48	0.157	6.5	1.3	13.7	3.5	7.8	4.5	0.2	0.2
GSH 134-43-062	0.09	0.033	0.3	0.1	3.2	0.8	0.1	0		
GSH292.0-01.5+50	0.14	0.049	3.5	0.9	25	6.3	3.4	0.9		
GSH250.0+01.5+67	0.34	0.196	10.7	5.2	31.7	9.8	10.1	5.5	1.5	0.2
GSH066.0-01.5-88	0.37	0.297	7.6	3	20.4	14	7.8	4.5	0.6	0.3
GSH243.5-02.5+43	0.37	0.407	9.2	9.6	25.1	10	4.7	3.4	0.6	0.3
GSH226.5-09.5+31	0.36	0.299	8.5	4.6	23.3	14.5	8.6	3.4	0.8	0.5

Table 4.6: Mean brightness temperature measurements in–, on– and in the vicinity of shells in H I datacubes. The 17 supernova remnant shells used for the measurements stem from table A.0.16 and are examples adopted from other studies (McClure-Griffiths et al. 2002; Ehlerová & Palouš 2013; Sallmen et al. 2015). The table contains mean intensity values for each shell $i \in \{1, 2, ..., 17\}$. These values have been derived from 20–30 individual measurements of brightness temperatures at points in the cavity of each shell $I_{\mathrm{cav},i,j}$, points on the shell $I_{\mathrm{s},i,j}$ and points outside of the shell $I_{\mathrm{a},i,j}$. The name of the shell is listed in column 1. The derived ratio c_{cav} between the mean intensity in the cavity $\overline{I}_{\mathrm{cav},i}$ and the one on the shell $\overline{I}_{\mathrm{s},i}$ is listed in column 2. Column 3 contains the standard deviation $\Delta c_{\mathrm{cav},i}$. $\overline{I}_{\mathrm{cav},i}$ and the mean uncertainties $\Delta\overline{I}_{\mathrm{cav},i}$ are listed in column 4 and 5 respectively. The mean on shell intensities $\overline{I}_{\mathrm{s},i}$ and its uncertainties $\Delta\overline{I}_{\mathrm{s},i}$ can be found in columns 6 and 7. Columns 8 and 9 contain the mean intensities of the ambient ISM around each shell $\overline{I}_{\mathrm{a},i}$ and its uncertainties $\Delta\overline{I}_{\mathrm{a},i}$ respectively. The measured mean difference between the center coordinates of the shell $\overline{\delta p}$ and its uncertainties $\Delta\overline{\delta p}$ of two neighboring channels k and l are listed in columns 10 and 11.

in total (McClure-Griffiths et al. 2002; Ehlerová & Palouš 2013; Sallmen et al. 2015) and they are all detectable visually even on low resolution data. It should also be considered that in previous studies, it is referred to the sizes of the outer edges of the shells and the Hough transformation here searches for the inner edges of the shells. Hence, the missing detections can be assumed a priori when choosing this as a limit. The CAR-projection (sec. 3.3.1) is equidistant in longitude and latitude near the Galactic plane and since the vast majority of shells is expected to be located in the Galactic plane, well suited for the search. It is also the one used in other studies that are compared. Since it is not expected to discover new shells above this angular size and since handling the projection effects, without significantly changing the algorithm at the cost of its general applicability, would go beyond this work, $R_{\mathrm{H,max}} = 20^{\circ}$ is also the maximum limit.

Each Hough circle contains an accumulator value (sec 4.1.2) of its quality. Observations show that shells often are not fully closed circular structures, but fragmented and sometimes open towards one or multiple directions. They also have shapes, different from the one of a perfect circle. So the algorithm aims to find arcs of the shell and not complete circles. For example an absolute accumulator value of 0.2 would mean that 20% of the pixels on the Hough circle are edge pixels. As mentioned in section 4.1.2 in the tests, it is empirically derived that a limit relative to the maximum accumulator value of $\mathrm{A_{H,min}} = 0.2$ leads to the best results. Similar to the step above, detections are accepted that are sorted out in later steps, when additional properties of expanding shells are included. The accumulator values have additionally been used in a post analysis as a quality measure to rank the resulting expanding shells (sec. 4.6.3). The Hough transformation for circles yields, not only edges of the inner part of a ring, but also the outer radius of circular-like blobs, which have to be distinguished.

Separation of cavities from blobs In section 4.1.3, it has been introduced how to distinguish structures like blobs or just random structures that lead to circle-like shapes in edge-maps from shells from cavities. Equation 4.14 is used and the limit for c_{cav} defines how strict this criterion is. The highest measured value from section 4.5.1 is $c_{\mathrm{cav}} = 0.71$. To go along the line with the previous steps and set the conditions loosely, to keep the detection rate high, the loosest value for this parameter to distinguish cavities from blobs is used, which is c_{cav}=1. The smaller c_{cav}, the higher the density gradient between the shell (ring) and inner cavity. Hence this value has been stored for each cavity candidate to later determine if shells with lower values of c_{cav} are better representations of shells (section 4.6.3). From observation of the 17 candidates, there seems to be no indication that a smaller value of c_{cav} is more likely than a higher one since the values are well distributed between 0.09-0.71. But since 17 shells are low statistics, additionally a possible relation is investigated for the shell catalog in section 4.6.3 to find a more strict criterion than $c_{\mathrm{cav}} = 1$.

The above explained steps of the algorithm have been applied to all channel maps of the specified velocity range of -150 to +150 km/s (section 3.3.2). The next step is to connect cavities of a sequence of channel maps to a three dimensional structure in the lbv–space.

Connection of detected cavities along the spectral axis The following criteria have to be met to connect cavities of different channels to one object, named **worm** hereafter. The name choice is due to its appearance in the H I datacube and to distinguish it from final shell candidates. Along the spectrum of the H I datacube, two cavities k and l of consecutive channel maps i and j (where $j = i + 1$) are connected if the absolute distance $\Delta P_{ik,jl}$ between their center coordinates l_0, b_0 is lower than a value that is specified below and in addition if the relative difference $\Delta R_{ik,jl}$ between the radii, R_{ik} and

R_{jl} of the channels i and j, is smaller than the other specified limit. If multiple cavities of channel j fulfill both conditions and would connect to the cavity of channel i, the two cavities are connected with each other that fulfill the criteria best. Then the circle of channel j is compared to all circles of channel $j + 1$ to search for another connection. This is done until either no connection is found or the comparison between the second last– $(n - 1)$ and the last channel (n) of the datacube are made. This procedure is repeated for every cavity of each channel map.

The maximum observable change in radius between two channels depends on the spectral bin-size (1.25 km/s for HI4PI, 0.8 km/s for GASS) and the minimum observable expansion velocity of a shell that is $v_{\mathrm{exp,min}}$. From observation and the dispersion of the ISM, a value of $v_{\mathrm{exp,min}} = 5$ km/s has been derived (section 4.5.1). Using the EHSS-model from section 4.2, this yields a mean radius change of $\Delta R_{ik,jl}$= 35% between the channels. The change is not linear between channels due to the radial velocity component of the expansion velocity that is observed (section 4.2). At channels close to v_0, the change in radius size is much smaller, since these parts of the shells almost move perpendicular to the observer as well as the ones near- and at $v_0 \pm v_{\mathrm{exp}}$. The visualization in figure 3.12 helps understanding these relations. In between these values, there are one to two channels, where the change in radius can be up to 50%. But since here already the case of the lowest expanding shell was taken, the mean value $\Delta R_{ik,jl} = 35\%$ has been used as the limit.

The difference between two center points $\Delta P_{ik,jl}$ that is allowed, is derived by redetermining the center points of the cavities in each channel map of the 17 shells from the literature, which has been done in section 4.5.1. The mean difference between the center points of all channel maps, where the respective shell is present is listed as δp in row 10 of table A.0.16. This value lies between 0.2° and 2.4°, depending on the shell and its radius. For these shells a maximum ratio of 30% between δp and the radius of the two neighboring cavities has been measured. Since this is the most extreme case that is found, the maximum connection limit for the distance between two circles of neighboring channels is specified as $\Delta P_{ik,jl} < 0.3\, R_{\mathrm{H,ij}}$.

The minimum number of connected cavities, $N_{\mathrm{ch,min}}$ depends on $v_{\mathrm{exp,min}}$. But since it is known from various examples (e.g. some shells of table A.0.16, the Usco-loop, the UCL-shell) that SNe can be open towards multiple directions, not $2 \cdot v_{\mathrm{exp,min}}$ is used, but the lowest limit possible of $N_{\mathrm{ch,min}} = 3$ to avoid to miss shells due to these properties. This limit is taken for the application, but additionally N_{ch} is used as one of multiple quality measures for the shell ranking below. This is because with increasing N_{ch}, it is less likely to have geometric patterns that randomly appear like parts of expanding shells and hence lead to false detections. The receding and ascending caps of the expanding shells (section 3.4.1) are not included in SAGHIS but have been considered in a post processing for the quality ranking of the results in section 4.6.3. Double-detections are produced by this step and the elimination of these is explained in the following.

Eliminating doubles The remaining worms have been thinned out because they contain doubles. The most straightforward thinning step is to measure if two worms share the exact same cavities but one worm has higher N_{ch} than the other one, i.e. additional cavities are detected in more channels. Then the shorter worm is ejected, since it is just a sub-feature of the longer worm. Then there are also similar worms, sharing a large fraction of cavities or neighboring cavities of the same channels. For this comparison, the mean center coordinates as well as the mean radii of each worm have been

determined and compared[20].

This last step resulted in a list of expanding shell candidates. The steps and parameters of SAGHIS are summarized in the following.

accumulator thresholding Over all circles, belonging to a shell candidate, the mean accumulator value has been calculated. While for single circles, the loose criterion is $a_{\mathrm{H,\,min}} \geq 0.2$ of the maximum intensity. Here, since it has been summed over multiple channels, the threshold for $a_{\mathrm{H,\,mean}}$ was adjusted to a value of $a_{\mathrm{H,\,mean}} \geq 0.4$. This is due to the tests of the algorithm described below in section 4.5.2.

Remaining parameter specifications

The tests of the different components of SAGHIS have already been presented in section 4.1. These tests have been continued for the full algorithm, first on the synthetic test dataset (sec 4.1.1). All shells of the test data have been detected using SAGHIS. The caps of the idealized spherical shells were not detected, due to the algorithm design. Not all real H I shells have caps but this sets the minimum expansion velocity uncertainty to $\Delta v_{\mathrm{exp}} = 1.25$ km/s with increasing value with increasing expansion velocity. All uncertainties are further discussed in section 4.6.4. For the synthetic dataset, the limit of $a_{\mathrm{H,\,mean}}$ has been tuned to detect all circles and to avoid too many predictions at the same position. The result is that a value of $a_{\mathrm{H,\,mean}} \geq 0.4$ gives the best predictions. The synthetic test dataset has then been expanded to higher latitudes. There, the distortion of the circle increases (fig. 3.5) and best results have been achieved if the threshold is not applied for objects with $b_0 \geq 20^\circ$.

The algorithm has been tested, not only on sub-sets of the HI4PI data but also on the LAB dataset. Due to the low resolution and hence small size of the LAB dataset, the full velocity, and longitude-latitude range could be used at once (see e.g. sec. 3.1). The properties of the test-results have been similar between both datasets. Due to different resolutions, shell detections differed. In both datasets, rarely objects have been detected at latitudes higher than 50°. After parameter tuning towards values that led to suppression of false positives, the algorithm did not detect shells at latitudes higher than 50°. Testing this on the full latitude range for the LAB-data for shells with $r_{\mathrm{max}} \leq 10^\circ$, it has been found that center coordinates of the detected shells are significantly below 50°. Figure B.0.12 shows the results of this test run. Technically it is difficult to detect shells at high latitudes because the intensity to noise ratio is small and in general less features are detected but also less H I shells are expected since the latitude is connected to the distance towards the Galactic disk.

The Galactic disk of stars has a vertical exponential profile (de Grijs & Peletier 1997). The ISM density of the Galactic disk is also approximated by exponential distributions (e.g. Kalberla & Kerp (2009) fig. 4 to 6). Hence less star clusters are located at higher distances from the Galactic plane and also in general at higher latitudes. The mean intensity distribution of H I along the Galactic latitude is shown in the right panel of figure 3.8. SNRs that are thought to be the main source of expanding shells, are usually also detected at low latitudes. For examples the vast majority of SNRs of Green (2013) have latitudes lower than 10° and there no objects have been detected with latitudes higher than 20°. H I shells have been detected up to higher latitudes but in the most complete catalog of Ehlerová

[20] Sorting out has been done for each of the four sub-datasets (tab. 3.2). After merging the datasets, also exact doubles had to be rejected since the sub datasets overlap so that the detection of large shells at the borders of the sub-datasets are still detectable.

& Palouš (2013), just 5 out of 333 shells are above $b = 50^\circ$. Due to the limits of the algorithm and a low expected number of missed detections, the limit is set to $b = 50^\circ$. In previous studies, maximum center H I shell velocities of 100 km/s were measured (Ehlerová & Palouš 2013). The signal to noise ratio at these velocities is very small (fig. 3.3.2. The algorithm does not detect shells near 150 km/s in the set of the LAB survey. This is why the algorithm is applied to the HI4PI data in the velocity range between -150 to +150 km/s. This is also in consensus with other H I surveys (e.g. Suad et al. (2014)) and shells of moving velocities higher than these values are not expected according to Galactic rotation velocities.

Summary of SAGHIS

The algorithm steps and the parameter specifications, introduced and discussed above, that have been used in the application of the algorithm on the HI4PI data as described below in section 4.6 are summarized here. In this case, i is the i-th channel with $i \in \{1, ..., 222\}$ and j is the j-th feature, detected in channel i, with $j \in \{1, ..., n_f\}$ and n_f being the number of features in channel j.

1.) Application of the customized zero parameter edge detection (sec. 4.1.1) on each channel map of the HI4PI data on a total of 220 channel maps, i.e. the range of $|V_{\rm rad}| < 150$ km/s in full longitude range and for $|b| \leq 50^\circ$, producing binary images of the edge-pixels.

2.) Application of the Hough transformation to each binary image to detect Hough circles with the parameters $R_{H,ij,\rm min} = 0.24^\circ$, $R_{H,ij,\rm max} = 20^\circ$ and $\Delta R_{H,ij} = 0.24^\circ$. All Hough circles with a relative accumulator value compared to the maximum value of $a_{\rm H,min} < 0.2$ are rejected.

3.) Rejection of blobs and separation of cavities with the loose cavity restriction of equation 4.14 and the value $c_{\rm cav}$=1.

4.) Connection of similar cavities of neighboring channel maps to 3D-features if the relative distance of the center points of two cavities k and l of channel i and j (j = i+1) is $\Delta P_{ik,jl} < 0.3\, R_{\rm H,i}$, where $R_{\rm H,i}$ is the radius of cavity i. Additionally the relative difference between the two radii of the cavities has to meet $\Delta R_{ik,jl} < 0.3$. If both criteria are met, the connected circle of channel j is compared to all other circles of channel j+1. This procedure is repeated until no connection is found or the maximum channel of the datacube is reached.

5.) Reject all connected 3D-features where $N_{\rm ch} < 3$ and eliminate doubles, produced during the search.

6.) Reject all 3D-features with mean accumulator values of $a_{\rm H,mean} < 0.4$ for objects with $b < 20^\circ$.

4.5.3 Parameter optimization for the Sco-Cen region

In chapter 6, the ISM in the vicinity of the Sco-Cen OB association is investigated in detail. For this analysis, some parameters of SAGHIS have been fine tuned towards the specifics of the properties of the ISM near Sco-Cen and the different dataset as explained in the following. The steps 2.)−5.) of section 4.5.2 are taken over. But the prior knowledge of the size, parameters and location of the SNRs has been used to improve the quality of the results. As shown in section 4.1.1, SAGHIS is adaptive for different regions and intensity variations. But the double thresholding of the Canny edge

detection is more accurate in specific regions, where prior knowledge about intensity distributions can be used. This is why the customized edge detection has been replaced by the Canny edge detection for the analysis of Sco-Cen. Also since the shells in the Sco-Cen region are all located in the southern hemisphere, the GASS survey (section 3.2.3 and table 3.1), which covers the whole southern hemisphere is chosen for investigation instead of the full sky survey HI4PI. The reason is that the GASS has a higher velocity resolution (1 km/s compared to 1.49 km/s of HI4PI), while having the same angular resolution, which enables a more detailed analysis of the shells in the spectral dimension.

The data to be investigated can be reduced to a region around the shells. This is realized by producing H I sub-datacubes that have an angular size of at least three times the observed maximum shell radius and are centered around the center coordinates of the estimated shell to ensure that the complete shell is contained in the datacube. To reduce the spectral limit only affects the efficiency of the search algorithm and not the quality of the results and hence a buffer of 50% of the velocity extent of the shell is used below the minimum observed velocity and above the maximum observed velocity as spectral limits for the datacube[21].

In the following just the parameters that change compared to the algorithm of section 4.5.2 are discussed. The parameter σ of the gaussian smoothing that is used prior to the Canny edge detection is set to 1, according to the tests of section 4.1.1. The hysteresis values of the CED are set to $T_l = 1$ K km/s and $T_h = 4$ K km/s respectively. The lowest radius for the Hough transformation is set to $R_{\mathrm{H,min}} = 1.5^\circ$, since the smallest known object in this region is the Usco-sub loop with a minimum radius of 2.1° (see e.g. table 6.10), $R_{\mathrm{H,max}} = 20^\circ$ and $\Delta R_{\mathrm{H}} = 0.24^\circ$ are not changed. Since the GASS has a higher velocity resolution than HI4PI and a binning of 0.8 km/s, $N_{\mathrm{ch}} = 5$ instead of 3 to result in a minimum expansion velocity of 3.2 km/s. The application of SAGHIS, with the parameter optimization that is explained here, is presented in chapter 6. In the following, the SAGHIS is applied to the Galactic H I data of the HI4PI survey.

[21] The uncertainty of the visual detection method is two channels, which is at most 2/7 = 28%. Since there is no influence on the quality of the result, the limit 50% is set to add an additional buffer

4.6 Application of SAGHIS to Galactic H I data

Here, the application of SAGHIS from section 4.5 to the HI4PI data to produce a catalog of Galactic H I shells is presented. In the following, it is always referred to the algorithm steps of sec. 4.5 if not explicitly stated otherwise.

Due to the insights of section 4.5.2, it has been applied for the full longitude range, the latitude limit is $|b| \leq 50^\circ$ and the velocity range is -150 km/s to +150 km/s. In the following, the results of each step of SAGHIS are presented. The reduction of the number of feature from a Hough circle detection in single channel maps towards cavities, three dimensional worm structures and finally H I shells by taking, for each step, additional physical properties into account, are explained along table 4.7. The final results are discussed and analyzed in chapter 5 and hence listed in table 5.1. Since the parameter specifications have been tested (sec. 4.1 and sec. 4.5.1) and summarized (sec. 4.5.2) beforehand, they are not discussed in this section if they are mentioned.

4.6.1 Channel-by-channel investigation

The results of the channel-by-channel search part of SAGHIS are presented here along figure 4.20, where the total number of features per channel are shown. Additionally, in figure 4.19 the results for the different steps for a zoom-in into a region of 120° range in longitude and 100° range in latitude for one H I channel map of the HI4PI dataset are visualized. This size is chosen so that smaller features below and near one degree are resolved, while still a major part of the large-scale features are visible. In the figure, H I data (top left panel), the detected edge features (top right panel), the center coordinates of the detected Hough circles (bottom left panel) and the center coordinates of the cavities (bottom right panel) are presented.

The application of the customized edge detection method of SAGHIS results in binary maps, where 1 (white) denotes edge pixels and 0 (dark blue) are none edge pixels, e.g. as shown in the top right panel of figure 4.19[22]. If compared to the non processed HI4PI data (top left panel of the figure) it can generally be seen that edge features follow the distribution of real H I features. It can also be seen that edges are detected at different intensity levels, for example near the Galactic plane at high intensities, as well as at high latitude regions of lower intensities, showing that the algorithm step works as tested in section 4.1.1.

After applying the edge detection method to each channel map of the H I datacube, the Hough transformation for circles is applied to the edge-images. A total number of 11.8 Mio. Hough circles are detected in the whole dataset as listed in table 4.7. This number is reduced by the application of the threshold of 20% of the maximum accumulator value that has been determined empirically in section 4.1.2. The number of Hough circles per channel can be followed in figure 4.20. The distribution peaks at 0 km/s and is not fully symmetric. When comparing these to the distribution of H I data itself, e.g. to figure 3.8, it can be seen that the number and density of Hough circles follows the highest mean H I intensity per channel. This is what is expected since the highest mean intensities itself represent channels with highest abundance of structures that are orders of magnitude above the sensitivity limit of the H I data. And these highest emissions lie mostly at low latitudes, where the overlap of the emission of the gas from the Galactic plane is visible as well as at radial velocities near $v_{\mathrm{rad}} \approx 0$ km/s.

[22] Due to maintaining the style, the colorbar is kept and limited between 0–1. But values in between don't exist for the top left, the bottom left and the bottom right panel.

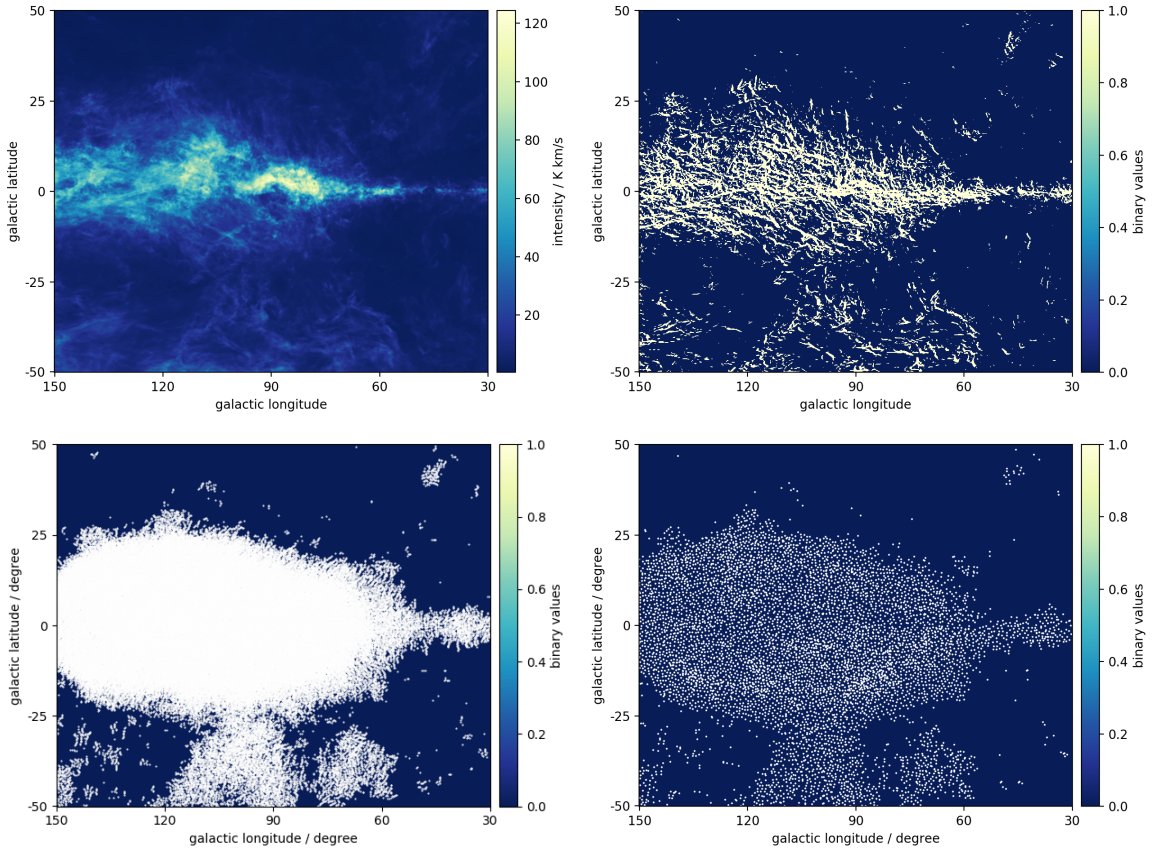

Figure 4.19: Results of one subset of the channel-by-channel investigation of the HI4PI data, for the velocity channel at 11.25 km/s. In the top left panel, the HI4PI data of this channel map is shown. The intensity range is color coded from blue to white with values in the range between 0 to 120 K km/s. The same region is shown in the other three panels but since the results are binary values for each pixel, the values are highlighted by the color bar values 0 and 1. In the top right panel, the results of the edge detection part of SAGHIS are shown. In the bottom left panel, 131090 center points of the circles, detected by the Hough Transformation on the binary edge maps are shown. The remaining 6796 Hough circles that fulfill the cavity condition from section 4.1.3 are shown in the bottom right panel.

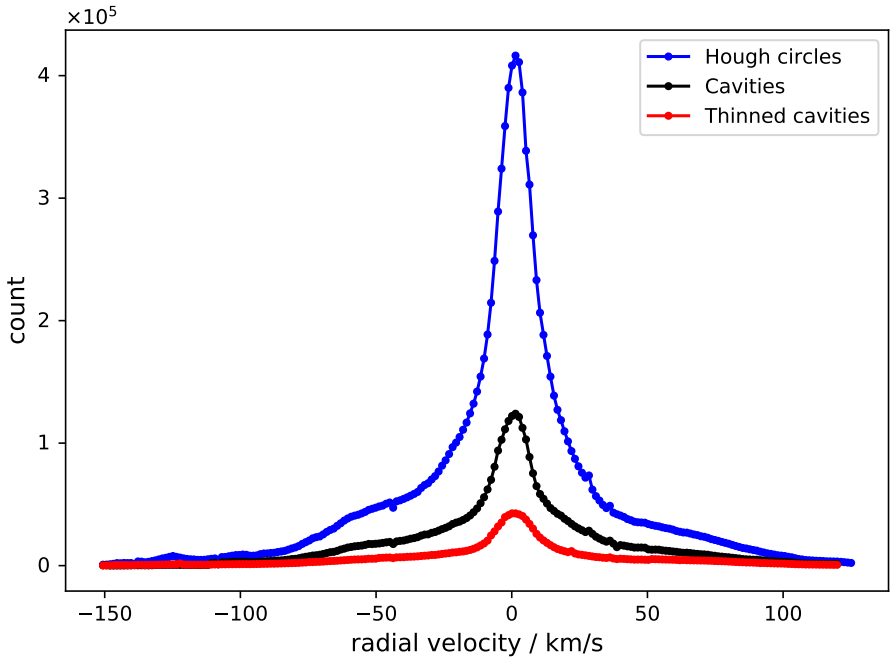

Figure 4.20: Detected number of features per channel of the channel-by-channel investigation for 211 channels, where channel 1 is starting at a velocity of -150 km/s. The connected blue dots represent the number of Hough circles detected in each channel. The remaining features that fulfill the cavity criterion (see 4.1.3) are color coded in black. The number of thinned out cavities per channel is marked in red. The total number of Hough circles, cavities and thinned cavities that are detected in the HI4PI data, are additionally listed in rows 1 to 3 of table 4.7.

The results of the Hough transformation on the edge maps for one particular region are shown in figure 4.19 in the bottom left panel. In this binary map of the velocity channel at 11.25 km/s, the center coordinates of the 131090 detected Hough circles are plotted.

To sort out results that are not physically connected to inner edges of shells, the cavity criterion (sec. 4.1.3) has been used as described in section 4.5[23]. This leads to a total rounded number of cavities of 4 Mio. cavities (row 2, table 4.7). This is a reduction to 1/3 of the initial Hough circle number. From the cavities with similar radii and similar center points that are too close to each other to be considered different cavities, the best candidate according to the definition of section 4.5.2 was kept. This reduced the total number of cavities further to 1.4 Mio. thinned cavities (row 3, table 4.7). Similar to the Hough circles, the distribution of cavities as well as thinned cavities are also plotted in figure 4.20 as the black and the red distribution, respectively. The reduction of features per channel by multiple orders of magnitude can be seen.

Focussing on the one channel map, in the bottom right panel of figure 4.19, center points of the remaining 6796 cavities of the velocity channel 11.25 km/s are plotted. When comparing it to all Hough circles, detected in this velocity channel, in the bottom left panel of the figure, it can be seen

[23] This is due to the approach of this work. It could also be tried to detect the outer edges of shells, which is not tackled in this thesis because there are often no clear edges visible for observed shells. At the inner edges, where the pressure from the stellar feedback hits the shell, it is often more sharply defined.

that the number of center points is reduced due to the cavity criterion and the accumulator threshold and that there are also less overlapping centers due to the thinning (sec. 4.5.2).

4.6.2 Derivation of expanding shell candidates

With the definitions of section 4.5.2 and the parameter specifications therein, 672642 (table 4.7) connections between cavities of sequential velocity channels have been derived. Out of the duplicates produced by the connection method, just the main features are kept and sub-features that contain the same, but just less Hough circle connections are sorted out (sec. 4.5.2). This leaves a remaining number of 59265 three dimensional objects (table 4.7). It is stated again that this "double" elimination does not aim to sort out merging shells or shells that are similar but just artificial doubles produced by the algorithm. Due to the minimum allowed expansion, velocity $v_{\mathrm{exp,min}}$ (section 4.5), set by the velocity dispersion of the ISM (sec. 2.1.1), the number of objects is reduced further to 35674. In the next step, the number was further reduced by sorting out objects that have mean accumulator lower than $a_{\mathrm{H,mean}} < 0.4$ for objects with $b < 20^{\circ}$ (section 4.5). The remaining 3D objects, with a total number of 6790 (table 4.7) are shell candidates.

These shell candidates have the mean parameters l_0, b_0, v_0, r_{mean}, the minimum- and maximum values for r_{min}, r_{mean} and finally the expansion velocity v_{exp}[24].

In figure 4.21, the binned distribution of the center velocities v_0 of the 3D-, thinned 3D features and shell candidates are shown. In the left panel, the count is plotted against the radial velocity to highlight how many features, not fulfilling the specifications, are rejected in the process. In the right panel log-normal histograms of the same values are shown to enable an easier comparison of the shapes of the distributions. If comparing the overall distributions to figure 4.20, the distributions are still peaking at 0 km/s and the left flank of the distribution towards negative velocities is higher than the right one. Interesting are the peaks at -40 to -50 km/s, which are also the velocities of prominent spiral arms and are more distinct than in the previous steps as will be analyzed in more detail in section 5.1.

As a post processing step, the 6790 candidates detected using SAGHIS have been investigated visually. Together with the quality measures, which are introduced in the following, that include additional physical properties, this leads too an interim number of 1082 shell candidates. The visual investigation is important to exclude detected patterns that are physically not related to expanding shells as is also done in all other known partly automated approaches (Ehlerová & Palouš 2005, 2013; Suad et al. 2014, 2019). Before discussing the uncertainties and deriving the final catalog, more details about the visual investigation and the ranking of the shell candidates are explained in the following.

[24] These values can be seen for the final shell catalog in table A.0.19.

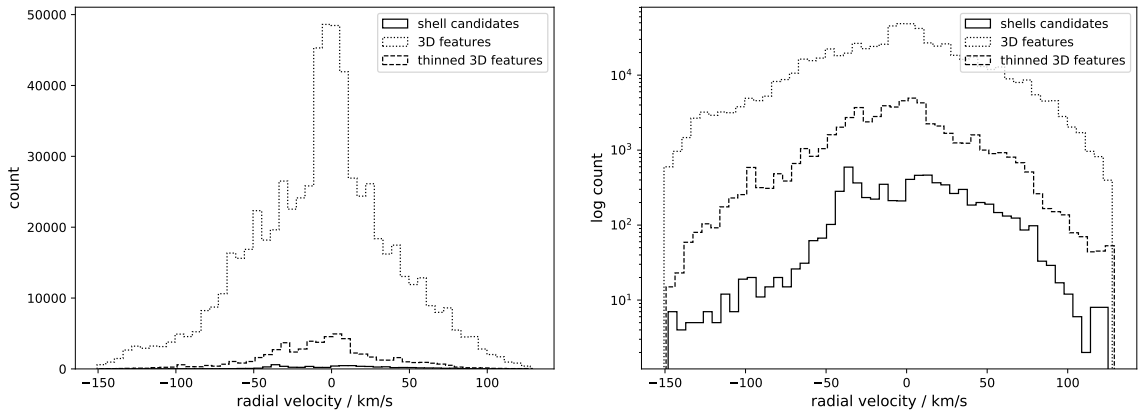

Figure 4.21: Plots, containing histograms of center velocities of detected 3D features in normal- and log-scale. In both plots, 3D features are marked by the dotted black line and thinned 3D features are marked by the dashed line. The remaining shell candidates after setting the loose criteria are marked by a black solid line. For more information see text.

Row	Feature Name	Number of features
1	Hough circles	11779039
2	Cavities	3970582
3	Thinned cavities	1410146
4	Worms	672642
5	Elimination of doubles	59265
6	Shell candidates	6790
7	Post processed shell candidates	1082
8	Shell catalog	842

Table 4.7: The total number of features, detected by the SAGHIS algorithm, in the HI4PI data for the different algorithm steps. The first column contains the row number, the second column describes the algorithm step and the third one lists the total number of features. Row 1 contains the Hough circles detected per channel, row 2 contains the number of Hough circles that meet the cavity criterion and in row 3 the thinned cavities are listed. Row 4 contains the three dimensional features. In row 5 the remaining non double 3D objects are listed. Row 6 lists the remaining shell candidates while row 7 contains the number of shell candidates after the post processing in section 4.6.3. Finally, row 8 contains the number of shells in the final shell catalog. For more detailed information about the table content see sections 4.6.1 to 4.6.2.

4.6.3 Ranking of the shell candidates

The shells, detected by SAGHIS, have been ranked by a quality measure Q_f, which consists of four components:

$$Q_f = Q_{\text{peak}} + Q_{\text{acc}} + Q_{\text{man}} + Q_{\text{vel}}. \tag{4.35}$$

Q_{peak} is a quality measure of the intensity features along the spectral axis, Q_{acc} is the mean Hough-Accumulator matrix value of all circles per shell, Q_{man} is the visual confirmation of a shell and Q_{vel} is the velocity quality value of a shell. Depending on the initial ISM environment, shells deviate from the idealized model of a spherical homogeneous shell (sec. 4.2). There are scenarios, where one, multiple of the quality measures are very low. The shell is closest to the idealized model if each of the quality measures has its maximum value. The maximum value is set to 1 for each measure. The determination of these quality measures and the distribution of the values between 0 and 1 is explained in the following.

Spectral peaks

For SAGHIS, eq. 4.14 has been used to identify cavities. Since an idealized expanding shell should have caps instead of rings near the maximum negative and -positive velocity channels, where it is present (e.g. fig. 3.11), this property should also be taken into account and hence has been measured additionally to collect more information about the shell properties. This was achieved by determining the peaks and dips of intensities along the velocity spectrum through a 3x3 pixel region in all channel maps around the center coordinates of the shell[25]. The peaks and dips have been derived using the automated peak-detection method, introduced in section 3.4. The resulting quality value for Q_{peak} has been measured and defined by:

1) high quality, if a shell candidate contains a dip in the velocity channels where it is present and is surrounded by two peaks outside of the border (see fig. 4.22, examples in the top row)

2) high-medium, if a shell candidate contains a dip in its velocity spread $2v_{\text{exp}}$ and at least one peak outside of its borders (fig. 4.22, middle row, example 1 and 2)

3) medium quality, if a shell candidate contains a dip in the velocity channels where it is present. $2 \cdot v_{\text{exp}}$ (fig. 4.22, middle row, example 3 on the right hand side)

4) low quality, if a shell candidate does not contain any dips or peaks in the velocity channels where it is present (fig. 4.22, examples in the bottom row)

A value of $Q_{\text{peak}} = 1$ has been assigned to shell candidates of category 1), while shells of the categories 2, 3 and 4 received values of $Q_{\text{peak}} = 0.75$, $Q_{\text{peak}} = 0.5$ and $Q_{\text{peak}} = 0$ respectively. It cannot be stated that a shell of lower Q_{peak} is not an expanding shell, e.g. due to turbulences, inhomogeneities in the regional ISM, the properties might differ from the idealized models, but it is more likely that an object of higher Q_{peak} actually is a shell as has been determined from the data. In the above quoted figure 4.22, results of different intensity profiles along the center of the shells with different values of Q_{peak} are shown exemplary. In this figure, the actual shell is present between the dashed vertical lines in each panel. It can be seen for the three top panels that the intensity minimum is inside this range,

[25] This size is the minimum size so that it contains independent pixels that do not belong to the same beam (sec. 3.1).

while surrounded by two maxima that either lie also inside the range where the shell is present or nearby. The shells in the panels of the middle row contain intensity minima but the missing intensity peaks induce that the shell-caps (sec. 3.4.1) are not present. In the bottom row, different examples of profiles are shown, which are usually not connected with idealized shells resulting in $Q_{\mathrm{peak}} = 0$. Since this is not the only quality measure it is still possible that a shell candidate of $Q_{\mathrm{peak}} = 0$ is in the final catalog.

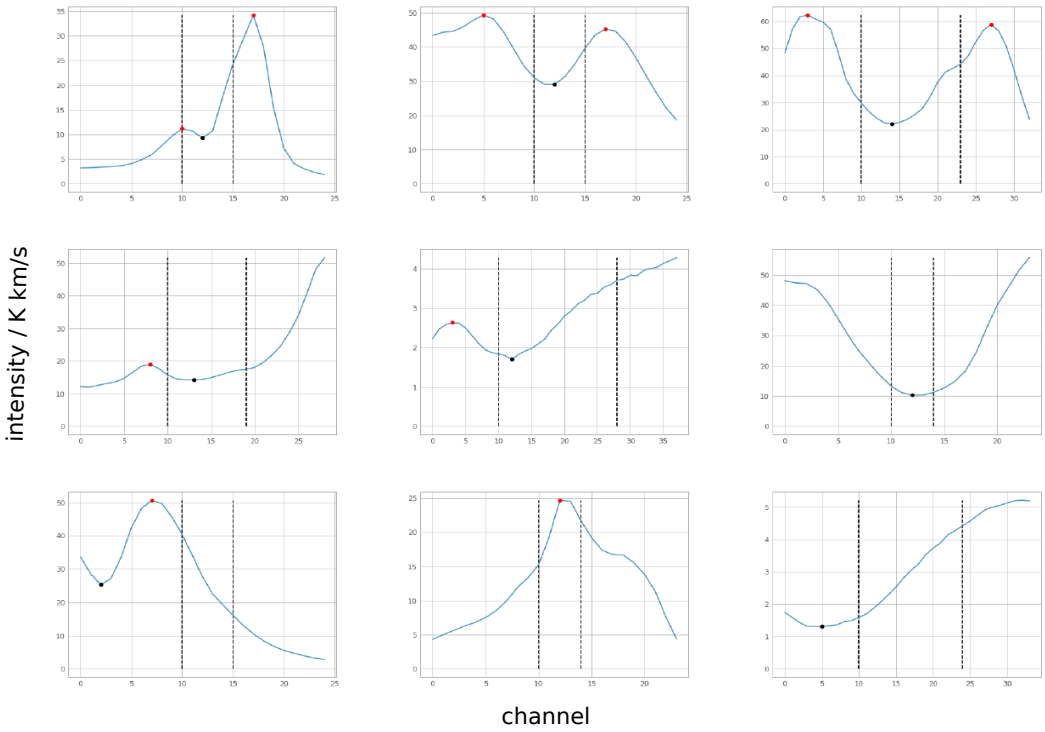

Figure 4.22: 9 plots, each containing an intensity profile through the center coordinate of the respective shell. The peaks and dips, detected by the method from section 3.4, are marked as red- and black dots respectively. In the top row, three examples classified as high quality ($Q_s = 1$) are shown. The row of images in the middle contains three examples that are ranked as high-medium or medium quality ($Q_s = 0.75$ and $Q_s = 0.5$ respectively). The bottom row of plots shows three examples, which are classified as low quality ($Q_s = 0$). For more information see text.

Visual confirmation

All 6796 shell candidates (see table 4.7) have been visually inspected along the assessment rules of section 3.4.3. This has been done efficiently by producing automated multi-plots for each shell in the respective velocity interval with adaptive intensity ranges[26]. To avoid biases, each investigation is done without knowing any other automatically determined quality measures of the object. Examples of these plots can be seen, e.g. in section 5.2.2, where some example shells are shown. The quality component, resulting from this visual investigation is divided into three categories

1) candidates where the visual investigation agrees with the proposed candidate ($Q_{\mathrm{vis}} = 1$)

2) candidates where the visual investigation has no clear result and no statement can be made ($Q_{\mathrm{vis}} = 0.5$)

3) candidates that can be clearly identified as false positives ($Q_{\mathrm{vis}} = 0$)

Category 3) are often H I cloud formations, which show a circular pattern but can clearly be identified as a random structure and which are sometimes of random shape. Sometimes random circles are detected in multiple channels, which match the Canny- and Hough criteria, where even the circular pattern cannot be identified, similar to what was found in the tests in section 4.1.2. In each case, choosing if these results get categorized into 2) or 3), then depends mostly on the surroundings. Examples of categories 1.) and 2.) are presented below in section 5.2.2.

Shells that could clearly be excluded are not present in the interim results of 1082 objects. Shells where the visual investigation results in $Q_{\mathrm{vis}} = 0.5$ have been kept if at least one of the other quality components Q_{peak}, Q_{acc}, Q_{vel} are > 0. This led to the 1082 post processed shell candidates. This list contains 458 shell candidates that have clearly been visually confirmed ($Q_{\mathrm{vis}} = 1$) and 625 objects that have not clearly been confirmed ($Q_{\mathrm{vis}} = 0.5$) but other quality measures are > 0. 20% of the 5714 objects that are rejected have values of $Q_{\mathrm{vis}} = 0.5$ and 80% have $Q_{\mathrm{vis}} = 0$.

More about the connection of the parameters is discussed below after the last two quality measures are introduced.

Intensity- and Hough accumulator values

The distributions of the mean intensity ratios and the mean Hough accumulator values of the shells have been investigated to determine to what extent they can be included into the quality measurement. All shell candidates have been compared to the ones of the interim list of 1082 post processed shell candidates, i.e. that fulfill the specifications of section 4.6.2 to derive patterns in the distributions. The comparison is illustrated in figure 4.23 and explained in the following.

intensity ratio For the intensity values of each shell candidate, two distributions are plotted in the left panel of figure 4.23. The dashed black distribution is the one of all shell candidates that have been rejected (5714), while the solid black distribution is the one of the remaining shell candidates (1082). There is in general no significant difference between the two distributions. The intensity ratio

[26] It took roughly 30 hours to investigate all objects. Even though this seems like a time consuming brute force task, it is very fast compared to searching for shells by hand. To investigate the data at the detail level and resolution of the algorithm would probably take years.

describes how much less intensity is in the interior of the shell compared to values on the shell itself. Hence the results can be explained by regions of low density, where the shell has minimal higher significant density than its interior and also the turbulence and complexity of structures in the Galactic disk show clouds in the inner of the shell at the same velocity channels, which might not belong to the shell but are overlapping in this longitude-latitude-velocity space. This is regularly the case as can also seen in the examples of section 5.2.2 and additionally for the Sco-Cen shells. It has been shown that the value ≤ 1 as a limit is necessary to separate blobs from cavities (see section 4.6.1). But in the tests of the observed SNR, it has also been found that the ratios spread over the range of 0–1 (sec. 4.5.1) and hence the quality should be independent of the ratio if it's below 1. In consensus with these observations, no pattern for this ratio and the quality could be derived and hence is not taken into account for Q_f.

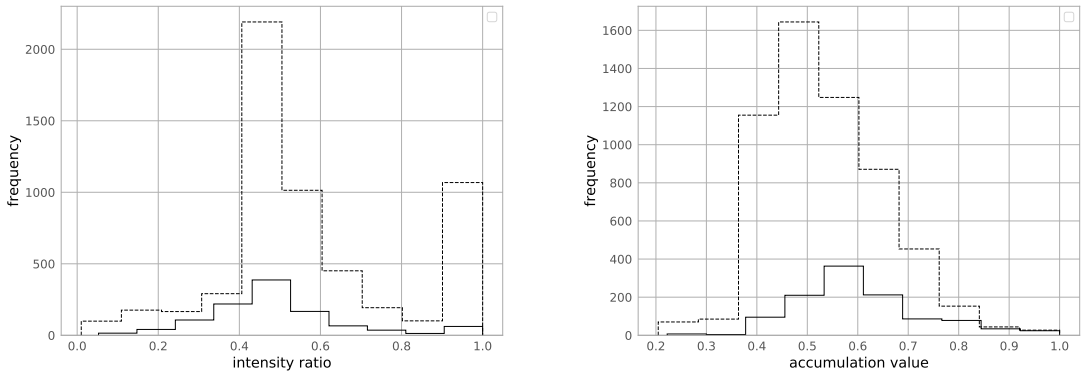

Figure 4.23: In the left panel of the figure, two distributions of intensity ratios between the mean intensities in the inner part of the shell against mean intensities on the shell are shown for all objects. The dashed histogram is the one of all shell candidates from section 4.6.2 and the solid-line histogram is the one of the 1082 post processed shell candidates. In the right panel of the figure, the two distributions with the same markers, for the same objects are shown for the mean Hough accumulator values of the shell candidates (dashed) and the post processed shells (solid line) are shown respectively. For more information see text.

Hough Accumulator As described in section 4.5.2, the mean Hough accumulator value of all circles belonging to a shell candidate has been stored. Since this value describes the ratio of pixels on the Hough circle that belong to an edge, this value measures how close the shape of a candidate is compared to a circle or how "closed" it is when its features are aligned on circles. For example, the fragmented clouds of the USco-loop are aligned on a circle (chapter 6). The hypothesis if the likelihood of detecting a real expanding shell is increasing with increasing accumulator value is tested. The tests of section 4.1.2 showed that the accumulator values do not reach values near 1 for H I clouds and that the relative accumulator value compared to the maximum accumulator value of all candidates is a better measure. This value cannot be ranked from highest to lowest as a quality measure. It is determined empirically here, by comparing the distributions of the rejected shell candidates with the one of the remaining 1082 shells as is shown in figure 4.23, if there is an optimal value.

As can be seen in the right hand side of figure 4.23, the distribution of the final shell ranking differs from the one of all objects. The distribution has a peak at the mean accumulator value of a shell of

0.6. For higher accumulator values than 0.6, there are less shell candidates in the final catalog but the distribution is also more symmetric around 0.6 compared to the one of all candidates, which peaks at 0.4–0.5. Hence the best fitting accumulator value, where most objects result in a shell has been measured as 0.6 and the equation for the accumulator quality is:

$$Q_{\mathrm{acc},i} = \left|0.6 - A_i\right| \tag{4.36}$$

where A_i is the mean accumulator value of the shell. $Q_{\mathrm{acc,i}}$ then contains values between 0 and 1 and the closer this value is to one, the higher the quality.

Velocity extent

Statistically, the false detection rate of shells should decrease for objects with higher velocity extent, since the number of channels where a Hough circle with sufficient quality is detected increases and it is less likely that multiple high quality Hough circles that are connected are related to random patterns. Since there might still be some random occurrences that extend over multiple velocity channels, it has been investigated if the shell length can be included into the quality ranking. For the test, the distribution of all shell candidates without minimal thresholding from section 4.6.2 have been compared to the ones of the catalog. This is shown in figure 4.24. The general downward trend towards higher velocity extents is the same in both distributions. But especially in the right panel, where the normalized density distributions are shown, it can be seen that relatively more shells of high velocity extent are contained in the shell candidate list. Significantly different is the relative amount of shells equal or below 5 km/s extent[27]. For the remaining 1082 shell candidates, the relative amount is 38%, while for all objects of section 4.6.2 it is (55%). This suggests that most rejected candidates stem from candidates of velocity extents below 5.5 km/s. This is why the velocity extent quality value, Q_{vel}, is set to 1 if the worm length is above 5 km/s and 0 if it is below as a more strict criterion, in agreement with the velocity dispersion (sec. 2.1.1). Since this is just a binary decision, it always has a higher impact on the final quality. The value of 1 is almost always mandatory for a shell candidate to reach at least a medium rank. The minimum expansion velocity criterion is already near the velocity dispersion (sec. 2.1.1) and hence its influence on the quality is important. On the other hand, the caps of the shells are not included in these considerations because they often cannot be observed. Hence shells below this value are not rejected by itself.

[27] Since the values are concrete in steps of the HI4PI data bin-widths of 1.25 km/s, this value is equivalent to a velocity extent of four spectral channels

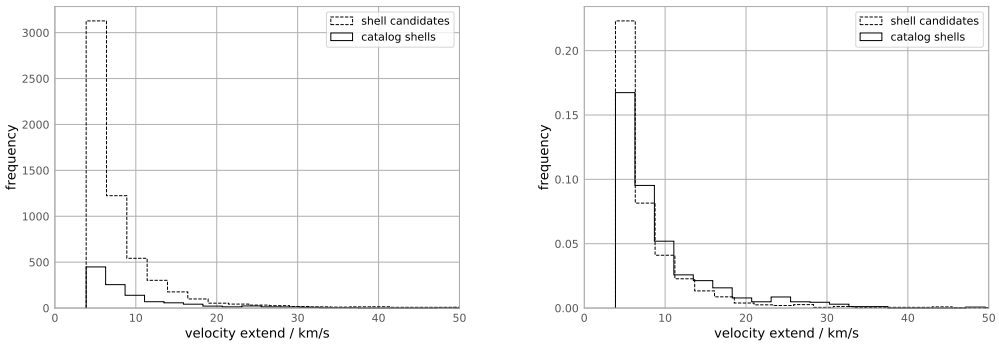

Figure 4.24: Comparison of the distributions of the velocity extents, i.e. the number of velocity channels where the shell is present for the catalog shells (solid line) and the one of the shell candidates (dashed line). While the standard histograms are shown in the left panel, in the right panel the normalized density distributions are shown for comparison (the integral over the area of bins is one, not the sum of the bins.)

Interim analysis of the ranking of the shell candidates

With the four quality components and the resulting value Q_{f} of eq. 5.3 for each shell candidate, a statistical analysis between the ranking and the parameters of the shell candidates has been made to investigate patterns in the ranking for the non included parameters like the radius. The quality values, as well as the rank are listed in table A.0.19 (or the excerpt in table 5.1)

The general distribution of the shells in longitude and latitude, as well as the other parameters are not discussed here since their analysis is presented in detail in chapter 5. For visualization, Q_f is plotted against the parameters of the shell in figure 4.25. As can be seen in the top left and the top right panel of the figure, the center coordinates of the shells are not dependent on the ranking, meaning shells of each region in the angular space can have a high- or low rank.

In the middle row of figure 4.25, Q_f is plotted against the minimum- and maximum radius of each shell. Both plots indicate that the shells of larger radii are more likely to have a higher rank because the distribution shows an upward trend towards the top right. Especially the number of shells with radii below 1° and $Q_f \geq 2$ is low. This is analyzed and discussed below in section 5.1.1. Further, as can be seen in the bottom row in the left panel, Q_f seems to be independent of the center velocity of the shell. Shells with high quality values can occur also at high absolute velocities. But the highest and lowest values of Q_f are reached at the lowest absolute velocities, which might be due to the low statistics of shells at high absolute velocities. The most interesting part is the velocity extent. Shells of high velocity extents (>10 km/s) always result in values of $Q_f > 2$ as can be seen in the bottom right panel of the figure. This is only possible if additionally, multiple other quality components are >0. Intuitively it is also unlikely that random circular patterns occur along a high number of channel maps compared to a low number of channel maps.

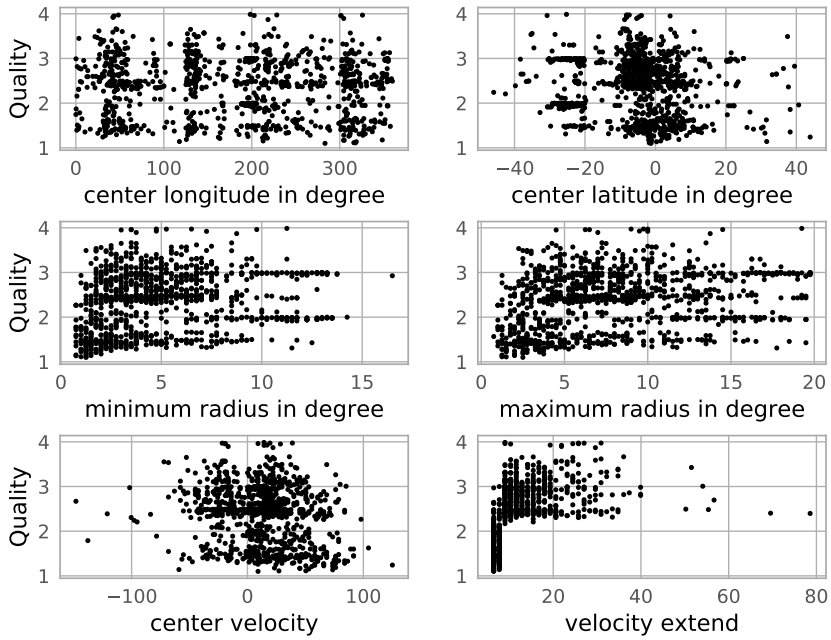

Figure 4.25: Multi plot showing the quality (Q_f) of each shell candidate plotted against its parameters. In the top left panels, the quality is plotted against the center longitude and latitude of the shells. In the middle row, Q_f is plotted against the minimum- and maximum radius in the left- and right panel respectively. In the bottom row, in the left panel, Q_f is plotted against the center velocity of the shells and in the right panel it is plotted against the velocity extent of the shells. For more information see text.

4.6.4 Determination of the uncertainties of the shell candidates

The parameters of the 1082 shell candidates are the center coordinates l_0 and b_0, the angular minimum-, mean-, and maximum radius, r_min, r_mean and r_max, the center velocity v_0 and the expansion velocity v_exp. Here it is explained how the uncertainties of these parameters have been derived. The values for each shell can be found in table 5.2, which is introduced in chapter 5.

Angular coordinate- and size uncertainties The uncertainties Δl_0 and Δb_0 of the mean center coordinates l_0 and b_0 of a shell candidate have been calculated as the standard deviation of the center coordinates of the belonging Hough circles. The minimum uncertainty of the center coordinates as well as the angular size is the Hough circle step width of $\Delta R_h = 0.27\,^\circ$ since this is also the HI4PI survey resolution. Additionally, the uncertainty of the detected maximum- or minimum radius of a shell candidate is dependent on its position relative to the second and third maximum radii. It is expected that the geometric shape of an expanding shell follows at least roughly the geometries of the EHSS-model from sec. 4.2. The largest radius of all Hough circles, belonging to the shell candidate due to this model, lies next to the other larger identified circles as visualized in figure 3.11. If this is not the case, the maximum radius is a potential outlier, which could lead to an overestimation of the shell size and hence the uncertainties increase. These outliers can be identified if the second and third

largest radii of the shell are not at neighboring velocities and are closer to the center velocity v_0 than $r_{\max}(v)$. From this, the additional uncertainty has been derived as $\Delta r_{\max} = \sqrt{(\Delta r^2 + \Delta r_d^2)}$ where r_d is the difference between the second largest and the largest radius, if both do not lie in neighboring channels. The uncertainty of $r_{\min}$ has been determined correspondingly in respect to the second smallest radius. Δr_{mean} has been calculated as the standard deviation of the mean radius r_0 of the shell.

Velocity uncertainties For an idealized spherical expanding shell, the maximum radius lies at the spectral position where the expansion velocity is perpendicular to the line of sight and hence at its moving velocity v_0 (sec. 3.4). Many observed expanding H I shells do not expand homogeneously into all direction and one reason are density fluctuations in the ISM. This has also been observed for most of the shell candidates. To name one specific extreme example, the USco-loop (fig. 3.12) is almost open towards its receding part and hence, the highest radius is not in the center of the observable part, but at the maximum observable velocity channel. In these cases, the position of the center of the velocity extent, v_0, has higher uncertainties. This is why for each of the catalog shells, the uncertainty $\Delta v_0 = \left|v(r_{\max}) - v_0\right| + \delta v$ has been determined, where $v(r_{\max})$ is the velocity channel, where the shell has its maximum radius and v_0 is the center velocity. The minimum uncertainty δv is the spectral resolution of HI4PI, which is 1.4 km/s. Hence $\Delta v_0 = \delta v$ if the position of $r_{\max}$ is at v_0. The idealized approximation that the center velocity channel of the shell is also its moving velocity v_0 for symmetric expansion. Since $r_{\max}$ itself has an uncertainty and could potentially be an outlier as explained above, its uncertainty propagates into Δv_0. This led to high relative uncertainties up to 50%.

In some cases, a second method could be used to determine the uncertainty of the center velocity, which includes the peaks of surrounding H I from the analysis of section 4.6.3, using the difference between the velocity position of the dip and v_0 of the shell. If no dip or not two peaks could be identified between the shells, the first method for calculating the uncertainties had to be used.

The minimum uncertainty of the expansion velocity v_{exp} is the propagated uncertainty of the sum of uncertainties at $v_{\min}$ and $v_{\max}$, which is half a bin width each. For the calculation of the uncertainties of v_{exp} again the uncertainty of the maximum radius position has been used. With increasing distance of the maximum radius from the center velocity channel v_0 of the shell, the more asymmetric, the expansion velocity between receding and ascending parts of the shell and hence the higher the uncertainties.

4.6.5 Derivation of the final H I shell catalog

In the list of the 1082 shell candidates, clusters of shells have been identified. The largest cluster of shell candidates is located in the region of the Orion-Eridanus superbubble at longitudes of -160° to -220° and latitudes from -20° to -30°. While it is known that this region contains multiple shells and also possible mergers, there have been 203 shell candidates detected just in this field. It has been confirmed visually that some of these detected objects are different parameterizations for the same ISM structure with small parameter variations between them.

The initial thinning with loose conditions that was performed during the application of SAGHIS in section 4.6.2 removed sub-features that are part of features with the same circles in the respective channels but with an extension over more velocity channels as defined therein. But it did not take care of shells, where a few channel features are different, but mainly the same object has been detected. Using the above derived uncertainties of the shell candidate parameters, these multiple detections have been determined and sorted out. The condition has been used that at least two shells overlap for

the values l_0, b_0, r_{mean} and v_0 within their uncertainty ranges. The parameter v_{exp} is excluded as a requirement, since the same object can still be traced, even though the expansion velocities might differ. By also using the above derived quality value Q_f, the most qualifying shell out of the multiple detections has been kept.

Applying this, 240 shell candidates have been rejected. Out of these 240 rejected shell candidates, for 192 shell candidates, they don't only overlap within the uncertainty ranges but all parameters of the rejected shell candidate itself are in the range of the uncertainties of the respective remaining shells. This leads to a **final shell catalog containing 802 expanding H I shells**.

The detailed analysis of the catalog, the physical properties of the shells and the comparison to other studies are presented in chapter 5. There, the shells, its parameters and its uncertainties are also listed in tables 5.1 and 5.2 as explained therein.

4.7 Methods to determine the distance towards H I shells

To be able to determine the distance towards H I clouds or shells is key to determine its other physical parameters, like the size, the density and hence the mass. In section 3.5.1, the tangential point method was introduced that can be used to determine distances on Galactic scales[28]. This method is based on approximations, like that all objects moving on a circular orbit and that the rotation speed is the same for all objects. To determine local[29] distances, more accurate methods have to be used to gain detailed information about the internal geometric structure of a region.

4.7.1 The density–distance problem of an expanding sphere

Two different shells on the same cone of sight cannot be distinguished from each other if the distance is not known. This effect is presented in figure 4.26. There, the observed column density is correlated to the size together with the distance. The phenomenon is explained by means of two filled spheres. Its parameters can be tuned in such a way that one shell with the particle density ρ_1, the radius R_1 and the distance D_1 has the exact same appearance as a shell with an appropriate larger distance D_2 and a respective smaller particle density ρ_2. The particle density has to be smaller because it is integrated over a larger spatial volume when calculating the column densities. If these criteria are met, both shells appear to be identical for the observer as highlighted in figure 4.26. This is why the distance cannot be fitted even if the other parameters are a priori known. This just holds if the observed angle is not too large. For shells that spread over large amounts of degree, the appearance changes as shown in the following.

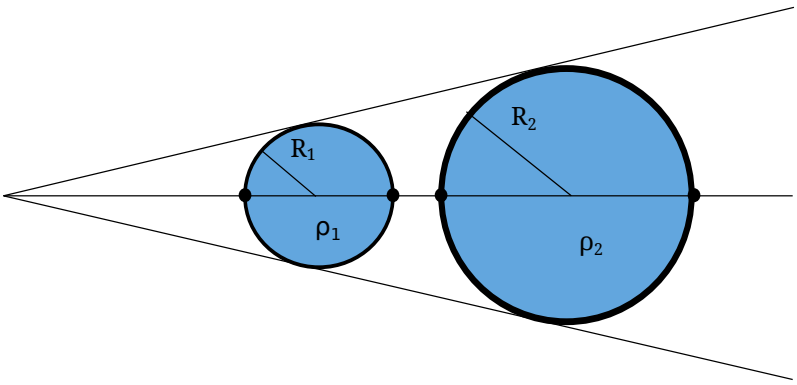

Figure 4.26: Profiles of two filled spheres with the respective radii R_1 and R_2 and the densities ρ_1 and ρ_2, located at different distances from the observer, which is located at the vertex of the three depicted lines of sights (black lines) on the left hand side.

[28] As described in section 3.5, even on Galactic scales it can just be applied to specific regions, which will become relevant for the investigation of the shells, detected using SAGHIS in chapter 5

[29] In this context local means distances of up to about 0.5 kpc

4.7.2 Visual- vs. real maximum radius of a spherical shell

In theory, if a shell has an spherical shape, it is possible to estimate a distance of the observed shape of a spherical shell if the angular size of the shell is ”large enough“. What this means in detail is explained below. First, some quantities that are needed are introduced in advance.

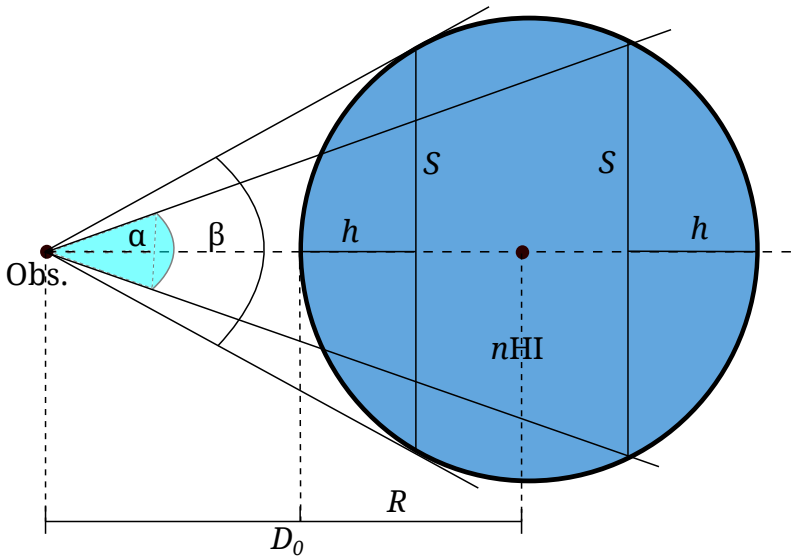

Figure 4.27: Illustration of the profile of a filled sphere with a particle density nH I, radius R at a distance D_0. The angular size β of a front part of the shell and the corresponding angular size α of the back of the shell are shown. S is the circle segment and h is the circle segment height. For more information see text, eq. 4.37 and 4.38.

The relation of the segment S of a circle, i.e. the profile of a cut of a sphere, in a datacube is shown for a given distance to the center D_0 and radius R of the shell. In figure 4.27 the following calculation can be followed by the geometry of this schematically shown filled circle.

$$S = 2 \cdot \sqrt{2 \cdot R \cdot h - h^2}, \tag{4.37}$$

where h is the perpendicular distance between S and the circle edge at the radius R. Knowing S, the center angle of the circle can be calculated by

$$\alpha/\beta = 2 \cdot \arctan\left(\frac{S}{2 \cdot d_{1/2}}\right) \tag{4.38}$$

where $d_1 = D_0 - R + h$ is needed for the front of the sphere, i.e. for the calculation of β, while $d_2 = D_0 + R - h$ is needed for the back of the sphere, i.e. for the calculation of α (fig. 4.27).

This means that S has two different angular sizes for the observer, despite having the same physical length. This implies two important effects. The first one is that the approaching cap of an object appears larger than the receding part[30]. The second effect is that the center of the object, if it is

[30] This is experienced commonly in our daily life, e.g. when looking down an avenue, where the closest tree seems to be the

considered a sphere, appears to be closer to the observer than it actually is, because the assumption for small spheres is that the center and radius of a sphere are seen where the angular radius is the largest. But since the UCL-shell of Sco-Cen has an angular size of up to 140° in one direction, this assumption does not hold anymore.

Both effects are illustrated in figure 4.28, where the observer is located at 0 pc and the observed profile of a shell at a distance of 130 pc is shown for different shell sizes. It can be seen that deviations of the shape from a circle-like shape increase with increasing angular radius of the shell. This effect is starting to be noticeable at objects of about 2–5 °. The black dots mark points where the observer sees the largest segment of the shell for the respective radius, while the red dots mark the largest physical segment, i.e. the real radius.

Theoretically, extracting additional distance information using this effect should be possible. In reality on the other hand, the shape of a shell is not perfectly spherical and can deviate quite significantly from the perfect shape of a sphere as shown for multiple examples of shells of Sco-Cen in chapter 6. Additionally, there are not many shells with angular radii larger than 10°, where this effect becomes significant enough to be measurable and even for most of these, the underestimation of the distance produced by this effect is still lower than the general uncertainties in the distance measurements. But when reaching sizes of above 50°, should be clearly visible, when a shell is nearly spherical and hence dedicated for the analysis of the UCL-shell.

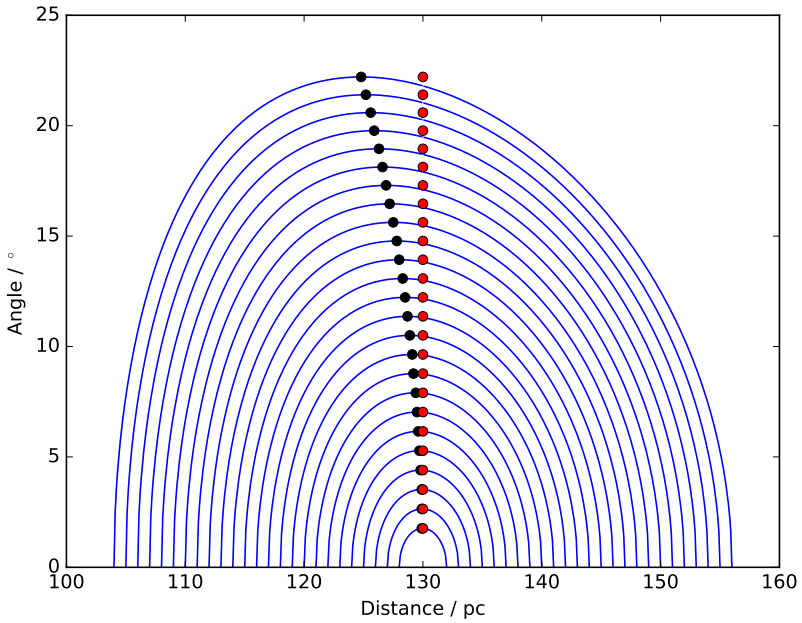

Figure 4.28: Plot of the observed angular size of spherical shells (blue lines) of different radii located at the same distance. The black dots mark the points of largest observed radii for the respective shell size, while the red dots mark the real x-position of the physical radius, which is not changing and always at the center position of the shell, at a distance of 130 pc. For more information about the context of this plot see text.

largest even if all trees have the same size.

4.7.3 Distance estimation by combining other measurements with H I

Since the H I emission itself does not imply distance information, except from what can be inferred by the kinematic distance estimations, its distance can be estimated if a connection to other objects, like star clusters or other wavelengths measurements can be made. For these, here, interstellar absorption lines, stellar distances from HIPPARCOS and GAIA have been used.

Distance constraints from interstellar absorption lines

In the spectra of stars, characteristic absorption lines can be observed, when the radiation ray of stars penetrates the ISM. If no dense ISM clouds are located between a star and the observer, just low column densities of absorption are observed. If another star is located more far away than the first star and in between a dense cloud is located, an increase of the observed column density, produced by the cloud, can be measured. With this, the distance of an observed cloud can be limited between the distance of those two stars as illustrated schematically in figure 4.29. Here four stars at different locations A, B, C and D around the ISM-Cloud are shown. Between A and C a significant increase in column density is expected, while for star B, the increase should be much lower since the cloud is not in the line of sight (black line connected with point B) and the increase between C and D should also be small. The more stars are included into such an analysis, the more accurate the distance limiting of the cloud. This can lead to a spatial distribution of the ISM as done by e.g. Vergely et al. (2001), Lallement et al. (2003) or Puspitarini & Lallement (2012) introduced in section 2.2. The concrete measurement is explained in the following.

The column density of species x for one line of sight (LoS) can be obtained by fist determining the equivalent width on the LoS by

$$\omega_\nu = \frac{I_{\mathrm{tot}}}{I_0} = \frac{\int d\nu (I(\nu) - I_0)}{I_0} \tag{4.39}$$

where ν is the frequency, I_0 is the intensity without absorption and I_{tot} is the total intensity. Given ω_ν, the column densities can be determined as ((Vergely et al. 2001))

$$N_x = 1.13 \cdot 10^{17} \frac{\omega_\lambda}{f\lambda^2} \tag{4.40}$$

with the "rest"-wavelength of the line λ and its oscillator strength f, e.g. $\log(\lambda f_{\mathrm{Na}}) = -2.83$, $\log(\lambda f_{\mathrm{H}}) = -8.52$, $\log(\lambda f_{\mathrm{Ca}}) = -2.86$, $\log(\lambda f_{\mathrm{K}}) = -1.65$ (Morton 1991, 1992) and with the relation $\omega_\lambda = \omega_\nu \frac{\lambda^2}{c}$, N_x can be determined for different LoSs when the inversion method of the absorption line is used[31].

Using inversion methods of multiple line of sights with interstellar lines (Vergely et al. 2001), the above mentioned maps of the LISM can be produced.

4.7.3.1 Na I absorption line analysis

One special case for absorption line analysis is the usage of the Natrium-D absorption line, because it traces the cold neutral ISM, meaning H I. Data tables from the literature (Welsh et al. 2010; Poeppel et al. 2010), containing LoSs towards stars with Na I absorption line detections, are available as well

[31] The gas has to be optically thin, meaning the opacity σ_τ has to be much smaller than one to make this method applicable.

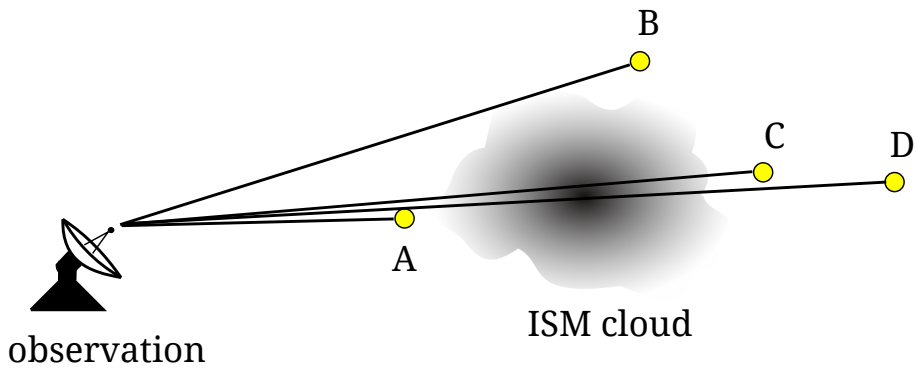

Figure 4.29: Schematics illustrating the distance estimation using interstellar absorption lines. Lines of sights towards the four exemplary illustrated stars marked as A, B, C and D, located in front, nearby and behind the cloud are depicted. For a description of the underlying method see text

as the peak velocities and their widths for each absorption line on the LoS. The distances, listed in these tables, have been calculated from the parallax measurements of the High Precision Parallax Collecting Satellite (**HIPARCOS**) data catalog (Perryman et al. 1997). The distance uncertainties are approximately 7% for 50 – 100 pc and 15% for 200 – 250 pc distance with large dispersions (Poeppel et al. 2010). For some, but not all, LoSs, Na I column densities are available, as derived by Welsh et al. (2010)[32]. These data have been used in this work as described in chapter 6 to limit the distances to the detected H I shells and clouds near Sco-Cen.

GAIA parallaxes The table of Poeppel et al. (2010) and Welsh et al. (2010) contains distance estimations to the stars from HIPPARCOS. If available, the distances have been replaced by more accurate parallax measurements towards the stars from the first data release of the GAIA mission[33] (Gaia Collaboration et al. 2016; Lindegren et al. 2016). A direct comparison of the distances towards the stars can be made in table A.0.6 between rows 3 (HIPPARCOS) and 4 (GAIA). For most cases, listed in table A.0.6, the distance estimation using parallax measurements led to similar results but there are also cases where the HIPPARCOS and the GAIA distances show significant differences, e.g. the star HD 146284 which has a distance of 264 pc according to the HIPPARCOS data and one of just 181.23 pc according to the GAIA data.

4.7.3.2 Connection between Na I- and H I peaks

Since from Welsh et al. (2010), 211 LoSs are available[32] and each LoS contains up to 10 absorption lines, an automated algorithm has been developed in this work and applied, to the data that determines,

[32] The study of Welsh et al. (2010) accounted for a much higher number of sight lines, but did not include the peak velocities in their tables. But after a data loss at their institute, the velocity values of the peaks are not available anymore (private communication with B.Y. Welsh 2014). Because of the release of the paper of (Poeppel et al. 2010), which was prior to the data loss but did not include the column densities of these sight lines, it is possible to check if a line of sight was target of both studies.

[33] The data have been downloaded using the GAIA web archive: https://gea.esac.esa.int/archive/ at

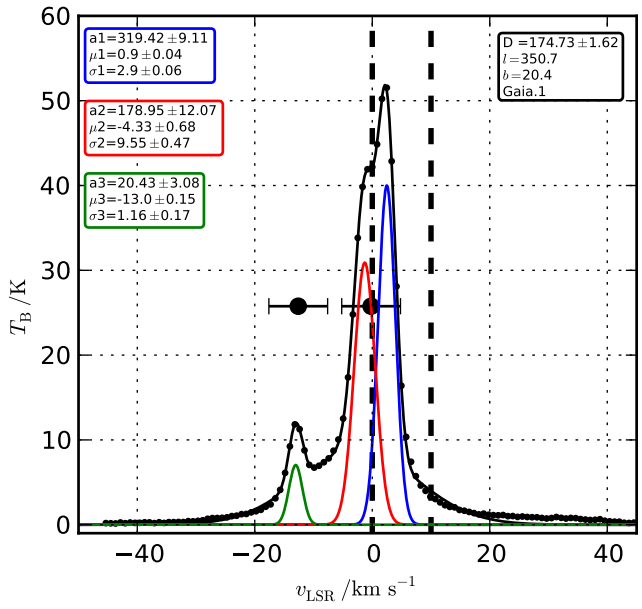

Figure 4.30: The H I profile of one line of sight (LoS) of the GASS data set, in the direction of l = 350.7 and b = 20, .4 (black dots), in the velocity range of -40 to +40 km/s. The H I profile is fitted by three Gaussian functions (green, red and blue) with the summed up function marked by the black line. The black, thick dots with error bars denote the Na I absorption line peaks with their velocity extensions. The two dashed vertical lines mark the velocity range in which the H I feature is detected. For more information about H I features, see section 6.1. An explanation of the fit to this profile is provided in the text in this section.

which of the Na I absorption line peaks are associated with the H I peaks of the GASS as explained in the following. For each LoS where Na I data were available, the H I profile has been extracted from the original GASS H I datacube in the velocity range -40 km/s to +40 km/s and the Gaussian decomposition fit from section 3.4 has been applied to each spectral line[34].

The connection between the resulting H I peaks of the multi component Gauss fit and the Na I absorption line has then been tested by setting a distance limit in velocity direction between the peaks to identify if one H I peak can be associated with the Na I absorption line. The connection is made if the following criteria i.) and ii.) are fulfilled:

i.) $\sigma_{\mathrm{H\,I}} \leq 3$ km/s and $\left|\mathrm{Na\,I}_0 - \mathrm{H\,I}_0\right| \leq \sigma_{\mathrm{H\,I}} \Rightarrow$ the peaks match

ii.) $\sigma_{\mathrm{H\,I}} > 3$ km/s and $\left|\mathrm{Na\,I}_0 - \mathrm{H\,I}_0\right| \leq (\Delta_{\mathrm{Na\,I}} + \sigma_{\mathrm{H\,I}}) \Rightarrow$ the peaks match

iii.) any other case $\Rightarrow$ the peaks don't match

Here $\mathrm{Na\,I}_0$ and $\mathrm{H\,I}_0$ are the velocities of the peaks of sodium and hydrogen respectively and $\sigma_{\mathrm{H\,I}}$ is the standard deviation of the H I peak and the limit of 3 km/s corresponds to $v_{\mathrm{FWHM}} = 7.1$ km/s (section 2.1.1). The specifications above prevents the absorption line peak to be fitted to a broad line

[34] The resolution of the position measurement of a star that has been used for the absorption line measurements is much higher than the H I resolution. The smallest area for a line of sight in an area of 1 pixel in the H I of GASS are used.

H I component, which would represent the Galactic disk background. It is also required that both peaks are close to each other compared to the velocity widths of the H I clouds. This is specified because it is expected that denser H I regions of a cloud, which define peak positions of high emission, also contain more sodium[35]. And it also reduces the amount of ambiguous results, i.e. one Na I peak should just connect to one H I peak and vice versa in most cases. But if the Na I absorption line still fits more than one H I component, the closest peak pair is chosen. The line fit and the peaks are automatically plotted, enabling the results to be cross checked afterwards to reject suspicious results.

A plot for one LoS is shown in fig. 4.30. The spectral data of the GASS are indicated by small black dots and are connected by the black solid line, which is the sum of the Gaussian components. The spectrum has two main peaks, while the larger one should be a convolution of two peaks itself. The fit result is in agreement with this and three Gaussian functions fit the spectrum best (green-, red- and blue solid lines). In this velocity range, two Na I peaks have been available that are marked by thick dots. The width of the lines in velocity is indicated by the black error bars. In this example the Na I peak at about 0 km/s matches two H I peaks (blue- and red solid lines) but the Na I peak is just associated with the red solid line since this is the best fit result.

This method has been performed for all 211 lines of sights and the profiles have been fitted, looping from 2 to 6 Gaussians per fit and taking the best fitting results automatically. Using these results. The distance limits can be derived as follows.

Determination of the distance limits The distance limits can be applied to each H I peak along each LoS of sodium absorption in the specified velocity range with the cases:

1.) No match between H I peak and Na I peak $\Rightarrow$ reject

2.) The fitted H I peak does not match any Na I peak but other H I peaks do. $\Rightarrow$ H I cloud behind star $\Rightarrow$lower distance limit

3.) The fitted H I peak matches the Na I peak $\Rightarrow$ H I cloud between Sun and star $\Rightarrow$ upper distance limit

Case 1 just appears for one single LoS of table A.0.6. The other two cases are possible for each H I peak along one LoS and limit the distance to the different components of the spectrum. In general it is expected that, in the direction of Sco-Cen, the more far away a cloud, the more positive should be its radial velocity because of the relative motion of the region compared to the Sun. In general, this does not have to be the case for clouds shocked by winds or SNe but is the case for each LoS here.

Continuing the example of figure 4.30, the green– and red H I peaks are of category 3 and hence are closer than the star and the blue line fit matches case 2 and has a higher distance than the star.

Example result In figure 6.3, feature X is represented by a small, dense ring with an inner region of low density at approximately $l = 350^\circ$, $b = 20^\circ$. For feature X, exemplary the confirmation method of the upper distance limit is explained for a single LoS. It has been checked if the sight line for which a match between H I and Na I had been detected is representative for the whole cloud, or at least a fraction of the cloud, by comparing the H I profile of the line of sight (LoS) to the profiles of neighboring

[35] In fact in visual test fits, in many cases the peaks of Na I and H I are closer than the limit, if not even on top of each other, both tracing the same region

pixels that are below 0.22° (GASS resolution) angular distance from the center. This ensures that the one matching LoS through one pixel does not appear due to random intensity variations and that they are still close enough to be dependant pixels[36], represent nearly the same H I line profile and hence the same cloud. Then also LoSs through random $l - b$ coordinates on other dense locations on the ring are chosen, to see if the profile is similar compared to the one of the LoS, where the Na I line is available. If this is the case for each tested location on the ring, it is suggested to have the same upper distance limit as the one given for the peak of the H I–Na I match. Lastly, some LoSs at coordinates in the region of low density have been investigated to see if the absence of the ring is also seen in the profile to distinguish it from the background.

In the upper plot of figure 6.3, the distance limit of 134 pc (yellow box) of feature X can be seen (see also (Krause et al. 2018)). Different profiles along coordinates, as described above, are presented in figure 4.31. The figure consists of 12 subplots. The first subplot with the label "center LoS", represents the profile along the LoS where the Na I–H I match has been determined and contains the position of the Na I peak (black dot with errorbar) and the fitted H I peak (blue vertical dashed line). These two markers are included in each subplot. By this, the overlap of the Na I peak with the respective H I line profiles, at the respective coordinates that are shown in the upper left of each subplot, have been determined. The plots are arranged from the top left to the bottom right, where the following three plots (upper LoS, left LoS, right LoS) show the H I emission at positions of 1 beamwidth away from the matching LoS as described above. The subplots "shell pos 1" to "shell pos 5" are the mentioned points on high emission regions on the ring. The remaining three plots "cavity pos 1" to "cavitiy pos 3" are regions near the center of the ring, where lower emission is expected. In all on-shell subplots 1–9, the Na I peak fits the H I profile within the uncertainties as described above. It can also be seen that for some velocity ranges, the profile in this region is a convolution of two H I peaks, e.g. subplot "shell pos 2". The profiles along the LoSs near the center positions show H I peaks that are shifted towards negative velocities and the peaks of subplot 1 lie at the right flank of these H I profile. The maximum intensities in these three subplots are different. For example the small peak in subplot "cavity pos 1" just has a maximum intensity of $T_b = 20$ K km/s compared to the main peaks on the shell that lie at about $T_b = 58$ K km/s. However, the profiles on the shell positions yield that the shell should indeed be closer than 134 pc, since they all match the Na I peak.

Since this method is applied for the Sco-Cen region for the 211 LoSs, the results are presented in section 6.1 in the tables and figures therein.

[36] Dependent pixels are pixels that contribute to the same beam. Since the binning is smaller than the resolution, pixel in a region of 0.22° are not independent.

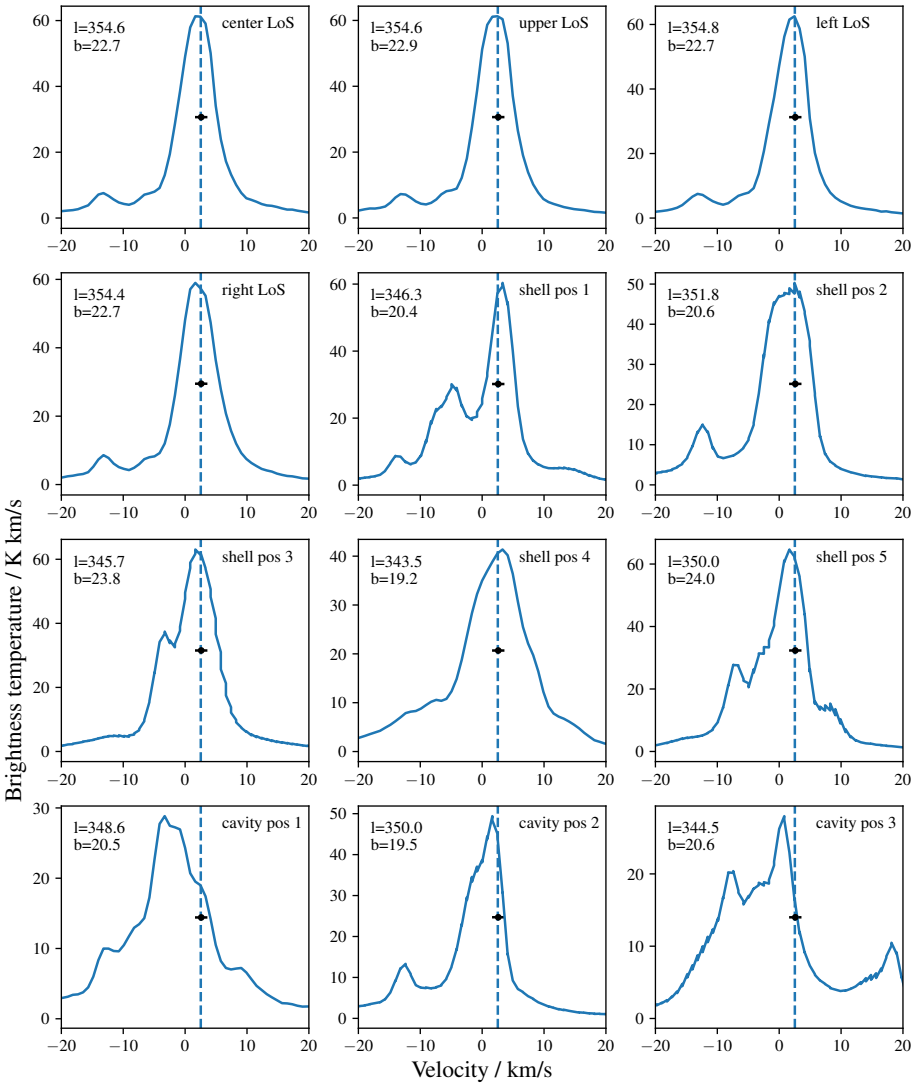

Figure 4.31: Plots showing 12 spectral lines of H I emission of LoSs in the region of feature X. At the top left in each plot, the angular LoS position of the match between the sodium absorption line and the H I emission peak is shown in units of degree. The vertical blue dashed line denotes the fitted H I peak of the position of subplot 1 and the black dot with errorbar denotes the position of the Na I absorption line peak. For more information see text.

4.8 Summary

In this chapter the tools and methods that are needed in preparation for the investigation of the local Galactic H I emission as well as for the detailed analysis of the Sco-Cen region have been introduced and their tests and applications to the data have been presented.

Pattern recognition algorithms that are also the foundation of SAGHIS have been introduced and tested. It has been shown that the customized edge detection serves the use case of blindly searching for expanding shells, while the Canny edge detection is better if the specifics of the ISM of a region are known a priori. The algorithm steps of SAGHIS have been introduced and it has been applied to the Galactic H I data of the HI4PI survey. The interim results of the application steps of SAGHIS to the HI4PI data have been presented. The result is a shell catalog containing 802 members that are ranked due to introduces quality measures. The shells of this catalog are analyzed in detail in the following chapter 5.

An astrophysically motivated shell representation, the EHSS-model has also been introduced in this chapter. This model is the baseline on which the SAGHIS algorithm has been developed. It has been tested with which methods the model can be fitted to synthetic data as well as real H I data. The results of the tests are that the model has limited applications for a general search and that the parameters have to be estimated a priori to ensure high quality fit results. If some parameters are known a priori, the model can be used to fit the remaining parameters as has been performed for the masses of the shells near Sco-Cen. A special H I emission background model has been developed for the ISM in the vicinity of Sco-Cen. It has been shown that, using this background model, the fit quality improved. Finally, methods to determine the distance towards local H I clouds and shells have been introduced. The application of these methods to the ISM in the vicinity of Sco-Cen is presented in chapter 6.

CHAPTER 5

H I shells in the HI4PI survey

This chapter builds upon the application of the **S**earch **A**lgorithm for **G**alactic **H** I **S**hells (SAGHIS) on the data of the HI4PI survey from section 4.6. The shell catalog that had been derived there has been analyzed statistically and used to derive physical properties of the H I shells that lead to astrophysical interpretations.

This chapter is structured as follows. The H I distribution properties of the shells in the longitude-latitude-velocity space as well as the statistical properties like angular size and the velocity range are presented in section 5.1. In section 5.2, the catalog is compared to other H I shell catalogs and examples of newly identified shells are presented. After that, in section 5.3, the derivation of the kinematic distance towards the shells to derive its physical properties as well as their spatial distribution in the local Milky Way is presented. An astrophysical interpretation of the results is derived in section 5.4. Finally the chapter is summarized in section 5.5.

5.1 Properties of the detected H I shells

The shell catalog, which has been derived in section 4.6, contains the results of the application of SAGHIS to the H I data of the HI4PI survey. The catalog contains 802 shells. An excerpt of the top 15 rows of the full table (table A.0.19) is presented in table 5.1. Columns 1 and 2 contain the mean coordinate pairs l_0, b_0 of the center of the shell. The mean-, minimum- and maximum radius are listed in columns 3, 5 and 6 respectively. The mean velocity v_0, the minimum- and maximum velocity channels, $v_{\rm min}$ and $v_{\rm max}$ where the shell is present are listed in columns 4, 7 and 8 respectively. The name of the shell is listed in column 9. The quality components $Q_{\rm m}$, $Q_{\rm ac}$, $Q_{\rm v}$, $Q_{\rm p}$, derived in section 4.6.3 are listed in columns 10–13 as well as the total quality value Q_f in column 14 that defines the ranking of the shells in the table. Table 5.2 lists the corresponding uncertainties Δl_0, Δb_0, Δr_0, Δv_0, $\Delta r_{\rm min}$, $\Delta r_{\rm max}$ and $\Delta v_{\rm exp}$ (sec. 4.6.4).

1 l_0 °	2 b_0 °	3 r_0 °	4 v_0 km/s	5 $r_{\rm min}$ °	6 $r_{\rm max}$ °	7 $v_{\rm min}$ km/s	8 $v_{\rm max}$ km/s	9 name -	10 Q_m -	11 Q_{ac} -	12 Q_v -	13 Q_p -	14 Q_f -
198.25	-25.25	13.2	14.3	11.2	19.2	10.4	16.8	DK_1476	1	0.99	1	1	3.99
228.42	-7.42	6.3	38.7	4.7	9.7	24.6	52.9	DK_2046	1	0.97	1	1	3.97
48.33	-8.08	7.7	19.4	6.5	9	10.4	33.6	DK_1303	1	0.97	1	1	3.97
325.83	-8.25	7.2	-21.8	5.2	10	-33.4	-8.9	DK_1286	1	0.97	1	1	3.97
202.75	-30.75	11.5	9.1	9.7	14.5	5.3	11.7	DK_b_356	1	0.96	1	1	3.96
301.33	-4	5	-19.2	3.5	6.5	-30.8	-7.6	DK_1187	1	0.96	1	1	3.96
301.42	-4.08	4.6	-19.2	3.5	6.2	-30.8	-8.9	DK_1188	1	0.96	1	1	3.96
43.5	4.17	3.8	28.4	3	4.5	24.6	32.3	DK_1119	1	0.95	1	1	3.95
42.33	-4.75	5.7	16.8	4.7	9.5	11.7	28.4	DK_857	1	0.93	1	1	3.93
42.33	-8.17	8.3	14.3	7.2	10	5.3	24.6	DK_810	1	0.92	1	1	3.92
304.5	-5.33	5	-16.6	3.7	7	-27	-7.6	DK_3462	1	0.9	1	1	3.9
218.42	-8.75	9.7	22	8.7	13.7	7.8	34.9	DK_457	1	0.87	1	1	3.87
225.25	-9.25	5.1	36.2	3.5	7.2	19.4	52.9	DK_1619	1	1	1	0.7	3.67
45.67	-8.58	10.4	16.8	8.5	13.5	10.4	23.3	DK_1701	1	1	1	0.7	3.66
130.42	4.33	3.2	-52.7	3	4.2	-57.9	-47.6	DK_1452	1	0.98	1	0.7	3.65
26.25	-8.42	8	23.3	6.7	11.5	9.1	37.5	DK_1117	1	0.95	1	0.7	3.62

Table 5.1: Excerpt of the first rows of the shell catalog, which represents the final results of SAGHIS (see appendix table A.0.19 for full catalog). Column 1 and 2 contain the mean center coordinates l_0, b_0 of the shell over all channels. Column 3 contains the mean angular radius r_0 of the shell, columns 4, 5 and 6 contain the center velocity v_0, the minimum radius $r_{\rm min}$ and the maximum radius $r_{\rm max}$ respectively. Column 7 and 8 present the lower ($v_{\rm min}$) and upper ($v_{\rm max}$) velocity channels where the shell is detected and columns 9 gives the name of the object. The quality components (section 4.6.3) are listed in columns 11, 12, 13 and 14 with a total quality value Q_f, used for the ranking that is listed in column 14.

1 name	2 Δl_0	3 Δb_0	4 $\Delta r_{\rm min}$	5 Δr_0	6 $\Delta r_{\rm max}$	7 Δv_0	8 $\Delta v_{\rm exp}$
DK_1476	2.08	0.67	1	2.83	4	0.74	0.53
DK_2046	1.25	0.27	1.19	1.58	2.5	2.58	2.83
DK_1303	1.17	0.33	0.5	1.25	0.25	3.54	2.83
DK_1286	1.25	1.08	1.31	1	2	2.58	2.58
DK_b_356	2.08	0.27	0.5	1.5	2.75	0.74	0.53
DK_1187	0.75	0.67	0.5	1.5	1.75	2.9	2.32
DK_1188	0.58	0.33	0.25	0.92	1.75	2.58	2.06

DK_1119	0.42	0.75	0.5	0.67	0.5	0.97	0.77
DK_857	0.92	0.27	1.19	1.42	0.25	2.9	2.32
DK_810	0.83	0.58	0.25	1.08	0.75	2.58	2.06
DK_3462	0.42	0.27	0.94	1.08	1.75	2.25	1.8
DK_457	1.08	1	1.25	2.42	1.75	3.22	2.58
DK_1619	0.58	0.27	0.87	1.42	1.81	4.19	3.35
DK_1701	1.25	0.33	1	1.67	3.25	1.61	1.29
DK_1452	0.42	0.27	0.75	0.5	1.25	1.29	1.03

Table 5.2: This table is an excerpt of table A.0.21. It contains the uncertainties of the parameters of the catalog shells from table A.0.19. Columns 1 and 2 contain the uncertainties of the center coordinates Δl_0, Δb_0 of each shell. Columns 3–5 list the uncertainties of the minimum-, mean- and maximum radius (Δr_{min}, Δr_0, Δr_{max}) respectively. The uncertainties of the center velocity Δv_0 and the expansion velocity Δv_{exp} are listed in the columns 7 and 8 respectively. For more information see text in section 5.1.

5.1.1 Distribution and angular extent of the shells

Angular distribution of the shells in Galactic coordinates

The Galactic disk of stars has a vertical exponential profile (de Grijs & Peletier 1997). The global ISM density of the Galactic disk is also approximated by exponential distributions (e.g. Kalberla & Kerp (2009) fig. 4 to 6). Since less star clusters are located at higher distances from the Galactic plane, the number of detectable shells with center coordinates there should also decrease (sec. 5.3). The mean intensity distribution of H I along the Galactic latitude is shown in the right panel of figure 3.8. It also decreases steeply towards higher latitudes, so is the general distribution of shells of the catalog. This is shown in figure 5.1, where the distribution of the shells in longitude and latitude is plotted. The density distribution of shells along Galactic longitudes is shown in the top panel and the one along the latitudes is shown in the right panel of the figure. The majority (74%) of the shells are located at latitudes lower than 20 °. If fitting a normal distribution in the range -20° to $+20^\circ$ in latitude to the binned data, the mean value is $b_{\mathrm{mean}} = -1.6^\circ$ (fig. B.0.26). This offset is also observed for the global ISM distribution due to the Galactic warp, which leads to an asymmetry in the distribution of the ISM into the direction of the Galactic center between the regions above- and below the Galactic plane. More gas at negative latitudes is observed than at positive latitudes (Kalberla & Kerp (2009), fig. 3 therein).

Figure B.0.26 also reveals clusters of shells at similar longitudes and latitudes in this two dimensional projection. Some of them have different center velocities v_0 and hence are located at different spatial positions but other shell clusters occur at regions with well known H I shells and supernova activities and share similar center velocities v_0 as will be shown in below. For example, the number of off-plane shells at $b = -40^\circ$ to -20° (180°–220°) stands out from the main distribution. This is the region of the Orion-Eridanus superbubble, which is close on galactic scales and reveals highly structured high density regions at high latitudes, even on all-sky H I maps. In this region it is observed that multiple nested shells exist inside the largest once, the Orion-Eridanus bubble (Ochsendorf et al. 2015). Catalog shells that are identified with the bubble are DK_1476, DK_b_489, DK_b_602. These shells lie at different velocities and have different center coordinates but share large radii between 18°-19.75°, similar to the one of the Orion-Eridanus Bubble. The nested shells inside the Orion-Eridanus bubble are not compared in detail here. However since the Orion-Erhidanus bubble shares a wide range of coordinates and velocities, 18 catalog shells are found to be lying within the Orion-Eridanus bubble. These are DK_1983, DK_182, DK_b_712, DK_b_338, DK_b_741, DK_168, DK_b_735, DK_b_628,

DK_b_672, DK_2433, DK_4918, DK_3442, DK_b_693, DK_b_692, DK_b_794, DK_b_808, DK_b_625, DK_2572 and DK_b_793. Also Sco-Cen contains partly overlapping shells and shells that are embedded into each other, e.g. in figures 6.5 to 6.10. A group of catalog shells is located near 20 ° latitude and at low positive radial velocities and is identified to belong to the Sco-Cen shells. The catalog shells overlap within their parameter uncertainties (sec. 4.6.4) with the known parameters of the Sco-Cen shells (sec. 2.5). For example, the object DK_1047 is within the uncertainty ranges of the USco-loop, DK_b_34 in the one of the USco-shell, DK_307 traces the LCC-Loop. These objects will be analyzed in more detail in chapter 6.

The distribution of shells along Galactic longitudes is not homogeneous but shows distinct peaks. This is analyzed below with derived physical locations of the shells in section 5.3.

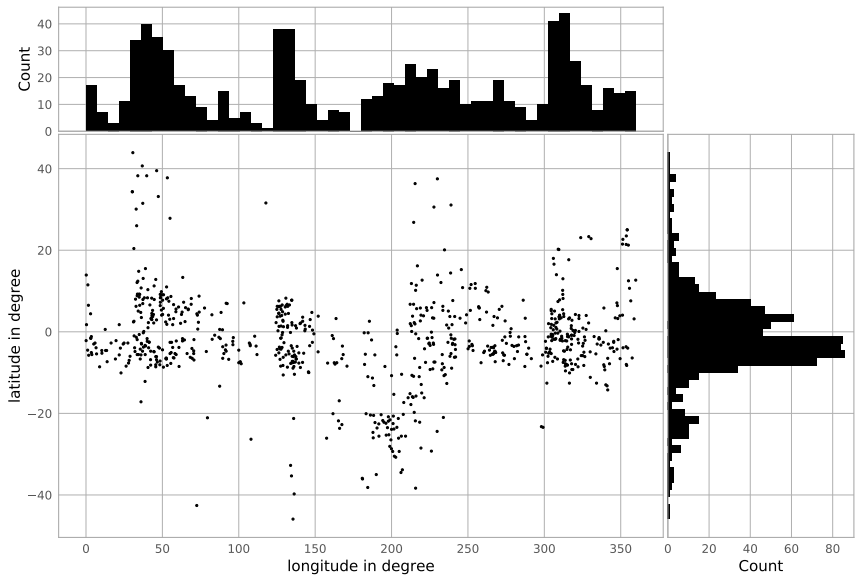

Figure 5.1: Distribution of shells of table A.0.19 for the whole 360° longitude range in the plate-carée projection for latitudes $\leq |50°|$. Each dot represents the center coordinate of one shell of the catalog. In the top- and right panel, the histograms of the latitude and longitude distribution of the shells are shown respectively.

Velocity distribution of shells

Complementing the angular distribution, now the center velocities of the shells v_0 are analyzed. On the left hand side of figure 5.2, the velocity is plotted against the Galactic longitude of the shells and in the right panel, the velocity-latitude distribution of the shells is plotted. Along the longitude axis of the left panel of figure 5.2, regions of high densities of shells of roughly 20° thickness can be seen at the longitudes $l = 140°, l = 40°, l = -50°$ and $l = -140°$.

Just about 1% of the shells are detected at velocities higher than $|v_{\mathrm{LSR}}| \geq 100$ km/s. The catalog contains some shells with high moving velocities, v_0, near $|v_{\mathrm{LSR}}| = 150$ km/s. Shells at these velocities have not been known before (Heiles 1979, 1984; McClure-Griffiths et al. 2002; Ehlerová & Palouš 2005, 2013; Sallmen et al. 2015). Generally, the intensities for shells at these velocities are low (fig 3.3.2) and at high latitude regions, near the noise level. However the catalog objects are identified as expanding structures. These are the catalog shells DK_b_102 ($v_0 = -150.6$ km/s), DK_b_278 ($v_0 = -139$ km/s), DK_b_226 ($v_0 = -123.6$ km/s), DK_5585 ($v_0 = -109.4$ km/s) and DK_5563 ($v_0 = -108.1$ km/s). Their ranking (Q_f of table 5.1) are rather low with values between $Q_f = 1.49 - 2.67$. Close objects following the Galactic rotation should have mean radial velocity variations of several 10- th of km/s. The radial velocities of these objects however are above 100 km/s. Such high velocity objects are also found at negative latitudes below $b = -20°$. Either these high latitude objects are close and rapidly approaching or the high radial velocities are components of the large-scale Galactic rotation velocity at different locations on the disk. They would then have also a vertical distance towards the plane of several kpc for latitudes of 20 degree. Even though generally, star formation takes place in the thin disk of scale heights 300–400 pc (e.g. Sparke & Gallagher (2007)) it still cannot be assumed a priori, that these shells do not originate from supernova explosions at high Galactic latitudes. But the formation of expanding H I shells due to the impact of intermediate- or high velocity clouds (e.g. Kulkarni & Heiles (1987), Tenorio-Tagle & Bodenheimer (1988),Rand & Stone (1996),Santillan et al. (1999), Braun & Burton (1999) and sec. 2.4.3) is also a candidate for the origin. This is why DK_b_102, which has one of the highest negative mean velocity is discussed in more detail in regards to this below in section 5.2.

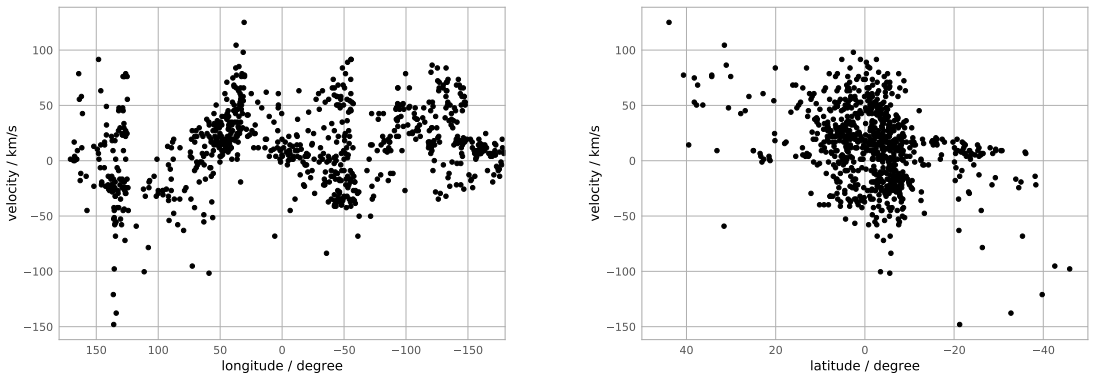

Figure 5.2: Longitude- and latitude-velocity plots of the detected H I shells using the SAGHIS. In the left panel, the longitude-velocity plot of the center coordinates of the shells is shown and in the right panel, the latitude-velocity plot is presented. The velocity range is -150 km/s−+150 km/s, while the full longitude range of 360° and latitudes in the range of -50° − +50° are shown.

Angular radius distribution and center velocities

The radial center- or moving velocity, v_0, of an object is connected to the distance of the object on Galactic scales. The distribution of angular sizes of the shells along the velocity spectrum can be seen in figure 5.3. For the majority of shells, the maximum angular radius increases with decreasing absolute mean center velocity v_0. If an object follows the Galactic rotation, shells of high v_0 are generally not located close to the Sun because locally, the stars move towards the same direction on the circular orbit. The further away a shell is located, the smaller is its angular radius if the physical size is the same (sec. 4.7.2). Together this leads to the distribution that can be seen in the figure, where the objects of higher radial velocities are more abundant for objects of smaller radii. An offset of the distribution towards positive velocities can be seen in the histogram on the right panel of figure 5.3, which correlates with the distribution of mean intensity values per velocity channel of the ISM along the range -150 km/s to +150 km/s (e.g. fig. 3.8). The Abundance distribution of radii can be seen in the top panel of figure 5.3. 50% of the detected objects have a maximum angular radius $r_{\mathrm{max}} \leq 7.2^{\circ}$ and 95 % of the objects lie in the range $0.5^{\circ} \leq r_{\mathrm{max}} \leq 17.7^{\circ}$. A more detailed analysis about the size and distance of shells is made below once the physical parameters of the shells are determined in section 5.3.

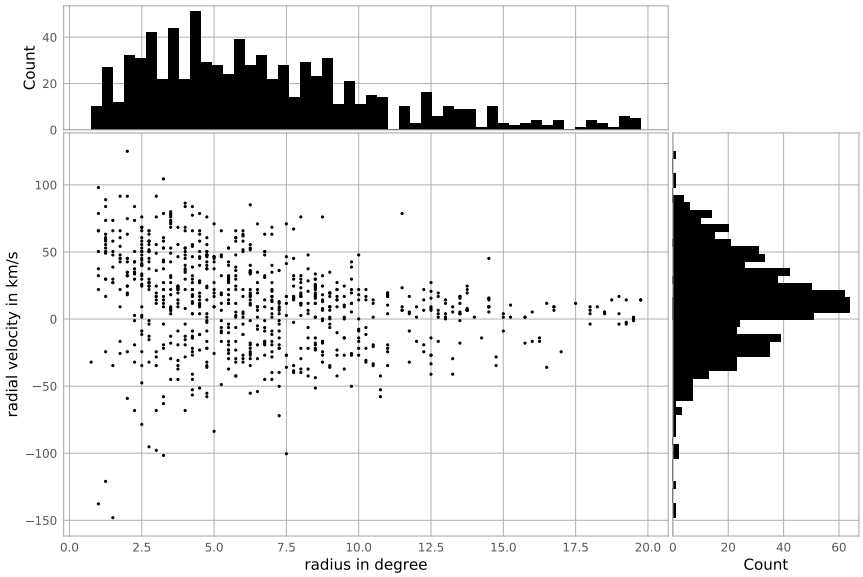

Figure 5.3: Plot of the center velocity against the maximum angular radius r_{max} of the catalog shells in the main panel in the velocity range −150 to +150 km/s and with the maximum shell radius of 20°. In the top panel of the figure, the abundance distribution of the radii are plotted in an histogram and the same is done for distribution of the velocity extent in the right panel.

5.2 Properties of known and new identified H I shells in the catalog

The derived H I shell catalog of table 5.1 is compared to other existing catalogs, mainly derived by H I surveys but also one containing SNR, based on radio continuum observation here.

5.2.1 Comparison with other catalogs

Previous catalogs of shells have been establishes by Heiles (1979), Heiles (1984), McClure-Griffiths et al. (2002),Ehlerová & Palouš (2005), Daigle et al. (2007), Ehlerová & Palouš (2013) and Sallmen et al. (2015) (sec. 2.4.3)[1]. The list of McClure-Griffiths et al. (2002) contains the results of Heiles (1979) and lists 19 objects. The catalog of Ehlerová & Palouš (2013) includes the results of Ehlerová & Palouš (2005) and contains the largest number of objects with 333 H I shells. The catalog of Sallmen et al. (2015) contains 69 objects. Comparable objects are the ones that lie within the searched coordinate ranges covered. This is $l = 0$–360°, $|b| \leq 50^\circ$ and $v < 150$ km/s (sec. 4.5.2). In the other catalogs, no shells with $v \approx 150$ km/s are present. In the catalog of Ehlerová & Palouš (2013), 4 shells are listed with latitudes $|b| \geq 50^\circ$, which leaves 329 out of 333 shells for comparison and 52 shells from Sallmen et al. (2015). The last catalog has been derived from an analysis of the SETHI data, which covers approximately a 10° strip along constant declination angle, meaning its distribution is not representative globally, which is taken into account for the comparison. The shells in these catalogs are listed in l-b-v-space and hence are directly comparable to the results of the H I shell catalog of this work. Calculating the physical properties of the shells introduces additional uncertainty sources from the kinematic distance estimation (section 5.3) and for a large fraction of shells this method is not applicable. This is why just for a fraction of the shells in the catalogs of the literature, the physical parameters are listed. Hence the statistical comparison has been done in the following in the l-b-v space. For readability, the catalogs of McClure-Griffiths et al. (2002), Ehlerová & Palouš (2013) and Sallmen et al. (2015) are abbreviated MCG2002, EP2013 and S2015 respectively. When mentioning the catalog of this work, derived with SAGHIS (section 4.6), it is named as "this" or "the" catalog in the following. The term "new shells" us used for all H I shells that are detected with SAGHIS that have not been listed in the studies of MCG2002, EP2013 and S2015.

Statistical comparison to other H I shell catalogs

The distributions of parameters of the catalogs are discussed along figures 5.4 and B.0.22 (normalized). In these figures, in each panel, the distribution H I shell of this catalog (black), the distribution of the shells MCG2002 (gray-dashed), the one from EP2013 (blue) and the one from S2015 (gray) are plotted for each shell parameter. A deviation can be seen in the top left panel, where the distributions of center longitudes are shown. The distribution of EP2013 is smoother than the one of the catalog and does not show the above described distinct peaks. In fig. B.0.22, the peak in the region around $l = 50^\circ$, $l = 180^\circ$ is also seen in S2015, while the peak around $l = 300$ of the catalog is also in MCG2002 (gray-dashed). In latitude (top-right panel), the distributions are similar. Most shells have been detected between -20° to 20° for all catalogs. A few new H I shells are listed at higher latitudes. The small peak at -20° latitude, discussed above, is not visible in EP2013. Due to the analyzed strip

[1] The catalog of Suad et al. (2014) that was refined in Suad et al. (2019) has been found after this analysis had been carried out. This is the reason why it is not included into this analysis.

of 10° at constant declination, the data of S2015 do not cover the same area. The small offset towards negative latitudes that was discussed above, is also present in EP2013.

The distributions of the mean radius $r_{\rm mean}$ (middle-left panel of the figures) are generally similar. Most shells have been detected with radii between 2–10° in all catalogs. The counter intuitively high number of shells at radii of 3–5° was discussed in section 5.1.1. The catalog of this work contains more shells of radii ≤ 5° (fig. 5.4) compared to EP2013. The peak at 5° is more distinct and more shells at larger radii are detected. The distributions of center velocities (v_0, middle-right panel of the figures) are similar for the different catalogs and spread mainly between -100 to 100 km/s. Most new shells are detected in ranges of v_0 from -50 km/s to 100 km/s but some new shells also at values of $v_0 \geq 100$ km/s (see section 5.1.1 and 5.2.2).

In the bottom panel of the figures, the distribution of expansion velocities are shown. In all catalogs, shells have expansion velocities between $v_{\rm exp}$ = 5–20 km/s. The 95% quantile of this catalog is at 12.3 km/s, similar to the one of S2015 with a value of 11.0 km/s for this quantile, whereas the one of EP2013 is at 19.4 km/s. This difference is due to the high abundance of shells with $v_{\rm exp} \leq 10$ km/s in the catalog of this work. In section 4.6.3, the properties of shell intensities along the velocity spectrum have been shown. Some shells in the catalog are open towards one- or both sides of the velocity spectrum and don't have the caps that are always present for an idealized model in a homogeneous environment (sec. 3.4). This observation is in agreement with what is observed for many of the best studied cases, like the USco-loop or the UCL-shell (ch. 6). The approach followed in this work (sec. 4.1, sec. 4.5) allows to detect these shells. In combination with the properties of the $r_{\rm mean}$ of the shells from above, new larger shells of lower measurable expansion velocities are detected by SAGHIS and are listed in this catalog.

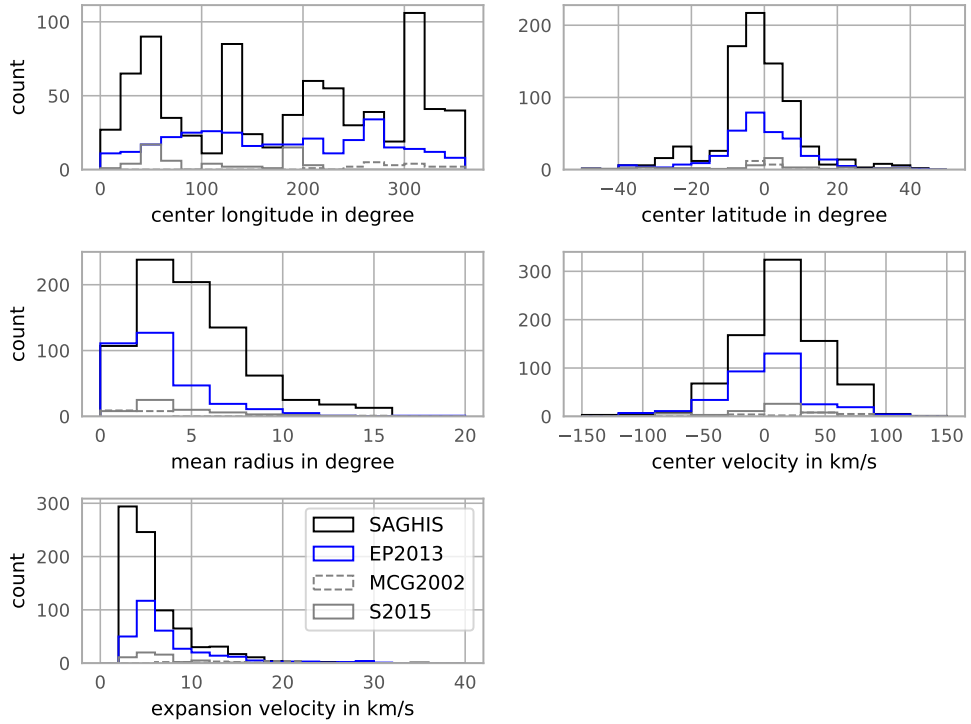

Figure 5.4: Distributions of the parameters of the shells of the thesis catalog, derived with SAGHIS (black), reference shells from the literature (blue) and overlapping objects that are present in both (dashed gray). In each of the five panels, separate distributions of the shell parameters are plotted. A similar version of these plots, containing the normalized distributions, can be found in figure B.0.22 in the appendix. For more information see text.

Overlapping and new objects in the H I shell catalog

To detemine if an object of this H I shell catalog traces the same shell as one of reference catalogs, the parameters l_0, b_0, v_0 and r_0 should be similar. The data used in this thesis have a higher resolution. The others have been carried out on the LAB survey (if not stated differently) with an effective angular resolution of 1° (tab. 3.1). Additionally the search methods are differend and also the parameterization of the objects differ between catalogs[2]. Hence it is unlikely to have objects of different catalogs, exactly matching in the 5 parameter space. This is why the approach from section 4.6.5 has been used again, where this time the uncertainties Δl_0, Δb_0, Δv_0, Δv_{exp} and Δr_{mean} of the shells of this catalog and the ones of MCG2002, EP2013 and S2015 have been used to determine if two shells of different catalogs match. If two shells of two different catalogs lie within the uncertainty ranges they are considered to trace the same object. Smaller shells in angular radius have smaller absolute uncertainties compared

[2] e.g. the catalogs of Ehlerová & Palouš (2013), Sallmen et al. (2015) and McClure-Griffiths et al. (2002) describe the objects with rectangular shapes of widths dl and db, which had to be normalized for comparison, resulting in additional uncertainies.

to larger ones. Hence they are sharper defined in the l-b-v-space. This indicates that if two small shells overlap, their parameter differences are also small. 5/19 shells of MCG2002 (26%), 10/52 shells of S2015 (19%) and 93/329 shells from EP2013 (28%) are also present in the catalog derived using SAGHIS. The results, presented in figure 5.5, are similar to the ones above (fig. 5.4) but this time, the normalized distributions of new shells that are not listed in the catalogs of MCG2002, EP2013 and S2015 (blue line), the overlaps with these (black-line) and the missing objects (dashed-gray line) are shown. Radii and expansion velocities are the striking parameters that show most differences between the surveys as mentioned above. Additionally, the characteristics of the new shells that are only present in the new SAGHIS catalog can be seen in this plot. For each panel (parameter) in figure 5.5, regions where these three distributions differ significantly, indicate that there is a systematic difference of new, overlapping and missing shells for this parameter as described below. Hence also a non normalized version of the plots is shown in figure B.0.13 in the appendix.

For the center longitude and -latitude (top left and top right panel) new, missing and overlapping objects are distributed along the whole longitude range and in the latitude range of $\|b\| \leq 50^\circ$. For longitudes, peaks in overlapping and new objects are connected to the high abundance of listed shells in the catalog at these longitudes due to high detections at close spiral-arm positions (more details below in sec. 5.3). For latitudes, apart from the above discussed region near b = -20°, no distinct differences between the distributions can be seen.

It has been presented above that in absolute numbers, a similar amount of new shells of radii smaller than 2°, compared to the other catalogs, are detected (fig. 5.4). In the middle left panel of figure 5.5, it can be seen that for the mean radius of the shells, many known objects with radii smaller than 2° are not included in the catalog (gray-dashed line). But the catalog of this work lists also a significant fraction of new shells (blue-line) of radii smaller than 2°, while the number of overlaps (black line) is just a few percent (see also middle-left panel of figure B.0.13). The number of overlaps is just 5, while the number of missed and newly detected shells are 96 and 108 respectively.

The abundance of shells of smaller angular radius should be higher in general compared to shells of larger angular size[3]. But smaller shells in angular radius are generally more difficult to detect due to the background emission of different sources that can overlay with larger fractions of the shell, especially near the Galactic plane. The smaller shells, especially at radii below $\leq 1^\circ$ are close to the resolution limit of the respective survey. This is why the abundance of shells in the bin up to 2° is lower for all catalogs than for their respective next bin. The distribution of center velocities are similar. Due to the above discussed reasons, the number of new objects is highest for expansion velocities near 2–4 km/s and the number of overlaps at this bin is the second highest after the one in the range of 4–6 km/s. (bottom left panel of fig. 5.5).

Comparison to supernova remnant catalogs derived by radio continuum observation

At the first stages, according to the evolution described in section 2.3.2, SNR can be observed in the radio continuum. For shell-type SNR, they can be traced by the synchrothon emission of electrons (Moffet 1975), accelarated by the SNR shockwave (Bell 1978a,b; Blandford & Ostriker 1978). For objects of the catalog, where this is the case[4], H I shells have been formed and hence here the comparison is made if some of the detected shells, maybe trace these radio continuum SNR. The

[3] This is because the further away an observed object, the smaller its angular radius. This means with increasing distance, the maximum possible angular radius decreases (because the maximum physical radius is limited).

[4] There are also types of SNR that can be observed in radio continuum without a shell (Blandford & Ostriker 1978)

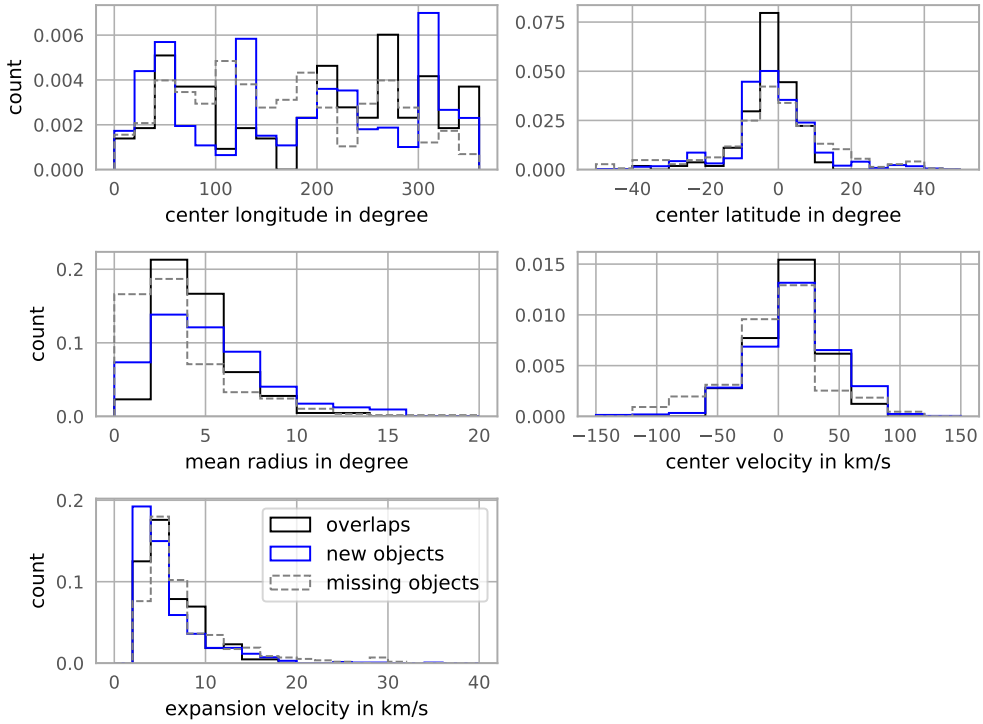

Figure 5.5: Distributions of new– (blue), overlapping– (black) and missing (gray-dashed) shells when comparing to the catalogs of MCG2002, EP2013 and S2015. In each of the five panels, separate distributions of the shell parameters are plotted. The distributions are normalized to 1.

most complete catalog of SNR objects found in the radio continuum is the catalog of Green (2019). This catalog is the result of a series of studies (Green & Gull 1984; Green 1988, 1991; Stephenson & Green 2002; Green 2004a, 2009, 2014). The angular resolution of the radio continuum data (0.05° resolution for lo-parkes Molonglo 408-MHz survey, 0.076° resolution for Effelsberg 2.7-GHz survey) is one order of magnitude higher than the one of the HI4PI survey (0.244°, see section 3.2.3) and hence the smaller objects that are connected to younger SNRs of this reference catalog cannot be resolved in H I. The catalog contains 294 objects in total. 95% of these objects are smaller than 1.78° and 123 Objects of this catalog have radii smaller than the resolution limit of HI4PI and hence are excluded from comparison. This leaves a total number of 173 objects to compare. The result is that the H I shell catalog of this work overlaps with 20 of these objects of Green (2019). At least mixing of different evolutionary phases occurring at the same time at different locations of a SNR (Dubner & Giacani 2015) is supported by these overlaps. To determine if they are physically connected and to draw conclusions regarding the physical processes is up to additional research that is out of the scope of this work.

5.2.2 Examples of new H I shells in the catalog

Examples of newly identified H I shells of the catalog are presented and discussed here. The shells are visualized in figures 5.6 and 5.7 or in the appendix. Each figure contains sub-plots in l and b along the velocities where the respective H I shell is present. The plots have been generated automatically[5] and the maximum brightness temperature, shown in the colorbar, depends on the maximum value in the respective velocity channel for each subplot[6] In each subplot, either the mean radius or the minimum-, mean- and maximum angular radii of the shell are plotted in red.

Catalog shell DK_1286 The shell DK_1286 has rank 5 in the catalog and hence a high quality value of $Q_f = 3.97$. The shell is located at $l_0 = 325.83^\circ$, $b_0 = -8.25^\circ$ and $v_0 = -21.8$ km/s. It has a mean angular radius of $r_0 = 7.1^\circ$ and a minimum velocity range of -33.4 km/s to -8.9 km/s. The shell is presented in figure 5.6, which consists of 20 sub-plots. r_{mean} of the shell is marked by the red ring. The brightness temperature is dominated by the Galactic plane emission that can be seen in the top of the respective subplot. The general brightness temperature increases with increasing velocity channels. At lower velocities, due to the colorbar scaling, the shell is barely visible. This example highlights why visual searches can easily lead to misclassification of objects and requires constant adjusting of the colorbar ranges (sec. 4.6.3). The algorithms are not deceived by these visual effects and work independent of such visualization scalings and hence can detect the corresponding features. However, filamentary structures of the south side of the H I shell are visual along the red circle. The expected caps predicted for an idealized expanding shell model (sec. 3.4.1) for this object are also detected. The caps, identified as intensity maxima (see peak detection sec. 4.6.3) at the center coordinate spectrum along velocity channels through the shell are present near highest and lowest velocity channels where the shell is present (see figure B.0.23). In this plot also the differences of the highest intensities of low velocities vs. the ones at high velocities can be seen. This indicates the inhomogeneities of the ISM in this region as is also visible in figure 5.6.

[5] For each member of the catalog for efficient visual investigation of section 4.6.3

[6] This is why in some channel maps, the colorbar range is not optimized. This is kept on purpose to highlight how, in some cases, visual identification of the shell is difficult, while the algorithm is still able to detect the pattern.

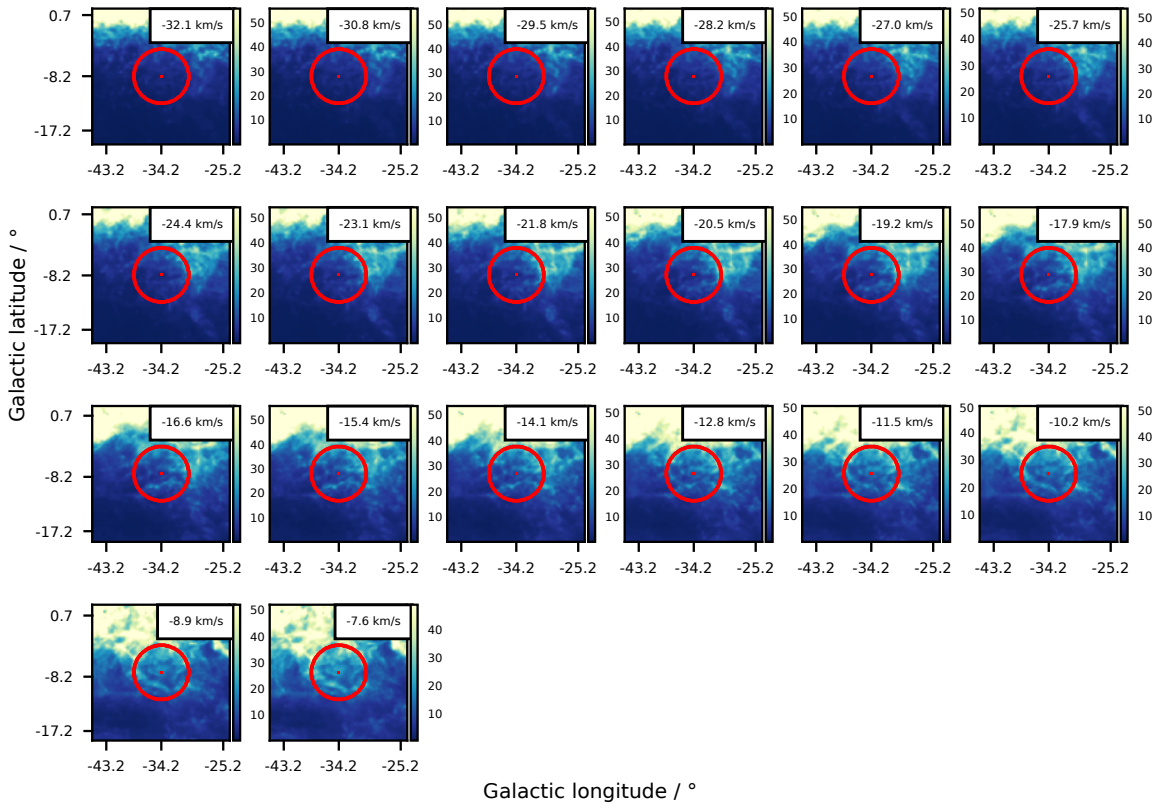

Figure 5.6: Plots of the shell DK_1286 for each channel, where it is present on top of the H I data of the HI4PI survey for this region. The red circle in each plot mark the maximum radius of the shell.

Catalog shell DK_102 The H I shell, DK_102 has a quality value of $Q_f = 2.67$ and is ranked at position 284 in the catalog. It was chosen for presentation, since it is special due to its high negative center velocity $v_0 = -148$ km/s and due to its presence in a very low intensity region of $0.02 - 0.2$ K km/s, which is at the limit of the HI4PI resolution of 0.043 K km/s as shown in figure 5.7. This value of v_0 is by far higher than the maximum value near 100 km/s, listed in other H I shell catalogs that were compared above. With center coordinates of $l_0 = 135.91^\circ$ and $b_0 = -21.25^\circ$ and including that local objects typically have velocity variations of just $\|v_{\text{rad}}\| \approx 10$ km/s, it is also far away from the Galactic plane, where generally star formation takes place for higher distances (McGehee 2008) and a SNR-progenitor is not expected. Since visually, and from the analysis steps of section 4.6.3, the object seems to be indeed an expanding shell, it is investigated if it could stem from another source than stellar feedback. For this, the data of the identified high velocity clouds of (Westmeier 2018) are used. In figure B.0.28, the comparison is visualized and it is found that a high-velocity cloud marked by a red circle in the figure, is present at this exact location. The circular structure might be a result of the impact of the high-velocity cloud on the ISM of the Milky Way. At least further investigations are needed to determine which processes lead to the observed structure. Similar objects of this type are the catalog shells DK_5563, DK_b_102, DK_b_225, DK_5585, DK_b_278, DK_b_80 and DK_b_142.

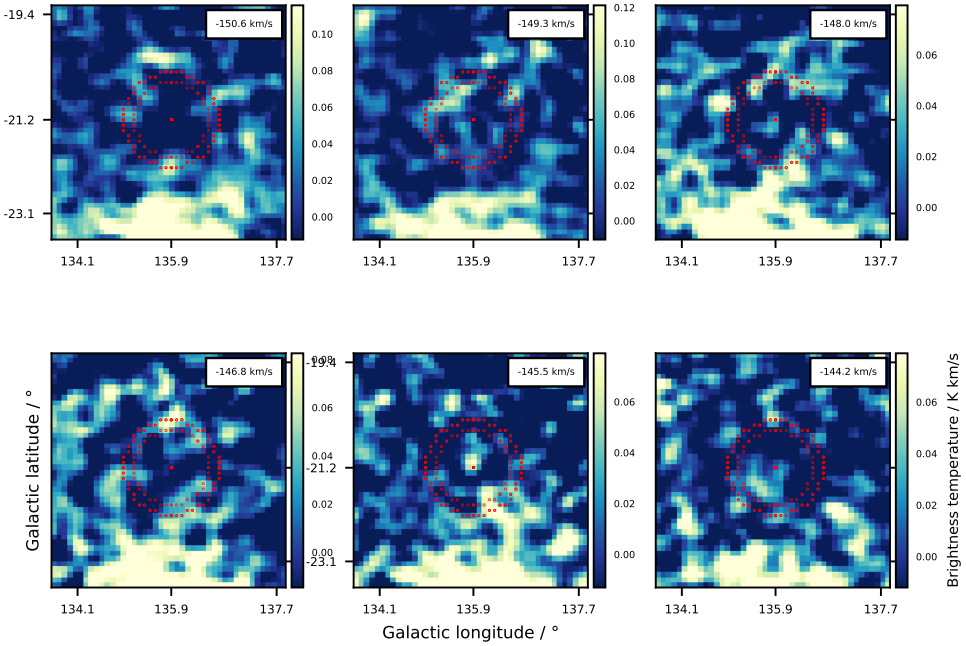

Figure 5.7: Plots of the shell DK_102 for each channel, where it is present on top of the H I data of the HI4PI survey for this region. The red circles in each plot mark the minimum-, mean- and maximum radius of the shell R_{min}, R_0 and R_{max}, respectively.

5.3 Spatial distribution and physical shell properties

The determination of distances of the 802 shells of the catalog (tab. 5.1) is mandatory to determine their physical properties. For a subset of shells, the distance can be determined using the kinematic distance estimation that is based on the tangential point method from section 3.5.1. This can be done if the following criteria are fulfilled. It is applicable to regions where the rotation curve is flat, i.e. for distances of the object from the Galactic center of 5 kpc $\leq R_{\mathrm{gc},i} \leq$ 27.5 kpc (Kalberla & Kerp 2009; Kalberla, P. M. W. et al. 2007; Levine et al. 2008; Fich et al. 1989). For these regions, the idealized rotation velocity around the Galactic center of 220 km/s can be used to solve equation 3.12. In the direction of the inner Galaxy, where the method has two solutions, the results of the distance estimations have high uncertainties up to 50% as discussed below. This is why the shells of the inner Galaxy have been excluded in the analyses of spatial distribution in other studies (e.g Ehlerová & Palouš (2005) and Ehlerová & Palouš (2013)) but are discussed here separately by dividing the shells into two segments:

$$\begin{aligned} \text{Seg 1} &= 90^\circ \leq l \leq 170^\circ \,\&\, 190^\circ \leq l \leq 270^\circ \\ \text{Seg 2} &= 10^\circ \leq l < \ 90^\circ \,\&\, 270^\circ < l \leq 360^\circ \end{aligned} \tag{5.1}$$

where l is the longitude (see fig B.0.30 for a schematic visualization). The two segments are chosen so that regions of longitudes, l_i, in the direction of the Galactic center with $350^\circ \leq l_i$ or $l_i \leq 10^\circ$ and the Galactic anticenter ($170^\circ \leq l_i \leq 190^\circ$), where the general rotation vector of objects is similar to the one of the Sun and comparable to local velocity variations (see e.g. Brand & Blitz (1993), Ehlerová & Palouš (2013)), are avoided. For the same reason the distances are only calculated for all shells with radial velocities in the range of $|v_0| \geq 10$ km/s. The tangential point method and mainly equation 3.12 is applied to the shells in the two segments, leading to a total number of 545 out of the 802 shells where a distance calculation is possible[7].

Table 5.3 contains the physical parameters (excerpt of table A.0.20) and table 5.4 (excerpt of table A.0.22) contains the respective uncertainties. The name of the shell is listed in column 1 of table 5.3. The resulting Distance solutions of the shells from the Sun, $D_{\mathrm{s,a}}$ and $D_{\mathrm{s,b}}$, are listed in columns 2 and 3. The final distance that is derived from these solutions is listed in column 4. The calculated distance of the shell from the Galactic plane (z) and the distance of the shell from the Galactic center D_{gc} are listed in the columns 5 and 6 respectively. The minimum- and maximum physical radii R_{min}, R_{max} are listed in column 7 and 8 in units of kpc. The age of each shell is listed in columns 9. The hydrogen mass $M_{\mathrm{H\,I}}$ and the total mass M_{tot}, derived by equation 3.23 from $M_{\mathrm{H\,I}}$ are listed in columns 10 and 11 respectively. The kinetic energy E_{kin}, derived using M_{tot}, is listed in column 12. For each physical shell parameter, the uncertainties, listed in table 5.4, have been derived, using Gaussian error propagation of the uncertainties from table 5.2 if not explicitly stated differently.

[7] It is accounted for the statistics of the remaining 257 shells, where no distance calculation is possible in section 5.4

1	2	3	4	5	6	7	8	9	10	11	12
Name	$D_{s,a}$	$D_{s,b}$	D_{sun}	z	D_{gc}	R_{min}	R_{max}	τ	$M_{H\,I}$	M_{tot}	E_{kin}
Unit:	kpc	kpc	kpc	kpc	kpc	kpc	kpc	10^6yr	$M_\odot$	$M_\odot$	ergs
DK_1476	2.9	20.75	2.9	1.37	11.03	0.58	1.01	7.89	1.31E+06	1.77E+06	8.67E+49
DK_2046	3.54	14.92	3.54	0.46	11.15	0.29	0.61	1.18	2.13E+06	2.88E+06	4.26E+51
DK_1303	9.82	1.49	9.82	1.39	7.59	1.12	1.55	3	1.59E+07	2.14E+07	3.17E+52
DK_1286	12.44	1.62	1.62	0.24	7.21	0.15	0.29	0.6	4.50E+05	6.07E+05	7.42E+50
DK_1188	7.04	1.82	7.04	0.5	7.71	0.43	0.77	1.99	4.66E+06	6.29E+06	4.92E+51
DK_1187	7.01	1.83	7.01	0.49	7.71	0.43	0.8	1.85	5.16E+06	6.97E+06	6.90E+51
DK_1119	10.28	2.05	2.05	0.15	7.15	0.11	0.16	0.94	2.38E+05	3.21E+05	3.53E+49
DK_857	11.33	1.24	1.24	0.1	7.63	0.1	0.21	0.48	2.27E+05	3.06E+05	3.03E+50
DK_810	11.5	1.06	1.06	0.15	7.75	0.14	0.19	0.48	2.12E+05	2.86E+05	2.24E+50
DK_3462	8.2	1.42	8.2	0.77	7.78	0.54	1.01	2.92	6.15E+06	8.31E+06	4.98E+51

Table 5.3: Physical parameters of 682 objects of the shell catalog of table 5.1. These are the remaining shells where a kinematic distance estimation is applicable. This table is an excerpt of the first 10 rows of table A.0.20 that can be found in the appendix. Column 1 contains the name of the shell, column 2 and 3 contain the two distance solutions of the tangential point method $D_{s,a}$ and $D_{s,b}$. Column 4 lists the derived final value for the distance, which is either one of the values of $D_{s,a}$ or $D_{s,b}$ or their mean value, depending on the observed direction. Columns 5 and 6 list the z-distance of the object to the Galactic plane z, and the distance of the shell towards the Galactic center D_{gc}, both also derived by this method. The calculated minimum- and maximum radius R_{min} and R_{max}, using $D_{s,a}$ or $D_{s,b}$ are listed in columns 7 and 8. Columns 9, 10 and 11 contain the calculated age τ, the hydrogen mass $M_{H\,I}$ and the total mass M_{tot} of the shell. Finally, column 12 contains the derived kinetic energy E_{kin} of the shells. For more information about the derivation of the parameters see text.

1	2	3	4	5	6	7	8	9	10	11	12
Name	$\Delta D_{s,a}$	$\Delta D_{s,b}$	ΔD_{sun}	Δz	ΔD_{gc}	ΔR_{min}	ΔR_{max}	$\Delta\tau$	ΔM_{own}	ΔM_{tot}	ΔE_{kin}
unit:	kpc	kpc	kpc	kpc	kpc	kpc	kpc	10^7yr	$M_\odot$	$M_\odot$	ergs
DK_1476	1.53	1.53	1.53	0.65	1.26	0.31	0.41	3.51	4.70E+05	5.88E+05	7.57E+49
DK_1476	1.16	1.16	1.16	0.5	0.91	0.24	0.41	3.51	4.70E+05	5.87E+05	7.57E+49
DK_2046	1.12	1.12	1.12	0.14	0.87	0.1	0.24	0.51	8.66E+05	1.08E+06	2.75E+51
DK_1303	1.51	1.51	1.51	0.21	0.58	0.17	0.62	1.38	2.83E+06	3.53E+06	2.26E+52
DK_1286	1.16	1.16	1.16	0.17	0.56	0.11	0.11	0.27	1.58E+05	1.97E+05	4.86E+50
DK_1188	2.38	2.38	2.38	0.17	0.58	0.15	0.31	0.91	2.00E+06	2.51E+06	4.00E+51
DK_1187	2.4	2.4	2.4	0.17	0.58	0.15	0.32	0.85	2.17E+06	2.71E+06	5.57E+51
DK_1119	1.43	1.43	1.43	0.1	0.53	0.08	0.06	0.42	6.23E+04	7.78E+04	2.60E+49
DK_857	1.27	1.27	1.27	0.11	0.58	0.11	0.08	0.22	4.04E+04	5.05E+04	2.16E+50
DK_810	1.25	1.25	1.25	0.18	0.59	0.16	0.08	0.22	4.81E+04	6.02E+04	1.63E+50
DK_3462	1.86	1.86	1.86	0.17	0.59	0.13	0.4	1.33	2.46E+06	3.08E+06	3.97E+51

Table 5.4: This table is an excerpt of table A.0.22 from the appendix. It contains the uncertainties of the values of table 5.3. Columns 1 contains the name of the shell. Columns 2 and 3 contain the uncertainties of the possible two distance solutions of the tangential point method calculation $\Delta D_{s,a}$ and $\Delta D_{s,b}$ respectively. Column 4 contains the uncertainties of the derived final distance towards the Sun. Columns 5 and 6 contain the uncertainties of the z-height of the shell to the Galactic plane, Δz, and the distance towards the Galactic center ΔD_{gc}, respectively. The uncertainties of the minimum- and maximum radius ΔR_{min} and ΔR_{max} can be found in columns 7 and 8. Column 9 contains the uncertainty of the age of the shell, $\Delta\tau$, while columns 10 and 11 list the uncertainty of the H I mass $\Delta M_{H\,I}$ and the ones of the total mass ΔM_{tot} respectively. Column 12 contains the derived kinetic energy of the shell ΔE_{kin}. For more information see text.

5.3.1 Distribution of shells in the solar neighborhood

Here, the positions and distributions of the catalog shells in the Galactic plane, their vertical distances from the Galactic plane as well as their physical sizes and velocities are presented and discussed.

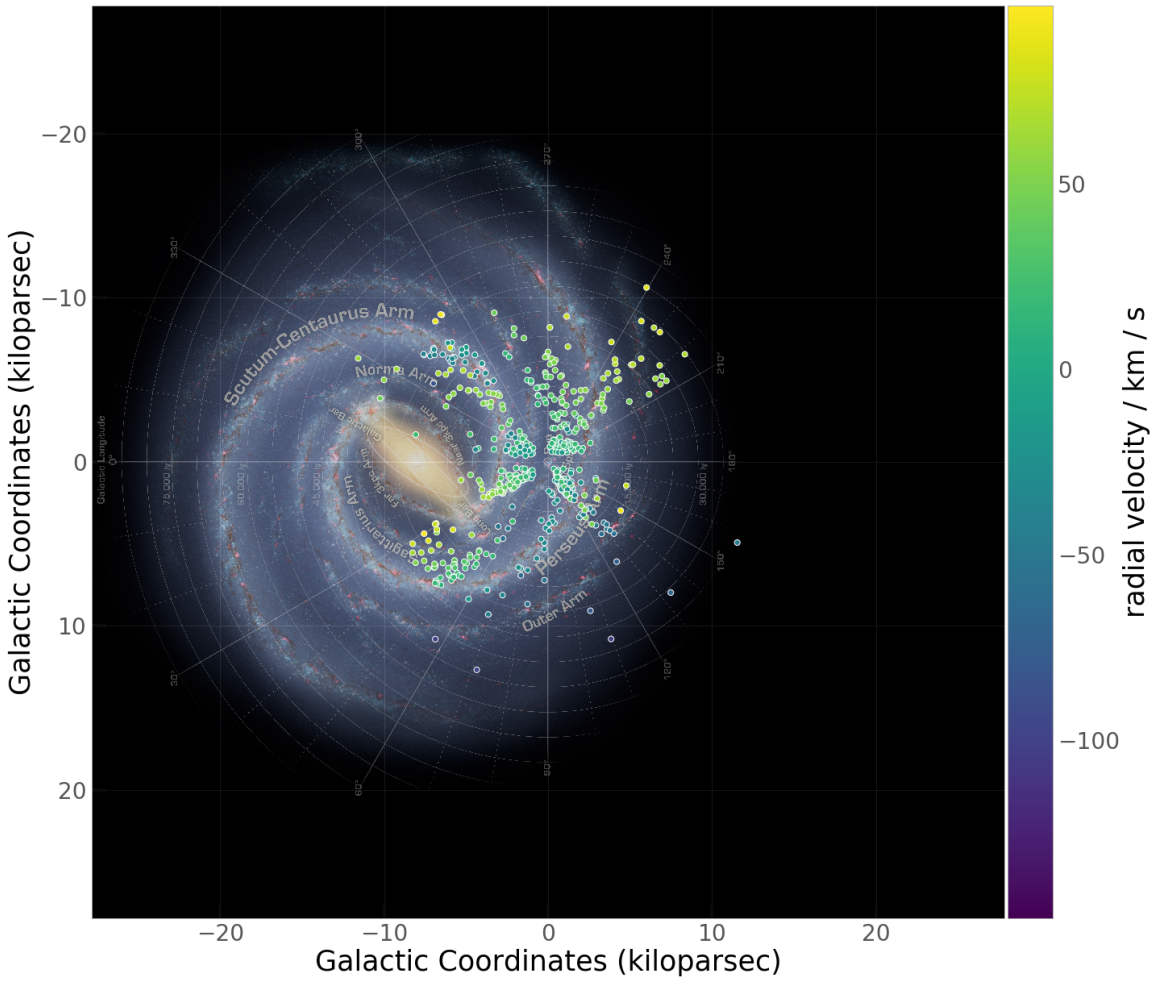

Figure 5.8: Plot in the galactocentric projection, showing the distribution of the shells in the Galactic plane. Each shell is color-coded by its radial velocity in respect to the Sun. The background image contains the Galactic center and the spiral arms to provide a high level comparison of the positions of the objects relative to the Galactic spiral arms. The location of the Sun lies at the center coordinates (0,0) kpc of the plot. A variation of this plot, containing the color coded size of the shells instead of the radial velocity, can be found in figure B.0.25 in the appendix. Background figure credits https://pypi.org/project/mw-plot (status 01.12.2020).

Distribution of shells in the Galactic plane

With the calculated distances of the shells from the Sun, $D_{\mathrm{a},i}$ or $D_{\mathrm{b},i}$ (tab. 5.3), as well as $l_{0,i}$ and $b_{0,i}$, $i \in \{1, .., 545\}$, the positions of the shells in the Galactic plane are presented in figure 5.8. The figure is superimposed onto a background of the spiral arms and the Galactic center. The position of the Sun lies at the center of the coordinate system. The shells are marked by filled circles and color coded by their respective mean radial velocity $v_{0,i}$. The excluded regions, where no distance calculation was possible can be seen e.g. by empty regions into the direction of the Galactic center and anti center in a range of $0^\circ \pm 10^\circ$. Also, the criterion that $v_{\mathrm{rad}} \geq 10\,\mathrm{km/s}$ leads to the absence of local shells around the Sun ($D_{\mathrm{a/b}} < 0.5\,\mathrm{kpc}$). The largest fraction of the shells are located at distances below 5 kpc. The same plot, but with the color coded sizes (R_{max}) of the shells instead of v_{rad} is presented in fig. B.0.25 to visualize the following presented properties. The knowledge about the spiral arm structures (sec. 2.2.2) is used for the discussion.

Shells below 2 kpc distance Shells at distances of below 2 kpc have mixed mean radial velocities. But a general trend is that shells behind the Sun on the circular orbit in respect to the rotation direction, have mainly positive radial velocities, v_0, and the ones in front of the Sun are seemingly approaching, i.e. having negative values of v_0 as expected due to the rotation on a circular orbit around the Galactic center. For example close shells in the fourth Galactic quadrant ($l = -270^\circ$ to 0°) are approaching, while shells in the first quadrant ($l = 0^\circ$ to 90°) are mainly moving away from the Sun. The density of shells, in general, is highest close to the Sun. This is a mixture of the Sun being part of the Orion arm and an observational bias, than a measure of the real distribution as further discussed below.

Shells in the region of the Scutum-Centaurus Arm In the fourth Galactic quadrant (fig. 5.8, clusters of shells with v_0 below -50 km/s (blue dots) coincide with the Scutum-Centaurus Arm ($l = 300 - 330^\circ$) that shares similar radial velocity components at these longitudes. Another group of shells, located closer between the Norma Arm, near and on the Scutum-Centaurus Arm, share positive velocities above 50 km/s (green-yellow dots). Their kinematics suggest that they are not connected to the Scutum-Centaurus Arm. Since these shells belong to Seg. 2 (two solutions for the kinematic distance estimation), it might be that their distances rather should be derived from the second solution of eq. 3.13 for these objects, which is above 14 kpc. In the first quadrant, up to longitudes of $l = 30^\circ$, there are clusters of shells, where especially the ones of high positive v_0 are aligned on the Scutum–Centaurus Arm, matching its radial velocity v_{rad} at that position. These clusters, following the spiral arm structures also explain the peaks at certain longitudes that have been identified in section 5.1, e.g fig. 5.1.

Shells in the inner- and outer segments of the Galaxy Most of the shells in the outer Galaxy (Seg 1), at angles between $90^\circ \leq l < 270^\circ$, are distributed around the Perseus Arm. In the third Galactic quadrant, in the direction of $l = 210^\circ - 240^\circ$, there is a group of shells located near the Outer Arm of the Milky Way and even further. Due to the high distance uncertainties at these distances, it is difficult to state if they follow the Outer Arm or belong to ISM structures apart. However, it can be seen in figure B.0.25 that there are more shells of larger radii (37 shells) detected in the inner Galaxy (Seg 2) compared to the outer Galaxy (6 shells). The highest number of shells larger than 1 kpc (23) and the largest shells (e.g. DK_1685, DK_1778,...) are detected in the Scutum-Centaurus Arm. Additional shells of radius above 1 kpc are detected in the Sagittarius Arm (sec. 2.2.2). This pattern is

expected from the higher number of star clusters that are located in the inner Galaxy compared to the outer Galaxy (Urquhart et al. (2013) fig.6) and hence more shells should be located along the line of sight in directions through the Galactic center.

In the inner Galaxy in Seg. 2, between two spiral arms, in the direction of $l = 270^\circ$ to 300° and the direction of $l = 40^\circ$ to 90°, there are voids, where no shells are detected. This supports the assumption that most of the expanding shells that have been detected are produced and driven by stellar winds and SNe, being the result of massive star formation, which generally takes place in the spiral arms, e.g. Elmegreen (2011). The distance uncertainties are too high to draw concrete conclusions if the shells lie exactly on the spiral arms (section 2.2.2) or lack behind in rotation, which would be explainable due to friction of the gas (e.g. Krause et al. (2015)). The kinematic distance estimations come along with high uncertainties, reaching up to $\Delta D_{\mathrm{s},i} > 2\,\mathrm{kpc}$ for the shells most far away, which propagates to the estimation of the radius and other physical shell properties that is done in section 5.3.2. What can be measured for closer shells and especially for shells of Seg 1 is if they also quantitatively follow the spiral arm densities or are distributed randomly along distances. The distances towards the Perseus Arm in the direction of Seg 1, in the longitude range $l = 180 - 270^\circ$, is in the mean 2 kpc (Xu et al. 2006), with a width that leads to distance ranges of of 1.5-2.2 kpc (Griv et al. 2017). In the same direction at a higher distance of about 6 kpc (Hachisuka et al. 2009) with a rough thickness of 0.25 kpc (Hou & Han 2014) lies the Outer Arm. The density distribution of the shells of Seg 1 is shown in figure 5.9, together with the distances of the Perseus- and the Outer Arm. A high number of shells with the peak at the exact mean distance of the Perseus Arm can be seen. It is suggested that the shells follow the structure of the spiral arms here, while between the arms, less shells are detected. At the distance of the Outer Arm no such peak is visible but at these distances the general number of shells is low and the absolute distance uncertainties are high as mentioned above.

Vertical distance towards the Galactic plane

The vertical distance (z-height) of the shells towards the Galactic plane is presented in figure 5.10 in the plot on the left hand side as a function of the distance of each shell towards the Sun $d_{\mathrm{sun},i}$. Using $\Delta D_{\mathrm{a},i}$ or / and $\Delta D_{\mathrm{s},b}$, $D_{\mathrm{sun},i}$ is calculated. The values and their uncertainties can be found in table 5.3 and 5.4 respectively. 90% of all shells have heights of $|z| \leq 1.07\,\mathrm{kpc}$ and 70% of all shells have $|z| \leq 0.50\,\mathrm{kpc}$. The highest position is at $z = 2.3 \pm 0.78\,\mathrm{kpc}$. As also visible in the Galactic plane view (fig. 5.8), the density of detected shells decreases with distance to the Sun. This is observed for both segments. It can also be seen that the general distribution of z-heights is getting broader with increasing distance towards the Sun. This reflects the increasing probability to detect shells more far away from the Galactic plane, when increasing the amount of spatial volume that is investigated. But additionally, Δz is increasing with increasing d_{sun}, which potentially could lead to partly higher vertical distances of the shells. While most of the shells of both segments up to 4 kpc distance share $z < 0.5\,\mathrm{kpc}$, there are some groups of outliers, at highest vertical distances while still being located relatively close to the Sun. Since these shells seem to be outliers of the general distribution, they will receive some additional attention in the analysis below. On the right hand side of the figure, the same plot is shown as on the left hand side but with the addition of the uncertainties $\Delta D_{\mathrm{sun},i}$ (horizontal errorbars) and Δz (vertical errorbars). The mean relative uncertainty of $\Delta D_{\mathrm{sun},i}$ is 54% and is the result of the kinematic distance estimation (eq. 3.12, eq. 3.13 and 3.16). Δz increases with increasing absolute z-height due to an increase of the uncertainties of the kinematic distance estimates. One reason is because the difference in rotation speed is higher for higher latitude objects (Kalberla &

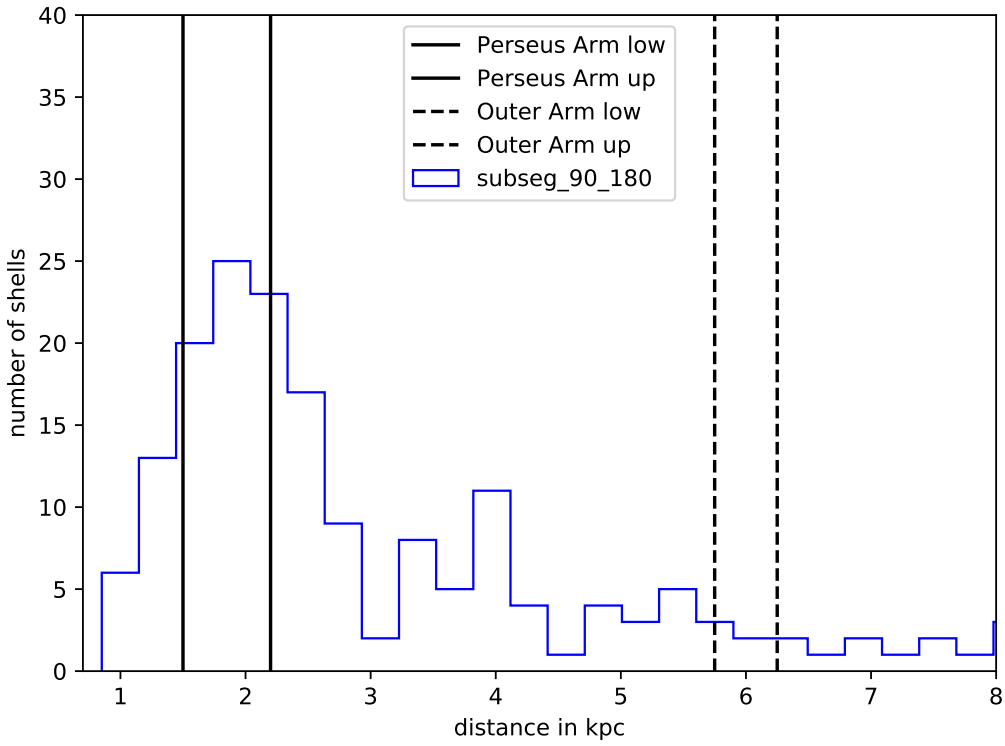

Figure 5.9: Distance distribution of shells of Seg 1 of the catalog of this work in the direction of spiral arms compared to the distances of the Perseus Arm, marked by the black-solid lines (distance limits from Griv et al. (2017)) and the Outer Arm markes by the black-dashed lines (distance from Hachisuka et al. (2009) and thickness from Hou & Han (2014).

Kerp 2009). The other reason is that the maximum absolute $z-$height is increasing with increasing distance towards the Sun and so do the uncertainties in $z-$direction (fig 5.10). At least for $z-$heights between 0.1–0.7 kpc the uncertainties increase linearly between 0.04–0.21 kpc.

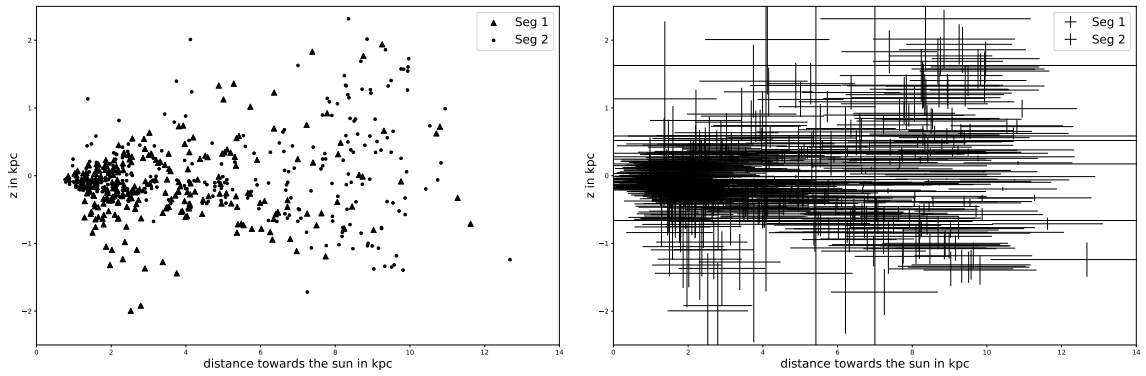

Figure 5.10: Vertical distances, z_i, of the shells i from the Galactic plane are plotted against the distances from the Sun $D_{\mathrm{sun},i}$. In the left panel and the right hand panel, the same shells are plotted. But in the right hand panel, the error bars are shown additionally. The shells of Seg 1 are marked by black filled triangles, while the ones of Seg 2 are marked by black filled circles. For an introduction of the two segments see relation 5.1 and for a discussion of the plots see in sec 5.3.1.

5.3.2 Derivation of physical shell properties

Sizes of the shells

In figure 5.11, the physical radius $R_{\mathrm{max},i}$, $i \in \{1, ..., 545\}$ of each H I shell is plotted as a function of its distance towards the Sun, $D_{\mathrm{sun},i}$. The physical radius is calculated by using the relation $R_{\mathrm{max},i} = D_{\mathrm{sun},i} \cdot \tan(r_{\mathrm{max},i})$. 91% of the shells have radii below 1 kpc and out of these, 79% share radii below 0.5 kpc, which is visualized by the distribution in the right panel of figure 5.11. Shells with $R_{\mathrm{s},i} \geq 1$ kpc start to appear at $D_{\mathrm{sun},i} \geq 3$ kpc, mostly for Seg 2 (39 shells) but also some from Seg 1 (10 shells). In general, with increasing distance in respect to the Sun, shells of increasing size are detected. This is expected from the point of view that, the larger the observed volume, the higher the statistics and rare parts of a distribution, which are the largest shells, are more likely to appear. On the other hand, apart from variations e.g. due to spiral arm structures, smaller shells per distance interval should dominate and even increase because the observed volume per distance interval increases. This is also what is observed up to distances of $D_{\mathrm{sun}} = 4$ kpc, where the majority of detected H I shells have radii <0.5 kpc. But for higher D_{sun}, the absolute number of smaller shells is lower. This can be shown by the distance intervals. In the interval (0–2 kpc), the relative amount of shells of $R_{\mathrm{max}} < 0.2$ kpc is 50%, for 2–4 kpc it is just 30%, for 4–6 kpc it is 13% and for 6–8 kpc it is 0%. This is also the case for all other known studies that contain spatial information about their shells (e.g. Ehlerová & Palouš (2013); Suad et al. (2014)). This is an observation bias and is visualized as the black-dotted line in figure 5.11 that shows how large the radius of a shell has to be with increasing distance to maintain a measured angular radius of 1° (ang_size_1deg) and the black-dashed line (ang_size_10deg) represents a shell with an angular radius of 10°. A typical shell of radius $R_{\mathrm{s}} = 50$ pc at a distance of 10 kpc would have an angular radius of 0.29°, which is comparable to the resolution of 0.22° of the HI4PI survey and cannot be detected as an expanding shell. Even for shells of angular radius close to 5°, its cavities would not be resolved in most cases to detect inner edges of the H I shell (sec. 3.4.1 and sec. 4.1.2) at these distances. This is why at high distances less shells of smaller radius are detected.

For Seg 1, 9 shells of $R_{\mathrm{max},i} \approx 1$ kpc and one shell with a value larger than 1.4 kpc are present.

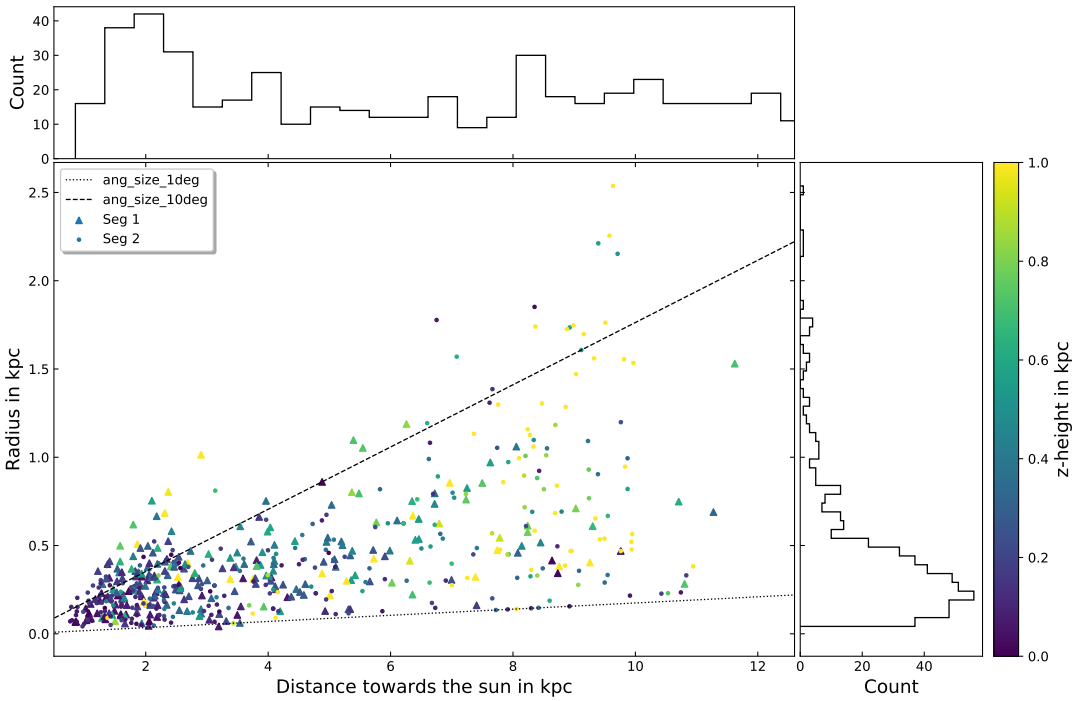

Figure 5.11: The physical size of the shells of table 5.3 is plotted against the distance of the center of the shell towards the Sun in the main panel. Along each axis a sub-plot, containing histograms of the distributions of shells along the respective axis, is shown. The markers are color coded by the vertical distance from the Galactic plane, $|z|$, of the respective shell. The colorbar is clipped at 1 kpc. For a discussion about the sizes of the shells, see text in sec. 5.3.2. The black dashed- and the black dotted line represent shell radii that shells of 10° and 1° angular radius would have at different distances between 0 and 12 kpc.

These shells all share a negative latitude of at least $b = -20^\circ$ with high uncertainties due to the above discussed reasons for high $z-$heights. Shells of these sizes have not previously been reported. But the compared catalogs of Ehlerová & Palouš (2005), Ehlerová & Palouš (2013) disregarded the largest shells for their analysis and the radius was effectively corrected to not exceed 1 kpc as stated in there. The focus of these studies was on the outer Galaxy only, where less larger shells are expected as discussed above. In external galaxies, multiple shells of radii larger than 1 kpc are detected where the largest ones there have radii up to 1.3 kpc (Bagetakos et al. 2010). The face-on view on the galaxies allows it only to measure the spread in the galactic plane– the direction where the density of the ISM is the highest, and possibly some shells might even be larger. This means that the maximum radius in this study is not an upper limit (Bagetakos et al. 2010) and larger radii would be expected in the vertical direction compared to the plane.

For different smaller external spiral galaxies (sec. 2.4.3), it is observed that the maximum radius is capped and it was interpreted that this is due to shearing at smaller galactic radii (Bagetakos et al. 2010). But this would be relevant only for shells that are closer than 3 kpc (Bagetakos et al. 2010) from the Galactic center (GC). Apart from one exception, the distance of all shells towards the GC is higher than that.

For the inner Galaxy in seg 2, where the distance uncertainties are higher and most large shells are detected, some even larger shells are detected. The largest one has a radius of 2.5 kpc. To produce shells of these sizes, more energetic events than single supernovae are needed. The impact of high-velocity clouds could be the source, which could be an explanation, especially at high $z-$heights (section 2.4.3). The observation of shells with radii above 1 kpc at least agree with numerical simulations and theoretical models that predict larger shells than commonly observed (section 2.4.2). While the relative number of shells, larger than $R_{max} \geq 1$ kpc, is low compared to the one for smaller sizes, they have the highest impact on the calculations of the total energies and volume statistics of shells or possible number of supernovae to produce the shells. Shells of radii of kpc-scale cover a noticeable area of the Galactic volume and hence the mass determination, the age determination as well as the derivations of the physical properties are affected. For the following calculations of the ages, masses and kinetic energies, all shells of both, Seg 1 and Seg 2 are considered, while evaluating them separately.

Ages of the shells

The upper limit for the age, τ, of the shells can be derived from assumed dynamics using the calculated maximum radius, R_{max}, of the shell and the expansion velocities $v_{exp,i}$ that can be estimated by the velocity range of the shell $\left|v_{min,i} - v_{max,i}\right|$ (table 5.1). $v_{exp,i}$ is then estimated to be half the velocity range. The uncertainties $\Delta v_{exp,i}$ and $\Delta R_{max,i}$ are listed in table 5.2. They have been calculated using the position of the maximum angular radius $r_{max,i}$ and the lowest values are limited by the uncertainties of the velocity resolution (section 4.6.4). The upper limit for τ, has then been calculated using eq 2.19 and is listed in column 9 of table 5.3. For shells in the radiative phase, which is plausible for all objects here, a value of $c = 0.35$ (Koo et al. 2020) in eq. 5.3 has been used. This age estimation, is an upper limit since $R_{max,i}$ and the determined $v_{exp,i}$ of the shells themselves are upper limits (section 5.2.1). The uncertainties, $\Delta\tau_i$, of the age, determined using error propagation are listed in column 9 of table 5.4. In figure 5.12, the radius of each shell is plotted against its age, color coded by v_{exp}. Since τ_i is a linear function of $v_{exp,i}$ and $R_{max,i}$ and since different values of v_{exp} are discrete and due to the spectral binning in datacubes, the distribution of the shells appears to fall on lines. Each line represents one measured value of v_{exp} as can be seen in the circle-colors for each line. 26% of the shells have ages $\tau \leq 10$ Myr and 61.5% have $\tau < 20$ Myr but there are also 1.2% of the shells with $\tau \geq 100$ Myr, where one shell even reaches an ages of 128 Myr (shell of Seg 1 near $R_{max} = 1$ kpc in fig. 5.12). The mean relative uncertainty, $\Delta\tau$, for all shells (table 5.4) is 44%. Shells of higher angular radius have lower expansion velocities, plausibly because they are in the latest stages of their evolution. But larger shells are not always older. This can be understood as follows. To produce supershells, multiple massive stars are needed. Since massive stars form in clusters and their lifetime is short, the energy input happens in short intervals and hence the shell grows substantially in a short amount of time (sec. 2.3.1 and sec. 2.3.2). Using eq. 2.20 for a single supernova explosion, the size of the shell at 1 Myr would be 350 pc and for 5 SNe it would be 483 pc at the same age. The theoretical age per fixed radius for different initial densities n_0 and number of SNe, n_{sn}, are also plotted into figure 5.12. The two extreme cases of $n_0 = 1000$ and $n_{sn} = 1$ (dashed-line) and $n_0 = 0.1$ and $n_{sn} = 10$ embed all observed H I shells in the plot and highlight the theoretical high impact of the initial conditions for the expansion of the shells. In numerical simulations, it is suggested that the shell velocity spikes due to the input momentum from different SNe inside a bubble in a case between 3-10 Myr (Krause & Diehl 2014) and hence creates variations in the observed expansion velocity for similar sized shells.

If comparing Seg 1 (filled triangles) and Seg 2 (filled dots) in figure 5.12, it can be seen that the majority of shells with ages higher than 20 Myr belong to Seg 2 (filled circles) but the oldest objects belong to Seg 1. Values of above 120 Myrs are still plausible since in external, similar hubble type galaxies, supershells of even higher ages and up to 150 Myr are observed (Bagetakos et al. 2010). But a high fraction of the higher age shells (>50 Myr) is due to clusters of shells at high latitudes, where the kinematic distance estimation and hence the radius of the shell can be overestimated and values have high uncertainties, which results again in high uncertainties of the age estimations for these shells.

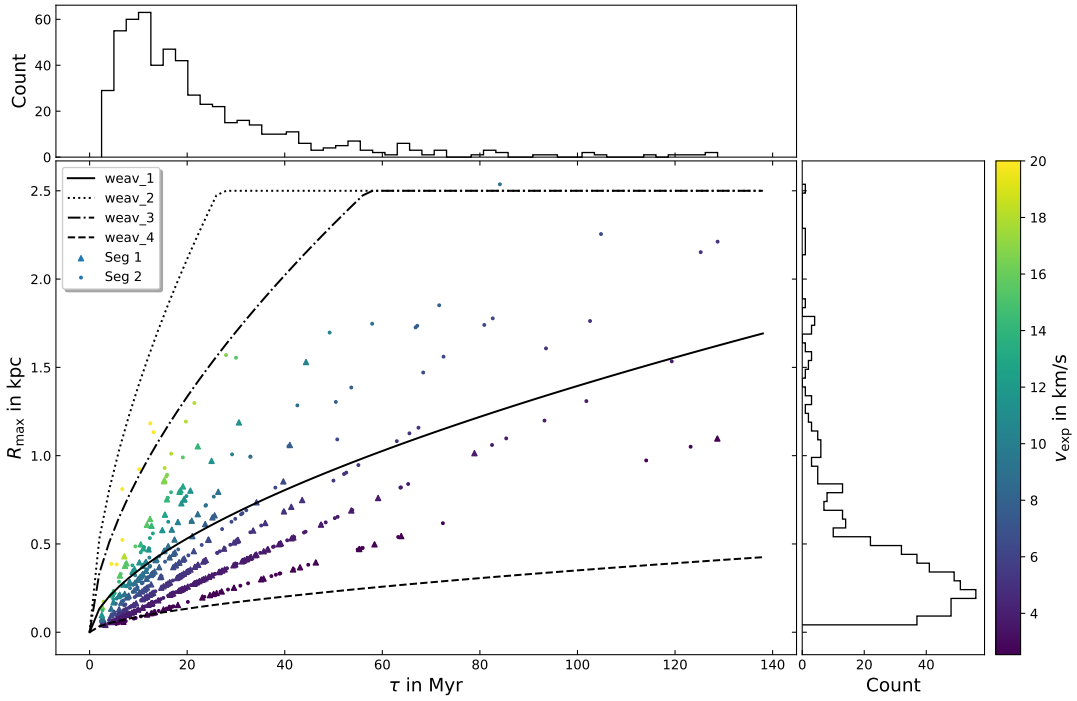

Figure 5.12: The radii of the H I shells of table 5.3 are plotted against their calculated ages, τ, with color coded expansion velocity of each shell $v_{\mathrm{exp},i}$ in the main panel. Shells of Seg 1 are marked by filled dots and shells of Seg 2 are marked by filled triangles. Introduction of Seg 1 and Seg 2 in relation 5.1. The top panel shows the distribution of the ages of the shells, while the vertical distribution of the radii is shown in the right panel. The normal-, dotted, dotted-dashed and dashed lines represent the theoretical radius relation for different ages, initial densities n_0 (0.1, 0.1, 10, 1000) and number of supernovae n_{sn} (1,10,1,1) using eq. 2.20 respectively. For a discussion about the pattern and structures see text.

Masses of the shells

With calculated distances, the derived minimum- and maximum radii, $R_{\mathrm{min},i}$ and $R_{\mathrm{max},i}$, are fixed and the H I masses, $M_{\mathrm{H\,I},i}$ with $i \in \{1, 2, ..., 545\}$, of the shells can be calculated using equation 3.20. The H I-mass is calculated for the rings between r_{min} and r_{max} plus the thickness Δr of the shell, which is

estimated to be $20\%^{+30\%}_{-10\%}$ (section 2.4.2)[8]. The resulting masses are listed in table 5.3 in column 10 and their respective uncertainties $\Delta M_{\mathrm{H\,I}}$, derived by error propagation from $\Delta r_{\mathrm{min,i}}$, $\Delta r_{\mathrm{max,i}}$ and Δv_{exp} and $D_{\mathrm{s},i}$ (table 5.4 in column 10).

The shell masses are shown in figure 5.13, where its dependence on R_{max} is plotted and b_0 of each shell is color coded. The dashed line marks the theoretical mass for shells with a mean density of 1 H I atom per cm^3 for different values of R_{max} for idealized spherical complete shells. Figure B.0.27 in the appendix shows $M_{\mathrm{H\,I}}$ against the velocity range ($2 \cdot v_{\mathrm{exp}}$). The masses of the shell range from $1 - 10^7\,\mathrm{M}_\odot$. The lowest mass members appear in Seg 1, while the vast majority of most massive shells are located in Seg 2. Shells of higher latitude (yellow) tend to have lower mass ($M_{\mathrm{H\,I}}$) at similar radii compared to shells in the Galactic plane (blue-violet). This is expected from the exponential density gradient of the ISM. The highest impact on $M_{\mathrm{H\,I}}$ has the velocity range $2 \cdot v_{\mathrm{exp}}$. While the mass magnitude range from above is covered by shells of $v_{\mathrm{exp}} \leq 8\,\mathrm{km/s}$, the vast majority of shells have H I masses above $10^4\,\mathrm{M}_\odot$ (fig. B.0.27) similar to what is observed in other works for H I shells (Ehlerová & Palouš 2013; Poeppel et al. 2010).

The mean uncertainties of the H I mass are $\Delta\overline{M_{\mathrm{H\,I}}} = 34\%$, which results from the uncertainties in the kinematic distance estimation as well as $\Delta R_{\mathrm{min,i}}$, $\Delta R_{\mathrm{max,i}}$ and $\Delta v_{\mathrm{exp},i}$. Systematic uncertainties that are not reflected in the mass uncertainty calculation that should especially affect the largest shells in the catalog are the derivation from a circle-like shape and the background intensity that should have a significant contribution to the total emission in H I. The uncertainties from the circular approximation is in the mean for all shells about 16%[9]. The thickness of a shell is an estimated parameter, which contains high uncertainties in observation because generally thickness variations of 20%–50% occur as mentioned above and in section 2.4.2.

The mass distribution found in this work is similar to the one of other similar hubble type galaxies listed in Bagetakos et al. (2010). Some very high mass objects, more massive than observed so far, are present above $10^7\,\mathrm{M}_\odot$. Comparing masses of Seg 1 to the ones of external galaxies, the values agree, while other surveys in the MW tend to find mean masses of $10^4\,\mathrm{M}_\odot$ (Ehlerová & Palouš 2013) but larger shells were not included or clipped at 1 kpc size in the physical analyses of these works. This might be a reason for their lower maximum mass values. In external galaxies, the most massive shells are found to have masses in the magnitude of $10^6\,\mathrm{M}_\odot$, the most massive shells here reach values of one magnitude above. The largest shell ($R_{\mathrm{max},i} \geq 2.5\,\mathrm{kpc}$) of Seg 2 also results in the highest mass of above $10^7\,\mathrm{M}_\odot$, which is a considerable amount of the total hydrogen mass of gas in the MW, which is about $8{\cdot}10^9\,\mathrm{M}_\odot$ (e.g. Goldstein (1972), Kalberla & Kerp (2009)). However, due to the large volume that is covered by these shells in combination with the above-mentioned uncertainty sources, the mass uncertainties for large shells are high. These high masses are also considered an upper limit, because of the variation of the thickness of the shells and that larger shells tend to have a smaller relative thickness compared to smaller shells[10].

The shell mass is not only dependent on the amount of neutral hydrogen atoms, $M_{\mathrm{sh,H\,I}}$, but also depends on the H_2–mass and the He–mass (section 3.5.2). Using equation 3.23, the total mass of each

[8] To achieve this, moment-0 maps are drawn from the regions of the shell in the HI4PI data using the angular size of the shell as well as the velocity range as introduced in equation 3.10 in section 3.3.3.

[9] This is estimated by using 200 elliptical samples from (Ehlerová & Palouš 2013) and calculating the mean uncertainty by estimating them as circles.

[10] A dedicated analysis of each object would be needed to increase the accuracy but is not the focus here. At least the high uncertainties are taken into account in the following calculations.

shell $M_{sh,tot,i}$ is calculated (see table 5.3 column 10). The factor for the H_2 mass should vary between different regions as introduced in section 2.1.1. The best guess is taken from the abundance in the solar neighborhood (Ehlerová & Palouš 2005; Suad et al. 2014). This is also adopted here. Note that the majority of the detected shells are located below 5 kpc distance to the Sun. The uncertainties due to variation of the H_2 abundances are taken into account.

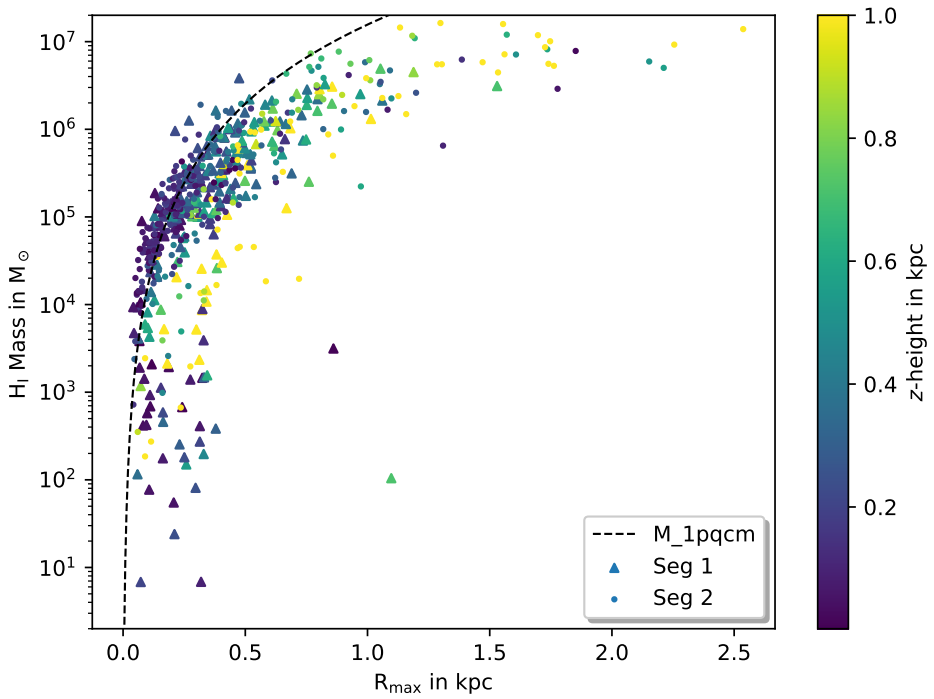

Figure 5.13: The hydrogen shell masses, $M_{\mathrm{H\,I}}$, are plotted against $R_{\mathrm{max},i}$ of the shells. Each shell is color coded with its vertical distance from the Galactic plane (z-height), capped at 1 kpc. Shells of Seg 1 and Seg 2 (see relation 5.1) are marked by filled triangles and filled circles respectively. The dashed line represents the H I mass of shells of different radii with an on-shell H I particle number density of $n = 1 \cdot \mathrm{cm}^{-3}$. For more information see text.

Kinetic shell energies

The kinetic energy of each shell is calculated by $E_{\mathrm{kin},i} = 0.5 M_{\mathrm{tot},i} v^2_{\mathrm{exp},i}$, where $M_{\mathrm{tot},i}$ is the total mass of the i-th shell, as described above, and $v_{\mathrm{exp},i}$ is its expansion velocity that has also been determined above. The resulting values of $E_{\mathrm{kin},i}$ are listed in column 11 of table 5.3 and the uncertainties ΔE_{kin} are listed in column 11 of table 5.4. The mean uncertainty of E_{kin} for all shells is 66%, derived by propagation of $\Delta M_{\mathrm{tot},i}$ and $\Delta v_{\mathrm{exp},i}$.

Visualized in figure 5.14, here $R_{\mathrm{max},i}$ is plotted against $E_{\mathrm{kin},i}$ with the color coded expansion velocity, for each shell i. Values of $E_{\mathrm{kin},i}$ range from 10^{44}–10^{53} ergs (1 erg = 10^{-7} J). A dashed line represents the theoretical kinetic energy of shells with $n_0 = 1$ but of different radii, which hence have different H I masses but a constant expansion velocity of $v_{\mathrm{exp}} = 10$ km/s for an idealized shape of a homogeneous spherical shell.

5% of the shells in the distribution are below 10^{47} ergs. These low values are derived from a combination of low expansion velocities of $v_{\mathrm{exp},i} = 2.56$ km/s and mainly due to small values of M_{tot}. These shells of the catalog of low M_{tot} are at high latitudes, plus they have high absolute values of v_0, where the intensities are near the sensitivity of the survey and even negative values of T_b (section 3.1.1) are present.

Large shells reach kinetic energies in the regime of 10^{53} ergs. For external galaxies, holes in their disk with $E_{\mathrm{kin}} \geq 10^{54}$ ergs are detected commonly (section 2.4.3). Hence objects like these could occur in the MW as well. Clustered massive stars with their supernovae, or the impact of high velocity clouds can produce shells of such radii. And above, in section 5.2.2, it was argued that some objects could plausibly be produced by such a kind of event.

There are differences between the results for Seg 1 and Seg 2 (fig. 5.14). Shells of Seg 1 are limited to $E_{\mathrm{kin}} \leq 10^{52}$ ergs, while multiple candidates of Seg 2 have higher values and also the mean values of Seg 1 ($5 \cdot 10^{50}$ ergs) are one order of magnitude lower than in Seg 2 ($3 \cdot 10^{51}$ ergs). This originates from the difference in size and hence mass of the objects in these segments. The outliers towards energies below $0.5 \cdot 10^{47}$ ergs appear mainly in Seg 1. It can also be seen that shells of Seg 1 and Seg 2 of higher kinetic energies are the ones with the highest value of v_{exp}, highlighting, apart from its quadratic term in the equation, that this value has a higher impact on E_{kin}. Since blow outs can occur (e.g. Callaway et al. (2000)) and especially at high latitudes, where the general ISM densities are low, parts of the shells might be open (see e.g. USco-shell, sec. 6.5.1). This leads to uncertainties, especially in the measurement of v_{exp}, which also go into the mass and overall lead to relative mean uncertainties of E_{kin} of 66%.

One special outlier shell, the object DK_4766, is present in fig 5.14 with a radius of 1.06 kpc and with $E_{\mathrm{kin}} = 2.6 \cdot 10^{45}$. The low kinetic energy originates from a mass of 100 $\mathrm{M}_\odot$. With $l_0, b_0 = (164°, 7°)$ and $v_0 = 78.6$ km/s it is in a region where the emission is near the limit of the sensitivity of the HI4PI survey. It also just has an "expansion velocity" of 2.5 km/s and has rank 765 out of 802 in the catalog due to the quality measures (sec. 4.6.3). Due to its low energy and mass, this shell could have been produced by different processes than supernova explosions. However, the small size, mass and kinetic energy of the shell does not affect the following analyses due to its small energy contribution and volume.

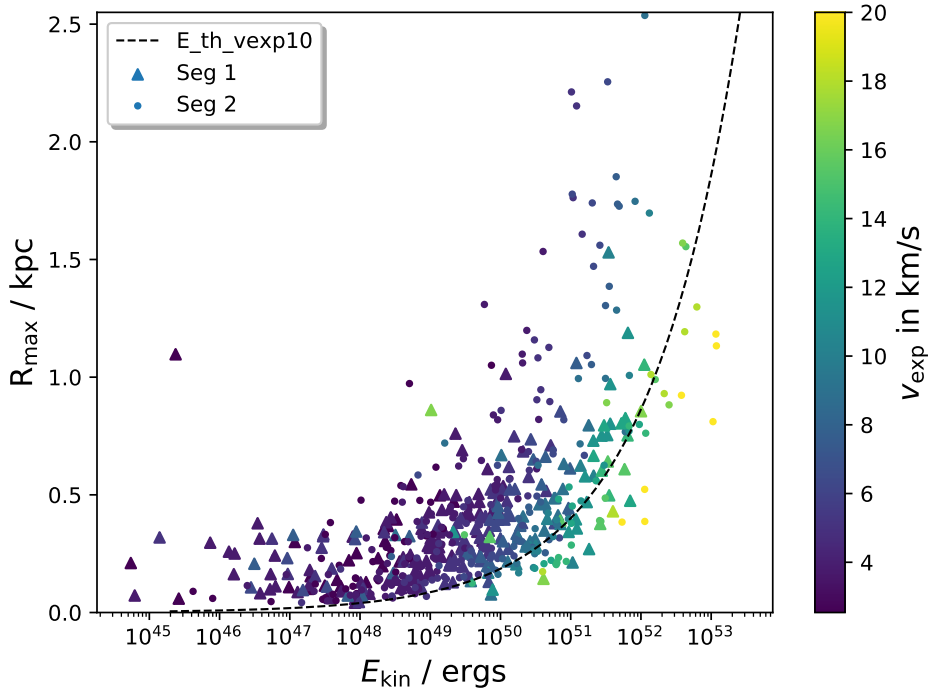

Figure 5.14: The age, τ, of the shells is plotted against their kinetic energy, E_{kin}. The $x-$ and $y-$scale are logarithmic and the values of $E_{\mathrm{kin},i}$ with $i \in \{1, 2, ..., 569\}$ are in a range of $3 \cdot 10^{44}$–$1 \cdot 10^{53}$ ergs in magnitudes and the τ_i are distributed in orders of 1–10^2 Myr. The filled triangles mark shells of Seg 1 and the filled circles denote the shells of Seg 2 (definition sec. 5.1). The dashed line represents the theoretical kinetic energies for shells of different radii, with $n_0 = 1$ and resulting masses (see derivation in the description of fig 5.13), together with $v_{\mathrm{exp}} = 10\,\mathrm{km/s}$.

5.4 Astrophysical interpretation

Using the derived physical properties of the shells, $R_{\max_i}$, τ_i, $M_{\mathrm{H\,I},i}$, $M_{\mathrm{tot},i}$ and $E_{\mathrm{kin},i}$, now astrophysical interpretations of the catalog are discussed. The volume filling factors (sec. 2.4.2) $f_{3D,\mathrm{Seg\,1}}$ and $f_{3D,\mathrm{Seg\,2}}$ have been derived[11]. The initial density $n_{0,i}$ of the ambient ISM of the progenitor of each shell, as well as the expected total energy output $E_i(t)$ at time t (with $t = \tau$) have been calculated to derive the ratio $\epsilon_e = E_{\mathrm{kin},i}(t)/E_i(t)$ (eq. 2.24). Values and uncertainties are listed in tables 5.5 and 5.6.

1	2	3	4	5	6	7	8	9	10
name:	V_{sh}	n_{obs}	$n_{\mathrm{obs,u}}$	$E_{\mathrm{w}}(t)$	$E_{\mathrm{w,u}}(t)$	$E_{\mathrm{c}}(t)$	$E_{\mathrm{c,u}}(t)$	ϵ_{w}	$\epsilon_{\mathrm{w,l}}$
unit:	kpc^3	cm^{-3}	cm^{-3}	erg	erg	erg	erg	-	-
DK_1476	4.37E+00	2.03E-02	7.23E+00	1.38E+50	4.91E+52	8.29E+51	5.98E+54	0.86	2.43E-03
DK_2046	9.46E-01	1.40E-01	1.17E+01	3.34E+51	2.80E+53	1.17E+53	1.67E+55	1.75	2.09E-02
DK_1303	1.57E+01	8.85E-02	8.74E+01	3.52E+52	3.48E+55	9.83E+53	2.22E+57	1.24	1.25E-03
DK_1286	9.84E-02	2.93E-01	2.48E+00	6.12E+50	5.17E+51	2.07E+52	2.26E+53	1.67	1.97E-01
DK_1188	1.92E+00	1.62E-01	2.56E+01	4.41E+51	6.98E+53	2.00E+53	5.82E+55	1.54	9.69E-03
DK_1187	2.14E+00	1.57E-01	2.84E+01	5.89E+51	1.06E+54	2.35E+53	7.91E+55	1.61	8.91E-03
DK_1119	1.76E-02	1.05E+00	1.31E+00	5.16E+49	6.40E+49	2.89E+51	3.68E+51	0.94	7.58E-01
DK_857	3.74E-02	3.80E-01	1.25E+00	2.49E+50	8.17E+50	5.95E+51	2.25E+52	1.67	5.09E-01
DK_810	2.77E-02	6.75E-01	1.17E+00	2.65E+50	4.59E+50	1.01E+52	1.87E+52	1.16	6.71E-01
DK_3462	4.28E+00	9.33E-02	3.39E+01	4.48E+51	1.63E+54	2.09E+53	1.54E+56	1.53	4.21E-03

Table 5.5: Derived physical quantities, using the physical shell parameters, are listed in this table. It is an excerpt of the first 10 rows of table A.0.23. In column 1, the name of the shell is listed. Column 2 contains the spatial volume of the shell, V_{sh}. The measured particle density, n_{obs}, and the upper particle density, $n_{\mathrm{obs,u}}$, of each shell are listed in column 3 and 4 respectively. Columns 5 and 6 list the corresponding theoretical total energies ejected from the stars, $E_{\mathrm{tot,w}}$ and $E_{\mathrm{w,u}}(t)$ respectively (eq. 2.21). The total energies, calculated using eq. 2.7, $E_{\mathrm{c}}(t)$ and $E_{\mathrm{c,u}}(t)$, are listed in column 7 and 8 respectively. Columns 9 and 10 list the ratio between the results of equation 2.24 for the energy ratio, using the values of $E_{\mathrm{weav}}(t)$ and $E_{\mathrm{chev}}(t)$, respectively. For more information see text.

1	2	3	4	5	6	7	8	9	10
name:	ΔV_{sh}	Δn_{obs}	$\Delta n_{\mathrm{obs,u}}$	$\Delta E_{\mathrm{w}}(t)$	$\Delta E_{\mathrm{w,u}}(t)$	$\Delta E_{\mathrm{c}}(t)$	$\Delta E_{\mathrm{c,u}}(t)$	$\Delta\epsilon_{\mathrm{w}}$	$\Delta\epsilon_{\mathrm{w,l}}$
unit:	kpc^3	cm^{-3}	cm^{-3}	erg	erg	erg	erg	-	-
DK_1476	5.34E+00	1.17E-02	2.01E+00	7.57E+49	2.81E+52	3.42E+52	1.97E+54	0.73	2.87E-03
DK_2046	9.17E-01	7.84E-02	3.69E+00	2.01E+51	1.73E+53	1.06E+53	4.29E+54	1.34	2.28E-02
DK_1303	7.27E+00	1.62E-02	1.24E+01	1.81E+52	1.83E+55	1.29E+54	9.51E+56	0.9	1.41E-03
DK_1286	2.14E-01	2.87E-01	6.73E-01	4.04E+50	3.50E+51	1.26E+52	7.26E+52	1.36	1.98E-01
DK_1188	1.96E+00	8.92E-02	8.52E+00	2.56E+51	4.27E+53	2.10E+53	1.92E+55	1.27	1.12E-02
DK_1187	2.21E+00	8.85E-02	9.21E+00	3.43E+51	6.48E+53	2.68E+53	2.78E+55	1.33	1.03E-02
DK_1119	3.71E-02	8.05E-01	2.68E-01	2.94E+49	3.77E+49	9.24E+50	1.51E+51	0.74	4.32E-01
DK_857	1.15E-01	5.18E-01	1.78E-01	1.75E+50	5.77E+50	4.27E+51	1.24E+52	1.46	4.42E-01
DK_810	9.79E-02	7.50E-01	2.09E-01	1.85E+50	3.27E+50	3.65E+51	8.25E+51	1.02	4.53E-01
DK_3462	2.94E+00	4.17E-02	1.05E+01	2.55E+51	9.64E+53	3.13E+53	5.03E+55	1.24	4.86E-03

Table 5.6: This table is an excerpt of the first 10 rows of table A.0.24 and contains the uncertainties of the values of table 5.5. The columns are arranged in the same order. The name of the respective shell is given in column 1. Column 2 contains the uncertainties of the shell volume ΔV_{sh}. Column 3 and 4 list the uncertainties of the particle density Δn_{obs} and the upper particle density $\Delta n_{\mathrm{obs,u}}$. Columns 5 and 6 contain the uncertainties of the theoretical total energies ejected from the stars, $\Delta E_{\mathrm{w}}(t)$ and $\Delta E_{\mathrm{w,u}}(t)$. Columns 7 and 8 list uncertainties of the total energies for the single point explosion approximation, $\Delta E_{\mathrm{c}}(t)$ and $\Delta E_{\mathrm{c,u}}(t)$, respectively. The columns 9 and 10 contain the energy ratios $\Delta\epsilon_{\mathrm{w}}$ and $\Delta\epsilon_{\mathrm{w,u}}$ respectively. For more information see text.

[11] The two segments are introduced in relation 5.1

5.4.1 Space filling factor of H I shells

With the size, $R_{\mathrm{max},i}$, of each shell, each shell volume can be calculated and further the ratio between the sum of the shell volumes and the volume of segments of the Milky Way, the so called volume filling factor $f_{3\mathrm{D}}$ (sec. 2.4.2), can be derived. It can be calculated for larger segments in the local Galaxy, where shell detection is not limited by the HI4PI survey resolution. The largest possible sub-segment of the Galactic volume, which does not contain ambiguous $D_{\mathrm{sun},i}$ has been chosen representatively, which is Seg 1 (definition see 5.3). The value of $f_{3\mathrm{D}}$ is dominated by the volumes of the largest shells and uncertainties due to possible missing detections of smaller shells due to an observational bias (sec. 5.3) are negligible compared to the remaining uncertainties[12].

The Galactic volume of Seg 1 consists of two equal cylinder-like sub-segments. The sub-segments are visualized in figure B.0.30. Both sub-segments together have the volume $V_{\mathrm{seg}} = 4\pi R_{\mathrm{seg}}^2 h_{\mathrm{seg}} \delta l / 360^\circ = 314\,\mathrm{kpc}^3$, with the radius of the segment, $R_{\mathrm{seg},j} = 15\,\mathrm{kpc}$, and the longitude range of the segment Δl[13]. The scale height of Galactic H I flaring increases exponentially with distance from the Galactic center but can be estimated to be $h_{\mathrm{seg}} = 0.5\,\mathrm{kpc}$ in the relevant regions (Kalberla & Kerp (2009), fig. 6 therein) and hence is also adopted for the height of the reference volume. Since all shells are approximated by a spherical shape, the total volume of the shells in Seg 1 is calculated by $V_{\mathrm{sh}} = \sum_{i=1}^{n} 4/3\pi R_{\mathrm{max},i}^3 = 112 \pm 71\,\mathrm{kpc}$[14], $i \in \{1, ..., n\}$ and $n = 268$ being the total number of shells in Seg 1 where a distance calculation is possible. The result of $V_{\mathrm{sh},i}$ for each individual shell can be found in column 2 of table 5.5. The resulting interim space filling factor is $f_{\mathrm{3D,raw}} = V_{\mathrm{sh}}/V_{\mathrm{seg}} = 0.29 \pm 0.22$. Due to the restriction that distances for shells with values of $v_0 < 10\,\mathrm{km/s}$ cannot be derived by its kinematics (section 5.3), 19% of the shells in Seg 1 have no physical result parameters because they were excluded from the kinematic distance estimation (sec. 5.3). Assumed, the volumes of these remaining shells to statistically distribute similar to the average of the others, an addition of $0.19 \cdot V_{\mathrm{sh}}$ has to be added to V_{sh}. By considering the statistical variation of the evaluated shells, the fractional filling factor is $f_{\mathrm{3D,\,seg}} = \mathbf{0.36 \pm 0.23}$. The resulting value of $f_{3\mathrm{D}}$ depends on the choice of the reference volume. If considered that this volume is not too small by including it to the furthest shell, detected in Seg 1. The ISM density towards higher Galactic radii decreases exponentially (e.g. Kalberla & Kerp (2009)) and especially at higher distances of Seg 1 of ($D_{\mathrm{sun}} \geq 5\,\mathrm{kpc}$, fig. B.0.30), apart from the Outer Arm, the density is generally lower. This can also be seen for the number of shells at these different regions. The shell densities, or number of shells, close to the Sun (Orion Arm) and near the Perseus Arm are higher compared to the distance segments in between (see section 5.3.1 and figure 5.9).

While the region covers a significant part of the MW, it is difficult to extrapolate this value for the inner Galaxy or the subsegment, Seg 2, because the structures and densities between the outer- and inner Galaxy are significantly different. For comparison, the space filling factor is calculated for Seg 2, similar to Seg 1, and results in $f_{\mathrm{3D,\,Seg2}} = \mathbf{1.34 \pm 0.54}$. Seg 1 and 2 have the same size. That this values is much higher than for Seg 1 is due to the high amount of shells of radii $\geq 1\,\mathrm{kpc}$ in Seg 2 (39), which have the highest impact on $f_{3\mathrm{D}}$. Additionally there are more shells in Seg 2, compared to Seg 1. It has been shown that many of these shells occur in clusters (sec 5.1.1) and hence could partly overlap with each other (sec. 4.6.5). This is why a value of $f_{3\mathrm{D}}$ that exceeds 1 is possible.

[12] e.g. the volume of a shell with $R_{\mathrm{max}} = 1\,\mathrm{kpc}$ is equal to the one of 1000 shells of $R_{\mathrm{max}} = 0.1\,\mathrm{kpc}$.

[13] The factor 4 is the product of having the same volume below and above the Galactic plane, times having two subsegments of the same size.

[14] The parts of the volume that is outside of $h = 0.5\,\mathrm{kpc}$ is not included

If reviewing section 2.4.2 and 2.4.3, while for external galaxies, a range of $f_{3D} = 0.01$–0.2 Bagetakos et al. (2010) is observed, the results of numerical simulations of (Krause et al. 2015) suggest a range of $f_{3D,sim} = 3.1 - 115$ for initial densities of $0.1\,\mathrm{cm}^{-3} \leq n_0 \leq 10\,\mathrm{cm}^{-3}$ for weak- and strong dissipation models and propose that the discrepancy of one magnitude to observation might result from efficient shell merging, especially for younger shells. From hot gas fraction in ISM simulations of de Avillez & Breitschwerdt (2005) a value of $f_{3D} = 0.2$ is expected. Ehlerová & Palouš (2013) found a value $f_{3D} = 0.05$ from the evaluation of their H I shell catalog, while also mentioning that this is more of a lower limit since they excluded the largest shells from their calculations. Since the largest shells dominate f_{3D}, the size of shells of this work are not capped at 1 kpc and more shells of this size are detected here, this would explain the difference of their value compared to the one of this work. On the other hand for the very local ISM around the Sun, they proposed a porosity (f_{3D}) that exceeds 1, due to the observation of merging shells, similar to what was observed above for Seg 2. If reviewing the distance distribution of shells discussed in section 5.3, especially for Seg 1, the density of shells closer to the Sun and near the Perseus Arm (≈ 2 kpc, sec. 5.3.1) is significantly higher than at $D_{sun} > 5$ kpc and hence, while already shells of radii of about 1 kpc are present, the local porosity is also higher. If calculating f_{3D} for a sub-segment of Seg 1 that contains shells up to 5 kpc distance $f_{3D,S1sub} = 1.33 \pm 0.55$ (which is also comparable to full Seg 2). These results are then consistent with the ones of Ehlerová & Palouš (2013), who also calculated f_{3D} for for close shells up to 1 kpc. But since this region is biased due to the local presence of the Perseus Arm, it is not representative for a mean Galactic value. This is why the value of the full segment $f_{3D,Seg1}$ gives a better approximation. As introduced in section 2.4.2, more recent investigations of (Sarkar et al. 2019) found that f_{3D} should self-regulate to a constant $f \approx 50\%$, which agrees with the value of $f_{3D} = 0.35 \pm 0.23$ of Seg 1.

Summarized, the value of f_{3D} depends strongly on the selection of the reference segment size. In the directions of spiral arms, f_{3D} exceeds 1. But in the voids between spiral arms, the density of shells is down to almost 0. This shows the strong dependence of the results on the environment that is investigated, especially if the reference volume is defined too small. These come from variations of shell densities, e.g. visible in figure 5.8. However, the segment of this work is large enough to contain a considerable amount of the Galactic volume and contains multiple spiral arm segments as well as voids. The results are consistent with the ones of Sarkar et al. (2019) and are also closer towards the results of numerical simulations that lead to higher values of f_{3D} compared to the observed ones.

5.4.2 Energy loss in H I shells

Approximations of the initial ambient ISM density For deriving the energy output, the initial density of the ambient ISM of a SNR, n_0 is of key importance. In some investigations (de Geus 1992; Poeppel et al. 2010; Ehlerová & Palouš 2013), the density of the ISM in the solar vicinity is used. But n_0 can differ significantly between different regions and is generally also dependent on the vertical distance of the shell center point towards the Galactic plane. Hence, here an approximation for n_0 (n_{obs}) is additionally derived from the H I data by dividing the derived $M_{tot,i}$ by the shell volume V_i. This yields an initial density $n_{0,obs,i}$, which is listed in column 3 of table 5.5 and can be compared to theoretical values of n_0. The resulting values are in the range of $1.42 \cdot 10^{-6}\,\mathrm{cm}^{-3}$ to $1.68 \cdot 10^{1}\,\mathrm{cm}^{-3}$ with a mean value of $\overline{n}_{0,obs} = 0.26 \pm 0.07\,\mathrm{cm}^{-3}$. The here derived value n_{obs} is an approximation since it describes the mean on-shell density. Possible systematic uncertainties in the approach here of deriving n_0 from the H I shells is the missing mass due to possible outflows and but also mass remnants in the inner parts of the shell due to Rayleigh Taylor– or Vishniac instabilities (sec. 2.4.2).

On top of that the on-shell volume is large and the same particle number might have been concentrated on a smaller volume, initially. This is why additionally, an upper limit $n_{\mathrm{obs,u}}$ is also derived. This is estimated by assuming that the on-shell mass was initially located in a volume, that is that of a massive star forming region of 10±5 pc^3 (Madrid et al. 2012; Tremblin et al. 2014)[15]. $n_{\mathrm{obs,u}}$ ranges from $3.76 \cdot 10^{-5}$ cm^{-3} to $27.07 \cdot 10^{1}$ cm^{-3} and has a mean value of $\overline{n}_{0,\mathrm{obs,u}} = 2.66 \pm 0.27\,\mathrm{cm}^{-3}$. The uncertainties for the lower limit Δn_{obs} as well as the upper limit $\Delta n_{\mathrm{obs,u}}$ is given by propagation of the uncertainties of the shell parameters. Both values are listed in column 3 and 4 of table 5.6.

The proposed or assumed values of other studies range over multiple magnitutes. Tremblin et al. (2014) argues for number densities of 500 cm^{-3}, Kim et al. (2016) and Gupta et al. (2016) conclude ranges of 1–1000 cm^{-3}, 1–800 cm^{-3} is used by Pittard (2022), also smaller ranges are used like 0.1–0.7 by Bagetakos et al. (2010) and $n_{\mathrm{th}} = 10$ by Rodgers-Lee et al. (2019) for Galactic-scale superbubble simulations. $\overline{n}_{0,\mathrm{obs}}$ is at the lower end of what is commonly assumed. The mean upper limit $\overline{n}_{0,\mathrm{obs,u}}$ is in the mean of the above-mentioned values and closest to the one from Rodgers-Lee et al. (2019). Additionally, to the here derived values of n_{obs} and $n_{\mathrm{obs,u}}$, also the mean value of $n_{\mathrm{th}} = 10$ from Rodgers-Lee et al. (2019) is adopted for further calculations.

Calculation of the theoretical total energy Now the total energy, $E(t)$, at a given age, t, can be calculated for Seg 1. Here, the main approach to calculate the theoretical total energy $E_i(t)$ of each shell i using the analytical description of a constant energy input with point explosions of multiple sources from Weaver et al. (1977) (eq. 2.21) and by inserting the above determined shell parameters $R_{\mathrm{max},i}$, τ_i and $n_{0,\mathrm{obs}}$. The resulting values $E_{\mathrm{w},i}(t)$ using $n_{\mathrm{obs},i}$ and the upper limits $E_{\mathrm{w,u},i}(t)$ using $n_{\mathrm{obs,u},i}$ are listed in columns 5 and 6 of table 5.5 with mean values of $\overline{E}_{\mathrm{w}}(t) = (2.89 \pm 0.61) \cdot 10^{50}$ ergs, where the uncertainties are the errors of the respective means. The mean relative uncertainty of all shells is 56% with the uncertainties $\Delta E_{\mathrm{w},i}(t)$ (tab. 5.6). For the upper limit, the values are $\overline{E}_{\mathrm{w,u}}(t) = (6.45 \pm 1.99) \cdot 10^{52}$ ergs with mean relative uncertainties of 70%.

A different description, where the time dependancy is eliminated to calculate $E(t)$ that has been used by Bagetakos et al. (2010) as "a best" approximation, which is the solution for one of a single SN-explosion in a symmetric environment without constant energy input from Chevalier (1974) (eq 2.7). This gives the values $E_{\mathrm{c},i}(t)$ as well as $E_{\mathrm{c,u},i}(t)$, which are listed in columns 7 and 8 of table 5.5 and their corresponding uncertainties in table 5.6. The results are $\overline{E}_{\mathrm{c}}(t) = (1.42 \pm 0.23) \cdot 10^{51}$ ergs and $\overline{E}_{\mathrm{c,u}}(t) = (4.64 \pm 1.54) \cdot 10^{54}$ ergs respectively.

Ratio between theoretical input- and kinetic energy Having calculated the total energy output, $E(t)$, at time, t, the fraction of $E_{\mathrm{kin},i}(t)$ of $E_i(t)$ of each shell from sec. 5.3.2 can be analyzed. This relation is shown in figure 5.15.

The triangles mark the $E_{\mathrm{w},i}(t)$ with the lower uncertainties $\Delta E_{\mathrm{w},i}(t)$. The upper limits $E_{\mathrm{w,u},i}(t)$ for the respective shells are marked by gray circles with the upper uncertainties $\Delta E_{\mathrm{w,u},i}(t)$. Both values are connected with gray lines to visualize the range between the upper limit, using a theoretical initial volume for the density approximation and the values derived using the on-shell density n_{obs}, from above, for the calculations.

The black points denote $E_{\mathrm{c},i}(t)$ for the single blast approximation without constant energy input of

[15] In a 5% of the cases, the on-shell volume was smaller than 5 pc^3 and here, the on-shell mass is kept as well as its uncertainties

Chevalier (1974) and are plotted for completeness. It can be seen that even when leaving out the upper limits $E_{\mathrm{c,u},i}(t)$, $E(t)$ is overestimated compared to the solution of Weaver et al. (1977), which is due to the missing constant energy input, which leads to underestimations in radius.

$\epsilon = E_{\mathrm{kin},i}(t)/E_i(t)$ indicates how much of the total energy is transferred into the expansion of the shells and how much energy is thermal energy or lost due to e.g. instabilities (Krause & Diehl 2014) and radiation. This value is not constant over time and generally, the older an expanding shell, the higher the fraction of kinetic energy compared to the total energy because the thermal energy inside a bubble decreases when the amount of existing massive stars, to produce winds and SNe, decreases. The theoretical description of the ratio, $\epsilon_{k,\mathrm{num}}$ ((Krause & Diehl 2014) and sec. 2.4.1) ranges from $\epsilon_{k,\mathrm{num}} = 0.2$ (see black solid line in fig. 5.15) to $\epsilon_{k,\mathrm{num}} = 0.8$. Since $E_{\mathrm{kin}}(t)$ of a shell is always a fraction of the total output energy, generally the values of $E_{\mathrm{w},i}(t)$ lie between the two lines, whereas for increasing values of $E_{\mathrm{kin}}(t)$ and $E_{\mathrm{w},i}(t)$ they are distributed around the limit of 1 (black solid line). For the upper limits, $E_{\mathrm{w,u},i}(t)$, it even surpasses the line of $\epsilon_{k,\mathrm{num}}$ =0.2 consistently. A value of ϵ_{w} that exceeds 1 (black dashed line in fig. 5.15) but within its uncertainties is compatible with the upper limit[16]. The median value $\overline{\epsilon}$ of ϵ_i (tab. 5.5) is discussed. These are $\overline{\epsilon}_{\mathrm{w}} = 1.01 \pm 0.30$ for using the relation of Weaver et al. (1977) with $E_{\mathrm{w}}(t), n_{\mathrm{obs}})$ and $\overline{\epsilon}_{\mathrm{w,u}} = 0.096 \pm 0.94$ for the upper limit using $E_{\mathrm{w},u}(t, n_{\mathrm{obs,u}})$.

The differences between the means, $\overline{\epsilon}_{\mathrm{w}}$ and $\overline{\epsilon}_{\mathrm{w,u}}$, highlight how the approximation of the initial density, n_0, influences the results. Based on the high uncertainties, on how large the general fraction of kinetic energy of the total energy is, no general conclusion can be drawn. However, increasing values of $E_i(t)$ are directly connected to higher ages/sizes (section 5.3.2) of the shells (eq. 2.21). The relation between age/radius and the estimated initial density n_{obs} is shown in figure B.0.29 in the left panel. There it is shown that larger shells have lower mean densities in general. This is because they reach up to higher z-heights, where the density of the ISM is lower. This is why in the right hand side of the figure, also the density is plotted against the z-height of the center coordinate, which indicates the same relation and leads to lower ratios between E_{kin} and $E_i(t)$.

[16] $E_{\mathrm{kin}}(t)$ cannot be larger than the total output energy $E_{\mathrm{i}}(t)$ at any time

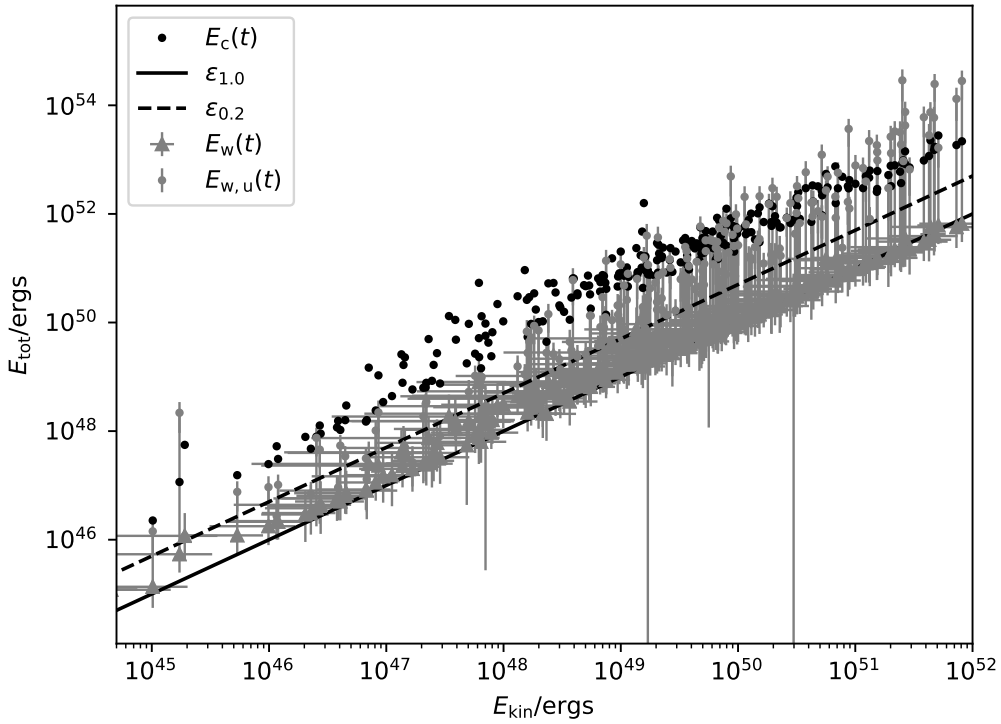

Figure 5.15: The theoretical input energy, $E_{\rm tot}$, is plotted against the kinetic energy, $E_{\rm kin}$, for each shell of Seg. 1. The gray trianlges mark the values $E_{\rm w}(t)$ caluclated using the constant energy input and multiple point source approximation from Weaver et al. (1977) (eq. 2.21) and the black dots mark the values $E_{\rm c}(t)$ calculated using the approximation of Chevalier (1974) (eq. 2.7). For the former one, the asymmetric errorbars are shown. The black line $\epsilon_{1.0}$ marks the theoretical upper limit where $E_{\rm tot} = E_{\rm kin}$. And the dashed black line $\epsilon_{0.2}$ marks the theoretical lower limit of $\epsilon = E_{\rm kin}/E_{\rm tot} = 0.2$ (Krause & Diehl 2014). For more information and the derivation of the uncertainty limits see text.

5.5 Summary

The 802 H I shell of the catalog, derived in section 4.6, has been analyzed in this chapter. The distributions of shells in longitude, latitude and velocity space show an exponential decrease towards higher latitudes and higher absolute velocities. This is similar to the distribution of the global ISM. But clusters of shells, standing out from the general distribution, have been identified. The largest clusters occur at high latitudes and have been connected to the two prominent massive star forming regions, the Orion complex and the Sco-Cen OB association, of which the surrounding ISM is known to contain multiple H I shells (sec. 5.1.1).

The H I shells, detected in this work, have been compared to other H I shell studies. This catalog overlaps with 108 objects of previous studies and contains 694 new H I shells (sec. 5.2.1). For a high fraction of the newly identified shells, expanding H I shell features have been identified (table 5.1), but can just be observed in a small velocity interval. In many cases, the caps that are expected from an idealized model of an expanding shell are not present. Some newly identified shells, which are outliers from the distribution of shells, have center velocities of up to $|v_0| = 150$ km/s. The most extreme case has been analyzed and it is suggested to be produced by the impact of an infalling high velocity cloud with the ISM of the Galactic disk (sec. 5.2.2), which is observed at the same coordinates (Westmeier 2018).

Further, the physical properties of the shells have been derived by determining their distance in respect to the Sun. Most of the identified H I shells scatter around the spiral arm structures and show similar kinematics at these regions (sec. 5.3.1). Also regions of low densities of shells are observed in the regions between spiral arms. A high density of shells is identified at the location of the Perseus Arm in the direction of the Galactic anticenter. The highest number of shells is detected in the vicinity of the Sun, while the largest shells are identified at distances of 6 kpc and above.

Using the derived physical values, astrophysical properties of the shells have been determined. The volume filling factor of H I shells has been calculated for a segment in the outer Galaxy. The resulting value of $f_{3D,Seg1} = 0.36 \pm 0.23$ indicates that a high fraction of the Galactic volume is filled with H I shells. This result is in agreement with studies like Sarkar et al. (2019) but higher than the value of comparably older studies as the one of Ehlerová & Palouš (2013). The analyses have also shown that the value depends on the observed direction as it is much higher for Seg 1 ($f_{3D,S1,sub} = 1.35 \pm 0.55$) and that even on Galactic scales, the values differ strongly between regions, as shown for the sub segment of Seg 2, where $f_{3D,S1,sub} = 1.33 \pm 0.55$, which is in agreement with the local value of Ehlerová & Palouš (2013). This indicates the difference in massive star formation between regions, e.g. spiral arms and voids. But in general these high values of f_{3D} support the idea of efficient shell merging Krause et al. (2015).

The ages, masses and kinetic energies of the shells have been derived, analyzed statistically and compared to Galactic and extragalactic known H I shells. With these values, the theoretical total expected energy output has been derived. The initial density has been approximated, directly from the H I data, by two approaches. It has been shown that the calculated theoretical energy input at a given time is strongly dependent on the approach. It has been shown that the ratio between kinetic- and total expected output energy is higher for larger (older) shells than for smaller (younger) shells.

CHAPTER 6

The Scorpius–Centaurus association

In this chapter, the analyses of the ISM in the vicinity of the Scorpius Centaurus OB association (Sco-Cen), of which the current state of research has been introduced in section 2.5, is presented.

Because of its proximity and the large angular sizes of the H I clouds that spread over almost one quarter of the whole sky, the investigation required additional approaches, compared to the Galactic large-scale shell search from the last chapter, to determine the characteristics of the ISM structures in detail. The H I data of GASS (sec. 3.2), that cover the whole region have been used as the main data source for the analyses here.

Physical parameters of the H I shells as well as their connection to the stellar groups have been determined to derive new insights about the history of Sco-Cen. First the analyses of the large scale features, mainly arc-like H I clouds in integrated maps are presented. Their distances have been determined, using additional data sources. A visual inspection of H I channel maps, using the assessment criteria from section 3.4.3, to estimate the parameters of cavities in the ISM, is presented. The determination of the distances towards the H I shells and their masses, using multiple independent methods from chapter 4 is presented. This is followed by the description of the derivation of the initial stellar masses to estimate the energy output of the stellar groups and compare it to the kinematics of the shells. Finally a scenario for the history of Sco-Cen is proposed in section 6.5.3[1].

[1] We published some partial results of this chapter (Na I absorption line analysis) Krause et al. (2018). For the respective images and results that have been published Krause et al. (2018) is cited

6.1 Analysis of the H I features near Scorpius Centaurus

The ISM around Sco-Cen is distributed across 100° in longitude and 70° in latitude, revealing many large scale structures. As a first insight of the investigation of the H I gas, three integrated maps (sec. 3.3.1) of the same angular region, of different velocity ranges, in a total velocity range of -40 km/s to +10 km/s are presented. These are figure 6.1 (-40 km/s to -20 km/s), figure 6.2 (-20 km/s to +0 km/s) and figure 6.3 (0 km/s to +10 km/s). The analyzed H I data are from the GASS survey (sec 3.2.2) because it has the higher spectal resolution (1 km/s), while having the same angular resolution as the HI4PI survey (sec. 3.2) and covers the region of Sco-Cen. The most striking H I features, detected visually in the integrated H I data are marked by white boxes with Roman capital numerals from I to XV.

The distance to these H I clouds cannot be measured directly because the structures are local ones and Galactic scale methods, like kinematic distance estimations are not applicable. Hence, distance measurements of ISM clouds from interstellar absorption lines (section 2.2) from (Welsh et al. 2010) of 211 sight lines, have been used as a first estimation to limit the distances towards the ISM clouds[2]. To make this method applicable, the H I clouds had to be connected to the measured sodium lines by their kinematics[3]. The automated method to determine matches between H I peaks and absorption line peaks, has been introduced in section 4.7.3. There the application of the method for the example of feature X has been presented and the results for lower- and upper distance limits have been discussed there along figure 4.30. This method has been applied to all available absorption lines of the 211 sight lines for each detected H I feature I to XV in specified velocity ranges (sec. 4.7.3). The preliminary results are listed in table 6.1 (excerpt of table A.0.7). The table contains all detected matches between H I- and Na I absorption peaks. The remaining peaks ($\mu_{\mathrm{H\,I}}$) of the gaussian component of the H I profile that fits the Na I absorption line best are listed in column 11 and the standard deviation $\sigma_{\mathrm{H\,I}}$ of the peak can be seen in column 12 and can be compared to the absorption line peaks ($v_{\mathrm{Na\,I}}$) that are listed in column 9. Doubles that should be sorted out according to the method in section 4.7.3 are still listed in this table. The remaining best matches for the lower distance limits are listed in table A.0.9, while the remaining best matches for the upper distance limits are listed in table A.0.8.

The final results of the latter two tables are visualized in the integrated H I maps in figures 6.1 to 6.3. In the plot in the upper panel of each figure, the determined upper distance limits are marked by yellow boxes, containing the distance in units of pc. This corresponds to case 3 of the scenarios in section 4.7.3 (Determination of the distance limits). In the lower panel of each figure, **the lower distance limits** are marked by red boxes, also containing the distance limits in units of pc, which corresponds to case 2 of the scenarios in section 4.7.3.

Inferences from distance limits It can be seen in the figures 6.1 to 6.3 that most clouds contain multiple distance limits. Since the distance limit directly depends on the distance of the star in respect to the Sun, the matches of Na I and H I of the closest stars are most important for an upper distance limit of the H I cloud, while the most distant stars, where no match for the respective feature has been found, yield the best lower distance limits. The lower limit has just been used if the Na I peak matches another H I peak of the spectrum that is not associated with the respective feature. If the Na I peak does

[2] The explained results presented here, are also published in (Krause et al. 2018). The figures are marked

[3] Here it is focussed on Na I as a tracer. Na I traces the colder neutral ISM, while Ca II is a better tracer for the warm component (Hobbs 1978; Lallement et al. 2003).

1	2	3	4	5	6	7	8	9	10	11	12	13	14
nm	n_{LoS}	l	b	fl	D	δD	$\delta v_{Na\,I}$	$v_{Na\,I}$	red $\chi^2_{H\,I}$	$\mu_{H\,I}$	$\sigma_{H\,I}$	$\Delta\mu_{H\,I}$	$\Delta\sigma_{H\,I}$
-	-	°	°	-	pc	pc	km s^{-1}	km s^{-1}	-	km s^{-1}	km s^{-1}	km s^{-1}	km s^{-1}
II	0	272.8	29.2	1	400	2.5	4	-20.4	0.037	-21.44	-2.49	1.39	1.95
II	0	272.8	29.2	1	400	2.5	4	-20.4	0.037	-16.89	6.09	4.13	2.42
IV	1	297.1	-18.3	1	329	2.2	5	-4.9	0.307	4.38	-8.41	2.23	0.76
IV	3	293.8	-13.1	1	375	3.8	4	-9.3	0.092	-21.82	-9.93	2.95	2.55
IV	3	293.8	-13.1	1	375	3.8	4	-9.3	0.092	2.17	-7.81	0.74	0.71
IV	3	293.8	-13.1	1	375	3.8	4	-2.2	0.092	2.17	-7.81	0.74	0.71
IV	4	293.7	-13.2	1	156	4.0	4	-15.5	0.146	-22.16	-9.91	3.38	2.79
IV	5	295.1	-13.6	1	433	3.7	4	-12.9	0.287	-20.25	-9.41	2.78	2.33
IV	6	297.7	-15.6	1	279	3.9	4	0.6	1.623	-0.9	17.81	4.15	1.94
IV	6	297.7	-15.6	1	279	3.9	4	3.8	1.623	-0.9	17.81	4.15	1.94
IV	11	294.4	-14.5	0	312	15.	4	2.7	0.139	-3.25	-16.16	1.73	1.96
V	0	366.2	29.1	0	279	14.0	4	-0.7	6.676	1	3.75	0.04	0.05
V	0	366.2	29.1	0	279	14.0	4	-12.7	6.676	-4.56	13.65	1.16	1.05
V	0	366.2	29.1	0	279	14.0	4	-0.7	6.676	-4.56	13.65	1.16	1.05
V	1	366.3	23.6	0	140	7.0	6	-0.7	0.379	1.06	2.55	0.08	0.07
V	1	366.3	23.6	0	140	7.0	6	-0.7	0.379	0.14	13.35	0.76	0.62
V	2	366.3	23.6	0	140	7.0	0.5	-1	0.379	1.06	2.55	0.08	0.07
V	2	366.3	23.6	0	140	7.0	0.5	-6.6	0.379	0.14	13.35	0.76	0.62
V	2	366.3	23.6	0	140	7.0	0.5	-5.1	0.379	0.14	13.35	0.76	0.62
V	2	366.3	23.6	0	140	7.0	0.5	-2.4	0.379	0.14	13.35	0.76	0.62
V	2	366.3	23.6	0	140	7.0	0.5	-1	0.379	0.14	13.35	0.76	0.62
V	3	366.3	23.6	0	140	7.0	0.5	0	0.379	1.06	2.55	0.08	0.07
V	3	366.3	23.6	0	140	7.0	0.5	0	0.379	0.14	13.35	0.76	0.62

Table 6.1: Accordances of H I profile with Na I lines for available lines that are in the angular range and in velocity intervals of the respective feature. Columns 1 denotes the name of the feature from I–XIII. Column 2 gives a mark for the sight line, columns 3 and 4 contain the (l, b) coordinate pair of the LoS towards a star. Column 5 flags if the distance is from Hipparcos (0) or GAIA (1). Columns 6 and 7 contain the distance of the star and the distance uncertainty respectively. Columns 8 and 9 list the velocity and the FWHM of the Na I line peak respectively. The remaining columns 10-14 contain the results of multi component Gaussian fits with the center μ, standard deviation σ of the thickness and the fit uncertainties $\Delta\mu$ and $\Delta\sigma$. This table is an excerpt of table A.0.7. For more information about the fitting procedure, see sec. 4.7.3.

not match any H I peak this is not considered a proof for a lower limit. This procedure is explained in detail along feature X in section 4.7.3 but has been applied to all relevant distance limits in the figures 6.1 to 6.3, yielding one total lower- and one total upper limit, D_{min} and D_{max}, for each feature. For example for feature X this resulted in $D_{min} = 74$ pc and $D_{max} = 141$ pc. The remaining distance limits have been used for the mass determination of these features (section 6.3.1) and are listed in the table 6.5. Below they are also compared to other derived distance information.

.

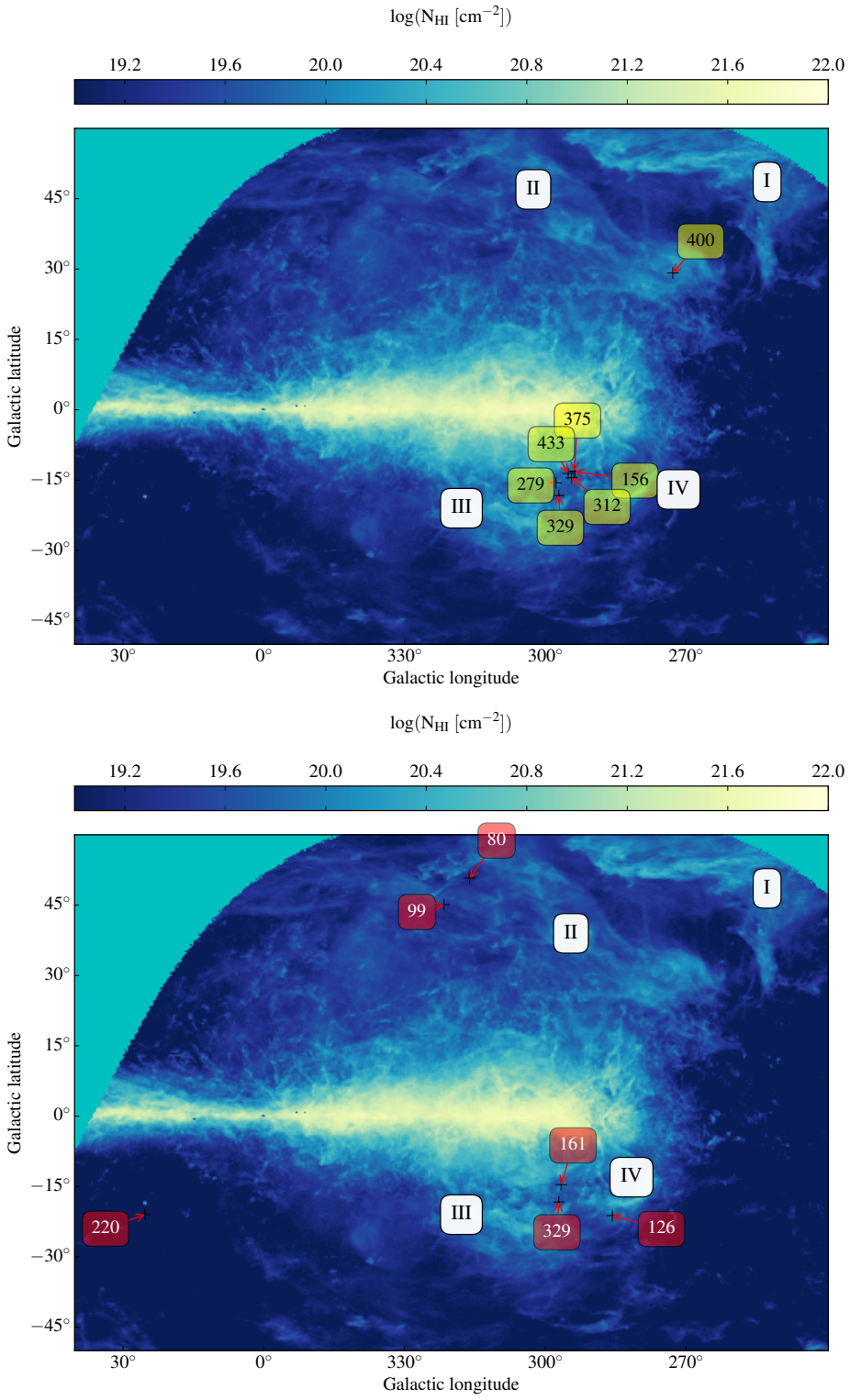

Figure 6.1: Integrated H I map, covering the velocity interval -40 km/s to -20 km/s, where the column density is color coded. In the top panel, the maximum distance matches between the fitted H I peaks and the Na I peaks are shown in yellow bounding boxes. In the lower panel, the lower distance limits are shown in red bounding boxes. The name of the respective feature is marked by a white box. For more information see text .

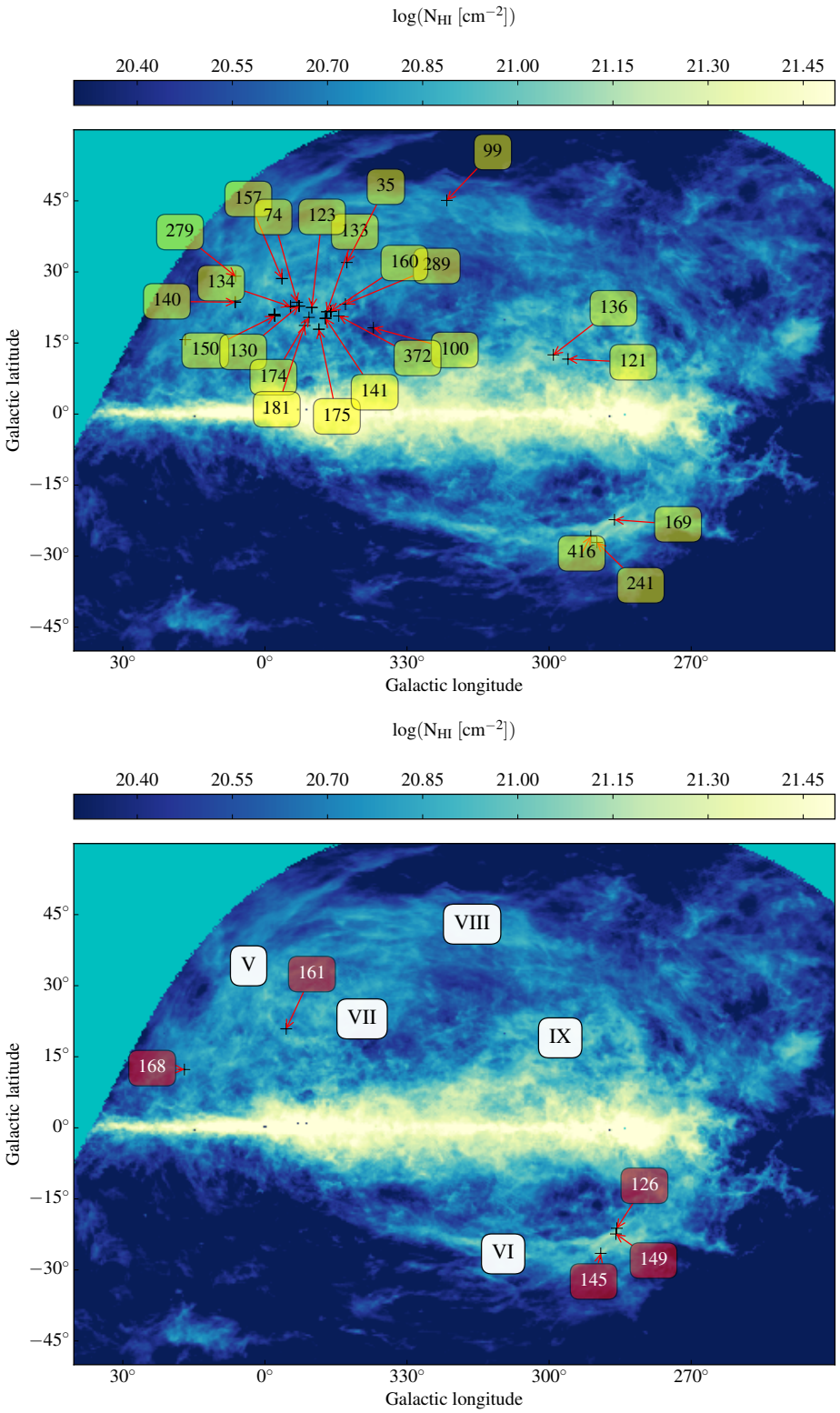

Figure 6.2: Similar to fig. 6.1 but the H I distribution of integrated velocities from -20 km/s to 0 km/s is shown. The upper- and lower distance limits are shown in the upper and lower panel, respectively. Upper panel figure has also been published in Krause et al. (2018) fig.4. left panel therein.

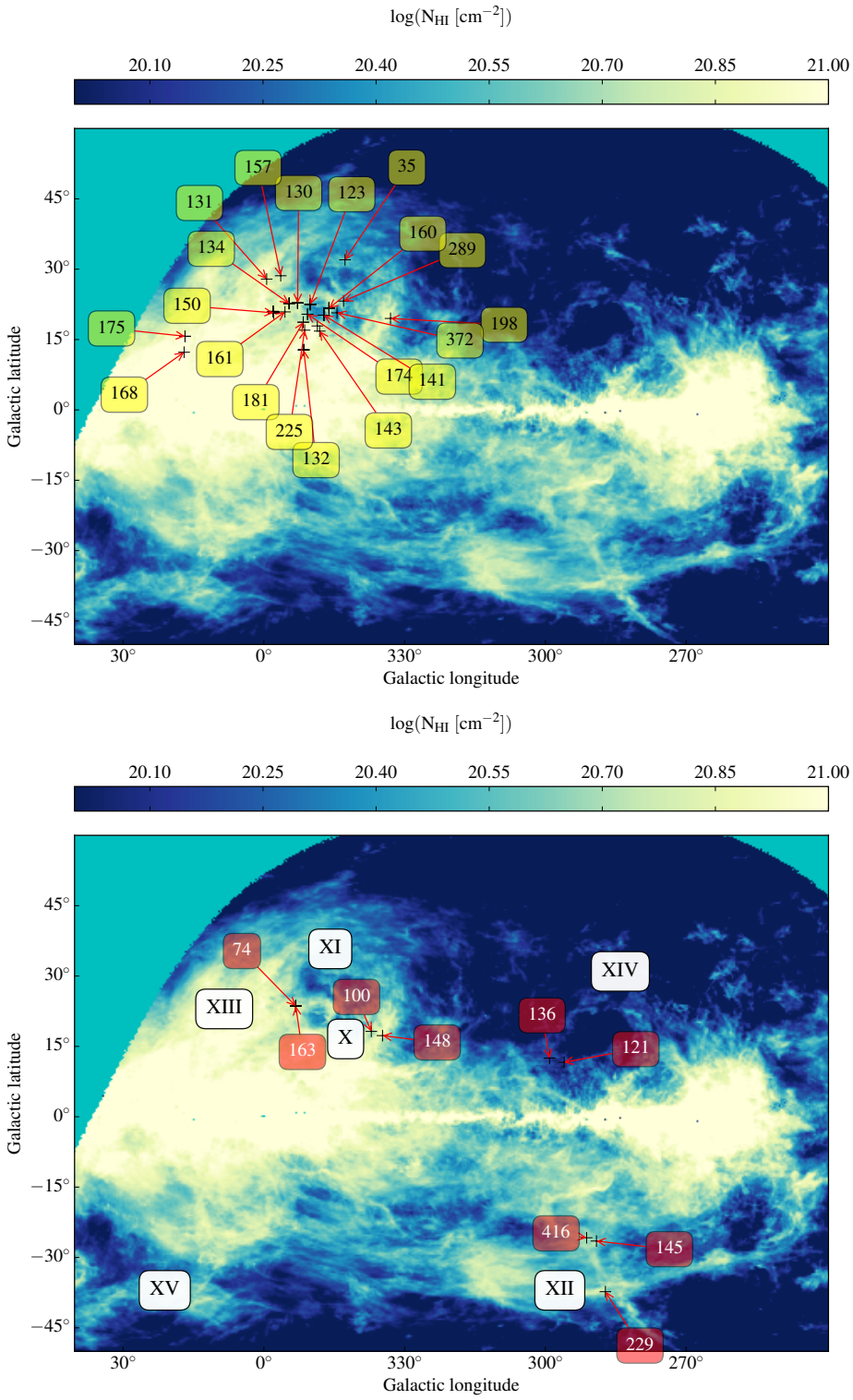

Figure 6.3: Similar figure to fig. 6.1 but the integrated H I emission over the velocities from 0 km/s to 10 km/s is shown. The upper- and lower distance limits are shown in the upper and lower panel, respectively. Upper panel figure has also been published in Krause et al. (2018) fig.4. right panel therein.

Distances inferred by interstellar reddening maps

The data of Green et al. (2015), introduced in section 2.2.1 have been published and are downloadable. They have been processed in this work to make them directly comparable to H I data as described in the following. From the data available, interstellar reddening maps by dust of distances 63 pc, 79 pc, 100.0 pc, 126 pc, 158.5 pc, 200 pc, 251 pc, 316 pc, 398 pc and 502 pc in the region of Sco-Cen have been produced since higher distance maps are not relevant for the analysis of this region[4]. The original angular resolution of the data lies in the range of 3.4′ to 13.7′ depending on the sight line. The data have been regridded in this work to match the resolution of the used H I data from GASS (16.1′) for a direct comparison[5].

A dust map integrated to a distance of 251 pc away from the Sun is shown in figure B.0.5 in the appendix. The angular size of the map is chosen based on the H I map size that covers all relevant H I structures near Sco-Cen (sec. 6.1, e.g. fig. 6.2) and range from 240° to 30° in longitude and from -50° to +50° in latitude. More than half of this region, which is also the most important part for the analysis of the ambient ISM of Sco-Cen, has not been covered by PAN-STARRS 1 nor 2MASS, which is almost the whole fourth Galactic quadrant.

But for the available sight lines, the total map reveals distinct filamentary structures on small- and large scales. One prominent filament on the northern sky, covering longitudes from 340° to 20° and latitudes 30–60°, is the counterpart of feature V that has been identified in the integrated H I maps (fig. 6.1).

To highlight the distances where new emission arises, also differential maps are computed that just contain the reddening added up to the respective distance bin. A multi-plot of these maps, covering distances from 79 pc to 398 pc, is shown in figure 6.4. It can be seen that the arc corresponding to feature V is already present at the nearest distances and hence can be assumed to be a very local feature. This insight is important for the discussion in section 6.5.2.

If the features that are present in these maps are also present in H I, they serve as a distance limit because it is probable that both trace the same cloud. The inversion of this argument is not made, because there might be regions of low gas to dust ratios, especially at high latitudes and the distance to the H I cloud can be overestimated. Detailed inferences of these maps and the H I shells are made in section 6.5.

[4] The complete fits files with a total size of 4.5 GB are available on http://argonaut.skymaps.info/usage. Full information about the compilation are provided in Green et al. (2015)

[5] The available sight lines are marked by ”non reliable distance“ and ”reliable distance“. For the analysis in this work, also sight lines of non reliable distances have been used, since it is dealt with large scale structures (+10°), containing hundred thousands of sight lines, which is a high enough statistic so that some outliers do not affect the results significantly.

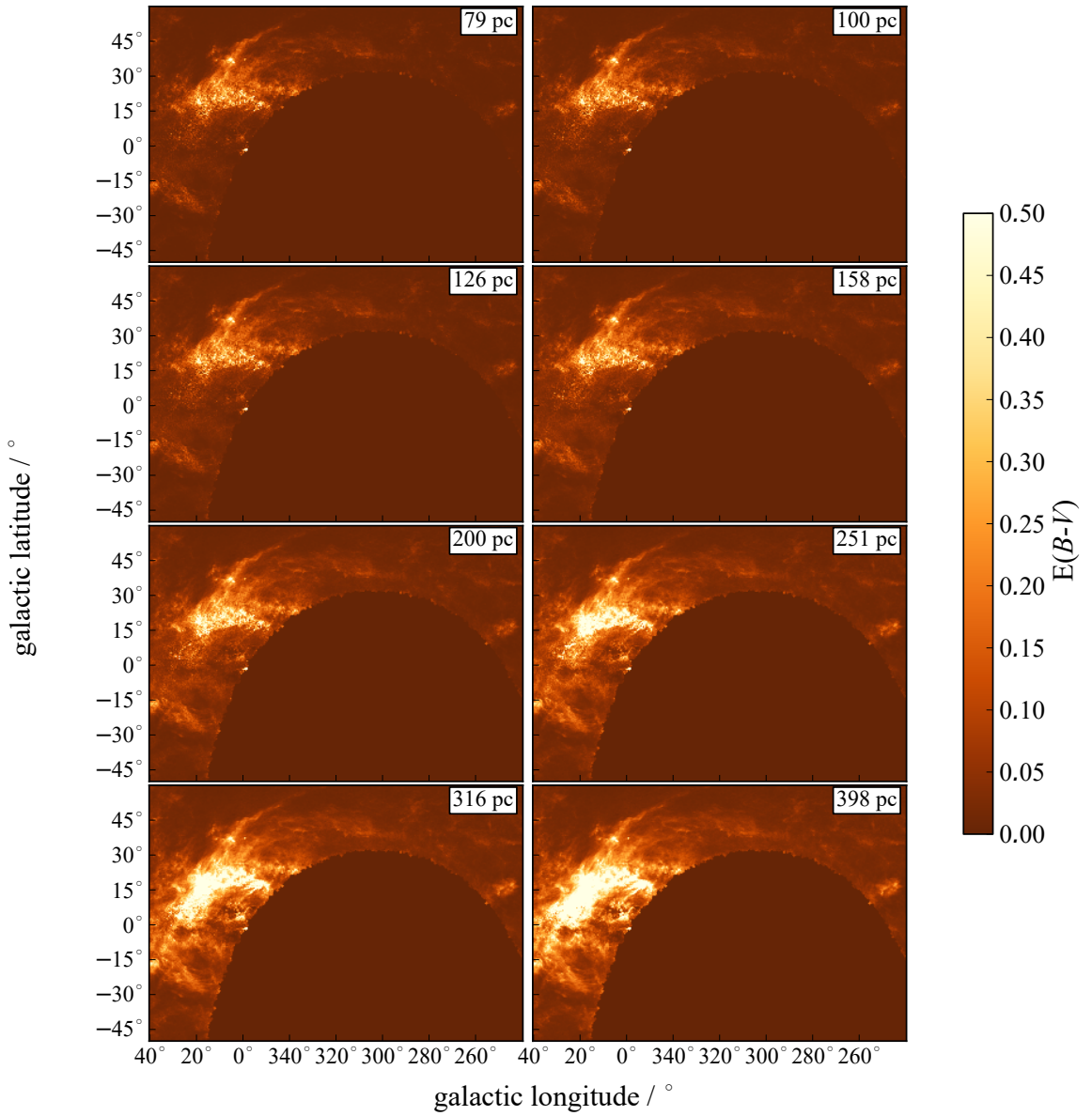

Figure 6.4: Integrated maps of interstellar reddening induced by dust of distances between 79 pc and 398 pc from top left to the bottom right. The color bar denotes the reddening in units of magnitudes of $E(B-V)$. Maps have been produced in this work using data from Green et al. (2015).

6.2 Analysis of cavities near Scorpius Centaurus

Here, the investigation of each individual channel map of the GASS data between velocities -30 km/s to +20 km/s is presented[6]. The angular size, the center positions and the velocity extent of the detected cavities, which are embedded by the above detected features I-XV, which again partly belong to H I shells, have been determined. To achieve this a combination of visual investigations and algorithms has been used. For the visual investigation part of the analyses, the assessment criteria, defined in section 3.4.3 have been applied[7].

In the following, the visual investigation of the H I data is presented in section 6.2.1. Then in section 6.2.2, the Hough-transformation from chapter 4 is also applied to the same data. The resulting detected cavities from both methods are then presented and discussed in section 6.2.3. In accordance to section 4.1 and 4.5, the terms circle, cavity, worm and shell candidate are used as descriptions for the detected structures in different slices and dimensions of the datacubes.

[6] This is a different velocity range than used for the integrated maps, since in these exact channel maps, the features are present. No distinct cavities have been detected in channels of higher positive or lower negative velocities.

[7] While the eye is strong at detecting patterns and complex structures, algorithms are better at determining the parameters of objects objectively. The attitude substituted here is that a combination of both methods is the best way to accurately detect and determine the parameters of the investigated H I structures.

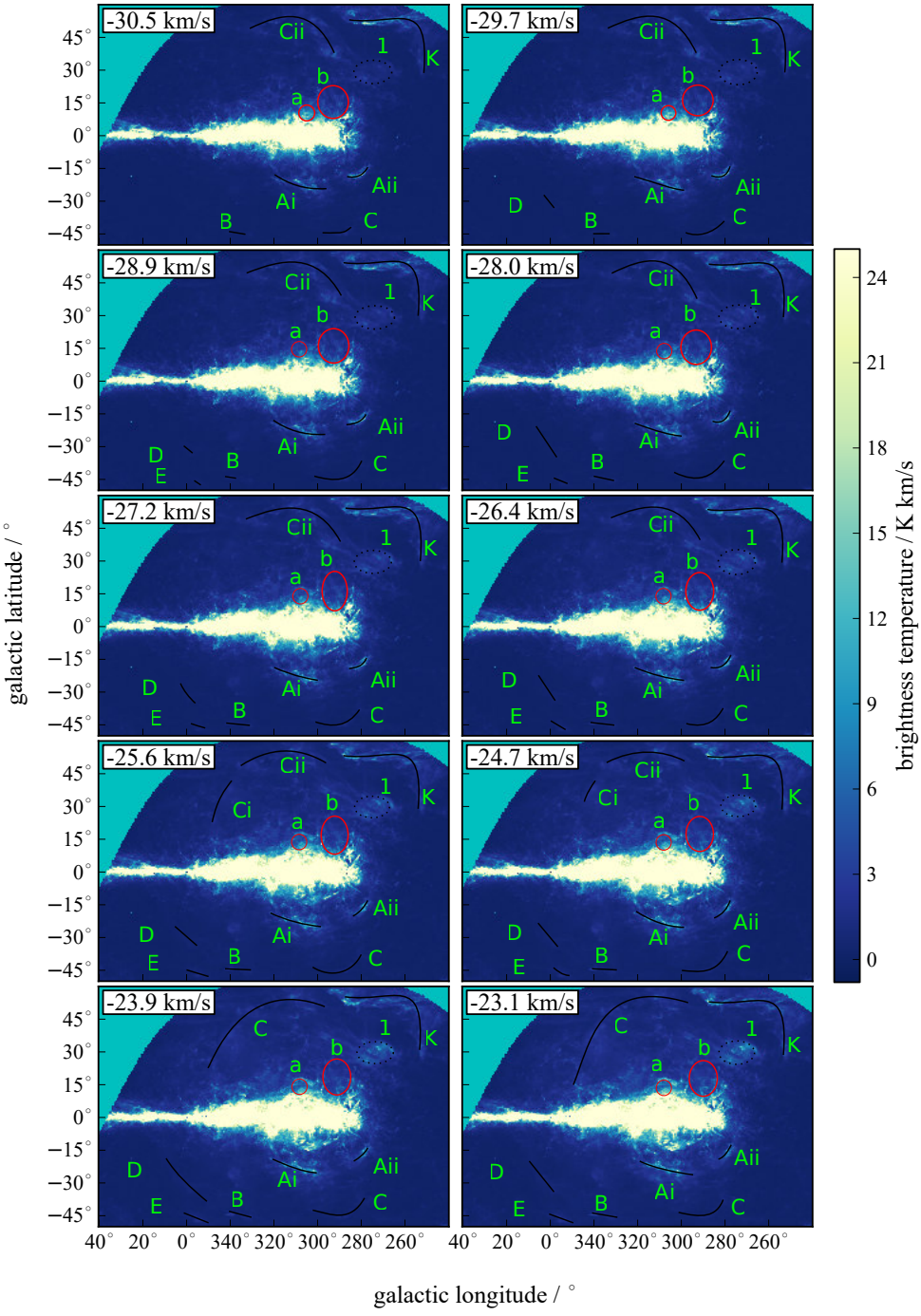

Figure 6.5: Mosaic map, showing the ISM of the same region around the Sco-Cen OB association for 10 consecutive velocity channels with increasing velocity from left to right and top to bottom, starting at −30.5 km/s -30.5 km/s. The colorbar shows the brightness temperature. The detected holes are illustrated by red circles or ellipses and are marked by lower-case letters. H I features are shown by black arcs and marked by capital letters. Some detected blobs or shells are illustrated and marked by dotted ellipses and marked with numbers.

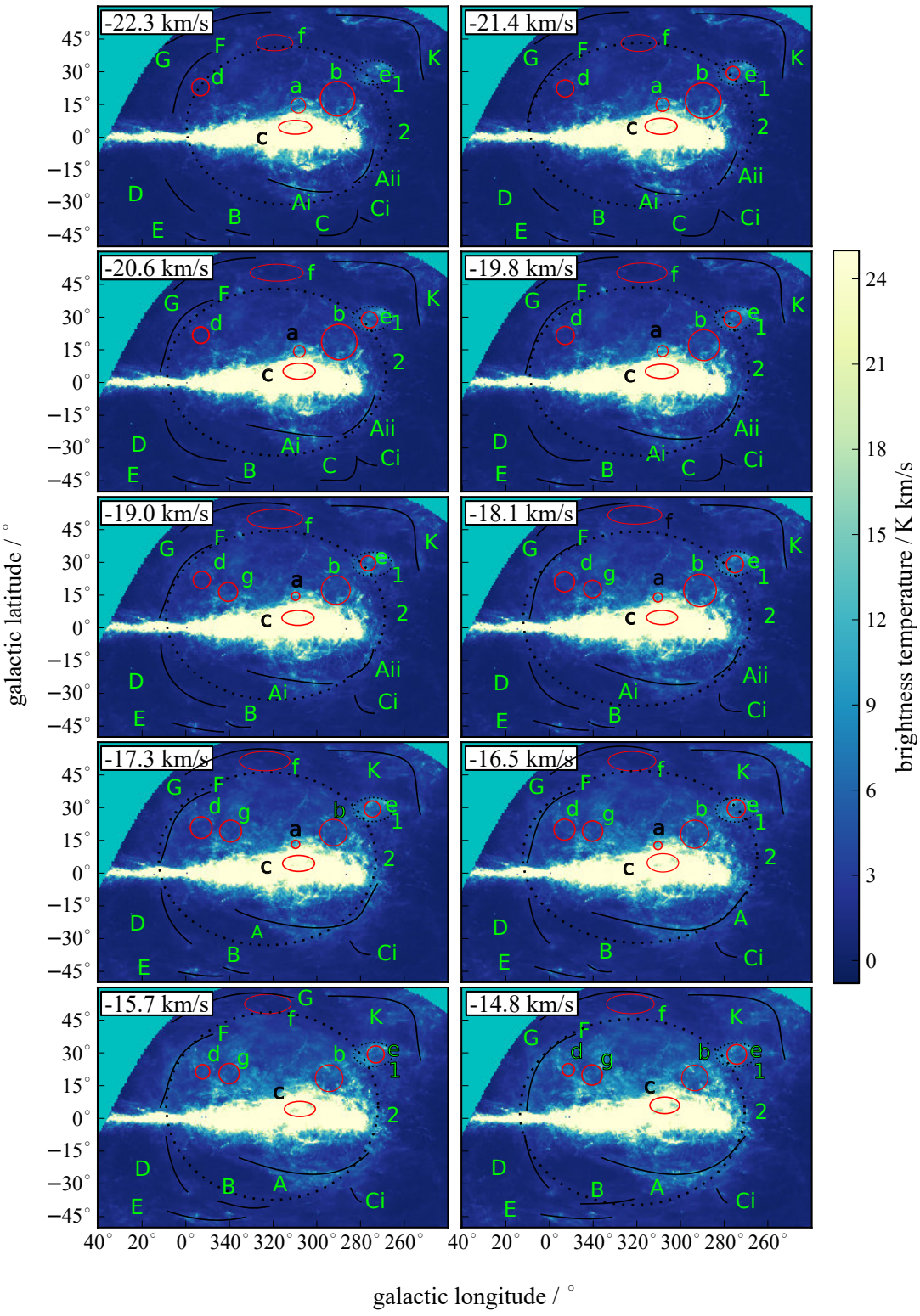

Figure 6.6: Continuation of figure 6.5 with the next 10 velocity channel maps. For more information see text.

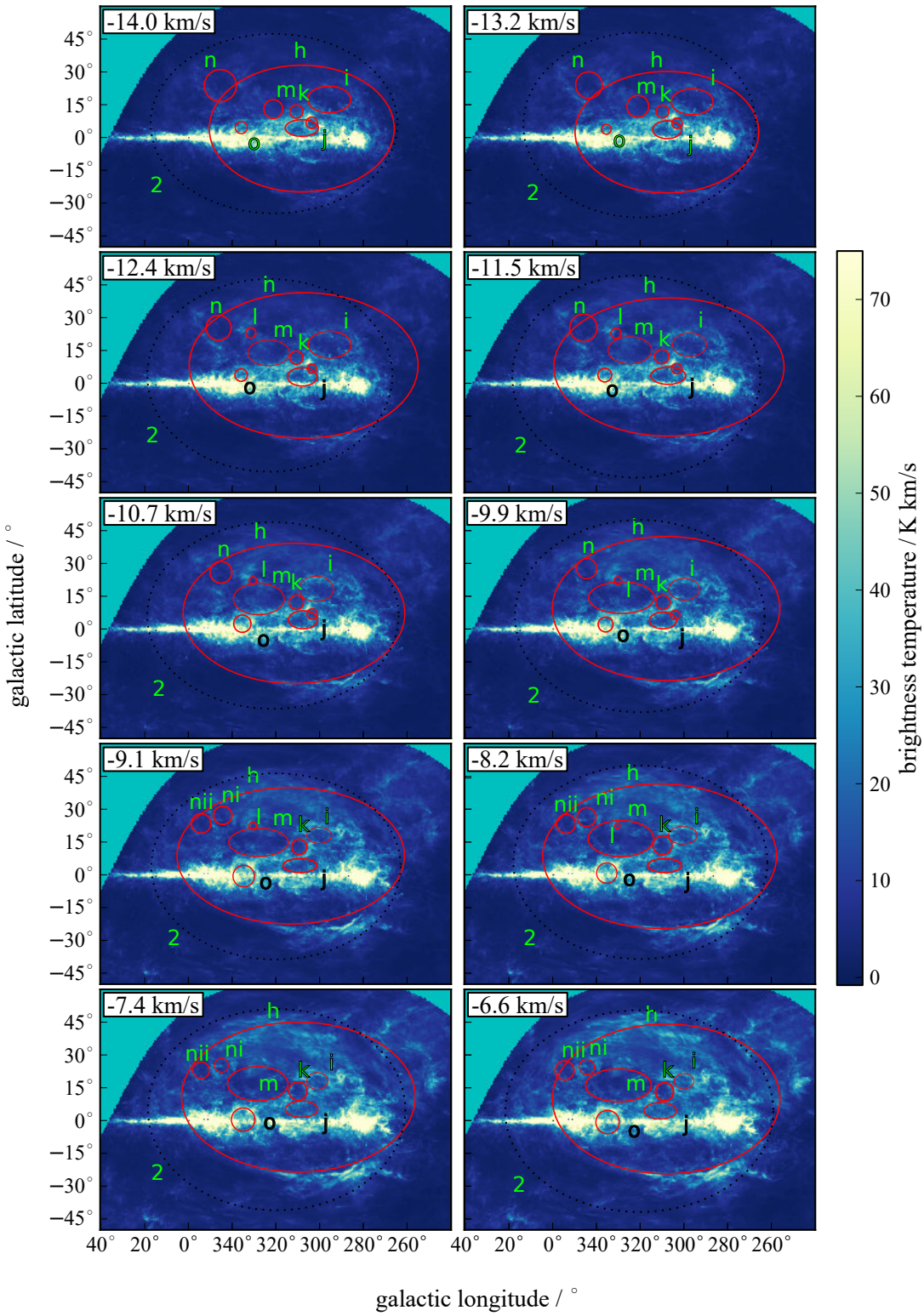

Figure 6.7: Continuation of figure 6.6 with the next 10 velocity channel maps and a different brightness temperature range.

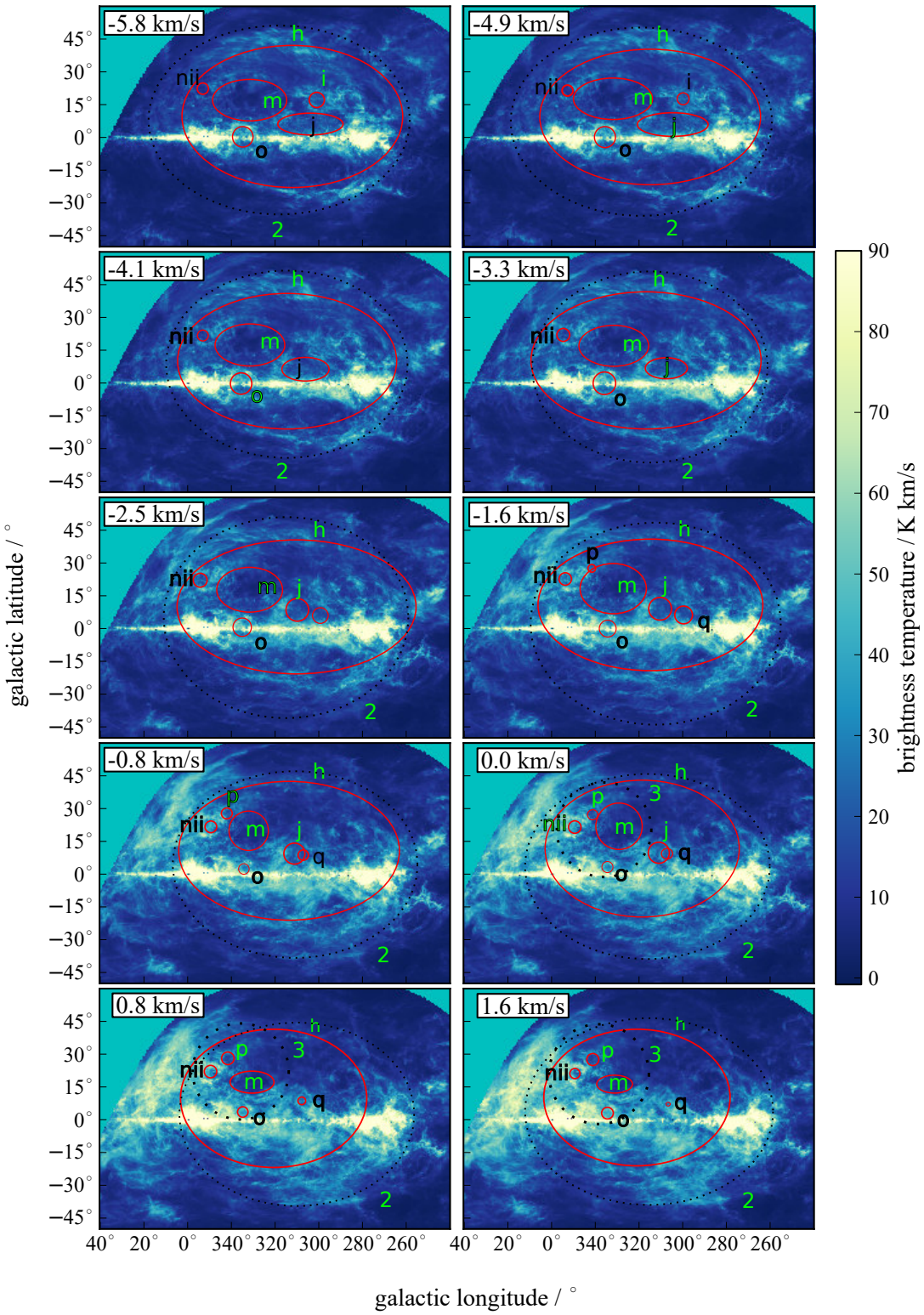

Figure 6.8: Continuation of figure 6.7 with the next 10 velocity channel maps and a different brightness temperature range.

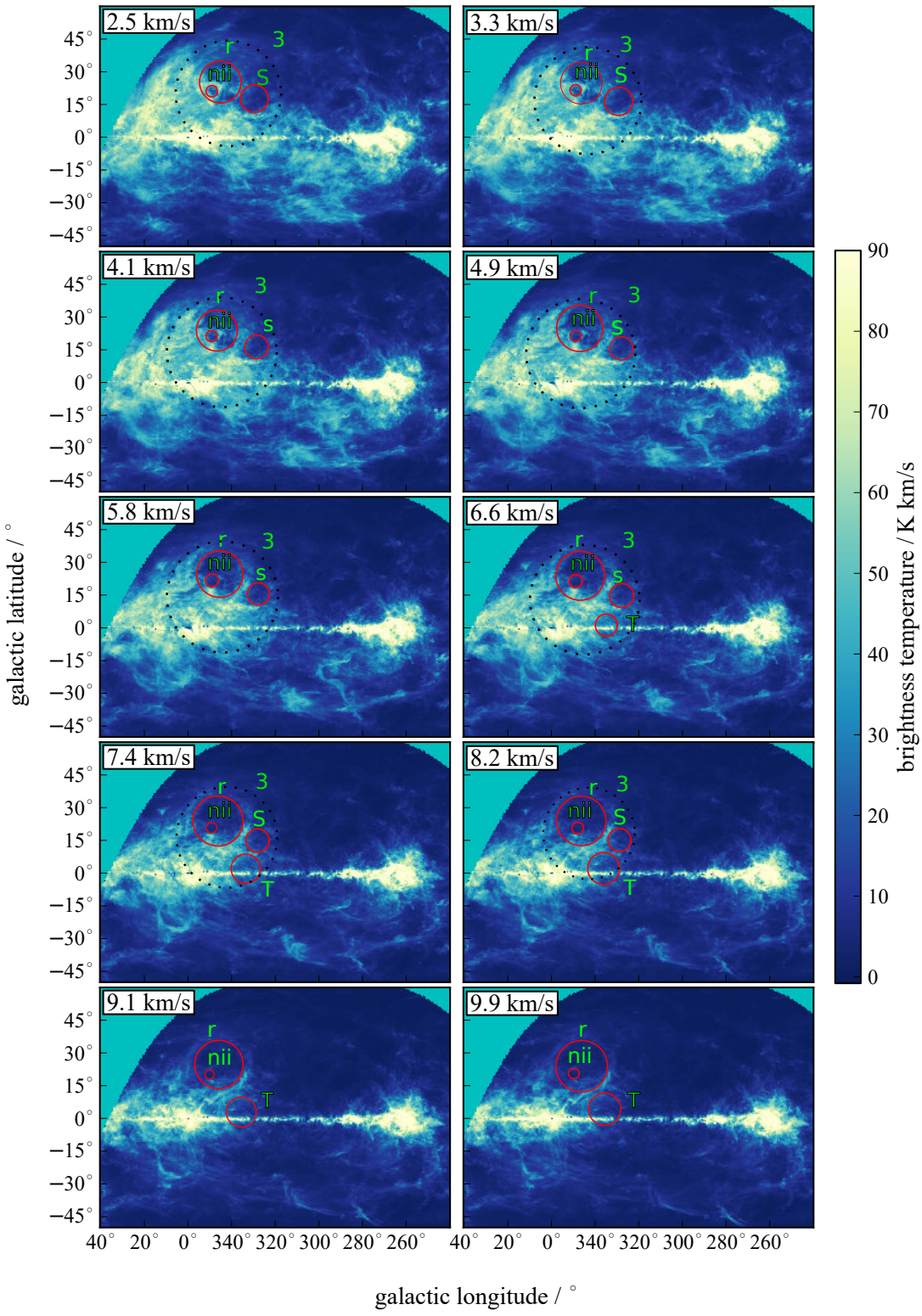

Figure 6.9: Continuation of for figure 6.6 with the next 10 velocity channel maps.

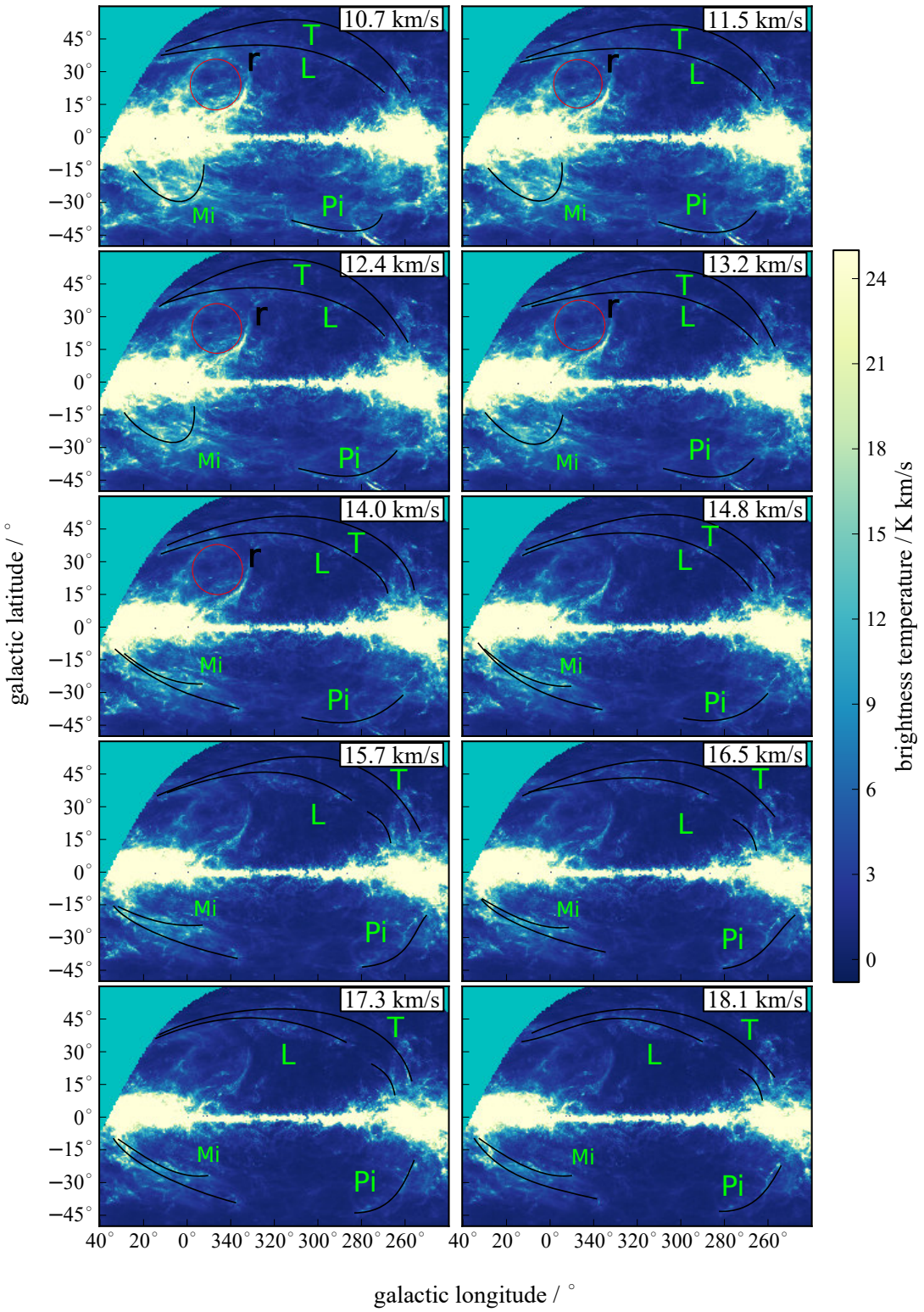

Figure 6.10: Continuation of figure 6.6 with the next 10 velocity channel maps.

6.2.1 Visual investigation

The interim results can be seen and are marked in figures 6.5 to 6.10. They include not only the final results but all cavity candidates, of which some do not fulfill both criteria 2.) and 3.) (section 3.4.3). For these figures, the maximum intensity value for the color bar has been chosen so that most of the cavities and features are visible in the related velocity channels. Especially for the most negative- and positive velocity channels, the maximum intensity of the color bar is set very low compared to the highest value (152 K for this data cube in one channel map with spectral width 0.8 km/s), highlighting fainter features that would otherwise be overshadowed by the emission of the Galactic disk. The data itself have been analyzed, using at least three different intensity ranges, that are 0–25 K km/s, 0–50 K km/s and 0–75 K km/s with the exception of the channels containing the highest intensities where the data are also analyzed for the range 0–90 K km/s[8].

In addition to the detected cavities, the most striking arcs that are detected, some of which are parts of the features I–XV from section 6.1 and are probably the corresponding clumps of the shells that surround the cavities, are labeled and included in these figures. These arcs, blobs or thick large clouds are indicated by black lines and marked by capital letters (green or black, depending on the background color). The cavities are marked by lower case letters and are indicated by red circles or -ellipses. For the largest features, almost describing a full circle or ellipse itself, which are suggested to be parts of shells, the outer edges are traced and marked by black dashed lines and labeled with numbers.

In some parts of H I data, too many features, arcs and cavities have been identified to illustrate them in one plot. In these cases the plots are split into two figures, one containing the features and arcs and another one showing the cavities. These are figures 6.7, 6.8 and 6.9. Plots including the cavities and the arcs at the same velocity channels are listed in figures B.0.37, B.0.38 and B.0.39 in appendix B.

Cavity candidates The circles, defining edges of cavities of consecutive channel maps, are connected to worms if they are close to each other in the sense of the definitions of sections 4.5. If multiple circles fulfill this criterion, the closest and best fitting ones are chosen to be connected.

Cavities (circles in the image) of different velocity channels that belong to the same worm are marked by the same letter in the tables and figures. All worms are listed in table A.0.13 in appendix A. Table 6.2 is a summary of the minimum, mean and maximum parameters of each worm, where each row contains the parameters of one worm.

Center coordinates and radii For each cavity, table 6.2 lists the mean center coordinates l_0, b_0 and their standard deviation Δl_0 and Δb_0, the mean-, minimum- and maximum radius ($r_{\mathrm{av}}, r_{\mathrm{min}}, r_{\mathrm{max}}$) in case of circles and the mean-, minimum- and maximum semi major- and minor axes ($a_{\mathrm{av}}, a_{\mathrm{min}}, a_{\mathrm{max}}$ and $a_{\mathrm{av}}, a_{\mathrm{min}}, a_{\mathrm{max}}$) and its uncertainties Δr_{av} and Δa_{av} in case of ellipses. This table also includes the minimum- and maximum velocities, v_{min} and v_{max}, where the cavity is detected as well as an estimated center velocity (v_0) of the cavity.

Center- and expansion velocities According to the description of section 3.4, if the worm belongs to an expanding spherical-like structure, the radius would increase towards the median of the velocity channels of the worm and would be the smallest at the minimum- and maximum velocities of the worm. But as was also discussed in section 2.4.2 and 3.4, the homogeneous expansion is an idealization and

[8] The effect of different intensity ranges can be revisited in fig 3.9 and text in section 3.3.

can be more complex in reality, especially for younger shells. This is why for the estimation of the center velocity, the channel of maximum radius and maximum intensity have been estimated to be its center source of the shell. Because of the possible asymmetries in the shape of a shell, for some cases the center velocity had been determined to be at different velocities than $v_{\mathrm{min}} + 1/2 \cdot (v_{\mathrm{max}} - v_{\mathrm{min}})$. There are some cases where it is not possible to determine a center velocity because the worm has multiple peaks at different velocities (see in table 6.2, columns 13, 14 and 15). The level of uncertainty in velocity is based on the characteristics of the velocity channel with the peak radius and the ones of the neighboring channels plus the systematic uncertainties. The systematic uncertainties stem from the estimation of the minimum- and maximum velocity channels that contribute to the shells and are at least the resolution uncertainties of the bin-widths of the two channels, which is 1.13km/s.

If the determined center velocity is near the mean velocity within ±20% of the total range, the expansion velocity (v_{exp}) can be estimated by $0.5 \cdot \left|v_{\mathrm{min}} - v_{\mathrm{max}}\right|$. The velocity range v_{min}–v_{max} of columns 14 and 15 of table 6.2 represent always minimum limits for the expansion velocity of the shell candidate, because with this method, the approaching- and receding caps of the shells that are expected to represent the real minimum- and maximum radial velocities values of the shell are not included. In most cases for the main shells of Sco-Cen it is not visible in the H I data.

1	2	3	4	5	6	7	8	9	10	11	12	13	14	15	16
n u:	l_0 /°	b_0 /°	r_{av} /°	a_{av} /°	r_{min} /°	a_{min} /°	r_{max} /°	a_{max} /°	Δr_{av} /°	Δa_{av} /°	Δlb_0 /°	$v_{0,\mathrm{est}}$ km/s	v_{min} km/s	v_{max} /°	Δv /°
a	307.8	13.4	3.1		1.9		3.7		0.7		1.9	-21.4	-30.5	-16.5	1.39
b	291.2	17.1	6.9	7.5	5.8	5.9	8.2	9.0	0.7	0.9	4.0	-20.4	-3.5	-16.5	1.39
c	307.9	4.8	6.9	7.4	6.8	3.1	7.7	4.2	0.2	0.3	0.9	-17.3	-22.3	-14.8	1.39
d	352.6	21.4	4.1	4.0	2.9	2.8	5.0	4.9	0.7	0.7	1.1	-17.3	-22.3	-14.8	1.39
e	274.4	29.1	29.1	3.8	28.4	3.1	4.5	4.5	0.4	0.4	1.1	–	-21.4	-14.8	1.13
f	320.0	47.9	11.1	4.2	8.2	3.7	12.8	4.5	1.6	0.3	4.6	-19.0	-22.3	-14.8	2.26
g	339.9	18.7	4.6	4.6	4.1	4.0	12.8	5.1	0.4	0.4	1.5	-17.3	-19.01	-14.8	2.26
h	312.1	8.9	50.1	31.2	42.4	25.0	55.3	34.1	4.2	2.1	5.0	–	-14	1.6	1.13
i	298.4	17.6	6.7	4.6	2.8	2.7	10.0	6.2	2.5	1.2	2.2	-10.7	-14	-4.9	1.13
j	307.9	5.6	8.1	4.4	4.8	3.2	16.4	5.5	3.3	0.7	3.0	-4.9	-14	0.0	2.26
k	309.6	12.4	3.6	3.6	3.0	2.9	4.4	4.5	0.5	0.5	0.9	-8.2	-14	-6.6	2.26
l	330.5	22.4	1.9	1.9	1.2	1.2	2.4	2.3	0.4	0.4	0.6	-8.2	-12.4	-8.2	2.26
m	328.5	16.3	5.9	7.8	4.4	4.2	18.3	11.4	3.9	2.2	4.1	-1.6	-14	1.6	2.26
ni	344.7	25.4	5.1	5.1	3.2	3.2	7.6	7.5	1.4	1.4	1.5	–	-14	-6.6	1.13
nii	350.2	21.3	2.9	2.9	2.1	2.1	4.0	4.0	0.4	0.4	1.3	–	-11.5	2.5	1.13
o	335.0	1.7	3.9	3.9	2.3	2.2	5.4	5.4	1.1	1.1	1.6	-6.6	-14	1.6	2.26
pi	303.1	6.6	2.4	2.3	2.1	2.1	2.7	2.6	0.2	0.2	0.3	–	-14	-9.9	1.13
p	341.4	27.5	2.5	2.5	1.8	1.8	2.9	2.9	0.4	0.4	0.5	–	-1.6	1.6	1.13
q	304.2	7.8	2.6	2.5	1.0	0.9	4.1	4.1	1.1	1.2	4.4	-1.6	-2.5	1.6	0.80
r	346.2	24.4	11.0	10.9	9.5	9.4	11.9	11.8	0.8	0.8	1.0	7.4	2.5	14	1.13
s	328.3	15.7	5.7	5.6	5.2	5.1	6.5	6.4	0.5	0.5	1.2	4.9	2.5	8.2	1.13
t	335.0	2.5	6.8	6.7	5.1	5.0	7.5	7.3	1.0	0.9	1.5	8.2	6.6	9.9	2.13
u	349.4	3.9	2.8	2.8	2.6	2.5	3.0	2.9	0.2	0.1	0.4	–	10.7	17.3	3.13

Table 6.2: Summary of the parameters of the visually detected cavities in the ISM of the region around Sco-Cen from table A.0.13 in the appendix. Each row contains the parameters of one cavity. The first column contains the name of the feature. Columns 2 and 3 list center coordinates l_0, b_0 of the cavity. column 4 lists either the mean radius or mean of the semi minor axis (both called r_{av}). Column 5 lists the mean semi major axis a_{av} (or the radius again). This is depending on the shape of the cavity that has been determined and is listed in table A.0.13. Columns 6–9 give the minimum- and maximum respective values of the cavity. The uncertainties of the radius and semi axes and center coordinates are listed in columns 10–12. Column 13 contains the estimated center velocity of the cavity if possible. The columns 14 and 15 give the velocity extent of the cavity. The uncertainty of the center velocity is listed in column 16. If no center velocity is available, the minimum uncertainty is listed.

Outer edges of large shell-like features The same visual procedure that is used to detect cavities is also used to determine the outer edges of the largest structures, i.e. the outer edges of the shell candidates. This is important for the final parameters of the shells, since the angular thickness of very large structures can reach sizes up to 10° and have different thicknesses at different locations. The largest shells that surround, or embed, most cavities are listed in table 6.3. These are three ellipsoid-like features of which two are assumed to be connected to the stellar clusters of Sco-Cen. Feature 1 (e.g. fig. 6.5) has no real connection and its center coordinates are off, compared to Sco-Cen and no physical connection could be made. The feature is listed since it fulfills all criteria for a cavity but most likely belongs to a different source and is not investigated further in this work.

The largest one is feature 2 that surrounds the UCL stellar sub-group of Sco-Cen and has a semi major axis of 55.1°. It is present in at least 29 channel maps, corresponding to a visible velocity width of 23.3 km/s. It is enclosing the cavity-*h* as can also be seen in the figures 6.5 to 6.7. The other striking shell candidate is the ring-like feature 3 around USco, which has a radius of 24.4° and is enclosing cavity-r. The source of these features is defined and discussed in more detail in section 6.2.3. Beforehand, the cavity parameters are analyzed using the specialization of SAGHIS for this region of section 4.5.3.

1	2	3	4	5	6	7	8	9	10	11	12	13	14	15	16
nm	l_0	b_0	r_{mean}	b_{mean}	r_{min}	b_{min}	r_{max}	b_{max}	Δr	Δb	Δl_0	v_0	v_{min}	v_{max}	Δv
Unit	/°	/°	/°	/°	/°	/°	/°	/°	/°	/°	/°	/ km/s	/ km/s	/ km/s	/ km/s
1	273.8	29.3	8.8	29.3	8.1	4.9	9.6	5.9	0.4	0.3	0.6	-20.6	-30.5	-16.5	1.7
2	318.0	5.1	55.1	42.1	47.2	36.0	61.8	46.1	2.3	1.5	3.7	-6.6	-22.3	1.6	2.4
3	341.2	16.8	24.4	16.8	21.2	20.9	27.2	26.9	2.2	2.1	5.2	5.8	0.0	8.2	1.7

Table 6.3: Similar to table 6.2, but containing the parameters of the shells, detected in the figures 6.5 to 6.10 and the summary of the results listed in table A.0.10 in the appendix. Column 1 contains the name of the shell as numbers. The meaning and description of the other columns is the same as in table 6.2.

6.2.2 Cavity detection with automated methods

Here the specialized H I shell search algorithm of section 4.5.3 is applied to the ISM in the region of Sco-Cen in the same angular range as the visual investigation from above was carried out. A subset of the H I data around the center coordinates of the visually detected shells is taken and the algorithm is applied to this image to specify the parameters of the shell objectively. The results are listed in table 6.4.

If comparing the results to the one of table 6.2, it can be seen that for most cavities, there is a good accordance between the visual- and the automated detections. The automated application of the algorithm was more efficient in the application compared to the time consuming manual investigation. But due to the limit of the Hough Transformation for circles for the shape of the objects, the determination of the center coordinates has higher uncertainties for the automated approach (see row 11 of tab. 6.4). The algorithm on the other hand is more robust in detecting the minimum and maximum channels where the cavity is present. That is why for the following analyses, the center coordinates, radii and center velocities from the visual method are adopted, while the velocity ranges from the algorithm are adopted if both results do agree within the uncertainties.

1	2	3	4	5	6	7	8	9	10	11	12	13
nm	l_0	b_0	r_{mean}	r_{min}	r_{max}	$v_{0,\mathrm{est}}$	v_{min}	v_{max}	Δr	$\Delta l_0/b_0$	Δv	fl
unit	/°	/°	/°	/°	/km/s	/km/s	/km/s	/km/s	/°	/°	/°	-
a	305.61	10.16	1.29	0.96	2.89	-22.05	-33.05	-14.05	0.58	2.51	1.39	(2)
b	296.72	12.30	4.36	0.96	4.82	-33.05	-33.05	-14.05	0.95	5.51	1.39	(3)
c	302.29	5.08	6.05	5.30	6.75	-21.21	-23.21	-10.21	0.58	1.72	1.39	(2)
d	345.67	16.56	2.96	2.41	4.58	-20.21	-23.21	-10.21	0.67	3.25	1.39	(4)
e	275.11	28.77	3.80	3.61	4.10	-13.57	-21.57	-10.57	0.20	1.31	1.13	(1)
f	312.53	34.61	3.86	2.81	7.15	-22.21	-23.21	-10.21	1.27	10.07	1.39	(3)
g	338.00	12.99	3.45	2.41	4.82	-12.57	-21.57	-10.57	0.72	5.11	1.39	(3)
j	308.85	0.18	4.08	3.21	8.03	-5.19	-14.19	2.81	1.49	10.67	2.26	(3)
k	307.38	11.65	3.68	3.05	4.26	-9.19	-14.19	-4.19	0.50	1.27	1.13	(1)
ni	345.16	23.60	2.75	1.85	3.77	-3.73	-11.73	-2.73	0.54	2.80	1.13	(2)
nii	349.55	21.09	2.55	2.25	2.89	-1.19	-14.19	2.81	0.22	1.70	2.26	(1)
o	334.35	0.18	2.37	1.61	4.50	4.81	-14.19	4.81	0.82	5.89	1.13	(1)
p	342.47	28.18	3.10	1.77	2.73	0.29	-2.71	1.29	0.36	2.29	1.13	(1)
q	303.25	5.81	1.74	1.20	2.41	-0.71	-2.71	2.29	0.46	2.16	0.80	(1)
r	348.84	21.95	11.06	9.24	11.89	7.39	1.39	16.39	0.83	3.67	1.13	(1)
s	335.29	18.73	5.39	5.06	6.02	3.21	2.21	9.21	0.40	5.27	1.13	(2)
t	339.61	-0.42	4.75	2.49	7.07	10.31	6.31	10.31	1.77	3.09	2.13	(3)
u	351.95	2.28	2.70	2.57	2.89	12.23	11.23	16.23	0.12	2.14	3.13	(1)

Table 6.4: Summed up results from the application of the pattern recognition methods of sections 4.1 and 4.5 of table A.0.14. The first column contains the name of the feature, column 2 and 3 list the mean center coordinates l_0, b_0. Column 4 contains the mean radius r_{mean} of the cavity. Columns 5 and 6 contain the minimum- and maximum radius of the cavity, r_{min} and r_{max}. $v_{0,\mathrm{est}}$ that denotes the center velocity, which is estimated by the velocity channel where the radius of the cavity is the largest, is listed in column 7. The minimum- and maximum velocities v_{min} and v_{max}, where the cavity is present, are listed in columns 8 and 9 respectively. In columns 10, 11 and 12, the uncertainties of the angular radius Δr, the ones of the center coordinates $\Delta l_0/\Delta b_0$ as well as the velocity uncertainty Δv are listed, respectively. In column 13, a flag (fl) is listed. See text for more information

6.2.3 Connection between the cavities and the stellar groups

Here the main cavities from tables 6.2 and 6.4 and figures 6.5 to 6.10 that fulfill all detection criteria from section 3.4.3 and 4.5.3 for both, the automated and visual analyses are presented and connected to the stellar subgroups of Sco-Cen if possible.

Cavities near LCC The mean center coordinates of cavity-c are $l = 307.9^\circ, b = 4.8^\circ$. While the center is 7° off compared to the center LCC, the stellar group is completely embedded in this ellipsoid-like cavity that has an angular maximum semi major of 7.7° along the Galactic longitude. It is also striking that a region of low density that is surrounded by a high density region is present this close to the Galactic plane without being dominated by background emission from the disk or other nearby sources.

Cavity-a has a smaller angular size ($r = 3.1^\circ$) and lies above the LCC group, and above cavity-c, and has a latitude of $b_0 = 13.4^\circ$ at the same velocity channels −22.3 to −14.8 km/s (fig. 6.6). cavity-k might be connected to cavity-a as it has similar center coordinates but larger radii and is detected at higher positive velocities. At the velocity channels −14.0–0.0 km/s, cavity-j is visible at very similar center coordinates ($l_0 = 307.9^\circ, b_0 = 5.6^\circ$) as cavity-c, but the coordinates of cavity-a are not well reflected by the results of the HT-method. Still, these two objects should belong to the same cavity. And hence the total velocity extent of the cavity enclosing the LCC group should be −22.3 to 0 km/s.

Cavity-i is present in the same velocity channels at even higher latitudes with center coordinates of $l = 298.4^\circ$, $b = 17.6^\circ$. It is part of a larger feature, which includes multiple small cavities such as cavity-b and -k. Especially cavity candidate-i and -b might not be formed by stellar feedback but being the results of overlapping clouds or also random projection effects since the former one was not even detected by the HT and the second one has different parameters compared to the results of the visual analysis. The center coordinates are also too high above the LCC stellar group and too far away from the other subgroups of Sco-Cen to be formed by their stars. Hence cavitiy-i and -b have been ejected for the analysis presented below. To conclude, the most striking cavity is cavity-c. Its parameters have been adopted for the further analyses of the LCC-shell.

The large UCL-cavity Cavity-h is the largest cavity. It has an ellipsoid-like shape in the datacube and spreads over 110.6° degree in longitude and 68.1° in latitude. Its center coordinates are $l = 312.1^\circ, b = 8.9^\circ$. The absolute systematic uncertainties that contribute to the uncertainties of the parameters are high on the one hand because the shell is large and on the other hand because the cavity is not fully closed, contains other shells and cavities, like all other Sco-Cen cavities, has components above and below the Galactic disk emission and itself is embedded into many large arc-like H I clouds. At some positions, the borders of the cavity are well defined, as at the enclosing feature I (sec. 6.1). At different positions they are not well defined, e.g. at the south-western part as can be seen in fig 6.7 as well as the part that is limited by feature XI. Overall this cavity should belong to the large UCL-shell that is also directly tracked by the features that are marked in the figures 6.5 to 6.10 and are also listed in table 6.5.

Small cavities near USco Cavity-d, -n, -ni and -nii are smaller cavities that are very close to each other in projection and might be connected to each other (figures 6.6 to 6.10). They are surrounded by the larger cavity-r and the belonging ring that traces the USco-loop. But these smaller cavities are present up to more negative velocities (-22.3 km/s) than the larger features, which suggests a

higher expansion velocity[9]. The circle-like H I shell that encloses these cavities is named USco-tunnel hereafter because it has a cylindrical, more specifically, a slightly conical shape in the datacube and differs from the typical ellipsoid-like shape that is expected for the idealized model of an expanding shell (sec 3.4). The parameters of the USco-tunnel are defined according to the cavities here, where cavity-nii is the most striking with center coordinates and extents, surrounding the remaining B-stars of USco in projection and also visible at the same velocities as the moving velocities of the stellar group.

The larger cavity near USco Cavity-r has mean center coordinates of $l = 346.1^\circ, b = 24.2^\circ$, which are similar to the center coordinates of the USco stellar group. The corresponding shell clouds (*Qi*, *Qii* or feature X) form a ring with decreasing density towards higher latitudes and with a radius towards the inner edges (radius of cavity-r) of 11.9°. Its center velocity lies at +7.4 km/s and the cavity has been from +2.5 to +14.0 km/s (see table 6.2 and 6.4). Cavity-r represents the inner edges of the H I shell that has been introduced as the USco-loop (section 2.5.1).

Cavities between USco and UCL The USco-loop shows a region of high density at the coordinate ranges $l = 320^\circ$–340° and $b = 12^\circ$–17°. Cavity-s lies in the south-east compared to this high density region, while cavity-t is located south compared to the USco-loop. It is possible that the collision of the shells belonging to cavity-r, -s and -t formed this region of high density, where ongoing star formation is observed (Lupus I complex, see e.g. Gaczkowski et al. (2015, 2017)). But cavity-s and cavity-t might also be the results of projection effects, which is confirmed by the analysis of the extinction maps, presented below. On top of that these two cavities are also small compared to the main shells and would hence be even younger. While cavity-t is not connected to any of the subgroups, cavity-s might be formed by one or a few stars from UCL but can be neglected for the following analyses since it would just be important for a small scale analysis of the star forming complex and does not contribute noticeably to the overall gas kinematics. Hence cavity-s and -t are not discussed further.

The rejected cavity candidates There are some cavities that show no connection to any of the subgroups of Sco-Cen in velocity or angular positions and do not fulfill the detection criteria 4.) or 5.) of the visual investigation criteria or are not detected using the automated methods from section 4.5.3. Namely these are cavity-f, which is located at very high latitudes, cavity-e that is also connected to cloud 1 (see fig. 6.5 and fig. 6.6) and cavity-m that does not fulfill criterion 5.). cavity-l, -p and -q might be younger small shells, formed by winds of single stars of Sco-Cen or again be random occurrences and have been neglected for the same reasons as stated above. Cavity-o is a noticeable region of low density near the Galactic plane. However it lies not near any of the three subgroups of Sco-Cen (criterion 4.)) and is not discussed any further[10].

[9] Towards higher positive velocities, the gas density decreases rapidly for this region and all shells seem to be "open" towards this spectral direction.

[10] Some of these excluded objects could be interesting different future studies and are hence included into the tables 6.2 and 6.4

6.2.4 Distance towards the cavities

In other studies, where Sco-Cen has been analyzed, as a first order of approximation, the distance towards the center of the respective stellar group has been estimated to trace the distance towards the center of the corresponding H I shells. But the center of a shell as it can be observed today and the origin of the shell do not have to be the same. This has two reasons. The first one is that the stellar groups move with a different center velocity than the gas particles (Mackey et al. 2015; Townsley et al. 2014), even after time spans of 1 Myr, which is less than the age of most expanding shells in the region. The other reason is that the expansion of H I shells is not symmetric in most cases. This is why here the color excess maps from Lallement et al. (2014), introduced in section 2.2.1 have been used as another independent distance estimation. With the angular sizes of the cavities and shells derived from the H I data, a comparison has been made to the regions of high- and low extinction in these maps.

The extinction maps, especially the available vertical plane cuts that are separated by 15° in longitude, are the main source that have been investigated to estimate a distance to the center of the shell D_0 in the line of sight if possible (figures B.0.40 to B.0.43). In cases where it is not possible to find accordances between extinction- and H I pattern, no distance assumption is made. All resulting distances to the centers of the cavities and shells explained in the following are listed in a sum up in table 6.10 in section 6.5.

The distance uncertainties have been calculated, based on the following known uncertainties. For the color-excess map uncertainties, the only values that are known is the range of 10 pc close to the Sun up to 100 pc at 1 kpc distance (see Lallement et al. (2014)). If a linear increase is assumed, this gives relative uncertainties of 10 % of the respective distance value. The uncertainties that arise from estimating the distance to the center in the maps itself, have been estimated to be around 10 pc.

Distance to the USco-loop The cavity of the USco-loop, denoted as "2" in figure B.0.43, which is a longitude slice, close to the center longitude of the cavity, is surrounded by multiple clumps of high opacity. This is in agreement to the H I data as it has a similar angular size and a similar center latitude. The distance to the center of this estimated cavity and the surrounding shell is measured to be 127 ± 15 pc.

Distance to the USco-tunnel It is assumed that the origin of the USco-tunnel lies in the USco group because of its striking correlation in angular projection with the remaining B-stars in the USco group. Using the region around the latitude inferred by the H I data, the measured distance to the origin of the USco-tunnel is 125±15 pc as shown by ring "1" in figure B.0.43. This distance is also consistent with the distance of the center of the USco-loop.

Distance to the USco-shell The analyses of the color-excess map suggest that the region of the USco stellar group is surrounded by multiple clumps in the vertical plane cut in figure B.0.43. The ring denoted as "3" in this figure marks the edges of the shell that could contain these clumps. On the other hand, these clumps might belong to the USco-loop or be randomly distributed in this matter. It is reminded that the presence of the USco-shell in H I is not as striking as in extinction maps (see sec 6.5.1). Nevertheless, the distance to the center of this shell is measured to 122.6±12.3 pc.

Distance to the UCL-shell The center longitude of the UCL-shell, inferred by H I is estimated to be $l_0 = 318° \pm 4°$ (see table 6.3). The color-excess vertical plane cut maps shown in figure B.0.41 and

B.0.42 (left hand side) for $l = 315$ and $l = 330$ respectively, have been used to identify a distance to the center of the shell and its cavity. For a shell of this size, asymmetries that have been already seen in the H I data, are expected. Hence the center of the shell (UCLe in fig B.0.42) might be at the same coordinates as the minimum intensity as stated above (see UCLd, fig. B.0.42). What is referred to as "center", here is the assumed origin of the shell, which is expected to lie at the minimum opacity region, i.e. a mean value between the center UCLa (fig. B.0.41) and UCLd. This distance has been measured to $D_0 = 135.1 \pm 13.5$ pc.

Distance to the LCC-loop In H I, the LCC-loop is characterized by the cavities listed in table 6.2. It is located near the Galactic plane with an elliptical shape and its center longitude is $l_0 \approx 308^\circ$. The color-excess map for the slice at $l = 300$ (fig. B.0.40) shows a cavity that is surrounded by high opacity clumps. The clump, located on top of the cavity, might trace the northern part of the corresponding H I cloud. The center has been inferred by the centers of the rings LCCa and LCCb in the figure B.0.40, which is 100±10 pc away from the Sun.

With the distance to the center of each shell and the determined angular radius, the physical sizes can be calculated as well as the masses, which is the topic of section 6.3.

6.3 Determination of physical parameters of the H I features and -shells

In the following the application of three different methods to determine the masses of the main H I shells in the vicinity of Sco-Cen are presented, the interim results are discussed and the determination of the ages as well as the kinetic energies of the shells are described.

6.3.1 Results of the H I mass determination approaches

Mass determination of the main features, detected in the integrated maps

Using equation 3.21, the masses, M_{feat}, of the features I–XI (section 6.1 and figures 6.1 to 6.3) have been determined. The features contain large fractions of the total H I shell mass in the region and serve as a direct comparison to the mass values that are determined with the methods below. M_{feat} determined here should be considered as lower limits since the features are just parts of the total shells. The shells, features and cavities as well as the distance limits used for the mass calculation are listed in table 6.5 if available. The calculated masses as well as the mass uncertainties can be found in columns 12 and 13. The results are discussed along with the other results below in section 6.3.2.

1	2	3	4	5	6	7	8	9	10	11	12	13
Shell	M-f.	Cavity	f.	D_{e}	D_{min}	D_{max}	flD_{min}	flD_{max}	V_{min}	V_{max}	M_{feat}	ΔM
-	-	-	-	/ pc	/ pc	/ pc	-	-	km/s	km/s	$M_\odot$	$M_\odot$
USco-	VII	r	Qi,Qii		0	123	-	-	-20	0	1847	370
loop	XI	r			100	157	1	1	0	10	1622	332
USco-	X	nii,n,d	-		74	141	1	1	0	10	1622	332
tunnel					0	0	-	-				
USco-		-	M		0	0	-	-	-	-	-	
shell		-			0	0	-	-	-	-	-	
		-			0	0	-	-	-	-	-	
UCL-	II	-	Cii,1		80	99	1	3	-30	-20	179	25
shell	III	-	Ai	-		-	1	-	-30	-20	129	26
	IV	-	Aii	-		126	-	1	-30	-20	451	90
	VI	h	Ai,Aii,	1	149	161	1	1	-20	0	3564	713
	VII	h,n	L-	1	1	123	-	1	-20	0	1847	370
	VIII	h	L,L$_i$,L$_{ii}$	1	1	99	-	1	-20	0	2074	415
	IX	h,i	L-			121	-	-	-20	0	2860	572
LCC-	-	j	1	100	1	121	1	3	-20	0	800	300
loop												

Table 6.5: Results for the main H I features and the shells they belong to. Column 1 contains the name of the shell, columns 2, 3 and 4 list the main features (M-f.) I–XI, cavities and channel map features that belong to the shell respectively. The Distance to the center of the cavity, determined using dust extinction maps if available, are given in column 5. The estimated minimum- and maximum distances, D_{min} and D_{max}, from the IS absorption lines (see sec. 6.1) are listed in columns 6 and 7. Columns 8 and 9 contain flags for the minimum- and maximum distances (see text, sec. 6.3). In columns 10 and 11, the minimum- and maximum velocities, where the features are present, are listed. The calculated masses for the main features and its uncertainties can be found in the columns 12 and 13.

Mass determination of the H I shells using integrated maps

Using the center coordinates, the angular radii, the velocity extensions from section 6.2 and the mean distances, derived from extinction data[11], the masses of the shells have been approximated by integrating the column densities within a circle of the largest angular radius of the shell along the respective velocity channels and by using equation 3.20. The results for the Sco-Cen shells are listed in table 6.6, where the total mass of each shell (column 1) is listed in column 2. $M_{\rm tot}$ is corrected by the mass induced by the developed background model from sec. 4.4.1 ($M_{\rm disk}$ in column 4) and the resulting shell mass $M_{\rm smax}$ is listed in column 5 of the table. The columns 6–9 list the uncertainties of the respective masses, which have been calculated using error propagation of the uncertainties from table 6.10.

This method overestimates the mass of the shells because it includes the mass of the cavity. Hence this mass estimation should serve as an upper limit for the masses but serves as an orientation for the modeled masses of section 6.3.1, which should not be higher.

1	2	3	4	5	6	7	8	9
Name	$M_{\rm tot}$	$M_{\rm cav}$	$M_{\rm disk}$	$M_{\rm smax}$	$\delta M_{\rm tot}$	$\Delta M_{\rm cav}$	$\Delta M_{\rm disk}$	$\Delta M_{\rm smax}$
Unit:	10^3 M$_\odot$	10^3 M$_\odot$	10^3 M$_\odot$	10^3 M$_\odot$	10^3 M$_\odot$	10^3 M$_\odot$	10^3 M$_\odot$	10^3 M$_\odot$
USco-loop	15.9	8.2	0.62	15.3	3.1	1.6	0.122	3.1
USco-tunnel	2.4	1.3	0.03	2.3	0.5	0.3	0.006	0.5
USco-shell	27.6	6.2	7.8	19.8	5.6	1.3	2.121	5.8
UCL-shell	216.1	174.3	91.5	124.6	40	32.3	16.944	43.4
LCC-loop	5	1.7	1.9	3.1	1.3	0.4	0.475	1.4

Table 6.6: Integrated masses of the H I data from the GASS for the regions of the five Sco-Cen shells. Column 1 lists the total integrated mass of the region without background correction. The mass that is contained up to the maximum radii of the cavities are presented in column 2. Column 3 contains the modeled background emission that is calculated from the data using the Hill function and the parameters, determined in section 4.4.1. The final shell mass that has been determined by $M_{\rm tot} - M_{\rm disk}$, is shown in column 4. The columns 5 to 8 contain the respective uncertainties of the values.

Masses determination of the H I shells by model fitting

The EHSS-model from section 4.2 has been applied to the USco-loop, the USco-tunnel, the USco-shell and the LCC-loop to fit the masses of the shells. The other model parameters have been fixed and given by the analyses from above and are also listed in table 6.10, introduced below. It has not been applicable to the UCL-shell because of its strong deviation from a spherical shape.

The fit results for each shell are listed in table 6.7. By the application of the background-model (sec 4.4.1) of the Galactic disk emission, χ^2 has been reduced by one order of magnitude compared to a fit without including a background model for each shell. This is why the background model has always been applied and equation 4.33 has been used for the χ^2-fit. The reduced χ^2 (normalized) has also been calculated since the datacubes of each shell have different dimensions, ranging from about 10^6–10^7 pixels. For the USco-loop and the USco-tunnel, the shell fit has been optimized by using two density parameters. This is also shown for the example of the USco-loop in section 4.4.2, where the variation of the parameters on a grid and the variation of χ^2 is also visualized in figure 4.18. One

[11] All values are listed in table 6.10 that is fully introduced in section 6.5

density parameter is determined for the front of the shell and another one for the back, as can be seen in table 6.7 in row 3 and 4. In $l-b-v$-space, the front of a shell (ρ_{front}) is defined as the emission of the shell that is located at the center velocity V_0 or lower, which is the approaching part of the shell and the density of the back (ρ_{back}) is the emission with more positive velocities than V_0 and is the receding part of the shell. By applying this, it is considered that the general emission at higher positive velocities (> 10 km/s) is lower than the ones at negative velocities for this region and it is accounted for asymmetries in the density of the shell itself[12]. The results for each shell are discussed below.

1	2	3	4	5	6	7	8	9	10	11
name	χ^2	χ^2_{red}	ρ_{front}	ρ_{back}	$\Delta\rho_{\mathrm{front}}$	$\Delta\rho_{\mathrm{back}}$	M_{front}	M_{back}	M_{mod}	$\Delta M_{\mathrm{front}}$
	10^7	-	$m_{\mathrm{p}}\,\mathrm{cm}^{-3}$	$m_{\mathrm{p}}\,\mathrm{cm}^{-3}$	$m_{\mathrm{p}}\,\mathrm{cm}^{-3}$	$m_{\mathrm{p}}\,\mathrm{cm}^{-3}$	$\mathrm{M}_\odot$	$\mathrm{M}_\odot$	$\mathrm{M}_\odot$	$\mathrm{M}_\odot$
Usco-loop	73.9	4.31	4.80	0.48	0.25	0.15	8.47	0.85	9.32	0.80
Usco-tunnel:	0.9	2.45	15.80	1.20	0.15	0.2	0.54	0.04	0.58	0.04
USco-Shell	73.8	4.30	1.15	1.15	0.15	0.15	10.49	10.49	20.99	3.11
LCC-loop	27.2	2.56	4.30	4.30	0.20	0.20	3.63	3.63	7.27	0.12

Table 6.7: Masses of shells in the region of Sco-Cen that are determined by fitting the EHSS-model to the H I data. Column 1 contains the name of the shell, column 2 and 3 list χ^2 and the reduced χ^2 respectively. The best fit parameters for the density of the front of the shell, ρ_{front}, and the one of the back of the shell, ρ_{back}, are listed in columns 3 and 4. The corresponding uncertainties are shown in column 5 and 6. The calculated mass of the front (approaching part of the shell), the back (receding part of the shell) and the sum of both are listed in columns 7, 8 and 9 respectively. The uncertainty of the mass that has been calculated using Gaussian error propagation is presented in column 10.

6.3.2 Interim discussion of the shell masses

Here, it is already referred to the summary table 6.10, where the results for the three mass determination methods from above are listed together and that will be fully introduced below in section 6.5.

USco-loop The mass of the USco-loop is about $M_{\mathrm{mod}}(9.3 \pm 0.8) \cdot 10^3\,\mathrm{M}_\odot$, which is in agreement with the upper limit of $M_{\mathrm{smax}} = (15.3 \pm 3.1) \cdot 10^3\,\mathrm{M}_\odot$ from the integrated maps. The fit of the USco-loop suggests that this shell is almost not present or open at its receding part since the fitted density of the back of the shell is about 10 times lower than the one at the front of the shell (see table 6.7 columns 4 and 5). This is in agreement of what can be identified visually in the integrated- (fig. 6.9) as well as channel maps (fig. 3.12) at positive velocities.

USco-shell The structures that could be visually connected to the USco-shell (feature 3 in fig. 3.12) has high uncertainties since not every part of it can be identified clearly along the velocity dimension. This is why the mass of the integrated map of $M_{\mathrm{smax}} = (19.8 \pm 5.8) \cdot 10^3\,\mathrm{M}_\odot$ comes with higher uncertainties compared to the one of the USco-loop.

The fitted mass, using the EHSS-model is $M_{\mathrm{mod}} = (21 \pm 3.1) \cdot 10^3\,\mathrm{M}_\odot$, which is in agreement at least in the range of the uncertainties. The most probable reason for the low mass of the integrated maps compared to the fitted mass is the closeness of the USco-shell to the Galactic plane and hence an overestimation of the Galactic disk background emission by the background model used above (M_{disk} table 6.6). But since the uncertainties are high it might also be an overestimation of the fitted mass.

[12] Doing this gives a 10% lower value of χ^2 compared to fitting just one parameter for the density of the shell.

UCL-shell The H I mass determination of the UCL-shell includes high uncertainties, since it covers such a significant fraction of the total sky. It contains parts of the USco-shell, the USco-loop, the LCC-loop and other features that might not belong to the UCL-shell. And since it is highly asymmetric in shape, the application of the EHSS-model is not possible. The integration of the mass minus the disk background emission has led to a value of $M_{\mathrm{smax}} = (124.6 \pm 43.4) \cdot 10^3\,\mathrm{M}_\odot$. The sum of the masses of the features in table 6.5 at the edges of the shell just covers parts of the total shell. Their mass is $M_{\mathrm{feat}} = (11.0 \pm 1.5) \cdot 10^3\,\mathrm{M}_\odot$. Also not all features have been covered since no Na I absorption lines were available for arc-Ai, -Aii, -D, -E, -G that are visible in figures 6.5 to 6.8. M_{feat} is the minimum value and M_{smax} should be a better estimation in this case.

LCC-loop The mass estimation of the LCC-loop is even more dependent on the background model than the other shells because of its closeness to the Galactic plane. Its mass is $M_{\mathrm{mod}} = (4.1 \pm 0.08) \cdot 10^3\,\mathrm{M}_\odot$ induced by the fit of the EHSS-model. Within the uncertainties, the result of the integrated map of $M_{\mathrm{smax}} = (3.1 \pm 1.4)\ 10^3\mathrm{M}_\odot$ are in agreement with the fitted mass.

USco-tunnel The USco-tunnel has a fitted mass of $(0.58{\pm}0.04) \cdot 10^3\,\mathrm{M}_\odot$, which could be an overestimation because of a nearby large, dense background cloud that either belongs to the USco-loop or -shell or might belong to some fractions of the Aquila rift (see section 2.2.2) and hence a distance estimation is difficult. This is why a correction mass estimation of the cloud has not been done. However, the upper limit of the USco-tunnel mass is $(2.3{\pm}0.5) \cdot 10^3\,\mathrm{M}_\odot$. Regarding its small size, this is a high mass compared to the other shells that is reached due to two properties. The first one is its high expansion velocity of 29.7–32.2 km/s (see table 6.10) and hence it is present in more velocity channels than the other shells, which compensates partly for its small radius. And the second one is the high intensities and the resulting fitted density of the shell of 15 atoms per cm^2, resulting from the USco-tunnel being a more compact object compared to the other shells, which should be the case for younger SNRs.

With the determined masses, more properties like the ages and kinetic energies can be calculated as is presented in the following.

6.3.3 Ages and kinetic energies of the main H I shells

From the H I mass, the total mass of the shell has been estimated by using equation 3.23. Along the lines of Poeppel et al. (2010) and for comparison for these regions with other studies, the value $M_{\mathrm{H}_2} = M_{\mathrm{H\,I,\,tot}}$ has been used. The resulting helium mass M_{He} as well as the resulting total mass $M_{\mathrm{sh,\,tot}}$ for each shell are listed in table 6.8 in column 2 and 3 respectively. Due to the high uncertainties of the mass estimation, the relative mass uncertainties are in the order of 50% as can be seen if comparing $M_{\mathrm{sh,\,tot}}$, to its uncertainties $\Delta M_{\mathrm{sh,\,tot}}$, which are listed in column 5 of the table.

Using the expansion velocity, v_{exp}, as well as the radius R_{max} of the shell, an upper limit for its age is estimated using equation 2.19 with $\alpha = 1$ as is done in comparable studies as Poeppel et al. (2010). The results, τ, and its uncertainties, $\Delta\tau$, for each shell are listed in column 6 and 7 respectively.

Using the expansion velocity v_{exp} as well as the mass of a shell M_{mod}, its kinetic energy E_{kin} has been calculated using eq. 2.23. The uncertainties ΔE_{kin} are listed in column 8. If not explicitly stated otherwise, the uncertainties have been calculated using gaussian error propagation. These results are discussed and compared to other studies in the following.

1	2	3	4	5	6	7	8	9
Name	$M_{\mathrm{H,tot}}$	M_{He}	$M_{\mathrm{sh,tot}}$	$\Delta M_{\mathrm{sh,tot}}$	τ	$\Delta\tau$	E_{kin}	ΔE_{kin}
unit	$\mathrm{M}_\odot$	$\mathrm{M}_\odot$	$\mathrm{M}_\odot$	$\mathrm{M}_\odot$	10^6 yr	10^6 yr	10^{50} ergs	10^{50} ergs
Usco loop	30.6	10.2	40.8	15.4	3.40	0.59	0.46	0.18
Usco tunnel	4.6	1.5	6.1	2.3	0.16	0.05	0.63	0.24
Usco shell	42.0	14.0	56.0	21.2	7.17	3.10	0.34	0.16
UCL shell	249.2	83.1	332.3	125.7	15.07	5.98	8.14	3.34
LCC loop	8.2	2.7	11.0	4.1	3.62	0.45	0.20	0.08

Table 6.8: Ages and kinetic energies of the H I shells. The name is listed in column 1. Columns 2 and 4 list the total hydrogen mass $M_{\mathrm{H,tot}}$ and the total Helium mass, M_{He} respectively. Columns 4 and 5 list the overall shell mass $M_{\mathrm{sh,tot}}$, which is the sum of col 2 and 3, and the uncertainties $\Delta M_{\mathrm{sh,tot}}$, respectively. Column 6 and 7 contain the age and the age uncertainty in Myrs and column 8 and 9 contain the kinetic energies E_{kin} and its uncertainties ΔE_{kin} in units of 10^{50} ergs.

6.4 Stellar feedback of the Scorpius Centaurus OB association

To make a connection between the ISM results from above to the properties of the stellar groups, the output energy of the latter ones have been calculated using the IMF (sec. 2.4.1) in combination with the stellar synthesis code of Voss et al. (2009). The output energy of stars of masses lower than 8 $M_\odot$ can be neglected in the first few million years of a star cluster because the winds plus SNe of the highest mass members dominate the output energy by multiple magnitudes (sec. 2.3.1). Using the stellar evolution code of Voss et al. (2009), some examples have been produced and after the first 5 Myr, wind energies produced by an 8 $M_\odot$ star, a 20 $M_\odot$ star and a 50 $M_\odot$ are 10^{45} erg, $1.4 \cdot 10^{49}$ erg and $1.7 \cdot 10^{51}$ erg respectively. A 60 $M_\odot$ star would already have exploded after 5 Myrs and its total energy output, together with the one of its supernova would be $3.23 \cdot 10^{51}$ erg.

The calibration of the IMF is important to estimate the numbers of the most massive stars that already have exploded. Here, the Kroupa–IMF (Kroupa & Weidner (2003)) has been used and in addition the stars have been not randomly– but optimally sampled[13] (Kroupa et al. 2013).

The number of observed B-stars in Sco-Cen, n_b, has been determined by de Bruijne (1999) for each stellar group of Sco-Cen. It is listed in column 2 the table 6.9.

Using this, the expected number of initially existing O-stars of the initial stellar distribution can be calculated using the restriction $n_b = A \cdot \int_{\mathrm{B9.5}}^{\mathrm{B2.5}} \xi(m)$ where A is the factor that has to be determined (see column 5 in table 6.9). It can be assumed that all stars of spectral type later than B2.5 should still exist since the UCL-, USco-, and the LCC- stellar groups are all younger than 20 Myrs (section 2.5). In practice, it is integrated over the mass and not the spectral type. There exist different conversions of spectral types to mass. The first one that has been used here is 2.34–15.6 $M_\odot$ for B type (Habets & Heintze 1981). This is listed in column 3 and 4 in row 1 for the respective stellar group. A more recent study concludes a range of 3.29–17 $M_\odot$ (Silaj et al. 2014), which is listed also in column 3 and 4 but in the second row for the respective stellar group.

The first one is listed in row 1 of the respective stellar group and the calculation for the second mass range is listed in the second row. The number of estimated O-stars $N_{O,c}$, determined by integrating the IMF from the upper B-star range to 150 $M_\odot$ is listed in column 7.

A different approach to calculate the expected number of O-stars is to use the total cluster mass. This mass has been determined by de Geus (1992) and the properties are adopted in table A.0.3. The IMF has been normalized and integrated for the respective mass. The resulting number of all stars, earlier than B2.5, i.e. more massive than 8.25 $M_\odot$, is listed in column 9 and by using the age of the stellar groups (see section 2.5) that are listed in column 8, the cumulative energy output of stars and the expected number of supernovae has been calculated using the stellar synthesis code of Voss et al. (2009). The results are shown in figure 6.11. The cumulative energies are shown there for the range of 0–17 Myrs. The upper and lower limits for the ages of the three stellar clusters are marked by dashed lines (red for USco, blue for LCC, black for UCL) and the cumulative energy of winds and SNe of massive stars output today of the sub-clusters are $(3\text{–}3.3) \cdot 10^{51}$ ergs for USco, $3.9 \cdot 10^{51}$ ergs for LCC and $(5.6\text{–}6.6) \cdot 10^{51}$ ergs for UCL. The steep increases in cumulative energy that appear in a very short time frame are the supernova events. It can be seen that the expected explosion of the first supernova in USco appears in the estimated age limits. The results of the H I shell of USco is that the upper age limit is 3.4±0.6 Myr (sec. 6.3.3). This is in agreement with these results when considering that the winds started producing the USco-loop but the SNe boosted its expansion after a few Myr.

[13] Optimal sampling deterministically reproduces the IMF and no Poisson noise is added as it is for random sampling.

By using equations eq 2.14, 2.15 and 2.16, the theoretical expected radii (column 13) $R_{s,\star}$, expansion velocities $v_{exp,\star}$ (column 14) and kinetic energies $E_{s,\star}$ (column 12) of the shells can be calculated respectively.

1	2	3	4	5	6	7	8	9	10	11	12	13	14
	N_B	$M_{B9.5}$	M_{B0}	A	$N_{B2.5}$	$N_{O,c}$	τ	N_O	M_{max}	N_{SN}	$E_{s,\star}$	$R_{s,\star}$	$v_{exp,\star}$
Unit:		$M_\odot$	$M_\odot$				Myr		$M_\odot$		10^{50}	pc	km/s
USco	49	3.2	17.2	2831	15	5.8	5	15	68.9	1	1.7	70	8.28
		2.3	15.6	1828	15	3.8	5	15			4.02		
LCC	42	3.2	17.2	2426	7	5.0	12	12	58.8	4	4.1	122	5.85
		2.3	15.6	1567	7	3.2	12	12			26.19		
UCL	66	3.2	17.2	3813	17	7.9	15	15	63.9	6	8.1	149	5.97
		2.3	15.6	2462	17	5.1	15	15			36.23		

Table 6.9: Parameters and the expected number as well as the masses of the O-stars, according to the IMF for the USco-, LCC- and UCL-stellar groups. For a concrete description of the columns and parameters see text[14].

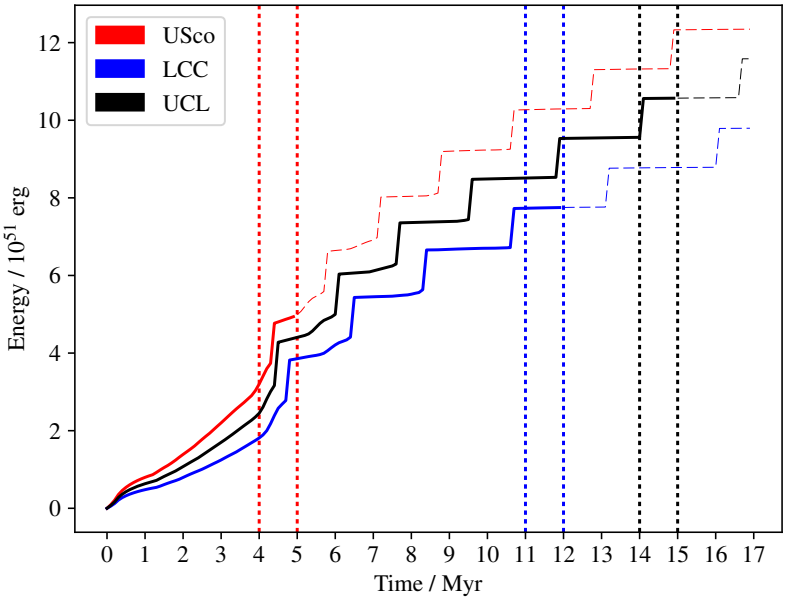

Figure 6.11: Cumulative energy output of the stellar groups USco (red), LCC (blue) and UCL (black). The output energy of each individual star has been derived from the stellar synthesis code of Voss et al. (2009). The stellar input masses have been optimally sampled from the IMF for each stellar group. The vertical red-dashed line represents the age of USco, the vertical blue-dashed line represents the age of LCC and the vertical black-dashed line represents the age estimation for the UCL stellar group from de Geus (1992)[15] (see section 2.5). .

6.5 Discussion of the H I shells and the history of Scorpius Centaurus

Here the shell parameters, determined sections 6.1 to 6.3, are summed up and discussed. For this, all determined shell parameters are put together in table 6.10, which is arranged as follows. Column 1 contains the parameters, while column 2 lists the corresponding unit. Column 3 gives the row number for referencing the parameter position. Columns 4 to 8 contain all parameters of the USco-loop, -tunnel, -shell, the UCL-shell and the LCC-loop, respectively. In each of the rows 1–24 one parameter is listed, while the rows 25 to 44 contain the corresponding parameter uncertainties.

The center coordinates (l_0, b_0) from sec 6.2.3 of table 6.3 are listed in rows 1 and 2. Also adopted from these tables are the angular radius, r_{min}, of the cavity and the one of the shell's outer edge, r_{max}, listed in rows 3 and 4, respectively. Using the distance to the center of the shells, D_{e}, of row 9 (tab. 6.1, the physical radii, R_{min} and R_{max} (rows 5 and 6), have been calculated using the general relation $R = D_{\mathrm{e}} \cdot \tan(r)$. The rows 7 and 8 contain the distance limits, D_{min} and D_{max}, from table 6.5 that have been derived in section 6.1.

The estimated minimum- (v_{min}), center- (v_0) and maximum velocity channels (v_{max}), where the cavities are visible, are listed in rows 10, 11 and 12 respectively. From these three values, the expansion velocity limits, $v_{\mathrm{exp,min}}$ and $v_{\mathrm{exp,max}}$, have been derived and are listed in rows 13 and 14. These two values also include channels of higher velocities than v_{max} and lower velocities than v_{min} if the caps or fractions of the shells have been detectable additionally in these channel maps. Even though these values are the minimum- and maximum measurable values, they are not the upper limits for the expansion velocities because features of the shells might not be detectable or not present in some maps, due to breakouts of the ISM or density gradients, especially towards higher latitudes. In the case of the USco-loop and the USco-tunnel, the shell is open at its back and hence the expansion velocity would be infinity. Here $v_{\mathrm{exp,min}}$ and $v_{\mathrm{exp,max}}$ denote the velocities of the receding and approaching parts where the shell and the interior material are present. The value, v_0, has been determined, based on a combination of the position of the largest radius in spectral space and a high presence of the loop.

If a shell has not a spherical- but an elliptical shape, the semi minor axis (here always in direction of Galactic latitude) is listed as $r_{2,\,\mathrm{min}}$ or $r_{2,\mathrm{max}}$ for the angular size and $R_{2,\mathrm{min}}$ and $R_{2,\mathrm{max}}$ for the physical size in rows 15 to 18. The radius in the LoS direction of each shell has been calculated, using $R_{\mathrm{LoS}} = D_0 - R_{\mathrm{max}}$ and is listed in row 19.

The rows 20–22 contain the hydrogen part of the shell masses M_{feat}, M_{smas}, M_{mod}, determined using the three methods in section 6.3.1 from tables 6.5, 6.6 and 6.7, respectively. The age, τ, and the kinetic energy, E_{kin}, of each shell from table 6.8 are given in rows 23 and 24. The uncertainties stem from the tables of the respective sections and its determination is explained therein. In the following, the H I shells of table 6.10 and its parameters are discussed.

Parameter	Unit	Row	Usco-loop	Usco-tunnel	Usco-shell	UCL-shell	LCC-loop
l_0	deg	1	346.2	350.2	341.2	318	307.9
b_0	deg	2	24.4	21.3	16.8	5.1	4.8
r_{min}	deg	3	11.9	2.1	11.9	55.3	7.7
r_{max}	deg	4	15.9	4	24.4	62.8	9.2
R_{min}	pc	5	26.8	4.6	-	195.2	13.5
R_{max}	pc	6	36.2	5.2	55.6	235.4	18.0
D_{min}	pc	7	100	74	70	70	64
D_{max}	pc	8	157	141	149	161	136
D_{e}	pc	9	127	125	122.6	135.1	100
V_0	km/s	10	7.4	7.4	5.8	-6.6	-17.3
V_{min}	km/s	11	-3.3	-22.3	0	-22.3	-22.3
V_{max}	km/s	12	11.2	9.9	8.2	1.6	0
$V_{\mathrm{exp,min}}$	km/s	13	4.9	29.7	5.8	8.2	5
$V_{\mathrm{exp,max}}$	km/s	14	10.7	32.2	7.8	15.7	13.5
$r_{2,\mathrm{min}}$	deg	15	-	-	-	34.1	3.1
$r_{2,\mathrm{max}}$	deg	16	-	-	-	46.1	5.6
$R_{2,\mathrm{min}}$	pc	17	-	-	-	91.5	5.4
$R_{2,\mathrm{max}}$	pc	18	-	-	-	140.3	9.8
R_{LoS}	pc	19	27	51	52.6	65.1	36
M_{feat}	10^3 M$_\odot$	20	3.5	1.1	-	11.1	0.8
M_{smax}	10^3 M$_\odot$	21	15.3	2.3	19.8	124.6	3.1
M_{mod}	10^3 M$_\odot$	22	9.32	0.58	20.99	-	4.11
τ	10^6 yr	23	3.40	0.16	7.17	15.07	3.62
E_{kin}	10^{50} ergs	24	0.46	0.63	0.34	8.14	0.2
Δl_0	deg	25	1.0	1.3	5.2	3.7	0.9
Δr_{min}	deg	26	0.8	0.4	2.2	2.2	0.5
Δr_{max}	deg	27	0.8	0.4	2.2	4.2	2.3
$\Delta r_{2,\mathrm{min}}$	deg	28	-	-	-	2.1	0.6
$\Delta r_{2,\mathrm{max}}$	deg	29	-	-	-	2.1	1.5
ΔR_{min}	pc	30	3.7	1.5	3.7	78.3	4.4
ΔR_{max}	pc	31	4.7	1.5	10.6	90.1	5.9
$\Delta R_{2,\mathrm{min}}$	pc	32	-	-	-	77.0	4.3
$\Delta R_{2,\mathrm{max}}$	pc	33	-	-	-	77.1	4.3
ΔR_{LoS}	pc	34	18	18	16	17	14
$\Delta D_{\mathrm{min/max}}$	pc	35	10	10	10	10	10
ΔD_{e}	pc	36	14.9	14.7	12.3	13.5	10.0
ΔV_0	km/s	37	1.1	4.8	1.7	2.4	1.4
$\Delta V_{\mathrm{min/max}}$	km/s	38	4.5	5.7	5.0	4.5	3.6
ΔV_{exp}	km/s	39	2.5	5.6	3.0	3.3	2.3
ΔM_{feat}	10^3 M$_\odot$	40	0.5	0.3	-	1.5	0.3
ΔM_{smax}	10^3 M$_\odot$	41	3.1	0.5	5.8	43.4	1.4
ΔM_{mod}	10^3 M$_\odot$	42	0.80	0.04	3.11	-	0.08
$\Delta \tau$	10^6 yr	43	0.59	0.05	3.10	5.98	0.45
ΔE_{kin}	10^{50} ergs	44	0.18	0.24	0.16	3.34	0.08

Table 6.10: Summary of the results for the parameters of the H I shells around Sco-Cen from the tables 6.1 to 6.8 are listed. The first column contains the name of the parameters, column 2 gives the units, column 3 lists the row numbers. The following five columns list all parameters of the USco-loop, the USco-tunnel, the USco-shell, the UCL-shell and the LCC-loop respectively. The listed masses denote the hydrogen part of the total shell masses (see section 6.3).

6.5.1 Discussion of each H I shell

The results of the previous sections and the summarized properties of table 6.10 are discussed here for each shell separately.

The USco-loop

A three dimensional visualisation in longitude-latitude-velocity space of the cavities is shown in figure 6.12. There the detected rings in each channel map, connected to feature-r that represents the cavity of the USco-loop (and the USco-tunnel) is shown. The determined distances at line of sights, where absorption line measurements have been available, are marked by color coded filled circles, where the color denotes the distances from blue (100 pc) to red (200 pc). Visually it is difficult to conclude distance constraints from the plot. This highlights the importance of the usage of fit methods of section 6.1 to the H I profiles that have been used. The USco-loop has mean center coordinates of $l = 346.2^\circ$ and $b = 24.4^\circ$, close to the center coordinates of the USco–subgroup. It can be seen that the center coordinates between the single-channel map cavities vary. The cavity has a maximum angular radius of 26.8±3.7 pc where it transitions into the shell, which has a maximum thickness of about 9±4.7 pc. The distance to the shell has been determined by two methods. A minimum- and maximum distance limit $D_{\mathrm{min/max}}$ of 100−148 pc is suggested by the results of the absorption line analysis (see also Krause et al. (2018)). This is in agreement with the distance towards the center of the shell induced by the color-excess maps of 127±10 pc (sec. 6.1).

The shell is fragmented and does not fill the complete surface of a sphere in H I. It shows low to none emission at positive velocities, where the back (receding part) of the shell should be present, especially in the coordinates of smaller distance towards the center in l_0, b_0, where for an idealized model, the caps should be present. This is supported by the results of the fit of the EHSS-model to the data, where the density of the back of the shell is about 10 times lower than the one of the front (sec. 6.3.1). However, the general properties of the ISM in this region towards higher velocity is the same. The density discrepancy is still remarkably enough to conclude that the shape of the shell in position-position-velocity space is that of a semi-sphere. Plausibly, the shell expanded into an inhomogeneous ISM reservoir and a breakthrough happened in one direction. This is supported by the idea that, observing objects at these high latitudes, higher velocities represent higher distances and higher distance at the same latitude means also looking at higher vertical distance. These regions then have lower densities in general due to the vertical exponential ISM density gradient of the Milky Way (sec. 2.4.2) and a break through is more likely.

The center velocity has been identified to lie at 7.4±1.1 km/s. At this position the radius is the largest, compared to the other channel maps and the shell has the highest densities at this channel map, suggesting that gas just expands perpendicular to the LoS at this position (section 4.2). The maximum limit for the age of the shell has been calculated to be 3.4±0.5 Myr (sec 6.3.3). This age is consistent with the age of the USco–subgroup of about 5 Myrs (Preibisch et al. 2002; Allen et al. 2003; Slesnick 2007) and fits the theoretical expected SN-explosion from about 0.5 Myr ago (fig. 6.11) that has been estimated by determining the IMF and using stellar synthesis models (sec. 6.4). These results do not support the suggestion of Pecaut et al. (2012) of an age of 11 Myrs.

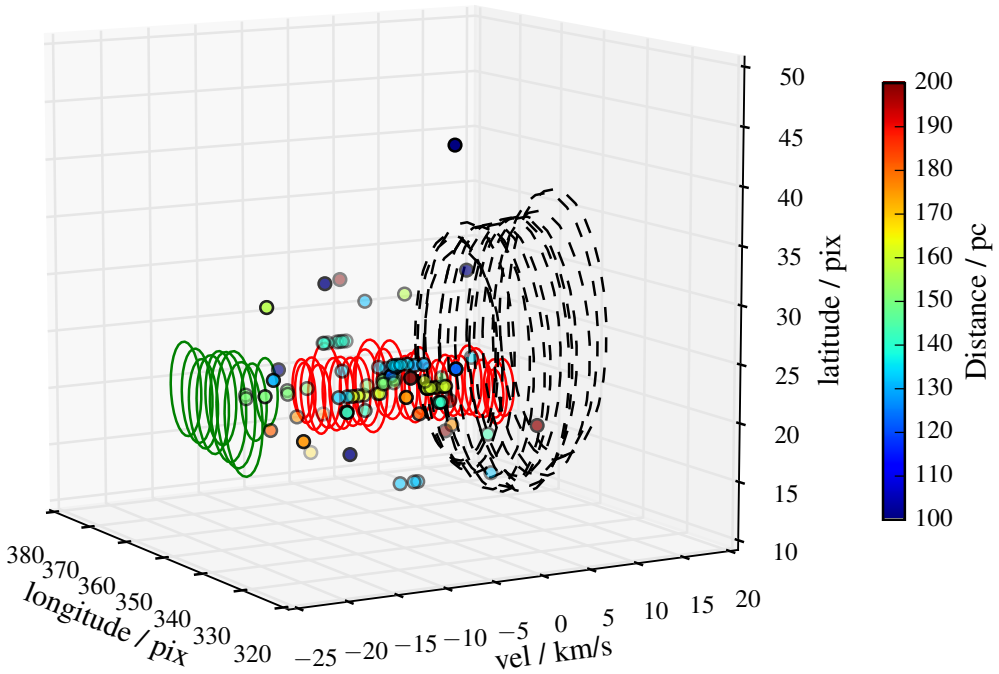

Figure 6.12: Three dimensional longitude-latitude-velocity-plot of feature-*ni*, −*nii* (red circles), cavity-d (green circles) that have been identified to belong to the USco-tunnel and cavity-r belonging to the USco-loop (black dashed circles). The colored dots denote line of sights of absorption lines that are associated with H I features, fitted in sec. 4.7.3. The color marks the distance limit they represent. All values of the circles are listed in table A.0.13 in the appendix. Similar figure also published in Krause et al. (2018).

The USco-tunnel

The USco-tunnel is the smallest of the main shells. It is included because of its striking appearance, its high density and its angular location close to the center of the USco stellar group. The location is especially overlapping with the coordinates of the remaining B-stars therein. It is present in up to 35 channel maps in the velocity range of -22.3 to 9.9 km/s indicating its high expansion velocity. It is difficult to estimate a center velocity from the H I data alone because of the tunnel- or worm-like shape of the USco-tunnel in datacubes. But the distance estimation of 125 pc implies that the origin lies at the same velocities as the one of the USco-loop and hence the center velocity is estimated to be at 7.4 km/s. This is also supported by the USco-tunnel showing the highest densities at this velocity channel.

This velocity is also in agreement with the ones of the stars of the USco–subgroup[16]. The expansion

[16] The mean velocity of the USco–subgroup is 4.2 km/s

velocity towards the Sun is at least 29.7 km/s if it is assumed that the two cavities-*ni* and -*nii* and *d* (see table 6.2 and fig. 6.12), which are separated by background emission at the negative velocities from -11 km/s to -14 km/s (fig. 6.7), still both belong to the USco-tunnel.

The center coordinates shift towards higher longitudes for high negative velocities and the radius increases with increasing positive velocities, implying a slightly rotated orientation of the tunnel towards higher latitudes, compared to the LoS and a cone-like shape that can be seen in figure 6.12, where the red circles belong to cavity *ni* and *nii* and the green ones denote cavity *d*.

At more positive velocities, ranging from -11.5–2.5 km/s (*nii*) the shape of the USco-tunnel is that of a tunnel or worm with similar radii in each velocity channel. Similar to the USco-loop, the USco-tunnel expands towards the Sun, but shows no sign of a receding part. The fit of the density, using the EHSS-model also results in a H I density of the front of $\rho_{\mathrm{front}} = 15.8\,\mathrm{cm}^{-3}$, while the density of the back is just $1.2\,\mathrm{cm}^{-3}$. This strengthens the assumption that the initial gas reservoir of the USco–subgroup was inhomogeneous and much lower towards higher latitudes, when the shells were formed.

The USco-shell

The USco-shell has not identified by de Geus (1992), but it is stated to be the main shell enclosing the USco-subgroup by Poeppel et al. (2010) (section 2.5.1).

The shell is different compared to the other ones because it does not have a separate cavity, except the one that belongs already to the USco-loop that is the interior of the USco-shell. That is why the USco-shell has not been detectable using the automated algorithm, applied for the other shells in section 6.2.2. But a filled shell with partly well defined outer edges can be identified at velocity channels mainly between 0–8.2 km/s (see figures 6.8 and 6.9).

Hence just a maximum radius has been measured. For the minimum radius or the radius of the cavity, the inner edges, r_{min}, of the USco-loop are again taken as an approximation. But the centers of the USco-shell and the USco-loop do not match and hence the uncertainties regarding the other parameters are higher compared to the other shells.

Color excess maps in the direction of the USco stellar subgroup show multiple high density clumps that can together be interpreted as the USco-shell. If a circle is "fitted" by hand to these clumps, it has a similar angular size as the measured Usco-shell in H I (circle 3 in fig B.0.43). From these maps, the distance to the center of this circle of 122.6±12.3 pc is used as the main distance source (sec. 6.1). The maximum radius of this shell, calculated from the angular radius is then 55.6 pc. The USco-shell has a slow expansion velocity of 7.8±3 km/s, at the limit of the general velocity dispersion of the ISM (sec 2.1.1). The mass of the shell is about $(21\pm3)\cdot10^3\mathrm{M}_\odot$ but includes the mass of the USco-loop minus the interior of the cavity of the USco-loop. The determined age, calculated by the size and its low expansion velocity using is $\tau = 7.2 \pm 1.8$ Myr.

The LCC-loop

The LCC-loop represents a well defined loop-like structure in Galactic coordinate projection that embeds a distinct cavity of low density, which is remarkable because of its location close to the Galactic disk, where the detection of such structures are limited due to overlapping emissions from multiple sources. The LCC-loop has an elliptical shape in Galactic projection and encloses the LCC–subgroup (sec. 6.2). Its center coordinates are $l_0 = 307.9^\circ$, $b_0 = 4.8^\circ$ and it has a semi major axis of 18±4.3 pc

(longitude direction) and a semi minor axis of 9.8 ± 5.9 pc (latitude direction) (sec. 6.2.3). Hence it traverses the GP and the background emission makes the detection of the shell down to negative latitudes more challenging.

From the color excess maps of Lallement et al. (2014) a radial cut in the direction of $l = 300$ is given. The LCC-loop has been identified in these maps and if approximating its shape by a ring along the LoS, the center lies at 100±10 pc, which is compatible with $D_{\rm min} = 64$ pc and $D_{\rm max} = 136$ pc, determined from absorption lines given in rows 8 and 9 in table 6.10 (sec. 6.1). The distance is also supported by the ISM distribution in the Galactic plane view of the color excess maps in the direction of $l = 300^\circ$ in figure 2.3. The distance to the center of the shell is close to the one of the center of the subgroup (120 pc (de Zeeuw et al. 1999)) and the shell embeds the subgroup completely. The density gradient in latitude direction is low, suggesting a homogeneous mass distribution on visible parts of the shell.

The LCC-loop contains multiple substructures, as well as other loops in its angular vicinity in Galactic projection (e.g. cavities -a,-l, sec. 6.2.3). In previous studies it has been suggested that the LCC-loop is also just a loop in 3D and does not show signs of expansion, since the visibility of the loop spectral cuts is not much larger than the dispersion of the H I (de Geus 1992). Nevertheless here the channel nap, representing the largest radius of the shell is taken as the center radius at v_0 and with the total spread in velocity channels, an estimation for the expansion velocity has been determined to be $V_{\rm exp}$= 13.5 km/s that could at least be interpreted as minimum expansion velocity of the loop[17], which is higher than the one of the USco-shell. Hence it is concluded that the LCC-loop belongs to an expanding shell. The calculated mass of the LCC-loop is $(4.1 \pm 1.4) \cdot 10^3$ M$_\odot$ and the upper limit for the age is determined to be $\tau = 3.62 \pm 0.45$Myrs, which is much younger than the age of the stellar group of 12 Myrs (de Geus 1992). The kinetic energy of the shell is $(1.8 \pm 0.9) \cdot 10^{49}$ ergs

It is suggested here that the LCC-loop is the second generation shell or loop that has been produced by the LCC–subgroup, in agreement with other studies (de Geus 1992; Poeppel et al. 2010) and that the subgroup additionally produced a larger shell that has already merged with the UCL–shell, which is discussed in the following.

The UCL-shell

The UCL-shell is by far the largest shell and should be mainly formed by the UCL–subgroup and partly by the LCC–subgroup.

On these large angular scales, projection effects become important. Since it is centered at low latitudes $l_0 = 318^\circ, b_0 = 5.1^\circ$, the Plate-carée projection (section 3.3.1) is a valid choice but deformations of the original shell shape have to be considered.

The shell has an elliptical shape with a maximum semi major (longitude) axis of 235 pc and a maximum semi-minor axis (latitude) of 140 pc (sec. 6.1 and 6.2). In the third dimension, the radial distance, the axis just spreads to about $D_0 - D_{\rm min} = 55 \pm 20$ pc, where $D_{\rm min}$ is the lower distance estimation from absorption line measurements and $D_e = 135.1 \pm 13.5$ pc is the center of a circle. fitted to the extinction maps in the direction of $l_0 = 315^\circ$, see also fig. B.0.6 (sec. 6.2.4). But this third value should serve as a minimum radius and the shape is discussed in the following.

[17] In table 6.10 it is denoted as the maximum expansion velocity. But this naming corresponds to the maximum expansion velocity that has been verified. Since the caps at highest and lowest velocities could not be identified, the real expansion velocity could be higher.

Some previous studies assumed a complete spherical shape and it has been discussed if the UCL-shell might already have passed the Sun (e.g. Poeppel et al. (2010)). But the ellipsoid-like shape measured here, indicates that the UCL-shell did not reach the solar system yet. This is in consensus with the scenario suggested by Egger & Aschenbach (1995). They found that Loop I (sec. 2.2.2) and the local bubble hit each other at 80-100 pc. It is suggested here, as discussed below, that Loop I and the UCL-shell are indeed connected.

Because of its large sky coverage, the shell embeds multiple other shells and contains emission from external sources that share the same velocities. Because of this and its high fragmentation, the mass of the shell has higher uncertainties than the other shells. With the Galactic disk-model from section 4.4.1 most of this background has been eliminated and the resulting mass of the shell is $124.6 \pm 43.4 \cdot 10^3\,M_\odot$. This is more of an upper mass limit since this shell contains also partially the USco-shell,-loop,-tunnel and the LCC-loop. Subtraction of these shells would lower the mass. The shell is discussed further in the following section.

6.5.2 The connection between Loop I and the UCL-shell

In the integrated maps of H I of the vicinity of Sco-Cen from section 6.1, the striking feature, named "V“ has been detected, having the shape of an arc and extending from the Galactic plane towards latitudes of about 50°. This feature has a high column density, well defined sharp edges and is present in many velocity channels as can be seen in the channel maps in figures 6.5 and 6.6 as well as in figures B.0.37 to B.0.39 in appendix B and is marked by the capital letters F, G and FG therein. There are few sight lines available for this feature. The ones fitted in section 6.1 suggest that this feature is closer than 279.1 pc and at slightly different coordinates closer than 140 pc, which is not very accurate but at least limits the distance of this feature to be a local one.

As introduced in section 2.2.2, the x-ray analysis of loop I, which reflects the H I feature V, together with the hydrogen column densities (NH I) showed that this loop could possibly hit the front of the hot local bubble at a distance of 80 pc (Egger & Aschenbach 1995). What also strengthens this statement is the analysis of the reddening maps introduced in section 2.2.1. Figure 6.4 represents an area that includes the dust counterpart of feature V that has a similar appearance that is even visually striking enough to assume that both, the gas and dust emission trace the same feature. This Dust feature is already present in the distance bin of 79^{+21}_{-16} pc. On top of that, this is also consistent with rough distance estimation that has been made here using color excess maps of Lallement et al. (2014), where two dense blobs of higher extinction are present at similar low distances (sec. 6.2.4). Both blobs can be seen in figure B.0.6 at the vertical plane slice at $l = 360°$. The distance towards the region closer to the GP is 76±15pc and the one to the higher latitude ($b \approx 45°$) is estimated to lie at 95 ± 23 pc. In direction towards the Galactic plane, both clouds lie at the same distance.

With the distance of the stellar reddening induced by dust, the results of Egger & Aschenbach (1995) and the upper distance limits from the absorption lines, it is concluded that the H I feature also lies at a distance of 79^{+21}_{-16} pc.

The next question to answer is if this feature belongs to a shell produced by the Sco-Cen group. It is the largest arc, reaching latitudes higher than the outer parts of the UCL-shell in projection and is too large and too near to belong to the USco-loop and also somewhat too near but definitely too large to belong to the USco-shell. But from the distance determination, it could very well be part of the UCL-shell, whose visible features hints that it is large enough to reach even lower distances.

But as is introduced in section 2.5, the UCL–subgroup lies 60 pc more far away. So if loop I belongs

to the UCL-shell, it should not be the largest feature since it does not represent the center of the shell and geometrically, the highest part of a shell in latitude that can be observed lies where the expansion velocity vector is perpendicular to the Galactic plane, which would be near the distances of the UCL-stellar group, since the source of the SNe and hence its center should lie approximately there. But since the UCL-shell is so large and near, this is an observational bias as explained in the following.

The visual size changes for large, close objects as described in detail in section 4.7.2 and as illustrated in figure 4.28. Loop I could represent a real world example of this projection effect that is observed for large close objects. By using eq. 4.37 and 4.38 and by inserting the parameters of the UCL-shell, the appearance of the shell is calculated and presented in figure 6.13. In this figure, the observer is located at 0 pc and the center of the shell lies at $D_0 = 135$ pc. The blue line follows the maximum radius seen at each given distance for the radius $R_{2,\mathrm{min}} = 91.5$ pc. The red dashed vertical line denotes the center of the shell and the region where the real largest radius is located, which is not the largest one seen by an observer. The black-dashed vertical line denotes the distance at which the shell has the largest angular size for an observer. This region lies at 75 pc for the distance and radius of the UCL-shell, which coincides with the location of loop I. Due to these results, it is proposed that loop I is part of the UCL-shell.

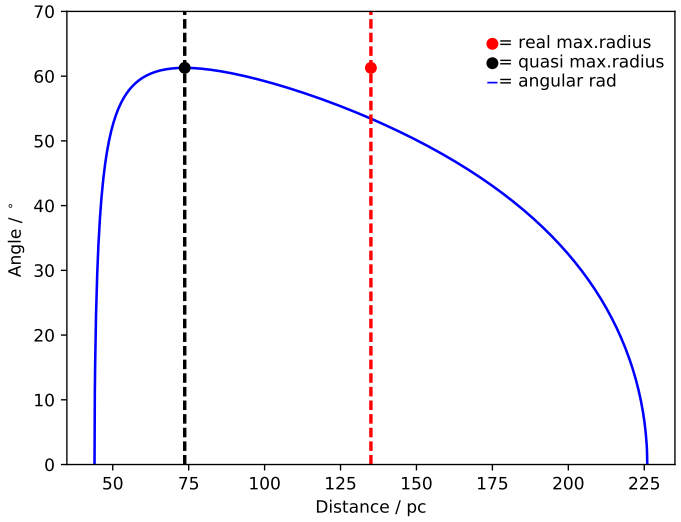

Figure 6.13: Plot showing the observed seeming radius compared to the distance of the physical maximum radius of the shell due to an angular size (dashed line) that is marked by the blue line. The observer is located at 0 pc. The red-dashed line denotes the real distance to the center of the shell, i.e. the distance where the shell is the largest if it is spherical. The black dashed line denotes the seeming distance at which the radius is the largest. For more information see text.

6.5.3 Proposed scenario for the history of Scorpius Centaurus and its interstellar medium

Considering the size and ages of the shells, a scenario of the history of the associations can be inferred. It has been shown that the UCL–subgroup of Sco-Cen is the oldest one with an age of 14-17 Myrs (e.g. sec. 6.5.1). The UCL-shell is suggested to be produced by the UCL stellar subgroup in agreement

with other studies (de Geus 1992; Poeppel et al. 2010).

The distance between the stellar groups of USco and UCL is roughly 80 pc. Considering the expansion velocity of the UCL-shell and using eq. 2.19, it should have passed the USco–subgroup after 5 Myrs, which should have been 10 Myrs ago, considering the age of the UCL-shell. Hence it is expected that it had traveled through the USco stellar region before the USco-loop was produced. It is suggested that this is the reason why the Usco-loop has its well defined loop-like shape if most surrounding inhomogeneous clouds are already swept away by the expanding UCL-shell as also indicated by the other wavelength measurements and hydrogynamic simulations in Krause et al. (2018). The fluctuation of the shell density of the Usco-loop at different positions still indicate that the initial ISM was inhomogeneous. For example on the one hand the shell is probably connected to the dense molecular cloud Lupus I (Gaczkowski et al. 2015, 2017) and on the other hand shows a density gradient towards higher latitudes and velocities.

The ages of the shells as well the estimated time stamps of supernova explosions (sec. 6.4) support the suggested scenario of Preibisch et al. (2002), where it has been concluded that the UCL-shell might have influenced or even triggered the star formation in the USco–subgroup. The strong elongated shape along the Galactic longitude, the position and age of the UCL-shell together with the mass and age of the LCC stellar groups and the absence of a large LCC-shell, lead to the conclusion that a larger LCC-shell has already merged with the UCL-shell as already suggested by Poeppel et al. (2010).

On top of that it has been shown that the UCL-shell also interacts with the Local Bubble at 79^{+21}_{-16} pc and that this interaction could have produced loop I (sec. 6.5.1) as is shown schematically in figure 6.14 in a Galactic plane view (sec. 6.5.2). This could explain why the H I cloud, describing loop I, has such sharp edges and does not show fragmentation, like expected for older shell (see feature V in fig 6.2 or the counterpart in stellar reddening maps in fig B.0.5).

The rough age estimation of 13 Myrs (table 6.8) and the size the of the LCC- loop suggest that it has been formed during the expansion and merging of the previous larger shell, after the most massive stars of the LCC-loop had already vanished.

The USco-loop is one of the younger shells in this region and has well defined edges but is also in the latest evolutionary stage and about to merge into the ISM as its low expansion velocity and the structures at the outer parts of the USco-loop indicate. As suggested by previous studies (e.g. Poeppel et al. (2010)), it has been formed by the stellar winds and the explosion of massive O-stars of the first generation of stars of the only 5 Myr old USco-stellar group. In the cavity of this loop, the USco-tunnel has been detected, which arised, probably due to the stellar winds of the currently radiating B-stars, which are embedded into the USco-tunnel cavity in angular projection. Hence, the USco-tunnel might be a younger arising second generation shell, similar to what has been observed for the ISM around the LCC-group.

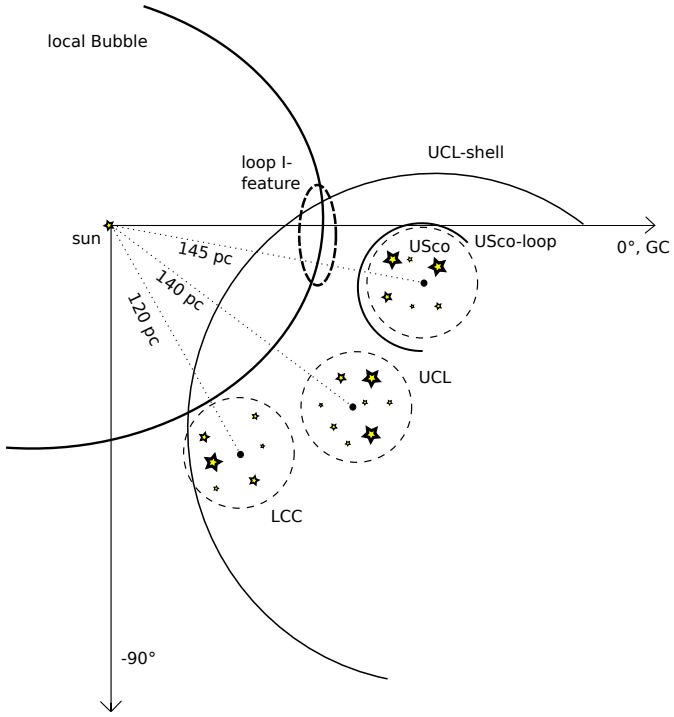

Figure 6.14: Illustration, showing Sco-Cen with its three stellar subgroups USco, UCL and LCC (dashed circles) as well as the open shells formed by these associations (semi circles) in the Galactic plane view. The position of the Sun lies at the origin. The Local Bubble is also marked by a black line with an ellipse segment. The region where loop I is observed is marked with a thick dashed ellipse at the overlap of the UCL-shell and the Local Bubble. For more information see text.

6.6 Summary

The new H I data from the Galactic All Sky Survey have been used as the main source to redetermine the parameters of the H I shells that embed the Scorpius Centaurus OB association in more detail compared to previous studies. Most of the parameters that have been redefined are in agreement with the results of previous studies, especially the two main studies of de Geus (1992) and Poeppel et al. (2010). Absorption line data have been used to determine distance limits for the detected H I clouds, using HIPPARCOS distances towards the stars. The first data release of GAIA has been used to reduce the uncertainties of these distance limits if available. To further limit the distance of the H I structures, extinction maps from Lallement et al. (2014) and data from Green et al. (2015), both representing the spatial distribution of dust, have been used. The masses of the shells have been determined by fitting the EHHS-model and a background model for this region. Also parameters of new structures, like the USco-tunnel have been determined and discussed.

The kinetic ages of the shells have been determined by their current parameters. The use of the stellar synthesis code of Voss et al. (2009), together with the use of the Kroupa IMF Kroupa & Weidner (2003) and optimal sampling, an independent estimation for the time stamps of SNe explosions for the stellar groups have been determined. The results support the age estimation of 5 Myr for the USco-stellar group Preibisch et al. (2002); Allen et al. (2003); Slesnick (2007) and have been connected to the ones of the H I shells.

Based on the results of the shell parameters, a scenario for the history of the Sco-Cen region has been proposed. Due to the new results it is suggested that the UCL-shell probably hit the local bubble at a distance of 79^{+21}_{-16} pc and that Loop I is part of the UCL-shell or a product of the collision.

CHAPTER 7

Conclusion

In this thesis two topics about expanding H I shells in the ISM have been tackled. The first topic is a general automated search for expanding H I shells in the local Galaxy. New algorithms have been developed with the core concept to detect the inner edges of shells to define their parameters. Multiple algorithms have been connected to result in a search algorithm for Galactic H I shells in the database of the 16.1' angular resolution all-sky HI4PI survey. Using the algorithm in combination with a visual investigation of the results, a catalog of local Galactic H I shells has been derived. The shell catalog contains 842 members, which are ranked using quality criteria, derived from the expectations of simplified shell models and observed shells. The detected shells can partly be identified with the objects of catalogs of other studies but mainly new shells have been detected. The majority of new detected shells have low expansion velocities below 10 km/s. This indicates the ability of the approach of this work to identify shells that can only be observed at small velocity ranges near the dispersion limit of the ISM.

The other physical parameters of the shells have been derived, using the kinematic distance estimation. The distribution of shells roughly follows the spiral arm structures but a general conclusion is limited by the high distance uncertainties. However, in the case of the nearest Perseus Arm segment, a clear correlation to the shell density distribution has been measured. Also clusters of shells have been detected at highly structured and turbulent interstellar medium regions. In these clusters, shells are partly overlapping or embedded into each other, indicating shell interactions and merging. Using the shell parameters, the volume filling factor of the shells has been calculated and compared to a reference volume. It has been shown that the determined value of this work agrees with other observations within the uncertainties. It has also been shown that the result is dependent on the choice of the observed segment of the Milky Way but that the high values generally support the efficient shell merging, predicted by hydrodynamic models (Krause et al. 2015).

Two approaches have been used to derive the initial density of the ISM, before the shell has been produced, from H I data and the derived shell parameters. By this it has been shown that the total expected output energies differ by multiple orders of magnitudes, depending on the assumptions of the initial environment. Despite the resulting uncertainties, it has been shown that statistically the ratio between kinetic and expected output energy is higher for older- and larger shells than for younger and smaller shells, which is in line with astrophysical expectations because the thermal energy is low at the latest stages of SNR evolution.

The second topic of this thesis is the investigation of the interstellar medium in the vicinity of

the Scorpius Centaurus OB association. By using the developed algorithms of this work, visual assessment criteria as well as combining Na I absorption line measurements and interstellar reddening maps from other studies with the H I data, the distance towards the H I structures have been determined. By using an idealized spherical shell model together with a developed background emission model of the interstellar medium of the region of the USco-subgroup, the shell masses have been fitted to the data. It has been tested how many parameters of the model can be fitted at the same time but it turned out that the model is very sensitive to parameter variations and that the optimal parameters are not found if the start parameters are off. The parameters, like the mass, the spread in each cartesian direction, kinetic energies, expected energy input by stars and the age of the UCL-shell, the LCC-loop, the USco-shell, the USco-loop and the USco-tunnel have been refined. Here the USco-tunnel is a new proposed shell. By combining the results of all shells, a conclusion for the history of this region has been presented. By using the initial mass function, the number of expected massive stars and also the number of expected supernovae for each stellar group of Sco-Cen have been estimated. From this, an upper age limit of 5 Myr has been derived for the USco-subgroup. The age of the USco-loop, derived from its kinematics, matches the expected time when a supernova event of one of the most massive stars is expected. By this result an age of 5 Myr, also derived by Preibisch et al. (2002), is supported, which stood against a different estimation of 11 Myr (Pecaut et al. 2012). Due to the determined ages of the shells and the stellar groups, the UCL-shell passed the USco region before or during the formation of the stars of the USco stellar group, probably triggering, but at least influencing the star formation in the USco-group. Due to the new distance estimation, it is proposed that the UCL-shell hit the local bubble at 79^{+21}_{-16} pc distance from the Sun, where also the feature Loop-I is visible and associated with this collision at this distance.

Outlook The main source of uncertainties of the catalog shell parameters stem from uncertainties of the kinematic distance estimations. The accuracy of the shell parameters could be increased by individually determining the distances for each object, e.g. by the combination with different wavelength data. This would further increase the accuracy of the statistical and physical shell properties of this work.

The pattern recognition methods that have been developed in this work could be applied to different datasets in the future. These could be new H I data, but also data of different wavelengths to search for features or basic geometric structures. The methods could potentially be combined with methods of other works such as the ones of Ehlerová & Palouš (2013); Suad et al. (2019), which could lead to the detection of even more new shells.

A promising different approach to detect expanding H I shells that became popular during the analysis phase of this work, is the use of neural networks. There are already different approaches for analyzing the general filamentary structure using artificial intelligence in combination with a rolling Hough transformation (Soler et al. 2022). The application of deep neural networks and architectures for a direct detection of expanding shells, which have already proven to be successful in different fields of computer vision (Tan & Le 2019; Ronneberger et al. 2015; Dosovitskiy et al. 2020), also on small amounts of data (Tan & Le 2021; Liu et al. 2022), could be tested. However, the data would have to be labeled and it has to be tested if such an approach is successful on this task.

Regarding the investigation of Sco-Cen, the scenario for its history, derived in this work might be challenged by new measurements, e.g. (Alves et al. 2020; Zucker et al. 2021; Lallement et al. 2022), or combinations of measurements of other wavelengths for this region. It might be worth investigating

the H I structures on even smaller angular scales. The methods developed for the analysis of Sco-Cen could also be applied in future studies to investigate interstellar medium structures in the vicinity of other nearby star clusters.

APPENDIX A

Tables

Mass/ $M_\odot$	Time/Myr
1	10000.0
2	1358.4
3	422.6
4	184.5
5	97.0
6	57.4
7	36.8
8	25.1
9	17.9
10	13.2
11	12.9
14	8.46
15	7.49
16	6.69
17	6.01
18	5.44
20	4.52
25	3.05
30	2.21
35	1.69
50	0.90
60	0.65
70	0.50
80	0.39
85	0.35

Table A.0.1: The resulting ages for specified stellar masses using the mass to main-sequence-lifetime relation of eq. 2.6 with $\eta_1 = 3.88$ for stellar masses lower than $10\,M_\odot$ and $\eta_2 = 2.76$ for higher stellar masses.

1	2	3	4	5	6	7	8	9	10	11a‖11b‖11c
sg	Extent	$\overline{D}_0$	H	$\overline{v}_\mathrm{r}$	$\overline{v}_\mathrm{l}$	$\overline{v}_\mathrm{b}$	τ	$\mathrm{n_b}$	$n_{\mathrm{B2.5}}$	$n_{\mathrm{a,s}}‖n_{\mathrm{b,s}}‖n_{\mathrm{c,s}}$
	$l/^\circ, b/^\circ$	pc	pc	km s^{-1}	km s^{-1}	km s^{-1}	Myr			
US	343-360,+10+30	145	50–60	+5.5	-0.3	-0.9	4-5	49	15	0.8‖1 ± 1‖1
UCL	312-343,0+25	140	50 ± 20	+7.0	-1.6	+1.6	14-15	66	17	3.5‖6 ± 3‖13
LCC	285-312,-10+21	118	30–40	+4.2	-1.6	+1.4	11-12	42	7	1.3‖3 ± 2‖6

Table A.0.2: Properties of the three stellar subgroups of Sco-Cen (Poeppel et al. 2010). Column 1 contains the name of the stellar subgroup, column 2 lists the location and the angular size of the respective stellar subgroup in galactic longitude l and -latitude b. Columns 3 and 4 contain the mean distances and the characteristic depth along the LoS respectively (de Bruijne 1999). The mean radial velocity v_r and the projected components v_l and v_b are listed in columns 5, 6 and 7 respectively (de Zeeuw et al. 1999). The age, the number of B-stars and the number of stars of spectral type earlier than B2.5 are listed in columns 8, 9 and 10 respectively. Column 11 is divided into three sub-columns describing the estimated number $n_{a,s}$, $n_{b,s}$, $n_{c,s}$ of SNe by the studies of Blaauw (1991), Maíz-Apellániz (2001b) and de Geus (1992) respectively. All values are adopted from Poeppel et al. (2010) and table 1 therein.

1	2	3	4	5	6	7	8	9	10	11
sg	ΔM	N_{obs}	N_{tot}	M_{tot}	τ_{nuc}	$\int_t E(t)\mathrm{d}t$	$E_{\mathrm{S,W,pr}}$	$E_{\mathrm{S,W,pa}}$	$E_{\mathrm{S,SN}}$	$E_{\mathrm{S,tot}}$
	$M_\odot$			$N_\odot$	10^6 yr	10^{50}	10^{50}	10^{50}	10^{50}	10^{50}
US	6-13	19	3300 ‖ 170	2350 ‖ 780	4-5	1±1	1.2±0.2	1.7±0.6	1.0±0.8	3±2
UCL	5-9	23	2950 ‖ 150	2100 ‖ 690	14-15	6±3	0.6±0.1	2.7 ± 0.8	6±2	9±3
LCC	5-12	16	1850 ‖ 100	1300 ‖ 430	11-12	3±2	0.6 ± 0.1	1.5 ± 0.4	3 ± 1	4 ± 2

Table A.0.3: Masses and estimated energy outputs of the stellar groups of Sco-Cen. In column 1, the name of the respective stellar group is listed. Column 2 contains the mass interval ΔM that is used for calculating the IMF (sec. 2.4.1) to determine the initial stellar content from the present day mass function for each stellar subgroup of Sco-Cen. In column 3, the observed number of stars N_{obs} of each subgroup is listed. The total number of stars N_{tot} for two different lower limits for the IMF of 0.1 $M_\odot$ and 2 $M_\odot$ are listed in column 4 and for both lower limits, the total mass M_{tot} is listed in column 5. Column 6 lists the nuclear age τ_{nuc} (de Geus et al. 1989). The integral of the evaporation function is listed in column 7. The fractions of the energy of the shells that is contributed by the subgroups are listed in column 8–10 and the sum, the total energy output $E_{\mathrm{S,tot}}$, is listed in column 11. All values are collected from de Geus (1992), table 2 and 3 therein.

1	2	3	4	5	6	7	8
ΔV	$\overline{D}_0$	$M_{\rm comp}$	$M_{\rm interp}$	$M_{\rm HI,tot}$	sub-	M	$E_{\rm kin}$
km s^{-1}	/ pc	/ M$_\odot$	/ 10^5 M$_\odot$	/ 10^5M$_\odot$	group	/ 10^5 M$_\odot$	10^{50} erg
[−42, −20]	100	1550	650	0.022	USco	0.8 ± 0.3	1.7 ± 0.8
[−20, −0.5]	100	43000	17000	0.60	UCL	3 ± 2	6 ± 2
[−0.5, +16]	150	115000	50000	1.65	LCC	1 ± 0.5	-
[+16, +41]	150	15000	7000	0.22			

Table A.0.4: Determined H I masses of Sco-Cen, investigated by Poeppel et al. (2010) (columns 1–5) and de Geus (1992) (columns 6–8). Column 1 provides the integrated velocity range, column 2 contains the mean assumed distance, column 3, 4 and 5 list the computed, interpolated and resulting total H I mass that is embedding Sco-Cen for the given velocity interval, respectively. Column 6 contains the name of the stellar subgroup, column 7 lists the mass in units of 10^5M$_\odot$ and column 8 shows the kinetic Energy.

1	2	3	4	5	6	7	8	9	10	11	12	13
subgr.	l	b	2 Θ	V_0	n	V$_{\rm exp}$	D_0	R	$d_{\rm min}$	$d_{\rm max}$	$d_{\rm obs}$	τ_S
& ref.	/ °	/ °	°	km/s		km/s	pc	pc	pc	pc	pc	Myr
UCL	325±5	17.5±5	130±10	+3	1	8	140	127	13	267	76	15.6
					2	10						12.7
					3	12						10.6
(2)	320±3	10 ± 3	100	1	-	10±2	115	110 ± 10				10
USco-	350±5	21 ± 3	46 ± 6	+3	1	10	145	57	88	202	< 130	5.7
shell					2	12						4.8
USco-	346±2	25±4	28	+3	1b	8	130	21	99	161	-	1.0
loop					2b	10						0.8
(2)	347±2	21 ± 2	30	0	-	10±2	152	40 ± 4				4
LCC-	300±5	10±5	90±8	+2	1	6	118	83	35	201	< 60	
shell					2	9						9.2
					3	12						6.2
LCC-												
loop(2)	300±5	8 ± 5	25	-	-	-	159	35 ± 10				10

Table A.0.5: Parameters of fitted H I shells using the method of Cappa de Nicolau & Poeppel (1986). In column 1, the name of the fitted shell and a reference markers are listed. If there is no marker, values are from Poeppel et al. (2010), table 3 therein and if the marker is (2) values of de Geus (1992) and table 1 therein are cited. In column 2 and 3, the galactic center coordinates l_0 and b_0 of the shells are listed respectively. Column 4 contains the angular diameter of the respective shell. The moving-, or mean velocity v_0 of the center is content of column 5. Column 6 contains the number of fits n and column 7 contains the expansion velocity $V_{\rm exp}$. The distance to the center of the shell D_0 and the radius R of it can be found in column 8 and 9. The minimum and maximum distance, $d_{\rm min}$ and $d_{\rm max}$, are listed in column 10 and 11. Distance estimations from interstellar lines are listed in column 12. Lastly column 13 contains the estimated age τ_s. For more information about how these values were derived, see text in section 2.5.

$l/^\circ$	$b/^\circ$	D_{HIP}	D_{GAIA}	ΔD_{GAIA}	HD name
272.8	29.2	278	400.83	2.51	94473
270	30.3	163	154.92	4.09	93474
321.6	45.1	104	99.81	1.86	119786
344.4	20.7	358	372.01	2.77	141180
350.7	20.4	131	174.73	1.62	144844
351.6	18.7	264	181.23	1.75	146284
285.7	-21.2	125	126.77	2.43	66920
289.9	-27.1	285	241.66	4.17	49835
286.2	-22.3	279	169.94	4.12	64409
285.9	-22.4	158	149.73	3.43	64033
289.1	-26.5	143	145.33	3.73	52365
291.2	-25.8	385	416.13	3.82	57336
287.2	-37.3	229	229.53	3.19	26594
282.3	-43.4	207	185.6	4.53	22488
281.4	-42.8	214	253.96	4.52	23509
285.2	-38.8	101	105.27	2.47	25938
284.1	-39.1	234	236.47	3.35	26109
285.3	-35.7	168	165.46	3.48	29769
336.7	10.8	204	226.84	3.45	141905
289.9	-27.1	285	241.66	4.17	49835
289.1	-26.5	143	145.33	3.73	52365
297.1	-18.3	255	329.21	2.16	93237
292.7	-19.8	340	359.44	3.41	80840
293.8	-13.1	300	375.03	3.81	92645
293.7	-13.2	120	156.42	4.03	92438
295.1	-13.6	280	433.82	3.71	94413
297.7	-15.6	334	279.3	3.91	98143
296.3	-15.8	230	264.86	3.13	94414
296.6	-14.6	164	161.11	3.52	96675
344.4	20.7	358	372.01	2.77	141180
333	19.5	174	198.73	2.56	134685
336.7	10.8	204	226.84	3.45	141905
330	8.9	198	242.32	3.11	137957
321.6	45.1	104	99.81	1.86	119786
350.7	20.4	131	174.73	1.62	144844
351.6	18.7	264	181.23	1.75	146284
350.7	20.4	131	174.73	1.62	144844
316.1	50.8	80	0	0	116658
365.5	39	125	0	0	140873
364.2	36.9	99	0	0	141569
364.2	36.9	99	0	0	141569
366.2	29.1	279	0	0	146931
366.3	23.6	140	0	0	149757
366.3	23.6	140	0	0	149757
366.3	23.6	140	0	0	149757
366.3	23.6	140	0	0	149757
366.3	23.6	140	0	0	149757
366.3	23.6	140	0	0	149757
366.3	23.6	140	0	0	149757
376.8	15.7	175	0	0	157841
316.1	50.8	80	0	0	116658
356.4	28.6	157	0	0	142983
359.4	27.9	131	0	0	144708

358	21	150	0	0	148184
358	21	150	0	0	148184
358	21	150	0	0	148184
358	21	150	0	0	148184
358	21	150	0	0	148184
315.3	25.3	131	0	0	119921
327	28.8	127	0	0	126769
327.7	22.1	63	0	0	129685
343	23.2	289	0	0	139094
346.1	21.7	160	0	0	141637
346.1	21.7	160	0	0	141637
346.1	21.7	160	0	0	141637
346.1	21.7	160	0	0	141637
346.1	21.7	160	0	0	141637
346.9	21.6	133	0	0	142114
346.9	21.6	133	0	0	142114
347.2	20.2	141	0	0	143018
347.2	20.2	141	0	0	143018
347.2	20.2	141	0	0	143018
347.2	20.2	141	0	0	143018
350.1	22.5	123	0	0	143275
350.1	22.5	123	0	0	143275
353.2	23.6	163	0	0	144217
353.2	23.6	163	0	0	144217
353.2	23.6	163	0	0	144217
353.2	23.6	163	0	0	144217
352.8	22.8	130	0	0	144470
352.8	22.8	130	0	0	144470
352.8	22.8	130	0	0	144470
352.8	22.8	130	0	0	144470
348.6	17.9	175	0	0	145102
348.1	16.8	143	0	0	145482
354.6	22.7	134	0	0	145502
354.6	22.7	134	0	0	145502
354.6	22.7	134	0	0	145502
354.6	22.7	134	0	0	145502
351.3	17	225	0	0	147165
351.3	17	225	0	0	147165
351.5	12.8	132	0	0	149438
351.5	12.8	132	0	0	149438
351.5	12.8	132	0	0	149438
351.5	12.8	132	0	0	149438
266.7	-12.3	119	0	0	65575
296	11.6	121	0	0	105435
299.1	12.5	136	0	0	108483
314.2	19.1	162	0	0	120324
314.1	14.2	118	0	0	121263
316	19.1	143	0	0	121743
316	19.1	143	0	0	121743
318.5	14.1	108	0	0	125238
366.8	-23.1	265	0	0	184597
369.4	-22.8	288	0	0	185163
369.3	-24.4	234	0	0	186417
368.3	-24.8	167	0	0	186500
368.7	-26.2	450	0	0	187741

385.3	-21	220	0	0	188220
365.5	-28.5	189	0	0	189103
282.2	-43.7	261	0	0	22252
282.2	-43.7	261	0	0	22252
295	-21	165	0	0	258538
337.1	18.2	100	0	0	138138
356.4	28.6	157	0	0	142983
339.9	10.8	146	0	0	143927
353.2	23.6	163	0	0	144217
353.2	23.6	163	0	0	144217
353.2	23.6	163	0	0	144217
353.2	23.6	163	0	0	144217
359.4	27.9	131	0	0	144708
354.6	22.7	134	0	0	145502
354.6	22.7	134	0	0	145502
354.6	22.7	134	0	0	145502
354.6	22.7	134	0	0	145502
354.6	22.7	134	0	0	145502
354.6	22.7	134	0	0	145502
355.5	20.9	161	0	0	147009
351.3	17	225	0	0	147165
351.3	17	225	0	0	147165
357.9	20.7	150	0	0	148184
357.9	20.7	150	0	0	148184
357.9	20.7	150	0	0	148184
357.9	20.7	150	0	0	148184
357.9	20.7	150	0	0	148184
345.9	9.2	229	0	0	148703
351.5	12.8	132	0	0	149438
351.5	12.8	132	0	0	149438
294.4	-14.5	312	0	0	92157
376.8	15.7	175	0	0	157841
376.8	15.7	175	0	0	157841
377	12.3	168	0	0	159975
389.7	12.6	435	0	0	164353
380.3	6.1	175	0	0	165402
379	0.7	188	0	0	169033
394	2.4	145	0	0	173370
394	2.4	145	0	0	173370
395.9	-0.1	338	0	0	175869
379.6	-36.3	279	0	0	198174
397.1	-51.8	350	0	0	210191
383.6	-53	350	0	0	209522
315.3	25.3	131	0	0	119921
314.2	19.1	162	0	0	120324
314.1	14.2	118	0	0	121263
316	19.1	143	0	0	121743
316	19.1	143	0	0	121743
316	19.1	143	0	0	121743
318.5	14.1	108	0	0	125238
321.7	21.7	76	0	0	125473
321.6	20	128	0	0	125823
322.8	16.7	95	0	0	127972
327.7	22.1	63	0	0	129685
326.9	14.8	165	0	0	132200

326.8	11.1	125	0	0	133955
334.7	17.3	148	0	0	136961
337.1	18.2	100	0	0	138138
339.9	10.8	146	0	0	143927
343	23.2	289	0	0	139094
346.1	21.7	160	0	0	141637
346.1	21.7	160	0	0	141637
346.1	21.7	160	0	0	141637
346.1	21.7	160	0	0	141637
346.1	21.7	160	0	0	141637
346.9	21.6	133	0	0	142114
346.9	21.6	133	0	0	142114
347.2	20.2	141	0	0	143018
347.2	20.2	141	0	0	143018
347.2	20.2	141	0	0	143018
347.2	20.2	141	0	0	143018
350.1	22.5	123	0	0	143275
352.8	22.8	130	0	0	144470
352.8	22.8	130	0	0	144470
352.8	22.8	130	0	0	144470
352.8	22.8	130	0	0	144470
348.6	17.9	175	0	0	145102
348.1	16.8	143	0	0	145482
351.3	17	225	0	0	147165
351.3	17	225	0	0	147165
342.7	32	35	0	0	6981
316.1	50.8	80	0	0	116658
365.5	39	125	0	0	140873
364.2	36.9	99	0	0	141569
364.2	36.9	99	0	0	141569
372.9	41.1	90	0	0	142039
373.1	39.7	132	0	0	142930
389.1	29.2	236	0	0	153562
353.2	23.6	74	0	0	144218
352.8	22.8	130	0	0	144470
357.9	20.7	150	0	0	148184
357.9	20.7	150	0	0	148184
347.2	20.2	141	0	0	143018
347.2	20.2	141	0	0	143018
353.2	23.6	163	0	0	144217
353.2	23.6	163	0	0	144217
353.2	23.6	163	0	0	144217
348.1	16.8	143	0	0	145482
348.6	17.9	175	0	0	145102
354.6	22.7	134	0	0	145502
354.6	22.7	134	0	0	145502
350.1	22.5	123	0	0	143275
356.4	28.6	157	0	0	142983

Table A.0.6: Table containing distances to stars with galactic coordinates given in column 1 and 2, calculated from parallax measurements from the HIPPARCOS catalog given in column 3, and the GAIA mission (column 4). The distance uncertainties for the HIPPARCOS data are $\approx$ 7% for $D_{\mathrm{HIP}} = 50 - 100\,\mathrm{pc}$, and $\approx$ 15% for $D_{\mathrm{HIP}} = 200 - 250\,\mathrm{pc}$ distance with "high dispersions" (Poeppel et al. 2010). The distance uncertainties for the GAIA data are listed in column 5. For line of sights where no GAIA data were available, the D_{GAIA} and ΔD_{GAIA} were set to 0 as a placeholder, not as a number. The HD name of the star is given in column 6.

1	2	3	4	5	6	7	8	9	10	11	12	13	14
nm	n_{LoS}	l	b	fl	D	δD	$\delta v_{Na\,I}$	$v_{Na\,I}$	red $\chi^2_{H\,I}$	$\mu_{H\,I}$	$\sigma_{H\,I}$	$\Delta\mu_{H\,I}$	$\Delta\sigma_{H\,I}$
-	-	°	°	-	pc	pc	km s^{-1}	km s^{-1}	-	km s^{-1}	km s^{-1}	km s^{-1}	km s^{-1}
V	4	366.3	23.6	0	140	7	0.7	-2	0.379	1.06	2.55	0.08	0.07
V	4	366.3	23.6	0	140	7	0.7	-0.5	0.379	1.06	2.55	0.08	0.07
V	4	366.3	23.6	0	140	7	0.7	-5	0.379	0.14	13.35	0.76	0.62
V	4	366.3	23.6	0	140	7	0.7	-2	0.379	0.14	13.35	0.76	0.62
V	4	366.3	23.6	0	140	7	0.7	-0.5	0.379	0.14	13.35	0.76	0.62
V	5	366.3	23.6	0	140	7	4.5	-2.5	0.379	1.06	2.55	0.08	0.07
V	5	366.3	23.6	0	140	7	4.5	-2.5	0.379	0.14	13.35	0.76	0.62
V	6	366.3	23.6	0	140	7	4	-2.4	0.379	1.06	2.55	0.08	0.07
V	6	366.3	23.6	0	140	7	4	-2.4	0.379	0.14	13.35	0.76	0.62
V	7	366.3	23.6	0	140	7	0.5	-0.4	0.379	1.06	2.55	0.08	0.07
V	7	366.3	23.6	0	140	7	0.5	-3.5	0.379	0.14	13.35	0.76	0.62
V	7	366.3	23.6	0	140	7	0.5	-0.4	0.379	0.14	13.35	0.76	0.62
V	9	376.8	15.7	0	175	8.75	4	-1	3.392	2.27	3.99	0.03	0.04
V	9	376.8	15.7	0	175	8.75	4	-1	3.392	6.65	14.12	0.69	0.72
VI	1	289.9	-27.1	1	241.66	4.17	4	-1	0.643	-3.64	4.74	0.25	0.35
VI	1	289.9	-27.1	1	241.66	4.17	4	-1	0.643	-1.2	-9.17	0.94	1.62
VI	2	286.2	-22.3	1	169.94	4.12	4	-11.4	2.654	-7.98	2.87	0.04	0.05
VI	2	286.2	-22.3	1	169.94	4.12	4	-11.4	2.654	-9.82	10.49	1.63	0.87
VI	5	291.2	-25.8	1	416.13	3.82	4	-7.2	1.037	-5.97	2.19	0.12	0.21
VI	5	291.2	-25.8	1	416.13	3.82	4	-7.2	1.037	-5.02	6.7	1.05	0.36
VI	5	291.2	-25.8	1	416.13	3.82	4	3	1.037	-5.02	6.7	1.05	0.36
VII	0	344,4	20,7	1	372,01	2,77	4	-9,3	0,422	-6,49	4,57	0,33	0,39
VII	0	344,4	20,7	1	372,01	2,77	4	1,7	0,422	-6,49	4,57	0,33	0,39
VII	0	344.4	20.7	1	372.01	2.77	4	-9.3	0.422	0.3	13.02	1.41	1
VII	1	350.7	20.4	1	174.73	1.62	5	-0.2	0.043	-1.32	1.7	0.17	0.13
VII	1	350.7	20.4	1	174.73	1.62	5	-12.6	0.043	-13.08	1.27	0.15	0.18
VII	1	350.7	20.4	1	174.73	1.62	5	-0.2	0.043	3.39	-25.53	5.97	8.95
VII	1	350.7	20.4	1	174.73	1.62	5	-12.6	0.043	-2.2	7.7	0.64	0.98
VII	1	350.7	20.4	1	174.73	1.62	5	-0.2	0.043	-2.2	7.7	0.64	0.98
VII	2	351.6	18.7	1	181.23	1.75	4	-14.2	3.169	-12.43	3.11	0.17	0.19
VII	3	356.4	28.6	0	157	7.85	3.6	-12.6	0.9	-2.96	10.94	0.37	0.35
VII	3	356.4	28.6	0	157	7.85	3.6	-4	0.9	-2.96	10.94	0.37	0.35
VII	3	356.4	28.6	0	157	7.85	3.6	2.1	0.9	-2.96	10.94	0.37	0.35
VII	3	356.4	28.6	0	157	7.85	3.6	-4	0.9	-3.43	1.37	0.09	0.1
VII	4	358	21	0	150	7.5	3.6	-14.2	2.177	-8.04	2.88	0.2	0.23
VII	4	358	21	0	150	7.5	3.6	-7.7	2.177	-8.04	2.88	0.2	0.23
VII	4	358	21	0	150	7.5	3.6	-7.7	2.177	0.88	14.28	0.87	1.28
VII	5	358	21	0	150	7.5	6	0.6	2.177	-8.04	2.88	0.2	0.23
VII	6	358	21	0	150	7.5	0.5	-9.8	2.177	-8.04	2.88	0.2	0.23
VII	6	358	21	0	150	7.5	0.5	-8.8	2.177	-8.04	2.88	0.2	0.23
VII	6	358	21	0	150	7.5	0.5	-8	2.177	-8.04	2.88	0.2	0.23
VII	6	358	21	0	150	7.5	0.5	-6.8	2.177	-8.04	2.88	0.2	0.23
VII	6	358	21	0	150	7.5	0.5	-8.8	2.177	0.88	14.28	0.87	1.28
VII	6	358	21	0	150	7.5	0.5	-8	2.177	0.88	14.28	0.87	1.28
VII	6	358	21	0	150	7.5	0.5	-6.8	2.177	0.88	14.28	0.87	1.28
VII	6	358	21	0	150	7.5	0.5	-4.3	2.177	0.88	14.28	0.87	1.28
VII	6	358	21	0	150	7.5	0.5	-1.3	2.177	0.88	14.28	0.87	1.28
VII	8	358	21	0	150	7.5	0.5	-7.7	2.177	-8.04	2.88	0.2	0.23
VII	8	358	21	0	150	7.5	0.5	-7.7	2.177	0.88	14.28	0.87	1.28
VII	9	343	23.2	0	289	14.45	4	-3.1	0.143	1.33	2.02	0.06	0.09
VII	9	343	23.2	0	289	14.45	4	-3.1	0.143	-0.04	-14.78	1.49	2.02
VII	9	343	23.2	0	289	14.45	4	-3.1	0.143	-3.46	6.36	0.62	0.62
VII	10	346.1	21.7	0	160	8	3.6	-6.7	0.3	-3.6	3.3	0.34	0.34
VII	10	346.1	21.7	0	160	8	3.6	1	0.3	-3.6	3.3	0.34	0.34
VII	10	346.1	21.7	0	160	8	3.6	-6.7	0.3	-0.35	9.42	0.82	1.85
VII	10	346.1	21.7	0	160	8	3.6	1	0.3	-0.35	9.42	0.82	1.85
VII	10	346.1	21.7	0	160	8	3.6	-6.7	0.3	0.88	-21.66	14.84	21.19
VII	11	346.1	21.7	0	160	8	0.5	-5.2	0.3	-3.6	3.3	0.34	0.34
VII	11	346.1	21.7	0	160	8	0.5	-3.5	0.3	-3.6	3.3	0.34	0.34

VII	11	346.1	21.7	0	160	8	0.5	0.1	0.3	-3.6	3.3	0.34	0.34
VII	11	346.1	21.7	0	160	8	0.5	-8.2	0.3	-0.35	9.42	0.82	1.85
VII	11	346.1	21.7	0	160	8	0.5	-5.2	0.3	-0.35	9.42	0.82	1.85
VII	11	346.1	21.7	0	160	8	0.5	-3.5	0.3	-0.35	9.42	0.82	1.85
VII	11	346.1	21.7	0	160	8	0.5	0.1	0.3	-0.35	9.42	0.82	1.85
VII	11	346.1	21.7	0	160	8	0.5	-8.2	0.3	0.88	-21.66	14.84	21.19
VII	11	346.1	21.7	0	160	8	0.5	-5.2	0.3	0.88	-21.66	14.84	21.19
VII	11	346.1	21.7	0	160	8	0.5	-3.5	0.3	0.88	-21.66	14.84	21.19
VII	12	346.1	21.7	0	160	8	0.8	0	0.3	1.79	1.83	0.07	0.07
VII	12	346.1	21.7	0	160	8	0.8	-5	0.3	-3.6	3.3	0.34	0.34
VII	12	346.1	21.7	0	160	8	0.8	0	0.3	-3.6	3.3	0.34	0.34
VII	12	346.1	21.7	0	160	8	0.8	-8	0.3	-0.35	9.42	0.82	1.85
VII	12	346.1	21.7	0	160	8	0.8	-5	0.3	-0.35	9.42	0.82	1.85
VII	12	346.1	21.7	0	160	8	0.8	0	0.3	-0.35	9.42	0.82	1.85
VII	12	346.1	21.7	0	160	8	0.8	-8	0.3	0.88	-21.66	14.84	21.19
VII	12	346.1	21.7	0	160	8	0.8	-5	0.3	0.88	-21.66	14.84	21.19
VII	12	346.1	21.7	0	160	8	0.8	0	0.3	0.88	-21.66	14.84	21.19
VII	13	346.1	21.7	0	160	8	0.5	-7.3	0.3	-3.6	3.3	0.34	0.34
VII	13	346.1	21.7	0	160	8	0.5	-4.3	0.3	-3.6	3.3	0.34	0.34
VII	13	346.1	21.7	0	160	8	0.5	-7.3	0.3	-0.35	9.42	0.82	1.85
VII	13	346.1	21.7	0	160	8	0.5	-4.3	0.3	-0.35	9.42	0.82	1.85
VII	13	346.1	21.7	0	160	8	0.5	-7.3	0.3	0.88	-21.66	14.84	21.19
VII	13	346.1	21.7	0	160	8	0.5	-4.3	0.3	0.88	-21.66	14.84	21.19
VII	14	346.1	21.7	0	160	8	1.1	-7.9	0.3	-3.6	3.3	0.34	0.34
VII	14	346.1	21.7	0	160	8	1.1	0.4	0.3	-3.6	3.3	0.34	0.34
VII	14	346.1	21.7	0	160	8	1.1	-7.9	0.3	-0.35	9.42	0.82	1.85
VII	14	346.1	21.7	0	160	8	1.1	0.4	0.3	-0.35	9.42	0.82	1.85
VII	14	346.1	21.7	0	160	8	1.1	-7.9	0.3	0.88	-21.66	14.84	21.19
VII	15	346.9	21.6	0	133	6.65	4	-8.1	0.89	-2.04	14	0.82	1.5
VII	15	346.9	21.6	0	133	6.65	4	-3.1	0.89	-2.04	14	0.82	1.5
VII	15	346.9	21.6	0	133	6.65	4	-8.1	0.89	-8.05	1.25	0.14	0.2
VII	15	346.9	21.6	0	133	6.65	4	-3.1	0.89	-8.05	1.25	0.14	0.2
VII	15	346.9	21.6	0	133	6.65	4	-8.1	0.89	-1.58	5.15	0.15	0.23
VII	15	346.9	21.6	0	133	6.65	4	-3.1	0.89	-1.58	5.15	0.15	0.23
VII	16	346.9	21.6	0	133	6.65	6	-9	0.89	-2.04	14	0.82	1.5
VII	16	346.9	21.6	0	133	6.65	6	-9	0.89	-8.05	1.25	0.14	0.2
VII	16	346.9	21.6	0	133	6.65	6	-9	0.89	-1.58	5.15	0.15	0.23
VII	17	347.2	20.2	0	141	7.05	0.5	-8	0.121	-7.17	1.24	0.12	0.19
VII	17	347.2	20.2	0	141	7.05	0.5	-7	0.121	-7.17	1.24	0.12	0.19
VII	17	347.2	20.2	0	141	7.05	0.5	-6	0.121	-7.17	1.24	0.12	0.19
VII	17	347.2	20.2	0	141	7.05	0.5	-8	0.121	-4.82	4.88	0.86	0.96
VII	17	347.2	20.2	0	141	7.05	0.5	-7	0.121	-4.82	4.88	0.86	0.96
VII	17	347.2	20.2	0	141	7.05	0.5	-6	0.121	-4.82	4.88	0.86	0.96
VII	17	347.2	20.2	0	141	7.05	0.5	-5.3	0.121	-4.82	4.88	0.86	0.96
VII	17	347.2	20.2	0	141	7.05	0.5	-3.7	0.121	-4.82	4.88	0.86	0.96
VII	17	347.2	20.2	0	141	7.05	0.5	-8	0.121	-1.58	14.08	3.02	2.52
VII	17	347.2	20.2	0	141	7.05	0.5	-7	0.121	-1.58	14.08	3.02	2.52
VII	17	347.2	20.2	0	141	7.05	0.5	-6	0.121	-1.58	14.08	3.02	2.52
VII	17	347.2	20.2	0	141	7.05	0.5	-5.3	0.121	-1.58	14.08	3.02	2.52
VII	17	347.2	20.2	0	141	7.05	0.5	-3.7	0.121	-1.58	14.08	3.02	2.52
VII	19	347.2	20.2	0	141	7.05	0.8	-8	0.121	-7.17	1.24	0.12	0.19
VII	19	347.2	20.2	0	141	7.05	0.8	-6	0.121	-7.17	1.24	0.12	0.19
VII	19	347.2	20.2	0	141	7.05	0.8	-8	0.121	-4.82	4.88	0.86	0.96
VII	19	347.2	20.2	0	141	7.05	0.8	-6	0.121	-4.82	4.88	0.86	0.96
VII	19	347.2	20.2	0	141	7.05	0.8	-3	0.121	-4.82	4.88	0.86	0.96
VII	19	347.2	20.2	0	141	7.05	0.8	-8	0.121	-1.58	14.08	3.02	2.52
VII	19	347.2	20.2	0	141	7.05	0.8	-6	0.121	-1.58	14.08	3.02	2.52
VII	19	347.2	20.2	0	141	7.05	0.8	-3	0.121	-1.58	14.08	3.02	2.52
VII	20	347.2	20.2	0	141	7.05	0.5	-6.1	0.121	-7.17	1.24	0.12	0.19
VII	20	347.2	20.2	0	141	7.05	0.5	-6.1	0.121	-4.82	4.88	0.86	0.96
VII	20	347.2	20.2	0	141	7.05	0.5	-4.1	0.121	-4.82	4.88	0.86	0.96
VII	20	347.2	20.2	0	141	7.05	0.5	-6.1	0.121	-1.58	14.08	3.02	2.52
VII	20	347.2	20.2	0	141	7.05	0.5	-4.1	0.121	-1.58	14.08	3.02	2.52

VII	22	350.1	22.5	0	123	6.15	5	-2.1	2.337	-1.29	3.36	0.07	0.12
VII	22	350.1	22.5	0	123	6.15	5	-2.1	2.337	0.33	10.64	0.44	0.53
VII	23	353.2	23.6	0	163	8.15	0.5	-12.6	3.497	-10.67	4.83	0.3	0.33
VII	23	353.2	23.6	0	163	8.15	0.5	-11.2	3.497	-10.67	4.83	0.3	0.33
VII	24	353.2	23.6	0	163	8.15	0.8	-13	3.497	-10.67	4.83	0.3	0.33
VII	24	353.2	23.6	0	163	8.15	0.8	-11	3.497	-10.67	4.83	0.3	0.33
VII	25	353.2	23.6	0	163	8.15	5	-0.4	3.497	1.68	2.88	0.03	0.03
VII	25	353.2	23.6	0	163	8.15	5	-12.6	3.497	-10.67	4.83	0.3	0.33
VII	26	353.2	23.6	0	163	8.15	0.5	-11.2	3.497	-10.67	4.83	0.3	0.33
VII	27	352.8	22.8	0	130	6.5	4	-13.4	0.144	-12.72	1.22	0.09	0.11
VII	27	352.8	22.8	0	130	6.5	4	-5.4	0.144	-1.03	10.32	1.34	1.95
VII	27	352.8	22.8	0	130	6.5	4	1.6	0.144	-1.03	10.32	1.34	1.95
VII	27	352.8	22.8	0	130	6.5	4	-5.4	0.144	4.17	20.03	20.12	23.24
VII	28	352.8	22.8	0	130	6.5	6	-0.4	0.144	0.1	1.34	0.07	0.11
VII	28	352.8	22.8	0	130	6.5	6	-0.4	0.144	-1.03	10.32	1.34	1.95
VII	28	352.8	22.8	0	130	6.5	6	-0.4	0.144	3.22	3.42	0.18	0.12
VII	28	352.8	22.8	0	130	6.5	6	-0.4	0.144	4.17	20.03	20.12	23.24
VII	29	352.8	22.8	0	130	6.5	0.5	-1.4	0.144	0.1	1.34	0.07	0.11
VII	29	352.8	22.8	0	130	6.5	0.5	-12.9	0.144	-12.72	1.22	0.09	0.11
VII	29	352.8	22.8	0	130	6.5	0.5	-5.9	0.144	-1.03	10.32	1.34	1.95
VII	29	352.8	22.8	0	130	6.5	0.5	-1.4	0.144	-1.03	10.32	1.34	1.95
VII	29	352.8	22.8	0	130	6.5	0.5	-1.4	0.144	4.17	20.03	20.12	23.24
VII	30	352.8	22.8	0	130	6.5	4	2.6	0.144	-1.03	10.32	1.34	1.95
VII	31	348.6	17.9	0	175	8.75	4	-12	0.086	-12	1.15	0.06	0.07
VII	31	348.6	17.9	0	175	8.75	4	-12	0.086	-2.34	-10.12	0.5	0.67
VII	31	348.6	17.9	0	175	8.75	4	3.8	0.086	-2.34	-10.12	0.5	0.67
VII	32	354.6	22.7	0	134	6.7	0.5	-5.4	1.03	-1.31	12.34	0.51	0.56
VII	33	354.6	22.7	0	134	6.7	8	1.6	1.03	-1.31	12.34	0.51	0.56
VII	35	354.6	22.7	0	134	6.7	5	0.5	1.03	-1.31	12.34	0.51	0.56
VII	36	337.1	18.2	0	100	5	4	-12	0.29	-10.56	1.49	0.51	0.56
VII	37	354.6	22.7	0	134	6.7	8	0.1	1.03	-1.31	12.34	0.51	0.56
VII	38	354.6	22.7	0	134	6.7	1.1	-1.5	1.03	1.94	2.53	0.03	0.04
VII	38	354.6	22.7	0	134	6.7	1.1	-1.5	1.03	-1.31	12.34	0.51	0.56
VII	38	354.6	22.7	0	134	6.7	1.1	0.9	1.03	-1.31	12.34	0.51	0.56
VII	39	355.5	20.9	0	161	8.05	8	3.9	0.137	-9.08	6.63	2.87	1.17
VII	41	357.9	20.7	0	150	7.5	0.5	-9.8	3.477	-9.01	3.54	0.22	0.2
VII	41	357.9	20.7	0	150	7.5	0.5	-8.8	3.477	-9.01	3.54	0.22	0.2
VII	41	357.9	20.7	0	150	7.5	0.5	-8	3.477	-9.01	3.54	0.22	0.2
VII	41	357.9	20.7	0	150	7.5	0.5	-6.8	3.477	-9.01	3.54	0.22	0.2
VII	42	357.9	20.7	0	150	7.5	0.5	-1.3	3.477	3.2	4.49	0.06	0.09
VII	43	357.9	20.7	0	150	7.5	0.5	-12.2	3.477	-9.01	3.54	0.22	0.2
VII	43	357.9	20.7	0	150	7.5	0.5	-7.7	3.477	-9.01	3.54	0.22	0.2
VII	45	346.1	21.7	0	160	8	0.8	-5	0.3	-3.6	3.3	0.34	0.34
VII	45	346.1	21.7	0	160	8	0.8	-8	0.3	-0.35	9.42	0.82	1.85
VII	45	346.1	21.7	0	160	8	0.8	-5	0.3	-0.35	9.42	0.82	1.85
VII	45	346.1	21.7	0	160	8	0.8	-8	0.3	0.88	-21.66	14.84	21.19
VII	45	346.1	21.7	0	160	8	0.8	-5	0.3	0.88	-21.66	14.84	21.19
VII	46	350.1	22.5	0	123	6.15	0.5	-2.1	2.337	-1.29	3.36	0.07	0.12
VII	46	350.1	22.5	0	123	6.15	0.5	-2.1	2.337	0.33	10.64	0.44	0.53
VII	47	342.7	32	0	35	1.75	4.6	-12.2	0.381	-3.53	10.01	0.41	0.27
VII	47	342.7	32	0	35	1.75	4.6	2.7	0.381	-3.53	10.01	0.41	0.27
VII	48	353.2	23.6	0	74	3.7	5	-12.7	3.497	-10.67	4.83	0.3	0.33
VII	49	352.8	22.8	0	130	6.5	3.6	-13.4	0.144	-12.72	1.22	0.09	0.11
VII	50	357.9	20.7	0	150	7.5	3.6	-14.2	3.477	-9.01	3.54	0.22	0.2
VII	51	357.9	20.7	0	150	7.5	0.5	-12.2	3.477	-9.01	3.54	0.22	0.2
VII	54	353.2	23.6	0	163	8.15	0.5	-12.6	3.497	-10.67	4.83	0.3	0.33
VII	54	353.2	23.6	0	163	8.15	0.5	-11.2	3.497	-10.67	4.83	0.3	0.33
VII	55	353.2	23.6	0	163	8.15	0.8	-13	3.497	-10.67	4.83	0.3	0.33
VII	55	353.2	23.6	0	163	8.15	0.8	-11	3.497	-10.67	4.83	0.3	0.33
VII	56	353.2	23.6	0	163	8.15	5	-12.6	3.497	-10.67	4.83	0.3	0.33
VII	57	348.6	17.9	0	175	8.75	4	-12	0.086	-12	1.15	0.06	0.07
VII	57	348.6	17.9	0	175	8.75	4	-12	0.086	-2.34	-10.12	0.5	0.67
VII	61	356.4	28.6	0	157	7.85	3.6	-12.6	0.9	-2.96	10.94	0.37	0.35

VIII	0	321.6	45.1	1	99.81	1.86	5.5	-8	0.059	-5.68	1.55	0.07	0.1
VIII	0	321.6	45.1	1	99.81	1.86	5.5	-8	0.059	-4.69	4.34	0.23	0.35
VIII	0	321.6	45.1	1	99.81	1.86	5.5	-8	0.059	1.75	-18.37	2.66	2.41
IX	0	296	11.6	0	121	6.05	3.6	-6.5	0.02	-1.79	2.44	0.75	0.43
IX	0	296	11.6	0	121	6.05	3.6	0	0.02	-1.79	2.44	0.75	0.43
IX	0	296	11.6	0	121	6.05	3.6	-6.5	0.02	-11.7	1.93	0.34	0.42
IX	0	296	11.6	0	121	6.05	3.6	-6.5	0.02	-5.88	1.83	0.79	0.58
IX	0	296	11.6	0	121	6.05	3.6	-6.5	0.02	-9.44	9.79	0.6	1.02
IX	0	296	11.6	0	121	6.05	3.6	0	0.02	-9.44	9.79	0.6	1.02
IX	1	299.1	12.5	0	136	6.8	3.6	-8	0.314	-2.92	2.51	0.09	0.11
IX	1	299.1	12.5	0	136	6.8	3.6	-2.5	0.314	-2.92	2.51	0.09	0.11
IX	1	299.1	12.5	0	136	6.8	3.6	-8	0.314	-10.49	-9.82	0.29	0.16
IX	1	299.1	12.5	0	136	6.8	3.6	-2.5	0.314	-10.49	-9.82	0.29	0.16
X	0	350.7	20.4	1	174.73	1.62	5	-0.2	0.043	2.43	1.48	0.11	0.07
X	0	350.7	20.4	1	174.73	1.62	5	-0.2	0.043	3.39	-25.53	5.97	8.95
X	1	351.6	18.7	1	181.23	1.75	4	1.6	3.169	1.74	3.97	0.04	0.05
X	1	351.6	18.7	1	181.23	1.75	4	1.6	3.169	1.87	30.13	5.13	8.33
X	2	346.1	21.7	0	160	8	3.6	1	0.3	1.79	1.83	0.07	0.07
X	2	346.1	21.7	0	160	8	3.6	1	0.3	-0.35	9.42	0.82	1.85
X	2	346.1	21.7	0	160	8	3.6	1	0.3	0.88	-21.66	14.84	21.19
X	3	346.1	21.7	0	160	8	0.5	0.1	0.3	1.79	1.83	0.07	0.07
X	3	346.1	21.7	0	160	8	0.5	2	0.3	1.79	1.83	0.07	0.07
X	3	346.1	21.7	0	160	8	0.5	0.1	0.3	-0.35	9.42	0.82	1.85
X	3	346.1	21.7	0	160	8	0.5	2	0.3	-0.35	9.42	0.82	1.85
X	3	346.1	21.7	0	160	8	0.5	0.1	0.3	0.88	-21.66	14.84	21.19
X	3	346.1	21.7	0	160	8	0.5	2	0.3	0.88	-21.66	14.84	21.19
X	4	346.1	21.7	0	160	8	0.8	0	0.3	1.79	1.83	0.07	0.07
X	4	346.1	21.7	0	160	8	0.8	2	0.3	1.79	1.83	0.07	0.07
X	4	346.1	21.7	0	160	8	0.8	0	0.3	-0.35	9.42	0.82	1.85
X	4	346.1	21.7	0	160	8	0.8	2	0.3	-0.35	9.42	0.82	1.85
X	4	346.1	21.7	0	160	8	0.8	0	0.3	0.88	-21.66	14.84	21.19
X	4	346.1	21.7	0	160	8	0.8	2	0.3	0.88	-21.66	14.84	21.19
X	5	346.1	21.7	0	160	8	0.5	1.7	0.3	1.79	1.83	0.07	0.07
X	5	346.1	21.7	0	160	8	0.5	2.7	0.3	1.79	1.83	0.07	0.07
X	5	346.1	21.7	0	160	8	0.5	1.7	0.3	-0.35	9.42	0.82	1.85
X	5	346.1	21.7	0	160	8	0.5	2.7	0.3	-0.35	9.42	0.82	1.85
X	5	346.1	21.7	0	160	8	0.5	1.7	0.3	0.88	-21.66	14.84	21.19
X	5	346.1	21.7	0	160	8	0.5	2.7	0.3	0.88	-21.66	14.84	21.19
X	6	346.1	21.7	0	160	8	1.1	0.4	0.3	1.79	1.83	0.07	0.07
X	6	346.1	21.7	0	160	8	1.1	2.4	0.3	1.79	1.83	0.07	0.07
X	6	346.1	21.7	0	160	8	1.1	0.4	0.3	-0.35	9.42	0.82	1.85
X	6	346.1	21.7	0	160	8	1.1	2.4	0.3	-0.35	9.42	0.82	1.85
X	6	346.1	21.7	0	160	8	1.1	0.4	0.3	0.88	-21.66	14.84	21.19
X	6	346.1	21.7	0	160	8	1.1	2.4	0.3	0.88	-21.66	14.84	21.19
X	10	347.2	20.2	0	141	7.05	0.5	1.8	0.121	2.42	1.37	0.1	0.15
X	10	347.2	20.2	0	141	7.05	0.5	1.8	0.121	-1.58	14.08	3.02	2.52
X	11	347.2	20.2	0	141	7.05	0.8	2	0.121	2.42	1.37	0.1	0.15
X	11	347.2	20.2	0	141	7.05	0.8	2	0.121	-1.58	14.08	3.02	2.52
X	13	350.1	22.5	0	123	6.15	0.5	4.9	2.337	0.33	10.64	0.44	0.53
X	14	350.1	22.5	0	123	6.15	5	-2.1	2.337	0.33	10.64	0.44	0.53
X	15	352.8	22.8	0	130	6.5	4	1.6	0.144	0.1	1.34	0.07	0.11
X	15	352.8	22.8	0	130	6.5	4	1.6	0.144	-1.03	10.32	1.34	1.95
X	15	352.8	22.8	0	130	6.5	4	1.6	0.144	3.22	3.42	0.18	0.12
X	15	352.8	22.8	0	130	6.5	4	1.6	0.144	4.17	20.03	20.12	23.24
X	16	352.8	22.8	0	130	6.5	6	-0.4	0.144	0.1	1.34	0.07	0.11
X	16	352.8	22.8	0	130	6.5	6	-0.4	0.144	3.22	3.42	0.18	0.12
X	16	352.8	22.8	0	130	6.5	6	-0.4	0.144	4.17	20.03	20.12	23.24
X	18	352.8	22.8	0	130	6.5	4	2.6	0.144	0.1	1.34	0.07	0.11
X	18	352.8	22.8	0	130	6.5	4	2.6	0.144	-1.03	10.32	1.34	1.95
X	18	352.8	22.8	0	130	6.5	4	2.6	0.144	3.22	3.42	0.18	0.12
X	18	352.8	22.8	0	130	6.5	4	2.6	0.144	4.17	20.03	20.12	23.24
X	19	346.1	21.7	0	160	8	0.8	2	0.3	1.79	1.83	0.07	0.07
X	19	346.1	21.7	0	160	8	0.8	2	0.3	-0.35	9.42	0.82	1.85

X	19	346.1	21.7	0	160	8	0.8	2	0.3	0.88	-21.66	14.84	21.19
X	20	350.1	22.5	0	123	6.15	0.5	4.9	2.337	0.33	10.64	0.44	0.53
XI	0	344.4	20.7	1	372.01	2.77	4	1.7	0.422	0.74	1.71	0.09	0.12
XI	0	344.4	20.7	1	372.01	2.77	4	1.7	0.422	0.3	13.02	1.41	1
XI	1	350.7	20.4	1	174.73	1.62	5	-0.2	0.043	2.43	1.48	0.11	0.07
XI	1	350.7	20.4	1	174.73	1.62	5	-0.2	0.043	3.39	-25.53	5.97	8.95
XI	2	351.6	18.7	1	181.23	1.75	4	1.6	3.169	1.74	3.97	0.04	0.05
XI	2	351.6	18.7	1	181.23	1.75	4	1.6	3.169	1.87	30.13	5.13	8.33
XI	3	333	19.5	1	198.73	2.56	4	5.9	0.403	5.97	2.58	0.04	0.04
XI	3	333	19.5	1	198.73	2.56	4	5.9	0.403	-3.94	-12.45	0.77	0.56
XI	4	356.4	28.6	0	157	7.85	3.6	2.1	0.9	3.14	2.51	0.05	0.07
XI	4	356.4	28.6	0	157	7.85	3.6	2.1	0.9	-2.96	10.94	0.37	0.35
XI	5	359.4	27.9	0	131	6.55	5	-0.9	0.01	2.07	1.36	0.46	0.57
XI	5	359.4	27.9	0	131	6.55	5	-0.9	0.01	1.85	3.26	0.77	0.49
XI	5	359.4	27.9	0	131	6.55	5	-0.9	0.01	3.88	13.79	4.34	2.03
XI	6	358	21	0	150	7.5	3.6	1.8	2.177	3.25	4.02	0.05	0.08
XI	6	358	21	0	150	7.5	3.6	1.8	2.177	0.88	14.28	0.87	1.28
XI	7	358	21	0	150	7.5	6	0.6	2.177	3.25	4.02	0.05	0.08
XI	7	358	21	0	150	7.5	6	0.6	2.177	0.88	14.28	0.87	1.28
XI	9	358	21	0	150	7.5	0.5	0.4	2.177	3.25	4.02	0.05	0.08
XI	9	358	21	0	150	7.5	0.5	2	2.177	3.25	4.02	0.05	0.08
XI	9	358	21	0	150	7.5	0.5	3.2	2.177	3.25	4.02	0.05	0.08
XI	9	358	21	0	150	7.5	0.5	4.8	2.177	3.25	4.02	0.05	0.08
XI	9	358	21	0	150	7.5	0.5	0.4	2.177	0.88	14.28	0.87	1.28
XI	9	358	21	0	150	7.5	0.5	2	2.177	0.88	14.28	0.87	1.28
XI	9	358	21	0	150	7.5	0.5	3.2	2.177	0.88	14.28	0.87	1.28
XI	9	358	21	0	150	7.5	0.5	4.8	2.177	0.88	14.28	0.87	1.28
XI	10	358	21	0	150	7.5	0.5	1.6	2.177	3.25	4.02	0.05	0.08
XI	10	358	21	0	150	7.5	0.5	6.8	2.177	3.25	4.02	0.05	0.08
XI	10	358	21	0	150	7.5	0.5	1.6	2.177	0.88	14.28	0.87	1.28
XI	10	358	21	0	150	7.5	0.5	6.8	2.177	0.88	14.28	0.87	1.28
XI	11	343	23.2	0	289	14.45	4	-3.1	0.143	1.33	2.02	0.06	0.09
XI	12	346.1	21.7	0	160	8	3.6	1	0.3	1.79	1.83	0.07	0.07
XI	12	346.1	21.7	0	160	8	3.6	1	0.3	-0.35	9.42	0.82	1.85
XI	12	346.1	21.7	0	160	8	3.6	1	0.3	0.88	-21.66	14.84	21.19
XI	13	346.1	21.7	0	160	8	0.5	0.1	0.3	1.79	1.83	0.07	0.07
XI	13	346.1	21.7	0	160	8	0.5	2	0.3	1.79	1.83	0.07	0.07
XI	13	346.1	21.7	0	160	8	0.5	0.1	0.3	-0.35	9.42	0.82	1.85
XI	13	346.1	21.7	0	160	8	0.5	2	0.3	-0.35	9.42	0.82	1.85
XI	13	346.1	21.7	0	160	8	0.5	0.1	0.3	0.88	-21.66	14.84	21.19
XI	13	346.1	21.7	0	160	8	0.5	2	0.3	0.88	-21.66	14.84	21.19
XI	14	346.1	21.7	0	160	8	0.8	0	0.3	1.79	1.83	0.07	0.07
XI	14	346.1	21.7	0	160	8	0.8	2	0.3	1.79	1.83	0.07	0.07
XI	14	346.1	21.7	0	160	8	0.8	0	0.3	-0.35	9.42	0.82	1.85
XI	14	346.1	21.7	0	160	8	0.8	2	0.3	-0.35	9.42	0.82	1.85
XI	14	346.1	21.7	0	160	8	0.8	0	0.3	0.88	-21.66	14.84	21.19
XI	14	346.1	21.7	0	160	8	0.8	2	0.3	0.88	-21.66	14.84	21.19
XI	15	346.1	21.7	0	160	8	0.5	1.7	0.3	1.79	1.83	0.07	0.07
XI	15	346.1	21.7	0	160	8	0.5	2.7	0.3	1.79	1.83	0.07	0.07
XI	15	346.1	21.7	0	160	8	0.5	1.7	0.3	-0.35	9.42	0.82	1.85
XI	15	346.1	21.7	0	160	8	0.5	2.7	0.3	-0.35	9.42	0.82	1.85
XI	15	346.1	21.7	0	160	8	0.5	1.7	0.3	0.88	-21.66	14.84	21.19
XI	15	346.1	21.7	0	160	8	0.5	2.7	0.3	0.88	-21.66	14.84	21.19
XI	16	346.1	21.7	0	160	8	1.1	0.4	0.3	1.79	1.83	0.07	0.07
XI	16	346.1	21.7	0	160	8	1.1	2.4	0.3	1.79	1.83	0.07	0.07
XI	16	346.1	21.7	0	160	8	1.1	0.4	0.3	-0.35	9.42	0.82	1.85
XI	16	346.1	21.7	0	160	8	1.1	2.4	0.3	-0.35	9.42	0.82	1.85
XI	16	346.1	21.7	0	160	8	1.1	0.4	0.3	0.88	-21.66	14.84	21.19
XI	16	346.1	21.7	0	160	8	1.1	2.4	0.3	0.88	-21.66	14.84	21.19
XI	20	347.2	20.2	0	141	7.05	0.5	1.8	0.121	2.42	1.37	0.1	0.15
XI	20	347.2	20.2	0	141	7.05	0.5	1.8	0.121	-1.58	14.08	3.02	2.52
XI	21	347.2	20.2	0	141	7.05	0.8	2	0.121	2.42	1.37	0.1	0.15
XI	21	347.2	20.2	0	141	7.05	0.8	2	0.121	-1.58	14.08	3.02	2.52

XI	23	350.1	22.5	0	123	6.15	0.5	4.9	2.337	0.33	10.64	0.44	0.53
XI	24	350.1	22.5	0	123	6.15	5	-2.1	2.337	0.33	10.64	0.44	0.53
XI	25	353.2	23.6	0	163	8.15	0.5	0.6	3.497	1.68	2.88	0.03	0.03
XI	25	353.2	23.6	0	163	8.15	0.5	2.5	3.497	1.68	2.88	0.03	0.03
XI	25	353.2	23.6	0	163	8.15	0.5	4	3.497	1.68	2.88	0.03	0.03
XI	26	353.2	23.6	0	163	8.15	0.8	1	3.497	1.68	2.88	0.03	0.03
XI	26	353.2	23.6	0	163	8.15	0.8	2.5	3.497	1.68	2.88	0.03	0.03
XI	27	353.2	23.6	0	163	8.15	5	-0.4	3.497	1.68	2.88	0.03	0.03
XI	28	353.2	23.6	0	163	8.15	0.5	0.8	3.497	1.68	2.88	0.03	0.03
XI	28	353.2	23.6	0	163	8.15	0.5	2.8	3.497	1.68	2.88	0.03	0.03
XI	29	352.8	22.8	0	130	6.5	4	1.6	0.144	0.1	1.34	0.07	0.11
XI	29	352.8	22.8	0	130	6.5	4	1.6	0.144	-1.03	10.32	1.34	1.95
XI	29	352.8	22.8	0	130	6.5	4	1.6	0.144	3.22	3.42	0.18	0.12
XI	29	352.8	22.8	0	130	6.5	4	1.6	0.144	4.17	20.03	20.12	23.24
XI	30	352.8	22.8	0	130	6.5	6	-0.4	0.144	0.1	1.34	0.07	0.11
XI	30	352.8	22.8	0	130	6.5	6	-0.4	0.144	3.22	3.42	0.18	0.12
XI	30	352.8	22.8	0	130	6.5	6	-0.4	0.144	4.17	20.03	20.12	23.24
XI	32	352.8	22.8	0	130	6.5	4	2.6	0.144	0.1	1.34	0.07	0.11
XI	32	352.8	22.8	0	130	6.5	4	2.6	0.144	-1.03	10.32	1.34	1.95
XI	32	352.8	22.8	0	130	6.5	4	2.6	0.144	3.22	3.42	0.18	0.12
XI	32	352.8	22.8	0	130	6.5	4	2.6	0.144	4.17	20.03	20.12	23.24
XI	33	348.6	17.9	0	175	8.75	4	3.8	0.086	5.96	1.72	0.07	0.06
XI	33	348.6	17.9	0	175	8.75	4	3.8	0.086	0.09	2.85	0.12	0.15
XI	33	348.6	17.9	0	175	8.75	4	3.8	0.086	-2.34	-10.12	0.5	0.67
XI	33	348.6	17.9	0	175	8.75	4	3.8	0.086	7.43	27.2	16.39	18.96
XI	34	348.1	16.8	0	143	7.15	5	7.5	1.3	5.04	3.33	0.05	0.07
XI	36	354.6	22.7	0	134	6.7	8	1.6	1.03	1.94	2.53	0.03	0.04
XI	36	354.6	22.7	0	134	6.7	8	1.6	1.03	-1.31	12.34	0.51	0.56
XI	37	354.6	22.7	0	134	6.7	0.5	8.6	1.03	-1.31	12.34	0.51	0.56
XI	38	354.6	22.7	0	134	6.7	5	0.5	1.03	1.94	2.53	0.03	0.04
XI	38	354.6	22.7	0	134	6.7	5	0.5	1.03	-1.31	12.34	0.51	0.56
XI	40	351.3	17	0	225	11.25	6	4.3	3.524	3.94	3.49	0.1	0.13
XI	40	351.3	17	0	225	11.25	6	4.3	3.524	-4.01	6.11	2.38	1.52
XI	40	351.3	17	0	225	11.25	6	4.3	3.524	2.5	16.49	2.09	1.83
XI	41	351.5	12.8	0	132	6.6	0.5	1.4	1.377	0.14	14.83	1.41	1.67
XI	41	351.5	12.8	0	132	6.6	0.5	5.2	1.377	0.14	14.83	1.41	1.67
XI	41	351.5	12.8	0	132	6.6	0.5	1.4	1.377	4.61	-3.98	0.13	0.1
XI	41	351.5	12.8	0	132	6.6	0.5	5.2	1.377	4.61	-3.98	0.13	0.1
XI	42	351.5	12.8	0	132	6.6	0.5	-0.5	1.377	0.14	14.83	1.41	1.67
XI	42	351.5	12.8	0	132	6.6	0.5	0.6	1.377	0.14	14.83	1.41	1.67
XI	42	351.5	12.8	0	132	6.6	0.5	1.5	1.377	0.14	14.83	1.41	1.67
XI	42	351.5	12.8	0	132	6.6	0.5	3.1	1.377	0.14	14.83	1.41	1.67
XI	42	351.5	12.8	0	132	6.6	0.5	4.9	1.377	0.14	14.83	1.41	1.67
XI	42	351.5	12.8	0	132	6.6	0.5	0.6	1.377	4.61	-3.98	0.13	0.1
XI	42	351.5	12.8	0	132	6.6	0.5	1.5	1.377	4.61	-3.98	0.13	0.1
XI	42	351.5	12.8	0	132	6.6	0.5	3.1	1.377	4.61	-3.98	0.13	0.1
XI	42	351.5	12.8	0	132	6.6	0.5	4.9	1.377	4.61	-3.98	0.13	0.1
XI	43	351.5	12.8	0	132	6.6	0.8	1	1.377	0.14	14.83	1.41	1.67
XI	43	351.5	12.8	0	132	6.6	0.8	5	1.377	0.14	14.83	1.41	1.67
XI	43	351.5	12.8	0	132	6.6	0.8	1	1.377	4.61	-3.98	0.13	0.1
XI	43	351.5	12.8	0	132	6.6	0.8	5	1.377	4.61	-3.98	0.13	0.1
XI	44	351.5	12.8	0	132	6.6	8	9.4	1.377	0.14	14.83	1.41	1.67
XI	44	351.5	12.8	0	132	6.6	8	9.4	1.377	4.61	-3.98	0.13	0.1
XI	46	354.6	22.7	0	134	6.7	8	0.1	1.03	1.94	2.53	0.03	0.04
XI	46	354.6	22.7	0	134	6.7	8	0.1	1.03	-1.31	12.34	0.51	0.56
XI	47	354.6	22.7	0	134	6.7	1.1	0.9	1.03	1.94	2.53	0.03	0.04
XI	47	354.6	22.7	0	134	6.7	1.1	2.6	1.03	1.94	2.53	0.03	0.04
XI	47	354.6	22.7	0	134	6.7	1.1	4.2	1.03	1.94	2.53	0.03	0.04
XI	47	354.6	22.7	0	134	6.7	1.1	0.9	1.03	-1.31	12.34	0.51	0.56
XI	47	354.6	22.7	0	134	6.7	1.1	2.6	1.03	-1.31	12.34	0.51	0.56
XI	47	354.6	22.7	0	134	6.7	1.1	4.2	1.03	-1.31	12.34	0.51	0.56
XI	48	355.5	20.9	0	161	8.05	8	3.9	0.137	0.69	1.74	0.22	0.32
XI	48	355.5	20.9	0	161	8.05	8	3.9	0.137	3.46	2.66	2.15	0.99

XI	48	355.5	20.9	0	161	8.05	8	3.9	0.137	7.96	7.83	5.81	2.49
XI	48	355.5	20.9	0	161	8.05	8	3.9	0.137	5.42	0.71	0.1	0.14
XI	49	357.9	20.7	0	150	7.5	6	0.6	3.477	3.2	4.49	0.06	0.09
XI	51	357.9	20.7	0	150	7.5	0.5	0.4	3.477	3.2	4.49	0.06	0.09
XI	51	357.9	20.7	0	150	7.5	0.5	2	3.477	3.2	4.49	0.06	0.09
XI	51	357.9	20.7	0	150	7.5	0.5	3.2	3.477	3.2	4.49	0.06	0.09
XI	51	357.9	20.7	0	150	7.5	0.5	4.8	3.477	3.2	4.49	0.06	0.09
XI	52	357.9	20.7	0	150	7.5	0.5	6.8	3.477	3.2	4.49	0.06	0.09
XI	53	357.9	20.7	0	150	7.5	7	1.6	3.477	3.2	4.49	0.06	0.09
XI	55	346.1	21.7	0	160	8	0.8	2	0.3	1.79	1.83	0.07	0.07
XI	55	346.1	21.7	0	160	8	0.8	2	0.3	-0.35	9.42	0.82	1.85
XI	55	346.1	21.7	0	160	8	0.8	2	0.3	0.88	-21.66	14.84	21.19
XI	56	350.1	22.5	0	123	6.15	0.5	4.9	2.337	0.33	10.64	0.44	0.53
XI	57	342.7	32	0	35	1.75	4.6	2.7	0.381	3.12	-2.93	0.1	0.12
XI	57	342.7	32	0	35	1.75	4.6	2.7	0.381	-3.53	10.01	0.41	0.27
XIII	0	376.8	15.7	0	175	8.75	0.3	1.9	3.392	2.27	3.99	0.03	0.04
XIII	0	376.8	15.7	0	175	8.75	0.3	4.7	3.392	2.27	3.99	0.03	0.04
XIII	0	376.8	15.7	0	175	8.75	0.3	1.9	3.392	6.65	14.12	0.69	0.72
XIII	0	376.8	15.7	0	175	8.75	0.3	4.7	3.392	6.65	14.12	0.69	0.72
XIII	1	376.8	15.7	0	175	8.75	4	-1	3.392	2.27	3.99	0.03	0.04
XIII	1	376.8	15.7	0	175	8.75	4	5	3.392	2.27	3.99	0.03	0.04
XIII	1	376.8	15.7	0	175	8.75	4	-1	3.392	6.65	14.12	0.69	0.72
XIII	1	376.8	15.7	0	175	8.75	4	5	3.392	6.65	14.12	0.69	0.72
XIII	2	377	12.3	0	168	8.4	0.5	0.6	1.603	1.55	2.19	0.04	0.04
XIII	2	377	12.3	0	168	8.4	0.5	0.6	1.603	5.62	12.69	0.21	0.24

Table A.0.7: Continuation of table 6.1. Accordances of H I profile with Na I lines for available lines that are in the angular range and in the velocity intervals of the respective feature. Columns 1 denotes the name of the feature from I–XIII. Column 2 gives a mark for the sight line, columns 3 and 4 contain the (l, b) coordinate pair of the LoS towards a star. Column 5 (n) flags if the distance is from Hipparcos (0) or GAIA (1). Columns 6 and 7 contain the distance of the star and the distance uncertainty respectively. Columns 8 and 9 list the velocity and the FWHM of the line peak respectively. The remaining columns 10–14 contain the results of multi component Gaussian fits with the center μ, standard deviation σ of the thickness and the fit uncertainties $\Delta\mu$ and $\Delta\sigma$. For more information about the fitting procedure, see text in the section 4.7.3.

nm	n_{LoS}	l	b	fl	D	δD	$\delta v_{Na\,I}$	$v_{Na\,I}$	red $\chi^2_{H\,I}$	$\mu_{H\,I}$	$\sigma_{H\,I}$	$\Delta\mu_{H\,I}$	$\Delta\sigma_{H\,I}$
-	-	°	°	-	pc	pc	km s^{-1}	km s^{-1}	-	km s^{-1}	km s^{-1}	km s^{-1}	km s^{-1}
II	0	272.8	29.2	1	400.83	2.51	4	-20.4	0.037	-21.44	-2.49	1.39	1.95
IV	1	297.1	-18.3	1	329.21	2.16	5	-4.9	0.307	4.38	-8.41	2.23	0.76
IV	3	293.8	-13.1	1	375.03	3.81	4	-2.2	0.092	2.17	-7.81	0.74	0.71
IV	4	293.7	-13.2	1	156.42	4.03	4	-15.5	0.146	-22.16	-9.91	3.38	2.79
IV	5	295.1	-13.6	1	433.82	3.71	4	-12.9	0.287	-20.25	-9.41	2.78	2.33
IV	6	297.7	-15.6	1	279.3	3.91	4	0.6	1.623	-0.9	17.81	4.15	1.94
IV	11	294.4	-14.5	0	312	15.6	4	2.7	0.139	-3.25	-16.16	1.73	1.96
V	0	366.2	29.1	0	279.0	13.95	4.0	-0.7	0.289	-1.19	1.79	0.08	0.06
V	3	366.3	23.6	0	140.0	7.0	0.5	0.0	0.379	1.06	2.55	0.08	0.07
V	9	376.8	15.7	0	175.0	8.75	4.0	-1.0	3.392	2.27	3.99	0.03	0.04
VI	1	289.9	-27.1	1	241.66	4.17	4.0	-1.0	0.000	-3.64	4.74	0.25	0.35
VI	2	286.2	-22.3	1	169.94	4.12	4.0	-11.4	0.154	-8.48	2.36	0.06	0.06
VI	5	291.2	-25.8	1	416.13	3.82	4.0	-7.2	1.037	-5.97	2.19	0.12	0.21
VI	5	291.2	-25.8	1	416.13	3.82	4.0	3.0	1.037	-5.02	6.7	1.05	0.36
VII	0	344.4	20.7	1	372.01	2.77	4.0	-9.3	0.422	-6.49	4.57	0.33	0.39
VII	1	350.7	20.4	1	174.73	1.62	5.0	-0.2	0.043	-1.32	1.7	0.17	0.13
VII	1	350.7	20.4	1	174.73	1.62	5.0	-12.6	0.043	-13.08	1.27	0.15	0.18
VII	2	351.6	18.7	1	181.23	1.75	4.0	-14.2	3.169	-12.43	3.11	0.17	0.19
VII	3	356.4	28.6	0	157.0	7.85	3.6	2.1	0.900	-2.96	10.94	0.37	0.35
VII	3	356.4	28.6	0	157.0	7.85	3.6	-4.0	0.900	-3.43	1.37	0.09	0.1
VII	6	358.0	21.0	0	150.0	7.5	0.5	-8.0	2.177	-8.04	2.88	0.2	0.23
VII	6	358.0	21.0	0	150.0	7.5	0.5	-1.3	2.177	0.88	14.28	0.87	1.28
VII	9	343.0	23.2	0	289.0	14.45	4.0	-3.1	0.134	-3.46	6.36	0.62	0.62
VII	11	346.1	21.7	0	160.0	8.0	0.5	-3.5	0.300	-3.6	3.3	0.34	0.34
VII	11	346.1	21.7	0	160.0	8.0	0.5	0.1	0.300	-0.35	9.42	0.82	1.85
VII	12	346.1	21.7	0	160.0	8.0	0.8	0.0	0.300	1.79	1.83	0.07	0.07
VII	15	346.9	21.6	0	133.0	6.65	4.0	-8.1	0.800	-8.05	1.25	0.14	0.2
VII	15	346.9	21.6	0	133.0	6.65	4.0	-3.1	0.800	-1.58	5.15	0.15	0.23
VII	17	347.2	20.2	0	141.0	7.05	0.5	-7.0	0.121	-7.17	1.24	0.12	0.19
VII	17	347.2	20.2	0	141.0	7.05	0.5	-5.3	0.121	-4.82	4.88	0.86	0.96
VII	19	347.2	20.2	0	141.0	7.05	0.8	-8.0	0.121	-1.58	14.08	3.02	2.52
VII	22	350.1	22.5	0	123.0	6.15	5.0	-2.1	2.377	-1.29	3.36	0.07	0.12
VII	24	353.2	23.6	0	163.0	8.15	0.8	-11.0	3.497	-10.67	4.83	0.3	0.33
VII	25	353.2	23.6	0	163.0	8.15	5.0	-0.4	3.497	1.68	2.88	0.03	0.03
VII	29	352.8	22.8	0	130.0	6.5	0.5	-12.9	0.144	-12.72	1.22	0.09	0.11
VII	29	352.8	22.8	0	130.0	6.5	0.5	-1.4	0.144	-1.03	10.32	1.34	1.95
VII	27	352.8	22.8	0	130.0	6.5	4.0	-5.4	0.144	4.17	20.03	20.12	23.24
VII	31	348.6	17.9	0	175.0	8.75	4.0	-12.0	0.086	-12.0	1.15	0.06	0.07
VII	35	354.6	22.7	0	134.0	6.7	5.0	0.5	0.086	-1.31	12.34	0.51	0.56
VII	47	342.7	32.0	0	35.0	1.75	4.6	-12.2	0.000	-3.53	10.01	0.41	0.27
VII	51	357.9	20.7	0	150.0	7.5	0.5	-12.2	0.000	-9.01	3.54	0.22	0.2
VIII	0	321.6	45.1	1	99.81	1.86	5.5	-8.0	0.059	-4.69	4.34	0.23	0.35
IX	0	296.0	11.6	0	121.0	6.05	3.6	-6.5	0.020	-5.88	1.83	0.79	0.58
IX	0	296.0	11.6	0	121.0	6.05	3.6	0.0	0.020	-1.79	2.44	0.75	0.43
IX	1	299.1	12.5	0	136.0	6.8	3.6	-2.5	0.314	-2.92	2.51	0.09	0.11
IX	1	299.1	12.5	0	136.0	6.8	3.6	-8.0	0.314	-10.49	-9.82	0.29	0.16
X	0	350.7	20.4	1	174.73	1.62	5.0	-0.2	0.043	2.43	1.48	0.11	0.07
X	1	351.6	18.7	1	181.23	1.75	4.0	1.6	3.169	1.74	3.97	0.04	0.05
X	3	346.1	21.7	0	160.0	8.0	0.5	2.0	0.300	1.79	1.83	0.07	0.07
X	6	346.1	21.7	0	160.0	8.0	1.1	0.4	0.300	-0.35	9.42	0.82	1.85
X	2	346.1	21.7	0	160.0	8.0	3.6	1.0	0.300	0.88	-21.66	14.84	21.19
X	11	347.2	20.2	0	141.0	7.05	0.8	2.0	0.121	2.42	1.37	0.1	0.15
X	10	347.2	20.2	0	141.0	7.05	0.5	1.8	0.121	-1.58	14.08	3.02	2.52
X	14	350.1	22.5	0	123.0	6.15	5.0	-2.1	0.144	0.33	10.64	0.44	0.53
X	15	352.8	22.8	0	130.0	6.5	4.0	1.6	0.144	-1.03	10.32	1.34	1.95
X	18	352.8	22.8	0	130.0	6.5	4.0	2.6	0.144	3.22	3.42	0.18	0.12
X	16	352.8	22.8	0	130.0	6.5	6.0	-0.4	0.144	0.1	1.34	0.07	0.11
X	17	352.8	22.8	0	130.0	6.5	1.0	3.2	0.144	0.1	1.34	0.07	0.11
XI	0	344.4	20.7	1	372.01	2.77	4.0	1.7	0.422	0.3	13.02	1.41	1.0
XI	1	350.7	20.4	1	174.73	1.62	5.0	-0.2	0.043	2.43	1.48	0.11	0.07

XI	2	351.6	18.7	1	181.23	1.75	4.0	1.6	3.169	1.74	3.97	0.04	0.05
XI	3	333.0	19.5	1	198.73	2.56	4.0	5.9	0.403	5.97	2.58	0.04	0.04
XI	4	356.4	28.6	0	157.0	7.85	3.6	2.1	0.040	3.14	2.51	0.05	0.07
XI	5	359.4	27.9	0	131.0	6.55	5.0	-0.9	0.010	1.85	3.26	0.77	0.49
XI	9	358.0	21.0	0	150.0	7.5	0.5	3.2	2.177	3.25	4.02	0.05	0.08
XI	7	358.0	21.0	0	150.0	7.5	6.0	0.6	2.177	0.88	14.28	0.87	1.28
XI	11	343.0	23.2	0	289.0	14.45	4.0	-3.1	0.143	1.33	2.02	0.06	0.09
XI	11	346.1	21.7	0	160.0	8.0	0.5	-3.5	0.300	-3.6	3.3	0.34	0.34
XI	11	346.1	21.7	0	160.0	8.0	0.5	0.1	0.300	-0.35	9.42	0.82	1.85
XI	12	346.1	21.7	0	160.0	8.0	0.8	0.0	0.300	1.79	1.83	0.07	0.07
XI	20	347.2	20.2	0	141.0	7.05	0.5	1.8	0.121	2.42	1.37	0.1	0.15
XI	24	350.1	22.5	0	123.0	6.15	5.0	-2.1	2.337	0.33	10.64	0.44	0.53
XI	25	353.2	23.6	0	163.0	8.15	0.5	2.5	3.497	1.68	2.88	0.03	0.03
XI	30	352.8	22.8	0	130.0	6.5	6.0	-0.4	0.144	-1.03	10.32	1.34	1.95
XI	32	352.8	22.8	0	130.0	6.5	4.0	2.6	0.144	3.22	3.42	0.18	0.12
XI	33	348.6	17.9	0	175.0	8.75	4.0	3.8	0.086	5.96	1.72	0.07	0.06
XI	34	348.1	16.8	0	143.0	7.15	5.0	7.5	1.300	5.04	3.33	0.05	0.07
XI	40	351.3	17.0	0	225.0	11.25	6.0	4.3	3.524	3.94	3.49	0.1	0.13
XI	41	351.5	12.8	0	132.0	6.6	0.5	1.4	1.377	0.14	14.83	1.41	1.67
XI	42	351.5	12.8	0	132.0	6.6	0.5	4.9	1.377	4.61	-3.98	0.13	0.1
XI	47	354.6	22.7	0	134.0	6.7	1.1	2.6	1.030	1.94	2.53	0.03	0.04
XI	46	354.6	22.7	0	134.0	6.7	8.0	0.1	1.030	-1.31	12.34	0.51	0.56
XI	48	355.5	20.9	0	161.0	8.05	8.0	3.9	0.137	3.46	2.66	2.15	0.99
XI	51	357.9	20.7	0	150.0	7.5	0.5	3.2	0.137	3.2	4.49	0.06	0.09
XI	55	346.1	21.7	0	160.0	8.0	0.8	2.0	0.300	1.79	1.83	0.07	0.07
XI	57	342.7	32.0	0	35.0	1.75	4.6	2.7	0.381	3.12	-2.93	0.1	0.12
XIII	0	376.8	15.7	0	175.0	8.75	0.3	1.9	3.392	2.27	3.99	0.03	0.04
XIII	1	376.8	15.7	0	175.0	8.75	4.0	5.0	3.392	6.65	14.12	0.69	0.72
XIII	2	377.0	12.3	0	168.0	8.4	0.5	0.6	1.603	1.55	2.19	0.04	0.04

Table A.0.8: Intensity accordances of H I lines with Na I lines for available Na I lines that are in the angular and in the velocity range of the respective H I feature. This table is the final version of table 6.1 after thinning containing the Na I lines that fitted the H I lines and the description of the columns can be found there.

name	l	b	gflag	d	Δd	$\Delta v_{\mathrm{Na\,I}}$	$v_{\mathrm{Na\,I}}$	$\mu_{\mathrm{H\,I}}$	$\sigma_{\mathrm{H\,I}}$
II	321.6	45.1	1	99.81	1.86	5.5	-8	0.059	23.67
II	316.1	50.8	0	80	4	3	-7.3	0.01	17.51
III	297.1	-18.3	1	329.21	2.16	5	-4.9	0.307	3.2
IV	285.7	-21.2	1	126.77	2.43	4	4.5	10	-26.56
IV	296.6	-14.6	1	161.11	3.52	5	3.8	0.156	-9.22
IV	385.3	-21	0	220	11	4	2.8	0.145	18.52
V	377	12.3	0	168	8.4	0.5	0.6	1.603	6.58
VI	285.7	-21.2	1	126.77	2.43	4	4.5	10	-26.56
VI	285.9	-22.4	1	149.73	3.43	4	6	3.042	-7.54
VI	289.1	-26.5	1	145.33	3.73	4	5.1	0.366	-8.47
VII	355.5	20.9	0	161	8.05	8	3.9	3.133	-10.72
X	353.2	23.6	0	74	3.7	5	-12.7	3.497	1.68
XI	353.2	23.6	0	163	8.15	5	-12.6	3.497	1.68
XI	337.1	18.2	0	100	5	4	-12	0.29	5.53
XI	334.7	17.3	0	148	7.4	4	-14.3	0.913	7.12
XI	353.2	23.6	0	163	8.15	0.5	-12.6	3.497	1.68
XI	353.2	23.6	0	163	8.15	0.8	-13	3.497	1.68
XI	353.2	23.6	0	163	8.15	5	-12.6	3.497	1.68
XII	289.1	-26.5	1	145.33	3.73	4	5.1	0.366	-8.47
XII	291.2	-25.8	1	416.13	3.82	4	3	1.037	-5.97
XII	287.2	-37.3	1	229.53	3.19	3.5	6.7	0.44	0.24
XIV	296	11.6	0	121	6.05	3.6	0	0.374	-12.99
XIV	299.1	12.5	0	136	6.8	3.6	-8	0.314	-18.94

Table A.0.9: Table containing the lower distance limits for H I features from interstellar Na I absorption lines towards stars in the region around Sco-Cen. The table is arranged in the same order as to table A.0.7.

nm	shape	V	l_0	b_0	r/a_e	r/b_e	Δr_{meas}
1	Ell	-30.5	274.1	29.0	8.8	5.4	0.7
1	Ell	-29.7	273.4	28.9	8.9	5.9	0.6
1	Ell	-28.9	273.2	29.0	9.2	5.4	0.6
1	Ell	-28.0	273.3	29.3	9.0	5.4	0.6
1	Ell	-27.2	274.1	29.4	8.7	5.2	0.6
1	Ell	-26.4	274.1	29.3	8.6	5.8	0.6
1	Ell	-25.6	274.5	29.6	8.1	4.9	0.6
1	Ell	-24.6	273.3	30.1	8.1	4.9	0.6
1	Ell	-23.9	273.1	29.5	8.4	5.0	0.6
1	Ell	-23.1	274.1	29.5	8.4	5.5	0.6
1	Ell	-22.3	273.3	29.4	9.0	5.5	0.6
1	Ell	-21.4	273.2	29.2	9.1	5.5	0.6
1	Ell	-20.6	274.2	29.2	9.6	5.6	0.6
1	Ell	-19.8	274.8	29.4	9.0	5.5	0.6
1	Ell	-19.0	274.0	28.9	9.0	5.7	0.6
1	Ell	-18.1	274.3	29.4	9.1	5.5	0.6
1	Ell	-17.3	273.8	28.9	9.0	5.5	0.6
1	Ell	-16.5	274.3	28.7	9.2	5.6	0.6
2	Ell	-22.3	312.6	5.3	47.2	36.0	0.6
2	Ell	-21.4	317.7	5.8	51.9	37.5	0.6
2	Ell	-20.6	318.1	4.7	50.5	38.0	0.6
2	Ell	-19.8	318.6	5.0	50.4	38.4	0.6
2	Ell	-19.0	318.6	5.0	50.7	38.6	0.6
2	Ell	-18.1	319.8	4.1	52.3	39.8	0.6

2	Ell	-17.3	322.4	6.5	50.2	39.5	0.6
2	Ell	-16.5	318.2	7.4	54.0	39.2	0.6
2	Ell	-15.7	320.2	5.6	48.9	42.9	0.6
2	Ell	-14.8	321.8	2.9	51.9	42.6	0.6
2	Ell	-14.0	320.6	6.3	56.8	40.8	0.6
2	Ell	-13.2	320.0	5.7	53.6	42.0	0.6
2	Ell	-12.4	322.5	3.6	56.6	43.8	0.6
2	Ell	-11.5	319.9	5.0	55.5	44.0	0.6
2	Ell	-10.7	319.9	5.0	56.9	43.6	0.6
2	Ell	-9.9	319.9	5.9	57.6	43.8	0.6
2	Ell	-9.1	319.7	3.8	57.5	42.2	0.6
2	Ell	-8.2	319.6	5.0	58.8	44.7	0.6
2	Ell	-7.4	319.4	5.0	59.4	45.8	0.6
2	Ell	-6.6	320.1	4.3	61.8	45.9	0.6
2	Ell	-5.8	317.9	7.9	60.1	43.0	0.6
2	Ell	-4.9	318.7	7.2	60.3	42.9	0.6
2	Ell	-4.1	314.3	8.5	55.8	42.6	0.6
2	Ell	-3.3	314.7	7.3	54.4	43.5	0.6
2	Ell	-2.5	314.6	5.0	56.5	45.8	0.6
2	Ell	-1.6	312.1	2.2	57.9	46.1	0.6
2	Ell	-0.8	310.5	4.4	56.4	42.6	0.6
2	Ell	0.0	315.9	3.5	56.4	42.1	0.6
2	Ell	0.8	309.7	2.5	54.1	41.8	0.6
2	Ell	1.6	321.3	3.7	57.1	42.7	0.6
3	circ	0.0	335.8	20.2	21.9	21.6	0.6
3	circ	0.8	335.6	22.0	22.1	22.0	0.6
3	circ	1.6	338.2	22.6	23.3	23.5	0.6
3	circ	2.5	341.4	19.9	24.5	24.2	0.6
3	circ	3.3	343.2	16.7	24.7	24.4	0.6
3	circ	4.1	342.6	12.0	27.2	26.8	0.6
3	circ	4.9	345.2	11.9	26.7	26.2	0.6
3	circ	5.8	342.6	12.6	27.1	26.9	0.6
3	circ	6.6	343.8	12.0	26.1	25.8	0.6
3	circ	7.4	342.0	16.3	23.3	23.0	0.6
3	circ	8.2	342.7	18.1	21.2	20.9	0.6

Table A.0.10: Shell parameters (of outer edges of circles high density regions) determined by visually fitting ellipsed to the GASS datacubes, shown in figures 6.5 to 6.10. Column 1 gives the name, column two contains the shape, which can be either ellipses or circles. Column 3 lists the velocity channel in which the structure is visible. Columns 4 and 5 give the center coordinates of the ellipses or circles in longitude and latitude respectively. If the shape is a circle, column 6 and 7 give the radius of this circle, else it gives the semi minor- and semi major axis of the ellipse respectively. Column 8 contains the read off error of the angular radius.

name	shape	v / km/s	l_0 / $^\circ$	b_0 / $^\circ$	r/a_e / $^\circ$	r/b_e / $^\circ$	Δr_{mean} / $^\circ$
a	circ	-30.5	304.4	10.2	3.7	3.6	0.3
a	circ	-29.7	305.5	10.2	3.4	3.3	0.3
a	circ	-28.9	307.9	14.4	3.5	3.6	0.3
a	circ	-28.0	307.4	13.6	3.5	3.5	0.3
a	circ	-27.2	307.3	13.8	3.5	3.5	0.3
a	circ	-26.4	307.8	13.8	3.5	3.6	0.3
a	circ	-25.6	307.9	13.6	3.5	3.5	0.3
a	circ	-24.6	307.7	13.4	3.5	3.5	0.3
a	circ	-23.9	307.7	14.0	3.5	3.5	0.3

a	circ	-23.1	307.6	13.4	3.6	3.6	0.3
a	circ	-22.3	308.1	14.4	3.4	3.3	0.5
a	circ	-21.4	307.7	14.8	3.2	3.2	0.5
a	circ	-20.6	307.6	14.1	2.7	2.7	0.6
a	circ	-19.8	307.7	14.2	2.6	2.6	0.6
a	circ	-19.0	309.3	14.4	1.9	1.9	0.6
a	circ	-18.1	309.9	13.8	2.1	2.1	0.6
a	circ	-17.3	309.3	13.0	1.9	1.9	0.6
a	circ	-16.5	309.9	12.5	1.9	1.9	0.6
b	circ	-30.5	292.2	15.2	7.3	7.6	0.7
b	circ	-29.7	292.2	15.9	7.1	7.0	0.7
b	Ell	-28.9	292.0	16.0	7.1	7.9	0.7
b	Ell	-28.0	292.7	15.3	7.0	7.8	0.7
b	Ell	-27.2	291.5	16.2	5.8	9.0	0.7
b	Ell	-26.4	291.0	16.0	6.5	8.6	0.7
b	Ell	-25.6	291.5	16.8	6.2	8.7	0.6
b	Ell	-24.7	291.0	17.3	6.3	8.1	0.6
b	Ell	-23.9	290.5	18.4	6.4	8.2	0.6
b	Ell	-23.1	289.4	17.7	6.5	8.2	0.6
b	circ	-22.3	290.0	17.6	8.0	7.9	0.7
b	circ	-21.4	289.0	16.7	8.2	8.1	0.6
b	circ	-20.6	289.2	18.3	8.2	8.1	0.6
b	circ	-19.8	288.5	16.9	7.2	7.1	0.6
b	circ	-19.0	290.8	17.2	6.7	6.6	0.5
b	circ	-18.1	290.3	17.0	7.5	7.4	0.6
b	circ	-17.3	291.9	18.3	6.4	6.1	0.5
b	circ	-16.5	293.0	17.6	6.5	6.4	0.5
b	circ	-15.7	293.9	18.3	6.4	6.1	0.5
b	circ	-14.8	292.9	18.4	6.1	5.9	0.5
c	Ell	-22.3	309.5	4.6	7.7	3.1	0.6
c	Ell	-21.4	308.4	5.0	7.5	3.8	0.7
c	Ell	-20.6	307.7	5.0	7.4	3.8	0.6
c	Ell	-19.8	308.1	5.0	7.6	3.3	0.6
c	Ell	-19.0	308.2	4.5	7.5	3.4	0.6
c	Ell	-18.1	307.9	4.7	7.2	3.3	0.6
c	Ell	-17.3	307.9	4.3	7.4	3.7	0.6
c	Ell	-16.5	307.6	4.6	7.3	4.2	0.5
c	Ell	-15.7	307.3	4.2	7.2	3.5	0.6
c	Ell	-14.8	306.7	5.9	6.8	3.8	0.6
d	circ	-22.3	353.2	22.8	4.0	4.0	0.6
d	circ	-21.4	352.6	22.2	4.0	3.9	0.6
d	circ	-20.6	353.0	21.4	3.8	3.8	0.8
d	circ	-19.8	352.6	21.3	4.2	4.2	0.6
d	circ	-19.0	352.5	21.8	4.0	3.9	0.6
d	circ	-18.1	352.9	20.9	4.7	4.6	0.6
d	circ	-17.3	352.9	20.6	5.0	4.9	0.6
d	circ	-16.5	352.9	19.7	4.9	4.9	0.6
d	circ	-15.7	352.2	21.2	3.3	3.3	0.6
d	circ	-14.8	351.2	22.1	2.9	2.8	0.6
e	circ	-21.4	275.3	29.2	3.1	3.1	0.6
e	circ	-20.6	275.2	28.4	3.8	3.7	0.7
e	circ	-19.8	275.5	28.9	4.0	3.9	0.6
e	circ	-19.0	275.3	29.4	3.5	3.4	0.6
e	circ	-18.1	274.2	29.4	3.9	3.9	0.6
e	circ	-17.3	273.9	28.8	3.8	3.7	0.7

e	circ	-16.5	273.7	29.2	4.3	4.2	0.7
e	circ	-15.7	273.7	29.2	3.9	3.9	0.6
e	circ	-14.8	272.4	29.1	4.5	4.5	0.6
f	Ell	-22.3	319.1	43.1	8.5	3.7	0.3
f	Ell	-21.4	318.4	43.7	8.2	3.9	0.3
f	Ell	-20.6	317.8	44.4	12.3	3.9	0.4
f	Ell	-19.8	317.1	45.0	11.7	4.4	0.4
f	Ell	-19.0	316.5	45.6	12.8	4.4	0.4
f	Ell	-18.1	320.5	51.4	12.5	4.2	0.4
f	Ell	-17.3	323.5	50.9	11.7	4.4	0.4
f	Ell	-16.5	321.8	50.9	11.0	4.5	0.4
f	Ell	-15.7	322.4	52.1	10.7	4.4	0.4
f	Ell	-14.8	322.6	52.1	11.1	4.4	0.4
g	circ	-19.0	340.4	16.3	4.4	4.3	0.6
g	circ	-18.1	340.0	17.6	4.1	4.0	0.7
g	circ	-17.3	339.1	19.0	5.1	5.1	0.6
g	circ	-16.5	340.0	19.0	4.7	4.7	0.6
g	circ	-15.7	340.0	20.4	4.8	4.7	0.6
g	circ	-14.8	340.2	19.8	4.7	4.7	0.6
h	Ell	-14.0	307.8	3.9	42.6	28.9	0.6
h	Ell	-13.2	307.4	2.3	42.4	27.8	0.6
h	Ell	-12.4	306.9	8.0	52.7	33.1	0.6
h	Ell	-11.5	306.5	7.4	53.0	31.4	0.6
h	Ell	-10.7	311.4	7.1	51.0	31.9	0.6
h	Ell	-9.9	307.8	9.3	52.6	32.8	0.6
h	Ell	-9.1	312.9	8.7	52.5	31.1	0.6
h	Ell	-8.2	310.8	8.5	53.9	32.9	0.6
h	Ell	-7.4	309.4	10.7	53.9	34.1	0.6
h	Ell	-6.6	307.6	9.8	52.6	34.1	0.6
h	Ell	-5.8	311.8	9.5	50.7	32.5	0.6
h	Ell	-4.9	314.6	9.3	51.0	30.8	0.6
h	Ell	-4.1	314.2	9.9	50.5	31.1	0.6
h	Ell	-3.3	316.5	10.3	53.1	31.3	0.6
h	Ell	-2.5	309.8	9.9	55.3	30.5	0.6
h	Ell	-1.6	314.5	10.8	52.2	29.9	0.6
h	Ell	-0.8	313.3	10.4	50.9	31.7	0.6
h	Ell	0.0	318.3	11.4	44.7	31.1	0.6
h	Ell	0.8	320.4	9.7	43.0	25.0	0.6
h	Ell	1.6	320.7	10.1	43.5	31.2	0.6
i	Ell	-14.0	295.2	17.3	10.0	6.1	0.6
i	Ell	-13.2	295.8	16.2	9.7	5.9	0.6
i	Ell	-12.4	295.0	17.5	9.9	6.2	0.5
i	Ell	-11.5	297.0	17.5	8.0	5.4	0.3
i	Ell	-10.7	301.1	18.2	8.0	5.8	0.3
i	Ell	-9.9	299.4	18.1	7.1	5.0	0.3
i	Ell	-9.1	299.8	17.9	5.7	3.7	0.0
i	Ell	-8.2	300.1	17.9	6.7	4.0	0.3
i	Ell	-7.4	300.7	17.9	4.9	3.8	0.2
i	Ell	-6.6	299.6	17.9	4.5	3.6	0.3
i	Ell	-5.8	297.9	17.0	3.7	3.5	0.6
i	circ	-4.9	299.4	17.5	2.8	2.7	0.6
j	Ell	-14.0	307.8	4.3	7.6	3.9	0.6
j	Ell	-13.2	307.3	3.5	6.8	4.1	0.7
j	Ell	-12.4	307.6	3.1	6.9	4.3	0.7
j	Ell	-11.5	306.8	3.4	8.1	4.0	0.6

j	Ell	-10.7	307.2	4.2	6.7	4.1	0.6
j	Ell	-9.9	309.3	3.9	6.2	3.8	0.6
j	Ell	-9.1	308.6	4.2	7.8	3.2	0.7
j	Ell	-8.2	308.5	4.2	7.8	3.2	0.7
j	Ell	-7.4	307.9	5.2	7.5	3.8	0.5
j	Ell	-6.6	310.5	4.4	7.5	3.7	0.5
j	Ell	-5.8	303.5	6.1	15.1	5.1	0.6
j	Ell	-4.9	304.2	5.9	16.4	5.4	0.6
j	Ell	-4.1	305.7	6.3	10.9	5.5	0.6
j	Ell	-3.3	307.2	6.7	9.8	4.8	0.6
j	circ	-2.5	309.5	8.5	5.3	5.3	0.6
j	circ	-1.6	310.0	9.0	5.3	5.2	0.6
j	circ	-0.8	310.8	9.1	5.0	4.9	0.6
j	circ	0.0	310.6	9.5	4.8	4.8	0.6
k	circ	-14.0	310.3	11.8	3.2	3.0	0.6
k	circ	-13.2	309.4	11.8	3.0	2.9	0.7
k	circ	-12.4	310.3	11.6	3.1	3.2	0.6
k	circ	-11.5	309.8	12.2	3.3	3.4	0.6
k	circ	-10.7	310.3	12.2	3.5	3.5	0.6
k	circ	-9.9	309.3	12.2	3.4	3.4	0.6
k	circ	-9.1	309.0	12.1	3.5	3.5	0.6
k	circ	-8.2	309.4	13.4	4.4	4.5	0.6
k	circ	-7.4	309.5	13.4	4.3	4.2	0.7
k	circ	-6.6	308.5	13.1	4.2	4.2	0.8
l	circ	12.9	292.6	17.3	28.0	16.9	12.3
l	circ	-12.4	331.3	22.9	2.4	2.3	0.6
l	circ	-11.5	330.9	22.7	2.4	2.3	0.6
l	circ	-10.7	330.3	22.1	1.7	1.7	0.6
l	circ	-9.9	330.0	22.0	1.9	1.9	0.5
l	circ	-9.1	330.4	22.2	1.7	1.7	0.6
l	circ	-8.2	330.3	22.2	1.2	1.2	0.6
m	circ	-14.0	320.9	12.9	4.4	4.4	0.6
m	circ	-13.2	320.8	14.2	5.1	4.9	0.6
m	Ell	-12.4	323.0	13.8	9.7	5.9	0.4
m	Ell	-11.5	324.5	15.0	10.0	6.1	0.5
m	Ell	-10.7	327.6	13.6	11.8	7.2	0.5
m	Ell	-9.9	328.3	14.3	15.2	7.4	0.6
m	Ell	-9.1	327.7	14.7	13.9	6.5	0.5
m	Ell	-8.2	328.6	16.5	15.1	8.3	0.6
m	Ell	-7.4	328.1	16.7	13.9	7.9	0.6
m	Ell	-6.6	329.7	16.0	15.2	7.6	0.7
m	Ell	-5.8	331.5	16.9	17.1	9.8	0.6
m	Ell	-4.9	331.7	17.6	18.3	9.6	0.6
m	Ell	-4.1	331.3	17.3	16.2	9.6	0.6
m	Ell	-3.3	331.4	16.9	16.2	9.4	0.6
m	Ell	-2.5	331.5	17.7	15.2	10.3	0.6
m	Ell	-1.6	331.6	18.2	15.4	11.4	0.6
m	circ	-0.8	331.9	19.5	9.2	8.9	0.5
m	circ	0.0	328.9	21.6	10.8	10.7	0.5
m	Ell	0.8	330.3	17.1	10.2	5.1	0.6
m	Ell	1.6	331.0	16.2	8.4	4.2	0.6
ni	circ	-14.0	345.3	23.6	7.6	7.5	0.6
ni	circ	-13.2	343.3	23.8	6.2	6.1	0.7
ni	circ	-12.4	346.1	25.2	5.8	5.7	0.6
ni	circ	-11.5	345.8	25.2	6.4	6.3	0.6

ni	circ	-10.7	345.0	25.8	5.1	5.1	0.6
ni	circ	-9.9	344.0	27.5	4.7	4.6	0.6
ni	circ	-9.1	344.2	27.0	4.4	4.3	0.7
ni	circ	-8.2	344.4	26.3	4.4	4.3	0.6
ni	circ	-7.4	344.8	25.1	3.2	3.2	0.5
ni	circ	-6.6	344.3	24.3	3.5	3.4	0.5
nii	circ	-11.5	350.0	22.2	2.5	2.5	0.3
nii	circ	-10.7	351.3	21.7	2.6	2.6	0.3
nii	circ	-9.9	351.2	21.5	3.1	3.1	0.3
nii	circ	-9.1	351.4	20.9	3.0	3.0	0.3
nii	circ	-8.3	351.7	22.0	3.6	3.6	0.3
nii	circ	-7.5	351.4	21.2	3.1	3.1	0.3
nii	circ	-6.6	351.9	21.2	3.1	3.1	0.3
nii	circ	-5.8	351.3	21.3	2.9	2.9	0.3
nii	circ	-4.9	351.6	21.3	2.9	2.9	0.3
nii	circ	-4.1	351.6	21.5	3.3	3.3	0.3
nii	circ	-3.3	352.2	21.5	4.0	4.0	0.3
nii	circ	-2.5	350.8	21.9	2.9	2.9	0.3
nii	circ	-1.6	351.3	22.0	3.4	3.4	0.3
nii	circ	-0.8	349.3	21.5	2.7	2.7	0.6
nii	circ	0.0	349.3	21.4	3.0	2.9	0.6
nii	circ	0.8	349.5	21.9	2.9	2.9	0.6
nii	circ	1.6	349.3	21.0	2.4	2.4	0.6
nii	circ	2.5	349.0	21.0	2.6	2.6	0.6
nii	circ	3.3	348.9	21.4	2.6	2.6	0.6
nii	circ	4.1	349.2	21.2	2.6	2.6	0.6
nii	circ	4.9	348.9	21.2	2.6	2.5	0.6
nii	circ	5.8	348.9	21.6	3.0	3.0	0.6
nii	circ	6.6	348.8	21.3	3.0	3.0	0.6
nii	circ	7.4	349.1	20.7	2.5	2.5	0.5
nii	circ	8.2	347.9	20.5	2.8	2.7	0.6
nii	circ	9.1	350.0	20.0	2.1	2.1	0.5
nii	circ	9.9	349.7	20.5	2.5	2.4	0.6
o	circ	-14.0	335.6	4.5	2.8	2.8	0.5
o	circ	-13.2	335.3	3.7	2.3	2.2	0.6
o	circ	-12.4	335.2	2.4	4.0	3.9	0.6
o	circ	-11.5	336.0	3.7	3.2	3.2	0.6
o	circ	-10.7	335.2	2.4	4.0	3.9	0.6
o	circ	-9.9	335.6	2.1	3.5	3.4	0.6
o	circ	-9.1	334.5	0.6	5.0	4.9	0.5
o	circ	-8.2	335.1	0.8	4.7	4.6	0.5
o	circ	-7.4	334.8	0.4	5.4	5.4	0.6
o	circ	-6.6	334.7	0.7	5.4	5.4	0.6
o	circ	-5.8	334.6	0.3	4.8	4.7	0.6
o	circ	-4.9	335.4	-0.1	4.9	4.8	0.6
o	circ	-4.1	335.4	-0.3	5.0	4.9	0.6
o	circ	-3.3	335.7	0.1	5.2	5.2	0.6
o	circ	-2.5	334.9	0.6	4.3	4.2	0.5
o	circ	-1.6	334.1	0.0	3.9	3.9	0.5
o	circ	-0.8	334.1	2.3	2.5	2.4	0.3
o	circ	0.0	334.3	3.2	2.6	2.5	0.3
o	circ	0.8	334.6	3.5	2.5	2.4	0.6
o	circ	1.6	334.3	3.0	2.8	2.7	0.6
pi	circ	-14.0	303.2	6.7	2.7	2.6	0.6
pi	circ	-13.2	302.8	6.5	2.4	2.4	0.6

pi	circ	-12.4	303.2	6.7	2.1	2.1	0.6
pi	circ	-11.5	302.9	6.7	2.5	2.3	0.6
pi	circ	-10.7	303.0	6.8	2.5	2.4	0.6
pi	circ	-9.9	303.6	6.4	2.2	2.2	0.6
p	circ	-1.6	341.5	27.4	1.8	1.8	0.6
p	circ	-0.8	342.0	27.6	2.6	2.5	0.6
p	circ	0.0	341.1	27.0	2.4	2.4	0.5
p	circ	0.8	341.5	27.9	2.9	2.9	0.6
p	circ	1.6	341.0	27.4	2.8	2.7	0.6
q	circ	-2.5	298.9	5.9	3.6	3.8	0.5
q	circ	-1.6	299.2	6.2	4.1	4.1	0.5
q	circ	-0.8	306.7	8.7	2.4	2.4	0.6
q	circ	0.0	306.8	10.6	2.6	2.4	0.5
q	circ	0.8	307.4	8.6	1.8	1.7	0.6
q	circ	1.6	306.3	7.1	1.0	0.9	0.3
r	circ	2.5	345.0	25.1	9.7	9.6	0.6
r	circ	3.3	346.2	24.6	9.7	9.6	0.5
r	circ	4.1	346.7	23.7	9.5	9.4	0.6
r	circ	4.9	346.9	24.7	10.8	10.5	0.6
r	circ	5.8	345.3	24.4	10.8	10.6	0.6
r	circ	6.6	346.7	23.7	11.4	10.8	0.6
r	circ	7.4	346.1	23.7	11.6	11.5	0.6
r	circ	8.2	346.3	23.8	11.4	11.3	0.6
r	circ	9.1	345.7	24.5	11.2	11.0	0.6
r	circ	9.9	346.1	23.7	11.9	11.8	0.6
r	circ	10.7	346.9	23.9	11.7	11.6	0.3
r	circ	11.5	347.1	24.3	11.2	11.1	0.3
r	circ	12.4	346.3	24.5	11.5	11.3	0.3
r	circ	13.2	346.3	25.9	11.6	11.5	0.3
r	circ	14.0	346.0	26.2	11.6	11.5	0.3
s	circ	2.5	329.3	17.6	6.4	6.3	0.6
s	circ	3.3	329.0	16.4	6.5	6.4	0.6
s	circ	4.1	328.4	16.2	5.5	5.4	0.6
s	circ	4.9	327.8	15.6	5.5	5.4	0.6
s	circ	5.8	327.5	15.5	5.2	5.1	0.6
s	circ	6.6	327.6	14.7	5.6	5.5	0.6
s	circ	7.4	327.9	14.8	5.4	5.4	0.6
s	circ	8.2	328.6	15.1	5.4	5.3	0.6
t	circ	6.6	334.7	1.2	5.1	5.0	0.6
t	circ	7.4	333.4	2.0	6.8	6.7	0.6
t	circ	8.2	335.9	2.1	7.5	7.3	0.6
t	circ	9.1	335.4	2.9	7.0	6.9	0.6
t	circ	9.9	335.4	4.2	7.4	7.3	0.6
u	circ	10.7	349.6	4.0	3.0	2.9	0.8
u	circ	11.5	349.9	4.0	2.6	2.5	0.7
u	circ	12.4	349.1	4.1	2.7	2.7	0.6
u	circ	13.2	348.9	4.1	2.7	2.7	0.6
u	circ	14.0	349.4	4.0	2.9	2.9	0.6
u	circ	14.8	349.1	3.7	2.9	2.9	0.6
u	circ	15.7	349.6	3.8	2.7	2.7	0.6
u	circ	17.3	349.7	3.3	3.0	2.9	0.6

Table A.0.13: All visually detected circles or ellipses in the ambient ISM of Sco-Cen using the datacines of the GASS at velocities between -40 km/s to 20 km/s. The circles or ellipses that are connected to a worm (shell candidates) share the same name as listed in column 1. The shapes of the objects (ellipse "ell" or circle "circ") are listed in column 2. Column 3 contains the velocity channels where the circle or the ellipse is detected. The center coordinates l_0 and b_0 are listed in columns 4 and 5 respectively. If the object is an ellipse, the semi axes are listed in columns 6 and 7. Otherwise, the radius is listed in column 6 and agian in columnd 7. The uncertainties of the radii or semi axes are listed in column 8.

name	l_0 / °	b_0 / °	r / °	v / K km/s
a	303.30	10.00	1.45	-33.05
a	308.11	9.12	0.96	-32.05
a	307.79	9.84	1.20	-31.05
a	309.08	8.88	0.96	-30.05
a	304.34	10.72	0.96	-29.05
a	307.39	10.40	0.96	-28.05
a	303.62	10.32	0.96	-27.05
a	303.06	10.00	1.20	-26.05
a	310.04	8.96	0.96	-25.05
a	302.41	9.76	0.96	-24.05
a	303.94	9.60	1.45	-23.05
a	302.57	11.68	2.89	-22.05
a	308.68	10.08	1.20	-21.05
a	304.42	10.88	1.45	-20.05
a	305.71	9.28	0.96	-19.05
a	307.95	10.88	2.89	-18.05
a	303.62	10.48	0.96	-17.05
a	304.90	11.04	1.20	-16.05
a	304.90	9.84	0.96	-15.05
a	306.43	11.44	1.20	-14.05
b	289.64	12.48	4.82	-33.05
b	298.56	12.40	4.58	-32.05
b	295.83	13.28	4.82	-31.05
b	301.21	12.40	4.58	-30.05
b	289.08	12.32	4.58	-29.05
b	300.24	13.20	4.58	-28.05
b	299.36	12.32	4.58	-27.05
b	286.91	12.72	4.82	-26.05
b	300.73	11.44	4.82	-25.05
b	287.56	13.28	4.82	-24.05
b	301.05	11.36	4.82	-23.05
b	287.32	13.12	4.58	-22.05
b	300.73	12.48	4.82	-21.05
b	300.08	12.56	4.82	-20.05
b	300.97	11.36	4.82	-19.05
b	296.07	13.76	4.82	-18.05
b	296.55	9.20	0.96	-17.05
b	299.04	12.56	4.34	-16.05
b	301.29	11.44	3.13	-15.05
b	302.17	12.32	3.13	-14.05
c	-	-	-	-23.21
c	-	-	-	-22.21

c	304.10	6.64	6.75	-21.21
c	-	-	-	-20.21
c	301.13	5.44	5.54	-19.21
c	304.02	6.16	6.75	-18.21
c	301.13	4.96	5.54	-17.21
c	301.61	4.56	6.26	-16.21
c	303.62	5.36	5.30	-15.21
c	301.61	3.60	6.50	-14.21
c	-	-	-	-13.21
c	301.13	3.92	5.78	-12.21
c	-	-	-	-11.21
c	-	-	-	-10.21
d	346.74	15.52	2.65	-23.21
d	346.90	15.36	2.41	-22.21
d	344.81	16.88	3.85	-21.21
d	349.47	19.68	4.58	-20.21
d	350.76	23.12	2.65	-19.21
d	343.93	14.40	2.65	-18.21
d	343.45	15.76	2.65	-17.21
d	343.85	14.08	2.41	-16.21
d	344.41	15.28	2.41	-15.21
d	344.98	17.76	2.89	-14.21
d	344.98	16.00	3.13	-13.21
d	343.93	15.76	2.89	-12.21
d	347.06	16.80	3.85	-11.21
d	344.09	15.44	2.41	-10.21
e	-	-	-	-21.57
e	-	-	-	-20.57
e	-	-	-	-19.57
e	-	-	-	-18.57
e	274.63	28.40	3.85	-17.57
e	273.98	30.08	3.85	-16.57
e	275.27	29.52	3.61	-15.57
e	-	-	-	-14.57
e	275.75	27.44	4.10	-13.57
e	275.91	28.40	3.61	-12.57
e	-	-	-	-11.57
e	-	-	-	-10.57
f	311.89	48.48	3.29	-23.21
f	312.45	38.00	7.15	-22.21
f	303.86	30.96	3.77	-21.21
f	309.88	33.92	3.29	-20.21
f	309.48	34.96	3.53	-19.21
f	302.98	32.80	3.77	-18.21
f	309.08	34.48	3.53	-17.21
f	311.73	36.32	6.18	-16.21
f	309.96	34.16	3.53	-15.21
f	308.60	32.72	3.05	-14.21
f	310.76	34.96	4.26	-13.21
f	309.56	33.52	2.81	-12.21
f	334.21	29.92	3.05	-11.21
f	331.00	29.36	2.81	-10.21
g	340.64	13.68	3.37	-21.57
g	342.73	14.24	3.61	-20.57
g	340.88	13.68	3.61	-19.57

g	338.15	13.52	4.10	-18.57
g	340.72	12.08	2.65	-17.57
g	339.59	12.64	3.13	-16.57
g	337.19	11.76	3.61	-15.57
g	338.23	11.20	2.89	-14.57
g	344.25	12.48	2.89	-13.57
g	335.18	12.96	4.82	-12.57
g	327.39	17.04	4.34	-11.57
g	331.08	10.56	2.41	-10.57
j	320.24	5.44	3.21	-14.19
j	299.84	-4.32	3.45	-13.19
j	321.69	-4.48	3.21	-12.19
j	315.66	7.92	3.21	-11.19
j	299.92	-4.32	3.45	-10.19
j	303.22	7.44	3.21	-9.19
j	318.55	3.60	4.42	-8.19
j	297.59	2.40	3.45	-7.19
j	303.70	-4.88	3.21	-6.19
j	303.38	0.64	8.03	-5.19
j	323.05	0.96	3.45	-4.19
j	300.24	-1.12	3.21	-3.19
j	300.73	-0.56	3.21	-2.19
j	322.49	-0.32	3.93	-1.19
j	302.73	-2.56	6.10	-0.19
j	298.96	-2.96	3.21	0.81
j	304.90	0.64	7.31	1.81
j	322.33	-0.24	4.18	2.81
k	-	-	-	-14.19
k	307.79	11.84	3.77	-13.19
k	-	-	-	-12.19
k	-	-	-	-11.19
k	-	-	-	-10.19
k	307.31	10.56	4.26	-9.19
k	308.68	12.96	4.02	-8.19
k	-	-	-	-7.19
k	-	-	-	-6.19
k	306.67	11.20	3.05	-5.19
k	306.43	11.68	3.29	-4.19
ni	342.41	27.44	3.05	-11.73
ni	347.14	22.64	2.57	-10.73
ni	-	-	-	-9.73
ni	-	-	-	-8.73
ni	348.11	25.68	1.85	-7.73
ni	342.65	22.80	2.81	-6.73
ni	345.14	22.00	2.57	-5.73
ni	346.10	22.72	2.81	-4.73
ni	345.14	23.68	3.77	-3.73
ni	344.57	21.84	2.57	-2.73
nii	-	-	-	-14.19
nii	348.83	20.72	2.57	-13.19
nii	348.75	19.60	2.57	-12.19
nii	349.55	19.76	2.57	-11.19
nii	349.15	21.20	2.25	-10.19
nii	349.07	20.64	2.25	-9.19
nii	352.20	21.12	2.73	-8.19

nii	347.79	22.48	2.57	-7.19
nii	349.31	22.08	2.41	-6.19
nii	348.35	21.60	2.41	-5.19
nii	348.59	20.32	2.25	-4.19
nii	-	-	-	-3.19
nii	-	-	-	-2.19
nii	350.68	20.08	2.89	-1.19
nii	351.00	23.04	2.73	-0.19
nii	351.80	21.92	2.41	0.81
nii	350.44	20.48	2.73	1.81
nii	347.79	21.28	2.89	2.81
o	325.94	-1.20	1.85	-14.19
o	326.91	-1.20	2.81	-13.19
o	341.20	-1.76	1.85	-12.19
o	332.21	1.68	1.85	-11.19
o	341.52	-2.32	1.61	-10.19
o	339.59	-2.40	1.61	-9.19
o	333.25	-1.60	1.85	-8.19
o	339.67	-1.60	1.61	-7.19
o	331.89	0.00	3.53	-6.19
o	332.05	1.20	2.57	-5.19
o	328.27	-1.68	1.85	-4.19
o	338.23	3.52	3.53	-3.19
o	327.87	2.88	1.61	-2.19
o	328.43	2.32	2.81	-1.19
o	337.75	3.92	2.09	-0.19
o	327.39	-1.68	2.33	0.81
o	339.03	3.68	1.61	1.81
o	340.64	-0.24	2.57	2.81
o	339.03	-0.72	3.29	3.81
o	336.06	0.72	4.50	4.81
p	339.19	27.44	1.77	-2.71
p	344.81	28.80	2.25	-1.71
p	341.36	28.72	2.01	-0.71
p	343.61	28.24	2.73	0.29
p	343.37	27.68	2.25	1.29
q	303.06	4.88	1.20	-2.71
q	306.19	5.20	1.45	-1.71
q	301.61	5.60	2.41	-0.71
q	304.10	6.64	1.93	0.29
q	301.29	6.72	1.69	1.29
q	-	-	-	2.29
r	347.22	23.44	10.44	1.39
r	351.64	21.52	9.24	2.39
r	353.33	23.52	10.68	3.39
r	348.91	22.88	11.64	4.39
r	-	-	-	5.39
r	346.42	21.04	11.64	6.39
r	345.22	24.08	11.89	7.39
r	345.54	23.92	11.89	8.39
r	345.06	23.68	10.92	9.39
r	344.17	19.92	10.44	10.39
r	350.28	22.40	11.89	11.39
r	349.07	20.80	11.64	12.39
r	350.60	19.12	9.96	13.39

r	353.01	20.32	10.92	14.39
r	-	-	-	15.39
r	353.33	20.72	11.64	16.39
s	337.51	23.20	5.30	2.21
s	337.02	20.48	6.02	3.21
s	333.89	21.12	5.06	4.21
s	337.11	23.36	5.30	5.21
s	338.23	17.52	6.02	6.21
s	338.63	14.56	5.06	7.21
s	328.51	15.28	5.30	8.21
s	331.40	14.32	5.06	9.21
t	337.35	-1.12	4.42	6.31
t	337.75	0.48	2.49	7.31
t	339.03	-3.44	5.86	8.31
t	342.32	2.32	3.93	9.31
t	341.60	-0.32	7.07	10.31
u	348.67	1.92	2.73	11.23
u	351.72	1.68	2.89	12.23
u	352.76	3.36	2.73	13.23
u	353.57	0.16	2.57	14.23
u	352.52	3.44	2.57	15.23
u	352.44	3.12	2.73	16.23

Table A.0.14: Detected circles using the Hough transformation for circles on the GASS data in the region of Sco-Cen at velocities between -40 km/s to 20 km/s. The circles that are connected to one worm share the same name as listed in column 1. The center coordinates are listed in columns 2 and 3. The radius is listed in column 4 and the velocity channel where the respective circle is detected is listed in column 5. For more information on the detection method see text in section 4.5.3.

b	$T_{\mathrm{b,mean}}$	$\Delta T_{\mathrm{b,mean}}$	$\mathrm{ch_{up}}$	$\mathrm{ch_{low}}$
/°	K km/s	K km/s	-	-
0.0	35.7	20.1	25	0
0.2	36.5	20.3	25	0
0.3	36.9	20.4	25	0
0.5	36.6	20.2	25	0
0.6	36.2	20.1	25	0
0.8	34.9	19.6	25	0
1.0	33.2	18.7	25	0
1.5	27.7	16.3	25	0
2.0	21.1	13.6	25	0
3.0	13.7	8.5	25	0
4.0	8.5	5.4	25	0
6.0	4.3	2.7	25	0
7.0	3.3	2.2	25	0
9.0	1.7	1.1	25	0
10.0	1.5	1.1	25	0
12.0	0.9	0.6	25	0
13.0	0.8	0.5	25	0
14.0	0.7	0.4	25	0
17.0	0.4	0.2	25	0
20.0	0.3	0.2	25	0
0.0	54.4	19.5	30	25
0.2	53.9	19.1	30	25
0.3	52.9	18.7	30	25

0.5	49.9	17.6	30	25
0.6	48.6	17.2	30	25
0.8	45.4	16.2	30	25
1.0	42.5	15.4	30	25
1.5	36.3	14.4	30	25
2.0	31.8	13.7	30	25
3.0	22.8	11.7	30	25
4.0	17.4	9.4	30	25
6.0	13.8	7.8	30	25
7.0	11.3	6.7	30	25
9.0	7.0	4.9	30	25
10.0	6.2	4.3	30	25
12.0	3.9	2.2	30	25
13.0	3.3	1.6	30	25
14.0	3.0	1.4	30	25
17.0	2.4	1.1	30	25
20.0	1.7	0.5	30	25
0.0	57.2	19.0	35	30
0.2	56.7	18.6	35	30
0.3	55.7	18.3	35	30
0.5	52.3	17.3	35	30
0.6	50.8	16.8	35	30
0.8	46.9	15.6	35	30
1.0	43.5	14.7	35	30
1.5	37.3	14.0	35	30
2.0	33.0	13.3	35	30
3.0	24.8	11.4	35	30
4.0	19.6	9.8	35	30
6.0	15.7	8.8	35	30
7.0	13.8	7.9	35	30
9.0	9.7	6.3	35	30
10.0	8.4	5.6	35	30
12.0	5.8	3.0	35	30
13.0	5.0	2.3	35	30
14.0	4.6	2.0	35	30
17.0	3.4	1.2	35	30
20.0	2.8	0.7	35	30
0.0	59.7	19.4	40	35
0.2	59.5	19.3	40	35
0.3	58.1	19.0	40	35
0.5	52.9	17.6	40	35
0.6	50.7	17.0	40	35
0.8	45.3	15.4	40	35
1.0	41.0	14.2	40	35
1.5	34.2	12.5	40	35
2.0	29.4	11.1	40	35
3.0	23.6	9.9	40	35
4.0	19.2	8.6	40	35
6.0	15.1	7.0	40	35
7.0	14.2	6.9	40	35
9.0	11.0	5.7	40	35
10.0	9.8	5.0	40	35
12.0	8.0	3.4	40	35
13.0	7.2	2.7	40	35
14.0	6.8	2.5	40	35

17.0	5.5	1.7	40	35
20.0	5.6	1.5	40	35
0.0	62.2	20.2	45	40
0.2	61.7	19.9	45	40
0.3	60.2	19.4	45	40
0.5	54.3	18.1	45	40
0.6	51.7	17.5	45	40
0.8	45.6	15.8	45	40
1.0	40.7	14.5	45	40
1.5	33.7	12.5	45	40
2.0	29.0	11.2	45	40
3.0	23.8	9.8	45	40
4.0	20.0	7.9	45	40
6.0	17.3	6.7	45	40
7.0	15.8	6.1	45	40
9.0	13.7	5.1	45	40
10.0	11.7	4.1	45	40
12.0	10.5	3.4	45	40
13.0	10.0	3.0	45	40
14.0	9.9	3.4	45	40
17.0	8.8	2.5	45	40
20.0	10.5	3.1	45	40
0.0	67.6	26.6	50	45
0.2	67.0	26.0	50	45
0.3	65.8	25.4	50	45
0.5	60.8	23.7	50	45
0.6	58.5	23.2	50	45
0.8	52.8	21.7	50	45
1.0	48.1	20.4	50	45
1.5	40.9	18.1	50	45
2.0	36.3	16.9	50	45
3.0	30.7	14.4	50	45
4.0	26.1	12.0	50	45
6.0	21.1	8.6	50	45
7.0	19.5	8.0	50	45
9.0	19.1	7.2	50	45
10.0	15.9	5.4	50	45
12.0	15.4	4.8	50	45
13.0	16.2	5.4	50	45
14.0	15.5	5.6	50	45
17.0	14.5	5.9	50	45
20.0	15.4	6.2	50	45
0.0	76.0	36.2	55	50
0.2	75.2	35.4	55	50
0.3	74.2	34.3	55	50
0.5	69.9	32.1	55	50
0.6	67.9	31.5	55	50
0.8	63.3	30.3	55	50
1.0	59.7	29.4	55	50
1.5	53.4	27.5	55	50
2.0	48.7	25.7	55	50
3.0	42.0	22.0	55	50
4.0	36.8	18.6	55	50
6.0	29.5	14.0	55	50
7.0	27.3	12.2	55	50

9.0	26.3	9.6	55	50
10.0	24.0	8.6	55	50
12.0	25.4	9.7	55	50
13.0	26.1	10.2	55	50
14.0	25.7	10.5	55	50
17.0	22.5	12.8	55	50
20.0	19.8	10.6	55	50
0.0	77.1	34.0	60	55
0.2	76.1	33.3	60	55
0.3	75.1	32.5	60	55
0.5	71.7	31.5	60	55
0.6	70.2	31.4	60	55
0.8	66.5	30.9	60	55
1.0	63.5	29.9	60	55
1.5	57.4	27.0	60	55
2.0	53.6	24.8	60	55
3.0	48.7	21.8	60	55
4.0	46.0	21.0	60	55
6.0	41.5	19.2	60	55
7.0	38.7	19.8	60	55
9.0	36.1	17.5	60	55
10.0	35.9	16.7	60	55
12.0	31.4	17.7	60	55
13.0	30.6	18.7	60	55
14.0	29.8	19.1	60	55
17.0	25.2	20.0	60	55
20.0	22.7	18.7	60	55
0.0	65.3	28.5	65	60
0.2	63.6	27.3	65	60
0.3	62.4	26.5	65	60
0.5	59.4	26.3	65	60
0.6	58.0	26.5	65	60
0.8	54.5	26.7	65	60
1.0	51.7	26.3	65	60
1.5	46.7	25.4	65	60
2.0	42.9	25.3	65	60
3.0	39.7	24.8	65	60
4.0	37.4	23.6	65	60
6.0	35.5	21.5	65	60
7.0	34.4	21.9	65	60
9.0	32.3	21.7	65	60
10.0	30.0	20.6	65	60
12.0	25.0	19.5	65	60
13.0	23.3	18.6	65	60
14.0	21.2	17.8	65	60
17.0	18.0	16.8	65	60
20.0	14.6	14.6	65	60
0.0	70.8	20.2	70	65
0.2	68.8	20.0	70	65
0.3	66.4	19.8	70	65
0.5	60.8	19.3	70	65
0.6	58.8	19.4	70	65
0.8	54.0	19.5	70	65
1.0	50.3	19.6	70	65
1.5	43.6	19.6	70	65

2.0	37.1	18.5	70	65
3.0	33.0	18.7	70	65
4.0	29.9	17.6	70	65
6.0	24.0	13.5	70	65
7.0	22.3	12.4	70	65
9.0	19.1	10.6	70	65
10.0	16.3	8.4	70	65
12.0	12.6	7.0	70	65
13.0	11.7	6.1	70	65
14.0	10.1	5.6	70	65
17.0	7.7	4.6	70	65
20.0	6.3	3.8	70	65
0.0	67.8	30.3	75	70
0.2	66.4	30.7	75	70
0.3	64.1	30.4	75	70
0.5	57.6	29.0	75	70
0.6	55.3	28.6	75	70
0.8	50.0	28.1	75	70
1.0	45.9	27.9	75	70
1.5	38.2	17.7	75	70
2.0	31.4	16.2	75	70
3.0	27.3	16.7	75	70
4.0	24.8	16.1	75	70
6.0	19.6	12.8	75	70
7.0	17.6	11.7	75	70
9.0	12.6	8.0	75	70
10.0	10.1	6.2	75	70
12.0	6.5	3.4	75	70
13.0	6.1	3.1	75	70
14.0	5.5	2.7	75	70
17.0	3.8	2.0	75	70
20.0	3.2	1.7	75	70
0.0	64.0	29.0	80	75
0.2	62.0	30.0	80	75
0.3	59.8	30.2	80	75
0.5	54.2	29.6	80	75
0.6	52.2	29.3	80	75
0.8	47.0	28.5	80	75
1.0	42.0	27.3	80	75
1.5	34.1	17.0	80	75
2.0	28.5	16.0	80	75
3.0	24.1	16.2	80	75
4.0	20.4	14.9	80	75
6.0	13.8	9.3	80	75
7.0	12.5	8.9	80	75
9.0	9.5	7.3	80	75
10.0	7.5	5.6	80	75
12.0	4.4	2.5	80	75
13.0	4.1	2.2	80	75
14.0	3.9	2.2	80	75
17.0	2.4	1.4	80	75
20.0	1.9	1.1	80	75
0.0	39.1	14.1	110	100
0.2	36.6	13.6	110	100
0.3	34.3	13.0	110	100

0.5	29.5	11.4	110	100
0.6	27.9	10.9	110	100
0.8	24.6	9.8	110	100
1.0	22.2	9.1	110	100
1.5	17.5	7.7	110	100
2.0	13.9	6.4	110	100
3.0	8.5	4.3	110	100
4.0	5.1	3.0	110	100
6.0	2.6	1.3	110	100
7.0	2.1	1.1	110	100
9.0	1.3	0.7	110	100
10.0	1.0	0.5	110	100
12.0	0.8	0.6	110	100
13.0	0.8	0.5	110	100
14.0	0.7	0.5	110	100
17.0	0.5	0.3	110	100
20.0	0.3	0.1	110	100

Table A.0.15: Mean brightness temperatures $T_{\mathrm{b,mean}}$ with standard deviations $\Delta T_{\mathrm{b,mean}}$ along the longitudes 240°–380° that are obtained for 20 different latitudes b summed up over 5 channels (from the lower channel $\mathrm{ch_{low}}$ in row 4 to the upper channel $\mathrm{ch_{up}}$ in row 5) between the channels 0–110, respectively. This channel range corresponds to the velocity range of -45 km/s to +45 km/s.

1	2	3	4	5	6	7	8	9	10	11a‖11b‖11c	12
sub-group	Center $l/^\circ, b/^\circ$	$\overline{D}_0$ pc	H pc	$\overline{V}_r$ km s^{-1}	$\overline{V}_l$ km s^{-1}	$\overline{V}_b$ km s^{-1}	τ Myr	n_b	$n_{B2.5}$	$n_{a,SN}\|\|n_{b,SN}\|\|n_{c,SN}$	M_{st} $M_\odot$
US	343-360,+10+30	145	50-60	+5.5	-0.3	-0.9	4-5	49	15	0.8‖1 ± 1‖1	2350
UCL	312-343,0+25	140	50 ± 20	+7.0	-1.6	+1.6	14-15	66	17	3.5‖6 ± 3‖13	2100
LCC	285-312,-10+21	118	30-40	+4.2	-1.6	+1.4	11-12	42	7	1.3‖3 ± 2‖6	1300

Table A.0.11: Table containing the main parameters of the stellar groups of Sco-Cen from Poeppel et al. (2010). Column 1 contains the name. Column 2 lists the range in longitude and latitude. Column 3 includes the mean distance from de Zeeuw et al. (1999). In column 4, the characteristic depth along the line of sight is given (de Bruijne 1999), column 5, 6 and 7 contain the average radial, -l-projected and -b-projected velocities, the number of stars with spectral type B and the ones earlier than B2.5 are given in columns 9 and 10 respectively (de Bruijne 1999). The number of supernovae according to (Blaauw 1991), de Geus (1992) and Maíz-Apellániz (2001b) are given in column 11 a), b) and c) respectively. Lastly, in column 12 the total stellar mass is given (de Geus 1992).

subgroup	Center l	b	2 Θ	V_0	n	V_{exp}	D_0	R	d_{min}	d_{max}	d_{obs}	τ_S
UCL	325±5	17,5±5	130±10	+3	1	8	140	127	13	267	76	15.6
					2	10						12.7
					3	12						10.6
US	350±5	21 ± 3	46 ± 6	+3	1	10	145	57	88	202	< 130	5.7
					2	12						4.8
US-loop	346±2	25±4	28	+3	1b	8	130	21	99	161	-	1.0
					2b	10						0.8
LCC	300±5	10±5	90±8	+2	1	6	118	83	35	201	< 60	
					2	9						9.2
					3	12						6.2

Table A.0.12: Fitted parameters of and expanding spherical shell using a 2D geometric model in position velocity space from Cappa de Nicolau & Poeppel (1986). Column 2 contains the center coordinates of the shell l_0, b_0. Column 3 contains the angular size 2Θ, the center- and expansion velocity are listed in column 4 and 6 respectively, while in between the number of fits n is given in colun 5. The distance D_0 to the center is listed in column 7 (this was set equal to the respective subgroups center), column 8 contains the radius of the shell given by $R = \sin\Theta \cdot D_0$, column 9 and 10 contains the minimum distance $d_{min} = D_0 - R$ and maximum distance $d_{max} = D_0 + R$. Column 11 contains the observed distance from interstellar lines D_{obs}. Column 12 contains the age of the shell calculated by $\tau_s = R/V_0$ and column 13 shows the names of the fitted H I features.

1	2	3	4	5	6	7	8	9	10
Autor	shellname	l_0	b_0	Δl	Δb	v_{exp}	v_0	v_{min}	v_{max}
mclure	GSH 263+00+47	262.9	-0.1	2.3	2.9	13	47	37.4	55
mclure	GSH 267-01+77	267.1	-1.1	5.3	3.5	12	77	59	95
mclure	GSH 327+04-25	327.2	3.4	7.7	5.6	7	-25	-32	-19
mclure	GSH 319-01+13	319.4	-1.1	2.1	1.7	18	13	2.6	27
mclure	GSH 255-00+52	255.2	-0.5	3.8	3.7	18	52	0	0
mclure	GSH 256+00+63	256.6	-0.1	2.2	2.2	12	63	0	0
mclure	GSH 292-01+55	292.4	-1.5	5.1	2	21	55	0	0
salmen	GSH 179-24+012	179	-24	11.75	20.75		12	11	14
salmen	GSH 052+10-087	52	10	0.75	1		87	-91	-82
salmen	GSH 040+04+048	40.01	4.29	1.75	1.75		48	39	54
salmen	GSH 052-05+023	52	-5	8.25	8		23	11	39
salmen	GSH 062+03-102	62	3	1.75	2		-102	-107	-99
salmen	GSH 134-43-062	134	-43	9	11.75		-62	-68	-51
elerovah	GSH292.0-01.5+050.5	292.25	-1.5	1.75	1.5	9.25	51.55	42.3	60.8
elerovah	GSH250.0+01.5+67.0	250.5	1.5	2	1	4.1	67	62.9	71.1
elerovah	GSH066.0-01.5-088.6	67.25	-1.75	5.25	1.75	10.3	10.3	-97.9	-77.3
elerovah	GSH243.5-02.5+043.3	241.75	2	9.75	9	30.9	47.4	16.5	78.3
elerovah	GSH226.5-09.5+031.9	226.25	-9.5	5.25	5	21.65	32.95	11.3	54.6

Table A.0.16: A collection of SNRs from McClure-Griffiths et al. (2002), Ehlerová & Palouš (2013) and Sallmen et al. (2015). The first column names the author. Column 2 lists the name of the shell. In columns 3 and 4, the center coordinates l_0 and b_0 are listed respectively. The spread of the shells in longitude Δl and latitude Δb are listed in columns 5 and 6 respectively. Column 7 and 8 contain the expansion velocity v_{exp} and the moving velocity v_0 of the shell respectively. Additionally v_{min} and v_{max}, which were measured in this work are shown in columns 8 and 9.

H I-feature (branch) (1)	$\bar{\Delta}\theta$ ° (2)	$\bar{T}_p$ K (3)	Na I k_V,$\bar{d}_{V12}$ pc (4)	Na I k_L,$\bar{d}_{L12}$ pc (5)	d pc (6)	d_A pc (7)	Panel of Table A.1 (8)	$\bar{d}$ pc (9)	$\bar{\Delta}d$ pc (10)	$\bar{\Delta}t$ pc (11)	N_{HI} 10^{20} cm^{-2} (12)	n_{HI} cm^{-3} (13)	δM_{HI} $M_\odot$ (14)
A_1	6	29 ± 10	2, 80–130	3, 80–145	<99		1	80[1]	60	8	5.3	2.9	5000
A_1'	9	15 ± 5	1, 80–130		<134	<132	2	80[3]	50	13	2.7	1.7	540
A_2	6	16 ± 6	2, 75–125	2, 75–130	<80		3	80[1]	55	8	2.9	1.7	670
A_2'	6	18 ± 7	1, 120–200	2, 125–200	–			120[2]	75	13	3.3	1.4	1700
B_1	6	19 ± 5	4, 75–120	4, 70–160	<150	<150	4	80[2]	70	8	3.5	1.6	)
B_2	7	16 ± 7	2, 75–125	2, 130–215	–			80[3]?	75	10?	2.9	1.3	} 4600
B′	5	16 ± 8	4, 75–130	4, 80–155	–			80[2]	65	7	2.9	1.4	)
B″	7	17 ± 6	2, 75–130?	2, 40-80?	<130	<130	5	75[3]?	50	9?	3.1	2.0	1800
C	3	25 ± 8	3, 160–220	4, 90–215	–	<143	6	100[1]	90	5	4.6	1.7	8300
C′, C″	4	9 ± 2			–			≥ 200[4]		≥14	1.6		≥280
J, K	3	9 ± 4			–			100[4]?		5?	1.6		200
LCC-br.	6	21 ± 4	2, 75–130	2, 60–100?	<143		7	70[2]	50	7	3.8	2.5	1400
LCC-cl.		25 ± 6			<120		7	70[3]?			4.6		730
A^+,A^{++}	6	18 ± 3	3, 70–115	3, 75–165	–			70[2]	70	7	3.3	1.5	800
D_0	9	31 ± 7	3, 100–150	3, 100–200	<190		8	160[1]	75	25	5.7	2.5	9700
D_0'	6	8 ± 3			<288		8	160[4]?	75?		1.5		1300
D_1	5	21 ± 8	4, 160–215	4, 100–160	–			130[3]	60	11	3.8	2.1	7800
D_2	5	24 ± 7	2, 120–180	2, 100–200	–			110[3]	80	10	4.4	1.8	1400
D_t	4	20 ± 5	1, 120–180?		<150		9	120[3]?	60	8?	3.7	2.0	1800
US-loop	8	35 ± 12	3, 75–130?	5, 50–130?	<132	<134	10	140[1]	40	20	6.4	5.2	22 000
Cha arc	9	37 ± 3		2, 100–250?	<175		11	100[3]?	75?	16?	6.8	2.9?	1500
M_1,M_2	4	5 ± 2			>278		16	280[4]?		>20	0.9		18 000
N	4	4 ± 1			<90?		17	90[4]?		6?	0.7		450
Aql Rift		>45	1, 70–200?	2, 50–250	–	<145	12				>8.2		
E	5	14 ± 6	2, 105–155	2, 110–210	<203		13	110[2]	75	10	2.6	1.1	3900

Table A.0.17: Image of table 2 of Poeppel et al. (2010) containing the parameters of the H I features near Sco-Cen. Column 1 contains the name of the feature. In Column 2, the mean angular transverse half-width is listed. Column 3 lists the mean peak brightness temperature and its dispersion. Columns 4 and 5 contain the number k of identifications of an H I feature as a counterpart of Na I clumps, and the average of the distance-ranges covered by the Na I clumps on the line of sight, as derived from different authors (Poeppel et al. 2010), respectively. Columns 6 and 7 contain upper distance limits derived in Poeppel et al. (2010). A reference number to a panel of another table is listed in column 8. Column 9 contains the adopted distanced for the near faces with the assigned group as a superscript, and column 10 shows the radial thicknesses. Column 11 contains the mean thickness across the line of sight. Column 12 lists the mean column density $N_{H\,I}$, derived from T_p. The mean spatial density is listed in column 13. Column 14 contains the H I mass of the feature. Some features of this table serve as a comparison in chapter 6. For a further discussion of the derivation of the values see Poeppel et al. (2010).

1 l_0 °	2 b_0 °	3 r_0 °	4 v_0 km/s	5 $r_{\min}$ °	6 $r_{\max}$ °	7 $v_{\min}$ km/s	8 $v_{\max}$ km/s	9 name -	10 Q_m -	11 Q_{ac} -	12 Q_v -	13 Q_p -	14 Q_f -
198.25	-25.25	13.2	14.3	11.2	19.2	10.4	16.8	DK_1476	1	0.99	1	1	3.99
228.42	-7.42	6.3	38.7	4.7	9.7	24.6	52.9	DK_2046	1	0.97	1	1	3.97
48.33	-8.08	7.7	19.4	6.5	9	10.4	33.6	DK_1303	1	0.97	1	1	3.97
325.83	-8.25	7.2	-21.8	5.2	10	-33.4	-8.9	DK_1286	1	0.97	1	1	3.97
202.75	-30.75	11.5	9.1	9.7	14.5	5.3	11.7	DK_b_356	1	0.96	1	1	3.96
301.33	-4	5	-19.2	3.5	6.5	-30.8	-7.6	DK_1187	1	0.96	1	1	3.96
301.42	-4.08	4.6	-19.2	3.5	6.2	-30.8	-8.9	DK_1188	1	0.96	1	1	3.96
43.5	4.17	3.8	28.4	3	4.5	24.6	32.3	DK_1119	1	0.95	1	1	3.95
42.33	-4.75	5.7	16.8	4.7	9.5	11.7	28.4	DK_857	1	0.93	1	1	3.93
42.33	-8.17	8.3	14.3	7.2	10	5.3	24.6	DK_810	1	0.92	1	1	3.92
304.5	-5.33	5	-16.6	3.7	7	-27	-7.6	DK_3462	1	0.9	1	1	3.9
218.42	-8.75	9.7	22	8.7	13.7	7.8	34.9	DK_457	1	0.87	1	1	3.87
225.25	-9.25	5.1	36.2	3.5	7.2	19.4	52.9	DK_1619	1	1	1	0.7	3.67
45.67	-8.58	10.4	16.8	8.5	13.5	10.4	23.3	DK_1701	1	1	1	0.7	3.66
130.42	4.33	3.2	-52.7	3	4.2	-57.9	-47.6	DK_1452	1	0.98	1	0.7	3.65
26.25	-8.42	8	23.3	6.7	11.5	9.1	37.5	DK_1117	1	0.95	1	0.7	3.62
52.75	11	3.5	19.4	2.5	4.5	15.6	23.3	DK_960	1	0.94	1	0.7	3.6
312	5.42	4.4	-37.3	3.5	5.5	-41.1	-32.1	DK_3275	1	0.9	1	0.7	3.57
145.67	-9.92	7.7	-20.5	6	10.5	-30.8	-11.5	DK_3296	1	0.9	1	0.7	3.57
145.58	-9.83	7.7	-19.2	6.2	10.5	-29.5	-11.5	DK_3295	1	0.9	1	0.7	3.57
145.83	-10	7.5	-21.8	5.5	10.2	-33.4	-11.5	DK_3297	1	0.9	1	0.7	3.57
190	-35	3	-19.2	2	4	-24.4	-15.4	DK_b_802	1	0.89	1	0.7	3.56
126.83	-4.17	4.6	-72	3.7	7.2	-82.3	-61.7	DK_3639	1	0.89	1	0.7	3.55
219.25	-28.5	3.8	-21.8	2.5	4.7	-33.4	-15.4	DK_b_823	1	0.87	1	0.7	3.54
134.5	-35.33	1.8	-68.2	1.7	2.2	-75.9	-61.7	DK_b_222	1	0.87	1	0.7	3.54
222.25	-7.5	7.1	29.7	6.2	9.7	19.4	40	DK_1580	0.5	1	1	1	3.5
65.17	5.92	2.2	24.6	1.7	2.7	18.1	29.7	DK_301	1	0.83	1	0.7	3.49
139.33	-5.17	7.8	-23.1	7.2	9.2	-28.2	-16.6	DK_1527	0.5	0.99	1	1	3.49
230	37.5	1.8	68.4	1.2	2.5	64.5	73.5	DK_1760	0.5	0.99	1	1	3.49
267.83	-7.33	6.4	37.5	5.5	8.2	25.9	49.1	DK_5129	1	0.82	1	0.7	3.49
21.75	1.75	2.8	24.6	2.2	3.7	22	28.4	DK_1483	0.5	0.99	1	1	3.49
214.17	-16.08	9.6	15.6	8.5	12.5	11.7	19.4	DK_1828	0.5	0.99	1	1	3.49
137	-7.42	2.2	-28.2	1.7	3	-33.4	-20.5	DK_1965	0.5	0.98	1	1	3.48
24.33	-3	2.5	27.2	2.2	2.7	23.3	29.7	DK_1281	0.5	0.97	1	1	3.47
3.5	-5.08	4.7	16.8	3.7	7	13	20.7	DK_184	1	0.78	1	0.7	3.45
344.58	-3.92	4.7	10.4	3.2	6.2	4	18.1	DK_165	1	0.77	1	0.7	3.44
162.5	-7.58	7.3	-11.5	5.5	10.2	-16.6	-1.2	DK_928	0.5	0.93	1	1	3.43
28.25	-7	6.6	41.3	5.7	7.5	16.8	65.8	DK_2819	0.5	0.92	1	1	3.42
127.42	-1.58	4.7	-25.7	3.5	6.2	-28.2	-19.2	DK_2820	0.5	0.92	1	1	3.42
87	-1.33	2.7	-34.7	2.5	3	-39.8	-28.2	DK_2873	0.5	0.92	1	1	3.42
281.83	-3.42	3.4	42.6	2.7	4.7	38.7	47.8	DK_3145	0.5	0.91	1	1	3.41
314.67	-2.25	3.7	22	2.5	5	14.3	29.7	DK_104	1	0.74	1	0.7	3.41
31.83	-3.92	5.6	29.7	4.7	8.5	19.4	38.7	DK_3277	0.5	0.9	1	1	3.4
40.83	2.25	7.4	19.4	6	11	13	27.2	DK_635	0.5	0.9	1	1	3.4
289.75	-4	3.4	1.4	2.7	4.7	-11.5	20.7	DK_3576	0.5	0.89	1	1	3.39
56	-2.58	3.7	-51.4	3.2	4.5	-56.6	-43.7	DK_4220	0.5	0.86	1	1	3.36
303.5	-4.92	3.9	-11.5	3	6	-25.7	4	DK_1514	1	0.99	1	0.3	3.32
107.5	-3.42	3.5	-24.4	2.7	4.2	-29.5	-20.5	DK_1785	1	0.99	1	0.3	3.32
107.42	-3.08	4.2	-19.2	3.5	5.5	-27	-10.2	DK_1784	1	0.99	1	0.3	3.32
106.92	-2.75	4.9	-17.9	4	8.5	-25.7	-10.2	DK_1783	1	0.99	1	0.3	3.32
27.83	-7.67	7.5	22	7	8.5	16.8	23.3	DK_5209	0.5	0.82	1	1	3.32
239.58	1.75	6	11.7	4.7	8	-1.2	27.2	DK_1846	1	0.99	1	0.3	3.32
325.08	-5.83	6	-19.2	5	7.2	-23.1	-16.6	DK_5238	0.5	0.82	1	1	3.32
307.58	1.08	8.3	-32.1	6.7	10.2	-39.8	-25.7	DK_1389	1	0.98	1	0.3	3.31
204.58	-26.08	11	6.5	9.5	11.5	4	10.4	DK_b_634	1	0.98	1	0.3	3.31
127.67	-4.25	4.3	33.6	3.5	6.2	29.7	37.5	DK_2009	1	0.97	1	0.3	3.31
167.42	-6.58	6.5	0.1	4.5	9	-3.8	4	DK_241	0.5	0.81	1	1	3.31
45.67	-8.08	7.7	11.7	6.7	9.7	6.5	15.6	DK_1299	1	0.97	1	0.3	3.3
132	1.5	3.6	-8.9	3	4.7	-11.5	-3.8	DK_232	0.5	0.8	1	1	3.3

124.17	-5.75	5.1	-45	4	7	-48.9	-42.4	DK_1267	1	0.97	1	0.3	3.3
203.5	-23.42	14	9.1	11.2	16.7	6.5	13	DK_b_360	1	0.97	1	0.3	3.3
45.67	-6.08	7.8	11.7	6.5	13	1.4	24.6	DK_1221	1	0.96	1	0.3	3.3
238.25	-6	6.7	-8.9	5.5	10	-10.2	10.4	DK_1050	1	0.95	1	0.3	3.28
163	-7.92	5.2	-17.9	4	6.2	-24.4	-12.8	DK_930	1	0.93	1	0.3	3.27
128.42	6.58	3.2	76.1	2.2	4.7	69.7	82.5	DK_136	0.5	0.76	1	1	3.26
36.25	-2.83	4.2	22	3	6	15.6	31	DK_120	0.5	0.75	1	1	3.25
46.67	-7.42	5.3	9.1	4.2	6.5	5.3	14.3	DK_757	1	0.91	1	0.3	3.25
46.17	-6.83	5.7	19.4	4.5	8.5	6.5	32.3	DK_756	1	0.91	1	0.3	3.25
184.5	-11	8.9	7.8	7.5	12.5	0.1	20.7	DK_723	1	0.91	1	0.3	3.24
165.75	-16.92	8	1.4	7.5	9	-2.5	4	DK_659	1	0.9	1	0.3	3.24
206.17	-34.5	6.2	-24.4	4.5	7	-36	-14.1	DK_b_785	1	0.9	1	0.3	3.24
58.92	5.58	7.4	22	5	10.2	6.5	38.7	DK_656	1	0.9	1	0.3	3.24
280.08	-3.58	3.8	14.3	2.7	4.7	7.8	20.7	DK_3575	1	0.89	1	0.3	3.22
48.5	-7.17	5.7	40	5	7	31	47.8	DK_3584	1	0.89	1	0.3	3.22
55.75	-5.08	8.8	27.2	7	12.5	13	42.6	DK_562	1	0.89	1	0.3	3.22
262.33	10.92	5	51.6	4.2	6	43.9	59.4	DK_3668	1	0.88	1	0.3	3.22
220	12.67	1.7	45.2	1.5	2.5	40	49.1	DK_456	1	0.87	1	0.3	3.2
313.83	-9.58	8.8	-16.6	7.5	10	-27	-5.1	DK_4380	1	0.85	1	0.3	3.19
258.58	-7.58	5.7	32.3	5.2	6.7	24.6	40	DK_4593	1	0.84	1	0.3	3.18
136.42	-10.42	10.7	-24.4	9.2	17	-29.5	-12.8	DK_4719	1	0.84	1	0.3	3.17
50.08	-4.42	4.7	4	4	7	-7.6	14.3	DK_338	1	0.84	1	0.3	3.17
205	-29.33	10.3	9.1	8.5	14.5	6.5	13	DK_b_540	1	1	1	0.2	3.17
312.75	3.75	8.3	-34.7	6.5	11	-41.1	-28.2	DK_1668	1	1	1	0.2	3.16
128.67	4.92	3.2	23.3	2.5	4.7	19.4	27.2	DK_1601	1	1	1	0.2	3.16
124.42	2.25	2.5	-24.4	2.2	3	-28.2	-20.5	DK_1555	0.5	0.99	1	0.7	3.16
139.33	-7.67	7.8	-27	7.2	9.2	-29.5	-23.1	DK_1528	0.5	0.99	1	0.7	3.16
131.92	1.08	3.5	45.2	2.7	5	41.3	47.8	DK_294	1	0.82	1	0.3	3.16
129.08	-6.25	6.5	-16.6	5	8.7	-20.5	-12.8	DK_1861	1	0.98	1	0.2	3.15
266.58	-3.75	2.8	31	2.2	3.5	28.4	34.9	DK_1906	1	0.98	1	0.2	3.15
37.58	-3.75	4	42.6	3.2	5	34.9	49.1	DK_1400	1	0.98	1	0.2	3.15
213.67	-15.92	10.2	20.7	6.7	12.5	13	28.4	DK_1958	0.5	0.98	1	0.7	3.14
321.92	-6.67	7.5	-19.2	5.7	8.5	-30.8	-6.3	DK_5458	1	0.81	1	0.3	3.14
219.75	-15	6.4	16.8	5	8	10.4	22	DK_1983	1	0.98	1	0.2	3.14
257	6.17	2.3	49.1	2	3.5	45.2	52.9	DK_1993	0.5	0.98	1	0.7	3.14
33.67	9.25	4	28.4	2.7	5.5	27.2	33.6	DK_1331	0.5	0.97	1	0.7	3.14
136	-4.75	7.4	-27	6.2	12.5	-30.8	-21.8	DK_2034	0.5	0.97	1	0.7	3.14
356.58	7.58	5.2	7.8	3.5	7	1.4	14.3	DK_209	1	0.8	1	0.3	3.13
351.17	21.5	15.7	4	9	18	1.4	7.8	DK_b_34	1	0.96	1	0.2	3.13
138.17	-3.58	9.8	-16.6	6.2	12.7	-21.8	-12.8	DK_2320	1	0.95	1	0.2	3.12
135.08	-7.58	6.8	-57.9	6	10.7	-69.5	-47.6	DK_2335	0.5	0.95	1	0.7	3.12
127.75	-1.5	3	-19.2	2.5	3.7	-23.1	-16.6	DK_2351	1	0.95	1	0.2	3.12
315.33	-3.75	5.2	-11.5	4.2	7	-16.6	-7.6	DK_2389	1	0.95	1	0.2	3.11
88.42	4.75	7.9	16.8	7.2	9.2	9.1	23.3	DK_1068	0.5	0.95	1	0.7	3.11
306.17	1.58	3.7	-21.8	3.5	4.2	-25.7	-19.2	DK_2496	0.5	0.94	1	0.7	3.11
132.42	-4.75	4.5	-29.5	3.2	6	-34.7	-25.7	DK_2513	0.5	0.94	1	0.7	3.11
334.58	-3	5.8	24.6	4.7	8.5	13	36.2	DK_1011	0.5	0.94	1	0.7	3.11
310	3.92	5.2	-8.9	3.7	7	-12.8	-3.8	DK_1003	0.5	0.94	1	0.7	3.11
349.42	3.92	6.2	9.1	5	7.2	6.5	13	DK_985	1	0.94	1	0.2	3.1
317.83	-3.08	9.7	-41.1	6.2	12.5	-45	-37.3	DK_2595	0.5	0.93	1	0.7	3.1
52.33	-6.58	5.2	36.2	4.7	6.2	24.6	47.8	DK_2598	0.5	0.93	1	0.7	3.1
264.67	-5.75	4.7	50.3	4	6.7	38.7	60.6	DK_2663	0.5	0.93	1	0.7	3.1
218.08	-11	9.5	16.8	6.7	13.5	14.3	23.3	DK_919	0.5	0.93	1	0.7	3.1
265.17	-3.83	3.7	46.5	3	4.5	37.5	47.8	DK_2740	1	0.93	1	0.2	3.1
136.08	-8.5	10.5	-16.6	7.7	16.2	-23.1	-11.5	DK_2779	1	0.93	1	0.2	3.09
54.83	3.08	7.5	33.6	5.7	8.5	19.4	47.8	DK_798	0.5	0.92	1	0.7	3.09
241.17	-6.25	6.5	27.2	5.7	9.2	23.3	36.2	DK_3004	0.5	0.92	1	0.7	3.08
220.92	3.92	5.7	47.8	4.5	8.2	45.2	58.1	DK_3099	1	0.91	1	0.2	3.08
48.83	8.42	2.6	22	1.7	3.2	18.1	24.6	DK_737	0.5	0.91	1	0.7	3.08
127	-6.75	6.6	-27	5.2	10	-29.5	-19.2	DK_3187	0.5	0.91	1	0.7	3.07
141.83	2.58	2.7	23.3	2.2	3.7	18.1	28.4	DK_609	1	0.89	1	0.2	3.06
253.33	-4.58	2.7	42.6	2.2	3.2	38.7	47.8	DK_3489	0.5	0.89	1	0.7	3.06
239.83	-3.08	3.1	80	2.2	3.5	76.1	83.8	DK_3722	1	0.88	1	0.2	3.05

33.5	-5.58	4.8	34.9	3.2	6.2	27.2	42.6	DK_3745	0.5	0.88	1	0.7	3.05
35.17	6.5	3.3	29.7	2.5	4.2	24.6	34.9	DK_3833	0.5	0.88	1	0.7	3.04
44.42	-4.83	3.5	40	2.7	4.7	32.3	47.8	DK_3894	1	0.87	1	0.2	3.04
282.42	-4.83	2.3	37.5	1.7	3.2	34.9	41.3	DK_4385	0.5	0.85	1	0.7	3.02
288.58	-5.5	2.5	14.3	2	3.2	6.5	23.3	DK_4456	1	0.85	1	0.2	3.02
34.83	-0.67	4.5	85.1	4	6.2	59.4	110.9	DK_4735	0.5	0.84	1	0.7	3.01
354.25	25	7.5	9.1	6.7	9	4	13	DK_1620	1	1	1	0	3
354.25	25	7.5	9.1	6.7	9	4	13	DK_b_47	1	1	1	0	3
137.75	0.92	2.8	22	2.2	4	18.1	24.6	DK_1602	1	1	1	0	3
193.17	-20.33	14.2	6.5	11	18	2.7	10.4	DK_b_528	1	1	1	0	3
199.58	-26.5	13.5	6.5	12.2	13.7	2.7	11.7	DK_b_513	1	1	1	0	3
196.5	-25.33	14.2	9.1	12.7	16.7	5.3	11.7	DK_b_516	1	1	1	0	3
307.08	3.17	6.7	-14.1	5.2	10	-19.2	-10.2	DK_306	1	0.83	1	0.2	2.99
308.33	2.33	6.2	-16.6	5.2	6.7	-21.8	-11.5	DK_307	1	0.83	1	0.2	2.99
197.92	-21.92	14.8	9.1	12.5	18	5.3	11.7	DK_b_489	1	0.99	1	0	2.99
198.83	-28.08	13.5	11.7	11.2	16.5	6.5	15.6	DK_b_486	1	0.99	1	0	2.99
40.08	-2.33	5.2	52.9	5.2	5.5	50.3	56.8	DK_5049	0.5	0.82	1	0.7	2.99
0.17	13.92	12.2	5.3	10	16	0.1	10.4	DK_1750	1	0.99	1	0	2.99
128.33	-0.75	2.4	45.2	2	2.7	40	51.6	DK_1771	1	0.99	1	0	2.99
238.92	-5.33	5.7	29.7	4.2	8	25.9	34.9	DK_1792	1	0.99	1	0	2.99
127.42	6.25	5	-19.2	3.5	7	-23.1	-12.8	DK_1802	1	0.99	1	0	2.99
273.92	-5.75	4.4	11.7	3.7	5.7	7.8	19.4	DK_5194	1	0.82	1	0.2	2.99
273.42	-5.67	4.7	16.8	3.7	6	9.1	24.6	DK_5193	1	0.82	1	0.2	2.99
272.75	-5.17	4.7	22	3.7	7	9.1	33.6	DK_5192	1	0.82	1	0.2	2.99
199.92	-28.67	13.5	6.5	11.7	13.7	4	10.4	DK_b_451	1	0.98	1	0	2.98
201.58	-23.83	9.8	6.5	9	12.7	4	10.4	DK_1857	1	0.98	1	0	2.98
201	-22.5	13.5	14.3	9	18.7	5.3	25.9	DK_b_449	1	0.98	1	0	2.98
351.42	22.67	11.1	1.4	7.5	15	0.1	6.5	DK_b_46	1	0.98	1	0	2.98
355	21.25	8.6	0.1	7	10	-5.1	2.7	DK_b_42	1	0.98	1	0	2.98
353.58	21.42	9	1.4	7.2	10.5	-3.8	4	DK_b_43	1	0.98	1	0	2.98
287.33	-1.17	4.7	14.3	3.5	6.7	2.7	27.2	DK_1879	1	0.98	1	0	2.98
215.75	-38.33	6.2	-21.8	5	7.2	-45	-7.6	DK_b_616	1	0.98	1	0	2.98
302.75	2	6	-34.7	4.2	7.7	-39.8	-29.5	DK_1387	1	0.98	1	0	2.98
201.5	-15.33	15.1	14.3	10.7	19.7	7.8	24.6	DK_1383	1	0.98	1	0	2.98
129.58	-2.67	4	-57.9	3.5	4.7	-69.5	-46.3	DK_5417	0.5	0.81	1	0.7	2.98
57.58	-6.42	6.1	-6.3	5.5	8.2	-20.5	6.5	DK_1365	1	0.98	1	0	2.98
355.08	12.5	11.2	5.3	10	14.5	4	10.4	DK_1321	1	0.97	1	0	2.97
89.33	0.5	5.4	11.7	4	8.5	2.7	23.3	DK_244	1	0.81	1	0.2	2.97
59	-5.58	2.5	-101.7	2.2	3.2	-108.1	-93.9	DK_5563	0.5	0.81	1	0.7	2.97
201.83	-30.5	13.8	9.1	12.2	14.5	5.3	11.7	DK_b_380	1	0.97	1	0	2.97
92.42	6.92	5	13	4.2	7	9.1	16.8	DK_1304	1	0.97	1	0	2.97
250.08	-4.17	4.8	27.2	3.2	6.5	23.3	32.3	DK_5707	1	0.8	1	0.2	2.97
146.75	3	4.1	-6.3	3.2	5.7	-11.5	-2.5	DK_224	1	0.8	1	0.2	2.97
226.08	-29.25	2.2	-15.4	1.7	2.7	-21.8	-8.9	DK_b_665	1	0.97	1	0	2.97
312.17	13	8.6	6.5	6.2	12.2	0.1	14.3	DK_1215	1	0.96	1	0	2.96
8.92	-8.58	7.3	9.1	5	9	2.7	11.7	DK_1146	1	0.95	1	0	2.95
216	-15.75	5.2	16.8	3.5	7	11.7	20.7	DK_182	1	0.78	1	0.2	2.95
200.75	-29.33	12.3	10.4	10.7	15.2	7.8	14.3	DK_2418	1	0.95	1	0	2.95
302.42	-6	4.9	-27	3.5	6.7	-38.5	-14.1	DK_1055	1	0.95	1	0	2.95
40.58	1	7.2	1.4	6	13	-1.2	13	DK_1049	1	0.95	1	0	2.95
135.5	-7.25	6.4	-45	6	6.7	-50.1	-37.3	DK_2424	1	0.95	1	0	2.95
186.17	-20.42	6.1	-6.3	5.5	6.7	-11.5	-2.5	DK_b_712	1	0.95	1	0	2.95
44.17	4.25	4.4	22	3.2	5.7	18.1	24.6	DK_2436	1	0.94	1	0	2.94
329.08	23.33	14.7	4	12.2	19	1.4	10.4	DK_b_26	1	0.94	1	0	2.94
201.17	-20.67	4.6	19.4	4	5.2	14.3	23.3	DK_b_338	1	0.94	1	0	2.94
55.5	-7.75	8	9.1	6.7	13.2	6.5	16.8	DK_1014	1	0.94	1	0	2.94
307.92	14	6	11.7	4.5	7.2	0.1	24.6	DK_1007	1	0.94	1	0	2.94
236.92	-2.58	4.5	14.3	4	5.5	9.1	18.1	DK_2524	1	0.94	1	0	2.94
309.08	20.25	6.3	24.6	4	8.5	11.7	38.7	DK_973	1	0.94	1	0	2.94
326.5	-6.08	5.5	-21.8	4.5	8	-29.5	-15.4	DK_2638	1	0.93	1	0	2.93
326.67	-2.08	2.3	6.5	2	3.5	2.7	9.1	DK_148	1	0.77	1	0.2	2.93
128.83	2.83	1.2	-24.4	1	1.2	-27	-20.5	DK_146	1	0.77	1	0.2	2.93
244.83	3.33	4.7	34.9	3.7	6.5	31	38.7	DK_937	1	0.93	1	0	2.93

197.92	-20.83	7.4	9.1	6.5	9.5	5.3	13	DK_b_741	1	0.93	1	0	2.93
125.08	-4.33	5.3	76.1	4.2	8	72.2	80	DK_2714	1	0.93	1	0	2.93
262.92	-3.5	4.2	50.3	3	6	45.2	64.5	DK_2738	1	0.93	1	0	2.93
151.92	-4.92	3.8	-23.1	3.2	4.5	-32.1	-14.1	DK_2798	1	0.93	1	0	2.93
315.08	-0.58	8.6	-27	8.2	12.5	-30.8	-21.8	DK_2804	1	0.93	1	0	2.93
223.33	-1.58	2.5	42.6	2	3.5	40	46.5	DK_129	1	0.76	1	0.2	2.93
168.33	-5.58	5.7	0.1	4.2	8.7	-3.8	4	DK_114	1	0.75	1	0.2	2.92
221.33	-16.17	9.7	14.3	8.2	12.2	7.8	22	DK_3122	1	0.91	1	0	2.91
52.5	-6.58	7.5	16.8	6.2	11	13	24.6	DK_713	1	0.91	1	0	2.91
52.67	-6.67	7.3	14.3	6.2	10.5	10.4	23.3	DK_714	1	0.91	1	0	2.91
52.5	-6.42	8.2	18.1	6.2	11	14.3	24.6	DK_712	1	0.91	1	0	2.91
236.17	-12.67	4.8	-28.2	3.7	7	-34.7	-21.8	DK_3274	1	0.9	1	0	2.9
89.5	-6.5	5.6	-16.6	4.7	6.7	-20.5	-10.2	DK_3338	1	0.9	1	0	2.9
34.33	-5.58	5.7	24.6	5	7.7	18.1	29.7	DK_3336	1	0.9	1	0	2.9
134	-7.75	4.9	-55.3	4.2	6.2	-64.3	-47.6	DK_3331	1	0.9	1	0	2.9
79.5	-21.08	2.8	-63	2	3.2	-66.9	-59.2	DK_b_230	1	0.9	1	0	2.9
218.42	-22.17	11.7	15.6	9.5	14.5	11.7	19.4	DK_b_303	1	0.89	1	0	2.89
131.83	-8.67	5.9	-42.4	4.7	8.2	-48.9	-32.1	DK_3551	1	0.89	1	0	2.89
274.17	-1.25	4	19.4	2.7	5	18.1	28.4	DK_3574	1	0.89	1	0	2.89
233.25	-7.83	4.4	65.8	3.2	5.2	58.1	74.8	DK_3609	1	0.89	1	0	2.89
240.75	-1.83	3.5	16.8	2.5	5	11.7	22	DK_535	1	0.88	1	0	2.88
35.5	-4.25	8.1	16.8	6	12.7	9.1	24.6	DK_530	1	0.88	1	0	2.88
333.75	-5.42	4.8	-29.5	4.2	6.5	-37.3	-20.5	DK_3756	1	0.88	1	0	2.88
233.92	-21	3.9	-34.7	3	4.7	-41.1	-29.5	DK_b_818	1	0.88	1	0	2.88
250.92	-3.58	4.1	37.5	3.2	4.7	31	42.6	DK_3804	1	0.88	1	0	2.88
126.5	6.25	4.2	-29.5	3.7	5.5	-36	-24.4	DK_3900	1	0.87	1	0	2.87
245.67	15.25	3	47.8	2.5	4	45.2	51.6	DK_466	1	0.87	1	0	2.87
310.42	-1.92	2.2	50.3	1.7	2.7	46.5	55.5	DK_70	1	0.7	1	0.2	2.87
135.5	-8.92	7.2	-51.4	6.5	8.5	-61.7	-41.1	DK_4223	1	0.86	1	0	2.86
57.17	-6.33	6.3	-14.1	5.5	8.2	-32.1	2.7	DK_4236	1	0.86	1	0	2.86
127.42	-8.42	6.2	-43.7	4.7	8.5	-47.6	-30.8	DK_4318	1	0.86	1	0	2.86
38.67	-3.33	3.5	50.3	2.5	4.7	46.5	52.9	DK_4341	1	0.85	1	0	2.85
338.58	-2.58	2.2	43.9	2	2.5	38.7	49.1	DK_4424	1	0.85	1	0	2.85
215.58	-21.83	14.5	16.8	11.7	19	13	20.7	DK_b_300	1	0.85	1	0	2.85
90.25	-5.33	5.5	-7.6	4.5	6.5	-15.4	0.1	DK_364	1	0.85	1	0	2.85
241.92	-6.17	8.2	16.8	6.7	11	9.1	24.6	DK_4548	1	0.85	1	0	2.85
41.33	-2.5	3	11.7	2.5	4.5	7.8	15.6	DK_48	1	0.68	1	0.2	2.84
207.67	-20.25	3.3	-17.9	2.7	3.5	-21.8	-14.1	DK_b_851	1	0.84	1	0	2.84
87.92	-1.67	6	1.4	4.7	8.5	-1.2	5.3	DK_343	1	0.84	1	0	2.84
91.25	-4.42	5.4	-54	5	6.5	-65.6	-42.4	DK_4802	1	0.84	1	0	2.84
32.92	-1.33	4.3	46.5	4	5	42.6	50.3	DK_4814	1	0.84	1	0	2.84
305.83	0.5	8.7	-34.7	6.7	14.7	-38.5	-29.5	DK_1640	0.5	1	1	0.3	2.83
320.33	0.33	7.9	-34.7	6.5	10.5	-38.5	-28.2	DK_1598	0.5	1	1	0.3	2.83
46.25	39.5	3	14.3	2.5	3.7	10.4	16.8	DK_b_210	1	0.83	1	0	2.83
22.5	-4	7.7	24.6	6.2	13.7	9.1	46.5	DK_1745	0.5	0.99	1	0.3	2.83
313.67	-7	9	-28.2	7	14.7	-34.7	-20.5	DK_1777	0.5	0.99	1	0.3	2.82
276.83	-8	4.2	9.1	3.5	5	0.1	13	DK_5195	1	0.82	1	0	2.82
128.33	-3.83	3.2	-45	2.2	3.7	-56.6	-34.7	DK_5190	1	0.82	1	0	2.82
302.08	-7.58	6.8	-14.1	6	9.5	-30.8	2.7	DK_1465	0.5	0.99	1	0.3	2.82
146.33	1.33	3.6	63.2	2.7	4.5	58.1	67.1	DK_275	1	0.82	1	0	2.82
1.58	6.5	9.2	9.1	6.7	11.5	7.8	14.3	DK_1436	0.5	0.98	1	0.3	2.82
10.42	-5.25	5	40	4.2	6.2	25.9	54.2	DK_5303	1	0.82	1	0	2.82
38.92	15.5	3.2	68.4	2.2	4	64.5	73.5	DK_1417	0.5	0.98	1	0.3	2.81
302.83	-5.25	3.2	11.7	3	3.2	2.7	13	DK_5354	1	0.81	1	0	2.81
227	-9.08	4.8	63.2	3.5	7	47.8	78.7	DK_5376	1	0.81	1	0	2.81
274.33	2.67	4.7	-17.9	3.5	6.7	-21.8	-14.1	DK_234	1	0.8	1	0	2.8
48.08	-4	4.7	5.3	4.2	5.7	0.1	10.4	DK_225	1	0.8	1	0	2.8
312.33	-7.5	10.2	-17.9	7.5	15.7	-36	1.4	DK_2128	0.5	0.97	1	0.3	2.8
124.92	5.5	3.3	55.5	2.2	4.2	50.3	61.9	DK_222	1	0.8	1	0	2.8
304.83	-2.17	1.8	-19.2	1.7	2.2	-24.4	-14.1	DK_2174	0.5	0.96	1	0.3	2.8
184.67	-0.25	6.2	-7.6	5	10	-10.2	-3.8	DK_206	1	0.79	1	0	2.79
3.83	-5.58	4.5	11.7	3.5	6.2	10.4	18.1	DK_185	1	0.78	1	0	2.78
234.33	-10.75	6.7	20.7	5.7	8.2	16.8	24.6	DK_2394	0.5	0.95	1	0.3	2.78

291.5	-6.58	6.5	-8.9	5.2	7.2	-29.5	-7.6	DK_1052	0.5	0.95	1	0.3	2.78
278.83	-3.33	3.2	22	2.2	3.7	18.1	29.7	DK_2453	0.5	0.94	1	0.3	2.78
206.58	-10.42	5.5	16.8	4.2	7.7	11.7	22	DK_168	1	0.78	1	0	2.78
215.42	36.33	3.9	50.3	3.2	6.7	45.2	71	DK_b_923	1	0.77	1	0	2.78
312.67	4.42	2.4	55.5	2	3	50.3	59.4	DK_1013	0.5	0.94	1	0.3	2.77
353.92	-8.25	7.1	1.4	6	9.5	0.1	9.1	DK_994	0.5	0.94	1	0.3	2.77
135.75	-6.08	4.9	-42.4	4.2	5.7	-51.4	-34.7	DK_2639	0.5	0.93	1	0.3	2.77
304.5	-0.58	1.2	60.6	1	1.2	58.1	64.5	DK_13	0.5	0.6	1	0.7	2.77
5.92	-2.75	2.5	-68.2	2.2	3	-70.8	-64.3	DK_2700	0.5	0.93	1	0.3	2.76
233.58	5.25	3	22	2.5	3.7	19.4	25.9	DK_2760	0.5	0.93	1	0.3	2.76
186.92	-2	5.3	-5.1	4.5	6.5	-7.6	1.4	DK_130	1	0.76	1	0	2.76
218.83	5.83	6.3	-2.5	3.7	7.7	-3.8	9.1	DK_816	0.5	0.92	1	0.3	2.76
140.08	2	4	-25.7	3	5.5	-29.5	-21.8	DK_119	1	0.75	1	0	2.75
126.33	4.58	5.9	22	5	10	14.3	28.4	DK_797	0.5	0.92	1	0.3	2.75
308.17	0.67	7.9	-42.4	6.7	9.2	-46.3	-38.5	DK_765	0.5	0.91	1	0.3	2.75
216.17	11.42	1.7	60.6	1.2	2.5	58.1	64.5	DK_698	0.5	0.91	1	0.3	2.74
262.17	4.83	4.5	31	3.7	5.5	25.9	36.2	DK_3450	0.5	0.9	1	0.3	2.73
202.83	-3.67	4.2	4	3.5	6	0.1	7.8	DK_92	1	0.73	1	0	2.73
13.5	-4.58	7.8	19.4	5.7	11	10.4	29.7	DK_616	0.5	0.9	1	0.3	2.73
306.25	-1.83	3.6	27.2	2.2	4.5	23.3	31	DK_89	1	0.73	1	0	2.73
232.92	-9.33	7.2	16.8	5.7	8	14.3	20.7	DK_3583	0.5	0.89	1	0.3	2.72
141.75	-7.5	4.3	32.3	3.7	5.7	28.4	37.5	DK_3666	0.5	0.88	1	0.3	2.72
32.75	6.25	1.8	50.3	1.5	2.5	47.8	54.2	DK_3735	0.5	0.88	1	0.3	2.71
91.67	-3.25	4.4	-36	4	4.7	-42.4	-29.5	DK_3757	0.5	0.88	1	0.3	2.71
260.33	-5.08	3.2	78.7	2.5	4.5	73.5	82.5	DK_3831	0.5	0.88	1	0.3	2.71
319.92	-0.17	1.7	33.6	1.5	2.2	31	36.2	DK_72	1	0.71	0	1	2.71
318.67	-9.25	10.9	-14.1	7.7	12.5	-25.7	-1.2	DK_3972	0.5	0.87	1	0.3	2.7
302.58	-1.25	2.2	51.6	1.7	2.7	46.5	56.8	DK_69	1	0.7	1	0	2.7
218.83	2.67	4.5	34.9	3.2	6.2	22	49.1	DK_4113	0.5	0.86	1	0.3	2.7
38.75	-5.58	6.1	67.1	4.7	7.7	40	94.1	DK_4128	0.5	0.86	1	0.3	2.7
56.75	1.75	3.2	-37.3	3	3.7	-41.1	-32.1	DK_4179	0.5	0.86	1	0.3	2.69
84.25	-0.83	2.3	-57.9	2.2	3.2	-63	-54	DK_4307	0.5	0.86	1	0.3	2.69
101.58	-7.83	5.2	-32.1	4.5	5.7	-33.4	-17.9	DK_4336	0.5	0.86	1	0.3	2.69
227.5	-3.08	5.2	63.2	3.7	6.7	56.8	71	DK_4648	0.5	0.84	1	0.3	2.68
135.92	-21.25	1.5	-148	1.2	1.5	-150.6	-144.2	DK_b_102	1	0.67	1	0	2.67
52.92	1.83	5.7	29.7	5.5	7.7	24.6	36.2	DK_1622	0.5	1	1	0.2	2.67
348.08	3.25	7.2	14.3	5.7	9.2	10.4	16.8	DK_1611	0.5	1	1	0.2	2.66
137.67	-6.67	5.4	-21.8	4.2	8.5	-27	-12.8	DK_1673	0.5	1	1	0.2	2.66
137.5	-6.67	6.7	-14.1	4.7	9.5	-21.8	-12.8	DK_1672	0.5	1	1	0.2	2.66
322.67	0.08	7.2	-37.3	5	8.2	-41.1	-33.4	DK_1600	0.5	1	1	0.2	2.66
349.58	-6.58	5.5	-34.7	4.2	6.2	-47.6	-23.1	DK_4995	0.5	0.83	1	0.3	2.66
314.75	-8.08	8.5	-33.4	7	10.5	-36	-29.5	DK_1779	0.5	0.99	1	0.2	2.66
50.67	-8.67	7.7	22	7	9.2	18.1	27.2	DK_1489	0.5	0.99	1	0.2	2.65
129.25	1.25	6.4	24.6	4.7	9.5	20.7	28.4	DK_1813	0.5	0.99	1	0.2	2.65
322.67	4	5.2	20.7	3.7	7	16.8	24.6	DK_1474	0.5	0.99	1	0.2	2.65
300.75	-2.33	4.7	-27	4.2	6	-29.5	-23.1	DK_1462	0.5	0.99	1	0.2	2.65
58.25	-5.33	4.7	-6.3	4.2	5.2	-19.2	6.5	DK_1455	0.5	0.98	1	0.2	2.65
30.33	34.33	3	77.4	2.2	4.2	73.5	82.5	DK_b_92	1	0.65	1	0	2.65
30.33	34.33	2.4	76.1	2.2	3	72.2	80	DK_b_91	1	0.65	1	0	2.65
184.42	-38.17	6.9	-14.1	5.5	7.2	-21.8	-7.6	DK_b_617	0.5	0.98	1	0.2	2.65
310.25	0.17	8	-33.4	6.5	12.5	-39.8	-27	DK_1420	0.5	0.98	1	0.2	2.65
306.92	-6.25	5.9	-24.4	5	6.2	-29.5	-20.5	DK_1912	0.5	0.98	1	0.2	2.65
353.5	-3.67	3.3	-45	3	4.2	-47.6	-41.1	DK_5349	0.5	0.81	1	0.3	2.65
42.5	3.25	4.2	34.9	3	6.2	27.2	42.6	DK_1401	0.5	0.98	1	0.2	2.65
40.25	8.33	1.6	19.4	1.2	2	18.1	22	DK_1940	1	0.98	0	0.7	2.65
140.5	2.17	4.3	-21.8	3.2	6.2	-25.7	-19.2	DK_1395	0.5	0.98	1	0.2	2.65
37.83	0.08	4.8	18.1	3.2	6.2	14.3	22	DK_1399	0.5	0.98	1	0.2	2.65
266.75	-3.92	5.4	51.6	4.7	6.2	46.5	56.8	DK_1943	0.5	0.98	1	0.2	2.65
161.17	-0.92	1.4	42.6	1.2	1.7	36.2	47.8	DK_28	1	0.65	1	0	2.65
312.67	-6.83	4.7	-3.8	3.2	5.5	-6.3	0.1	DK_5645	0.5	0.8	1	0.3	2.64
47.33	33.17	5.2	9.1	4.2	6.7	6.5	10.4	DK_b_83	1	0.64	0	1	2.64
315.58	-1	4.2	58.1	3.2	5.7	52.9	63.2	DK_5709	0.5	0.8	1	0.3	2.64
135	-4	8.6	-19.2	6.5	12.2	-23.1	-16.6	DK_2152	0.5	0.96	1	0.2	2.63

339	5.83	2.7	27.2	2.2	3.2	23.3	29.7	DK_1219	0.5	0.96	1	0.2	2.63
43.17	3.92	3.1	40	2.7	4	36.2	45.2	DK_2266	0.5	0.96	1	0.2	2.62
41	-3.92	5.9	11.7	4.2	8.2	9.1	15.6	DK_1128	0.5	0.95	1	0.2	2.62
147.83	4.75	8.5	1.4	6.7	14	-2.5	5.3	DK_1095	0.5	0.95	1	0.2	2.62
308.92	7.42	7.7	6.5	5.5	11.5	2.7	9.1	DK_1091	0.5	0.95	1	0.2	2.62
48.67	8.33	4.2	32.3	2.7	5.5	28.4	34.9	DK_1031	0.5	0.94	1	0.2	2.61
167.5	-22.75	7.2	4	6.2	8.2	1.4	6.5	DK_b_722	1	0.94	0	0.7	2.61
91.75	7	2.2	-3.8	1.7	2.7	-7.6	-1.2	DK_2526	0.5	0.94	1	0.2	2.61
135.92	-7.5	6.7	-52.7	5.5	10.7	-64.3	-39.8	DK_2542	0.5	0.94	1	0.2	2.6
32.08	-4.83	4.4	42.6	3.2	5.5	36.2	49.1	DK_2544	0.5	0.94	1	0.2	2.6
305.92	18	6.3	15.6	5	7.7	11.7	19.4	DK_983	0.5	0.94	1	0.2	2.6
207.08	-33.83	4.9	-16.6	4.5	5.2	-19.2	-14.1	DK_b_735	1	0.93	0	0.7	2.6
19.25	-6.67	6.3	11.7	5.5	8	5.3	18.1	DK_927	0.5	0.93	1	0.2	2.6
22.92	-10.08	10.7	11.7	9.2	13.5	7.8	15.6	DK_2676	0.5	0.93	1	0.2	2.6
13.83	-7.33	8.4	11.7	7.2	10.5	6.5	18.1	DK_863	0.5	0.93	1	0.2	2.59
12.58	0.58	5.3	19.4	3.7	6.2	15.6	23.3	DK_855	0.5	0.93	1	0.2	2.59
170.83	-8.42	10	1.4	7.5	15.7	0.1	6.5	DK_836	0.5	0.92	1	0.2	2.59
239.33	-8.92	2.6	29.7	2.5	2.7	24.6	33.6	DK_2871	0.5	0.92	1	0.2	2.59
341.5	-6.5	7.5	4	6.2	12.7	0.1	6.5	DK_790	0.5	0.92	1	0.2	2.59
42.25	-6.83	8.5	10.4	7.7	11	5.3	15.6	DK_788	0.5	0.92	1	0.2	2.59
336	-1.75	6.4	14.3	4.5	7.7	9.1	16.8	DK_710	0.5	0.91	1	0.2	2.57
335.67	-1.75	6.4	15.6	5.2	7.7	11.7	19.4	DK_709	0.5	0.91	1	0.2	2.57
134.33	-3.42	8.7	1.4	6.2	13	-1.2	5.3	DK_693	0.5	0.91	1	0.2	2.57
225.25	-3.33	3.3	-11.5	3	4.5	-15.4	-5.1	DK_634	0.5	0.9	1	0.2	2.56
200	-10.75	9.7	15.6	8.7	13.5	7.8	24.6	DK_618	0.5	0.9	1	0.2	2.56
126.58	-3.75	7.5	-24.4	5.2	11	-27	-20.5	DK_3471	0.5	0.89	1	0.2	2.56
152	3.83	7.7	13	5.5	8.7	4	22	DK_606	0.5	0.89	1	0.2	2.56
28.83	-6	6	28.4	4.2	8.2	22	34.9	DK_3496	0.5	0.89	1	0.2	2.56
353.67	-8	7.7	14.3	7.2	9.2	10.4	18.1	DK_3507	0.5	0.89	1	0.2	2.56
322.42	-2.75	3.7	55.5	2.7	4.7	50.3	59.4	DK_3577	0.5	0.89	1	0.2	2.56
347.83	6.42	2.2	22	1.7	3.2	19.4	25.9	DK_576	0.5	0.89	1	0.2	2.56
140.33	-8.75	10.8	-14.1	7.7	16.2	-16.6	-10.2	DK_3761	0.5	0.88	1	0.2	2.55
358.75	3.17	4.4	11.7	3	5.5	7.8	15.6	DK_502	0.5	0.88	1	0.2	2.55
126.33	1.33	2	25.9	1.7	2.5	20.7	31	DK_437	0.5	0.87	1	0.2	2.53
41.33	-2.58	1.8	24.6	1.7	2	20.7	27.2	DK_62	0.5	0.69	1	0.3	2.52
167.83	-3.5	6.9	16.8	5.7	10.2	9.1	23.3	DK_388	0.5	0.86	1	0.2	2.52
214.42	-10.92	7.5	14.3	6.2	13	10.4	22	DK_367	0.5	0.85	1	0.2	2.52
227.33	-2.75	5.9	71	3.7	7.5	65.8	77.4	DK_4647	0.5	0.84	1	0.2	2.51
354.58	-4	9.6	22	6	12.2	6.5	37.5	DK_1658	0.5	1	1	0	2.5
355.75	10.67	7.7	-3.8	6.7	9	-7.6	0.1	DK_1597	0.5	1	1	0	2.5
316.5	3.42	8.3	-41.1	6.7	13.2	-43.7	-37.3	DK_1685	0.5	1	1	0	2.5
305.5	-7.25	7.9	-16.6	6.2	8.7	-23.1	-10.2	DK_1708	0.5	0.99	1	0	2.49
70.67	-1.92	4.7	-42.4	3.7	5.7	-51.4	-34.7	DK_4979	0.5	0.83	1	0.2	2.49
137.33	-6.08	5.8	-21.8	3.7	7.2	-24.4	-16.6	DK_1572	0.5	0.99	1	0	2.49
181	-36.08	8.3	6.5	7	13.7	2.7	11.7	DK_1726	0.5	0.99	1	0	2.49
180.83	-35.92	8.6	7.8	7	13.7	4	11.7	DK_1725	0.5	0.99	1	0	2.49
50.17	7.75	2.2	24.6	1.7	3	23.3	31	DK_299	0.5	0.83	1	0.2	2.49
53.17	-8.25	6.9	32.3	5.5	8.7	9.1	56.8	DK_1734	0.5	0.99	1	0	2.49
277.75	-1.08	4.7	16.8	3.7	7.5	11.7	22	DK_1551	0.5	0.99	1	0	2.49
359.83	12.67	10.6	4	7.7	15	1.4	10.4	DK_1550	0.5	0.99	1	0	2.49
318	-9.25	11.4	-2.5	8.7	19.2	-8.9	4	DK_1538	0.5	0.99	1	0	2.49
78.75	-4.83	3	-27	2.2	4.2	-32.1	-21.8	DK_5078	0.5	0.82	1	0.2	2.49
73.58	2.33	2	-34.7	2	2.5	-37.3	-29.5	DK_5101	0.5	0.82	1	0.2	2.49
315.17	-8.17	7.5	-37.3	6.5	9.5	-43.7	-32.1	DK_1780	0.5	0.99	1	0	2.49
313.83	-7.83	8.7	-29.5	7	13.2	-34.7	-24.4	DK_1778	0.5	0.99	1	0	2.49
44.67	7.92	4.3	55.5	3	6.2	51.6	59.4	DK_1507	0.5	0.99	1	0	2.49
317.08	-4.42	3.5	-10.2	2.7	5.2	-14.1	-6.3	DK_5148	0.5	0.82	1	0.2	2.49
129	2.58	5.5	23.3	4.2	8.5	19.4	27.2	DK_1793	0.5	0.99	1	0	2.49
131	6.42	9	-16.6	7.5	16	-17.9	-11.5	DK_1801	0.5	0.99	1	0	2.49
240	-2.83	5.8	6.5	4	7.2	-2.5	13	DK_1848	0.5	0.99	1	0	2.49
126.25	-5.17	6.5	1.4	4.7	8.5	-1.2	5.3	DK_1438	0.5	0.98	1	0	2.48
5.08	-3	2.9	4	2.2	4.5	0.1	7.8	DK_30	0.5	0.65	1	0.3	2.48
87.5	0.58	6.8	19.4	5.2	9.7	13	24.6	DK_1434	0.5	0.98	1	0	2.48

39	-3.5	6.7	45.2	5.2	7.7	41.3	47.8	DK_5285	0.5	0.82	1	0.2	2.48
96.08	-2.33	6	-27	4.7	9.7	-34.7	-20.5	DK_5318	0.5	0.81	1	0.2	2.48
261.75	10.08	3.2	46.5	2.2	4.2	41.3	49.1	DK_1904	0.5	0.98	1	0	2.48
126.08	4.5	3.8	-29.5	3.2	6.2	-37.3	-20.5	DK_1920	0.5	0.98	1	0	2.48
310	7.83	8.4	-32.1	6.5	11.7	-33.4	-27	DK_1928	0.5	0.98	1	0	2.48
195	-22.17	7.2	11.7	6	8.5	7.8	14.3	DK_b_628	0.5	0.98	1	0	2.48
42.92	3.08	4.2	22	3	5.5	20.7	24.6	DK_1402	0.5	0.98	0	1	2.48
346.42	3.42	4.5	63.2	3.2	6	46.5	78.7	DK_1396	0.5	0.98	1	0	2.48
267.67	-4.75	5.2	47.8	4.5	5.7	46.5	54.2	DK_1944	0.5	0.98	1	0	2.48
267.67	-4.83	4.1	47.8	3	4.7	42.6	50.3	DK_1945	0.5	0.98	1	0	2.48
268.17	-5.08	3.8	46.5	2.7	4.7	42.6	49.1	DK_1946	0.5	0.98	1	0	2.48
353.67	23.5	9.8	6.5	6	12.5	-1.2	15.6	DK_1369	0.5	0.98	1	0	2.48
222.83	5.92	5.1	-1.2	3	6.2	-5.1	2.7	DK_1979	0.5	0.98	1	0	2.48
66.92	5.58	5.1	-19.2	3.7	6.7	-20.5	-2.5	DK_2001	0.5	0.98	1	0	2.48
317.58	0.83	7.3	-36	5.2	9	-38.5	-33.4	DK_1356	0.5	0.98	0	1	2.48
322.08	-8.58	10	0.1	7	13	-3.8	4	DK_1353	0.5	0.98	1	0	2.48
233.58	6.25	1.5	63.2	1.2	2	60.6	64.5	DK_1343	0.5	0.98	0	1	2.48
136.5	-5.67	1.7	9.1	1.5	1.7	5.3	11.7	DK_1338	0.5	0.98	1	0	2.48
72.58	4.42	2.8	27.2	2.2	4.2	24.6	31	DK_2016	0.5	0.97	1	0	2.47
317.83	-7.83	7.4	-30.8	6.7	10.2	-33.4	-24.4	DK_1324	0.5	0.97	1	0	2.47
343.08	-4	3.6	-1.2	3.2	4.7	-5.1	2.7	DK_245	0.5	0.81	1	0.2	2.47
132.92	-5.42	7.2	-42.4	5.7	10.7	-56.6	-29.5	DK_2048	0.5	0.97	1	0	2.47
235.17	-10.5	7.2	29.7	6.2	8.5	23.3	34.9	DK_5601	0.5	0.81	1	0.2	2.47
215.33	1.92	3.3	11.7	2.7	4.2	2.7	19.4	DK_2070	0.5	0.97	1	0	2.47
330.08	-11.17	12.4	-1.2	10.5	19.5	-5.1	4	DK_2084	0.5	0.97	1	0	2.47
6.58	-3.92	1.7	34.9	1.5	2	31	37.5	DK_2089	0.5	0.97	1	0	2.47
227.67	3.33	3.2	83.8	2	4	80	87.7	DK_1272	0.5	0.97	1	0	2.47
347.58	-4.25	6.5	9.1	4.5	9.2	4	16.8	DK_219	0.5	0.8	1	0.2	2.47
60.92	-8.5	10.4	6.5	8.7	13.7	5.3	19.4	DK_2145	0.5	0.96	1	0	2.46
135	-7.25	8.4	-24.4	6.5	12.2	-25.7	-19.2	DK_2153	0.5	0.96	1	0	2.46
68.25	-6.25	5.2	-3.8	4.5	6	-6.3	0.1	DK_2160	0.5	0.96	1	0	2.46
191.67	-22.58	6.5	6.5	5.5	9	4	11.7	DK_b_672	0.5	0.96	1	0	2.46
182.08	-0.25	7	11.7	6.5	7.5	6.5	16.8	DK_2176	0.5	0.96	1	0	2.46
131.67	6.75	4	47.8	3.5	4.7	40	54.2	DK_2179	0.5	0.96	1	0	2.46
238.83	-0.75	6.2	15.6	4.7	8.5	9.1	22	DK_2247	0.5	0.96	1	0	2.46
239.08	-1.58	5.3	9.1	4.2	6.5	6.5	15.6	DK_2248	0.5	0.96	1	0	2.46
260.83	-4.75	7.7	-27	6.7	9.5	-28.2	-19.2	DK_1179	0.5	0.96	1	0	2.46
330	-4.92	4.8	46.5	4	7.5	36.2	61.9	DK_2271	0.5	0.96	1	0	2.46
297.83	-8.42	6.7	-50.1	4.7	9.7	-54	-47.6	DK_2294	0.5	0.95	1	0	2.45
272.5	-2.08	4.2	-11.5	3.5	6	-20.5	5.3	DK_2325	0.5	0.95	1	0	2.45
283.08	-3.25	3.9	-16.6	3.5	5.7	-28.2	-11.5	DK_2329	0.5	0.95	1	0	2.45
43	8.25	3.9	29.7	3	5.5	24.6	34.9	DK_1118	0.5	0.95	1	0	2.45
37.5	-0.25	3.8	45.2	2.5	4.5	41.3	50.3	DK_176	0.5	0.78	1	0.2	2.45
237.42	0.92	6	18.1	4.2	8	15.6	25.9	DK_2396	0.5	0.95	1	0	2.45
210.83	-16.17	5.7	19.4	4.5	8	14.3	23.3	DK_2433	0.5	0.95	1	0	2.45
347.75	15.5	8.2	4	6.2	13	1.4	7.8	DK_1047	0.5	0.94	1	0	2.44
40.58	-8.75	8.4	34.9	7.5	9	20.7	49.1	DK_2502	0.5	0.94	1	0	2.44
68.83	6.75	6.1	22	5	9.2	11.7	31	DK_982	0.5	0.94	1	0	2.44
37	-4.75	4.4	65.8	4	5.7	52.9	82.5	DK_2584	0.5	0.94	1	0	2.44
309.5	20.17	6.2	18.1	4	8.5	11.7	24.6	DK_b_62	0.5	0.94	1	0	2.44
128.08	4	3.1	9.1	2.2	4.5	6.5	13	DK_150	0.5	0.77	1	0.2	2.44
19.67	-2.17	2.8	52.9	2.2	4	47.8	59.4	DK_149	0.5	0.77	1	0.2	2.44
194.25	-21.75	12.2	-8.9	8.5	15	-14.1	-5.1	DK_b_329	0.5	0.94	1	0	2.44
158.17	-7.67	9.2	-14.1	6.7	14.2	-15.4	-6.3	DK_2614	0.5	0.93	1	0	2.43
57.33	6.67	3.1	16.8	2.5	4.2	13	19.4	DK_2617	0.5	0.93	1	0	2.43
126.25	7.58	6	27.2	3.7	8	22	31	DK_2622	0.5	0.93	1	0	2.43
342.67	-7.83	4.1	-21.8	3.5	4.7	-30.8	-12.8	DK_2628	0.5	0.93	1	0	2.43
128.67	-0.17	8.3	47.8	7.5	10	31	63.2	DK_2637	0.5	0.93	1	0	2.43
304.92	4.42	2.2	-8.9	2	2.5	-10.2	-6.3	DK_947	0.5	0.93	0	1	2.43
188.42	-13.17	10.9	15.6	9.7	14.5	4	27.2	DK_932	0.5	0.93	1	0	2.43
341.5	-14.25	13.8	-3.8	11.5	18	-12.8	5.3	DK_2707	0.5	0.93	1	0	2.43
341.08	-13.25	13.8	-3.8	11.7	19	-12.8	5.3	DK_2706	0.5	0.93	1	0	2.43
340.25	-13	14	-3.8	11.7	19.2	-10.2	5.3	DK_2705	0.5	0.93	1	0	2.43

251.58	5.25	4.2	27.2	3.2	5.5	23.3	29.7	DK_2696	0.5	0.93	1	0	2.43
316.42	-12.58	14.6	0.1	11.7	19.5	-1.2	5.3	DK_2703	0.5	0.93	1	0	2.43
59.08	-2.25	4.9	34.9	4.2	7	27.2	42.6	DK_2715	0.5	0.93	1	0	2.43
323.83	23.08	5.7	-1.2	3.7	6.7	-5.1	2.7	DK_b_65	0.5	0.93	1	0	2.43
312.08	9.17	5.8	-39.8	4.5	7.7	-45	-36	DK_2753	0.5	0.93	1	0	2.43
312.25	8.17	5.4	-39.8	4.5	7.2	-45	-37.3	DK_2754	0.5	0.93	1	0	2.43
312	10.17	5.9	-39.8	4.5	8	-42.4	-36	DK_2752	0.5	0.93	1	0	2.43
187.5	-11.33	9.8	14.3	8.5	14.5	6.5	20.7	DK_871	0.5	0.93	1	0	2.43
270.5	5.5	3.3	-11.5	2.7	4.5	-15.4	-2.5	DK_2807	0.5	0.93	1	0	2.43
82.42	4.17	2.5	11.7	2.2	3	7.8	16.8	DK_123	0.5	0.76	1	0.2	2.43
234.67	20.08	3.5	83.8	2.2	4.2	81.3	87.7	DK_2824	0.5	0.92	1	0	2.42
339.25	-8.5	7.2	-10.2	5.7	9.2	-15.4	-3.8	DK_2935	0.5	0.92	1	0	2.42
309.58	3.67	3.9	65.8	3	4.5	63.2	67.1	DK_2949	0.5	0.92	0	1	2.42
233.17	-5.58	4.7	71	3.7	6.5	65.8	76.1	DK_2959	0.5	0.92	1	0	2.42
241.83	-4.33	3.9	11.7	3.2	5.2	0.1	22	DK_3019	0.5	0.92	1	0	2.42
36	-5.67	3.7	24.6	3.2	4.7	19.4	28.4	DK_3025	0.5	0.92	1	0	2.42
36.33	-3	9.2	1.4	7	12.7	0.1	9.1	DK_766	0.5	0.91	1	0	2.41
303.75	-4.25	3.8	52.9	3	5.5	49.1	56.8	DK_3069	0.5	0.91	1	0	2.41
128.92	-8.25	6.5	-24.4	5.2	8.7	-30.8	-16.6	DK_3071	0.5	0.91	1	0	2.41
125.17	3.67	6.1	24.6	4.2	8.7	18.1	32.3	DK_759	0.5	0.91	1	0	2.41
50.75	9.08	4.3	11.7	3.2	5.5	9.1	15.6	DK_3094	0.5	0.91	1	0	2.41
267.33	-4.92	4	37.5	3.2	5	34.9	40	DK_3095	0.5	0.91	0	1	2.41
48.58	6.42	2.9	9.1	2.5	3.7	7.8	11.7	DK_3131	0.5	0.91	0	1	2.41
341.92	-3	4	-23.1	3.2	5.5	-27	-19.2	DK_3174	0.5	0.91	1	0	2.41
215.75	10.17	4.3	-2.5	3	4.7	-6.3	1.4	DK_706	0.5	0.91	1	0	2.41
267.67	-3.42	3.3	22	2.5	4.2	19.4	25.9	DK_3226	0.5	0.91	1	0	2.41
212.17	6.75	2.8	52.9	2	4	50.3	59.4	DK_690	0.5	0.91	1	0	2.41
35.5	-6.67	5.3	31	4.5	6.7	22	40	DK_3276	0.5	0.9	1	0	2.4
38.67	-12.17	11.9	45.2	11.2	14.5	13	80	DK_3280	0.5	0.9	1	0	2.4
347.5	7.08	1.7	37.5	1.5	2.7	33.6	40	DK_3340	0.5	0.9	1	0	2.4
70.67	-6.92	5.7	-8.9	5	6.7	-16.6	0.1	DK_3441	0.5	0.9	1	0	2.4
277.58	-0.17	4.7	18.1	4	5.2	14.3	22	DK_3509	0.5	0.89	1	0	2.39
58.83	4.92	5.2	32.3	3.7	7.7	24.6	38.7	DK_3512	0.5	0.89	1	0	2.39
238.17	3.75	2.6	49.1	1.7	3	46.5	51.6	DK_3516	0.5	0.89	0	1	2.39
182.33	-8	9.1	19.4	7.5	12.7	13	25.9	DK_587	0.5	0.89	1	0	2.39
267.08	3.75	3.9	36.2	3	5.7	31	41.3	DK_3570	0.5	0.89	1	0	2.39
136.25	-39.75	1.2	-121	1.2	1.2	-123.6	-118.4	DK_b_226	0.5	0.89	0	1	2.39
280.42	-6.58	3.3	-12.8	3	4.2	-17.9	-7.6	DK_3622	0.5	0.89	1	0	2.39
330.58	22.83	3.9	60.6	2.7	5.7	56.8	65.8	DK_549	0.5	0.89	1	0	2.39
100	-7.58	5.7	-27	4.7	7.5	-32.1	-19.2	DK_3644	0.5	0.89	1	0	2.39
317	-6.92	8.2	-16.6	7	12	-17.9	-11.5	DK_3646	0.5	0.89	1	0	2.39
308.58	-6.67	6	-21.8	4.7	8.2	-25.7	-14.1	DK_529	0.5	0.88	1	0	2.38
73.17	0.67	6.1	19.4	4.2	9	14.3	24.6	DK_512	0.5	0.88	1	0	2.38
74	8.75	2.8	7.8	2	3.5	6.5	14.3	DK_495	0.5	0.88	1	0	2.38
100	-4.5	5.6	-29.5	4.5	8	-34.7	-25.7	DK_3824	0.5	0.88	1	0	2.38
324.17	-5.83	4.1	-83.6	3.2	5	-90.1	-75.9	DK_3839	0.5	0.88	1	0	2.38
266.58	-5.42	2.8	65.8	2.5	4	60.6	69.7	DK_3834	0.5	0.88	1	0	2.38
266.58	-5.42	2.8	65.8	2.5	4.2	60.6	72.2	DK_3832	0.5	0.88	1	0	2.38
44.58	-4.92	4.2	71	3.7	5	61.9	81.3	DK_3837	0.5	0.88	1	0	2.38
254.75	11.83	7	25.9	4.2	8.5	22	32.3	DK_3848	0.5	0.88	1	0	2.38
275.17	-2.83	5.6	7.8	4.2	7.2	-6.3	22	DK_3850	0.5	0.88	1	0	2.38
63.92	7.25	3.2	22	2.5	3.5	14.3	29.7	DK_3940	0.5	0.87	1	0	2.37
252.08	11.58	4.3	19.4	3.7	6.5	14.3	25.9	DK_3990	0.5	0.87	1	0	2.37
257.42	5.83	5	24.6	3.5	5.7	20.7	31	DK_4042	0.5	0.87	1	0	2.37
306.67	5.08	8.9	5.3	6.7	11.7	-1.2	11.7	DK_425	0.5	0.86	1	0	2.36
53.25	37.75	3	50.3	2.2	4.5	42.6	56.8	DK_4140	0.5	0.86	1	0	2.36
148.25	0.42	4.7	6.5	4	6.5	1.4	11.7	DK_411	0.5	0.86	1	0	2.36
234.42	-8.75	2.6	72.2	2.2	3.5	68.4	76.1	DK_4304	0.5	0.86	1	0	2.36
96.42	-1.42	4.2	-27	3.2	6.2	-30.8	-21.8	DK_4322	0.5	0.86	1	0	2.36
12.83	-4.58	4.7	61.9	4	6	50.3	73.5	DK_4370	0.5	0.85	1	0	2.35
143.33	1.58	6.5	16.8	4	8.5	14.3	20.7	DK_383	0.5	0.85	1	0	2.35
46.17	-6.08	5	60.6	4.5	5.7	50.3	71	DK_4513	0.5	0.85	1	0	2.35
93.42	-6.75	4.7	-25.7	3.5	5	-36	-15.4	DK_4516	0.5	0.85	1	0	2.35

21.75	-5.67	6.3	32.3	5.5	8	25.9	43.9	DK_4595	0.5	0.84	1	0	2.34
66.92	5.42	1.9	29.7	1.5	2.5	27.2	33.6	DK_340	0.5	0.84	1	0	2.34
313.17	-4.75	4.2	47.8	3.2	5.2	38.7	56.8	DK_4858	0.5	0.83	1	0	2.33
312.58	-4.67	4.2	58.1	3.2	6	50.3	65.8	DK_4856	0.5	0.83	1	0	2.33
91.75	-4.75	3.8	-32.1	3.2	6	-37.3	-28.2	DK_4877	0.5	0.83	1	0	2.33
219.25	4.08	3.2	68.4	2.5	3.7	64.5	71	DK_4897	0.5	0.83	1	0	2.33
208	-17.33	6.5	19.4	5.5	9	16.8	23.3	DK_4918	0.5	0.83	1	0	2.33
70.5	-4.67	6.5	22	5.5	9.7	10.4	33.6	DK_308	0.5	0.83	1	0	2.33
70.5	-5.33	6	16.8	5	9	10.4	28.4	DK_309	0.5	0.83	1	0	2.33
143.5	0.67	4.3	-6.3	3.2	5.5	-8.9	-3.8	DK_291	0.5	0.82	0	1	2.32
345.42	-2.33	2.2	14.3	1.7	3	11.7	18.1	DK_33	0.5	0.65	1	0.2	2.32
69.5	-6.5	6.4	27.2	5.5	7	23.3	31	DK_5202	0.5	0.82	1	0	2.32
55.58	8.67	2.2	-11.5	2	2.5	-14.1	-7.6	DK_5467	0.5	0.81	1	0	2.31
3.08	-1.58	1.4	60.6	1.2	1.7	56.8	64.5	DK_5479	0.5	0.81	1	0	2.31
3.17	-1.58	1.3	47.8	1.2	1.7	42.6	51.6	DK_5480	0.5	0.81	1	0	2.31
63.17	-1.67	3.8	-48.9	3.2	5.2	-51.4	-46.3	DK_5558	0.5	0.81	0	1	2.31
111.33	-3.5	5.9	-100.4	4.5	7.5	-109.4	-91.4	DK_5585	0.5	0.81	1	0	2.31
47.33	-3.75	5.7	18.1	4.7	8.7	6.5	29.7	DK_236	0.5	0.8	1	0	2.3
130.83	8.25	3.1	29.7	2	4	27.2	33.6	DK_226	0.5	0.8	1	0	2.3
304.5	5.5	3.7	-41.1	3.2	4.2	-47.6	-34.7	DK_166	0.5	0.78	1	0	2.28
44.33	2.17	1.9	42.6	1.5	2.2	40	43.9	DK_164	0.5	0.77	0	1	2.27
317.92	-0.83	1.2	59.4	1	1.2	56.8	60.6	DK_15	1	0.6	0	0.7	2.27
31.42	2.58	0.9	98	0.7	1	95.4	100.6	DK_6	1	0.6	0	0.7	2.27
319.5	-0.92	0.8	65.8	0.7	1	63.2	67.1	DK_8	1	0.6	0	0.7	2.27
317.75	-0.83	0.8	65.8	0.7	1	63.2	69.7	DK_5	0.5	0.6	1	0.2	2.27
135.5	-45.92	2.7	-97.8	2.5	3	-101.7	-93.9	DK_b_143	0.5	0.74	1	0	2.24
130.83	-5.67	7.2	-21.8	5.7	11	-24.4	-20.5	DK_3909	1	0.87	0	0.3	2.21
72.5	-42.58	2.2	-95.2	2	2.7	-101.7	-88.8	DK_b_123	0.5	0.71	1	0	2.21
311.5	-1.58	1.5	34.9	1.2	2	31	37.5	DK_42	0.5	0.67	1	0	2.17
133.17	6.58	8	-6.3	5.2	10.2	-7.6	-3.8	DK_1545	1	0.99	0	0.2	2.16
1.25	11.5	11	-1.2	10	13.5	-2.5	1.4	DK_1751	1	0.99	0	0.2	2.16
165.25	-21.83	9.6	9.1	8	12.5	6.5	10.4	DK_1511	1	0.99	0	0.2	2.16
320.33	4.25	3.7	-8.9	2.7	5.2	-10.2	-6.3	DK_1967	0.5	0.98	0	0.7	2.14
213.33	-10.67	1.6	-25.7	1.5	1.7	-28.2	-24.4	DK_1340	1	0.98	0	0.2	2.14
287.75	-2.42	1.7	42.6	1.5	2	40	43.9	DK_5550	1	0.81	0	0.3	2.14
310	4.08	5.3	1.4	3.7	7	-1.2	4	DK_1002	0.5	0.94	0	0.7	2.11
206.42	-25.58	14.2	11.7	10	17.5	10.4	14.3	DK_b_335	1	0.94	0	0.2	2.11
48.58	9.17	2.3	16.8	1.7	3.2	14.3	19.4	DK_977	0.5	0.94	0	0.7	2.1
57.33	3.25	3.1	19.4	2.5	3.7	18.1	22	DK_940	1	0.93	0	0.2	2.1
304.83	-1	3.7	46.5	3	5.2	43.9	49.1	DK_2735	1	0.93	0	0.2	2.1
89.5	-3.67	5.9	-27	4.2	7.5	-29.5	-24.4	DK_2842	0.5	0.92	0	0.7	2.09
49.75	9.08	2	33.6	1.7	2.5	31	36.2	DK_2856	1	0.92	0	0.2	2.09
224.67	-2.75	4.2	-23.1	3.7	5.5	-25.7	-20.5	DK_2878	0.5	0.92	0	0.7	2.09
96.17	-3.17	3.5	-30.8	3	3.7	-33.4	-28.2	DK_2956	1	0.92	0	0.2	2.09
264.08	-4.5	3.5	40	2.7	5.5	38.7	42.6	DK_3046	0.5	0.92	0	0.7	2.08
325.5	-2.83	2.8	-21.8	2.5	3.2	-24.4	-19.2	DK_3129	1	0.91	0	0.2	2.08
212.08	-15.17	7.9	18.1	6.5	10	15.6	20.7	DK_3442	1	0.9	0	0.2	2.06
269.33	3.42	2.3	27.2	2	2.7	24.6	29.7	DK_3504	1	0.89	0	0.2	2.06
214.83	-19.75	9.4	16.8	7.2	11.7	14.3	18.1	DK_3521	0.5	0.89	0	0.7	2.06
34.83	9.25	2.3	40	2	2.5	37.5	41.3	DK_3634	1	0.89	0	0.2	2.05
241.33	3.75	4.4	52.9	3.2	6.2	50.3	54.2	DK_520	0.5	0.88	0	0.7	2.05
61.92	2.08	1.5	-16.6	1.5	1.7	-17.9	-14.1	DK_3738	0.5	0.88	0	0.7	2.05
316	17.67	4.6	16.8	3.7	6.2	14.3	19.4	DK_420	1	0.86	0	0.2	2.03
38.17	8.33	1.8	34.9	1.5	2.2	33.6	37.5	DK_405	1	0.86	0	0.2	2.03
322.67	3.25	4.9	4	3.5	7.2	2.7	7.8	DK_400	1	0.86	0	0.2	2.03
166	-23.67	14.7	1.4	14.2	15.7	-1.2	4	DK_b_537	1	1	0	0	2
266.08	-5.5	5.3	22	4.2	6.2	19.4	23.3	DK_4954	0.5	0.83	0	0.7	2
188.25	-20.5	15.2	9.1	13.5	18.2	6.5	10.4	DK_b_426	1	0.98	0	0	1.98
190.5	-23.58	13	4	11.7	13.5	2.7	6.5	DK_b_415	1	0.98	0	0	1.98
191.75	-25.58	12.5	4	10.2	13.5	2.7	6.5	DK_b_413	1	0.98	0	0	1.98
189.17	-22.25	14.6	6.5	13.2	16.7	5.3	9.1	DK_b_419	1	0.98	0	0	1.98
237.17	5.08	7.1	0.1	5	9.5	-2.5	2.7	DK_2004	1	0.98	0	0	1.98
226.5	-1.42	1.2	50.3	1	1.5	47.8	51.6	DK_246	1	0.81	0	0.2	1.98

72.92	4.08	1.9	2.7	1.7	2.2	0.1	5.3	DK_1341	1	0.98	0	0	1.98
226.25	5.92	2.4	52.9	1.7	3.2	50.3	54.2	DK_1335	1	0.98	0	0	1.98
36.83	40.67	2.8	77.4	1.7	3.5	74.8	80	DK_1203	1	0.96	0	0	1.96
199	-21.58	8.2	7.8	7.5	8.7	5.3	10.4	DK_b_693	1	0.96	0	0	1.96
345.58	-4.83	4.8	2.7	3	5.7	0.1	5.3	DK_196	1	0.79	0	0.2	1.95
313.75	-2.17	1.9	50.3	1.7	2.2	49.1	52.9	DK_195	1	0.79	0	0.2	1.95
325.25	0.92	2	52.9	1.5	2.5	50.3	54.2	DK_186	1	0.78	0	0.2	1.95
316.5	-10.08	13.7	4	11	18.5	2.7	7.8	DK_2408	1	0.95	0	0	1.95
40.5	10.33	2.3	32.3	1.7	3.5	31	34.9	DK_976	1	0.94	0	0	1.94
34.5	14.83	0.8	50.3	0.7	1	47.8	51.6	DK_2575	1	0.94	0	0	1.94
60.83	-3.83	3.6	37.5	3.2	4.7	34.9	38.7	DK_2582	1	0.94	0	0	1.94
223.58	-1.58	3.2	32.3	2.2	4.2	29.7	33.6	DK_151	1	0.77	0	0.2	1.94
226.83	3.42	2.6	71	2	3.5	68.4	72.2	DK_948	1	0.93	0	0	1.93
299.17	-23.42	3.4	-29.5	2.7	3.5	-32.1	-27	DK_b_1014	1	0.93	0	0	1.93
298.08	-23.25	3.5	-28.2	3	4	-29.5	-25.7	DK_b_1015	1	0.93	0	0	1.93
45.67	12.83	2.2	40	1.7	2.5	38.7	42.6	DK_2855	1	0.92	0	0	1.92
229.83	-24.42	3.7	-3.8	3.2	4	-6.3	-1.2	DK_b_783	1	0.9	0	0	1.9
183.33	-20.08	4.5	-1.2	4	5.2	-5.1	0.1	DK_b_794	1	0.9	0	0	1.9
287.5	3.33	6.6	-23.1	5.2	8.5	-25.7	-20.5	DK_3526	1	0.89	0	0	1.89
108	-26.33	1.9	-78.5	1.2	2.5	-79.8	-75.9	DK_b_225	1	0.89	0	0	1.89
209.17	-25.58	3.7	-12.8	3.2	4	-15.4	-10.2	DK_b_808	1	0.89	0	0	1.89
226.08	-0.08	1.7	73.5	1.5	2.2	71	76.1	DK_73	1	0.71	0	0.2	1.87
0.33	1.75	1.7	42.6	1.5	2.2	41.3	45.2	DK_454	1	0.87	0	0	1.87
214.42	6.75	3.8	4	2.7	4.7	1.4	5.3	DK_434	1	0.87	0	0	1.87
307.17	-1.83	1.8	2.7	1.5	2.5	0.1	5.3	DK_65	1	0.7	0	0.2	1.86
41.83	6.58	2.2	32.3	1.5	2.5	29.7	33.6	DK_67	1	0.7	0	0.2	1.86
157.5	-26.08	3.2	-45	2.7	3.5	-47.6	-43.7	DK_b_843	1	0.86	0	0	1.86
33.92	38.25	2.7	52.9	2	3.5	50.3	55.5	DK_b_219	1	0.86	0	0	1.86
273.08	-7.08	4.1	16.8	3.2	4.5	14.3	18.1	DK_5013	1	0.83	0	0	1.83
305.5	-0.92	1.7	22	1.7	1.7	19.4	23.3	DK_277	1	0.82	0	0	1.82
126.25	6.17	2.7	78.7	1.7	3.5	77.4	82.5	DK_276	1	0.82	0	0	1.82
203.42	-5.67	5.7	2.7	4.2	8	0.1	5.3	DK_268	1	0.82	0	0	1.82
149.17	-0.5	3.1	10.4	2.5	4.5	7.8	13	DK_257	1	0.81	0	0	1.81
236.08	1.67	2.2	40	2	2.5	37.5	42.6	DK_1991	0.5	0.98	0	0.3	1.81
37.25	7.92	2.7	46.5	2	3.7	43.9	49.1	DK_228	1	0.8	0	0	1.8
214.5	26.83	3.1	45.2	2.7	4	42.6	46.5	DK_b_932	1	0.8	0	0	1.8
43.67	3.75	3	7.8	2.7	4	5.3	10.4	DK_2267	0.5	0.96	0	0.3	1.79
133.92	-32.75	1	-137.7	1	1	-139	-135.2	DK_b_278	1	0.62	0	0.2	1.79
252.92	-3.42	3.7	38.7	3.2	4.2	37.5	41.3	DK_2308	0.5	0.95	0	0.3	1.79
125.67	0.25	1.8	-24.4	1.7	2	-25.7	-21.8	DK_1125	0.5	0.95	0	0.3	1.78
141.83	3.58	1.1	49.1	1	1.2	46.5	51.6	DK_175	1	0.78	0	0	1.78
34.83	8.5	0.9	29.7	0.7	1.2	27.2	31	DK_170	1	0.78	0	0	1.78
307.5	-1.67	2.4	36.2	1.7	3	33.6	38.7	DK_158	1	0.77	0	0	1.77
308.83	-0.33	0.9	78.7	0.7	1	77.4	81.3	DK_3	1	0.6	0	0.2	1.77
132.08	6.25	3.1	27.2	2.2	4.5	24.6	29.7	DK_137	1	0.76	0	0	1.76
189.08	-5.67	3.3	-12.8	2.7	3.5	-15.4	-10.2	DK_134	1	0.76	0	0	1.76
60.58	6.08	1.6	24.6	1.2	2.5	22	25.9	DK_126	1	0.76	0	0	1.76
0.08	-2.17	2.4	19.4	2	3	16.8	22	DK_109	1	0.75	0	0	1.75
31.33	20.42	1.3	54.2	1	1.7	51.6	56.8	DK_b_277	1	0.74	0	0	1.74
33.5	-1.92	2.8	-19.2	2.5	3.2	-20.5	-16.6	DK_3474	0.5	0.89	0	0.3	1.73
43.08	3	1.5	32.3	1.2	2	29.7	33.6	DK_86	1	0.73	0	0	1.73
223.25	5.25	0.8	37.5	0.7	1	34.9	40	DK_546	0.5	0.89	0	0.3	1.72
307.58	2.17	1.2	55.5	1	1.2	52.9	58.1	DK_79	1	0.71	0	0	1.71
130.42	6.08	3.7	-34.7	3.5	3.7	-36	-30.8	DK_3901	0.5	0.87	0	0.3	1.71
161.67	-20.08	7.4	11.7	6.5	9.7	9.1	13	DK_b_526	0.5	1	0	0.2	1.66
317.67	1.5	5.1	-39.8	4.2	7	-42.4	-37.3	DK_1544	0.5	0.99	0	0.2	1.66
240.08	7.67	1.6	45.2	1.2	1.7	43.9	47.8	DK_1763	0.5	0.99	0	0.2	1.66
327.33	0.58	9.5	1.4	7	15.2	0.1	4	DK_1806	0.5	0.99	0	0.2	1.65
49.5	4.08	1.8	34.9	1.5	2.2	32.3	36.2	DK_1833	0.5	0.99	0	0.2	1.65
257.25	5.92	4.2	65.8	3.7	6	63.2	68.4	DK_1473	0.5	0.99	0	0.2	1.65
6.92	-5.42	8	10.4	6.7	9.5	7.8	13	DK_1418	0.5	0.98	0	0.2	1.65
249.08	4.17	1.7	32.3	1.5	2	29.7	33.6	DK_2115	0.5	0.97	0	0.2	1.63
315.92	3.17	1.9	58.1	1.5	2.7	56.8	60.6	DK_1238	0.5	0.97	0	0.2	1.63

304.83	3.25	6.3	-37.3	4	8	-38.5	-34.7	DK_2141	0.5	0.97	0	0.2	1.63
62.5	4.25	3.2	13	2.5	4.2	10.4	15.6	DK_2168	0.5	0.96	0	0.2	1.63
36.08	10.75	2.9	34.9	2.2	4	33.6	37.5	DK_2190	0.5	0.96	0	0.2	1.63
351.5	-3.92	5.7	13	4.7	7.2	9.1	14.3	DK_2211	0.5	0.96	0	0.2	1.63
37.17	31.5	2.6	104.4	2.2	3.2	101.9	105.7	DK_b_80	1	0.63	0	0	1.62
339.58	-9.33	9.7	4	8.2	11.7	2.7	6.5	DK_1167	0.5	0.96	0	0.2	1.62
252.58	-3.08	3.9	47.8	3.5	4.7	45.2	50.3	DK_2307	0.5	0.95	0	0.2	1.62
311	3.42	5.7	-36	4	7.5	-38.5	-33.4	DK_2350	0.5	0.95	0	0.2	1.62
49.33	9.83	6.8	14.3	4.7	8.7	11.7	16.8	DK_1115	0.5	0.95	0	0.2	1.62
246.5	10.83	3.7	38.7	3.2	5.7	36.2	41.3	DK_1000	0.5	0.94	0	0.2	1.61
35.17	9.17	2	63.2	1.5	2.7	61.9	65.8	DK_2533	0.5	0.94	0	0.2	1.61
305.42	-0.67	3.2	54.2	2.5	4.2	52.9	58.1	DK_962	0.5	0.94	0	0.2	1.6
36.25	3.5	2.2	24.6	2	2.7	23.3	27.2	DK_2606	0.5	0.93	0	0.2	1.6
31.08	2.42	1.2	65.8	1	1.7	64.5	68.4	DK_14	1	0.6	0	0	1.6
304.25	1	1.2	91.6	1	1.7	89	94.1	DK_12	1	0.6	0	0	1.6
307.17	-0.33	0.9	89	0.7	1.2	87.7	91.6	DK_2	1	0.6	0	0	1.6
335.83	-1.42	3.3	-8.9	2.5	4.2	-11.5	-7.6	DK_916	0.5	0.93	0	0.2	1.6
325.08	-3.5	4.8	-10.2	3.5	5.5	-12.8	-7.6	DK_2725	0.5	0.93	0	0.2	1.6
53.5	8.33	2.7	27.2	2	3.5	24.6	28.4	DK_862	0.5	0.93	0	0.2	1.59
132.5	4.5	5.3	-27	4.5	8.7	-29.5	-24.4	DK_2885	0.5	0.92	0	0.2	1.59
49.33	5.33	8.7	4	7.7	11	2.7	6.5	DK_2887	0.5	0.92	0	0.2	1.59
219.42	-12.92	11	19.4	9	13.7	18.1	22	DK_2909	0.5	0.92	0	0.2	1.59
345.42	-2.58	2.7	-12.8	2.5	2.7	-15.4	-10.2	DK_3012	0.5	0.92	0	0.2	1.58
37.17	6.92	1.9	22	1.5	2.7	19.4	23.3	DK_3157	0.5	0.91	0	0.2	1.58
103.33	7.08	6.5	-14.1	5.5	8.5	-16.6	-11.5	DK_719	0.5	0.91	0	0.2	1.58
300.92	-5	6.3	-38.5	4.5	7.7	-41.1	-36	DK_3242	0.5	0.91	0	0.2	1.57
340.25	0.25	6.5	6.5	4.2	8.2	5.3	10.4	DK_676	0.5	0.9	0	0.2	1.57
248.5	2.17	3.2	22	2.5	4.2	20.7	24.6	DK_652	0.5	0.9	0	0.2	1.57
320.42	-8	3.7	-14.1	2.7	4.2	-15.4	-11.5	DK_3330	0.5	0.9	0	0.2	1.57
110.42	-1.08	0.7	-32.1	0.7	0.7	-34.7	-29.5	DK_3372	0.5	0.9	0	0.2	1.57
36	-17.17	5.4	5.3	4.2	6	2.7	7.8	DK_3413	0.5	0.9	0	0.2	1.57
31.5	-1	3.7	58.1	3	4.5	56.8	60.6	DK_3460	0.5	0.9	0	0.2	1.56
50.17	4.25	6.5	-1.2	5.5	8.7	-3.8	1.4	DK_3716	0.5	0.88	0	0.2	1.55
134.75	7.75	1.9	-32.1	1.5	2.2	-34.7	-30.8	DK_3718	0.5	0.88	0	0.2	1.55
134.58	7.75	2.4	-32.1	2.2	2.7	-33.4	-29.5	DK_3717	0.5	0.88	0	0.2	1.55
43.08	4.5	3.7	18.1	2.7	5.5	15.6	20.7	DK_3766	0.5	0.88	0	0.2	1.55
351.17	4.08	4.6	1.4	4	6	-1.2	4	DK_499	0.5	0.88	0	0.2	1.55
298.83	-5.67	3.1	-68.2	2.2	4	-70.8	-65.6	DK_3795	0.5	0.88	0	0.2	1.55
250.83	-2.25	1.3	29.7	1.2	1.5	28.4	32.3	DK_4085	0.5	0.87	0	0.2	1.53
216.92	16.17	1.8	68.4	1.2	2.5	65.8	69.7	DK_417	0.5	0.86	0	0.2	1.53
1.75	-5.75	5	1.4	4.2	5.7	-1.2	4	DK_346	0.5	0.84	0	0.2	1.51
224.42	-2.92	2.7	50.3	2.2	4.7	49.1	52.9	DK_4913	0.5	0.83	0	0.2	1.5
142.5	-5.25	4.4	-23.1	3.7	5.7	-25.7	-20.5	DK_1610	0.5	1	0	0	1.5
54	4.08	1.2	16.8	1	1.2	15.6	19.4	DK_1680	0.5	1	0	0	1.5
77.58	5.83	2	-24.4	1.7	2.5	-27	-21.8	DK_4939	0.5	0.83	0	0.2	1.5
68.92	8.17	1.7	-1.2	1.5	2.2	-3.8	0.1	DK_1694	0.5	1	0	0	1.5
69.33	-4.08	5.6	-6.3	4.2	9	-8.9	-5.1	DK_1756	0.5	0.99	0	0	1.49
272.25	6.25	3.7	9.1	2.5	5	7.8	11.7	DK_1757	0.5	0.99	0	0	1.49
230.08	13.92	1.7	65.8	1.2	2.5	63.2	68.4	DK_1761	0.5	0.99	0	0	1.49
52.67	8.08	2.6	16.8	2.2	3	14.3	18.1	DK_1523	0.5	0.99	0	0	1.49
203.75	-0.42	9.7	9.1	8.2	12	7.8	11.7	DK_1776	0.5	0.99	0	0	1.49
134.92	-6	7.9	-19.2	6.7	11	-21.8	-16.6	DK_1824	0.5	0.99	0	0	1.49
188	-26	11.5	5.3	9.2	13.2	2.7	6.5	DK_b_620	0.5	0.98	0	0	1.48
187.83	-24.67	11.7	5.3	9.2	13.5	4	7.8	DK_b_621	0.5	0.98	0	0	1.48
35.83	4.75	3.9	46.5	2.7	5	43.9	49.1	DK_265	0.5	0.81	0	0.2	1.48
357.5	-6.42	6.7	16.8	5.7	7.5	15.6	19.4	DK_1404	0.5	0.98	0	0	1.48
197.33	-23.5	6.2	9.1	5.7	6.5	6.5	11.7	DK_b_625	0.5	0.98	0	0	1.48
64.83	2.5	2.1	-1.2	1.7	2.7	-3.8	0.1	DK_1964	0.5	0.98	0	0	1.48
32.42	8	2.3	78.7	1.7	3.2	77.4	81.3	DK_260	0.5	0.81	0	0.2	1.48
3.5	-1.17	2.2	27.2	2	2.7	25.9	29.7	DK_1987	0.5	0.98	0	0	1.48
63.17	-2.25	3.7	-55.3	3.2	4.7	-56.6	-52.7	DK_5559	0.5	0.81	0	0.2	1.47
287.25	-8.5	7.7	-34.7	6.5	9	-37.3	-33.4	DK_2045	0.5	0.97	0	0	1.47
143.25	0.25	4.6	14.3	3.7	6.2	11.7	16.8	DK_1305	0.5	0.97	0	0	1.47

238.67	14.42	2.2	52.9	1.7	3.2	50.3	54.2	DK_1256	0.5	0.97	0	0	1.47
203.67	0.42	5.7	1.4	4.7	6.5	0.1	4	DK_1234	0.5	0.96	0	0	1.46
227.75	30.58	2.1	47.8	1.2	2.5	46.5	50.3	DK_1229	0.5	0.96	0	0	1.46
251.25	10.67	1.7	37.5	1.2	2.2	34.9	38.7	DK_1231	0.5	0.96	0	0	1.46
254.83	10.67	1.7	24.6	1.2	2	22	25.9	DK_1232	0.5	0.96	0	0	1.46
278.25	0.75	8.7	42.6	7.5	9.7	41.3	45.2	DK_2171	0.5	0.96	0	0	1.46
315.17	-1.17	2.1	50.3	1.7	2.7	47.8	52.9	DK_207	0.5	0.8	0	0.2	1.46
227.75	7.17	6.1	-32.1	4.5	8.7	-34.7	-29.5	DK_2263	0.5	0.96	0	0	1.46
64.42	-2	3	6.5	2.7	3.5	5.3	9.1	DK_2269	0.5	0.96	0	0	1.46
301.67	-12.58	12.4	-36	8.5	16.5	-38.5	-33.4	DK_2270	0.5	0.96	0	0	1.46
338.92	-8.08	11.6	5.3	8.7	18.5	2.7	7.8	DK_1166	0.5	0.96	0	0	1.46
310.75	-1.75	2.7	68.4	2.2	3.5	67.1	71	DK_2283	0.5	0.96	0	0	1.46
101	-7.33	9.1	1.4	6.5	12	0.1	4	DK_2287	0.5	0.96	0	0	1.46
33.17	26	1.1	58.1	1	1.2	55.5	59.4	DK_2288	0.5	0.96	0	0	1.46
213.17	0.08	2.2	58.1	1.7	2.7	55.5	60.6	DK_2297	0.5	0.95	0	0	1.45
55	-2.58	4.9	14.3	3.7	7	11.7	15.6	DK_1139	0.5	0.95	0	0	1.45
127.67	5.5	5	29.7	3.7	5.7	28.4	32.3	DK_1135	0.5	0.95	0	0	1.45
56.75	-3.83	6.8	5.3	5	9.7	4	7.8	DK_1127	0.5	0.95	0	0	1.45
63.33	13.33	2.9	4	2.2	3.5	1.4	6.5	DK_2359	0.5	0.95	0	0	1.45
304.5	5.17	1.5	91.6	1.2	2	89	92.9	DK_179	0.5	0.78	0	0.2	1.45
54.25	7.5	0.8	22	0.7	1	20.7	24.6	DK_171	0.5	0.78	0	0.2	1.45
125.17	6.25	3.2	-16.6	2.2	4.7	-17.9	-14.1	DK_1037	0.5	0.94	0	0	1.44
148.17	-2.58	2.7	91.6	2.2	3	90.3	94.1	DK_2458	0.5	0.94	0	0	1.44
286.17	7.75	3.5	-32.1	3	4.7	-34.7	-30.8	DK_2473	0.5	0.94	0	0	1.44
32.83	30.08	2	76.1	1.2	2.5	73.5	78.7	DK_b_271	0.5	0.94	0	0	1.44
50.67	5.75	1.7	29.7	1.5	2.2	28.4	32.3	DK_2534	0.5	0.94	0	0	1.44
212.67	-17.83	6.7	16.8	5	7.7	14.3	19.4	DK_2572	0.5	0.94	0	0	1.44
137.17	1.5	3	18.1	2.2	4.2	16.8	20.7	DK_138	0.5	0.76	0	0.2	1.43
55	-5.33	5.1	32.3	4.7	5.2	29.7	33.6	DK_2778	0.5	0.93	0	0	1.43
334.17	-12.58	14.1	1.4	12.5	19.5	-1.2	4	DK_2793	0.5	0.93	0	0	1.43
44.58	11.25	3	37.5	2	4	36.2	40	DK_860	0.5	0.93	0	0	1.43
3	4.42	3.2	50.3	2.2	4	47.8	51.6	DK_844	0.5	0.93	0	0	1.43
74.08	4.83	3.2	4	2.5	4.2	2.7	6.5	DK_2872	0.5	0.92	0	0	1.42
332.58	-1.17	3.2	55.5	2	3.7	52.9	58.1	DK_117	0.5	0.75	0	0.2	1.42
66.17	-5.33	5.8	-1.2	5.2	7.2	-3.8	0.1	DK_2940	0.5	0.92	0	0	1.42
221.58	-4.17	3.7	36.2	3	4	33.6	38.7	DK_2953	0.5	0.92	0	0	1.42
232.33	12.08	4.5	-29.5	3.7	5.7	-30.8	-27	DK_2974	0.5	0.92	0	0	1.42
257.75	3	1.3	47.8	1.2	1.5	45.2	49.1	DK_783	0.5	0.92	0	0	1.42
16.42	-2.75	4.8	47.8	3.2	6.7	45.2	49.1	DK_2996	0.5	0.92	0	0	1.42
55	27.83	2.1	42.6	1.5	2.7	41.3	45.2	DK_775	0.5	0.92	0	0	1.42
129.08	-10.58	7.1	-17.9	5.2	8.7	-20.5	-15.4	DK_3035	0.5	0.92	0	0	1.42
34.17	5.08	3.5	27.2	3	5	24.6	28.4	DK_3067	0.5	0.91	0	0	1.41
33.92	12.42	3.4	60.6	2.2	4.7	58.1	61.9	DK_746	0.5	0.91	0	0	1.41
309.83	3.17	4.8	22	3.5	6.5	19.4	24.6	DK_738	0.5	0.91	0	0	1.41
127.67	1.42	7.7	76.1	6.5	8.7	73.5	77.4	DK_736	0.5	0.91	0	0	1.41
314.83	-4.33	5.5	68.4	3.7	7	65.8	69.7	DK_3137	0.5	0.91	0	0	1.41
48.67	7.25	2.2	16.8	1.7	3	14.3	19.4	DK_3196	0.5	0.91	0	0	1.41
27.42	-2.75	2.2	41.3	2	2.5	38.7	43.9	DK_3205	0.5	0.91	0	0	1.41
327.42	4	1.1	63.2	1	1.2	60.6	64.5	DK_687	0.5	0.91	0	0	1.41
313.67	-8.42	10.1	-17.9	7.7	13.5	-19.2	-15.4	DK_3269	0.5	0.9	0	0	1.4
216.42	5.67	1.5	18.1	1.2	2	15.6	20.7	DK_96	0.5	0.74	0	0.2	1.4
213	11.83	1.7	58.1	1.2	2.5	55.5	60.6	DK_95	0.5	0.74	0	0.2	1.4
43.58	5.25	1.5	45.2	1.2	1.7	42.6	46.5	DK_3379	0.5	0.9	0	0	1.4
204.42	-21.25	3.7	-14.1	3	4.2	-16.6	-12.8	DK_b_793	0.5	0.9	0	0	1.4
1.08	-4.5	5.5	10.4	5	8	7.8	13	DK_613	0.5	0.89	0	0	1.39
306.33	16.58	2.4	43.9	2	3.2	41.3	46.5	DK_597	0.5	0.89	0	0	1.39
133.83	-0.17	5.8	23.3	3.7	8	20.7	25.9	DK_592	0.5	0.89	0	0	1.39
288.58	-5.5	5.8	-50.1	4.7	7.2	-51.4	-46.3	DK_3527	0.5	0.89	0	0	1.39
318.08	2.83	5.4	2.7	5	7.5	0.1	5.3	DK_585	0.5	0.89	0	0	1.39
227.75	-7.42	2.5	58.1	2.5	2.7	56.8	60.6	DK_3593	0.5	0.89	0	0	1.39
182.83	-5.5	2.9	-3.8	2.7	3.2	-6.3	-2.5	DK_81	0.5	0.72	0	0.2	1.39
82.58	-1.83	1.5	-34.7	1.5	1.5	-37.3	-32.1	DK_3740	0.5	0.88	0	0	1.38
62.92	4.83	4.7	-3.8	4.2	7.2	-6.3	-1.2	DK_3755	0.5	0.88	0	0	1.38

134.92	1.67	2.8	18.1	2	3.5	16.8	20.7	DK_496	0.5	0.88	0	0	1.38
111.92	-5.58	7.2	-25.7	5.7	9.7	-28.2	-23.1	DK_3866	0.5	0.88	0	0	1.38
134.75	2.25	3.4	-56.6	3.2	4.2	-59.2	-54	DK_3907	0.5	0.87	0	0	1.37
33.42	12.08	1.8	55.5	1.2	2.5	54.2	58.1	DK_416	0.5	0.86	0	0	1.36
337	-3.25	3.5	-15.4	3.2	4	-17.9	-12.8	DK_4218	0.5	0.86	0	0	1.36
52.17	2.42	0.8	32.3	0.7	1	29.7	33.6	DK_58	0.5	0.69	0	0.2	1.36
39.75	38.25	1.6	74.8	1.2	2	72.2	77.4	DK_b_215	0.5	0.85	0	0	1.35
10.33	-4.58	3.8	4	3.5	4.2	1.4	5.3	DK_385	0.5	0.85	0	0	1.35
40	-1.67	1.5	27.2	1.5	1.5	24.6	28.4	DK_57	0.5	0.69	0	0.2	1.35
263.25	9.75	2.6	9.1	2	3.2	7.8	11.7	DK_4588	0.5	0.84	0	0	1.34
241.58	-3.17	5.4	16.8	3.5	6.2	14.3	19.4	DK_4666	0.5	0.84	0	0	1.34
37.42	13.08	1.9	83.8	1.2	2.2	81.3	86.4	DK_335	0.5	0.84	0	0	1.34
164.17	-7.58	8.9	78.7	7.5	11.5	76.1	80	DK_4766	0.5	0.84	0	0	1.34
325.92	-5	4.3	-16.6	3.5	5.5	-19.2	-14.1	DK_4776	0.5	0.84	0	0	1.34
241.5	-1.75	8.3	14.3	7	10.2	11.7	15.6	DK_4796	0.5	0.84	0	0	1.34
238.92	31.08	3.3	86.4	3	4	83.8	89	DK_4985	0.5	0.83	0	0	1.33
146.42	-3.42	3.2	14.3	2.5	4.5	13	16.8	DK_304	0.5	0.83	0	0	1.33
24.92	-2.75	2.7	60.6	2.2	3.2	56.8	61.9	DK_5044	0.5	0.82	0	0	1.32
311.83	-2.25	8.6	-8.9	7.2	11.7	-11.5	-7.6	DK_5139	0.5	0.82	0	0	1.32
87.5	-13.33	1.8	-47.6	1.5	2.5	-50.1	-45	DK_5315	0.5	0.81	0	0	1.31
329	2.17	2.8	11.7	2.2	3.7	10.4	14.3	DK_262	0.5	0.81	0	0	1.31
322	-1.83	2.2	1.4	2	2.5	-1.2	2.7	DK_26	0.5	0.64	0	0.2	1.31
185.5	2.58	3.2	-8.9	3.2	3.7	-10.2	-5.1	DK_215	0.5	0.8	0	0	1.3
46.17	2.92	3.2	40	2.2	4.5	38.7	42.6	DK_203	0.5	0.79	0	0	1.29
215.08	-6.5	4.3	6.5	3.7	5.2	5.3	9.1	DK_193	0.5	0.79	0	0	1.29
266.33	1.58	1.4	38.7	1.2	1.5	36.2	41.3	DK_178	0.5	0.78	0	0	1.28
304.58	1.83	1.4	73.5	1.2	1.5	71	74.8	DK_180	0.5	0.78	0	0	1.28
326.25	-1.25	1.1	29.7	1	1.2	27.2	32.3	DK_22	0.5	0.61	0	0.2	1.28
311.33	-1.08	1.2	83.8	1	1.2	82.5	86.4	DK_19	0.5	0.61	0	0.2	1.28
127.08	3.83	3	76.1	1.7	3.5	73.5	77.4	DK_174	0.5	0.78	0	0	1.28
33.5	8.83	1.9	65.8	1.5	2.7	63.2	67.1	DK_159	0.5	0.77	0	0	1.27
214.83	2.25	2.4	58.1	1.7	3.2	55.5	60.6	DK_157	0.5	0.77	0	0	1.27
215.83	-0.5	2.2	65.8	1.7	2.7	64.5	68.4	DK_143	0.5	0.76	0	0	1.26
310.33	-2.08	2.4	9.1	2	3.5	7.8	11.7	DK_127	0.5	0.76	0	0	1.26
195.67	-8.5	2.8	24.6	2.5	3.7	22	27.2	DK_118	0.5	0.75	0	0	1.25
30.67	43.92	1.6	125.1	1.2	2	123.8	127.6	DK_b_142	0.5	0.74	0	0	1.24
162	-1.67	1.3	58.1	1.2	1.5	55.5	59.4	DK_97	0.5	0.74	0	0	1.24
213.75	3.83	1.2	65.8	1	1.5	63.2	68.4	DK_88	0.5	0.73	0	0	1.23
212.25	2	1.7	50.3	1.2	2.5	47.8	52.9	DK_84	0.5	0.73	0	0	1.23
217.75	-1.67	2.7	73.5	1.7	3.5	72.2	76.1	DK_80	0.5	0.72	0	0	1.22
163.67	3.25	2.2	55.5	1.7	2.7	52.9	56.8	DK_77	0.5	0.71	0	0	1.21
348.33	-1.92	2.7	23.3	2	3.7	20.7	25.9	DK_47	0.5	0.68	0	0	1.18
304.33	-1.08	1.7	45.2	1.2	2	43.9	49.1	DK_39	0.5	0.67	0	0	1.17
305.08	-1.33	1.7	45.2	1.2	2	42.6	46.5	DK_40	0.5	0.67	0	0	1.17
212.92	1.5	1.1	52.9	0.7	1.2	51.6	55.5	DK_32	0.5	0.65	0	0	1.15
117.75	31.58	1.7	-59.2	1.5	2	-61.7	-56.6	DK_b_85	0.5	0.64	0	0	1.14
318.75	0.33	0.9	73.5	0.7	1.2	71	74.8	DK_24	0.5	0.64	0	0	1.14
316	-1.25	1.1	50.3	1	1.2	47.8	51.6	DK_20	0.5	0.61	0	0	1.11
317.83	-1.75	1.3	27.2	1.2	1.5	24.6	28.4	DK_18	0.5	0.61	0	0	1.11
283.25	-1.25	1.7	9.1	1.2	2.5	7.8	11.7	DK_10	0.5	0.6	0	0	1.1

Table A.0.19: Results of the SNR survey for galactic H I shells from chapter 5 containing 802 objects. Column 1 and 2 contain the mean center coordinates l_0, b_0 of the shell over all channels. Column 3 contains the mean angular radius r_0 of the shell, columns 4, 5 and 6 contain the center velocity v_0, the minimum radius r_{min} and the maximum radius r_{max} respectively. Column 7 and 8 present the lower (v_{min}) and upper (v_{max}) velocity channels where the shell is detected and columns 9 gives the name of the object. The quality components (section 4.6.3) are listed in columns 11, 12, 13 and 14 with a total quality value Q_f used for the ranking that is listed in column 14. For more information about the generation of the content see section 4.6 and 5.1.

	τ	M_0	$M(t)$	$E_{\mathrm{cum,tot}}$	E_{sw}	$E(\tau_1)_{\mathrm{cum}}$	$E(\tau_2)_{\mathrm{cum}}$
	Myr	$M_\odot$	$M_\odot$	10^{51} erg	10^{51} erg	10^{51} erg	10^{51} erg
Usco	43.2	8.38	1.4	1	0	0	0
	38.3	8.87	1.4	1	0	0	0
	34	9.43	1.4	1.006	0.006	0.001	0.001
	29.8	10.1	1.4	1.008	0.008	0.001	0.001
	26.2	10.82	1.4	1.01	0.01	0.001	0.001
	23	11.68	1.4	1.013	0.013	0	0
	20.1	12.69	1.4	1.017	0.017	0.001	0.001
	17.4	13.97	1.4	1.022	0.022	0.001	0.001
	14.9	15.61	1.4	1.032	0.032	0.003	0.003
	12.8	17.67	1.4	1.052	0.052	0.006	0.008
	10.7	20.57	1.4	1.095	0.095	0.014	0.018
	8.8	24.62	1.4	1.242	0.242	0.039	0.053
	7.2	30.93	7	1.736	0.736	0.23	0.306
	5.8	42.49	7	2.455	1.455	0.66	0.909
	4.4	68.92	7	3.686	2.686	2.247	3.686
LCC	43.2	8.38	1.4	1	0	0	0
	37.5	8.98	1.4	1	0	0	0
	32.2	9.69	1.4	1.007	0.007	0.001	0.002
	27.2	10.6	1.4	1.01	0.01	0.001	0.001
	23	11.68	1.4	1.013	0.013	0.001	0.001
	19.2	13.04	1.4	1.018	0.018	0.002	0.003
	16.1	14.77	1.4	1.025	0.025	0.005	0.006
	13.2	17.19	1.4	1.047	0.047	0.027	0.044
	10.7	20.57	1.4	1.095	0.095	1.095	1.095
	8.4	26.02	7	1.345	0.345	1.345	1.345
	6.5	35.75	7	2.064	1.064	2.064	2.064
	4.8	58.79	7	3.19	2.19	3.19	3.19
UCL	45.4	8.19	1.4	1	0	0	0
	40.2	8.67	1.4	1	0	0	0
	26.9	10.67	1.4	1.01	0.01	0.002	0.002
	35.4	9.23	1.4	1.005	0.005	0.002	0.002
	31	9.89	1.4	1.008	0.008	0.002	0.002
	26.9	10.67	1.4	1.01	0.01	0.002	0.002
	23	11.68	1.4	1.013	0.013	0.002	0.003
	19.7	12.86	1.4	1.017	0.017	0.006	0.007
	16.7	14.37	1.4	1.023	0.023	0.014	0.021
	14.1	16.27	1.4	1.039	0.039	0.039	1.039
	11.9	18.81	1.4	1.062	0.062	1.062	1.062
	9.6	22.66	1.4	1.174	0.174	1.174	1.174
	7.7	28.47	7	1.548	0.548	1.548	1.548
	6.1	39.11	7	2.268	1.268	2.268	2.268
	4.5	63.87	7	3.44	2.44	3.44	3.44

Table A.0.18: Cumulative energy loss of stars of different mass during the lifetime of the respective stellar cluster predicted by the stellar synthesis code of Voss et al. (2009). The stellar masses are drawn from the IMF using optimal sampling as described in section 6.4. Column 1 contains the maximum age, τ. The star of initial stellar mass M_0 is listed in column 2. Column 3 contains the remaining mass after the SN explosion $M(t)$. The cumulative output energy over the whole lifetime of the star, $E_{\mathrm{cum,tot}}$ in units of 10^{51} erg is listed in column 4, while the total energy cumulated up to the age of the stellar group $E(\tau_1)$ and $E(\tau_1)$ are listed in the columns 5 and 6 respectively, for the respective ages τ_1 and τ_2. The values are used in section 6.4 for calculating the theoretical energy input to the shells.

1	2	3	4	5	6	7	8	9	10	11	12
Name	$D_{s,a}$	$D_{s,b}$	D_{sun}	z	D_{gc}	R_{min}	R_{max}	τ	$M_{H\,I}$	M_{tot}	E_{kin}
Unit:	kpc	kpc	kpc	kpc	kpc	kpc	kpc	10^6yr	$M_\odot$	$M_\odot$	ergs
DK_1476	2.9	20.75	2.9	1.37	11.03	0.58	1.01	7.89	1.31E+06	1.77E+06	8.67E+49
DK_2046	3.54	14.92	3.54	0.46	11.15	0.29	0.61	1.18	2.13E+06	2.88E+06	4.26E+51
DK_1303	9.82	1.49	9.82	1.39	7.59	1.12	1.55	3	1.59E+07	2.14E+07	3.17E+52
DK_1286	12.44	1.62	1.62	0.24	7.21	0.15	0.29	0.6	4.50E+05	6.07E+05	7.42E+50
DK_1188	7.04	1.82	7.04	0.5	7.71	0.43	0.77	1.99	4.66E+06	6.29E+06	4.92E+51
DK_1187	7.01	1.83	7.01	0.49	7.71	0.43	0.8	1.85	5.16E+06	6.97E+06	6.90E+51
DK_1119	10.28	2.05	2.05	0.15	7.15	0.11	0.16	0.94	2.38E+05	3.21E+05	3.53E+49
DK_857	11.33	1.24	1.24	0.1	7.63	0.1	0.21	0.48	2.27E+05	3.06E+05	3.03E+50
DK_810	11.5	1.06	1.06	0.15	7.75	0.14	0.19	0.48	2.12E+05	2.86E+05	2.24E+50
DK_3462	8.2	1.42	8.2	0.77	7.78	0.54	1.01	2.92	6.15E+06	8.31E+06	4.98E+51
DK_457	2.04	15.51	2.04	0.31	10.15	0.31	0.5	1.05	1.56E+06	2.10E+06	2.57E+51
DK_1619	3.38	15.51	3.38	0.55	11.1	0.21	0.43	0.71	1.04E+06	1.41E+06	2.90E+51
DK_1701	10.62	1.26	1.26	0.19	7.67	0.19	0.3	1.18	3.31E+05	4.47E+05	1.36E+50
DK_1452	5.1	16.16	5.1	0.39	12.42	0.27	0.38	1.76	1.64E+06	2.21E+06	4.32E+50
DK_1895	10.01	1.65	1.65	0.23	7.46	0.11	0.22	0.56	2.50E+05	3.38E+05	2.64E+50
DK_1117	13.34	1.9	1.9	0.28	6.84	0.23	0.39	0.75	9.79E+05	1.32E+06	1.95E+51
DK_960	8.69	1.6	8.69	1.69	7.64	0.38	0.68	3.98	1.23E+06	1.66E+06	1.82E+50
DK_809	11.19	1.43	1.43	0.18	7.5	0.19	0.25	0.53	4.77E+05	6.44E+05	7.88E+50
DK_3275	8.51	2.87	8.51	0.81	6.92	0.52	0.82	3.81	2.20E+06	2.96E+06	5.80E+50
DK_3295	1.88	16.11	1.88	0.33	10.08	0.21	0.35	1.15	5.16E+05	6.96E+05	3.06E+50
DK_3297	2.19	16.47	2.19	0.39	10.36	0.21	0.4	1.02	8.18E+05	1.10E+06	8.64E+50
DK_3296	2.03	16.28	2.03	0.35	10.21	0.21	0.38	1.09	6.45E+05	8.70E+05	5.21E+50
DK_3639	7.63	17.85	7.63	0.56	14.41	0.5	0.97	2.5	2.52E+06	3.40E+06	2.66E+51
DK_b_823	2.02	12.96	2.02	1.1	7.21	0.09	0.17	0.65	5.24E+03	7.07E+03	2.16E+48
DK_1580	2.73	15.42	2.73	0.36	10.66	0.3	0.47	1.21	1.17E+06	1.57E+06	1.23E+51
DK_1527	2.05	15	2.05	0.19	10.14	0.26	0.33	1.29	2.99E+05	4.04E+05	1.23E+50
DK_5129	5.48	6.13	5.48	0.71	10.26	0.53	0.8	1.84	1.62E+06	2.19E+06	2.17E+51
DK_1483	13.62	2.17	2.17	0.07	6.53	0.09	0.14	0.83	1.62E+05	2.18E+05	2.40E+49
DK_1828	1.57	16.21	1.57	0.45	9.78	0.23	0.35	2.02	3.34E+05	4.52E+05	4.97E+49
DK_1965	2.55	15.09	2.55	0.33	10.49	0.08	0.13	0.44	4.64E+04	6.26E+04	2.75E+49
DK_1281	13.27	2.22	2.22	0.12	6.54	0.09	0.11	0.83	5.13E+04	6.92E+04	3.38E+48
DK_165	18.33	1.91	1.91	0.13	10.35	0.11	0.21	0.69	2.10E+05	2.83E+05	1.24E+50
DK_928	1.89	18.25	1.89	0.25	10.31	0.18	0.34	0.88	6.45E+05	8.70E+05	6.81E+50
DK_2819	12.04	2.94	2.94	0.36	6.07	0.3	0.39	0.45	1.39E+06	1.87E+06	8.25E+51
DK_2820	2.16	12.5	2.16	0.06	9.96	0.13	0.24	0.92	9.24E+04	1.25E+05	3.81E+49
DK_2873	5.91	5.02	5.91	0.14	10.09	0.26	0.31	1.2	8.68E+05	1.17E+06	3.58E+50
DK_3145	8.31	4.83	8.31	0.5	10.6	0.4	0.69	3.21	1.55E+06	2.09E+06	4.09E+50
DK_104	13.81	1.85	1.85	0.07	9.89	0.08	0.16	0.54	1.13E+05	1.52E+05	6.71E+49
DK_3277	12.29	2.16	2.16	0.15	6.76	0.18	0.32	0.93	5.04E+05	6.81E+05	4.08E+50
DK_635	11.45	1.41	1.41	0.06	7.49	0.15	0.27	0.91	2.69E+05	3.63E+05	1.60E+50
DK_471	12.43	2.18	2.18	0.16	6.72	0.16	0.22	0.36	4.32E+05	5.83E+05	1.20E+51
DK_4220	14.27	4.76	4.76	0.21	11.84	0.27	0.37	1.24	7.68E+05	1.04E+06	4.56E+50
DK_1514	8.39	0.99	8.39	0.72	8	0.44	0.88	1.57	7.69E+06	1.04E+07	1.83E+52
DK_1785	2.63	7.75	2.63	0.16	9.62	0.13	0.2	1.14	1.43E+05	1.93E+05	2.12E+49
DK_1783	2.03	6.98	2.03	0.1	9.29	0.14	0.3	1	3.23E+05	4.36E+05	1.92E+50
DK_1784	2.13	7.22	2.13	0.11	9.36	0.13	0.2	0.59	1.51E+05	2.04E+05	1.22E+50
DK_1846	1.02	9.63	1.02	0.03	9.06	0.08	0.14	0.26	1.25E+05	1.69E+05	2.98E+50
DK_5238	12.5	1.43	1.43	0.15	7.37	0.13	0.18	1.42	6.94E+04	9.37E+04	4.58E+48
DK_1389	7.66	2.7	7.66	0.14	7.18	0.91	1.39	5.36	6.24E+06	8.43E+06	2.58E+51
DK_1966	2.97	15.55	2.97	0.39	10.85	0.09	0.13	0.6	4.25E+04	5.74E+04	1.12E+49
DK_2009	2.87	7.55	2.87	0.21	7.12	0.18	0.31	1.83	2.73E+02	3.68E+02	4.05E+46
DK_1299	10.99	0.89	0.89	0.13	7.91	0.1	0.15	0.89	7.75E+04	1.05E+05	1.15E+49
DK_1267	4.1	13.7	4.1	0.41	11.31	0.29	0.5	3.92	5.37E+05	7.25E+05	3.54E+49
DK_1221	11	0.88	0.88	0.09	7.91	0.1	0.2	0.43	2.74E+05	3.70E+05	4.52E+50
DK_930	3.47	19.88	3.47	0.48	11.83	0.24	0.38	1.77	5.59E+05	7.55E+05	1.48E+50
DK_120	12.11	1.6	1.6	0.08	7.27	0.08	0.17	0.49	1.63E+05	2.20E+05	1.32E+50
DK_756	10.32	1.45	1.45	0.17	7.57	0.11	0.22	0.46	3.81E+05	5.14E+05	6.29E+50
DK_b_785	2.79	15.72	2.79	1.92	6.51	0.22	0.34	0.88	1.46E+04	1.97E+04	1.54E+49
DK_656	6.6	2.18	6.6	0.64	7.61	0.58	1.19	1.97	1.10E+07	1.48E+07	3.05E+52

DK_3575	5.06	2.09	5.06	0.32	9.1	0.24	0.42	1.63	1.62E+06	2.19E+06	6.68E+50
DK_3584	8.1	3.16	8.1	1.02	6.83	0.71	0.99	3.3	3.83E+06	5.17E+06	2.28E+51
DK_562	7.08	2.49	7.08	0.63	7.39	0.87	1.57	2.8	1.20E+07	1.62E+07	2.85E+52
DK_3668	6.36	8.67	6.36	1.23	11.2	0.47	0.67	2.22	1.26E+05	1.70E+05	7.48E+49
DK_456	5.01	18.36	5.01	1.13	12.64	0.13	0.22	1.27	2.05E+04	2.77E+04	3.05E+48
DK_4380	10.52	1.26	1.26	0.21	7.68	0.17	0.22	0.51	2.86E+05	3.86E+05	3.83E+50
DK_4593	3.91	7.3	3.91	0.52	10.01	0.36	0.46	1.53	5.30E+05	7.16E+05	3.15E+50
DK_339	1.56	15.47	1.56	0.27	9.79	0.16	0.28	0.71	4.15E+05	5.60E+05	4.38E+50
DK_4719	2.18	14.7	2.18	0.4	10.16	0.35	0.67	1.54	1.15E+06	1.55E+06	1.54E+51
DK_1668	8.93	2.61	8.93	0.59	7	1.02	1.74	6.72	8.18E+06	1.10E+07	3.38E+51
DK_1601	1.86	8.8	1.86	0.16	7.48	0.08	0.15	0.9	1.13E+03	1.52E+03	1.67E+47
DK_1555	2.07	11.69	2.07	0.08	9.82	0.08	0.11	0.63	3.62E+04	4.88E+04	5.37E+48
DK_1528	2.48	15.49	2.48	0.33	10.49	0.32	0.4	2.35	2.57E+05	3.47E+05	3.81E+49
DK_294	3.59	7.77	3.59	0.07	6.66	0.17	0.31	2.44	4.10E+02	5.54E+02	2.71E+46
DK_1861	1.38	12.16	1.38	0.15	9.42	0.12	0.21	1.23	9.41E+04	1.27E+05	1.40E+49
DK_1906	4.61	5.62	4.61	0.3	9.9	0.18	0.28	1.64	2.88E+05	3.89E+05	4.28E+49
DK_1400	10.57	2.9	2.9	0.19	6.45	0.16	0.25	0.98	7.65E+05	1.03E+06	3.16E+50
DK_1958	2.19	16.91	2.19	0.63	10.32	0.26	0.49	1.61	7.38E+05	9.96E+05	4.38E+50
DK_5458	11.97	1.41	1.41	0.17	7.44	0.14	0.21	0.44	2.81E+05	3.79E+05	4.63E+50
DK_1983	1.56	15.09	1.56	0.42	9.7	0.14	0.22	1.02	1.43E+05	1.92E+05	3.76E+49
DK_1993	5.42	9.27	5.42	0.59	11.04	0.19	0.33	1.93	1.15E+05	1.55E+05	1.70E+49
DK_1331	12.08	2.07	2.07	0.34	6.88	0.1	0.2	0.93	3.67E+04	4.96E+04	9.70E+48
DK_2034	2.37	14.64	2.37	0.2	10.33	0.26	0.52	2.44	4.42E+05	5.97E+05	1.17E+50
DK_1298	10.84	1.16	1.16	0.13	7.72	0.14	0.2	0.47	2.19E+05	2.95E+05	2.92E+50
DK_2320	1.4	14.1	1.4	0.09	9.59	0.15	0.32	1.85	2.49E+05	3.37E+05	3.70E+49
DK_2335	6.26	18.4	6.26	0.83	13.62	0.66	1.19	3.06	4.50E+06	6.07E+06	4.75E+51
DK_2351	1.59	12	1.59	0.04	9.56	0.07	0.1	0.81	4.21E+04	5.68E+04	2.78E+48
DK_2389	11.23	0.86	0.86	0.06	7.91	0.06	0.11	0.62	2.98E+04	4.03E+04	4.43E+48
DK_2496	8.21	1.82	8.21	0.23	7.57	0.5	0.61	4.75	3.61E+06	4.88E+06	2.38E+50
DK_2513	2.56	14.07	2.56	0.21	10.4	0.15	0.27	1.57	1.37E+05	1.85E+05	2.04E+49
DK_1011	18.58	3.23	3.23	0.17	11.5	0.27	0.48	1.12	3.65E+05	4.93E+05	4.88E+50
DK_2595	9.71	2.89	9.71	0.52	6.65	1.06	2.15	12.53	5.94E+06	8.02E+06	8.82E+50
DK_2598	7.23	3.16	7.23	0.83	7.03	0.6	0.79	1.84	3.18E+06	4.30E+06	4.25E+51
DK_2663	6.35	7.94	6.35	0.64	11.05	0.44	0.75	1.94	1.90E+06	2.56E+06	2.00E+51
DK_919	1.54	15.17	1.54	0.3	9.73	0.18	0.37	1.43	3.38E+05	4.56E+05	1.39E+50
DK_2740	5.99	7.42	5.99	0.4	10.79	0.31	0.47	5.53	9.53E+05	1.29E+06	1.57E+49
DK_2779	1.41	13.79	1.41	0.21	9.55	0.19	0.41	1.91	3.79E+05	5.12E+05	1.00E+50
DK_2901	13.54	1.61	1.61	0.25	7.1	0.2	0.24	1.87	8.67E+04	1.17E+05	5.72E+48
DK_798	6.62	3.17	6.62	0.36	7.16	0.67	0.99	1.91	5.82E+06	7.86E+06	1.16E+52
DK_3004	2.45	10.69	2.45	0.27	9.9	0.25	0.4	1.15	4.16E+05	5.61E+05	3.36E+50
DK_3099	5.04	17.91	5.04	0.34	12.73	0.4	0.73	1.88	1.45E+06	1.95E+06	1.53E+51
DK_737	9.5	1.7	9.5	1.4	7.49	0.29	0.54	4.19	9.21E+05	1.24E+06	6.08E+49
DK_3187	2.32	12.62	2.32	0.27	10.05	0.21	0.41	1.35	2.56E+05	3.46E+05	1.52E+50
DK_609	1.68	11.7	1.68	0.08	7.26	0.07	0.11	0.51	9.28E+02	1.25E+03	2.45E+47
DK_3489	4.46	9.35	4.46	0.36	10.66	0.18	0.25	1.18	2.70E+05	3.64E+05	7.13E+49
DK_3722	8.45	17.01	8.45	0.46	14.68	0.33	0.52	3.01	2.20E+06	2.97E+06	3.26E+50
DK_3745	11.72	2.45	2.45	0.24	6.6	0.14	0.27	0.89	3.02E+05	4.07E+05	1.79E+50
DK_3833	11.78	2.12	2.12	0.24	6.88	0.09	0.16	0.73	1.83E+05	2.47E+05	4.82E+49
DK_3894	9.24	2.9	9.24	0.78	6.74	0.44	0.77	2.55	7.33E+06	9.90E+06	4.35E+51
DK_4385	7.93	4.27	7.93	0.67	10.3	0.24	0.45	2.62	6.37E+05	8.60E+05	9.46E+49
DK_4456	7	1.58	7	0.67	9.13	0.24	0.4	1.15	8.34E+05	1.13E+06	6.75E+50
DK_4735	8.43	5.53	8.43	0.1	5.07	0.59	0.92	1.02	4.16E+06	5.61E+06	2.74E+52
DK_1625	2.59	19.95	2.59	1.21	10.71	0.44	0.93	3.59	2.00E+06	2.70E+06	8.26E+50
DK_1602	1.59	10.99	1.59	0.03	7.4	0.06	0.11	0.87	6.90E+02	9.32E+02	4.56E+46
DK_b_518	2.27	20.26	2.27	1.04	10.5	0.52	0.74	5.74	1.05E+06	1.42E+06	6.95E+49
DK_b_520	2.71	20.57	2.71	1.16	10.93	0.63	0.97	4.53	1.63E+06	2.21E+06	4.31E+50
DK_b_517	2.19	20.14	2.19	1.01	10.42	0.5	0.66	5.12	9.61E+05	1.30E+06	6.35E+49
DK_b_519	2.66	20.66	2.66	1.22	10.85	0.61	0.89	5.18	1.15E+06	1.56E+06	1.71E+50
DK_306	9.12	1.13	9.12	0.5	7.87	0.84	1.61	9.35	7.13E+06	9.63E+06	1.06E+51
DK_307	9.23	1.32	9.23	0.38	7.75	0.85	1.09	5.08	4.70E+06	6.34E+06	1.24E+51
DK_b_560	3.87	21.52	3.87	1.53	12.01	0.65	1.31	3.38	7.21E+06	9.74E+06	7.62E+51
DK_b_486	2.31	20.55	2.31	1.23	10.45	0.46	0.68	3.98	1.03E+06	1.39E+06	1.53E+50
DK_5049	9.39	3.62	9.39	0.38	6.19	0.86	0.9	5.26	1.61E+06	2.18E+06	2.40E+50

DK_1771	4.31	6.23	4.31	0.06	6.74	0.15	0.21	0.8	5.51E+01	7.44E+01	2.27E+46
DK_5105	13.1	2.17	2.17	0.33	6.62	0.32	0.47	1.56	7.65E+05	1.03E+06	4.55E+50
DK_1792	2.63	11.44	2.63	0.25	10.1	0.2	0.37	1.72	2.34E+05	3.16E+05	6.18E+49
DK_1802	1.61	12	1.61	0.18	9.56	0.1	0.2	0.77	1.14E+05	1.53E+05	4.69E+49
DK_5194	3.54	2.38	3.54	0.36	8.98	0.23	0.36	1.18	3.81E+05	5.15E+05	2.27E+50
DK_5192	4.56	3.74	4.56	0.41	9.45	0.3	0.56	1.3	1.25E+06	1.69E+06	1.67E+51
DK_5193	4.09	3.08	4.09	0.41	9.21	0.27	0.43	1.42	5.53E+05	7.46E+05	3.28E+50
DK_1879	6.7	1.63	6.7	0.14	9.12	0.41	0.79	1.67	3.00E+06	4.05E+06	4.95E+51
DK_b_616	2.53	15.06	2.53	2	6.99	0.22	0.32	0.62	2.56E+04	3.46E+04	5.12E+49
DK_b_409	1.75	18.95	1.75	0.81	9.98	0.26	0.55	2.56	6.66E+05	8.99E+05	1.76E+50
DK_1387	4.95	4.24	4.95	0.17	7.16	0.37	0.67	3.13	1.55E+06	2.09E+06	4.08E+50
DK_1383	2.1	18.5	2.1	0.58	10.41	0.4	0.75	1.94	2.28E+06	3.08E+06	2.41E+51
DK_5417	5.72	16.56	5.72	0.27	12.91	0.35	0.47	1.1	3.82E+06	5.16E+06	5.11E+51
DK_5563	21.43	12.68	12.68	1.24	18.55	0.5	0.72	2.39	1.97E+04	2.66E+04	1.17E+49
DK_1283	1.88	19.83	1.88	1.1	10	0.26	0.35	4.09	8.36E+04	1.13E+05	1.38E+48
DK_5707	2.76	8.57	2.76	0.2	9.79	0.16	0.31	1.46	2.75E+05	3.71E+05	7.26E+49
DK_b_665	1.5	12.01	1.5	0.84	7.65	0.05	0.07	0.28	1.18E+03	1.59E+03	4.86E+47
DK_182	1.65	15.94	1.65	0.47	9.83	0.1	0.2	1.18	1.01E+05	1.37E+05	1.51E+49
DK_1055	6.44	2.68	6.44	0.68	7.42	0.39	0.76	1.6	5.15E+06	6.96E+06	8.51E+51
DK_2424	4.44	16.66	4.44	0.56	12.04	0.47	0.53	1.74	9.47E+05	1.28E+06	5.62E+50
DK_2436	10.58	1.61	1.61	0.12	7.43	0.09	0.16	1.26	6.85E+04	9.25E+04	4.52E+48
DK_b_338	3.38	20.32	3.38	1.28	11.51	0.24	0.31	1.81	1.09E+05	1.47E+05	1.62E+49
DK_1007	11.43	0.98	0.98	0.24	9.13	0.08	0.12	0.26	1.74E+04	2.36E+04	2.88E+49
DK_2524	1.21	10.5	1.21	0.05	9.21	0.08	0.12	0.68	3.27E+04	4.42E+04	4.86E+48
DK_973	12.93	2.21	2.21	0.81	10.04	0.15	0.33	0.64	1.12E+04	1.51E+04	2.23E+49
DK_2638	12.55	1.63	1.63	0.17	7.2	0.13	0.23	0.88	1.88E+05	2.54E+05	7.77E+49
DK_146	2.05	12.72	2.05	0.1	9.91	0.04	0.04	0.26	4.73E+03	6.38E+03	7.02E+47
DK_937	3.25	10.49	3.25	0.19	10.31	0.21	0.37	2.16	6.33E+04	8.55E+04	9.40E+48
DK_2738	6.11	8.21	6.11	0.37	11.05	0.32	0.64	1.24	1.23E+06	1.66E+06	2.46E+51
DK_2798	2.7	17.76	2.7	0.23	10.95	0.15	0.21	0.62	9.58E+05	1.29E+06	7.75E+50
DK_2800	3.42	21.32	3.42	1.37	11.62	1.01	1.21	5.62	2.79E+06	3.76E+06	7.36E+50
DK_2804	10.07	1.96	1.96	0.02	7.24	0.28	0.44	2.02	3.44E+05	4.65E+05	9.09E+49
DK_129	4.13	16.5	4.13	0.11	11.84	0.14	0.25	1.47	3.26E+05	4.40E+05	4.84E+49
DK_2939	1.77	14.84	1.77	0.45	9.85	0.21	0.4	2.33	3.43E+05	4.62E+05	5.09E+49
DK_3122	1.29	14.58	1.29	0.37	9.47	0.19	0.28	0.93	2.79E+05	3.76E+05	1.66E+50
DK_3168	4.18	16.65	4.18	0.54	11.86	0.46	0.79	2.63	2.26E+06	3.05E+06	1.34E+51
DK_712	8.88	1.47	8.88	1	7.7	0.97	1.73	6.68	8.64E+06	1.17E+07	3.57E+51
DK_714	9.16	1.15	9.16	1.07	7.85	1	1.7	4.92	1.19E+07	1.60E+07	9.59E+51
DK_713	8.99	1.36	8.99	1.04	7.75	0.98	1.75	5.79	1.01E+07	1.36E+07	6.00E+51
DK_3274	2.8	6.9	2.8	0.63	7.34	0.18	0.34	1.33	1.56E+03	2.10E+03	6.43E+47
DK_3338	3.6	3.45	3.6	0.41	9.2	0.3	0.43	1.65	4.59E+05	6.19E+05	1.89E+50
DK_3336	12.24	1.8	1.8	0.18	7.09	0.16	0.24	1.14	2.09E+05	2.82E+05	5.52E+49
DK_3331	5.77	17.69	5.77	0.78	13.13	0.43	0.63	2.09	9.77E+05	1.32E+06	5.80E+50
DK_b_303	1.58	15.97	1.58	0.64	9.69	0.26	0.41	2.38	2.99E+05	4.03E+05	4.44E+49
DK_3551	3.99	15.46	3.99	0.61	11.51	0.33	0.58	1.49	1.10E+06	1.49E+06	1.16E+51
DK_3552	4.34	16.06	4.34	0.68	11.85	0.36	0.53	4.15	3.30E+05	4.46E+05	2.18E+49
DK_3574	4.5	3.27	4.5	0.1	9.33	0.22	0.39	1.14	5.68E+05	7.67E+05	4.59E+50
DK_3609	6.79	17.06	6.79	0.93	13.64	0.39	0.62	1.81	1.24E+06	1.67E+06	1.00E+51
DK_535	1.49	9.8	1.49	0.05	9.32	0.07	0.13	0.61	1.87E+05	2.53E+05	4.94E+49
DK_530	12.58	1.26	1.26	0.09	7.51	0.13	0.29	0.95	2.94E+05	3.96E+05	1.74E+50
DK_3756	12.94	2.3	2.3	0.22	6.51	0.17	0.26	0.76	2.66E+05	3.60E+05	2.15E+50
DK_b_818	3.76	6.97	3.76	1.44	7.03	0.2	0.31	1.45	2.35E+03	3.17E+03	6.19E+47
DK_3804	3.79	9.36	3.79	0.24	10.37	0.22	0.31	1.46	4.89E+05	6.61E+05	1.29E+50
DK_3900	2.55	12.73	2.55	0.28	10.22	0.17	0.25	1.14	1.11E+05	1.50E+05	2.93E+49
DK_466	4.88	12.14	4.88	1.33	11.29	0.21	0.34	1.99	1.08E+04	1.46E+04	1.61E+48
DK_70	15.8	4.78	4.78	0.16	12.16	0.15	0.23	1.07	2.51E+05	3.39E+05	6.63E+49
DK_4223	5.37	17.64	5.37	0.84	12.83	0.61	0.8	2.07	2.52E+06	3.40E+06	2.66E+51
DK_4236	10.42	1.2	1.2	0.13	9.2	0.12	0.17	0.29	1.04E+05	1.40E+05	2.90E+50
DK_4318	4.03	14.48	4.03	0.6	11.38	0.34	0.6	1.27	1.22E+06	1.65E+06	2.02E+51
DK_4341	9.87	3.4	9.87	0.57	6.22	0.43	0.82	6.38	3.86E+06	5.21E+06	2.55E+50
DK_b_300	1.8	16.69	1.8	0.72	9.9	0.37	0.62	3.6	6.46E+05	8.72E+05	9.60E+49
DK_4548	1.53	9.58	1.53	0.17	9.31	0.18	0.3	0.99	3.48E+05	4.70E+05	2.07E+50
DK_48	11.89	0.87	0.87	0.04	7.87	0.04	0.07	0.4	4.32E+04	5.83E+04	6.41E+48

DK_b_851	1.66	14.39	1.66	0.61	7.16	0.08	0.1	0.59	5.41E+03	7.30E+03	8.03E+47
DK_4802	7.25	7.62	7.25	0.56	11.28	0.63	0.83	1.91	3.27E+06	4.42E+06	4.37E+51
DK_4814	11.15	3.12	3.12	0.07	6.12	0.22	0.27	1.59	3.63E+05	4.91E+05	5.40E+49
DK_1640	6.75	3.2	6.75	0.06	7.12	0.8	1.78	8.26	2.90E+06	3.91E+06	7.65E+50
DK_1598	10.67	2.42	2.42	0.01	6.82	0.28	0.45	1.73	4.46E+05	6.02E+05	1.84E+50
DK_b_210	10.38	1.38	1.38	1.13	7.61	0.06	0.09	0.7	2.44E+03	3.30E+03	1.61E+47
DK_1745	13.57	2.14	2.14	0.15	6.58	0.23	0.52	0.67	1.72E+06	2.33E+06	8.22E+51
DK_5096	1.89	10	1.89	0.25	9.53	0.25	0.4	2.33	2.82E+05	3.81E+05	4.19E+49
DK_1777	9.64	2.1	9.64	1.18	7.21	1.18	2.54	8.41	1.39E+07	1.88E+07	8.26E+51
DK_5190	4.11	14.68	4.11	0.28	11.51	0.16	0.27	0.69	1.26E+06	1.70E+06	1.33E+51
DK_1465	7.76	1.27	7.76	1.03	7.9	0.82	1.3	2.15	1.63E+07	2.20E+07	4.55E+52
DK_275	4.05	10.1	4.05	0.09	5.6	0.19	0.32	1.86	6.86E+00	9.26E+00	1.02E+45
DK_5303	12.35	4.44	4.44	0.41	4.23	0.33	0.49	0.94	1.13E+06	1.53E+06	2.26E+51
DK_1417	8.35	4.87	8.35	2.32	5.62	0.33	0.58	2.72	1.84E+04	2.49E+04	4.87E+48
DK_5354	10.21	0.99	0.99	0.09	9.08	0.05	0.06	0.66	1.30E+04	1.75E+04	2.14E+47
DK_5376	6.97	18.71	6.97	1.11	14.12	0.43	0.86	1.52	3.07E+06	4.14E+06	7.29E+51
DK_2174	8.07	1.64	8.07	0.31	7.68	0.25	0.32	1.47	1.91E+06	2.57E+06	5.03E+50
DK_2394	1.8	11.89	1.8	0.34	9.64	0.18	0.26	1.52	1.51E+05	2.04E+05	2.24E+49
DK_2453	5.66	3.04	5.66	0.33	9.46	0.22	0.37	1.23	8.04E+05	1.08E+06	4.77E+50
DK_168	1.99	17.45	1.99	0.37	10.29	0.15	0.27	1.26	3.57E+05	4.82E+05	9.43E+49
DK_2509	6.67	3.68	6.67	0.71	6.91	0.5	1.06	3.06	4.02E+06	5.43E+06	3.25E+51
DK_1013	17.11	5.59	5.59	0.43	12.96	0.2	0.29	1.71	6.46E+04	8.72E+04	9.59E+48
DK_2639	4.1	16.35	4.1	0.44	11.77	0.3	0.41	1.37	8.09E+05	1.09E+06	4.80E+50
DK_13	15.49	5.87	5.87	0.06	12.77	0.1	0.13	0.74	2.09E+04	2.82E+04	3.10E+48
DK_929	2.49	18.88	2.49	0.34	10.88	0.23	0.37	2.89	4.50E+05	6.08E+05	2.97E+49
DK_2760	1.86	11.99	1.86	0.17	9.71	0.08	0.12	0.71	7.87E+04	1.06E+05	1.17E+49
DK_119	2.33	15.37	2.33	0.08	10.39	0.12	0.22	1.3	1.09E+05	1.47E+05	1.62E+49
DK_797	1.84	8.26	1.84	0.15	7.56	0.16	0.32	1.26	8.89E+03	1.20E+04	3.67E+48
DK_765	6.64	3.86	6.64	0.08	6.83	0.79	1.08	6.3	1.67E+06	2.26E+06	2.48E+50
DK_698	8.76	22.76	8.76	1.77	16.24	0.19	0.38	2.22	3.73E+04	5.04E+04	5.55E+48
DK_636	11.75	1.06	1.06	0.1	7.73	0.11	0.21	0.53	2.30E+05	3.11E+05	2.43E+50
DK_3450	4.09	6.42	4.09	0.35	9.92	0.27	0.39	1.83	1.95E+05	2.64E+05	5.16E+49
DK_616	14.14	2.44	2.44	0.2	6.16	0.25	0.47	1.22	9.66E+05	1.30E+06	1.02E+51
DK_89	12.36	2.31	2.31	0.07	10.04	0.09	0.18	1.06	1.29E+05	1.74E+05	1.91E+49
DK_3583	1.43	11.81	1.43	0.23	9.42	0.14	0.2	1.17	9.36E+04	1.26E+05	1.39E+49
DK_3666	2.3	11.17	2.3	0.3	6.86	0.15	0.23	1.07	2.54E+02	3.43E+02	6.70E+46
DK_3735	10.94	3.35	3.35	0.37	5.96	0.09	0.15	0.85	2.44E+04	3.30E+04	3.63E+48
DK_3757	5.34	5.84	5.34	0.3	10.17	0.37	0.44	1.72	1.64E+06	2.21E+06	6.75E+50
DK_3831	9.03	11.89	9.03	0.8	13.37	0.39	0.71	4.13	2.54E+06	3.44E+06	3.78E+50
DK_72	16.21	3.2	3.2	0.01	11.14	0.08	0.13	0.98	6.22E+04	8.39E+04	4.10E+48
DK_3972	11.71	1.05	1.05	0.17	7.74	0.14	0.23	0.49	2.96E+05	3.99E+05	4.88E+50
DK_69	13.93	4.78	4.78	0.1	11.78	0.15	0.23	1.07	1.98E+05	2.67E+05	5.22E+49
DK_4113	3.44	16.7	3.44	0.16	11.38	0.2	0.38	0.73	9.59E+05	1.29E+06	1.91E+51
DK_4128	8.69	4.57	8.69	0.85	5.71	0.72	1.18	1.24	1.17E+07	1.58E+07	8.50E+52
DK_4179	12.6	3.28	3.28	0.1	10.66	0.17	0.22	1	1.07E+05	1.44E+05	2.81E+49
DK_4307	8.73	7.02	8.73	0.13	11.56	0.34	0.5	2.88	1.20E+06	1.62E+06	1.78E+50
DK_4336	3.87	7.32	3.87	0.53	10	0.3	0.39	0.75	2.59E+05	3.50E+05	5.18E+50
DK_4648	6.72	18.22	6.72	0.36	13.94	0.44	0.8	2.64	2.21E+06	2.98E+06	1.31E+51
DK_1622	7.74	2.51	7.74	0.25	7.27	0.75	1.05	4.08	3.48E+06	4.70E+06	1.44E+51
DK_1611	20.63	3.97	3.97	0.23	12.4	0.4	0.65	5.03	5.89E+05	7.95E+05	3.89E+49
DK_1673	1.9	14.55	1.9	0.22	9.98	0.14	0.28	0.82	2.85E+05	3.85E+05	2.31E+50
DK_1672	1.18	13.8	1.18	0.14	9.4	0.1	0.2	2.31	9.20E+04	1.24E+05	1.52E+48
DK_1600	10.95	2.57	2.57	0	6.64	0.22	0.37	2.17	2.46E+05	3.32E+05	3.66E+49
DK_4995	12.7	4.13	4.13	0.48	4.53	0.31	0.45	1.05	5.73E+05	7.73E+05	7.66E+50
DK_1779	9.51	2.46	9.51	1.35	6.99	1.17	1.76	10.26	5.30E+06	7.15E+06	7.87E+50
DK_1489	9.03	1.74	9.03	1.38	7.52	1.11	1.47	6.84	5.82E+06	7.86E+06	1.54E+51
DK_1813	1.94	8.82	1.94	0.04	7.43	0.16	0.32	1.89	1.46E+03	1.97E+03	2.17E+47
DK_1474	15.41	1.89	1.89	0.13	10.07	0.12	0.23	1.35	3.16E+04	4.26E+04	4.69E+48
DK_1462	5.75	2.94	5.75	0.23	7.44	0.43	0.6	3.52	1.26E+06	1.70E+06	1.87E+50
DK_1420	8.35	2.63	8.35	0.02	7.09	0.95	1.85	7.17	7.83E+06	1.06E+07	3.23E+51
DK_1912	8.18	2.03	8.18	0.9	7.46	0.72	0.9	5.22	2.47E+06	3.33E+06	3.67E+50
DK_1401	10.06	2.47	2.47	0.14	6.88	0.13	0.27	0.9	3.60E+05	4.86E+05	2.14E+50
DK_1940	11.55	1.43	1.43	0.21	7.47	0.03	0.05	0.39	3.81E+03	5.14E+03	2.51E+47

DK_1399	12.09	1.33	1.33	0	7.49	0.08	0.15	0.85	6.22E+04	8.40E+04	9.24E+48
DK_1395	1.94	15.06	1.94	0.07	10.07	0.11	0.21	1.65	7.60E+04	1.03E+05	5.02E+48
DK_1943	6.72	7.69	6.72	0.46	11.12	0.56	0.74	3.42	7.44E+05	1.00E+06	1.97E+50
DK_28	3.5	12.6	3.5	0.06	5.31	0.08	0.11	0.5	7.73E+01	1.04E+02	2.04E+46
DK_5709	18.35	6.21	6.21	0.11	13.65	0.35	0.63	2.91	2.50E+05	3.37E+05	6.59E+49
DK_2152	1.61	13.66	1.61	0.11	9.7	0.18	0.35	2.72	1.71E+05	2.30E+05	1.13E+49
DK_1226	1.17	13.78	1.17	0.07	9.4	0.12	0.22	1.72	1.01E+05	1.36E+05	6.64E+48
DK_1219	20.57	4.7	4.7	0.48	13	0.18	0.27	2.08	1.62E+04	2.19E+04	1.07E+48
DK_2266	9.55	2.85	9.55	0.65	6.71	0.46	0.67	3.1	4.31E+06	5.81E+06	1.14E+51
DK_1128	11.96	0.87	0.87	0.06	7.86	0.06	0.13	0.74	4.15E+04	5.60E+04	6.16E+48
DK_1031	8.72	2.51	8.72	1.28	7.1	0.42	0.84	6.53	8.73E+05	1.18E+06	5.77E+49
DK_2454	5.43	2.75	5.43	0.33	9.34	0.21	0.33	3.9	6.68E+05	9.01E+05	1.10E+49
DK_2544	11.48	2.92	2.92	0.25	6.22	0.17	0.28	1.09	2.73E+05	3.69E+05	1.13E+50
DK_983	11.33	1.36	1.36	0.44	9.36	0.12	0.18	1.07	2.59E+03	3.50E+03	3.85E+47
DK_b_735	1.97	16.25	1.97	1.32	7.08	0.15	0.18	1.41	2.12E+03	2.87E+03	1.40E+47
DK_927	14.88	1.28	1.28	0.15	7.31	0.12	0.18	0.7	1.51E+05	2.04E+05	6.22E+49
DK_2676	14.52	1.14	1.14	0.2	7.46	0.19	0.27	1.59	1.80E+05	2.43E+05	2.67E+49
DK_877	20.35	3.6	3.6	0.23	12.05	0.43	0.57	4.43	7.46E+05	1.01E+06	4.93E+49
DK_863	15.02	1.63	1.63	0.21	6.94	0.21	0.3	1.17	3.57E+05	4.82E+05	1.47E+50
DK_855	14.05	2.54	2.54	0.03	6.05	0.17	0.28	1.62	2.65E+05	3.57E+05	3.93E+49
DK_2833	2.21	10.29	2.21	0.19	9.74	0.18	0.24	1.89	1.78E+05	2.40E+05	1.17E+49
DK_2865	2.15	14.41	2.15	0.38	10.12	0.18	0.36	0.93	4.54E+05	6.13E+05	4.80E+50
DK_2871	2.68	11.45	2.68	0.42	10.11	0.12	0.13	0.75	1.02E+05	1.38E+05	1.52E+49
DK_788	11.8	0.78	0.78	0.09	7.94	0.11	0.15	0.71	8.30E+04	1.12E+05	2.19E+49
DK_763	6.17	3.91	6.17	0.12	6.94	0.73	1.57	9.11	1.65E+06	2.22E+06	2.44E+50
DK_3146	8.14	4.54	8.14	0.5	10.45	0.39	0.61	3.52	1.21E+06	1.63E+06	1.80E+50
DK_3180	13.02	2.25	2.25	0.3	6.56	0.25	0.39	1.12	5.46E+05	7.37E+05	4.42E+50
DK_710	17.27	1.74	1.74	0.05	10.11	0.14	0.24	1.84	5.46E+04	7.37E+04	3.60E+48
DK_709	17.39	1.9	1.9	0.06	10.26	0.17	0.26	1.51	6.04E+04	8.16E+04	8.97E+48
DK_634	0.86	11.12	0.86	0.05	7.92	0.05	0.07	0.26	1.91E+03	2.57E+03	7.87E+47
DK_618	2.42	18.68	2.42	0.46	10.77	0.37	0.58	1.69	1.91E+06	2.58E+06	1.54E+51
DK_3471	2.06	12.21	2.06	0.13	9.86	0.19	0.4	2.33	1.33E+05	1.79E+05	1.97E+49
DK_606	1.1	13.94	1.1	0.07	7.55	0.11	0.17	0.49	6.02E+04	8.13E+04	4.87E+49
DK_3577	20.28	6.81	6.81	0.33	14.51	0.33	0.57	3.29	6.54E+05	8.83E+05	9.72E+49
DK_576	24.63	7.91	7.91	0.89	16.27	0.24	0.45	2.61	1.46E+05	1.97E+05	2.17E+49
DK_3761	1.22	14.46	1.22	0.19	9.46	0.17	0.36	2.07	2.18E+05	2.95E+05	3.24E+49
DK_437	2.19	7.89	2.19	0.05	7.42	0.07	0.1	0.44	4.23E+02	5.72E+02	1.12E+47
DK_62	11	1.76	1.76	0.08	7.27	0.05	0.06	0.48	3.22E+04	4.35E+04	2.13E+48
DK_388	2.35	14.3	2.35	0.14	6.23	0.24	0.42	1.64	1.64E+05	2.21E+05	6.76E+49
DK_367	1.35	15.64	1.35	0.26	9.63	0.15	0.31	1.04	3.82E+05	5.15E+05	2.27E+50
DK_4647	8.05	19.59	8.05	0.39	15.15	0.53	1.06	4.1	2.13E+06	2.87E+06	8.78E+50
DK_1685	9.39	2.94	9.39	0.56	6.68	1.11	2.21	12.87	5.02E+06	6.78E+06	7.46E+50
DK_1708	8.47	1.4	8.47	1.08	7.77	0.93	1.3	5.05	5.52E+06	7.45E+06	2.28E+51
DK_4979	9.87	4.24	9.87	0.33	10.68	0.65	0.99	3.3	1.58E+06	2.13E+06	9.36E+50
DK_299	8.96	1.93	8.96	1.22	7.41	0.27	0.47	1.82	6.57E+05	8.87E+05	2.71E+50
DK_1734	7.36	2.83	7.36	1.07	7.17	0.71	1.13	1.31	1.45E+07	1.96E+07	8.63E+52
DK_1551	4.88	2.59	4.88	0.09	9.21	0.32	0.64	2.99	8.89E+05	1.20E+06	2.35E+50
DK_1547	1.63	13.43	1.63	0.25	9.68	0.14	0.27	1.27	1.69E+05	2.28E+05	4.46E+49
DK_5078	6.65	3.34	6.65	0.56	9.72	0.26	0.49	2.3	9.10E+05	1.23E+06	2.40E+50
DK_5101	8.49	3.68	8.49	0.35	10.17	0.3	0.37	1.72	5.67E+05	7.65E+05	1.50E+50
DK_1780	9.33	2.73	9.33	1.34	6.84	1.06	1.56	7.25	7.17E+06	9.68E+06	1.89E+51
DK_1513	1.6	12.41	1.6	0.14	9.59	0.14	0.27	1.55	7.90E+04	1.07E+05	1.17E+49
DK_1507	7.84	4.25	7.84	1.09	6.24	0.41	0.86	5	5.00E+05	6.75E+05	7.42E+49
DK_5148	11.68	0.77	0.77	0.06	7.96	0.04	0.07	0.41	1.40E+04	1.89E+04	2.08E+48
DK_1801	1.38	12.6	1.38	0.15	9.45	0.18	0.39	1.83	2.55E+05	3.44E+05	6.73E+49
DK_1490	9.13	1.55	9.13	1.43	7.62	1.12	1.41	4.66	5.67E+06	7.66E+06	3.37E+51
DK_1467	2.25	18.28	2.25	0.6	10.52	0.27	0.51	2.37	9.05E+05	1.22E+06	2.39E+50
DK_5285	10.13	3.08	3.08	0.19	6.41	0.28	0.42	3.26	2.45E+05	3.31E+05	1.62E+49
DK_1884	12.38	2.76	2.76	0.37	6.17	0.28	0.44	0.46	1.97E+06	2.66E+06	1.43E+52
DK_5318	3.85	5.66	3.85	0.16	9.7	0.32	0.66	2.56	7.72E+05	1.04E+06	3.18E+50
DK_1904	5.73	8.2	5.73	1.02	10.85	0.22	0.43	3.31	1.06E+05	1.43E+05	6.99E+48
DK_1920	2.54	12.58	2.54	0.2	10.2	0.14	0.28	0.81	2.39E+05	3.22E+05	1.93E+50
DK_1928	8.37	2.56	8.37	1.15	7.13	0.95	1.74	8.09	5.59E+06	7.54E+06	1.48E+51

DK_b_628	2.69	20.42	2.69	1.09	10.92	0.28	0.4	3.12	3.17E+05	4.28E+05	2.10E+49
DK_1402	10.85	1.6	1.6	0.09	7.41	0.08	0.15	1.2	4.56E+04	6.16E+04	3.01E+48
DK_1945	6.46	7.16	6.46	0.55	10.87	0.34	0.54	4.18	1.21E+06	1.63E+06	7.96E+49
DK_1944	6.46	7.16	6.46	0.54	10.87	0.51	0.65	2.52	5.17E+05	6.98E+05	2.13E+50
DK_1946	6.4	6.95	6.4	0.57	10.79	0.31	0.53	4.14	1.04E+06	1.41E+06	6.89E+49
DK_2001	8.54	1.88	8.54	0.84	9.4	0.56	1.01	1.67	3.62E+06	4.89E+06	1.01E+52
DK_1356	10.01	2.54	2.54	0.04	6.84	0.23	0.4	3.13	2.31E+05	3.12E+05	1.53E+49
DK_1343	6.36	16.51	6.36	0.7	13.27	0.14	0.22	2.6	3.06E+04	4.14E+04	5.06E+47
DK_1324	10.39	2.21	2.21	0.3	7.02	0.26	0.4	1.55	3.19E+05	4.30E+05	1.31E+50
DK_2048	3.97	15.59	3.97	0.38	11.56	0.4	0.75	1.59	2.84E+06	3.84E+06	4.69E+51
DK_5601	2.64	12.52	2.64	0.49	10.21	0.29	0.39	1.84	3.14E+05	4.24E+05	8.30E+49
DK_2070	1.03	14.91	1.03	0.03	9.36	0.05	0.08	0.25	8.98E+04	1.21E+05	5.34E+49
DK_1272	10.71	22.18	10.71	0.62	17.58	0.37	0.75	4.36	7.66E+05	1.03E+06	1.14E+50
DK_2153	2.12	14.23	2.12	0.27	10.09	0.24	0.46	2.14	2.45E+05	3.30E+05	6.46E+49
DK_2154	2.4	14.68	2.4	0.35	10.33	0.24	0.33	1.52	1.80E+05	2.43E+05	4.76E+49
DK_2179	3.97	7.41	3.97	0.47	6.58	0.24	0.33	1.28	1.97E+02	2.66E+02	8.13E+46
DK_2271	21.49	6.77	6.77	0.58	14.76	0.47	0.89	1.59	9.94E+05	1.34E+06	2.36E+51
DK_2334	5.84	17.97	5.84	0.73	13.25	0.61	1.16	3.85	3.49E+06	4.72E+06	2.08E+51
DK_1118	10.28	2.15	2.15	0.31	7.08	0.11	0.21	0.96	1.06E+05	1.43E+05	2.80E+49
DK_176	10.43	3.05	3.05	0.01	6.36	0.13	0.24	1.12	4.29E+05	5.79E+05	1.13E+50
DK_2396	1.54	10.7	1.54	0.02	9.42	0.11	0.22	0.72	1.56E+05	2.10E+05	9.25E+49
DK_2433	2.18	17.38	2.18	0.63	10.36	0.17	0.31	1.79	1.50E+05	2.03E+05	2.23E+49
DK_2502	10.44	2.47	2.47	0.38	6.82	0.32	0.39	0.75	9.39E+05	1.27E+06	1.88E+51
DK_2584	9.24	4.34	9.24	0.77	5.67	0.65	0.93	1.54	5.60E+06	7.56E+06	1.56E+52
DK_b_62	12.41	1.59	1.59	0.58	9.59	0.11	0.24	0.92	4.93E+03	6.66E+03	2.03E+48
DK_149	12.06	3.96	3.96	0.15	4.96	0.16	0.28	1.07	5.01E+05	6.76E+05	2.07E+50
DK_b_328	1.75	16	1.75	0.71	6.94	0.24	0.47	1.82	1.13E+05	1.52E+05	4.65E+49
DK_2614	1.91	17.84	1.91	0.26	10.28	0.23	0.49	1.61	7.10E+05	9.59E+05	4.22E+50
DK_2617	7.66	1.52	7.66	0.9	7.79	0.33	0.57	4.43	1.51E+06	2.03E+06	9.94E+49
DK_2622	2.36	7.78	2.36	0.31	7.36	0.15	0.33	1.93	1.48E+03	1.99E+03	2.19E+47
DK_2628	14.08	2.3	2.3	0.32	6.36	0.14	0.19	0.55	2.65E+05	3.58E+05	2.14E+50
DK_2637	4.88	5.74	4.88	0.01	6.65	0.64	0.86	1.53	3.15E+03	4.26E+03	7.49E+48
DK_2696	2.85	8.25	2.85	0.26	9.78	0.16	0.27	2.14	1.09E+05	1.47E+05	7.19E+48
DK_2753	8.28	3.12	8.28	1.34	6.82	0.65	1.13	6.56	2.39E+06	3.23E+06	3.55E+50
DK_2755	8.4	3.07	8.4	0.91	6.82	0.66	0.96	7.44	2.60E+06	3.52E+06	1.72E+50
DK_2752	8.24	3.13	8.24	1.48	6.81	0.65	1.16	6.74	1.49E+06	2.01E+06	2.21E+50
DK_2754	8.34	3.09	8.34	1.2	6.82	0.66	1.06	8.25	2.27E+06	3.07E+06	1.50E+50
DK_830	8.55	1	8.55	1	7.98	0.94	1.66	9.67	9.94E+06	1.34E+07	1.48E+51
DK_2935	14.82	1.07	1.07	0.16	7.51	0.11	0.17	0.68	1.13E+05	1.53E+05	4.66E+49
DK_2949	17.69	6.85	6.85	0.44	13.91	0.36	0.54	6.32	1.68E+05	2.27E+05	2.78E+48
DK_2959	7.5	17.74	7.5	0.73	14.28	0.49	0.85	3.97	1.96E+06	2.65E+06	5.18E+50
DK_3015	6.37	16.48	6.37	0.78	13.25	0.47	0.95	3.16	2.88E+06	3.89E+06	1.71E+51
DK_3019	1.06	9.11	1.06	0.08	9.05	0.06	0.1	0.25	5.33E+04	7.19E+04	5.63E+49
DK_3025	11.97	1.78	1.78	0.18	7.14	0.1	0.15	0.86	1.28E+05	1.73E+05	1.90E+49
DK_3071	2.09	12.88	2.09	0.3	9.93	0.19	0.32	1.06	2.19E+05	2.95E+05	1.30E+50
DK_3069	14.39	4.94	4.94	0.37	11.97	0.26	0.48	2.77	1.68E+05	2.27E+05	2.50E+49
DK_759	2.14	7.67	2.14	0.14	7.48	0.16	0.33	1.09	3.91E+03	5.28E+03	2.32E+48
DK_3094	9.83	0.92	9.83	1.57	7.95	0.56	0.95	5.51	1.84E+06	2.48E+06	2.73E+50
DK_3095	5.37	6.17	5.37	0.46	10.25	0.31	0.47	3.66	5.52E+05	7.45E+05	3.64E+49
DK_107	12.21	1.43	1.43	0.02	7.4	0.07	0.16	0.73	9.09E+04	1.23E+05	2.40E+49
DK_3174	13.88	2.31	2.31	0.12	6.35	0.13	0.22	1.29	1.35E+05	1.83E+05	2.01E+49
DK_3226	3.8	4.49	3.8	0.23	9.45	0.17	0.28	1.64	3.19E+05	4.31E+05	4.74E+49
DK_690	7.78	22.27	7.78	0.92	15.6	0.27	0.54	2.11	6.78E+05	9.15E+05	2.80E+50
DK_3280	10.14	3.14	3.14	0.68	6.36	0.62	0.81	0.67	6.42E+06	8.67E+06	7.72E+52
DK_3443	10.02	3.27	3.27	0.53	6.28	0.5	0.79	0.55	5.95E+06	8.03E+06	1.00E+53
DK_3516	4.52	13.5	4.52	0.3	11.53	0.14	0.24	1.84	1.59E+05	2.15E+05	1.05E+49
DK_3570	5.2	6.06	5.2	0.34	10.18	0.27	0.52	2.43	3.73E+05	5.03E+05	9.84E+49
DK_3644	3.49	6.47	3.49	0.47	9.72	0.29	0.46	1.52	4.38E+05	5.92E+05	2.60E+50
DK_3646	11.2	1.23	1.23	0.15	7.65	0.15	0.26	1.22	1.06E+05	1.43E+05	2.79E+49
DK_529	8.86	1.74	8.86	1.04	7.54	0.74	1.28	4.26	5.51E+06	7.44E+06	3.27E+51
DK_3824	3.72	6.68	3.72	0.29	9.85	0.29	0.52	3.04	3.56E+05	4.81E+05	5.29E+49
DK_3839	8.19	5.59	8.19	0.84	5.14	0.47	0.72	2.38	1.67E+06	2.25E+06	9.90E+50
DK_3834	8.24	9.26	8.24	0.78	12.16	0.36	0.58	3.35	1.24E+06	1.67E+06	1.84E+50

DK_3832	8.24	9.26	8.24	0.78	12.16	0.36	0.61	2.37	1.72E+06	2.33E+06	7.11E+50
DK_3848	3.03	7.59	3.03	0.63	9.71	0.22	0.45	1.75	1.63E+05	2.20E+05	6.71E+49
DK_3940	4.08	3.39	4.08	0.52	7.64	0.18	0.25	0.83	3.76E+05	5.08E+05	2.24E+50
DK_3961	1.31	9.25	1.31	0.14	9.18	0.14	0.17	0.8	1.18E+05	1.60E+05	3.13E+49
DK_3990	2.2	7.54	2.2	0.45	9.39	0.14	0.25	0.97	5.96E+04	8.04E+04	2.46E+49
DK_4042	3.01	6.73	3.01	0.31	9.61	0.18	0.3	1.17	1.92E+05	2.59E+05	7.91E+49
DK_4304	7.74	17.75	7.74	1.19	14.37	0.3	0.47	2.76	6.05E+05	8.16E+05	8.98E+49
DK_4323	3.77	5.77	3.77	0.1	9.7	0.21	0.35	2.02	2.43E+05	3.28E+05	3.61E+49
DK_4322	3.81	5.71	3.81	0.09	9.7	0.22	0.42	1.94	3.49E+05	4.71E+05	9.22E+49
DK_4370	11.56	5.07	5.07	0.41	3.74	0.35	0.53	1.24	5.15E+05	6.96E+05	6.89E+50
DK_383	1.25	12.39	1.25	0.03	7.53	0.09	0.19	1.09	1.94E+03	2.61E+03	2.88E+47
DK_4516	4.08	5.1	4.08	0.48	9.63	0.25	0.36	0.92	8.43E+05	1.14E+06	8.90E+50
DK_4513	6.21	5.56	6.21	0.66	6.14	0.49	0.63	1.61	2.06E+06	2.78E+06	2.18E+51
DK_4575	1.92	14.39	1.92	0.36	9.95	0.29	0.57	1.65	8.97E+05	1.21E+06	7.25E+50
DK_4595	13.09	2.7	2.7	0.27	6.08	0.26	0.38	0.88	5.55E+05	7.49E+05	7.42E+50
DK_4856	17.46	5.96	5.96	0.49	13.27	0.34	0.63	2.07	4.20E+05	5.67E+05	2.50E+50
DK_4858	16.23	4.6	4.6	0.38	12.12	0.26	0.42	1.23	4.30E+05	5.80E+05	3.47E+50
DK_4877	4.95	5.47	4.95	0.41	9.96	0.28	0.52	3.03	5.19E+05	7.01E+05	7.71E+49
DK_4897	9.3	22.5	9.3	0.66	16.75	0.41	0.61	4.74	7.22E+05	9.75E+05	4.77E+49
DK_4918	2.41	18.13	2.41	0.75	10.59	0.23	0.38	2.22	1.20E+05	1.62E+05	1.78E+49
DK_33	19.49	3.03	3.03	0.12	11.45	0.09	0.16	0.92	1.73E+05	2.34E+05	2.57E+49
DK_5320	5.04	5.81	5.04	0.69	10.05	0.55	1.12	1.72	3.13E+06	4.22E+06	1.01E+52
DK_5467	10.58	0.97	0.97	0.15	9.08	0.03	0.04	0.25	7.21E+02	9.73E+02	1.07E+47
DK_5558	12.24	4.56	4.56	0.13	11.32	0.26	0.42	3.26	1.14E+05	1.54E+05	7.53E+48
DK_5585	11.62	17.82	11.62	0.71	16.69	0.91	1.53	4.44	3.11E+06	4.21E+06	2.52E+51
DK_236	10.16	1.36	1.36	0.09	7.64	0.11	0.21	0.49	3.32E+05	4.48E+05	4.44E+50
DK_226	2.34	8.89	2.34	0.34	7.2	0.08	0.16	0.95	4.59E+02	6.19E+02	6.81E+46
DK_164	9.08	3.08	9.08	0.34	6.65	0.24	0.36	4.18	6.75E+05	9.12E+05	1.11E+49
DK_15	19.35	6.73	6.73	0.1	14.23	0.12	0.15	1.72	3.79E+04	5.12E+04	6.26E+47
DK_6	8.42	6.09	8.42	0.38	4.58	0.11	0.15	1.14	1.95E+04	2.64E+04	1.29E+48
DK_8	21.22	8.3	8.3	0.13	15.76	0.11	0.14	1.7	3.86E+04	5.21E+04	6.36E+47
DK_5	20.5	7.91	7.91	0.12	15.31	0.1	0.14	0.8	5.19E+04	7.01E+04	7.71E+48
DK_3909	1.83	13	1.83	0.18	9.79	0.18	0.36	4.17	9.58E+04	1.29E+05	1.58E+48
DK_42	14.34	3.07	3.07	0.08	10.78	0.07	0.11	0.83	7.36E+04	9.94E+04	4.86E+48
DK_1340	1.93	12.52	1.93	0.36	6.99	0.05	0.06	0.69	1.16E+02	1.56E+02	1.91E+45
DK_2033	2.11	14.35	2.11	0.15	10.12	0.23	0.5	2.89	1.82E+05	2.45E+05	2.70E+49
DK_5550	9.55	4.36	9.55	0.4	10.67	0.25	0.33	3.91	4.84E+05	6.53E+05	7.98E+48
DK_b_335	1.58	18.46	1.58	0.76	9.8	0.28	0.5	3.88	2.58E+05	3.49E+05	1.71E+49
DK_977	9.95	1.3	9.95	1.61	7.7	0.3	0.56	4.39	9.91E+05	1.34E+06	6.54E+49
DK_940	7.41	1.77	7.41	0.42	7.69	0.32	0.49	3.78	1.11E+06	1.50E+06	7.32E+49
DK_2735	13.93	4.22	4.22	0.07	11.45	0.22	0.39	3.02	9.69E+04	1.31E+05	6.40E+48
DK_2842	4.73	4.58	4.73	0.3	9.69	0.35	0.62	4.84	2.80E+05	3.77E+05	1.85E+49
DK_2856	8.3	2.69	8.3	1.33	7.07	0.25	0.36	2.82	1.59E+05	2.14E+05	1.05E+49
DK_2878	1.69	10.41	1.69	0.08	7.39	0.11	0.16	1.27	1.76E+02	2.38E+02	1.16E+46
DK_2956	4.24	6.07	4.24	0.23	9.9	0.22	0.28	2.16	3.09E+05	4.17E+05	2.04E+49
DK_2950	2.08	11.88	2.08	0.17	9.84	0.11	0.23	1.77	4.99E+04	6.73E+04	3.29E+48
DK_3046	5.21	6.97	5.21	0.41	10.41	0.25	0.5	3.91	1.74E+05	2.35E+05	1.15E+49
DK_3129	12.4	1.61	1.61	0.08	7.23	0.07	0.09	0.71	5.70E+04	7.70E+04	3.77E+48
DK_3442	1.93	16.86	1.93	0.52	10.13	0.22	0.34	2.65	1.46E+05	1.98E+05	9.67E+48
DK_3504	4.58	4.78	4.58	0.27	9.7	0.16	0.22	1.71	9.71E+04	1.31E+05	6.41E+48
DK_3521	1.77	16.59	1.77	0.63	9.91	0.22	0.37	4.31	1.11E+05	1.49E+05	1.82E+48
DK_3634	11.19	2.77	2.77	0.45	6.43	0.1	0.12	1.42	1.02E+04	1.37E+04	1.68E+47
DK_520	4.97	13.15	4.97	0.33	11.72	0.28	0.54	6.39	2.37E+05	3.20E+05	3.91E+48
DK_3738	9.5	1.5	9.5	0.35	9.3	0.25	0.29	2.26	1.61E+05	2.17E+05	1.06E+49
DK_420	13.7	1.47	1.47	0.47	9.61	0.1	0.16	1.25	9.83E+02	1.33E+03	6.49E+46
DK_405	10.92	2.44	2.44	0.36	6.75	0.06	0.1	0.75	1.16E+04	1.57E+04	7.67E+47
DK_4954	3.61	4.78	3.61	0.35	9.45	0.27	0.4	4.64	1.46E+05	1.97E+05	2.41E+48
DK_246	4.93	16.64	4.93	0.12	12.42	0.09	0.13	1.51	5.38E+04	7.26E+04	8.87E+47
DK_1335	5.36	17.17	5.36	0.56	12.78	0.16	0.3	3.57	1.00E+05	1.35E+05	1.66E+48
DK_195	16.7	4.95	4.95	0.19	12.45	0.15	0.19	1.51	8.08E+04	1.09E+05	5.33E+48
DK_186	20.87	6.9	6.9	0.11	14.71	0.18	0.3	3.53	1.90E+05	2.56E+05	3.13E+48
DK_976	10.62	2.3	2.3	0.42	6.91	0.07	0.14	1.1	2.10E+04	2.84E+04	1.39E+48
DK_2575	10.58	3.43	3.43	0.91	5.99	0.04	0.06	0.7	3.52E+02	4.75E+02	5.81E+45

DK_151	2.92	15.24	2.92	0.08	10.8	0.11	0.22	2.54	1.62E+05	2.18E+05	2.67E+48
DK_948	8.14	19.79	8.14	0.49	15.26	0.28	0.5	5.84	6.05E+05	8.17E+05	9.99E+48
DK_135	11.68	1.06	1.06	0.08	7.74	0.05	0.08	0.98	4.36E+04	5.89E+04	7.20E+47
DK_2855	8.85	3.03	8.85	2.02	6.74	0.27	0.39	3.01	7.16E+04	9.67E+04	4.73E+48
DK_b_808	1.29	15.17	1.29	0.62	7.51	0.07	0.09	0.7	5.94E+03	8.02E+03	3.92E+47
DK_73	8.73	20.52	8.73	0.01	15.86	0.23	0.34	2.67	5.15E+05	6.95E+05	3.40E+49
DK_67	10.37	2.3	2.3	0.27	6.96	0.06	0.1	1.18	2.76E+04	3.73E+04	4.56E+47
DK_5013	4.04	3.12	4.04	0.5	9.21	0.23	0.32	3.73	1.38E+05	1.86E+05	2.28E+48
DK_277	11.72	1.85	1.85	0.03	9.69	0.06	0.06	0.66	1.36E+04	1.83E+04	2.24E+47
DK_257	0.85	13.75	0.85	0.01	7.78	0.04	0.07	0.52	3.84E+03	5.18E+03	2.53E+47
DK_1991	3.55	13.04	3.55	0.1	10.89	0.12	0.16	1.21	7.95E+04	1.07E+05	5.25E+48
DK_228	10.38	3.16	3.16	0.44	6.29	0.11	0.21	1.61	4.78E+04	6.45E+04	3.15E+48
DK_2308	4.04	9.04	4.04	0.24	10.42	0.23	0.3	2.34	1.44E+05	1.94E+05	9.48E+48
DK_1125	2.06	11.97	2.06	0.01	9.84	0.06	0.07	0.56	1.06E+04	1.43E+04	7.01E+47
DK_175	3.32	10.08	3.32	0.21	6.24	0.06	0.07	0.56	6.83E+00	9.22E+00	4.51E+44
DK_170	11.82	2.13	2.13	0.32	6.86	0.03	0.05	0.55	2.39E+03	3.22E+03	3.94E+46
DK_158	13.51	3.16	3.16	0.09	10.72	0.1	0.17	1.29	1.12E+05	1.51E+05	7.36E+48
DK_3	19.58	8.92	8.92	0.05	15.72	0.12	0.16	1.21	4.43E+04	5.98E+04	2.92E+48
DK_137	2.07	9.39	2.07	0.23	7.28	0.08	0.16	1.27	5.88E+02	7.94E+02	3.88E+46
DK_133	19.22	2.63	2.63	0.17	11.07	0.15	0.23	1.79	2.48E+05	3.35E+05	1.64E+49
DK_126	5.54	2.81	5.54	0.59	7.53	0.12	0.24	2.84	1.17E+05	1.58E+05	1.93E+48
DK_b_277	10.77	3.75	3.75	1.4	5.65	0.07	0.11	0.89	2.73E+02	3.69E+02	1.80E+46
DK_3474	16.03	1.86	1.86	0.06	10.1	0.08	0.11	0.82	2.46E+04	3.32E+04	1.62E+48
DK_86	10.11	2.31	2.31	0.12	6.99	0.05	0.08	0.95	3.93E+04	5.30E+04	6.48E+47
DK_546	3.54	15.97	3.54	0.33	11.33	0.05	0.06	0.48	4.10E+03	5.54E+03	2.71E+47
DK_537	10.43	2.13	2.13	0.26	7.07	0.05	0.09	0.72	2.21E+04	2.98E+04	1.46E+48
DK_79	15.68	5.31	5.31	0.2	12.47	0.09	0.12	0.9	3.10E+04	4.18E+04	2.05E+48
DK_3901	3.07	14.16	3.07	0.33	10.74	0.19	0.2	1.17	9.14E+04	1.23E+05	1.36E+49
DK_b_526	1.47	15.71	1.47	0.54	7.2	0.17	0.25	2.96	3.94E+04	5.32E+04	6.50E+47
DK_1588	1.16	11.78	1.16	0.14	9.26	0.13	0.23	1.8	7.51E+04	1.01E+05	4.96E+48
DK_1544	9.76	2.8	9.76	0.26	6.7	0.73	1.2	9.32	2.61E+06	3.52E+06	1.72E+50
DK_1763	4.2	12.75	4.2	0.56	11.17	0.09	0.13	1	1.12E+04	1.52E+04	7.42E+47
DK_1833	8.29	2.75	8.29	0.59	7.03	0.22	0.33	3.82	3.83E+05	5.18E+05	6.33E+48
DK_1473	7.23	11.01	7.23	0.75	12.29	0.47	0.76	5.91	2.52E+05	3.40E+05	1.66E+49
DK_2115	3.2	9.29	3.2	0.23	10.09	0.08	0.11	1.31	2.35E+04	3.17E+04	3.88E+47
DK_1238	18.47	6.26	6.26	0.35	13.71	0.16	0.3	2.34	5.35E+04	7.22E+04	3.53E+48
DK_2141	5.83	3.88	5.83	0.33	7.04	0.41	0.82	6.37	1.00E+06	1.36E+06	6.63E+49
DK_2168	6.5	1.35	6.5	0.48	7.97	0.28	0.48	3.76	1.95E+06	2.64E+06	1.29E+50
DK_2190	11.28	2.46	2.46	0.47	6.67	0.1	0.17	1.34	2.08E+04	2.81E+04	1.37E+48
DK_2307	4.91	10	4.91	0.26	11.01	0.3	0.41	3.17	3.47E+05	4.68E+05	2.29E+49
DK_1115	9.97	1.11	9.97	1.73	7.82	0.83	1.53	11.93	4.45E+06	6.01E+06	2.94E+50
DK_1000	3.81	10.71	3.81	0.73	10.57	0.22	0.38	2.99	2.60E+04	3.52E+04	1.72E+48
DK_2533	9.76	4.14	9.76	1.58	5.65	0.26	0.47	3.65	4.41E+04	5.95E+04	2.91E+48
DK_2545	10.14	2.22	2.22	0.13	7.05	0.15	0.28	2.2	1.40E+05	1.89E+05	9.23E+48
DK_962	14.95	5.1	5.1	0.06	12.18	0.22	0.38	2.2	1.59E+05	2.15E+05	2.37E+49
DK_2606	11.94	1.77	1.77	0.11	7.15	0.06	0.09	0.66	4.31E+04	5.82E+04	2.85E+48
DK_14	10.39	4.17	4.17	0.18	5.38	0.07	0.13	0.99	3.91E+04	5.27E+04	2.58E+48
DK_12	20.4	10.83	10.83	0.19	17.12	0.19	0.33	2.57	1.00E+05	1.36E+05	6.63E+48
DK_2	21.01	10.74	10.74	0.06	17.26	0.14	0.23	1.82	1.22E+05	1.65E+05	8.08E+48
DK_2725	13.15	0.79	0.79	0.05	7.86	0.05	0.08	0.6	9.67E+03	1.31E+04	6.39E+47
DK_862	7.79	2.33	7.79	1.14	7.36	0.27	0.48	5.58	3.13E+05	4.22E+05	5.16E+48
DK_2885	2.31	13.83	2.31	0.18	10.2	0.18	0.36	2.77	8.28E+04	1.12E+05	5.47E+48
DK_3012	14.81	1.66	1.66	0.08	6.91	0.07	0.08	0.62	6.71E+04	9.06E+04	4.43E+48
DK_3117	5.68	6.38	5.68	0.5	10.4	0.45	0.65	3.77	3.94E+05	5.31E+05	5.85E+49
DK_3157	11.94	1.61	1.61	0.19	7.29	0.04	0.08	0.9	1.82E+04	2.46E+04	3.01E+47
DK_719	1.86	5.81	1.86	0.23	9.1	0.18	0.28	2.16	1.47E+05	1.99E+05	9.73E+48
DK_652	2.19	8.43	2.19	0.08	9.52	0.1	0.16	1.27	1.14E+05	1.54E+05	7.52E+48
DK_3330	12.05	1.05	1.05	0.15	7.72	0.05	0.08	0.61	1.57E+04	2.13E+04	1.04E+48
DK_3372	3.19	9.12	3.19	0.06	10.07	0.04	0.04	0.33	9.34E+03	1.26E+04	6.17E+47
DK_3460	10.73	3.76	3.76	0.07	5.65	0.2	0.3	2.3	2.27E+05	3.07E+05	1.50E+49
DK_3670	10.9	1.05	1.05	0.06	7.8	0.06	0.12	0.93	2.55E+04	3.45E+04	1.68E+48
DK_3718	2.91	14.98	2.91	0.4	10.72	0.08	0.11	1.34	1.39E+04	1.88E+04	2.30E+47
DK_3717	2.9	14.94	2.9	0.39	10.72	0.11	0.14	1.08	2.85E+04	3.85E+04	1.88E+48

DK_3766	11.08	1.33	1.33	0.1	7.58	0.06	0.13	1	3.55E+04	4.80E+04	2.35E+48
DK_4085	3.04	8.62	3.04	0.12	9.92	0.07	0.08	0.62	1.51E+04	2.03E+04	9.94E+47
DK_4467	12.78	1.09	1.09	0.09	7.64	0.1	0.21	2.47	7.33E+04	9.89E+04	1.21E+48
DK_4913	5.08	17.24	5.08	0.26	12.64	0.2	0.42	3.29	5.57E+05	7.53E+05	3.68E+49
DK_1610	2.15	15.69	2.15	0.2	10.28	0.14	0.22	1.68	6.46E+04	8.73E+04	4.27E+48
DK_1680	8.6	1.39	8.6	0.61	7.76	0.15	0.19	1.46	1.05E+05	1.42E+05	6.94E+48
DK_4939	6.64	2.98	6.64	0.68	9.59	0.2	0.29	2.25	1.47E+05	1.99E+05	9.71E+48
DK_1761	7.39	18.63	7.39	1.83	14.21	0.16	0.32	2.51	8.67E+03	1.17E+04	5.72E+47
DK_1523	8.94	1.37	8.94	1.27	7.75	0.35	0.47	5.49	4.47E+05	6.03E+05	7.38E+48
DK_265	10.66	3.13	3.13	0.26	6.24	0.15	0.27	2.13	3.43E+05	4.63E+05	2.26E+49
DK_260	9.42	4.93	9.42	1.32	5.08	0.29	0.53	4.16	4.54E+04	6.13E+04	3.00E+48
DK_5559	12.92	5.25	5.25	0.21	11.84	0.3	0.44	3.39	3.90E+05	5.26E+05	2.57E+49
DK_1305	1.07	12.55	1.07	0	7.67	0.07	0.12	0.91	2.08E+03	2.81E+03	1.38E+47
DK_1256	5.28	14.41	5.28	1.36	11.98	0.16	0.3	3.52	5.19E+03	7.01E+03	8.57E+46
DK_1231	3.93	9.49	3.93	0.74	10.4	0.09	0.15	1.81	8.73E+03	1.18E+04	1.44E+47
DK_1232	2.88	7.4	2.88	0.54	9.63	0.06	0.1	1.18	8.16E+03	1.10E+04	1.35E+47
DK_2171	7.62	5.18	7.62	0.1	10.57	1	1.31	10.18	6.50E+05	8.78E+05	4.29E+49
DK_207	17.09	5.04	5.04	0.1	12.59	0.15	0.24	1.88	1.45E+05	1.95E+05	9.54E+48
DK_2263	2.46	9.06	2.46	0.31	7.09	0.19	0.38	2.95	3.84E+02	5.18E+02	2.53E+46
DK_2283	18.45	7.35	7.35	0.22	14.42	0.29	0.45	3.5	2.16E+05	2.91E+05	1.43E+49
DK_2288	10.11	4.12	4.12	2.01	5.53	0.07	0.09	1.05	1.85E+02	2.50E+02	3.05E+45
DK_2297	8.64	22.87	8.64	0.01	16.42	0.26	0.41	3.23	8.05E+05	1.09E+06	5.31E+49
DK_1139	8.56	1.19	8.56	0.39	7.88	0.56	1.05	12.32	3.28E+06	4.42E+06	5.41E+49
DK_1135	2.49	7.95	2.49	0.24	7.26	0.16	0.25	1.95	1.81E+02	2.44E+02	1.19E+46
DK_179	20.57	10.94	10.94	0.99	17.24	0.24	0.38	4.48	1.67E+04	2.25E+04	2.76E+47
DK_171	8.06	1.87	8.06	1.06	7.56	0.11	0.14	1.09	3.50E+04	4.73E+04	2.31E+48
DK_1037	1.4	11.25	1.4	0.15	9.37	0.06	0.12	0.91	4.97E+04	6.71E+04	3.28E+48
DK_2458	5.66	8.8	5.66	0.26	4.75	0.22	0.3	2.31	8.11E+01	1.09E+02	5.35E+45
DK_2534	8.4	2.38	8.4	0.85	7.23	0.22	0.33	2.57	2.07E+05	2.79E+05	1.37E+49
DK_2537	4.64	9.8	4.64	0.28	10.84	0.24	0.39	3	1.93E+05	2.60E+05	1.27E+49
DK_2572	1.8	16.84	1.8	0.58	9.99	0.16	0.25	1.91	5.74E+04	7.76E+04	3.79E+48
DK_138	1.33	11.14	1.33	0.03	7.58	0.05	0.1	0.77	5.76E+02	7.77E+02	3.80E+46
DK_2778	6.72	3.03	6.72	0.63	7.2	0.56	0.62	7.24	5.31E+05	7.17E+05	8.77E+48
DK_860	9.35	2.76	9.35	1.86	6.81	0.33	0.65	5.08	3.27E+05	4.41E+05	2.16E+49
DK_2953	3.45	16.2	3.45	0.25	11.31	0.18	0.24	1.88	2.24E+05	3.02E+05	1.48E+49
DK_2974	2.57	8.06	2.57	0.55	7.24	0.17	0.26	2.01	1.50E+02	2.02E+02	9.89E+45
DK_783	5.31	8.92	5.31	0.28	10.93	0.12	0.14	1.63	2.07E+04	2.80E+04	3.42E+47
DK_2996	12.33	4	4	0.19	4.8	0.23	0.47	5.55	1.37E+05	1.85E+05	2.26E+48
DK_3035	1.53	12.43	1.53	0.28	9.52	0.14	0.23	1.83	4.53E+04	6.12E+04	2.99E+48
DK_3067	12.1	1.96	1.96	0.17	6.96	0.1	0.17	2.01	1.42E+05	1.92E+05	2.35E+48
DK_746	10.11	3.99	3.99	0.88	5.64	0.16	0.33	3.89	1.41E+04	1.91E+04	2.33E+47
DK_738	12.72	1.83	1.83	0.1	9.77	0.11	0.21	1.62	2.70E+04	3.64E+04	1.78E+48
DK_3137	19.91	7.92	7.92	0.6	15.17	0.52	0.97	11.41	2.23E+05	3.01E+05	3.68E+48
DK_3196	9.93	1.29	9.93	1.26	7.71	0.3	0.52	4.05	9.38E+05	1.27E+06	6.19E+49
DK_3205	12.14	2.95	2.95	0.14	6.04	0.1	0.13	1	6.36E+04	8.59E+04	4.20E+48
DK_687	24.86	10.53	10.53	0.74	18.28	0.18	0.23	2.7	1.24E+04	1.67E+04	2.05E+47
DK_96	1.66	15.41	1.66	0.16	9.88	0.04	0.06	0.45	9.34E+03	1.26E+04	6.16E+47
DK_95	9.26	23.82	9.26	1.94	16.84	0.2	0.4	3.14	3.01E+04	4.07E+04	1.99E+48
DK_3379	9.07	3.25	9.07	0.83	6.54	0.2	0.28	3.25	1.04E+05	1.41E+05	1.72E+48
DK_b_793	1.45	15.16	1.45	0.56	7.29	0.08	0.11	1.26	4.29E+03	5.80E+03	7.09E+46
DK_597	14.23	4.16	4.16	1.24	11.46	0.15	0.24	1.84	6.67E+02	9.01E+02	4.41E+46
DK_592	1.72	10.05	1.72	0.01	7.41	0.11	0.24	1.88	6.76E+02	9.12E+02	4.46E+46
DK_3593	6.02	17.55	6.02	0.78	13.27	0.26	0.29	2.25	1.28E+05	1.72E+05	8.42E+48
DK_569	10.38	2.48	2.48	0.48	6.82	0.07	0.12	0.93	1.42E+04	1.92E+04	9.39E+47
DK_3740	6.68	4.48	6.68	0.21	10.11	0.17	0.17	1.36	1.38E+05	1.86E+05	9.08E+48
DK_496	1.34	10.67	1.34	0.04	7.61	0.05	0.08	0.64	4.17E+02	5.64E+02	2.76E+46
DK_3866	2.54	8.91	2.54	0.25	9.73	0.26	0.44	3.39	1.61E+05	2.18E+05	1.07E+49
DK_3907	5.91	17.88	5.91	0.23	13.33	0.34	0.44	3.41	1.00E+06	1.36E+06	6.63E+49
DK_416	10.5	3.69	3.69	0.79	5.79	0.08	0.16	1.25	3.90E+03	5.26E+03	2.57E+47
DK_4218	14.22	1.42	1.42	0.08	7.21	0.08	0.1	0.78	7.54E+04	1.02E+05	4.98E+48
DK_58	7.72	2.71	7.72	0.33	7.17	0.1	0.13	1.58	8.00E+04	1.08E+05	1.32E+48
DK_57	11.09	1.93	1.93	0.06	7.13	0.05	0.05	0.59	2.01E+04	2.71E+04	3.31E+47
DK_353	2.51	7.87	2.51	0.25	7.26	0.11	0.22	1.71	3.50E+02	4.73E+02	2.31E+46

DK_335	7	6.5	7	1.63	5.17	0.15	0.28	2.14	1.97E+03	2.66E+03	1.30E+47
DK_4766	5.39	11.11	5.39	0.72	3.66	0.71	1.1	12.87	1.04E+02	1.41E+02	1.72E+45
DK_4776	12.81	1.27	1.27	0.11	7.49	0.08	0.12	0.95	2.97E+04	4.01E+04	1.96E+48
DK_4796	1.28	9.39	1.28	0.04	9.18	0.16	0.23	2.71	7.98E+04	1.08E+05	1.32E+48
DK_319	7.14	1.82	7.14	0.75	7.7	0.28	0.59	4.62	1.48E+06	1.99E+06	9.75E+49
DK_304	1.1	13.08	1.1	0.07	7.61	0.05	0.09	0.68	1.42E+03	1.92E+03	9.40E+46
DK_5044	11.39	4.03	4.03	0.19	5.14	0.16	0.23	2.68	2.21E+05	2.99E+05	3.65E+48
DK_5315	7.25	6.51	7.25	1.72	10.93	0.19	0.32	2.46	1.35E+04	1.83E+04	8.92E+47
DK_262	15.69	1.12	1.12	0.04	9.48	0.04	0.07	0.57	8.02E+03	1.08E+04	5.29E+47
DK_5460	4.81	23.03	4.81	2.3	12.75	0.98	1.54	18.06	1.02E+06	1.37E+06	1.68E+49
DK_203	8.79	2.98	8.79	0.45	6.79	0.35	0.69	5.38	2.20E+06	2.97E+06	1.45E+50
DK_180	17.31	7.66	7.66	0.25	14.31	0.17	0.2	2.35	2.23E+04	3.01E+04	3.68E+47
DK_178	5.34	6.43	5.34	0.15	10.32	0.12	0.14	1.09	6.02E+04	8.12E+04	3.97E+48
DK_19	21.65	10.42	10.42	0.2	17.26	0.18	0.23	1.77	1.30E+05	1.76E+05	8.60E+48
DK_22	17.26	3.12	3.12	0.07	11.23	0.05	0.07	0.53	2.54E+04	3.43E+04	1.68E+48
DK_159	9.94	4.24	9.94	1.54	5.49	0.26	0.48	5.6	4.56E+04	6.15E+04	7.52E+47
DK_157	8.08	22.04	8.08	0.32	15.81	0.25	0.46	3.57	9.20E+05	1.24E+06	6.07E+49
DK_143	9.76	23.54	9.76	0.09	17.38	0.3	0.47	3.65	3.96E+05	5.35E+05	2.62E+49
DK_118	6.32	22.87	6.32	0.94	14.61	0.28	0.41	3.22	4.02E+05	5.42E+05	2.65E+49
DK_88	10.8	24.97	10.8	0.72	18.46	0.19	0.28	2.2	1.02E+05	1.37E+05	6.70E+48
DK_84	7	21.38	7	0.24	14.89	0.15	0.31	2.38	6.10E+05	8.24E+05	4.03E+49
DK_80	11.28	24.72	11.28	0.33	18.73	0.34	0.69	5.36	3.14E+05	4.24E+05	2.07E+49
DK_77	4.38	11.96	4.38	0.25	4.48	0.13	0.21	2.47	2.40E+01	3.24E+01	3.96E+44
DK_40	13.85	4.08	4.08	0.1	11.35	0.09	0.14	1.67	7.67E+04	1.04E+05	1.27E+48
DK_39	13.67	4.08	4.08	0.08	11.32	0.09	0.14	0.83	8.30E+04	1.12E+05	1.23E+49
DK_32	7.41	21.68	7.41	0.19	15.25	0.1	0.16	1.26	1.01E+05	1.36E+05	6.66E+48
DK_24	22.69	9.91	9.91	0.06	17.24	0.13	0.22	2.54	6.71E+04	9.06E+04	1.11E+48
DK_20	17.33	5.1	5.1	0.11	12.68	0.09	0.11	1.31	3.49E+04	4.71E+04	5.76E+47
DK_18	15.01	2.41	2.41	0.07	10.42	0.05	0.06	0.74	1.43E+04	1.93E+04	2.35E+47

Table A.0.20: Physical parameters of 682 objects of the shell catalog of table 5.1. These are the remaining shells where a kinematic distance estimation is applicable. Column 1 contains the name of the shell, column 2 and 3 contain the two distance solutions of the tangential point method $D_{\mathrm{s,a}}$ and $D_{\mathrm{s,b}}$. Column 4 lists the derived final value for the distance, which is either one of the values of $D_{\mathrm{s,a}}$ or $D_{\mathrm{s,b}}$ or their mean value, depending on the observed direction. Columns 5 and 6 list the z-distance of the object to the galactic plane z, and the distance of the shell towards the galactic center D_{gc}, both also derived by this method. The calculated minimum- and maximum radius R_{min} and R_{max}, using $D_{\mathrm{s,a}}$ or $D_{\mathrm{s,b}}$ are listed in columns 7 and 8. Columns 9, 10 and 11 contain the calculated age τ, the hydrogen mass $M_{\mathrm{H\,I}}$ and the total mass M_{tot} of the shell. Finally, column 12 contains the derived kinetic energy E_{kin} of the shells. For more information about the derivation of the parameters see text.

1	2	3	4	5	6	7	8
shellname	Δl_0	Δb_0	Δr_{min}	Δr_{mean}	Δr_{max}	Δv_0	Δv_{exp}
DK_1476	2.08	0.67	1	2.83	4	0.74	0.53
DK_2046	1.25	0.27	1.19	1.58	2.5	2.58	2.83
DK_1303	1.17	0.33	0.5	1.25	0.25	3.54	2.83
DK_1286	1.25	1.08	1.31	1	2	2.58	2.58
DK_b_356	2.08	0.27	0.5	1.5	2.75	0.74	0.53
DK_1187	0.75	0.67	0.5	1.5	1.75	2.9	2.32
DK_1188	0.58	0.33	0.25	0.92	1.75	2.58	2.06
DK_1119	0.42	0.75	0.5	0.67	0.5	0.97	0.77
DK_857	0.92	0.27	1.19	1.42	0.25	2.9	2.32
DK_810	0.83	0.58	0.25	1.08	0.75	2.58	2.06
DK_3462	0.42	0.27	0.94	1.08	1.75	2.25	1.8
DK_457	1.08	1	1.25	2.42	1.75	3.22	2.58
DK_1619	0.58	0.27	0.87	1.42	1.81	4.19	3.35
DK_1701	1.25	0.33	1	1.67	3.25	1.61	1.29
DK_1452	0.42	0.27	0.75	0.5	1.25	1.29	1.03
DK_1117	0.75	0.42	1.69	1.33	2.87	3.54	2.83
DK_960	0.5	1.17	1.25	0.92	2	0.97	0.77
DK_3275	0.33	0.67	0.87	0.92	1.37	1.29	1.03

DK_3296	0.75	0.58	0.25	1.67	2.62	0.74	1.8
DK_3295	0.83	0.42	0.25	1.67	2.62	1.29	1.55
DK_3297	0.27	1.08	1.37	1.58	2.56	0.74	2.06
DK_b_802	0.27	0.58	0.25	0.17	0.25	0.74	0.77
DK_3639	0.67	0.27	0.25	0.92	0.75	2.58	2.06
DK_b_823	0.42	0.5	0.62	0.25	1.19	1.61	1.29
DK_b_222	0.27	0.33	0.44	0.46	0.56	0.74	1.29
DK_1580	1.25	0.27	1.56	0.83	1.25	2.58	2.06
DK_301	0.27	0.27	0.75	0.42	0.75	1.29	1.03
DK_1527	1.67	1	0.5	0.58	1	1.61	1.29
DK_1760	0.33	0.27	0.5	0.67	1.25	1.29	1.03
DK_5129	0.75	0.5	1.37	0.67	0.75	1.93	2.32
DK_1483	0.27	1	0.25	0.75	0.5	0.97	0.77
DK_1828	1.08	0.27	0.75	1.42	2	0.97	0.77
DK_1965	0.27	1.17	0.44	0.5	0.75	1.93	1.55
DK_1281	0.33	0.92	0.25	0.17	0.25	0.74	0.53
DK_184	0.83	0.83	0.75	1.33	2.75	0.97	0.77
DK_165	0.58	0.27	0.25	0.92	0.25	1.93	1.55
DK_928	1.08	0.67	0.25	2	2.5	2.58	2.06
DK_2819	0.75	0.27	1.44	0.58	1.87	6.12	4.9
DK_2820	0.67	0.67	0.25	1	1.5	1.61	1.29
DK_2873	0.33	0.27	0.25	0.33	0.25	1.61	1.29
DK_3145	0.5	0.27	0.25	0.92	1.25	1.29	1.03
DK_104	0.5	0.27	1.25	0.75	0.75	1.93	1.55
DK_3277	0.92	0.92	1.19	1.42	3.25	2.25	1.8
DK_635	1.33	0.27	0.75	1.33	3.25	1.93	1.55
DK_3576	0.33	0.27	0.69	0.58	0.25	3.22	3.86
DK_4220	0.58	0.27	0.81	0.5	1	1.93	1.55
DK_1514	0.42	0.42	0.75	1	0.25	3.86	3.09
DK_1785	0.27	0.58	0.69	0.5	1.06	0.97	0.77
DK_1784	0.58	0.27	0.87	0.58	0.75	2.25	1.8
DK_1783	0.83	0.27	1	1.25	2.5	1.93	1.55
DK_5209	0.58	0.5	1.75	0.83	2.12	0.74	0.53
DK_1846	0.92	0.33	0.5	1.25	2.75	3.86	3.09
DK_5238	0.83	0.92	1.25	0.83	1	0.74	0.53
DK_1389	1.17	0.27	1.25	1.75	2.5	1.61	1.29
DK_b_634	1.17	0.58	0.25	0.92	0.25	0.97	0.77
DK_2009	0.58	0.58	0.75	1.25	1	0.97	0.77
DK_241	0.92	0.27	0.25	1.92	0.25	0.97	0.77
DK_1299	1	0.67	0.5	1	1.25	0.97	0.77
DK_232	0.27	0.33	0.75	0.75	0.5	1.29	1.03
DK_1267	0.5	0.42	0.25	1.25	0.25	0.74	0.53
DK_b_360	1.58	0.27	2.81	1.25	0.5	0.97	0.77
DK_1221	1.33	0.27	0.75	1.42	4	3.22	2.58
DK_1050	0.92	1	1.25	1.75	1.75	3.86	3.86
DK_930	0.67	0.58	0.25	1.08	1.56	1.29	1.03
DK_136	0.42	0.27	0.5	1	1.25	1.61	1.29
DK_120	0.58	1	0.75	1.33	1	2.25	1.8
DK_757	0.75	0.83	1.06	0.83	1.62	1.29	1.03
DK_756	0.92	0.33	1.12	1.25	1	3.22	2.58
DK_723	1.25	0.27	1.5	2.25	1.25	3.22	2.58
DK_659	0.33	1.25	1.87	0.83	1.5	0.74	0.53
DK_b_785	0.5	1	1.12	0.58	1.75	1.93	2.06
DK_656	1.08	0.27	0.75	1.92	1.5	2.58	3.35
DK_3575	0.42	0.33	0.25	0.67	0.75	1.61	1.29
DK_3584	0.92	0.27	1.25	0.42	0.25	1.93	1.55
DK_562	1.25	0.83	1.25	1.83	3	3.86	3.09
DK_3668	0.5	0.27	2	0.92	0.25	1.93	1.55
DK_456	0.27	0.42	0.25	0.42	0.5	0.97	0.77
DK_4380	0.58	0.33	1.87	0.58	2.5	2.9	2.32
DK_4593	0.83	0.27	0.25	0.67	1.5	1.93	1.55
DK_4719	2	0.67	0.25	2.42	0.5	2.9	2.32
DK_338	0.75	0.27	1	0.75	1.75	2.58	2.06

DK_b_540	0.58	0.92	2.12	2.08	0.25	0.97	0.77
DK_1668	0.75	1.83	0.5	1.75	2	1.61	1.29
DK_1601	0.42	0.27	0.25	1.17	1.25	0.97	0.77
DK_1555	0.42	0.42	0.56	0.42	0.5	0.74	0.77
DK_1528	1.67	0.67	0.5	0.58	2.31	0.97	0.77
DK_294	0.5	0.27	1	0.92	0.5	0.74	0.53
DK_1861	0.58	0.75	1.25	1.58	0.25	0.97	0.77
DK_1906	0.33	0.75	0.25	0.42	0.25	0.97	0.77
DK_1400	0.5	1.17	0.81	0.5	0.25	1.61	1.29
DK_1958	1	0.83	1.69	2.17	3.12	0.74	1.55
DK_5458	0.83	0.5	2.5	1.25	0.25	3.22	2.58
DK_1983	0.83	0.92	1.25	1.25	0.25	1.29	1.03
DK_1993	0.42	0.27	0.5	0.58	1	0.97	0.77
DK_1331	0.75	0.42	0.5	1.25	0.75	1.29	1.03
DK_2034	1.25	0.33	0.25	2.08	0.25	1.29	1.03
DK_209	0.42	0.27	0.5	1.33	0.75	1.61	1.29
DK_b_34	1.92	0.33	7	3.75	7.25	0.97	0.77
DK_2320	1.5	0.27	0.5	2.5	1.25	0.97	0.77
DK_2335	0.92	0.33	1.5	1.17	0.5	2.5	2.06
DK_2351	0.42	0.92	0.5	0.67	1.25	0.74	0.53
DK_2389	0.42	0.83	0.25	0.92	2	0.97	0.77
DK_1068	0.67	0.27	3.25	1.5	2	1.61	1.29
DK_2496	0.67	0.27	0.87	0.33	0.75	0.74	0.53
DK_2513	0.75	0.92	0.75	1	0.5	0.97	0.77
DK_1011	0.92	1.25	0.25	1.33	2.75	2.9	2.32
DK_1003	0.67	0.27	0.94	1.42	0.25	0.74	1.03
DK_985	0.75	0.42	1	0.92	0.5	0.97	0.77
DK_2595	1.42	0.27	0.75	1.83	2	0.97	0.77
DK_2598	0.83	0.27	1.19	0.42	0.25	2.9	2.32
DK_2663	0.67	0.92	0.5	1	1.5	2.58	2.06
DK_919	1.33	0.92	2	2.33	3.25	1.61	1.29
DK_2740	0.42	0.27	0.25	0.58	0.75	0.74	0.53
DK_2779	1.5	0.27	0.25	2.67	3.25	1.29	1.03
DK_798	1	0.27	2.5	1.25	2	3.54	2.83
DK_3004	1.08	0.58	1.44	0.83	1.75	2.25	1.8
DK_3099	1.08	0.27	0.5	1.17	1.25	2.58	2.06
DK_737	0.5	0.27	1	0.67	1	0.74	0.53
DK_3187	1.25	0.27	1.31	1.5	1.5	1.93	1.55
DK_609	0.42	1.25	0.25	0.58	0.25	1.29	1.03
DK_3489	0.27	0.5	0.25	0.5	1	1.29	1.03
DK_3722	0.5	0.27	1	0.67	1	0.97	0.77
DK_3745	0.83	0.58	0.81	1.08	0.25	1.93	1.55
DK_3833	0.33	0.27	0.75	0.75	1	1.29	1.03
DK_3894	0.33	0.27	0.25	0.58	0.25	1.93	1.55
DK_4385	0.42	0.27	0.25	0.5	1	0.97	0.77
DK_4456	0.27	0.75	0.5	0.42	0.81	1.93	1.8
DK_4735	0.83	0.27	1.5	0.92	0.5	6.44	5.15
DK_1620	0.83	0.67	2	1.25	0.5	0.97	0.77
DK_b_47	0.83	0.67	2	1.25	0.5	0.97	0.77
DK_1602	0.27	0.67	0.25	0.58	0.5	0.74	0.53
DK_b_528	1.5	0.27	0.25	2.25	1.25	0.97	0.77
DK_b_513	1.67	0.27	3.06	0.33	3.44	1.29	1.03
DK_b_516	2	0.27	0.25	1.58	0.25	0.74	0.53
DK_306	1.42	0.58	0.75	1.42	2.25	0.97	0.77
DK_307	0.5	0.27	1.31	0.5	1.69	1.29	1.03
DK_b_489	1.83	0.42	0.25	1.58	1.5	0.74	0.53
DK_b_486	2	0.58	0.75	1.67	1.25	0.97	0.77
DK_5049	1	0.67	0.5	1	0.5	0.97	0.77
DK_1750	1.33	0.27	1	1.92	3.25	1.29	1.03
DK_1771	0.27	0.42	0.5	0.33	0.5	1.61	1.29
DK_1792	0.67	0.33	0.5	1.58	1.5	1.29	1.03
DK_1802	0.67	1.17	0.5	1.42	3.25	1.61	1.29
DK_5194	0.58	0.83	0.94	0.92	0.25	1.93	1.55

DK_5193	0.58	0.42	0.25	1	0.25	1.93	1.55
DK_5192	0.67	0.42	0.25	1.17	0.5	2.9	2.32
DK_b_451	1.17	0.67	0.25	0.17	0.25	0.97	0.77
DK_1857	0.58	0.27	2.25	1.33	0.75	0.97	0.77
DK_b_449	2.25	1.42	0.5	3.83	3.25	2.9	2.32
DK_b_43	0.67	0.27	0.25	1.25	0.25	0.74	0.53
DK_b_42	0.58	0.33	0.25	1.17	0.25	0.74	0.53
DK_b_46	1.58	0.67	1.75	2.42	1.5	1.29	1.03
DK_1879	0.83	0.92	1.25	1.17	1.75	3.22	2.58
DK_b_616	0.27	0.27	1.25	0.25	1.81	2.5	2.83
DK_1387	0.75	0.33	1.06	1.25	0.5	0.74	1.03
DK_1383	2.33	0.27	2.5	3.83	4.25	2.58	2.06
DK_5417	0.27	0.27	0.87	0.5	0.5	1.29	2.32
DK_1365	0.75	0.75	1.37	0.75	0.5	3.22	2.58
DK_1321	1.83	0.83	2	1.58	3.25	1.29	1.03
DK_244	1	0.33	0.75	1.67	2	2.9	2.32
DK_5563	0.27	0.92	0.56	0.25	0.81	1.93	1.55
DK_b_380	1.58	0.27	3.06	0.33	0.75	0.74	0.53
DK_1304	0.58	0.27	1.06	1.17	1.5	0.97	0.77
DK_5707	0.75	0.58	1.5	1.25	2	1.29	1.03
DK_224	0.67	1.25	1	1.17	0.75	0.97	0.77
DK_b_665	0.27	0.92	0.44	0.33	0.69	0.74	1.29
DK_1215	0.92	0.27	1	2.42	3	1.93	1.55
DK_1146	0.67	0.27	1.25	1.33	0.5	0.74	0.53
DK_182	0.27	1.67	0.75	1.58	1.75	0.97	0.77
DK_2418	1.75	0.27	0.25	1.83	0.75	0.97	0.77
DK_1055	0.75	0.27	0.25	1.25	0.25	3.22	2.58
DK_1049	1.33	0.58	1.5	1.42	3.75	2.9	2.32
DK_2424	1.17	0.67	1.5	0.42	0.25	1.93	1.55
DK_b_712	0.33	0.58	0.25	0.5	0.25	0.97	0.77
DK_2436	0.67	0.27	0.5	0.75	0.75	0.74	0.53
DK_b_26	2.75	0.27	0.75	3	3	1.61	1.29
DK_b_338	0.27	0.33	1	0.5	1.31	0.97	0.77
DK_1014	1.58	0.27	0.75	1.75	3.75	1.93	1.55
DK_1007	0.83	0.75	0.75	1.17	1	3.22	2.58
DK_2524	0.42	0.27	0.5	0.75	1.25	0.97	0.77
DK_973	0.83	0.27	0.5	1.5	1.25	3.54	2.83
DK_2638	0.33	0.27	0.25	1	0.75	1.61	1.29
DK_148	0.27	0.27	0.25	0.67	1.5	0.74	0.53
DK_146	0.27	0.27	0.25	0.08	0.31	0.97	0.77
DK_937	0.58	0.27	0.25	1.17	2	0.97	0.77
DK_b_741	1.5	0.27	1.62	1	1.5	0.97	0.77
DK_2714	0.83	0.33	1.25	1.17	1.5	0.97	0.77
DK_2738	0.58	0.67	0.75	1.08	0.75	3.54	2.83
DK_2798	0.67	0.67	0.81	0.58	0.25	1.93	1.8
DK_2804	1.33	0.42	2.5	2.08	2.75	1.29	1.03
DK_129	0.42	0.75	0.75	0.75	0.75	0.97	0.77
DK_114	0.83	0.27	0.5	1.92	2.25	0.97	0.77
DK_3122	1.42	1.58	0.25	1.42	0.5	1.93	1.55
DK_713	1.17	1	0.5	1.75	1.5	1.93	1.55
DK_714	1.08	0.27	0.25	1.5	0.75	2.25	1.8
DK_712	1.25	0.27	2	2.08	1.75	1.61	1.29
DK_3274	0.42	0.27	0.94	1.17	1.75	1.61	1.29
DK_3338	0.67	0.67	1.19	0.83	0.25	1.61	1.29
DK_3336	1.08	0.58	0.25	0.92	1.25	1.29	1.03
DK_3331	0.67	0.5	1.06	0.58	0.75	0.74	1.55
DK_b_230	0.27	0.42	0.5	0.17	0.81	0.74	0.77
DK_b_303	1.33	0.27	0.25	1.83	1.25	0.97	0.77
DK_3551	0.83	0.67	1.19	1.33	1	2.58	2.06
DK_3574	0.58	0.27	1	0.92	1.25	2.25	1.8
DK_3609	0.33	0.75	0.75	0.83	0.75	1.93	1.8
DK_535	0.5	0.92	0.5	1	1	1.29	1.03
DK_530	1.25	0.33	0.25	2.5	6	1.93	1.55

DK_3756	0.42	0.67	1.06	0.58	1	2.25	1.8
DK_b_818	0.27	0.58	0.75	0.25	1.19	1.29	1.03
DK_3804	0.33	0.27	1	0.58	0.75	1.29	1.03
DK_3900	0.67	0.92	0.94	0.75	1.37	1.29	1.03
DK_466	0.5	0.27	0.75	0.75	0.75	0.97	0.77
DK_70	0.27	0.33	0.5	0.25	0.5	1.29	1.03
DK_4223	0.67	0.67	1.62	0.58	0.25	2.58	2.06
DK_4236	1.17	0.5	1.37	0.83	1.75	2.58	3.35
DK_4318	0.58	1.08	1.19	1	2.12	3.22	2.58
DK_4341	0.42	0.27	0.25	1	0.75	0.74	0.53
DK_4424	0.27	0.5	0.25	0.17	0.25	1.29	1.03
DK_b_300	1.33	0.75	1	2.5	1.5	0.97	0.77
DK_364	0.83	1	1.12	1.17	0.5	1.93	1.55
DK_4548	0.67	0.5	0.25	1.17	1.75	1.93	1.55
DK_48	0.33	0.67	1	0.67	1	0.97	0.77
DK_b_851	0.27	1.33	0.69	0.33	0.87	0.97	0.77
DK_343	1	0.75	0.25	1.33	1.75	0.97	0.77
DK_4802	1	0.5	0.25	0.58	0.25	2.9	2.32
DK_4814	0.75	0.27	1	0.58	0.5	0.97	0.77
DK_1640	0.83	0.27	0.25	2.5	4.5	1.29	1.03
DK_1598	1.42	0.27	0.25	1.83	1.25	1.61	1.29
DK_b_210	0.42	0.27	0.75	0.5	1.25	0.74	0.53
DK_1745	1	0.33	1	2.42	1.25	5.47	4.38
DK_1777	1.17	0.27	0.25	2.67	1	1.93	1.55
DK_5195	0.42	0.75	0.87	0.42	0.25	0.97	0.77
DK_5190	0.27	0.5	0.56	0.25	0.94	2.5	2.06
DK_1465	0.75	1	1.5	1.17	1.75	4.19	3.35
DK_275	0.5	0.5	0.5	0.58	0.75	0.97	0.77
DK_1436	1.17	0.67	1.75	2.25	4.25	1.29	1.03
DK_5303	0.33	0.5	1.06	0.83	1.56	3.54	2.83
DK_1417	0.42	0.27	1.5	0.75	1.5	1.29	1.03
DK_5354	0.33	1.58	0.75	0.25	0.81	0.74	0.53
DK_5376	0.67	0.27	0.87	1.25	1.75	3.86	3.09
DK_234	0.75	0.67	1.75	1.33	1.75	0.97	0.77
DK_225	0.58	0.27	0.25	0.5	1	1.29	1.03
DK_2128	1.08	0.27	1	2.33	3	4.83	3.86
DK_222	0.42	0.33	1	0.75	1.5	1.61	1.29
DK_2174	0.27	0.5	0.44	0.25	0.25	1.29	1.03
DK_206	0.92	1.33	0.25	1.67	3.25	0.97	0.77
DK_185	0.5	0.42	0.25	0.92	0.25	1.61	1.29
DK_2394	0.75	0.58	0.25	0.75	1.25	0.97	0.77
DK_1052	0.83	0.33	1.31	0.75	1.25	0.74	0.53
DK_2453	0.33	0.27	0.25	0.58	0.5	1.93	1.55
DK_168	0.67	0.27	0.25	1.25	1	0.74	1.03
DK_b_923	0.5	0.27	1	0.92	0.5	5.15	4.12
DK_1013	0.42	0.92	0.5	0.5	0.25	0.97	0.77
DK_994	0.92	0.33	0.25	1.33	2.75	1.93	1.55
DK_2639	0.75	0.83	0.25	0.5	1.44	1.93	1.55
DK_13	0.27	0.27	0.25	0.08	0.25	0.97	0.77
DK_2700	0.27	0.33	0.56	0.33	0.25	0.74	0.77
DK_2760	0.33	0.27	0.62	0.58	0.25	0.74	0.77
DK_130	0.75	0.92	0.75	0.75	0.25	1.61	1.29
DK_816	0.75	0.58	0.75	1.42	3	2.9	2.32
DK_119	0.58	0.27	0.25	0.92	0.75	0.97	0.77
DK_797	1	0.27	2.25	1.33	3.75	1.61	1.29
DK_765	1.42	0.42	0.25	1.17	2.31	0.97	0.77
DK_698	0.33	0.27	0.25	0.5	0.5	0.97	0.77
DK_3450	0.58	0.27	0.25	0.67	1.37	1.29	1.03
DK_92	0.33	0.83	0.87	0.83	0.75	0.97	0.77
DK_616	0.75	2.5	1.75	2.25	4.25	2.58	2.06
DK_89	0.5	0.33	1.75	1	2	0.97	0.77
DK_3583	0.92	0.58	1.44	0.33	0.25	0.74	0.77
DK_3666	0.58	0.33	0.94	0.92	1.25	1.29	1.03

DK_3735	0.27	0.33	0.25	0.42	0.75	0.97	0.77
DK_3757	0.5	0.42	0.25	0.58	0.5	1.61	1.29
DK_3831	0.5	1.75	0.25	0.75	1.25	0.97	0.77
DK_72	0.27	0.27	0.25	0.25	0.5	0.74	0.53
DK_3972	1.17	0.27	4.75	2.25	0.5	3.22	2.58
DK_69	0.27	0.5	0.5	0.5	1	1.29	1.03
DK_4113	0.67	0.27	0.25	1.25	2.75	3.54	2.83
DK_4128	1	0.67	0.75	1.08	1.5	6.76	5.41
DK_4179	0.5	0.67	0.25	0.25	0.5	1.29	1.03
DK_4307	0.33	0.27	0.25	0.5	0.25	0.97	0.77
DK_4336	0.5	0.5	1.12	0.42	0.5	2.58	2.83
DK_4648	0.92	0.27	0.94	1.33	1.69	1.93	1.55
DK_b_102	0.27	0.27	0.31	0.37	0.37	0.74	0.77
DK_1622	0.83	0.58	0.25	0.83	1.5	1.61	1.29
DK_1611	1	1.33	1	1.25	2.25	0.74	0.53
DK_1673	0.5	0.27	0.25	1.25	0.75	2.25	1.8
DK_1672	0.83	0.42	0.5	1.75	0.75	0.74	0.53
DK_1600	0.83	0.42	1.25	0.67	0.5	0.97	0.77
DK_4995	0.58	0.67	1.06	0.5	1.56	2.5	2.32
DK_1779	1	0.42	1.75	1.42	0.25	0.74	0.77
DK_1489	1	1.5	0.5	0.83	0.5	1.29	1.03
DK_1813	0.75	0.42	0.5	1.83	0.5	0.97	0.77
DK_1474	0.92	0.27	0.94	1.5	3	0.97	0.77
DK_1462	0.42	0.67	0.25	0.58	0.5	0.97	0.77
DK_1455	0.5	0.27	1.06	0.33	1.31	1.93	2.58
DK_b_92	0.33	0.27	0.25	0.83	0.75	1.29	1.03
DK_b_91	0.27	0.27	0.25	0.42	0.25	0.97	0.77
DK_b_617	0.27	0.75	1.37	0.58	1.81	0.74	1.29
DK_1420	1.42	0.83	0.25	1.92	3.25	1.61	1.29
DK_1912	0.33	0.42	0.25	0.5	1.56	0.97	0.77
DK_5349	0.33	0.27	0.75	0.5	0.5	0.97	0.77
DK_1401	0.83	0.27	1.25	1.25	2.25	1.93	1.55
DK_1940	0.27	0.83	0.25	0.25	0.25	0.74	0.53
DK_1395	0.92	0.33	0.25	1.33	2.75	0.74	0.53
DK_1399	0.92	1.08	1.75	1.25	2.5	0.97	0.77
DK_1943	0.67	0.27	1.5	0.92	1	1.29	1.03
DK_28	0.27	1.33	0.31	0.17	0.25	1.29	1.03
DK_5645	0.75	0.27	0.81	0.58	1.37	0.74	0.77
DK_b_83	0.58	0.27	0.5	1.08	2	0.74	0.53
DK_5709	0.5	0.27	0.5	1	2	1.29	1.03
DK_2152	1.42	0.27	0.25	2.75	5.75	0.74	0.53
DK_1219	0.42	0.67	0.5	0.42	1	0.74	0.53
DK_2266	0.5	0.27	0.25	0.5	0.75	1.29	1.03
DK_1128	0.58	0.27	1.06	1.83	2.06	0.97	0.77
DK_1095	1.75	0.27	0.75	2.42	4.5	0.97	0.77
DK_1091	1.25	0.27	0.5	2.17	5	0.74	0.53
DK_1031	0.58	0.42	1.5	1.33	2.5	0.74	0.53
DK_b_722	0.42	0.27	0.25	0.83	1	0.74	0.53
DK_2526	0.27	0.42	0.25	0.5	0.5	0.74	0.53
DK_2542	0.75	0.5	1.37	1.25	1.25	3.22	2.58
DK_2544	0.42	0.27	0.81	0.83	0.25	0.74	1.29
DK_983	1	0.27	1.25	1.08	2.25	0.97	0.77
DK_b_735	0.27	0.67	1.12	0.17	1.31	0.74	0.53
DK_927	1.08	0.27	1.37	0.67	1.25	1.61	1.29
DK_2676	1.17	0.27	0.25	1.33	2	0.97	0.77
DK_863	1	0.42	1.81	1.25	0.25	1.61	1.29
DK_855	0.42	0.83	1	1.17	0.5	0.97	0.77
DK_836	1.83	1	2.5	2.92	5	1.29	1.03
DK_2871	0.27	0.42	0.62	0.08	0.69	0.97	0.77
DK_790	1.92	0.27	1.5	2.17	6	0.74	0.53
DK_788	1.5	0.27	0.5	1.17	1.75	1.29	1.03
DK_710	0.58	0.27	0.5	1.25	0.5	0.74	0.53
DK_709	0.75	0.27	1.75	1.33	0.5	0.97	0.77

DK_693	1.17	0.27	1.5	2.83	3.75	0.97	0.77
DK_634	0.42	0.27	0.25	0.67	1.5	1.61	1.29
DK_618	1.33	2.25	0.75	1.5	1	2.25	1.8
DK_3471	1.33	0.58	0.25	2.42	0.75	0.97	0.77
DK_606	1.08	0.67	1	1.33	1.5	2.25	1.8
DK_3496	0.67	1.83	0.25	1	1.5	1.61	1.29
DK_3507	0.67	0.5	1.81	0.75	1	0.97	0.77
DK_3577	0.5	0.5	0.69	0.92	0.25	0.97	0.77
DK_576	0.27	1.08	0.44	0.67	0.25	0.97	0.77
DK_3761	2	0.27	1.25	3.5	4.75	0.97	0.77
DK_502	0.5	0.27	1	0.83	1	0.97	0.77
DK_437	0.27	0.27	0.44	0.33	0.5	1.29	1.03
DK_62	0.27	1.58	0.44	0.17	0.5	0.74	0.53
DK_388	1	0.42	0.5	1.42	1.75	1.61	1.29
DK_367	1.33	0.83	1.56	2	5.75	1.93	1.55
DK_4647	1	0.27	0.94	1.42	0.5	1.61	1.29
DK_1658	1.25	0.58	1.25	2.25	1.25	3.86	3.09
DK_1597	0.92	1.33	1.69	0.83	1.25	0.97	0.77
DK_1685	1.58	0.27	0.25	2.5	5.25	0.97	0.77
DK_1708	1.33	0.67	2.5	1.17	1.5	1.61	1.29
DK_4979	0.58	1	0.5	0.92	0.75	1.93	1.55
DK_1572	0.75	0.27	0.25	1.08	0.25	1.29	1.03
DK_1726	1	0.75	1.75	2.25	3.5	1.29	1.03
DK_1725	1	0.5	1.75	2.33	4	0.74	0.77
DK_299	0.33	0.5	0.75	0.5	0.75	1.61	1.29
DK_1734	1.17	0.58	1	1.17	1.75	6.12	4.9
DK_1551	0.33	0.27	0.25	1.08	2.75	1.29	1.03
DK_1550	1.67	0.42	0.5	2.67	5.25	1.61	1.29
DK_1538	1.58	0.27	2.19	3.17	2.5	1.61	1.29
DK_5078	0.33	0.33	0.56	0.42	1.06	0.74	1.03
DK_5101	0.27	0.33	0.25	0.25	0.25	1.29	1.03
DK_1778	1.08	0.27	1.75	2.67	1	1.29	1.03
DK_1780	0.92	0.27	1.62	0.83	0.25	0.74	1.03
DK_1507	0.58	0.27	0.75	1.08	0.75	0.97	0.77
DK_5148	0.27	0.83	0.69	1.08	0.25	0.97	0.77
DK_1793	1.08	0.5	1	1.42	1	0.97	0.77
DK_1801	1.58	0.67	0.25	2.67	5	1.29	1.03
DK_1848	0.75	0.5	0.5	1.25	1.81	1.61	1.29
DK_1438	1.17	0.33	0.75	1.42	2.75	0.97	0.77
DK_30	0.27	0.5	0.56	0.92	0.5	0.97	0.77
DK_1434	1.25	0.27	1.25	2.08	4.25	1.29	1.03
DK_5285	1.08	0.27	2	1.08	1	0.74	0.53
DK_5318	1.08	0.27	0.5	1.75	0.75	1.61	1.29
DK_1904	0.42	0.27	0.5	0.75	0.25	0.74	0.53
DK_1920	0.58	0.27	0.5	1	1.75	2.25	1.8
DK_1928	1.25	0.5	2.75	2.08	2.25	1.29	1.03
DK_b_628	0.75	0.27	0.25	1.17	0.25	0.74	0.53
DK_1402	0.75	0.33	0.75	1	1.75	0.74	0.53
DK_1396	0.67	0.27	1	1.08	0.75	3.86	3.09
DK_1944	0.42	0.27	0.5	0.83	0.25	1.61	1.29
DK_1945	0.27	0.42	0.25	0.75	0.25	0.74	0.53
DK_1946	0.27	0.58	0.25	0.58	0.25	0.74	0.53
DK_1369	0.67	0.27	2.5	2.75	4	2.25	1.8
DK_1979	0.75	0.27	0.75	1.5	1.56	0.97	0.77
DK_2001	0.75	0.27	0.5	1	2	2.58	3.35
DK_1353	1.42	1.42	0.75	2.17	1.75	0.97	0.77
DK_1356	0.92	0.27	1	1.5	0.5	0.74	0.53
DK_1343	0.33	0.75	0.25	0.33	0.75	0.74	0.53
DK_1338	0.27	0.27	0.37	0.08	0.25	0.74	0.53
DK_2016	0.33	0.27	0.25	0.83	1.5	0.97	0.77
DK_1324	1.08	0.27	1.69	1.08	0.25	1.61	1.29
DK_245	0.58	0.27	0.81	0.5	1.25	0.97	0.77
DK_2048	1.17	1.5	0.25	1.5	1.75	3.22	2.58

DK_5601	0.75	0.75	0.5	0.83	0.75	1.29	1.03
DK_2070	0.58	0.5	0.5	0.58	0.5	1.93	1.55
DK_2084	1.5	0.33	2.62	2.83	6.75	1.29	1.03
DK_2089	0.27	0.42	0.37	0.08	0.25	0.74	0.53
DK_1272	0.42	0.33	1.75	0.83	0.75	0.97	0.77
DK_219	0.67	0.33	0.75	1.83	2.25	1.93	1.55
DK_2145	1.5	0.27	3	1.67	2.25	3.22	2.58
DK_2153	1.25	0.5	0.25	2.17	1.75	1.29	1.03
DK_2160	0.75	0.27	0.25	0.58	1.5	0.97	0.77
DK_b_672	0.83	0.33	0.25	1.08	1.5	1.29	1.03
DK_2176	0.67	0.75	0.75	0.83	0.75	1.29	1.03
DK_2179	0.67	0.33	0.25	0.58	0.25	1.61	1.29
DK_2247	0.92	0.5	0.5	1.58	0.25	1.61	1.29
DK_2248	0.75	0.58	0.5	0.83	0.25	1.61	1.29
DK_1179	1.25	0.27	1.75	1.25	1	1.93	1.55
DK_2271	1	1	0.25	1.17	3.5	3.86	3.09
DK_2294	1.33	0.27	1	1.58	2.25	0.74	0.53
DK_2325	0.58	0.27	0.25	0.83	0.5	4.19	3.35
DK_2329	0.42	0.27	0.25	0.83	0.25	1.29	1.03
DK_1118	0.75	0.33	1.25	0.83	1.25	1.29	1.03
DK_176	0.58	0.27	2	1	2	1.29	1.03
DK_2396	0.67	0.27	0.75	1.5	1.25	1.93	1.55
DK_2433	0.67	0.42	1.12	1.17	1.25	0.97	0.77
DK_1047	1.33	1.5	2	2.17	4	0.97	0.77
DK_2502	0.67	0.27	1.25	0.58	2.25	3.54	2.83
DK_982	0.92	0.33	0.75	1.42	1.75	2.25	1.8
DK_2584	0.5	0.27	0.25	0.58	1	4.19	3.35
DK_b_62	0.83	0.27	0.25	1.5	1.25	1.61	1.29
DK_150	0.42	0.5	0.25	0.83	0.5	0.97	0.77
DK_149	0.33	0.42	0.25	0.75	0.25	1.61	1.29
DK_b_329	0.42	1.33	0.25	0.58	3.75	0.74	0.77
DK_2614	2	1.67	0.25	3.5	7.5	1.93	1.55
DK_2617	0.33	0.27	0.75	0.58	0.25	0.74	0.53
DK_2622	0.75	0.58	0.5	1.42	2.5	0.97	0.77
DK_2628	0.42	0.27	0.87	0.5	1.19	2.25	1.8
DK_2637	0.92	1.42	0.5	1.17	1.75	3.86	3.09
DK_947	0.27	1.25	0.5	0.17	0.25	0.74	0.53
DK_932	1.42	0.27	0.25	1.92	3	2.9	2.32
DK_2707	1.67	0.27	0.25	2.33	1	2.25	1.8
DK_2706	1.83	0.27	0.25	2.42	1	2.25	1.8
DK_2705	1.92	1.67	0.25	2.58	1.25	2.25	1.8
DK_2696	0.5	2.5	0.75	0.92	1.25	0.74	0.53
DK_2703	2.5	0.27	0.5	2.75	2	1.29	1.03
DK_2715	0.92	0.27	1.75	1.08	1	1.93	1.55
DK_b_65	0.67	1	1	1.08	0.25	0.97	0.77
DK_2753	0.5	0.33	1.12	1	0.25	0.97	0.77
DK_2754	0.5	0.33	1.12	0.92	0.25	0.74	0.53
DK_2752	0.75	1.08	0.25	1.17	0.5	0.97	0.77
DK_871	1.58	0.5	3.25	2.33	5.25	1.61	1.29
DK_2807	0.42	0.5	0.5	0.58	0.75	2.25	1.8
DK_123	0.27	0.42	0.25	0.25	0.25	1.29	1.03
DK_2824	0.5	0.5	1.75	0.92	1.25	0.97	0.77
DK_2935	1.17	0.27	1.44	1.25	0.5	1.61	1.29
DK_2949	0.33	0.42	1	0.5	0.25	0.74	0.53
DK_2959	0.5	0.5	0.94	0.83	0.75	1.29	1.03
DK_3019	0.27	0.33	0.81	0.42	1.31	0.74	2.06
DK_3025	0.42	0.27	0.25	0.5	0.75	0.97	0.77
DK_766	1.67	1.33	3.25	2.17	3.5	1.93	1.55
DK_3069	0.33	0.27	0.25	1.17	2.5	0.97	0.77
DK_3071	0.67	0.5	1.31	1.25	0.25	1.93	1.55
DK_759	1	0.5	0.5	1.92	4	1.93	1.55
DK_3094	0.67	0.27	0.75	0.75	1.5	0.97	0.77
DK_3095	0.5	0.27	0.25	0.67	0.5	0.74	0.53

DK_3131	0.27	0.27	0.25	0.58	0.75	0.74	0.53
DK_3174	0.42	0.58	0.81	0.58	0.25	0.97	0.77
DK_706	0.5	0.27	1.75	0.75	0.25	0.97	0.77
DK_3226	0.42	0.5	1.25	0.58	0.75	0.97	0.77
DK_690	0.33	0.75	1.25	0.67	1.5	1.61	1.29
DK_3276	1	0.27	0.25	1.08	2.25	2.25	1.8
DK_3280	2.5	0.27	0.25	0.75	0.25	8.7	6.96
DK_3340	0.27	0.27	0.25	0.5	1.25	0.74	0.53
DK_3441	0.67	0.27	1.25	0.67	0.25	1.29	1.8
DK_3509	0.33	0.27	0.25	0.42	0.25	0.97	0.77
DK_3512	0.33	0.27	0.25	1.83	3.75	1.61	1.29
DK_3516	0.27	0.27	1	0.5	0.25	0.74	0.53
DK_587	1.58	1.17	1.5	2	3.5	1.61	1.29
DK_3570	0.42	1	1	1.17	2.25	1.29	1.03
DK_b_226	0.27	0.5	0.31	0.31	0.31	0.74	0.53
DK_3622	0.27	0.27	0.75	0.58	0.75	1.29	1.03
DK_549	0.58	1	1.25	1.17	1.75	1.29	1.03
DK_3644	1.08	0.27	0.25	1.25	0.5	1.93	1.55
DK_3646	0.92	1.25	1.75	2.17	5	1.29	1.03
DK_529	0.92	0.58	1.5	1.08	0.75	1.93	1.55
DK_512	0.92	0.58	0.75	2.17	4.5	1.29	1.03
DK_495	0.33	0.67	0.25	0.67	0.5	1.61	1.29
DK_3824	0.75	0.27	0.25	1.42	1	0.97	0.77
DK_3839	0.5	0.27	0.81	0.5	0.75	1.93	1.55
DK_3834	0.42	1.33	0.62	0.5	0.5	0.97	0.77
DK_3832	0.42	0.27	0.25	0.75	0.5	1.61	1.29
DK_3837	0.5	0.33	0.94	0.42	0.25	2.58	2.06
DK_3848	0.75	1.17	4	1.92	2	1.61	1.29
DK_3850	0.33	0.27	0.75	1.25	0.25	1.93	2.83
DK_3940	0.42	0.27	0.75	0.5	0.5	1.93	1.55
DK_3990	0.5	0.27	0.5	0.83	1	1.61	1.29
DK_4042	0.67	2.33	1.5	0.92	0.5	1.61	1.29
DK_425	1.17	0.27	2.5	2.08	0.75	1.61	1.29
DK_4140	0.42	0.27	0.5	0.92	1.25	1.61	1.29
DK_411	0.58	0.92	0.25	1	0.75	1.29	1.03
DK_4304	0.27	0.83	0.56	0.5	1	0.97	0.77
DK_4322	0.67	0.42	0.25	1.08	1.5	1.29	1.03
DK_4370	0.75	1.33	1	0.67	0.5	2.9	2.32
DK_383	0.75	0.42	3	1.83	3.75	0.97	0.77
DK_4513	1	0.27	1.12	1.08	0.25	2.58	2.06
DK_4516	0.5	0.27	0.87	0.33	1.25	2.58	2.06
DK_4595	1	0.58	0.5	1.17	2.5	2.9	2.32
DK_340	0.27	0.75	0.5	0.5	1	0.97	0.77
DK_4856	0.67	0.27	0.81	0.83	0.75	1.93	1.55
DK_4858	0.58	1.08	0.81	0.75	0.5	0.74	1.8
DK_4877	0.5	0.92	0.81	0.92	1.75	0.97	0.77
DK_4897	0.5	1.33	1	0.5	0.25	0.74	0.53
DK_4918	0.83	0.27	1.37	1.25	2	0.97	0.77
DK_308	1	0.5	0.75	1.83	3.5	2.9	2.32
DK_309	1	0.27	0.25	1.42	1	2.9	2.32
DK_291	0.75	0.58	0.25	1.08	1	0.74	0.53
DK_33	0.33	0.67	0.25	0.58	1.25	0.97	0.77
DK_5202	0.83	0.33	0.75	0.92	1	0.97	0.77
DK_5467	0.33	0.27	0.25	0.5	0.5	0.97	0.77
DK_5479	0.27	0.75	0.31	0.25	0.44	0.97	0.77
DK_5480	0.27	0.33	0.31	0.17	0.44	0.74	0.77
DK_5558	0.33	0.27	0.25	0.92	2	0.74	0.53
DK_5585	0.75	0.5	1.12	1	1.87	2.25	1.8
DK_236	0.83	0.33	0.5	1.5	0.75	2.9	2.32
DK_226	0.5	0.27	0.5	0.92	2	0.97	0.77
DK_166	0.33	0.58	1.5	0.75	0.5	1.61	1.29
DK_164	0.27	1	0.5	0.25	0.25	0.74	0.53
DK_15	0.27	1.75	0.25	0.08	0.31	0.74	0.53

DK_6	0.27	1.33	0.25	0.08	0.25	0.74	0.53
DK_8	0.27	0.67	0.19	0.08	0.25	0.74	0.53
DK_5	0.27	0.27	0.19	0.08	0.25	0.97	0.77
DK_b_143	0.27	0.33	0.62	0.17	0.75	0.74	0.77
DK_3909	0.5	1.08	1.25	1.67	3.75	0.74	0.53
DK_b_123	0.27	0.58	0.5	0.17	0.25	0.74	1.29
DK_42	0.27	2.67	0.31	0.33	0.25	0.74	0.53
DK_1545	0.83	0.27	0.25	1.92	3.5	0.74	0.53
DK_1751	1.33	0.27	0.5	1.58	1	0.74	0.53
DK_1511	1.08	0.5	0.25	1.92	3.25	0.74	0.53
DK_1967	0.5	0.83	0.75	1	1.75	0.74	0.53
DK_1340	0.27	0.75	0.37	0.4	0.44	0.74	0.53
DK_5550	0.27	0.27	0.37	0.17	0.25	0.74	0.53
DK_1002	0.67	0.83	0.25	1.5	0.5	0.74	0.53
DK_b_335	1.42	0.27	2.25	3.25	0.25	0.74	0.53
DK_977	0.42	0.33	0.25	0.67	1.25	0.74	0.53
DK_940	0.27	0.27	0.62	0.58	0.75	0.74	0.53
DK_2735	0.75	1.25	0.75	0.67	1	0.74	0.53
DK_2842	0.83	1.42	1	1.33	0.5	0.74	0.53
DK_2856	0.33	0.5	0.25	0.42	0.5	0.74	0.53
DK_2878	0.75	0.42	1.25	0.58	0.5	0.74	0.53
DK_2956	0.42	0.42	1	0.5	0.25	0.74	0.53
DK_3046	0.5	0.27	0.25	0.92	0.5	0.74	0.53
DK_3129	0.27	1.08	0.25	0.25	0.5	0.74	0.53
DK_3442	0.42	1	0.25	1.42	0.75	0.74	0.53
DK_3504	0.27	0.5	0.25	0.42	0.25	0.74	0.53
DK_3521	1.33	0.67	1.5	1.75	1.25	0.74	0.53
DK_3634	0.27	0.33	0.5	0.25	0.5	0.74	0.53
DK_520	0.75	0.58	1.75	1.33	2.5	0.74	0.53
DK_3738	0.27	0.33	0.37	0.08	0.25	0.74	0.53
DK_420	0.58	0.27	1.25	1	1	0.74	0.53
DK_405	0.27	0.42	0.5	0.42	0.5	0.74	0.53
DK_400	0.58	0.27	1	1.5	1	0.97	0.77
DK_b_537	1.5	0.27	0.5	0.83	1.5	0.74	0.53
DK_4954	1	0.33	1	0.75	0.75	0.74	0.53
DK_b_426	1.67	0.75	1.75	2	3.25	0.74	0.53
DK_b_415	0.5	1	2.94	0.92	3.37	0.74	0.53
DK_b_413	0.27	0.67	2.56	0.33	3.37	0.74	0.53
DK_b_419	1.33	0.33	0.75	1.67	2.25	0.74	0.53
DK_2004	0.92	0.27	0.25	2	2.5	0.74	0.53
DK_246	0.27	0.27	0.25	0.17	0.25	0.74	0.53
DK_1341	0.27	0.67	0.25	0.33	0.25	0.74	0.53
DK_1335	0.27	0.27	1	0.67	0.75	0.74	0.53
DK_1203	0.33	0.67	1.5	0.75	1.5	0.74	0.53
DK_b_693	0.67	0.33	0.25	0.83	1	0.74	0.53
DK_196	0.58	0.33	1.75	1.08	0.75	0.74	0.53
DK_195	0.27	0.92	0.25	0.25	0.25	0.74	0.53
DK_186	0.27	0.27	0.37	0.5	0.75	0.74	0.53
DK_2408	2.17	0.27	1.5	3.33	6.75	0.97	0.77
DK_976	0.42	0.27	0.5	0.75	1.75	0.74	0.53
DK_2575	0.27	0.67	0.19	0.08	0.25	0.74	0.53
DK_2582	0.27	0.27	0.5	0.83	1	0.74	0.53
DK_151	0.58	0.27	0.25	0.83	1.5	0.74	0.53
DK_948	0.42	0.27	0.75	0.67	1.5	0.74	0.53
DK_b_1014	0.27	0.27	0.69	0.85	0.87	0.74	0.53
DK_b_1015	0.27	0.27	0.75	0.17	1	0.74	0.53
DK_2855	0.33	0.27	0.5	0.42	0.75	0.74	0.53
DK_b_783	0.27	1.08	0.81	0.25	1	0.74	0.53
DK_b_794	0.5	0.27	0.25	0.5	0.25	0.74	0.53
DK_3526	1.08	0.27	0.5	1.42	1.25	0.74	0.53
DK_b_225	0.27	0.27	0.31	0.08	0.62	0.74	0.53
DK_b_808	0.27	0.27	0.81	0.25	1	0.74	0.53
DK_73	0.33	1.25	0.25	0.33	0.75	0.74	0.53

DK_454	0.27	0.83	0.37	0.33	0.25	0.74	0.53
DK_434	0.67	0.27	1.25	0.92	2	0.74	0.53
DK_65	0.27	0.27	0.37	0.5	1	0.74	0.53
DK_67	0.27	0.75	1	0.5	0.5	0.74	0.53
DK_b_843	0.27	0.27	0.69	0.17	0.25	0.74	0.53
DK_b_219	0.33	0.27	0.25	0.67	0.75	0.74	0.53
DK_5013	0.27	0.27	0.81	0.75	1.12	0.74	0.53
DK_277	0.27	0.5	0.44	0.08	0.44	0.74	0.53
DK_276	0.5	1.25	1.25	0.75	1	0.97	0.77
DK_268	0.83	0.33	0.25	1.33	1.75	0.74	0.53
DK_257	0.33	2.67	0.25	0.83	1	0.74	0.53
DK_1991	0.42	0.83	0.5	0.25	0.5	0.74	0.53
DK_228	0.27	0.27	0.5	0.75	1	0.74	0.53
DK_b_932	0.42	1.08	0.25	0.58	1.25	0.74	0.53
DK_2267	0.33	0.27	0.69	0.5	0.5	0.74	0.53
DK_b_278	0.27	0.67	0.25	0.25	0.25	0.74	0.53
DK_2308	0.42	0.27	0.5	0.67	0.75	0.74	0.53
DK_1125	0.27	1	0.44	0.08	0.25	0.74	0.53
DK_175	0.27	0.27	0.25	0.08	0.25	0.74	0.53
DK_170	0.27	0.58	0.19	0.25	0.5	0.74	0.53
DK_158	0.42	0.83	0.75	0.5	1	0.74	0.53
DK_3	0.27	0.83	0.25	0.08	0.25	0.74	0.53
DK_137	0.42	1.08	0.5	0.92	1.25	0.74	0.53
DK_134	0.27	0.58	0.69	0.08	0.25	0.74	0.53
DK_126	0.33	0.27	0.25	0.5	1.25	0.74	0.53
DK_109	0.27	0.27	0.25	0.5	0.75	0.74	0.53
DK_b_277	0.33	0.27	0.25	0.33	0.5	0.74	0.53
DK_3474	0.27	0.83	0.25	0.25	0.5	0.74	0.53
DK_86	0.27	0.33	0.25	0.33	0.25	0.74	0.53
DK_546	0.27	0.92	0.19	0.08	0.25	0.74	0.53
DK_79	0.27	0.67	0.25	0.08	0.31	0.74	0.53
DK_3901	0.67	0.27	0.87	0.5	0.94	0.97	0.77
DK_b_526	0.58	0.33	0.25	1.42	1.75	0.74	0.53
DK_1544	0.5	0.5	1.06	0.83	1.75	0.74	0.53
DK_1763	0.27	0.27	0.31	0.25	0.25	0.74	0.53
DK_1806	1.67	0.5	0.5	2.25	4.25	0.74	0.53
DK_1833	0.27	0.27	0.25	0.33	0.5	0.74	0.53
DK_1473	0.58	1.83	0.25	1.08	2.25	0.74	0.53
DK_1418	1.5	0.33	1	1	1.5	0.74	0.53
DK_2115	0.27	1.25	0.25	0.25	0.25	0.74	0.53
DK_1238	0.33	0.42	0.25	0.58	1.25	0.74	0.53
DK_2141	0.75	0.27	1.5	1.67	0.25	0.74	0.53
DK_2168	0.5	0.27	0.25	0.83	1.75	0.74	0.53
DK_2190	0.5	0.27	0.25	0.75	1	0.74	0.53
DK_2211	0.75	0.42	1.5	1	0.25	0.74	0.53
DK_b_80	0.27	0.75	0.25	0.5	1	0.74	0.53
DK_1167	1.08	0.27	0.75	1.33	1	0.74	0.53
DK_2307	0.42	0.27	0.75	0.83	1	0.74	0.53
DK_2350	1	0.27	0.5	1.33	0.75	0.74	0.53
DK_1115	1.33	0.92	2.5	1.58	3.75	0.74	0.53
DK_1000	0.5	0.27	0.25	0.75	0.75	0.74	0.53
DK_2533	0.42	0.27	0.5	0.5	1.25	0.74	0.53
DK_962	0.58	0.27	0.5	0.67	1	0.97	0.77
DK_2606	0.27	0.27	0.25	0.33	0.25	0.74	0.53
DK_12	0.27	1.08	0.25	0.25	0.75	0.74	0.53
DK_14	0.27	0.33	0.25	0.33	0.75	0.74	0.53
DK_2	0.27	0.27	0.25	0.17	0.25	0.74	0.53
DK_916	0.5	0.27	0.25	0.75	0.75	0.74	0.53
DK_2725	0.33	0.27	1.25	0.83	0.75	0.74	0.53
DK_862	0.42	0.33	0.75	0.67	1.25	0.74	0.53
DK_2885	0.75	1.17	0.5	1.42	2.5	0.74	0.53
DK_2887	1.42	0.27	1.25	1.33	1.75	0.74	0.53
DK_2909	1.92	0.33	1.5	2.67	3	0.74	0.53

DK_3012	0.27	0.27	0.25	0.08	0.69	0.74	0.53
DK_3157	0.33	1.25	0.25	0.5	1.25	0.74	0.53
DK_719	1.08	0.67	1.25	1.25	2.75	0.74	0.53
DK_3242	0.42	0.5	1.12	0.83	1.94	0.74	0.53
DK_676	0.75	0.27	1	1.42	2.75	0.97	0.77
DK_652	0.33	0.67	0.25	0.75	1.5	0.74	0.53
DK_3330	0.42	0.42	1.25	0.58	0.25	0.74	0.53
DK_3372	0.27	0.33	0.19	0.19	0.19	0.74	0.53
DK_3413	0.75	0.42	1.5	0.75	0.25	0.74	0.53
DK_3460	0.5	0.27	0.75	0.75	0.75	0.74	0.53
DK_3716	1.42	0.27	2	1.17	1.25	0.74	0.53
DK_3718	0.27	1.42	0.37	0.25	0.56	0.74	0.53
DK_3717	0.27	1.08	0.56	0.25	0.25	0.74	0.53
DK_3766	0.42	0.58	1	1.33	2.75	0.74	0.53
DK_499	0.67	0.42	0.5	1.08	2	0.74	0.53
DK_3795	0.58	0.75	0.25	0.67	0.5	0.74	0.53
DK_4085	0.27	0.27	0.31	0.08	0.37	0.74	0.53
DK_417	0.27	0.27	0.25	0.58	0.75	0.74	0.53
DK_346	0.58	1.08	0.5	0.5	0.5	0.74	0.53
DK_4913	0.42	0.27	0.5	0.83	1.75	0.74	0.53
DK_1610	0.67	1.42	0.25	0.92	2	0.74	0.53
DK_1680	0.27	0.33	0.25	0.08	0.31	0.74	0.53
DK_4939	0.33	0.33	0.44	0.33	0.25	0.74	0.53
DK_1694	0.27	0.92	0.25	0.33	0.5	0.74	0.53
DK_1756	0.83	0.27	0.5	2	4.25	0.74	0.53
DK_1757	0.42	0.27	0.62	1	0.75	0.74	0.53
DK_1761	0.27	0.27	0.25	0.58	0.25	0.74	0.53
DK_1523	0.33	0.27	0.5	0.5	0.75	0.74	0.53
DK_1776	1	0.58	0.5	1.67	3.25	0.74	0.53
DK_1824	1.17	0.27	1.69	1.58	3	0.74	0.53
DK_b_620	1	0.27	1.75	1.42	0.5	0.74	0.53
DK_b_621	1	0.42	2.5	1.75	1.75	0.74	0.53
DK_265	0.83	0.83	1.25	0.92	1.75	0.74	0.53
DK_1404	0.58	0.27	1.25	0.92	0.5	0.74	0.53
DK_b_625	0.67	0.27	1.44	0.25	1.62	0.74	0.53
DK_1964	0.27	0.58	0.25	0.5	0.5	0.74	0.53
DK_260	0.33	0.27	0.75	0.58	0.75	0.74	0.53
DK_1987	0.27	1	0.5	0.33	0.5	0.74	0.53
DK_5559	0.33	0.58	0.81	0.58	1	0.74	0.53
DK_2045	0.92	0.27	1	0.83	0.75	0.74	0.53
DK_1305	0.75	0.27	0.25	0.75	1.25	0.74	0.53
DK_1256	0.33	0.27	0.25	0.58	1.25	0.74	0.53
DK_1234	0.27	0.27	0.75	0.67	0.75	0.74	0.53
DK_1229	0.27	0.83	0.75	0.58	1.25	0.74	0.53
DK_1231	0.27	0.27	0.25	0.42	0.5	0.74	0.53
DK_1232	0.27	0.5	0.25	0.33	0.25	0.74	0.53
DK_2171	0.75	0.27	0.5	1.08	0.75	0.74	0.53
DK_207	0.27	0.27	0.25	0.5	0.25	0.74	0.53
DK_2263	0.67	0.27	0.25	1.33	1	0.74	0.53
DK_2269	0.27	0.27	0.69	0.33	0.25	0.74	0.53
DK_2270	1.08	0.27	2.75	2.75	2.25	0.74	0.53
DK_1166	1.58	0.33	1.5	3.75	6	0.74	0.53
DK_2283	0.27	0.27	0.25	0.5	1	0.74	0.53
DK_2287	1.42	0.33	2.25	2.25	3.5	0.74	0.53
DK_2288	0.27	0.27	0.25	0.08	0.25	0.74	0.53
DK_2297	0.33	0.42	0.5	0.42	0.75	0.74	0.53
DK_1139	0.67	0.27	0.5	1.42	2	0.74	0.53
DK_1135	1	0.5	1.75	0.92	0.5	0.74	0.53
DK_1127	0.75	0.67	0.25	1.67	1.5	0.74	0.53
DK_2359	0.33	0.27	0.25	0.67	0.5	0.74	0.53
DK_179	0.27	0.27	0.25	0.33	0.75	0.74	0.53
DK_171	0.27	0.67	0.19	0.08	0.25	0.74	0.53
DK_1037	0.5	0.92	0.75	1.17	0.25	0.74	0.53

DK_2458	0.27	1.42	0.56	0.33	0.5	0.74	0.53
DK_2473	0.58	0.27	0.5	0.58	1	0.74	0.53
DK_b_271	0.33	0.67	0.75	0.5	1	0.74	0.53
DK_2534	0.27	0.27	0.37	0.33	0.5	0.74	0.53
DK_2572	0.27	0.83	0.25	1.25	1.94	0.74	0.53
DK_138	0.42	0.27	0.5	0.75	0.75	0.74	0.53
DK_2778	1.08	0.27	0.5	0.83	1.75	0.74	0.53
DK_2793	3.17	1.08	1.25	2.75	6.75	0.74	0.53
DK_860	0.42	0.83	1.5	0.83	1.5	0.74	0.53
DK_844	0.27	0.27	1	0.58	0.75	0.74	0.53
DK_2872	0.42	1.5	0.5	0.67	0.5	0.74	0.53
DK_117	0.42	0.67	1.75	0.83	0.25	0.74	0.53
DK_2940	0.92	0.27	0.25	1	2	0.74	0.53
DK_2953	0.42	0.5	0.5	0.42	0.5	0.74	0.53
DK_2974	0.42	0.67	0.5	0.67	1.25	0.74	0.53
DK_783	0.27	0.58	0.31	0.08	0.25	0.74	0.53
DK_2996	0.42	0.27	1	1.67	0.5	0.74	0.53
DK_775	0.33	1.17	0.25	0.5	1	0.74	0.53
DK_3035	0.33	0.58	0.25	1.5	0.25	0.74	0.53
DK_3067	0.33	0.33	1	0.83	2	0.74	0.53
DK_746	0.42	0.27	1	0.92	2	0.74	0.53
DK_738	0.75	0.75	1.25	1.33	1.25	0.74	0.53
DK_736	0.83	0.83	0.25	0.92	0.25	0.74	0.53
DK_3137	0.92	1.17	0.75	1.5	0.5	0.74	0.53
DK_3196	0.27	0.27	0.5	0.5	1	0.74	0.53
DK_3205	0.27	0.27	0.5	0.17	0.25	0.74	0.53
DK_687	0.27	0.27	0.25	0.08	0.25	0.74	0.53
DK_3269	1.25	0.27	1.25	2.75	5.75	0.74	0.53
DK_95	0.27	0.27	0.25	0.5	1	0.74	0.53
DK_96	0.27	0.33	0.25	0.33	0.75	0.74	0.53
DK_3379	0.27	0.42	0.25	0.25	0.5	0.74	0.53
DK_b_793	0.33	0.27	0.75	0.5	1.06	0.74	0.53
DK_613	0.58	0.92	1.25	1	2	0.74	0.53
DK_597	0.33	1.25	0.25	0.58	0.75	0.74	0.53
DK_592	0.92	0.27	1.25	2.17	0.5	0.74	0.53
DK_3527	0.75	0.67	0.25	0.83	1.25	0.97	0.77
DK_585	0.58	0.27	1	0.83	0.75	0.74	0.53
DK_3593	0.27	1	0.62	0.42	0.25	0.74	0.53
DK_81	0.27	0.42	0.69	0.17	0.25	0.74	0.53
DK_3740	0.27	0.33	0.37	0.08	0.37	0.74	0.53
DK_3755	0.75	0.33	1.5	1	2	0.74	0.53
DK_496	0.5	1	1.25	0.67	1.5	0.74	0.53
DK_3866	1.33	0.27	2	1.33	2.75	0.74	0.53
DK_3907	0.42	0.67	0.25	0.58	0.5	0.74	0.53
DK_416	0.27	1.08	0.75	0.5	1	0.74	0.53
DK_4218	0.5	0.33	0.5	0.33	0.5	0.74	0.53
DK_58	0.27	0.27	0.19	0.08	0.25	0.74	0.53
DK_b_215	0.27	0.27	0.25	0.33	0.5	0.74	0.53
DK_385	0.67	0.83	0.25	0.25	0.5	0.74	0.53
DK_57	0.27	0.67	0.37	0.17	0.25	0.74	0.53
DK_4588	0.27	0.27	0.75	0.58	0.25	0.74	0.53
DK_4666	0.75	0.27	2.25	1	0.25	0.74	0.53
DK_335	0.27	0.92	1	0.5	1	0.74	0.53
DK_4766	0.92	0.27	1.5	1.42	2.25	0.74	0.53
DK_4776	0.42	0.33	0.87	0.5	0.25	0.74	0.53
DK_4796	1	0.27	0.75	1.42	2.5	0.74	0.53
DK_4985	0.42	0.83	0.25	0.75	0.5	0.74	0.53
DK_304	0.33	0.33	0.5	0.75	1.5	0.74	0.53
DK_5044	0.27	0.42	0.56	0.5	0.81	0.74	0.53
DK_5139	0.92	0.75	0.25	1.83	4	0.74	0.53
DK_5315	0.27	0.27	0.37	0.08	0.25	0.74	0.53
DK_262	0.33	1.08	0.75	0.67	1.25	0.74	0.53
DK_26	0.27	0.33	0.5	0.25	0.5	0.74	0.53

DK_215	0.27	0.27	0.25	0.33	0.25	0.97	0.77
DK_203	0.67	0.42	1	1.08	2.25	0.74	0.53
DK_193	0.5	0.58	0.25	0.58	0.75	0.74	0.53
DK_180	0.27	0.27	0.31	0.08	0.25	0.74	0.53
DK_178	0.27	0.27	0.31	0.17	0.25	0.74	0.53
DK_22	0.27	0.33	0.25	0.08	0.31	0.74	0.53
DK_19	0.27	0.27	0.25	0.08	0.25	0.74	0.53
DK_174	0.5	0.27	1.5	0.75	0.25	0.74	0.53
DK_159	0.33	0.83	0.5	0.5	0.25	0.74	0.53
DK_157	0.42	0.33	1	0.67	1.5	0.74	0.53
DK_143	0.33	0.5	0.5	0.5	1	0.74	0.53
DK_127	0.42	1.17	0.5	0.58	1.25	0.74	0.53
DK_118	0.27	0.67	0.25	0.5	1	0.74	0.53
DK_b_142	0.27	0.27	0.25	0.33	0.5	0.74	0.53
DK_97	0.27	0.58	0.31	0.08	0.25	0.74	0.53
DK_88	0.27	1.08	0.25	0.25	0.5	0.74	0.53
DK_84	0.27	0.27	0.25	0.5	0.5	0.74	0.53
DK_80	0.33	0.58	1	0.75	0.75	0.74	0.53
DK_77	0.33	0.42	0.25	0.42	0.75	0.74	0.53
DK_47	0.42	0.33	0.25	0.83	0.75	0.74	0.53
DK_39	0.27	0.58	0.5	0.33	0.75	0.97	0.77
DK_40	0.27	0.27	0.25	0.33	0.5	0.74	0.53
DK_32	0.27	0.27	0.5	0.25	0.25	0.74	0.53
DK_b_85	0.27	1.08	0.37	0.17	0.25	0.74	0.53
DK_24	0.27	0.42	0.19	0.25	0.5	0.74	0.53
DK_20	0.27	1.08	0.25	0.08	0.25	0.74	0.53
DK_18	0.27	0.75	0.31	0.08	0.37	0.74	0.53
DK_10	0.27	1.25	0.25	0.58	1.25	0.74	0.53

Table A.0.21: Uncertainties of the parameters of the catalog shells from table A.0.19. Columns 1 and 2 contain the uncertainties of the center coordinates Δl_0, Δb_0 of each shell respectively. Columns 3–5 list the uncertainties of the minimum-, mean- and maximum radius ($\Delta r_{\rm min}$, Δr_0, $\Delta r_{\rm max}$) respectively. The uncertainties of the center velocity Δv_0 and the expansion velocity $\Delta v_{\rm exp}$ are listed in the columns 7 and 8 respectively. For more information see text in section 5.1.

1	2	3	4	5	6	7	8	9	10	11	12
Name	$\Delta D_{\rm s,a}$	$\Delta D_{\rm s,b}$	$\Delta D_{\rm sun}$	Δz	$\Delta D_{\rm gc}$	$\Delta R_{\rm min}$	$\Delta R_{\rm max}$	$\Delta \tau$	$\Delta M_{\rm own}$	$M_{\rm tot}$	$\Delta E_{\rm kin}$
unit:	kpc	kpc	kpc	kpc	kpc	kpc	kpc	10^7yr	$M_\odot$	$M_\odot$	ergs
DK_1476	1.16	1.16	1.16	0.5	0.91	0.24	0.41	3.51	4.70E+05	5.87E+05	7.57E+49
DK_2046	1.12	1.12	1.12	0.14	0.87	0.1	0.24	0.51	8.66E+05	1.08E+06	2.75E+51
DK_1303	1.51	1.51	1.51	0.21	0.58	0.17	0.62	1.38	2.83E+06	3.53E+06	2.26E+52
DK_1286	1.16	1.16	1.16	0.17	0.56	0.11	0.11	0.27	1.58E+05	1.97E+05	4.86E+50
DK_1188	2.38	2.38	2.38	0.17	0.58	0.15	0.31	0.91	2.00E+06	2.51E+06	4.00E+51
DK_1187	2.4	2.4	2.4	0.17	0.58	0.15	0.32	0.85	2.17E+06	2.71E+06	5.57E+51
DK_1119	1.43	1.43	1.43	0.1	0.53	0.08	0.06	0.42	6.23E+04	7.78E+04	2.60E+49
DK_857	1.27	1.27	1.27	0.11	0.58	0.11	0.08	0.22	4.04E+04	5.05E+04	2.16E+50
DK_810	1.25	1.25	1.25	0.18	0.59	0.16	0.08	0.22	4.81E+04	6.02E+04	1.63E+50
DK_3462	1.86	1.86	1.86	0.17	0.59	0.13	0.4	1.33	2.46E+06	3.08E+06	3.97E+51
DK_457	1.04	1.04	1.04	0.16	0.81	0.16	0.2	0.48	4.32E+05	5.39E+05	1.91E+51
DK_1619	1.16	1.16	1.16	0.19	0.92	0.08	0.17	0.33	4.17E+05	5.21E+05	2.32E+51
DK_1701	1.36	1.36	1.36	0.2	0.58	0.21	0.12	0.53	1.29E+05	1.62E+05	1.08E+50
DK_1452	1.14	1.14	1.14	0.09	0.93	0.06	0.15	0.79	7.27E+05	9.09E+05	3.54E+50
DK_1117	1.09	1.09	1.09	0.16	0.55	0.14	0.15	0.34	3.92E+05	4.90E+05	1.56E+51
DK_960	1.74	1.74	1.74	0.33	0.57	0.08	0.27	1.76	7.30E+05	9.13E+05	1.66E+50
DK_3275	2	2	2	0.19	0.52	0.12	0.33	1.59	8.79E+05	1.10E+06	3.28E+50
DK_3297	0.98	0.98	0.98	0.17	0.77	0.1	0.16	0.41	3.27E+05	4.09E+05	3.89E+50
DK_3295	0.97	0.97	0.97	0.17	0.76	0.12	0.14	0.49	2.06E+05	2.58E+05	1.87E+50
DK_3296	0.97	0.97	0.97	0.17	0.76	0.11	0.15	0.44	2.58E+05	3.22E+05	2.41E+50
DK_3639	1.32	1.32	1.32	0.1	1.13	0.09	0.39	1.14	6.39E+05	7.99E+05	1.96E+51
DK_b_823	1.02	1.02	1.02	0.49	0.54	0.05	0.07	0.27	2.10E+03	2.62E+03	1.11E+48
DK_1580	1.06	1.06	1.06	0.14	0.83	0.12	0.19	0.55	3.25E+05	4.06E+05	9.16E+50

DK_1527	1	1	1	0.09	0.77	0.13	0.13	0.58	7.73E+04	9.66E+04	9.08E+49
DK_5129	1.38	1.38	1.38	0.18	0.77	0.13	0.32	0.79	3.91E+05	4.89E+05	1.13E+51
DK_1483	1.04	1.04	1.04	0.03	0.49	0.04	0.06	0.37	4.59E+04	5.74E+04	1.79E+49
DK_1828	0.98	0.98	0.98	0.27	0.73	0.15	0.14	0.89	1.04E+05	1.30E+05	3.76E+49
DK_1965	1.03	1.03	1.03	0.13	0.8	0.03	0.05	0.2	1.86E+04	2.32E+04	2.20E+49
DK_1281	1.07	1.07	1.07	0.06	0.49	0.04	0.04	0.37	1.25E+04	1.56E+04	2.82E+48
DK_165	1.02	1.02	1.02	0.07	0.88	0.06	0.08	0.31	4.01E+04	5.01E+04	8.91E+49
DK_928	1.07	1.07	1.07	0.14	0.92	0.11	0.14	0.4	2.54E+05	3.18E+05	5.41E+50
DK_2819	1.25	1.25	1.25	0.15	0.53	0.13	0.15	0.21	5.55E+05	6.93E+05	6.58E+51
DK_2820	1.06	1.06	1.06	0.03	0.75	0.07	0.09	0.41	3.61E+04	4.51E+04	3.02E+49
DK_2873	1.6	1.6	1.6	0.04	0.76	0.07	0.12	0.54	2.03E+05	2.54E+05	2.61E+50
DK_3145	1.44	1.44	1.44	0.09	0.79	0.07	0.28	1.44	6.39E+05	7.99E+05	3.28E+50
DK_104	1.15	1.15	1.15	0.04	0.75	0.05	0.06	0.24	3.40E+04	4.25E+04	5.05E+49
DK_3277	1.17	1.17	1.17	0.08	0.52	0.11	0.13	0.43	2.69E+05	3.36E+05	3.55E+50
DK_635	1.25	1.25	1.25	0.05	0.56	0.14	0.11	0.41	1.20E+05	1.50E+05	1.31E+50
DK_4220	1.24	1.24	1.24	0.06	0.9	0.07	0.15	0.56	2.86E+05	3.57E+05	3.57E+50
DK_1514	1.78	1.78	1.78	0.15	0.62	0.09	0.35	0.73	1.48E+06	1.84E+06	1.31E+52
DK_1785	1.34	1.34	1.34	0.08	0.72	0.07	0.08	0.5	5.72E+04	7.15E+04	1.69E+49
DK_1783	1.45	1.45	1.45	0.07	0.7	0.11	0.12	0.46	1.44E+05	1.80E+05	1.57E+50
DK_1784	1.42	1.42	1.42	0.08	0.7	0.09	0.08	0.27	4.35E+04	5.43E+04	9.12E+49
DK_5209	1.07	1.07	1.07	0.14	0.52	0.14	0.11	1.53	4.85E+04	6.07E+04	3.28E+48
DK_1846	1.22	1.22	1.22	0.04	0.7	0.11	0.06	0.12	6.20E+04	7.76E+04	2.53E+50
DK_5238	1.14	1.14	1.14	0.12	0.55	0.1	0.07	0.63	2.01E+04	2.51E+04	3.89E+48
DK_1389	2.34	2.34	2.34	0.04	0.54	0.28	0.55	2.42	2.46E+06	3.07E+06	2.05E+51
DK_2009	1.65	1.65	1.65	0.12	0.53	0.1	0.13	0.81	8.49E+01	1.06E+02	3.07E+46
DK_1299	1.3	1.3	1.3	0.18	0.59	0.15	0.06	0.39	2.18E+04	2.72E+04	8.57E+48
DK_1267	1.12	1.12	1.12	0.11	0.84	0.08	0.2	1.74	9.99E+04	1.25E+05	2.90E+49
DK_1221	1.32	1.32	1.32	0.14	0.61	0.17	0.08	0.2	1.26E+05	1.57E+05	3.74E+50
DK_930	1.09	1.09	1.09	0.15	0.95	0.08	0.15	0.79	2.24E+05	2.80E+05	1.18E+50
DK_120	1.18	1.18	1.18	0.06	0.55	0.06	0.07	0.22	5.19E+04	6.49E+04	1.00E+50
DK_756	1.42	1.42	1.42	0.17	0.58	0.11	0.09	0.21	1.03E+05	1.28E+05	4.65E+50
DK_b_785	0.92	0.92	0.92	0.52	0.5	0.08	0.14	0.38	5.85E+03	7.31E+03	1.01E+49
DK_656	2.77	2.77	2.77	0.27	0.57	0.24	0.48	0.84	3.25E+06	4.06E+06	1.59E+52
DK_3575	2.1	2.1	2.1	0.13	0.68	0.1	0.17	0.74	4.99E+05	6.24E+05	5.04E+50
DK_3584	2.25	2.25	2.25	0.28	0.51	0.2	0.4	1.5	7.13E+05	8.91E+05	1.63E+51
DK_562	2.61	2.61	2.61	0.23	0.57	0.33	0.63	1.29	4.69E+06	5.86E+06	2.26E+52
DK_3668	1.3	1.3	1.3	0.25	0.84	0.1	0.27	1.01	2.42E+04	3.02E+04	5.35E+49
DK_456	1.15	1.15	1.15	0.25	0.95	0.03	0.09	0.56	7.19E+03	8.99E+03	2.36E+48
DK_4380	1.38	1.38	1.38	0.23	0.59	0.19	0.09	0.24	1.15E+05	1.44E+05	3.05E+50
DK_4593	1.38	1.38	1.38	0.18	0.76	0.13	0.18	0.7	1.98E+05	2.47E+05	2.47E+50
DK_4719	1.05	1.05	1.05	0.19	0.79	0.17	0.27	0.71	2.07E+05	2.58E+05	1.10E+51
DK_1668	1.81	1.81	1.81	0.12	0.53	0.21	0.69	3.03	2.72E+06	3.39E+06	2.58E+51
DK_1601	1.25	1.25	1.25	0.11	0.56	0.06	0.06	0.4	4.66E+02	5.82E+02	1.34E+47
DK_1555	1.08	1.08	1.08	0.04	0.73	0.04	0.04	0.27	1.15E+04	1.44E+04	3.33E+48
DK_1528	1.01	1.01	1.01	0.14	0.79	0.13	0.16	1.04	1.03E+05	1.28E+05	3.04E+49
DK_294	1.63	1.63	1.63	0.03	0.5	0.08	0.13	1.09	1.03E+02	1.29E+02	2.26E+46
DK_1861	1.04	1.04	1.04	0.11	0.7	0.09	0.08	0.55	1.69E+04	2.11E+04	9.96E+48
DK_1906	1.43	1.43	1.43	0.09	0.74	0.06	0.11	0.73	6.39E+04	7.99E+04	3.10E+49
DK_1400	1.43	1.43	1.43	0.09	0.48	0.08	0.1	0.44	1.54E+05	1.92E+05	2.27E+50
DK_1958	1	1	1	0.28	0.77	0.13	0.19	0.66	2.95E+05	3.69E+05	2.12E+50
DK_5458	1.21	1.21	1.21	0.14	0.58	0.12	0.08	0.2	5.10E+04	6.37E+04	3.30E+50
DK_1983	0.99	0.99	0.99	0.26	0.73	0.09	0.09	0.46	2.60E+04	3.25E+04	2.68E+49
DK_1993	764.77	764.77	764.77	82.15	502.83	26.71	0.13	0.85	8.53E+05	1.07E+06	1.27E+50
DK_1331	1.18	1.18	1.18	0.19	0.52	0.06	0.08	0.41	1.06E+04	1.32E+04	7.25E+48
DK_2034	1.02	1.02	1.02	0.08	0.78	0.11	0.21	1.09	7.53E+04	9.41E+04	8.29E+49
DK_2320	0.97	0.97	0.97	0.06	0.72	0.11	0.13	0.82	6.19E+04	7.74E+04	2.71E+49
DK_2335	1.2	1.2	1.2	0.16	1.02	0.13	0.48	1.24	8.84E+05	1.10E+06	1.35E+51
DK_2351	1.05	1.05	1.05	0.03	0.71	0.05	0.04	0.36	2.04E+04	2.55E+04	2.59E+48
DK_2389	1.27	1.27	1.27	0.08	0.59	0.1	0.04	0.27	1.31E+04	1.64E+04	3.62E+48
DK_2496	1.91	1.91	1.91	0.05	0.56	0.12	0.24	2.11	1.18E+06	1.47E+06	2.05E+50
DK_2513	1.03	1.03	1.03	0.09	0.78	0.06	0.11	0.69	3.21E+04	4.02E+04	1.48E+49
DK_1011	1.2	1.2	1.2	0.06	0.98	0.11	0.19	0.51	1.73E+05	2.16E+05	4.08E+50
DK_2595	1.65	1.65	1.65	0.09	0.52	0.18	0.86	5.54	1.84E+06	2.30E+06	6.67E+50

DK_2598	2.8	2.8	2.8	0.32	0.53	0.23	0.32	0.84	6.08E+05	7.60E+05	3.04E+51
DK_2663	1.31	1.31	1.31	0.13	0.84	0.1	0.3	0.89	7.07E+05	8.83E+05	1.57E+51
DK_919	0.98	0.98	0.98	0.19	0.74	0.13	0.15	0.64	1.32E+05	1.65E+05	1.11E+50
DK_2740	1.3	1.3	1.3	0.09	0.8	0.07	0.19	2.74	3.02E+05	3.77E+05	2.55E+49
DK_2779	0.99	0.99	0.99	0.15	0.72	0.15	0.16	0.86	1.33E+05	1.66E+05	7.74E+49
DK_798	3.35	3.35	3.35	0.18	0.55	0.34	0.4	0.88	2.24E+06	2.81E+06	9.18E+51
DK_3004	1.17	1.17	1.17	0.13	0.75	0.12	0.16	0.53	1.41E+05	1.76E+05	2.58E+50
DK_3099	1.2	1.2	1.2	0.08	1.02	0.1	0.29	0.86	4.36E+05	5.45E+05	1.15E+51
DK_737	1.56	1.56	1.56	0.23	0.56	0.05	0.22	1.87	4.22E+05	5.27E+05	5.59E+49
DK_3187	1.08	1.08	1.08	0.13	0.76	0.1	0.16	0.61	7.70E+04	9.63E+04	1.15E+50
DK_609	0.88	0.88	0.88	0.04	0.54	0.03	0.04	0.23	2.02E+02	2.53E+02	1.77E+47
DK_3489	1.25	1.25	1.25	0.1	0.8	0.05	0.1	0.53	1.24E+05	1.54E+05	5.90E+49
DK_3722	1.35	1.35	1.35	0.07	1.15	0.06	0.21	1.33	9.57E+05	1.20E+06	2.66E+50
DK_3745	1.23	1.23	1.23	0.12	0.5	0.07	0.11	0.4	5.79E+04	7.23E+04	1.28E+50
DK_3833	1.22	1.22	1.22	0.14	0.51	0.06	0.06	0.33	7.05E+04	8.81E+04	3.81E+49
DK_3894	1.76	1.76	1.76	0.15	0.51	0.08	0.31	1.16	1.49E+06	1.86E+06	3.13E+51
DK_4385	1.48	1.48	1.48	0.12	0.77	0.05	0.18	1.16	2.92E+05	3.65E+05	7.83E+49
DK_4456	1.77	1.77	1.77	0.17	0.68	0.06	0.16	0.51	3.34E+05	4.18E+05	4.82E+50
DK_4735	3.29	3.29	3.29	0.04	0.41	0.23	0.37	0.47	9.62E+05	1.20E+06	2.00E+52
DK_1602	0.94	0.94	0.94	0.02	0.55	0.04	0.04	0.39	1.90E+02	2.38E+02	3.84E+46
DK_306	1.6	1.6	1.6	0.09	0.59	0.15	0.64	4.14	2.67E+06	3.34E+06	8.31E+50
DK_307	1.59	1.59	1.59	0.06	0.58	0.15	0.44	2.27	1.88E+06	2.35E+06	9.88E+50
DK_b_486	1.13	1.13	1.13	0.53	0.84	0.23	0.27	1.76	2.32E+05	2.90E+05	1.11E+50
DK_5049	1.82	1.82	1.82	0.07	0.46	0.17	0.36	2.33	3.89E+05	4.87E+05	1.75E+50
DK_1771	3.56	3.56	3.56	0.05	0.5	0.12	0.08	0.36	2.01E+01	2.51E+01	1.77E+46
DK_1792	1.13	1.13	1.13	0.1	0.76	0.09	0.15	0.77	7.90E+04	9.88E+04	4.74E+49
DK_1802	1.06	1.06	1.06	0.12	0.72	0.09	0.08	0.35	6.98E+04	8.73E+04	4.33E+49
DK_5194	2.5	2.5	2.5	0.25	0.67	0.16	0.14	0.54	7.47E+04	9.34E+04	1.62E+50
DK_5192	1.93	1.93	1.93	0.17	0.72	0.13	0.22	0.6	2.77E+05	3.47E+05	1.21E+51
DK_5193	2.14	2.14	2.14	0.21	0.69	0.14	0.17	0.65	1.07E+05	1.33E+05	2.35E+50
DK_b_449	1.22	1.22	1.22	0.47	0.99	0.2	0.32	0.86	9.30E+05	1.16E+06	2.93E+51
DK_1879	1.84	1.84	1.84	0.04	0.69	0.12	0.32	0.77	1.23E+06	1.53E+06	3.97E+51
DK_b_616	1.08	1.08	1.08	0.67	0.52	0.1	0.13	0.25	1.03E+04	1.28E+04	2.19E+49
DK_1387	16.14	16.14	16.14	0.56	0.53	1.2	0.27	1.31	3.80E+05	4.74E+05	1.92E+50
DK_1383	1.11	1.11	1.11	0.29	0.92	0.22	0.3	0.89	8.33E+05	1.04E+06	1.88E+51
DK_5417	1.17	1.17	1.17	0.06	0.97	0.07	0.19	0.45	9.76E+05	1.22E+06	2.05E+51
DK_5563	2.59	2.59	2.59	0.25	2.35	0.1	0.29	0.97	7.87E+03	9.84E+03	5.64E+48
DK_5707	1.28	1.28	1.28	0.09	0.73	0.08	0.13	0.66	1.26E+05	1.57E+05	6.01E+49
DK_b_665	1.16	1.16	1.16	0.57	0.57	0.04	0.03	0.11	4.75E+02	5.93E+02	2.51E+47
DK_182	0.98	0.98	0.98	0.27	0.74	0.07	0.08	0.52	4.06E+04	5.07E+04	1.20E+49
DK_2418	1.08	1.08	1.08	0.53	0.78	0.21	0.2	1.31	7.77E+04	9.71E+04	4.15E+49
DK_1055	3.18	3.18	3.18	0.33	0.56	0.19	0.3	0.74	9.70E+05	1.21E+06	6.08E+51
DK_2424	1.13	1.13	1.13	0.14	0.92	0.12	0.21	0.79	1.77E+05	2.22E+05	4.02E+50
DK_2436	1.37	1.37	1.37	0.1	0.55	0.08	0.06	0.56	1.94E+04	2.42E+04	3.82E+48
DK_b_338	1.1	1.1	1.1	0.39	0.88	0.08	0.12	0.8	4.37E+04	5.46E+04	1.29E+49
DK_1007	1.28	1.28	1.28	0.31	0.7	0.1	0.05	0.12	5.08E+03	6.35E+03	2.15E+49
DK_2524	1.12	1.12	1.12	0.05	0.69	0.08	0.05	0.3	1.24E+04	1.55E+04	3.82E+48
DK_973	1.23	1.23	1.23	0.43	0.79	0.09	0.13	0.29	3.32E+03	4.15E+03	1.67E+49
DK_2638	1.14	1.14	1.14	0.12	0.54	0.09	0.09	0.4	4.61E+04	5.77E+04	5.68E+49
DK_146	1.04	1.04	1.04	0.05	0.74	0.02	0.02	0.12	1.91E+03	2.39E+03	5.61E+47
DK_937	1.18	1.18	1.18	0.07	0.77	0.08	0.15	0.95	2.90E+04	3.62E+04	7.78E+48
DK_2738	1.33	1.33	1.33	0.08	0.85	0.07	0.26	0.57	3.39E+05	4.23E+05	1.82E+51
DK_2798	1.02	1.02	1.02	0.09	0.86	0.06	0.09	0.27	1.97E+05	2.47E+05	4.85E+50
DK_2804	1.47	1.47	1.47	0.02	0.55	0.22	0.17	0.91	1.28E+05	1.59E+05	7.12E+49
DK_129	1.08	1.08	1.08	0.03	0.89	0.04	0.1	0.65	1.19E+05	1.48E+05	3.77E+49
DK_3122	1.01	1.01	1.01	0.28	0.72	0.15	0.11	0.42	5.34E+04	6.67E+04	1.18E+50
DK_712	1.68	1.68	1.68	0.19	0.58	0.19	0.69	3.02	2.67E+06	3.34E+06	2.69E+51
DK_713	1.65	1.65	1.65	0.19	0.58	0.18	0.7	2.63	2.89E+06	3.62E+06	4.48E+51
DK_714	1.6	1.6	1.6	0.19	0.59	0.18	0.68	2.25	2.63E+06	3.28E+06	6.94E+51
DK_3274	2.08	2.08	2.08	0.46	0.55	0.14	0.14	0.6	6.24E+02	7.81E+02	5.13E+47
DK_3338	2.16	2.16	2.16	0.24	0.69	0.18	0.17	0.74	8.65E+04	1.08E+05	1.35E+50
DK_3336	1.16	1.16	1.16	0.11	0.53	0.1	0.1	0.51	6.53E+04	8.16E+04	4.18E+49
DK_3331	1.17	1.17	1.17	0.16	0.98	0.09	0.25	0.86	2.64E+05	3.30E+05	2.22E+50

DK_b_303	1.03	1.03	1.03	0.39	0.73	0.17	0.16	1.05	7.07E+04	8.83E+04	3.23E+49
DK_3551	1.13	1.13	1.13	0.17	0.89	0.1	0.23	0.68	2.99E+05	3.74E+05	8.62E+50
DK_3574	2.01	2.01	2.01	0.04	0.7	0.1	0.16	0.52	2.27E+05	2.84E+05	3.66E+50
DK_3609	1.25	1.25	1.25	0.17	1.05	0.07	0.25	0.8	3.63E+05	4.54E+05	6.62E+50
DK_535	1.18	1.18	1.18	0.04	0.7	0.05	0.05	0.27	6.56E+04	8.21E+04	3.82E+49
DK_530	1.14	1.14	1.14	0.08	0.57	0.16	0.11	0.43	1.82E+05	2.28E+05	1.62E+50
DK_3756	1.1	1.1	1.1	0.1	0.5	0.08	0.1	0.35	8.12E+04	1.01E+05	1.62E+50
DK_b_818	2.65	2.65	2.65	0.95	0.52	0.14	0.12	0.6	9.40E+02	1.17E+03	3.51E+47
DK_3804	1.24	1.24	1.24	0.08	0.78	0.07	0.13	0.66	1.51E+05	1.89E+05	9.76E+49
DK_3900	1.08	1.08	1.08	0.12	0.76	0.07	0.1	0.51	4.44E+04	5.55E+04	2.34E+49
DK_466	1.22	1.22	1.22	0.32	0.84	0.05	0.14	0.88	3.65E+03	4.56E+03	1.23E+48
DK_70	1.2	1.2	1.2	0.04	0.91	0.04	0.09	0.48	8.34E+04	1.04E+05	5.07E+49
DK_4223	1.21	1.21	1.21	0.19	1.01	0.14	0.32	0.95	4.52E+05	5.65E+05	1.89E+51
DK_4236	1.35	1.35	1.35	0.15	0.7	0.13	0.07	0.12	3.79E+04	4.73E+04	1.62E+50
DK_4318	1.16	1.16	1.16	0.17	0.89	0.1	0.24	0.58	4.89E+05	6.12E+05	1.61E+51
DK_4341	1.63	1.63	1.63	0.1	0.46	0.07	0.33	2.84	1.19E+06	1.48E+06	2.17E+50
DK_b_300	1.03	1.03	1.03	0.38	0.75	0.21	0.25	1.59	1.48E+05	1.85E+05	6.97E+49
DK_4548	1.21	1.21	1.21	0.13	0.7	0.15	0.12	0.45	1.08E+05	1.35E+05	1.56E+50
DK_48	1.2	1.2	1.2	0.05	0.59	0.06	0.03	0.18	1.62E+04	2.02E+04	5.03E+48
DK_b_851	0.83	0.83	0.83	0.29	0.53	0.04	0.04	0.25	2.17E+03	2.71E+03	5.35E+47
DK_4802	1.31	1.31	1.31	0.1	0.86	0.12	0.33	0.88	6.17E+05	7.71E+05	3.12E+51
DK_4814	1.34	1.34	1.34	0.03	0.46	0.09	0.11	0.7	9.10E+04	1.14E+05	3.96E+49
DK_1640	3.22	3.22	3.22	0.03	0.53	0.39	0.71	3.7	1.32E+06	1.65E+06	6.32E+50
DK_1598	1.4	1.4	1.4	0.01	0.53	0.16	0.18	0.78	1.20E+05	1.50E+05	1.36E+50
DK_b_210	1.39	1.39	1.39	0.88	0.57	0.06	0.04	0.31	1.19E+03	1.48E+03	1.50E+47
DK_1745	1.12	1.12	1.12	0.08	0.6	0.12	0.21	0.31	4.16E+05	5.20E+05	6.00E+51
DK_1777	1.57	1.57	1.57	0.19	0.54	0.19	1.01	3.82	3.03E+06	3.78E+06	5.97E+51
DK_5190	1.1	1.1	1.1	0.07	0.86	0.05	0.11	0.28	5.04E+05	6.29E+05	5.98E+50
DK_1465	2	2	2	0.26	0.61	0.21	0.52	0.99	5.45E+06	6.81E+06	3.48E+52
DK_275	0.95	0.95	0.95	0.02	0.46	0.05	0.13	0.82	3.38E+00	4.22E+00	8.63E+44
DK_5303	0.7	0.7	0.7	0.06	0.46	0.06	0.19	0.43	4.52E+05	5.65E+05	1.80E+51
DK_1417	2.82	2.82	2.82	0.75	0.42	0.11	0.23	1.22	9.68E+03	1.21E+04	4.22E+48
DK_5354	1.36	1.36	1.36	0.12	0.68	0.07	0.02	0.33	5.24E+03	6.54E+03	3.51E+47
DK_5376	1.4	1.4	1.4	0.22	1.2	0.09	0.34	0.7	1.23E+06	1.53E+06	5.81E+51
DK_2128	1.48	1.48	1.48	0.19	0.61	0.2	0.15	0.26	3.59E+05	4.49E+05	3.01E+51
DK_2174	1.93	1.93	1.93	0.07	0.57	0.06	0.13	0.66	4.98E+05	6.23E+05	3.71E+50
DK_2394	1.09	1.09	1.09	0.2	0.72	0.11	0.1	0.67	4.57E+04	5.71E+04	1.69E+49
DK_2453	1.83	1.83	1.83	0.11	0.71	0.07	0.15	0.56	2.28E+05	2.85E+05	3.56E+50
DK_168	0.96	0.96	0.96	0.17	0.77	0.07	0.11	0.53	9.98E+04	1.25E+05	4.61E+49
DK_1013	1.22	1.22	1.22	0.09	0.97	0.04	0.12	0.75	1.51E+04	1.89E+04	6.98E+48
DK_2639	1.11	1.11	1.11	0.12	0.9	0.09	0.17	0.62	3.24E+05	4.05E+05	3.83E+50
DK_13	1.24	1.24	1.24	0.01	0.96	0.02	0.05	0.33	7.33E+03	9.17E+03	2.40E+48
DK_2760	1.07	1.07	1.07	0.1	0.72	0.05	0.05	0.3	1.72E+04	2.14E+04	6.72E+48
DK_119	0.99	0.99	0.99	0.04	0.78	0.05	0.09	0.58	3.13E+04	3.91E+04	1.21E+49
DK_797	1.37	1.37	1.37	0.11	0.57	0.14	0.13	0.57	4.67E+03	5.84E+03	3.18E+48
DK_765	4	4	4	0.05	0.52	0.48	0.43	2.79	6.70E+05	8.38E+05	1.98E+50
DK_698	1.39	1.39	1.39	0.28	1.23	0.03	0.15	0.98	1.31E+04	1.63E+04	4.29E+48
DK_3450	3.44	3.44	3.44	0.29	1.81	0.23	0.16	0.82	7.86E+04	9.82E+04	4.12E+49
DK_616	0.76	0.76	0.76	0.06	0.55	0.11	0.19	0.56	5.18E+05	6.48E+05	8.91E+50
DK_89	1.21	1.21	1.21	0.04	0.75	0.06	0.07	0.47	7.65E+04	9.57E+04	1.74E+49
DK_3583	1.07	1.07	1.07	0.17	0.7	0.11	0.08	0.5	1.71E+04	2.14E+04	7.83E+48
DK_3666	0.9	0.9	0.9	0.12	0.52	0.06	0.09	0.48	9.34E+01	1.17E+02	5.24E+46
DK_3735	1.39	1.39	1.39	0.15	0.45	0.04	0.06	0.38	1.10E+04	1.38E+04	2.99E+48
DK_3757	1.39	1.39	1.39	0.08	0.76	0.1	0.18	0.78	4.18E+05	5.23E+05	4.97E+50
DK_3831	1.29	1.29	1.29	0.11	1	0.06	0.28	1.83	1.09E+06	1.36E+06	3.07E+50
DK_72	1.12	1.12	1.12	0	0.83	0.03	0.05	0.44	2.32E+04	2.90E+04	3.61E+48
DK_3972	1.24	1.24	1.24	0.2	0.6	0.17	0.09	0.23	5.67E+04	7.09E+04	3.49E+50
DK_69	1.23	1.23	1.23	0.03	0.88	0.04	0.09	0.48	1.02E+05	1.27E+05	4.49E+49
DK_4113	1.13	1.13	1.13	0.05	0.93	0.08	0.15	0.34	5.66E+05	7.07E+05	1.74E+51
DK_4128	2.47	2.47	2.47	0.24	0.47	0.21	0.47	0.58	4.01E+06	5.02E+06	6.55E+52
DK_4179	1.23	1.23	1.23	0.04	0.8	0.06	0.09	0.45	3.03E+04	3.78E+04	2.10E+49
DK_4307	1.38	1.38	1.38	0.02	0.86	0.05	0.2	1.28	2.73E+05	3.41E+05	1.29E+50
DK_4336	1.38	1.38	1.38	0.19	0.76	0.11	0.16	0.33	6.16E+04	7.69E+04	2.88E+50

DK_4648	1.27	1.27	1.27	0.07	1.09	0.09	0.32	1.2	8.84E+05	1.10E+06	1.05E+51
DK_1622	2.24	2.24	2.24	0.07	0.54	0.22	0.42	1.84	1.20E+06	1.49E+06	1.11E+51
DK_1611	1.13	1.13	1.13	0.06	1.01	0.12	0.26	2.24	2.32E+05	2.90E+05	3.46E+49
DK_1672	0.97	0.97	0.97	0.11	0.7	0.08	0.08	1.15	2.11E+04	2.64E+04	2.44E+48
DK_1673	1.01	1.01	1.01	0.12	0.76	0.08	0.11	0.38	6.81E+04	8.51E+04	1.68E+50
DK_1600	1.35	1.35	1.35	0	0.51	0.12	0.15	0.96	5.21E+04	6.51E+04	2.64E+49
DK_4995	1.08	1.08	1.08	0.12	0.9	0.08	0.18	0.42	2.29E+05	2.87E+05	3.37E+50
DK_1779	1.63	1.63	1.63	0.23	0.53	0.2	0.71	4.37	9.22E+05	1.15E+06	4.41E+50
DK_1489	1.67	1.67	1.67	0.25	0.56	0.21	0.59	3.06	1.19E+06	1.49E+06	1.11E+51
DK_1813	1.24	1.24	1.24	0.03	0.55	0.1	0.13	0.83	2.97E+02	3.71E+02	1.56E+47
DK_1474	1.08	1.08	1.08	0.08	0.75	0.09	0.09	0.6	1.83E+04	2.29E+04	4.22E+48
DK_1462	4.22	4.22	4.22	0.17	0.55	0.31	0.24	1.56	2.97E+05	3.71E+05	1.36E+50
DK_1420	2.02	2.02	2.02	0.01	0.54	0.24	0.74	3.24	3.21E+06	4.01E+06	2.59E+51
DK_1912	1.95	1.95	1.95	0.21	0.56	0.17	0.36	2.31	9.88E+05	1.23E+06	2.92E+50
DK_1401	1.51	1.51	1.51	0.08	0.52	0.09	0.11	0.41	1.84E+05	2.30E+05	1.83E+50
DK_1940	1.23	1.23	1.23	0.18	0.56	0.03	0.02	0.17	1.07E+03	1.34E+03	2.12E+47
DK_1399	1.18	1.18	1.18	0	0.56	0.08	0.06	0.38	3.43E+04	4.28E+04	8.15E+48
DK_1395	0.97	0.97	0.97	0.04	0.75	0.07	0.08	0.73	4.49E+04	5.61E+04	4.98E+48
DK_1943	1.29	1.29	1.29	0.09	0.83	0.11	0.29	1.53	2.31E+05	2.89E+05	1.49E+50
DK_28	0.69	0.69	0.69	0.01	0.43	0.02	0.04	0.22	2.27E+01	2.83E+01	1.53E+46
DK_5709	1.25	1.25	1.25	0.02	1.03	0.08	0.25	1.3	1.24E+05	1.55E+05	5.61E+49
DK_2152	0.99	0.99	0.99	0.07	0.72	0.15	0.14	1.21	1.06E+05	1.32E+05	1.14E+49
DK_1219	1.17	1.17	1.17	0.12	0.99	0.05	0.11	0.92	7.44E+03	9.30E+03	9.86E+47
DK_2266	1.66	1.66	1.66	0.11	0.5	0.08	0.27	1.39	1.45E+06	1.82E+06	8.73E+50
DK_1128	1.19	1.19	1.19	0.08	0.59	0.1	0.05	0.33	1.67E+04	2.08E+04	4.92E+48
DK_1031	1.86	1.86	1.86	0.27	0.53	0.1	0.34	2.9	5.28E+05	6.60E+05	5.77E+49
DK_2542	1.25	1.25	1.25	0.16	1.06	0.12	0.42	1.02	1.31E+06	1.64E+06	6.00E+51
DK_2544	1.27	1.27	1.27	0.11	0.46	0.07	0.11	0.45	5.39E+04	6.73E+04	4.26E+49
DK_983	1.26	1.26	1.26	0.39	0.7	0.12	0.07	0.47	1.14E+03	1.43E+03	3.15E+47
DK_b_735	0.93	0.93	0.93	0.52	0.53	0.08	0.07	0.63	8.51E+02	1.06E+03	1.25E+47
DK_927	0.78	0.78	0.78	0.09	0.57	0.08	0.07	0.31	4.63E+04	5.78E+04	4.70E+49
DK_2676	1.01	1.01	1.01	0.18	0.56	0.17	0.11	0.7	5.37E+04	6.72E+04	2.01E+49
DK_863	0.78	0.78	0.78	0.1	0.57	0.1	0.12	0.53	6.22E+04	7.77E+04	1.05E+50
DK_855	0.7	0.7	0.7	0.01	0.48	0.05	0.11	0.72	6.09E+04	7.61E+04	2.86E+49
DK_2871	1.14	1.14	1.14	0.18	0.75	0.05	0.05	0.33	4.11E+04	5.13E+04	1.21E+49
DK_788	1.21	1.21	1.21	0.14	0.59	0.17	0.06	0.32	2.58E+04	3.23E+04	1.66E+49
DK_710	1.03	1.03	1.03	0.03	0.76	0.08	0.09	0.82	1.18E+04	1.47E+04	2.98E+48
DK_709	1.04	1.04	1.04	0.03	0.78	0.1	0.1	0.67	1.31E+04	1.63E+04	6.48E+48
DK_634	0.98	0.98	0.98	0.06	0.59	0.06	0.03	0.12	9.24E+02	1.16E+03	6.63E+47
DK_618	1.09	1.09	1.09	0.2	0.92	0.17	0.23	0.77	4.28E+05	5.35E+05	1.12E+51
DK_3471	1.06	1.06	1.06	0.07	0.74	0.1	0.16	1.03	2.90E+04	3.63E+04	1.43E+49
DK_606	0.82	0.82	0.82	0.06	0.58	0.08	0.07	0.22	1.94E+04	2.42E+04	3.70E+49
DK_3496	1.12	1.12	1.12	0.12	0.51	0.09	0.12	0.55	9.61E+04	1.20E+05	9.13E+49
DK_3577	1.28	1.28	1.28	0.06	1.09	0.06	0.23	1.46	1.33E+05	1.66E+05	6.99E+49
DK_576	1.48	1.48	1.48	0.16	1.38	0.05	0.18	1.16	3.31E+04	4.14E+04	1.57E+49
DK_3761	0.96	0.96	0.96	0.15	0.71	0.16	0.14	0.91	9.66E+04	1.21E+05	2.66E+49
DK_437	1.47	1.47	1.47	0.03	0.55	0.05	0.04	0.2	1.49E+02	1.86E+02	8.66E+46
DK_62	1.31	1.31	1.31	0.06	0.54	0.04	0.02	0.21	1.30E+04	1.62E+04	1.90E+48
DK_388	0.83	0.83	0.83	0.05	0.64	0.09	0.17	0.74	5.25E+04	6.57E+04	5.14E+49
DK_367	0.96	0.96	0.96	0.18	0.74	0.15	0.12	0.47	2.26E+05	2.83E+05	2.06E+50
DK_4647	1.36	1.36	1.36	0.06	1.2	0.09	0.42	1.85	4.61E+05	5.76E+05	6.34E+50
DK_1685	1.75	1.75	1.75	0.1	0.53	0.23	0.88	5.69	2.74E+06	3.43E+06	6.56E+50
DK_1708	1.78	1.78	1.78	0.22	0.58	0.2	0.52	2.28	1.77E+06	2.22E+06	1.73E+51
DK_4979	1.37	1.37	1.37	0.05	0.81	0.09	0.4	1.5	4.42E+05	5.53E+05	6.97E+50
DK_1572	0.99	0.99	0.99	0.1	0.75	0.07	0.1	0.5	2.59E+04	3.24E+04	2.63E+49
DK_299	1.71	1.71	1.71	0.23	0.55	0.05	0.19	0.82	2.63E+05	3.29E+05	2.16E+50
DK_1734	2.63	2.63	2.63	0.38	0.57	0.26	0.45	0.61	5.07E+06	6.34E+06	6.67E+52
DK_1551	2.04	2.04	2.04	0.04	0.69	0.14	0.26	1.34	4.60E+05	5.75E+05	2.02E+50
DK_5078	1.65	1.65	1.65	0.14	0.72	0.07	0.2	0.96	3.64E+05	4.55E+05	1.36E+50
DK_5101	1.46	1.46	1.46	0.06	0.76	0.05	0.15	0.77	1.42E+05	1.77E+05	1.10E+50
DK_1780	1.71	1.71	1.71	0.24	0.52	0.2	0.62	3.02	1.26E+06	1.58E+06	8.29E+50
DK_1778	1.59	1.59	1.59	0.22	0.54	0.2	0.9	4.69	2.09E+06	2.61E+06	1.77E+51
DK_1507	2.89	2.89	2.89	0.4	0.47	0.15	0.34	2.21	1.35E+05	1.69E+05	5.50E+49

DK_5148	1.22	1.22	1.22	0.09	0.59	0.06	0.03	0.18	2.95E+03	3.69E+03	1.50E+48
DK_1793	1.23	1.23	1.23	0.06	0.56	0.09	0.11	0.71	3.74E+02	4.67E+02	1.53E+47
DK_1801	1.02	1.02	1.02	0.11	0.71	0.16	0.16	0.82	1.18E+05	1.47E+05	5.59E+49
DK_5285	1.54	1.54	1.54	0.09	0.48	0.14	0.17	1.45	6.86E+04	8.58E+04	1.37E+49
DK_5318	1.48	1.48	1.48	0.06	0.73	0.12	0.26	1.16	1.75E+05	2.19E+05	2.31E+50
DK_1904	1.3	1.3	1.3	0.23	0.81	0.05	0.17	1.47	2.21E+04	2.76E+04	5.75E+48
DK_1920	1.09	1.09	1.09	0.09	0.77	0.07	0.11	0.37	1.03E+05	1.28E+05	1.57E+50
DK_1928	2	2	2	0.27	0.54	0.23	0.7	3.62	1.91E+06	2.39E+06	1.13E+51
DK_b_628	1.07	1.07	1.07	0.4	0.85	0.11	0.16	1.39	5.70E+04	7.13E+04	1.71E+49
DK_1402	1.33	1.33	1.33	0.07	0.55	0.08	0.06	0.53	2.14E+04	2.68E+04	2.79E+48
DK_1944	1.31	1.31	1.31	0.11	0.81	0.1	0.26	1.14	1.00E+05	1.25E+05	1.53E+50
DK_1945	1.3	1.3	1.3	0.11	0.81	0.07	0.21	1.86	2.44E+05	3.06E+05	6.54E+49
DK_1946	1.31	1.31	1.31	0.12	0.8	0.06	0.21	1.84	2.12E+05	2.65E+05	5.67E+49
DK_2001	1.53	1.53	1.53	0.15	0.71	0.11	0.4	0.71	1.62E+06	2.02E+06	6.24E+51
DK_1356	1.53	1.53	1.53	0.02	0.52	0.14	0.16	1.39	4.78E+04	5.97E+04	1.26E+49
DK_1343	1.2	1.2	1.2	0.13	0.99	0.03	0.09	1.29	1.61E+04	2.01E+04	8.47E+47
DK_1324	1.43	1.43	1.43	0.2	0.53	0.17	0.16	0.7	5.60E+04	6.99E+04	9.35E+49
DK_2048	1.14	1.14	1.14	0.11	0.92	0.12	0.3	0.73	8.90E+05	1.11E+06	3.55E+51
DK_5601	1.1	1.1	1.1	0.2	0.76	0.12	0.16	0.82	7.50E+04	9.38E+04	6.06E+49
DK_2070	0.93	0.93	0.93	0.03	0.71	0.05	0.03	0.12	2.42E+04	3.02E+04	3.95E+49
DK_1272	1.48	1.48	1.48	0.09	1.34	0.05	0.3	1.93	2.58E+05	3.23E+05	8.73E+49
DK_2153	1.02	1.02	1.02	0.13	0.76	0.12	0.18	0.96	7.17E+04	8.96E+04	4.84E+49
DK_2179	1.96	1.96	1.96	0.23	0.5	0.12	0.13	0.58	4.15E+01	5.18E+01	5.86E+46
DK_2247	1.15	1.15	1.15	0.02	0.69	0.1	0.08	0.35	2.35E+04	2.93E+04	3.81E+49
DK_2271	1.58	1.58	1.58	0.14	1.42	0.13	0.36	0.73	6.13E+05	7.67E+05	2.19E+51
DK_1118	1.44	1.44	1.44	0.21	0.53	0.08	0.08	0.43	4.01E+04	5.01E+04	2.20E+49
DK_176	1.47	1.47	1.47	0.01	0.48	0.07	0.1	0.5	2.55E+05	3.19E+05	1.03E+50
DK_2396	1.12	1.12	1.12	0.02	0.71	0.09	0.09	0.33	4.78E+04	5.98E+04	6.98E+49
DK_2433	1	1	1	0.28	0.78	0.08	0.12	0.79	4.61E+04	5.76E+04	1.68E+49
DK_2502	1.44	1.44	1.44	0.22	0.53	0.19	0.16	0.35	3.76E+05	4.70E+05	1.50E+51
DK_2584	2.05	2.05	2.05	0.17	0.44	0.14	0.37	0.71	1.81E+06	2.27E+06	1.19E+52
DK_b_62	1.2	1.2	1.2	0.42	0.72	0.09	0.1	0.42	1.47E+03	1.84E+03	1.53E+48
DK_149	0.67	0.67	0.67	0.02	0.38	0.03	0.11	0.48	1.07E+05	1.33E+05	1.49E+50
DK_2614	1	1	1	0.13	0.84	0.18	0.19	0.73	4.80E+05	6.00E+05	4.07E+50
DK_2617	2.04	2.04	2.04	0.24	0.58	0.09	0.23	1.97	3.15E+05	3.93E+05	8.19E+49
DK_2622	1.55	1.55	1.55	0.2	0.55	0.11	0.13	0.85	6.83E+02	8.54E+02	1.82E+47
DK_2628	0.74	0.74	0.74	0.1	0.51	0.05	0.08	0.25	1.06E+05	1.33E+05	1.71E+50
DK_2637	8.02	8.02	8.02	0.02	0.52	1.06	0.34	0.71	1.05E+03	1.32E+03	5.74E+48
DK_2696	1.3	1.3	1.3	0.12	0.73	0.08	0.11	0.95	4.11E+04	5.14E+04	6.34E+48
DK_2753	2.15	2.15	2.15	0.34	0.51	0.17	0.45	2.9	4.37E+05	5.47E+05	2.54E+50
DK_2752	2.18	2.18	2.18	0.38	0.51	0.17	0.46	2.98	3.17E+05	3.96E+05	1.60E+50
DK_2754	2.12	2.12	2.12	0.3	0.51	0.17	0.42	3.67	4.21E+05	5.26E+05	1.23E+50
DK_2935	1	1	1	0.15	0.58	0.1	0.07	0.31	2.33E+04	2.91E+04	3.36E+49
DK_2949	1.27	1.27	1.27	0.08	1.04	0.07	0.22	3.14	3.46E+04	4.32E+04	4.45E+48
DK_2959	1.28	1.28	1.28	0.12	1.09	0.08	0.34	1.78	5.21E+05	6.51E+05	3.83E+50
DK_3019	1.23	1.23	1.23	0.09	0.67	0.07	0.04	0.1	2.15E+04	2.69E+04	2.55E+49
DK_3025	1.19	1.19	1.19	0.12	0.53	0.07	0.06	0.38	3.95E+04	4.93E+04	1.43E+49
DK_3069	1.22	1.22	1.22	0.09	0.89	0.08	0.19	1.23	1.02E+05	1.27E+05	2.29E+49
DK_3071	1.06	1.06	1.06	0.15	0.75	0.1	0.13	0.48	3.92E+04	4.90E+04	9.26E+49
DK_759	1.55	1.55	1.55	0.1	0.56	0.13	0.13	0.5	2.38E+03	2.97E+03	2.14E+48
DK_3094	1.46	1.46	1.46	0.23	0.59	0.09	0.38	2.44	7.77E+05	9.71E+05	2.21E+50
DK_3095	1.37	1.37	1.37	0.12	0.76	0.08	0.19	1.63	1.38E+05	1.72E+05	3.04E+49
DK_3174	0.72	0.72	0.72	0.04	0.49	0.04	0.09	0.57	2.65E+04	3.31E+04	1.44E+49
DK_3226	1.61	1.61	1.61	0.1	0.7	0.07	0.11	0.73	1.04E+05	1.30E+05	3.62E+49
DK_690	1.36	1.36	1.36	0.16	1.23	0.05	0.22	0.95	3.56E+05	4.45E+05	2.42E+50
DK_3276	1.24	1.24	1.24	0.14	0.52	0.11	0.1	0.34	1.47E+05	1.84E+05	2.07E+50
DK_3280	1.66	1.66	1.66	0.35	0.58	0.33	0.32	0.31	1.08E+06	1.35E+06	5.48E+52
DK_3509	1.99	1.99	1.99	0.01	0.69	0.14	0.18	1.18	7.10E+04	8.88E+04	3.81E+49
DK_3516	1.14	1.14	1.14	0.07	0.86	0.04	0.09	0.82	3.72E+04	4.65E+04	8.72E+48
DK_3570	1.38	1.38	1.38	0.09	0.76	0.08	0.21	1.09	2.02E+05	2.52E+05	8.62E+49
DK_3644	1.45	1.45	1.45	0.19	0.73	0.12	0.18	0.69	9.52E+04	1.19E+05	1.88E+50
DK_3646	1.28	1.28	1.28	0.15	0.57	0.18	0.1	0.54	5.99E+04	7.48E+04	2.49E+49
DK_529	1.72	1.72	1.72	0.2	0.57	0.14	0.51	1.93	1.33E+06	1.66E+06	2.39E+51

DK_3824	1.4	1.4	1.4	0.11	0.73	0.11	0.21	1.35	9.81E+04	1.23E+05	3.93E+49
DK_3839	3.87	3.87	3.87	0.39	0.51	0.22	0.29	1.08	5.02E+05	6.27E+05	7.45E+50
DK_3832	1.28	1.28	1.28	0.12	0.91	0.06	0.24	1.07	4.61E+05	5.77E+05	5.26E+50
DK_3834	1.27	1.27	1.27	0.12	0.91	0.06	0.23	1.48	3.40E+05	4.25E+05	1.36E+50
DK_3848	1.39	1.39	1.39	0.29	0.73	0.11	0.18	0.79	6.27E+04	7.84E+04	5.30E+49
DK_3940	17.54	17.54	17.54	2.21	0.57	0.77	0.1	0.38	1.30E+05	1.62E+05	1.72E+50
DK_3990	1.42	1.42	1.42	0.28	0.7	0.09	0.1	0.44	1.82E+04	2.27E+04	1.85E+49
DK_4042	1.44	1.44	1.44	0.15	0.72	0.09	0.12	0.53	4.57E+04	5.71E+04	5.77E+49
DK_4304	1.28	1.28	1.28	0.2	1.08	0.05	0.19	1.22	2.64E+05	3.29E+05	7.33E+49
DK_4322	1.48	1.48	1.48	0.04	0.72	0.09	0.17	0.87	1.36E+05	1.70E+05	7.30E+49
DK_4370	0.86	0.86	0.86	0.07	0.6	0.06	0.21	0.57	1.20E+05	1.51E+05	5.02E+50
DK_383	0.86	0.86	0.86	0.02	0.56	0.09	0.07	0.48	1.15E+03	1.43E+03	2.61E+47
DK_4516	1.55	1.55	1.55	0.18	0.73	0.1	0.14	0.42	3.37E+05	4.22E+05	7.10E+50
DK_4513	15.69	15.69	15.69	1.66	0.46	1.23	0.25	0.74	5.19E+05	6.48E+05	1.60E+51
DK_4595	1.11	1.11	1.11	0.11	0.5	0.12	0.15	0.4	2.57E+05	3.21E+05	6.16E+50
DK_4856	1.26	1.26	1.26	0.1	1.02	0.07	0.25	0.94	1.16E+05	1.44E+05	1.85E+50
DK_4858	1.18	1.18	1.18	0.1	0.9	0.07	0.17	0.5	1.06E+05	1.32E+05	1.18E+50
DK_4877	1.43	1.43	1.43	0.12	0.74	0.09	0.21	1.34	2.29E+05	2.87E+05	6.31E+49
DK_4897	1.4	1.4	1.4	0.1	1.27	0.06	0.24	2.11	1.57E+05	1.96E+05	3.94E+49
DK_4918	1.02	1.02	1.02	0.3	0.8	0.1	0.15	0.98	4.47E+04	5.58E+04	1.40E+49
DK_33	1.03	1.03	1.03	0.04	0.9	0.04	0.06	0.41	9.83E+04	1.23E+05	2.30E+49
DK_5467	1.33	1.33	1.33	0.2	0.68	0.05	0.02	0.11	2.58E+02	3.22E+02	8.32E+46
DK_5558	1.26	1.26	1.26	0.04	0.84	0.08	0.17	1.45	6.06E+04	7.58E+04	7.22E+48
DK_5585	1.48	1.48	1.48	0.09	1.29	0.12	0.61	2.02	1.25E+06	1.56E+06	2.01E+51
DK_236	1.44	1.44	1.44	0.09	0.58	0.12	0.08	0.22	7.89E+04	9.86E+04	3.24E+50
DK_226	1.25	1.25	1.25	0.18	0.54	0.06	0.07	0.42	2.98E+02	3.73E+02	6.46E+46
DK_164	1.83	1.83	1.83	0.07	0.5	0.05	0.14	2.08	1.77E+05	2.21E+05	1.80E+49
DK_15	1.26	1.26	1.26	0.02	1.06	0.02	0.06	0.85	1.52E+04	1.90E+04	1.03E+48
DK_5	1.33	1.33	1.33	0.02	1.15	0.02	0.06	0.36	2.08E+04	2.60E+04	6.15E+48
DK_8	1.35	1.35	1.35	0.02	1.18	0.02	0.06	0.84	1.55E+04	1.93E+04	1.04E+48
DK_6	3.92	3.92	3.92	0.18	0.34	0.05	0.06	0.51	7.99E+03	9.99E+03	1.16E+48
DK_3909	1.03	1.03	1.03	0.1	0.73	0.12	0.14	2.07	4.70E+04	5.88E+04	2.63E+48
DK_42	1.16	1.16	1.16	0.03	0.8	0.03	0.04	0.37	2.04E+04	2.55E+04	4.10E+48
DK_1340	0.83	0.83	0.83	0.15	0.52	0.02	0.02	0.34	4.65E+01	5.81E+01	3.13E+45
DK_5550	1.37	1.37	1.37	0.06	0.79	0.04	0.13	1.94	1.33E+05	1.66E+05	1.29E+49
DK_b_335	1.02	1.02	1.02	0.44	0.74	0.18	0.2	1.73	4.25E+04	5.32E+04	1.39E+49
DK_977	1.46	1.46	1.46	0.23	0.57	0.05	0.23	1.95	5.30E+05	6.62E+05	6.28E+49
DK_940	2.19	2.19	2.19	0.12	0.57	0.1	0.19	1.68	3.88E+05	4.85E+05	6.37E+49
DK_2735	1.21	1.21	1.21	0.02	0.85	0.07	0.16	1.34	3.30E+04	4.13E+04	5.54E+48
DK_2842	1.76	1.76	1.76	0.11	0.72	0.13	0.25	2.15	6.07E+04	7.58E+04	1.52E+49
DK_2856	2.04	2.04	2.04	0.32	0.53	0.06	0.14	1.25	5.56E+04	6.95E+04	9.12E+48
DK_2878	1	1	1	0.05	0.55	0.07	0.07	0.56	4.26E+01	5.33E+01	9.68E+45
DK_2956	1.42	1.42	1.42	0.08	0.74	0.07	0.11	0.96	6.70E+04	8.38E+04	1.68E+49
DK_3046	1.33	1.33	1.33	0.1	0.78	0.06	0.2	1.74	4.20E+04	5.25E+04	9.57E+48
DK_3129	1.15	1.15	1.15	0.06	0.54	0.05	0.04	0.32	1.74E+04	2.18E+04	3.21E+48
DK_3442	0.98	0.98	0.98	0.26	0.76	0.11	0.14	1.18	3.30E+04	4.13E+04	8.00E+48
DK_3504	1.5	1.5	1.5	0.09	0.72	0.05	0.09	0.76	2.35E+04	2.93E+04	5.34E+48
DK_3521	1.01	1.01	1.01	0.34	0.74	0.13	0.15	2.14	2.84E+04	3.55E+04	2.94E+48
DK_3634	1.31	1.31	1.31	0.21	0.48	0.05	0.05	0.7	3.57E+03	4.46E+03	2.73E+47
DK_520	1.17	1.17	1.17	0.08	0.88	0.08	0.22	3.17	1.30E+05	1.63E+05	6.58E+48
DK_3738	1.42	1.42	1.42	0.05	0.69	0.04	0.12	1	4.72E+04	5.90E+04	9.02E+48
DK_420	1.13	1.13	1.13	0.34	0.72	0.08	0.06	0.56	3.06E+02	3.82E+02	5.55E+46
DK_405	1.34	1.34	1.34	0.19	0.5	0.04	0.04	0.33	4.34E+03	5.43E+03	6.75E+47
DK_4954	1.6	1.6	1.6	0.15	0.7	0.12	0.16	2.3	3.96E+04	4.95E+04	3.89E+48
DK_246	1.12	1.12	1.12	0.03	0.93	0.02	0.05	0.75	1.71E+04	2.13E+04	1.44E+48
DK_1335	1.15	1.15	1.15	0.12	0.96	0.04	0.12	1.77	3.82E+04	4.78E+04	2.71E+48
DK_195	1.19	1.19	1.19	0.04	0.93	0.04	0.08	0.67	2.11E+04	2.64E+04	4.47E+48
DK_186	1.28	1.28	1.28	0.02	1.1	0.04	0.12	1.75	8.54E+04	1.07E+05	5.17E+48
DK_976	1.39	1.39	1.39	0.25	0.51	0.05	0.06	0.49	1.37E+04	1.71E+04	1.43E+48
DK_2575	1.47	1.47	1.47	0.38	0.45	0.02	0.02	0.35	1.42E+02	1.78E+02	9.53E+45
DK_151	1.03	1.03	1.03	0.03	0.81	0.05	0.09	1.26	8.13E+04	1.02E+05	4.45E+48
DK_948	1.31	1.31	1.31	0.08	1.15	0.05	0.2	2.9	3.50E+05	4.38E+05	1.69E+49
DK_2855	1.9	1.9	1.9	0.42	0.5	0.06	0.15	1.34	3.23E+04	4.03E+04	4.33E+48

DK_b_808	0.89	0.89	0.89	0.38	0.56	0.05	0.04	0.31	2.39E+03	2.99E+03	3.50E+47
DK_73	1.34	1.34	1.34	0	1.19	0.04	0.14	1.19	2.49E+05	3.11E+05	3.17E+49
DK_67	1.43	1.43	1.43	0.16	0.52	0.04	0.04	0.58	9.72E+03	1.21E+04	7.43E+47
DK_5013	2.13	2.13	2.13	0.26	0.69	0.12	0.13	1.85	5.52E+04	6.90E+04	3.73E+48
DK_277	1.24	1.24	1.24	0.02	0.72	0.04	0.02	0.33	5.49E+03	6.86E+03	3.68E+47
DK_257	0.82	0.82	0.82	0.01	0.58	0.04	0.03	0.23	1.43E+03	1.79E+03	2.23E+47
DK_1991	1.1	1.1	1.1	0.03	0.81	0.04	0.06	0.54	2.79E+04	3.49E+04	4.57E+48
DK_228	1.49	1.49	1.49	0.2	0.47	0.05	0.08	0.72	1.99E+04	2.49E+04	2.84E+48
DK_2308	1.25	1.25	1.25	0.08	0.78	0.07	0.12	1.04	4.69E+04	5.87E+04	8.17E+48
DK_1125	1.07	1.07	1.07	0	0.73	0.03	0.03	0.25	2.95E+03	3.68E+03	5.92E+47
DK_175	0.95	0.95	0.95	0.06	0.47	0.02	0.03	0.25	2.45E+00	3.06E+00	3.94E+44
DK_170	1.21	1.21	1.21	0.18	0.51	0.02	0.02	0.27	1.32E+03	1.65E+03	6.63E+46
DK_158	1.19	1.19	1.19	0.04	0.8	0.04	0.07	0.57	5.40E+04	6.75E+04	6.87E+48
DK_3	1.37	1.37	1.37	0.01	1.18	0.02	0.06	0.54	1.78E+04	2.22E+04	2.61E+48
DK_137	1.14	1.14	1.14	0.12	0.54	0.05	0.07	0.56	2.52E+02	3.15E+02	3.51E+46
DK_126	4.39	4.39	4.39	0.47	0.56	0.1	0.1	1.41	7.63E+04	9.54E+04	3.32E+48
DK_b_277	1.45	1.45	1.45	0.51	0.42	0.03	0.05	0.4	1.19E+02	1.49E+02	1.64E+46
DK_3474	1.06	1.06	1.06	0.04	0.75	0.05	0.04	0.36	7.52E+03	9.40E+03	1.39E+48
DK_86	1.48	1.48	1.48	0.08	0.52	0.03	0.03	0.47	1.10E+04	1.37E+04	1.05E+48
DK_546	1.06	1.06	1.06	0.1	0.85	0.01	0.02	0.21	1.65E+03	2.06E+03	2.42E+47
DK_79	1.22	1.22	1.22	0.05	0.93	0.02	0.05	0.4	1.24E+04	1.55E+04	1.82E+48
DK_3901	1.06	1.06	1.06	0.11	0.8	0.07	0.08	0.52	3.66E+04	4.57E+04	1.08E+49
DK_b_526	0.8	0.8	0.8	0.28	0.55	0.1	0.1	1.47	1.30E+04	1.62E+04	1.06E+48
DK_1544	1.6	1.6	1.6	0.04	0.5	0.12	0.48	4.15	1.04E+06	1.31E+06	1.54E+50
DK_1763	1.15	1.15	1.15	0.15	0.83	0.03	0.05	0.44	3.30E+03	4.13E+03	6.31E+47
DK_1833	2.06	2.06	2.06	0.15	0.52	0.05	0.13	1.89	1.43E+05	1.79E+05	1.03E+49
DK_1473	1.26	1.26	1.26	0.13	0.92	0.09	0.3	2.63	1.32E+05	1.66E+05	1.59E+49
DK_2115	1.23	1.23	1.23	0.09	0.75	0.03	0.04	0.65	6.49E+03	8.12E+03	6.26E+47
DK_1238	1.24	1.24	1.24	0.07	1.02	0.04	0.12	1.04	3.24E+04	4.04E+04	3.53E+48
DK_2141	5.81	5.81	5.81	0.33	0.53	0.41	0.33	2.83	1.86E+05	2.32E+05	5.42E+49
DK_2168	2.48	2.48	2.48	0.18	0.59	0.11	0.19	1.67	1.10E+06	1.37E+06	1.26E+50
DK_2190	1.29	1.29	1.29	0.24	0.5	0.05	0.07	0.6	8.33E+03	1.04E+04	1.22E+48
DK_2307	1.23	1.23	1.23	0.07	0.82	0.08	0.16	1.41	1.25E+05	1.56E+05	2.00E+49
DK_2350	2.06	2.06	2.06	0.12	0.52	0.14	0.44	3.8	5.63E+05	7.04E+05	1.24E+50
DK_1115	1.44	1.44	1.44	0.25	0.58	0.14	0.61	5.31	2.58E+06	3.22E+06	2.89E+50
DK_1000	1.21	1.21	1.21	0.23	0.79	0.07	0.15	1.33	7.32E+03	9.14E+03	1.45E+48
DK_2533	1.78	1.78	1.78	0.28	0.42	0.05	0.19	1.62	2.66E+04	3.33E+04	2.91E+48
DK_962	1.22	1.22	1.22	0.01	0.91	0.06	0.15	0.98	6.14E+04	7.68E+04	1.87E+49
DK_2606	1.19	1.19	1.19	0.07	0.53	0.04	0.03	0.29	1.05E+04	1.31E+04	2.37E+48
DK_14	1.59	1.59	1.59	0.07	0.4	0.03	0.05	0.44	2.27E+04	2.83E+04	2.54E+48
DK_12	1.46	1.46	1.46	0.02	1.28	0.03	0.13	1.15	5.81E+04	7.27E+04	6.53E+48
DK_2	1.46	1.46	1.46	0.01	1.29	0.02	0.09	0.81	4.29E+04	5.36E+04	7.03E+48
DK_2725	1.09	1.09	1.09	0.07	0.59	0.07	0.03	0.26	2.83E+03	3.54E+03	5.42E+47
DK_862	2.17	2.17	2.17	0.31	0.55	0.08	0.19	2.77	1.59E+05	1.98E+05	8.62E+48
DK_2885	1.02	1.02	1.02	0.08	0.76	0.09	0.14	1.23	3.61E+04	4.51E+04	4.97E+48
DK_2909	0.99	0.99	0.99	0.22	0.75	0.17	0.18	1.52	7.69E+04	9.61E+04	1.21E+49
DK_3012	0.73	0.73	0.73	0.03	0.52	0.03	0.03	0.28	2.69E+04	3.36E+04	3.95E+48
DK_3157	1.19	1.19	1.19	0.14	0.54	0.04	0.03	0.45	1.10E+04	1.38E+04	5.12E+47
DK_719	1.64	1.64	1.64	0.2	0.68	0.17	0.11	0.96	6.99E+04	8.73E+04	9.02E+48
DK_652	1.29	1.29	1.29	0.05	0.71	0.06	0.07	0.56	5.74E+04	7.17E+04	7.09E+48
DK_3330	1.18	1.18	1.18	0.16	0.58	0.06	0.03	0.27	3.35E+03	4.18E+03	8.57E+47
DK_3372	1.24	1.24	1.24	0.02	0.75	0.02	0.02	0.14	3.79E+03	4.74E+03	5.51E+47
DK_3460	1.46	1.46	1.46	0.03	0.42	0.08	0.12	1.02	7.20E+04	9.00E+04	1.29E+49
DK_3718	1.04	1.04	1.04	0.14	0.8	0.03	0.05	0.66	5.57E+03	6.97E+03	3.77E+47
DK_3717	1.04	1.04	1.04	0.14	0.8	0.04	0.06	0.48	6.90E+03	8.62E+03	1.57E+48
DK_3766	1.29	1.29	1.29	0.1	0.56	0.08	0.05	0.44	2.32E+04	2.89E+04	2.42E+48
DK_4085	1.27	1.27	1.27	0.05	0.74	0.03	0.03	0.28	6.05E+03	7.57E+03	8.87E+47
DK_4913	1.13	1.13	1.13	0.06	0.95	0.05	0.17	1.46	2.89E+05	3.61E+05	3.50E+49
DK_1610	0.98	0.98	0.98	0.09	0.77	0.07	0.09	0.75	3.22E+04	4.03E+04	4.01E+48
DK_1680	1.74	1.74	1.74	0.12	0.58	0.03	0.08	0.65	4.21E+04	5.26E+04	6.19E+48
DK_4939	1.68	1.68	1.68	0.17	0.71	0.05	0.12	1	3.69E+04	4.61E+04	8.11E+48
DK_1761	1.28	1.28	1.28	0.31	1.06	0.03	0.13	1.12	2.17E+03	2.71E+03	4.78E+47
DK_1523	1.66	1.66	1.66	0.23	0.58	0.07	0.19	2.73	1.79E+05	2.24E+05	1.21E+49

DK_1824	0.99	0.99	0.99	0.1	0.72	0.13	0.13	1.09	4.73E+04	5.91E+04	6.66E+48
DK_265	1.43	1.43	1.43	0.12	0.47	0.08	0.11	0.95	1.71E+05	2.14E+05	2.13E+49
DK_260	2.12	2.12	2.12	0.3	0.38	0.07	0.21	1.85	1.73E+04	2.16E+04	2.65E+48
DK_5559	1.26	1.26	1.26	0.05	0.88	0.07	0.17	1.51	1.41E+05	1.76E+05	2.25E+49
DK_1305	0.86	0.86	0.86	0	0.57	0.06	0.05	0.41	7.32E+02	9.15E+02	1.20E+47
DK_1256	1.19	1.19	1.19	0.3	0.89	0.04	0.12	1.74	2.78E+03	3.47E+03	1.44E+47
DK_1232	1.4	1.4	1.4	0.26	0.72	0.03	0.04	0.58	2.26E+03	2.82E+03	2.17E+47
DK_1231	1.26	1.26	1.26	0.23	0.77	0.03	0.06	0.9	3.26E+03	4.07E+03	2.36E+47
DK_2171	1.46	1.46	1.46	0.02	0.79	0.19	0.52	4.53	1.48E+05	1.85E+05	3.56E+49
DK_207	1.19	1.19	1.19	0.02	0.94	0.04	0.1	0.84	3.49E+04	4.36E+04	7.94E+48
DK_2263	1.2	1.2	1.2	0.15	0.53	0.1	0.15	1.31	1.02E+02	1.27E+02	2.13E+46
DK_2283	1.29	1.29	1.29	0.04	1.08	0.05	0.18	1.56	9.41E+04	1.18E+05	1.29E+49
DK_2288	1.66	1.66	1.66	0.73	0.41	0.03	0.04	0.52	6.56E+01	8.20E+01	4.98E+45
DK_2297	1.36	1.36	1.36	0	1.24	0.04	0.17	1.44	3.40E+05	4.25E+05	4.79E+49
DK_1139	1.73	1.73	1.73	0.08	0.59	0.12	0.42	6.11	1.43E+06	1.78E+06	8.92E+49
DK_1135	1.49	1.49	1.49	0.14	0.54	0.1	0.1	0.87	4.32E+01	5.40E+01	9.94E+45
DK_179	1.46	1.46	1.46	0.13	1.29	0.03	0.15	2.22	8.77E+03	1.10E+04	4.62E+47
DK_171	1.97	1.97	1.97	0.26	0.56	0.03	0.06	0.49	1.41E+04	1.76E+04	2.06E+48
DK_1037	1.09	1.09	1.09	0.12	0.7	0.04	0.05	0.4	1.01E+04	1.27E+04	2.70E+48
DK_2458	1.43	1.43	1.43	0.06	0.45	0.06	0.12	1.03	2.59E+01	3.23E+01	4.60E+45
DK_2534	1.94	1.94	1.94	0.19	0.54	0.05	0.13	1.14	7.71E+04	9.64E+04	1.20E+49
DK_2572	0.99	0.99	0.99	0.3	0.75	0.09	0.1	0.85	2.30E+04	2.87E+04	3.38E+48
DK_138	0.95	0.95	0.95	0.02	0.56	0.04	0.04	0.34	1.88E+02	2.36E+02	3.27E+46
DK_2778	3.13	3.13	3.13	0.29	0.54	0.26	0.25	3.59	2.57E+05	3.22E+05	1.46E+49
DK_860	1.7	1.7	1.7	0.33	0.51	0.06	0.26	2.26	1.72E+05	2.14E+05	2.06E+49
DK_2953	1.05	1.05	1.05	0.08	0.85	0.06	0.1	0.84	6.16E+04	7.70E+04	1.24E+49
DK_2974	1.52	1.52	1.52	0.32	0.54	0.1	0.1	0.89	5.52E+01	6.90E+01	8.68E+45
DK_783	7.04	7.04	7.04	0.37	4.57	0.15	0.06	0.81	7.14E+03	8.92E+03	5.57E+47
DK_2996	0.66	0.66	0.66	0.03	0.39	0.04	0.19	2.75	3.07E+04	3.84E+04	3.64E+48
DK_3035	1.05	1.05	1.05	0.19	0.71	0.1	0.09	0.81	8.14E+03	1.02E+04	2.44E+48
DK_3067	1.18	1.18	1.18	0.1	0.52	0.07	0.07	1	7.83E+04	9.79E+04	3.95E+48
DK_746	1.65	1.65	1.65	0.35	0.42	0.07	0.13	1.93	8.06E+03	1.01E+04	3.94E+47
DK_738	1.18	1.18	1.18	0.06	0.73	0.08	0.08	0.72	9.30E+03	1.16E+04	1.55E+48
DK_3137	1.32	1.32	1.32	0.1	1.14	0.09	0.39	5.66	4.94E+04	6.17E+04	5.91E+48
DK_3196	1.46	1.46	1.46	0.18	0.57	0.05	0.21	1.8	4.53E+05	5.67E+05	5.77E+49
DK_3205	1.18	1.18	1.18	0.06	0.45	0.04	0.05	0.45	1.60E+04	2.00E+04	3.51E+48
DK_687	1.51	1.51	1.51	0.1	1.38	0.03	0.09	1.34	4.35E+03	5.43E+03	3.34E+47
DK_3269	1.39	1.39	1.39	0.2	0.57	0.21	0.13	1.12	4.70E+04	5.87E+04	5.29E+48
DK_95	1.42	1.42	1.42	0.29	1.27	0.04	0.16	1.4	1.66E+04	2.07E+04	1.93E+48
DK_96	0.95	0.95	0.95	0.09	0.74	0.02	0.02	0.2	4.92E+03	6.14E+03	5.89E+47
DK_3379	1.86	1.86	1.86	0.17	0.49	0.04	0.11	1.61	4.55E+04	5.68E+04	2.84E+48
DK_b_793	0.83	0.83	0.83	0.3	0.55	0.05	0.04	0.63	1.72E+03	2.15E+03	1.16E+47
DK_597	1.2	1.2	1.2	0.34	0.85	0.04	0.09	0.82	2.54E+02	3.18E+02	3.89E+46
DK_592	1.04	1.04	1.04	0	0.55	0.07	0.1	0.84	1.44E+02	1.80E+02	3.68E+46
DK_3593	1.19	1.19	1.19	0.15	0.99	0.05	0.12	1	3.08E+04	3.85E+04	7.01E+48
DK_3740	1.56	1.56	1.56	0.05	0.75	0.04	0.07	0.6	5.51E+04	6.89E+04	8.10E+48
DK_496	0.99	0.99	0.99	0.03	0.57	0.04	0.03	0.28	2.42E+02	3.02E+02	2.71E+46
DK_3866	1.26	1.26	1.26	0.12	0.72	0.14	0.17	1.51	6.98E+04	8.72E+04	9.66E+48
DK_3907	1.17	1.17	1.17	0.05	1	0.07	0.18	1.52	2.69E+05	3.36E+05	5.57E+49
DK_416	1.51	1.51	1.51	0.32	0.43	0.04	0.06	0.56	2.15E+03	2.68E+03	2.49E+47
DK_4218	1.01	1.01	1.01	0.06	0.54	0.06	0.04	0.34	2.08E+04	2.60E+04	4.20E+48
DK_58	2.3	2.3	2.3	0.1	0.53	0.03	0.05	0.78	3.22E+04	4.03E+04	2.17E+48
DK_57	1.3	1.3	1.3	0.04	0.53	0.03	0.02	0.29	6.47E+03	8.09E+03	5.38E+47
DK_4666	1.19	1.19	1.19	0.07	0.69	0.07	0.07	0.57	1.24E+04	1.56E+04	3.50E+48
DK_335	18.79	18.79	18.79	4.25	0.39	0.41	0.11	0.95	1.24E+03	1.55E+03	1.32E+47
DK_4766	3.05	3.05	3.05	0.4	2.31	0.4	0.44	6.38	3.79E+01	4.74E+01	2.81E+45
DK_4776	1.11	1.11	1.11	0.1	0.56	0.07	0.05	0.42	5.94E+03	7.43E+03	1.61E+48
DK_4796	1.2	1.2	1.2	0.04	0.68	0.15	0.09	1.34	3.15E+04	3.94E+04	2.16E+48
DK_304	0.83	0.83	0.83	0.05	0.57	0.04	0.03	0.3	6.89E+02	8.62E+02	8.77E+46
DK_5044	1.35	1.35	1.35	0.06	0.39	0.05	0.09	1.33	8.87E+04	1.11E+05	6.00E+48
DK_5315	1.43	1.43	1.43	0.33	0.81	0.04	0.13	1.1	3.38E+03	4.23E+03	7.45E+47
DK_262	1.04	1.04	1.04	0.04	0.71	0.05	0.03	0.25	3.89E+03	4.87E+03	4.94E+47
DK_203	1.91	1.91	1.91	0.1	0.51	0.08	0.28	2.4	1.43E+06	1.79E+06	1.49E+50

DK_178	1.35	1.35	1.35	0.04	0.77	0.03	0.06	0.48	1.91E+04	2.39E+04	3.41E+48
DK_180	1.3	1.3	1.3	0.04	1.07	0.03	0.08	1.17	7.07E+03	8.83E+03	5.97E+47
DK_22	1.1	1.1	1.1	0.02	0.84	0.02	0.03	0.24	1.02E+04	1.28E+04	1.50E+48
DK_19	1.45	1.45	1.45	0.03	1.29	0.03	0.09	0.79	4.57E+04	5.71E+04	7.49E+48
DK_159	1.74	1.74	1.74	0.27	0.41	0.05	0.19	2.78	1.10E+04	1.37E+04	1.21E+48
DK_157	1.32	1.32	1.32	0.05	1.2	0.05	0.18	1.59	5.62E+05	7.03E+05	6.10E+49
DK_143	1.43	1.43	1.43	0.01	1.31	0.05	0.19	1.62	2.04E+05	2.55E+05	2.48E+49
DK_118	1.26	1.26	1.26	0.19	1.14	0.06	0.17	1.43	1.67E+05	2.09E+05	2.38E+49
DK_88	1.51	1.51	1.51	0.1	1.4	0.03	0.11	0.98	4.91E+04	6.14E+04	6.25E+48
DK_84	1.25	1.25	1.25	0.04	1.12	0.03	0.12	1.06	2.14E+05	2.67E+05	3.51E+49
DK_80	1.53	1.53	1.53	0.04	1.42	0.05	0.28	2.39	1.14E+05	1.43E+05	1.82E+49
DK_77	0.78	0.78	0.78	0.04	0.52	0.03	0.08	1.22	1.02E+01	1.28E+01	6.53E+44
DK_40	1.21	1.21	1.21	0.03	0.85	0.03	0.06	0.83	3.07E+04	3.84E+04	2.08E+48
DK_39	1.21	1.21	1.21	0.02	0.84	0.03	0.06	0.37	4.36E+04	5.45E+04	1.07E+49
DK_32	1.28	1.28	1.28	0.03	1.15	0.02	0.06	0.56	3.54E+04	4.42E+04	5.80E+48
DK_24	1.44	1.44	1.44	0.01	1.29	0.02	0.09	1.26	3.69E+04	4.62E+04	1.86E+48
DK_20	1.19	1.19	1.19	0.03	0.95	0.02	0.04	0.65	1.23E+04	1.53E+04	9.39E+47
DK_18	1.11	1.11	1.11	0.03	0.78	0.03	0.03	0.37	5.77E+03	7.21E+03	3.87E+47

Table A.0.22: Uncertainties of the values of table 5.3 arranged in the same order. Columns 1 contains the name of the catalog shell. Columns 2 and 3 contain the uncertainties of the possible two distance solutions of the tangential point method calculation $\Delta D_{\mathrm{s,a}}$ and $\Delta D_{\mathrm{s,b}}$ respectively. Column 4 contains the uncertainties of the derived final distance towards the Sun. Columns 5 and 6 contain the uncertainties of the z-height of the shell from the galactic plane, Δz, and the distance towards the galactic center ΔD_{gc}, respectively. The uncertainties of the minimum- and maximum radius ΔR_{min} and ΔR_{max} can be found in columns 7 and 8. Column 9 contains the uncertainty of the age of the shell, $\Delta \tau$, while columns 10 and 11 list the uncertainty of the H I mass $\Delta M_{\mathrm{H\,I}}$ and the ones of the total mass ΔM_{tot} respectively. Column 12 contains the derived kinetic energy of the shell ΔE_{kin}. For more information see text in section 5.3.

1	2	3	4	5	6	7	8	9	10
name:	V_{sh}	n_{obs}	$n_{\mathrm{obs,u}}$	$E_{\mathrm{w}}(t)$	$E_{\mathrm{w,u}}(t)$	$E_{\mathrm{c}}(t)$	$E_{\mathrm{c,u}}(t)$	ϵ_{w}	$\epsilon_{\mathrm{w,l}}$
unit:	kpc^3	cm^{-3}	cm^{-3}	erg	erg	erg	erg	-	-
DK_1476	4.37E+00	2.03E-02	7.23E+00	1.38E+50	4.91E+52	8.29E+51	5.98E+54	0.86	2.43E-03
DK_2046	9.46E-01	1.40E-01	1.17E+01	3.34E+51	2.80E+53	1.17E+53	1.67E+55	1.75	2.09E-02
DK_1303	1.57E+01	8.85E-02	8.74E+01	3.52E+52	3.48E+55	9.83E+53	2.22E+57	1.24	1.25E-03
DK_1286	9.84E-02	2.93E-01	2.48E+00	6.12E+50	5.17E+51	2.07E+52	2.26E+53	1.67	1.97E-01
DK_1188	1.92E+00	1.62E-01	2.56E+01	4.41E+51	6.98E+53	2.00E+53	5.82E+55	1.54	9.69E-03
DK_1187	2.14E+00	1.57E-01	2.84E+01	5.89E+51	1.06E+54	2.35E+53	7.91E+55	1.61	8.91E-03
DK_1119	1.76E-02	1.05E+00	1.31E+00	5.16E+49	6.40E+49	2.89E+51	3.68E+51	0.94	7.58E-01
DK_857	3.74E-02	3.80E-01	1.25E+00	2.49E+50	8.17E+50	5.95E+51	2.25E+52	1.67	5.09E-01
DK_810	2.77E-02	6.75E-01	1.17E+00	2.65E+50	4.59E+50	1.01E+52	1.87E+52	1.16	6.71E-01
DK_3462	4.28E+00	9.33E-02	3.39E+01	4.48E+51	1.63E+54	2.09E+53	1.54E+56	1.53	4.21E-03
DK_457	5.17E-01	2.20E-01	8.56E+00	2.42E+51	9.40E+52	9.72E+52	5.86E+54	1.46	3.75E-02
DK_1619	3.33E-01	1.94E-01	5.73E+00	2.22E+51	6.57E+52	7.17E+52	3.19E+54	1.8	6.08E-02
DK_1701	1.17E-01	2.04E-01	1.82E+00	1.51E+50	1.34E+51	6.76E+51	7.82E+52	1.24	1.40E-01
DK_1452	2.29E-01	6.07E-01	9.01E+00	6.04E+50	8.97E+51	3.35E+52	6.87E+53	0.98	6.62E-02
DK_1117	2.44E-01	2.75E-01	5.39E+00	1.69E+51	3.32E+52	6.08E+52	1.70E+54	1.59	8.10E-02
DK_960	1.34E+00	6.09E-02	6.76E+00	2.27E+50	2.52E+52	1.07E+52	2.09E+54	1.11	9.97E-03
DK_3275	2.30E+00	7.06E-02	1.21E+01	7.08E+50	1.21E+53	2.75E+52	8.74E+54	1.13	6.58E-03
DK_3297	2.60E-01	2.04E-01	4.50E+00	7.53E+50	1.66E+52	3.24E+52	1.04E+54	1.58	7.15E-02
DK_3295	1.77E-01	2.02E-01	2.84E+00	3.06E+50	4.30E+51	1.64E+52	3.16E+53	1.37	9.79E-02
DK_3296	2.23E-01	1.94E-01	3.55E+00	4.86E+50	8.87E+51	2.20E+52	5.69E+53	1.47	8.08E-02
DK_3639	3.83E+00	4.20E-02	1.39E+01	2.28E+51	7.54E+53	8.31E+52	5.51E+55	1.6	4.85E-03
DK_b_823	1.98E-02	1.71E-02	2.88E-02	2.12E+48	3.58E+48	1.05E+50	1.89E+50	1.4	8.30E-01
DK_1580	4.33E-01	2.00E-01	6.42E+00	1.23E+51	3.94E+52	4.95E+52	2.41E+54	1.38	4.29E-02
DK_1527	1.57E-01	2.01E-01	1.65E+00	1.98E+50	1.62E+51	7.72E+51	8.15E+52	0.86	1.05E-01
DK_5129	2.11E+00	6.00E-02	8.94E+00	2.22E+51	3.30E+53	7.86E+52	2.13E+55	1.35	9.04E-03
DK_1483	1.21E-02	9.35E-01	8.90E-01	3.15E+49	3.00E+49	1.33E+51	1.26E+51	1.05	1.10E+00
DK_1828	1.75E-01	1.51E-01	1.84E+00	7.38E+49	8.98E+50	3.58E+51	5.89E+52	0.93	7.61E-02
DK_1965	9.99E-03	3.19E-01	2.55E-01	2.73E+49	2.18E+49	8.57E+50	6.68E+50	1.39	1.73E+00

DK_1281	5.10E-03	1.22E+00	2.82E-01	9.70E+48	2.24E+48	7.28E+50	1.41E+50	0.48	2.08E+00
DK_165	3.81E-02	3.52E-01	1.15E+00	1.15E+50	3.76E+50	4.40E+51	1.66E+52	1.49	4.55E-01
DK_928	1.68E-01	2.48E-01	3.55E+00	5.93E+50	8.48E+51	1.58E+52	3.10E+53	1.58	1.10E-01
DK_2819	2.43E-01	5.68E-01	7.62E+00	9.71E+51	1.30E+53	2.93E+53	5.37E+54	1.17	8.72E-02
DK_2820	5.58E-02	1.10E-01	5.09E-01	3.87E+49	1.78E+50	9.50E+50	5.26E+51	1.35	2.94E-01
DK_2873	1.24E-01	9.12E-01	4.78E+00	7.12E+50	3.73E+51	3.30E+52	2.11E+53	0.69	1.32E-01
DK_3145	1.38E+00	7.64E-02	8.52E+00	4.60E+50	5.13E+52	1.77E+52	3.47E+54	1.22	1.10E-02
DK_104	1.79E-02	3.97E-01	6.22E-01	6.08E+49	9.53E+49	2.59E+51	4.29E+51	1.52	9.68E-01
DK_3277	1.40E-01	2.39E-01	2.78E+00	3.76E+50	4.37E+51	1.71E+52	2.67E+53	1.49	1.28E-01
DK_635	8.68E-02	2.02E-01	1.48E+00	1.50E+50	1.10E+51	5.58E+51	5.18E+52	1.46	2.00E-01
DK_4220	2.21E-01	3.06E-01	4.23E+00	5.80E+50	8.00E+51	2.05E+52	3.88E+53	1.08	7.84E-02
DK_1514	2.88E+00	1.68E-01	4.23E+01	1.43E+52	3.61E+54	4.85E+53	2.37E+56	1.75	6.95E-03
DK_1785	3.12E-02	3.46E-01	7.86E-01	3.00E+49	6.82E+49	1.86E+51	4.67E+51	0.97	4.28E-01
DK_1783	1.16E-01	1.70E-01	1.78E+00	1.70E+50	1.77E+51	7.05E+51	9.74E+52	1.55	1.49E-01
DK_1784	3.60E-02	3.10E-01	8.31E-01	1.25E+50	3.35E+50	4.56E+51	1.37E+52	1.34	5.01E-01
DK_5209	7.66E-02	1.95E-01	6.67E-01	1.02E+49	3.50E+49	1.56E+51	6.18E+51	0.27	7.86E-02
DK_1846	1.23E-02	7.06E-01	6.90E-01	2.58E+50	2.52E+50	7.83E+51	7.64E+51	1.59	1.62E+00
DK_5238	2.55E-02	2.22E-01	3.82E-01	8.81E+48	1.52E+49	5.75E+50	1.05E+51	0.72	4.16E-01
DK_1389	1.12E+01	4.28E-02	3.44E+01	3.00E+51	2.41E+54	1.53E+53	2.74E+56	1.18	1.47E-03
DK_2009	1.30E-01	1.40E-04	1.50E-03	5.06E+46	5.41E+47	1.05E+48	1.49E+49	1.1	1.03E-01
DK_1299	1.48E-02	4.29E-01	4.27E-01	1.76E+49	1.75E+49	1.09E+51	1.08E+51	0.9	9.04E-01
DK_1267	5.36E-01	6.77E-02	2.95E+00	5.64E+49	2.46E+51	3.60E+51	2.47E+53	0.86	1.98E-02
DK_1221	3.54E-02	4.85E-01	1.51E+00	3.64E+50	1.13E+51	1.16E+52	4.14E+52	1.71	5.49E-01
DK_930	2.30E-01	1.81E-01	3.08E+00	1.81E+50	3.08E+51	1.02E+52	2.45E+53	1.12	6.58E-02
DK_120	2.00E-02	5.11E-01	8.98E-01	1.15E+50	2.02E+50	3.88E+51	7.28E+51	1.58	9.00E-01
DK_756	4.28E-02	5.73E-01	2.10E+00	5.21E+50	1.91E+51	1.98E+52	8.48E+52	1.66	4.54E-01
DK_b_785	1.69E-01	6.47E-03	8.04E-02	1.55E+49	1.93E+50	4.34E+50	7.30E+51	1.37	1.10E-01
DK_656	7.11E+00	9.55E-02	6.03E+01	2.34E+52	1.48E+55	7.43E+53	1.02E+57	1.79	2.85E-03
DK_3575	3.12E-01	3.54E-01	8.91E+00	6.94E+50	1.75E+52	3.46E+52	1.28E+54	1.32	5.25E-02
DK_3584	4.12E+00	8.01E-02	2.11E+01	2.83E+51	7.45E+53	1.38E+53	7.11E+55	1.11	4.20E-03
DK_562	1.62E+01	4.92E-02	6.61E+01	2.36E+52	3.18E+55	7.39E+53	2.36E+57	1.66	1.24E-03
DK_3668	1.25E+00	8.55E-03	6.93E-01	9.18E+49	7.44E+51	2.93E+51	4.02E+53	1.12	1.38E-02
DK_456	4.38E-02	3.29E-02	1.13E-01	4.01E+48	1.38E+49	1.90E+50	7.58E+50	1.05	3.05E-01
DK_4380	4.57E-02	5.91E-01	1.58E+00	4.73E+50	1.26E+51	1.75E+52	5.24E+52	1.11	4.17E-01
DK_4593	4.14E-01	1.33E-01	2.92E+00	4.70E+50	1.04E+52	1.99E+52	6.36E+53	0.92	4.19E-02
DK_4719	1.24E+00	6.02E-02	6.33E+00	1.31E+51	1.37E+53	2.88E+52	5.29E+54	1.62	1.54E-02
DK_1668	2.19E+01	2.58E-02	4.50E+01	3.55E+51	6.20E+54	1.53E+53	6.54E+56	1.31	7.49E-04
DK_1601	1.55E-02	4.66E-03	6.19E-03	2.01E+47	2.68E+47	5.85E+48	8.05E+48	1.14	8.58E-01
DK_1555	5.36E-03	6.42E-01	1.99E-01	9.57E+48	2.97E+48	4.81E+50	1.30E+50	0.77	2.49E+00
DK_1528	2.77E-01	9.75E-02	1.41E+00	7.51E+49	1.09E+51	2.73E+51	5.46E+52	0.7	4.82E-02
DK_294	1.30E-01	2.08E-04	2.26E-03	4.21E+46	4.56E+47	1.27E+48	1.83E+49	0.88	8.16E-02
DK_1861	4.00E-02	1.59E-01	5.18E-01	1.76E+49	5.76E+49	8.13E+50	3.06E+51	1.09	3.34E-01
DK_1906	9.37E-02	2.30E-01	1.59E+00	6.00E+49	4.13E+50	2.32E+51	2.01E+52	0.98	1.42E-01
DK_1400	6.86E-02	8.45E-01	4.21E+00	3.64E+50	1.81E+51	2.17E+52	1.31E+53	1.19	2.39E-01
DK_1958	4.82E-01	9.93E-02	4.06E+00	4.10E+50	1.68E+52	1.69E+52	1.08E+54	1.47	3.59E-02
DK_5458	3.94E-02	5.64E-01	1.54E+00	4.72E+50	1.29E+51	1.66E+52	5.14E+52	1.35	4.92E-01
DK_1983	4.38E-02	2.36E-01	7.85E-01	4.51E+49	1.50E+50	2.46E+51	9.44E+51	1.15	3.46E-01
DK_1993	1.53E-01	5.07E-02	6.30E-01	2.15E+49	2.68E+50	9.13E+50	1.53E+52	1.09	8.74E-02
DK_1331	3.30E-02	6.98E-02	2.02E-01	1.01E+49	2.91E+49	2.06E+50	6.77E+50	1.33	4.58E-01
DK_2034	6.05E-01	4.57E-02	2.43E+00	1.21E+50	6.42E+51	4.22E+51	3.62E+53	1.33	2.50E-02
DK_2320	1.34E-01	1.15E-01	1.37E+00	4.30E+49	5.13E+50	2.48E+51	3.99E+52	1.18	9.93E-02
DK_2335	7.03E+00	4.24E-02	2.47E+01	4.23E+51	2.47E+54	1.72E+53	2.16E+56	1.54	2.64E-03
DK_2351	4.74E-03	6.93E-01	2.32E-01	5.12E+48	1.71E+48	3.57E+50	1.05E+50	0.75	2.23E+00
DK_2389	4.95E-03	4.27E-01	1.64E-01	5.87E+48	2.26E+48	3.47E+50	1.19E+50	1.04	2.70E+00
DK_2496	9.53E-01	4.72E-01	1.99E+01	6.99E+50	2.95E+52	5.77E+52	3.81E+54	0.47	1.11E-02
DK_2513	8.20E-02	1.09E-01	7.56E-01	2.49E+49	1.72E+50	1.40E+51	1.22E+52	1.12	1.63E-01
DK_1011	4.69E-01	5.18E-02	2.01E+00	4.26E+50	1.65E+52	1.40E+52	8.41E+53	1.58	4.06E-02
DK_2595	4.18E+01	8.90E-03	3.27E+01	1.03E+51	3.79E+54	4.45E+52	4.37E+56	1.17	3.20E-04
DK_2598	2.08E+00	1.49E-01	1.75E+01	5.45E+51	6.39E+53	2.16E+53	4.47E+55	1.07	9.15E-03
DK_2663	1.78E+00	7.39E-02	1.04E+01	1.87E+51	2.64E+53	7.69E+52	1.97E+55	1.48	1.04E-02
DK_919	2.10E-01	1.01E-01	1.86E+00	1.33E+50	2.45E+51	3.40E+51	8.90E+52	1.44	7.82E-02
DK_2740	4.38E-01	1.70E-01	5.25E+00	5.10E+49	1.57E+51	1.58E+52	7.38E+53	0.42	1.37E-02
DK_2779	2.91E-01	7.98E-02	2.09E+00	1.01E+50	2.64E+51	5.23E+51	2.02E+53	1.36	5.21E-02

DK_798	4.07E+00	1.13E-01	3.20E+01	1.17E+52	3.29E+54	4.21E+53	2.34E+56	1.37	4.86E-03
DK_3004	2.64E-01	1.13E-01	2.29E+00	3.36E+50	6.78E+51	8.12E+51	2.35E+53	1.38	6.82E-02
DK_3099	1.63E+00	5.81E-02	7.96E+00	1.34E+51	1.84E+53	2.55E+52	6.31E+54	1.56	1.14E-02
DK_737	6.57E-01	9.14E-02	5.07E+00	9.34E+49	5.18E+51	6.23E+51	5.60E+53	0.89	1.61E-02
DK_3187	2.85E-01	5.77E-02	1.41E+00	1.41E+50	3.45E+51	3.02E+51	1.08E+53	1.49	6.08E-02
DK_609	5.58E-03	1.17E-02	5.11E-03	2.84E+47	1.24E+47	8.43E+48	3.34E+48	1.19	2.71E+00
DK_3489	6.81E-02	3.26E-01	1.49E+00	9.68E+49	4.40E+50	3.93E+51	2.15E+52	1.01	2.22E-01
DK_3722	5.78E-01	2.84E-01	1.21E+01	4.57E+50	1.94E+52	2.51E+52	1.68E+54	0.98	2.31E-02
DK_3745	8.11E-02	2.38E-01	1.66E+00	1.65E+50	1.15E+51	7.05E+51	6.20E+52	1.49	2.14E-01
DK_3833	1.64E-02	7.70E-01	1.01E+00	5.49E+49	7.17E+49	2.82E+51	3.80E+51	1.21	9.24E-01
DK_3894	1.90E+00	2.64E-01	4.03E+01	4.28E+51	6.56E+53	2.10E+53	5.87E+55	1.4	9.13E-03
DK_4385	3.82E-01	1.09E-01	3.51E+00	1.15E+50	3.73E+51	4.31E+51	2.11E+53	1.13	3.49E-02
DK_4456	2.63E-01	2.28E-01	4.59E+00	6.70E+50	1.35E+52	2.55E+52	7.37E+53	1.38	6.86E-02
DK_4735	3.29E+00	9.39E-02	2.29E+01	2.40E+52	5.85E+54	6.32E+53	2.98E+56	1.57	6.46E-03
DK_1602	5.78E-03	7.99E-03	3.80E-03	7.19E+46	3.42E+46	2.96E+48	1.29E+48	0.87	1.83E+00
DK_306	1.74E+01	2.63E-02	3.93E+01	1.27E+51	1.90E+54	7.47E+52	2.68E+56	1.15	7.67E-04
DK_307	5.45E+00	8.91E-02	2.58E+01	2.12E+51	6.14E+53	1.06E+53	6.06E+55	0.81	2.78E-03
DK_b_486	1.34E+00	6.04E-02	5.66E+00	2.26E+50	2.11E+52	1.32E+52	2.13E+54	0.93	9.93E-03
DK_5049	3.09E+00	2.19E-01	8.89E+00	1.89E+51	7.64E+52	8.33E+52	5.26E+54	0.17	4.31E-03
DK_1771	3.73E-02	1.32E-04	3.03E-04	3.10E+46	7.11E+46	4.74E+47	1.20E+48	1.01	4.40E-01
DK_1792	2.10E-01	7.18E-02	1.29E+00	6.58E+49	1.18E+51	2.33E+51	5.91E+52	1.29	7.20E-02
DK_1802	3.24E-02	2.20E-01	6.25E-01	4.48E+49	1.27E+50	1.41E+51	4.53E+51	1.44	5.06E-01
DK_5194	1.89E-01	1.53E-01	2.10E+00	2.48E+50	3.41E+51	6.94E+51	1.30E+53	1.25	9.15E-02
DK_5192	7.34E-01	1.11E-01	6.88E+00	1.42E+51	8.85E+52	5.61E+52	5.73E+54	1.62	2.60E-02
DK_5193	3.32E-01	1.21E-01	3.04E+00	3.44E+50	8.67E+51	1.43E+52	5.30E+53	1.31	5.21E-02
DK_b_449	2.17E+00	8.10E-02	1.58E+01	3.09E+51	6.03E+53	9.64E+52	3.55E+55	1.71	8.76E-03
DK_1879	2.09E+00	9.18E-02	1.65E+01	4.06E+51	7.30E+53	1.35E+53	4.52E+55	1.67	9.32E-03
DK_b_616	1.39E-01	1.51E-02	1.41E-01	5.28E+49	4.95E+50	1.93E+51	2.36E+52	1.33	1.42E-01
DK_1387	1.28E+00	7.93E-02	8.51E+00	4.43E+50	4.76E+52	2.06E+52	3.88E+54	1.27	1.18E-02
DK_1383	1.80E+00	8.21E-02	1.26E+01	2.09E+51	3.20E+53	5.99E+52	1.68E+55	1.58	1.04E-02
DK_5417	4.49E-01	7.80E-01	2.10E+01	6.14E+51	1.66E+53	2.78E+53	1.11E+55	1.15	4.24E-02
DK_5563	1.56E+00	1.04E-03	1.08E-01	1.39E+49	1.45E+51	3.07E+50	5.60E+52	1.16	1.11E-02
DK_5707	1.31E-01	1.32E-01	1.51E+00	7.53E+49	8.63E+50	2.82E+51	4.32E+52	1.33	1.16E-01
DK_b_665	1.57E-03	5.56E-02	6.48E-03	5.48E+47	6.39E+46	1.77E+49	1.59E+48	1.22	1.05E+01
DK_182	3.50E-02	1.82E-01	5.58E-01	1.77E+49	5.42E+49	1.02E+51	3.58E+51	1.17	3.82E-01
DK_2418	5.51E-01	5.87E-02	2.14E+00	9.00E+49	3.28E+51	3.17E+51	1.78E+53	0.88	2.42E-02
DK_1055	1.85E+00	1.78E-01	2.84E+01	6.99E+51	1.12E+54	2.50E+53	7.34E+55	1.67	1.05E-02
DK_2424	6.07E-01	2.87E-01	5.21E+00	1.49E+51	2.71E+52	5.45E+52	1.40E+54	0.52	2.86E-02
DK_2436	1.78E-02	2.58E-01	3.77E-01	7.15E+48	1.05E+49	4.68E+50	7.17E+50	0.87	5.94E-01
DK_b_338	1.26E-01	8.55E-02	6.01E-01	2.99E+49	2.10E+50	1.66E+51	1.47E+52	0.75	1.06E-01
DK_1007	8.09E-03	1.55E-01	9.60E-02	2.67E+49	1.65E+49	7.57E+50	4.41E+50	1.48	2.40E+00
DK_2524	6.59E-03	4.43E-01	1.80E-01	8.11E+48	3.30E+48	4.88E+50	1.78E+50	0.82	2.03E+00
DK_973	1.51E-01	4.54E-03	6.14E-02	1.73E+49	2.34E+50	3.48E+50	6.44E+51	1.77	1.31E-01
DK_2638	5.00E-02	2.51E-01	1.04E+00	7.90E+49	3.26E+50	4.01E+51	1.96E+52	1.35	3.28E-01
DK_146	3.74E-04	1.43E+00	2.60E-02	1.48E+48	2.70E+46	5.71E+49	6.44E+47	0.65	3.57E+01
DK_937	2.13E-01	2.02E-02	3.48E-01	1.20E+49	2.07E+50	4.60E+50	1.12E+52	1.08	6.26E-02
DK_2738	1.11E+00	6.98E-02	6.77E+00	1.95E+51	1.90E+53	3.70E+52	6.21E+54	1.73	1.78E-02
DK_2798	4.03E-02	2.09E+00	5.27E+00	9.46E+50	2.38E+51	4.83E+52	1.36E+53	1.13	4.47E-01
DK_2804	3.46E-01	7.61E-02	1.89E+00	1.15E+50	2.85E+51	4.17E+51	1.53E+53	1.09	4.38E-02
DK_129	6.74E-02	3.27E-01	1.79E+00	6.13E+49	3.36E+50	2.43E+51	1.64E+52	1.09	1.98E-01
DK_3122	9.27E-02	2.35E-01	1.53E+00	1.87E+50	1.22E+51	7.09E+51	5.78E+52	1.22	1.87E-01
DK_712	2.16E+01	2.69E-02	4.76E+01	3.64E+51	6.45E+54	1.15E+53	5.01E+56	1.35	7.61E-04
DK_713	2.23E+01	3.03E-02	5.56E+01	5.80E+51	1.06E+55	1.62E+53	7.30E+56	1.42	7.75E-04
DK_714	2.05E+01	4.02E-02	6.53E+01	9.21E+51	1.50E+55	2.34E+53	9.25E+56	1.43	8.80E-04
DK_3274	1.71E-01	5.92E-04	8.58E-03	6.36E+47	9.21E+48	1.43E+49	2.86E+50	1.39	9.60E-02
DK_3338	3.23E-01	1.19E-01	2.53E+00	2.43E+50	5.13E+51	7.77E+51	2.37E+53	1.07	5.07E-02
DK_3336	6.12E-02	2.56E-01	1.15E+00	6.83E+49	3.07E+50	3.81E+51	2.05E+52	1.11	2.47E-01
DK_3331	1.06E+00	7.41E-02	5.38E+00	6.70E+50	4.86E+52	3.08E+52	3.73E+54	1.19	1.64E-02
DK_b_303	2.87E-01	7.85E-02	1.64E+00	6.27E+49	1.31E+51	2.87E+51	8.66E+52	0.97	4.65E-02
DK_3551	8.12E-01	9.20E-02	6.06E+00	1.06E+51	6.99E+52	2.98E+52	3.25E+54	1.51	2.29E-02
DK_3574	2.56E-01	1.46E-01	3.13E+00	4.20E+50	8.98E+51	7.66E+51	2.36E+53	1.5	7.04E-02
DK_3609	1.02E+00	8.76E-02	6.82E+00	1.00E+51	7.79E+52	3.58E+52	4.70E+54	1.38	1.77E-02
DK_535	9.27E-03	1.27E+00	1.03E+00	5.13E+49	4.16E+49	2.73E+51	2.16E+51	1.33	1.63E+00

DK_530	9.79E-02	1.83E-01	1.62E+00	1.54E+50	1.36E+51	6.40E+51	7.32E+52	1.56	1.77E-01
DK_3756	7.57E-02	2.68E-01	1.47E+00	2.27E+50	1.24E+51	8.38E+51	5.62E+52	1.3	2.38E-01
DK_b_818	1.27E-01	1.35E-03	1.29E-02	7.51E+47	7.17E+48	2.30E+49	2.88E+50	1.13	1.19E-01
DK_3804	1.31E-01	3.02E-01	2.69E+00	1.72E+50	1.54E+51	1.01E+52	1.17E+53	1.03	1.16E-01
DK_3900	6.23E-02	1.43E-01	6.11E-01	3.89E+49	1.66E+50	2.03E+51	1.03E+52	1.04	2.43E-01
DK_466	1.67E-01	4.72E-03	5.95E-02	2.19E+48	2.75E+49	5.42E+49	9.25E+50	1.01	8.01E-02
DK_70	5.07E-02	3.67E-01	1.38E+00	8.10E+49	3.05E+50	3.30E+51	1.46E+52	1.12	2.99E-01
DK_4223	2.16E+00	1.15E-01	1.39E+01	3.53E+51	4.25E+53	1.42E+53	3.04E+55	1.04	8.60E-03
DK_4236	2.20E-02	3.68E-01	5.72E-01	2.78E+50	4.32E+50	9.18E+51	1.50E+52	1.43	9.22E-01
DK_4318	9.19E-01	8.85E-02	6.73E+00	1.73E+51	1.31E+53	3.25E+52	4.15E+54	1.61	2.11E-02
DK_4341	2.31E+00	1.07E-01	2.12E+01	3.86E+50	7.64E+52	2.76E+52	1.03E+55	0.91	4.58E-03
DK_b_300	9.92E-01	4.60E-02	3.56E+00	1.27E+50	9.81E+51	5.72E+51	7.46E+53	1.04	1.35E-02
DK_4548	1.10E-01	2.25E-01	1.92E+00	2.12E+50	1.81E+51	9.08E+51	1.00E+53	1.34	1.57E-01
DK_48	1.35E-03	2.12E+00	2.38E-01	7.97E+48	8.95E+47	4.37E+50	3.78E+49	1.11	9.85E+00
DK_b_851	4.36E-03	1.33E-01	2.98E-02	1.60E+48	3.60E+47	6.62E+49	1.24E+49	0.69	3.06E+00
DK_4802	2.36E+00	1.39E-01	1.80E+01	5.77E+51	7.45E+53	2.27E+53	5.26E+55	1.04	8.07E-03
DK_4814	8.52E-02	4.80E-01	2.00E+00	1.14E+50	4.74E+50	6.16E+51	3.05E+52	0.65	1.57E-01
DK_1640	2.35E+01	7.45E-03	1.59E+01	7.64E+50	1.63E+54	2.49E+52	1.34E+56	1.38	6.43E-04
DK_1598	3.76E-01	8.49E-02	2.45E+00	2.01E+50	5.81E+51	6.21E+51	2.69E+53	1.26	4.36E-02
DK_b_210	3.07E-03	6.22E-02	1.34E-02	2.97E+47	6.42E+46	1.53E+49	2.75E+48	0.75	3.45E+00
DK_1745	6.00E-01	1.74E-01	9.48E+00	5.93E+51	3.24E+53	1.36E+53	1.20E+55	1.9	3.49E-02
DK_1777	6.84E+01	1.24E-02	7.65E+01	7.30E+51	4.48E+55	2.53E+53	4.43E+57	1.56	2.53E-04
DK_5190	8.22E-02	1.07E+00	6.93E+00	1.25E+51	8.07E+51	6.29E+52	5.07E+53	1.46	2.26E-01
DK_1465	9.17E+00	1.30E-01	8.97E+01	4.11E+52	2.83E+55	1.44E+54	2.18E+57	1.52	2.21E-03
DK_275	1.36E-01	3.59E-06	3.77E-05	1.36E+45	1.43E+46	2.26E+46	3.15E+47	1.03	9.81E-02
DK_5303	4.82E-01	1.88E-01	6.22E+00	2.29E+51	7.57E+52	8.05E+52	4.06E+54	1.36	4.10E-02
DK_1417	8.35E-01	1.48E-03	1.01E-01	5.37E+48	3.69E+50	1.26E+50	1.44E+52	1.25	1.81E-02
DK_5354	7.50E-04	4.45E+00	7.13E-02	2.28E+48	3.66E+46	8.13E+50	7.95E+48	0.13	8.02E+00
DK_5376	2.62E+00	7.35E-02	1.69E+01	5.72E+51	1.31E+54	1.85E+53	8.17E+55	1.75	7.63E-03
DK_2128	2.38E-01	2.72E-01	5.80E+00	2.91E+51	6.20E+52	8.60E+52	2.65E+54	1.85	8.68E-02
DK_2174	1.33E-01	1.48E+00	1.05E+01	8.63E+50	6.10E+51	5.20E+52	4.65E+53	0.8	1.13E-01
DK_2394	7.41E-02	1.69E-01	8.32E-01	3.48E+49	1.71E+50	1.65E+51	9.87E+51	0.89	1.80E-01
DK_2453	2.13E-01	2.64E-01	4.42E+00	4.83E+50	8.09E+51	1.45E+52	3.40E+53	1.36	8.12E-02
DK_168	8.36E-02	2.81E-01	1.97E+00	1.02E+50	7.16E+50	4.96E+51	4.39E+52	1.27	1.81E-01
DK_1013	1.05E-01	4.79E-02	3.55E-01	1.40E+49	1.04E+50	7.22E+50	6.82E+51	0.94	1.27E-01
DK_2639	2.95E-01	2.52E-01	4.45E+00	6.38E+50	1.12E+52	3.22E+52	8.02E+53	1.04	5.87E-02
DK_13	8.78E-03	2.68E-01	1.15E-01	6.55E+48	2.81E+48	2.34E+50	9.07E+49	0.65	1.52E+00
DK_2760	7.54E-03	8.15E-01	4.33E-01	1.71E+49	9.08E+48	6.94E+50	3.42E+50	0.94	1.77E+00
DK_119	4.70E-02	1.52E-01	6.00E-01	1.99E+49	7.84E+49	9.17E+50	4.26E+51	1.12	2.84E-01
DK_797	1.43E-01	3.89E-03	4.90E-02	3.51E+48	4.41E+49	1.13E+50	1.92E+51	1.44	1.14E-01
DK_765	5.31E+00	2.82E-02	9.21E+00	4.15E+50	1.36E+53	1.89E+52	1.24E+55	0.82	2.51E-03
DK_698	2.34E-01	1.00E-02	2.06E-01	6.53E+48	1.34E+50	1.80E+50	5.28E+51	1.17	5.70E-02
DK_3450	2.56E-01	6.13E-02	1.08E+00	6.84E+49	1.20E+51	2.89E+51	7.16E+52	1.04	5.90E-02
DK_616	4.46E-01	1.38E-01	5.32E+00	8.77E+50	3.37E+52	3.09E+52	1.84E+54	1.6	4.16E-02
DK_89	2.50E-02	3.23E-01	7.08E-01	2.25E+49	4.92E+49	1.11E+51	2.66E+51	1.17	5.33E-01
DK_3583	3.38E-02	2.41E-01	5.15E-01	2.27E+49	4.84E+49	8.45E+50	1.97E+51	0.84	3.95E-01
DK_3666	5.17E-02	3.73E-04	1.40E-03	8.41E+46	3.15E+47	1.50E+48	6.58E+48	1.1	2.93E-01
DK_3735	1.31E-02	1.30E-01	1.34E-01	4.77E+48	4.91E+48	1.59E+50	1.64E+50	1.05	1.02E+00
DK_3757	3.66E-01	6.09E-01	9.01E+00	1.40E+51	2.08E+52	7.50E+52	1.53E+54	0.66	4.47E-02
DK_3831	1.50E+00	1.12E-01	1.40E+01	4.70E+50	5.85E+52	2.98E+52	6.61E+54	1.11	8.89E-03
DK_72	8.34E-03	5.83E-01	3.42E-01	7.56E+48	4.44E+48	3.87E+50	2.13E+50	0.75	1.27E+00
DK_3972	5.33E-02	3.97E-01	1.63E+00	4.49E+50	1.84E+51	1.54E+52	7.46E+52	1.49	3.64E-01
DK_69	5.06E-02	2.89E-01	1.09E+00	6.38E+49	2.40E+50	3.04E+51	1.34E+52	1.12	2.99E-01
DK_4113	2.24E-01	2.74E-01	5.28E+00	1.55E+51	2.98E+52	5.19E+52	1.42E+54	1.7	8.83E-02
DK_4128	6.94E+00	1.20E-01	6.43E+01	7.08E+52	3.79E+55	1.93E+54	2.20E+57	1.65	3.08E-03
DK_4179	4.17E-02	2.88E-01	5.87E-01	5.23E+49	1.07E+50	2.05E+51	4.56E+51	0.74	3.63E-01
DK_4307	5.09E-01	1.94E-01	6.61E+00	2.75E+50	9.36E+51	1.78E+52	9.27E+53	0.89	2.62E-02
DK_4336	2.49E-01	1.10E-01	1.43E+00	6.90E+50	8.97E+51	9.50E+51	1.68E+53	1.03	7.94E-02
DK_4648	2.11E+00	6.94E-02	1.22E+01	1.25E+51	2.20E+53	4.65E+52	1.51E+55	1.44	8.21E-03
DK_1622	4.90E+00	6.05E-02	1.92E+01	1.86E+51	5.90E+53	7.23E+52	4.57E+55	1.06	3.35E-03
DK_1611	1.13E+00	3.76E-02	3.24E+00	6.61E+49	5.70E+51	4.05E+51	5.97E+53	0.81	9.38E-03
DK_1672	3.20E-02	1.80E-01	5.06E-01	3.95E+48	1.11E+49	9.22E+50	2.94E+51	0.53	1.88E-01
DK_1673	9.62E-02	1.86E-01	1.57E+00	2.00E+50	1.69E+51	5.65E+51	6.16E+52	1.58	1.87E-01

DK_1600	2.16E-01	8.05E-02	1.36E+00	4.83E+49	8.13E+50	2.19E+51	5.18E+52	1.04	6.19E-02
DK_4995	3.87E-01	1.18E-01	3.15E+00	8.04E+50	2.14E+52	3.12E+52	1.23E+54	1.31	4.92E-02
DK_1779	2.29E+01	1.79E-02	2.92E+01	1.14E+51	1.86E+54	4.05E+52	1.60E+56	0.95	5.82E-04
DK_1489	1.33E+01	4.21E-02	3.21E+01	2.44E+51	1.86E+54	9.59E+52	1.62E+56	0.87	1.14E-03
DK_1813	1.42E-01	6.42E-04	8.03E-03	2.54E+47	3.18E+48	6.36E+48	1.08E+50	1.17	9.37E-02
DK_1474	5.22E-02	3.92E-02	1.74E-01	5.69E+48	2.52E+49	2.24E+50	1.19E+51	1.13	2.56E-01
DK_1462	9.25E-01	1.16E-01	6.93E+00	2.98E+50	1.78E+52	1.16E+52	1.14E+54	0.86	1.44E-02
DK_1420	2.66E+01	1.88E-02	4.31E+01	3.14E+51	7.21E+54	1.31E+53	7.63E+56	1.42	6.17E-04
DK_1912	3.01E+00	9.19E-02	1.36E+01	7.71E+50	1.14E+53	4.90E+52	1.32E+55	0.65	4.43E-03
DK_1401	8.33E-02	2.67E-01	1.98E+00	1.91E+50	1.41E+51	8.24E+51	7.77E+52	1.54	2.08E-01
DK_1940	5.17E-04	5.35E-01	2.09E-02	4.31E+47	1.69E+46	1.31E+49	3.47E+47	0.8	2.05E+01
DK_1399	1.30E-02	3.06E-01	3.42E-01	1.11E+49	1.24E+49	5.27E+50	5.97E+50	1.15	1.03E+00
DK_1395	4.00E-02	1.21E-01	4.18E-01	7.56E+48	2.61E+49	4.67E+50	1.87E+51	0.91	2.65E-01
DK_1943	1.67E+00	4.36E-02	4.10E+00	3.17E+50	2.98E+52	1.39E+52	2.25E+54	0.85	9.07E-03
DK_28	5.11E-03	1.31E-03	4.25E-04	2.91E+46	9.46E+45	7.83E+47	2.22E+47	0.96	2.96E+00
DK_5709	1.03E+00	1.63E-02	1.37E+00	7.30E+49	6.14E+51	2.78E+51	3.98E+53	1.24	1.48E-02
DK_2152	1.79E-01	6.14E-02	9.39E-01	1.71E+49	2.61E+50	1.03E+51	2.19E+52	0.91	5.93E-02
DK_1219	7.98E-02	1.68E-02	8.94E-02	2.08E+48	1.11E+49	1.04E+50	6.80E+50	0.71	1.33E-01
DK_2266	1.25E+00	2.81E-01	2.37E+01	1.53E+51	1.29E+53	6.85E+52	9.83E+54	1.02	1.21E-02
DK_1128	8.52E-03	3.10E-01	2.28E-01	7.33E+48	5.41E+48	2.67E+50	1.89E+50	1.15	1.57E+00
DK_1031	2.48E+00	2.22E-02	4.81E+00	8.54E+49	1.85E+52	5.07E+51	2.10E+54	0.93	4.28E-03
DK_2542	4.89E+00	6.36E-02	2.71E+01	6.61E+51	2.81E+54	2.17E+53	1.91E+56	1.69	3.97E-03
DK_2544	9.31E-02	2.03E-01	1.50E+00	1.19E+50	8.79E+50	5.27E+51	4.96E+52	1.3	1.76E-01
DK_983	2.63E-02	7.39E-03	1.43E-02	5.40E+47	1.04E+48	1.69E+49	3.53E+49	0.98	5.08E-01
DK_b_735	2.48E-02	1.27E-02	1.17E-02	4.89E+47	4.51E+47	1.65E+49	1.51E+49	0.39	4.27E-01
DK_927	2.43E-02	5.03E-01	8.30E-01	7.69E+49	1.27E+50	3.61E+51	6.32E+51	1.11	6.74E-01
DK_2676	8.54E-02	1.69E-01	9.90E-01	4.00E+49	2.35E+50	1.91E+51	1.39E+52	0.92	1.56E-01
DK_863	1.15E-01	2.53E-01	1.96E+00	1.82E+50	1.42E+51	7.23E+51	7.19E+52	1.11	1.43E-01
DK_855	8.99E-02	2.06E-01	1.46E+00	5.15E+49	3.64E+50	2.53E+51	2.26E+52	1.05	1.48E-01
DK_2871	8.89E-03	2.55E+00	5.64E-01	6.30E+49	1.39E+49	4.73E+51	8.74E+50	0.33	1.50E+00
DK_788	1.48E-02	4.70E-01	4.57E-01	3.03E+49	2.95E+49	1.46E+51	1.41E+51	0.99	1.02E+00
DK_710	5.56E-02	6.71E-02	3.01E-01	5.80E+48	2.60E+49	4.36E+50	2.34E+51	0.85	1.91E-01
DK_709	7.26E-02	6.62E-02	3.33E-01	1.34E+49	6.71E+49	5.67E+50	3.46E+51	0.92	1.84E-01
DK_634	1.32E-03	1.13E-01	1.05E-02	9.36E+47	8.68E+46	2.39E+49	1.67E+48	1.16	1.25E+01
DK_618	8.23E-01	1.73E-01	1.05E+01	1.60E+51	9.68E+52	6.15E+52	6.10E+54	1.33	2.19E-02
DK_3471	2.69E-01	3.04E-02	7.31E-01	2.27E+49	5.46E+50	7.18E+50	2.53E+52	1.19	4.97E-02
DK_606	2.03E-02	2.16E-01	3.31E-01	4.92E+49	7.54E+49	1.86E+51	3.00E+51	1.36	8.88E-01
DK_3496	1.27E-01	1.44E-01	1.59E+00	1.16E+50	1.27E+51	4.99E+51	7.33E+52	1.42	1.29E-01
DK_3577	7.60E-01	5.88E-02	3.60E+00	1.24E+50	7.61E+51	7.08E+51	7.12E+53	1.08	1.76E-02
DK_576	3.79E-01	2.51E-02	8.03E-01	2.64E+49	8.47E+50	8.28E+50	4.02E+52	1.13	3.52E-02
DK_3761	1.88E-01	7.12E-02	1.20E+00	3.72E+49	6.28E+50	1.28E+51	3.04E+52	1.2	7.10E-02
DK_437	3.64E-03	9.74E-03	2.33E-03	1.54E+47	3.70E+46	4.42E+48	8.90E+47	1	4.16E+00
DK_62	9.80E-04	5.48E+00	1.77E-01	8.35E+48	2.70E+47	7.02E+50	1.50E+49	0.35	1.08E+01
DK_388	3.19E-01	3.41E-02	9.01E-01	6.85E+49	1.81E+51	2.94E+51	1.15E+53	1.36	5.13E-02
DK_367	1.28E-01	1.84E-01	2.10E+00	2.02E+50	2.30E+51	5.67E+51	8.65E+52	1.55	1.36E-01
DK_4647	4.99E+00	2.67E-02	1.17E+01	8.40E+50	3.68E+53	2.96E+52	2.68E+55	1.44	3.28E-03
DK_1685	4.53E+01	6.98E-03	2.76E+01	8.80E+50	3.48E+54	2.86E+52	3.06E+56	1.17	2.94E-04
DK_1708	9.29E+00	5.11E-02	3.04E+01	2.99E+51	1.77E+54	1.35E+53	1.73E+56	1.05	1.76E-03
DK_4979	4.11E+00	2.91E-02	8.67E+00	1.03E+51	3.06E+53	4.45E+52	2.62E+55	1.25	4.21E-03
DK_1572	5.84E-02	1.53E-01	7.69E-01	3.88E+49	1.96E+50	1.15E+51	7.06E+51	1.31	2.59E-01
DK_299	4.33E-01	1.04E-01	3.62E+00	2.84E+50	9.85E+51	6.04E+51	3.21E+53	1.31	3.79E-02
DK_1734	6.09E+00	1.73E-01	7.97E+01	7.43E+52	3.42E+55	2.13E+54	2.05E+57	1.6	3.47E-03
DK_1551	1.11E+00	5.03E-02	4.90E+00	2.43E+50	2.37E+52	1.06E+52	1.79E+54	1.33	1.36E-02
DK_5078	5.06E-01	1.16E-01	5.01E+00	2.56E+50	1.10E+52	1.20E+52	8.13E+53	1.29	2.99E-02
DK_5101	2.13E-01	3.00E-01	3.12E+00	2.78E+50	2.90E+51	9.44E+51	1.30E+53	0.74	7.11E-02
DK_1780	1.59E+01	3.62E-02	3.95E+01	2.51E+51	2.74E+54	1.39E+53	3.49E+56	1.04	9.51E-04
DK_1778	4.80E+01	1.24E-02	5.09E+01	2.58E+51	1.07E+55	1.11E+53	1.24E+57	1.3	3.15E-04
DK_1507	2.65E+00	1.16E-02	2.75E+00	8.59E+49	2.03E+52	3.42E+51	1.56E+54	1.19	5.03E-03
DK_5148	1.46E-03	6.16E-01	7.70E-02	2.50E+48	3.12E+47	1.19E+50	1.15E+49	1.14	9.15E+00
DK_1793	8.74E-02	1.00E-03	7.67E-03	2.43E+47	1.86E+48	6.29E+48	6.15E+49	1.17	1.53E-01
DK_1801	2.57E-01	6.04E-02	1.40E+00	6.77E+49	1.57E+51	1.48E+51	5.02E+52	1.37	5.88E-02
DK_5285	3.09E-01	6.31E-02	1.35E+00	3.03E+49	6.49E+50	1.88E+51	5.81E+52	0.73	3.43E-02
DK_5318	1.22E+00	3.94E-02	4.25E+00	3.01E+50	3.25E+52	1.39E+52	2.63E+54	1.45	1.35E-02

DK_1904	3.23E-01	2.12E-02	5.82E-01	1.06E+49	2.93E+50	7.47E+50	3.06E+52	0.9	3.28E-02
DK_1920	9.02E-02	1.69E-01	1.31E+00	1.71E+50	1.33E+51	6.01E+51	5.97E+52	1.55	2.00E-01
DK_1928	2.21E+01	1.67E-02	3.07E+01	1.60E+51	2.96E+54	3.59E+52	1.63E+56	1.27	6.86E-04
DK_b_628	2.71E-01	9.88E-02	1.75E+00	4.17E+49	7.37E+50	2.71E+51	6.77E+52	0.69	3.91E-02
DK_1402	1.53E-02	1.96E-01	2.51E-01	4.66E+48	5.96E+48	1.43E+50	1.89E+50	0.89	6.95E-01
DK_1944	1.15E+00	4.72E-02	2.85E+00	3.42E+50	2.06E+52	6.90E+51	6.80E+53	0.86	1.42E-02
DK_1945	6.48E-01	1.37E-01	6.64E+00	1.38E+50	6.70E+51	1.25E+52	9.64E+53	0.79	1.63E-02
DK_1946	6.31E-01	1.13E-01	5.74E+00	1.11E+50	5.64E+51	7.57E+51	6.18E+53	0.86	1.68E-02
DK_2001	4.33E+00	5.55E-02	1.99E+01	8.27E+51	2.97E+54	1.07E+53	7.80E+55	1.68	4.67E-03
DK_1356	2.73E-01	5.78E-02	1.27E+00	2.46E+49	5.41E+50	1.10E+51	3.50E+52	0.85	3.88E-02
DK_1343	4.58E-02	4.86E-02	1.69E-01	1.53E+48	5.29E+48	9.44E+49	3.80E+50	0.46	1.31E-01
DK_1324	2.67E-01	9.13E-02	1.75E+00	1.53E+50	2.94E+51	3.91E+51	1.07E+53	1.18	6.14E-02
DK_2048	1.79E+00	1.03E-01	1.56E+01	3.90E+51	5.94E+53	1.50E+53	4.18E+55	1.65	1.09E-02
DK_5601	2.58E-01	1.11E-01	1.73E+00	1.24E+50	1.95E+51	6.65E+51	1.45E+53	0.92	5.87E-02
DK_2070	1.89E-03	3.58E+00	4.94E-01	5.80E+49	8.02E+48	3.29E+51	3.59E+50	1.26	9.15E+00
DK_1272	1.76E+00	2.74E-02	4.22E+00	1.34E+50	2.06E+52	5.81E+51	1.64E+54	1.17	7.59E-03
DK_2153	4.07E-01	3.87E-02	1.35E+00	6.86E+49	2.39E+51	1.45E+51	7.70E+52	1.3	3.72E-02
DK_2179	1.50E-01	1.20E-04	1.08E-03	1.13E+47	1.02E+48	2.40E+48	2.83E+49	0.99	1.09E-01
DK_2247	3.38E-02	2.54E-01	7.12E-01	5.41E+49	1.51E+50	2.37E+51	7.50E+51	1.36	4.85E-01
DK_2271	2.97E+00	2.17E-02	5.47E+00	1.91E+51	4.82E+53	4.16E+52	2.04E+55	1.7	6.74E-03
DK_1118	3.71E-02	1.87E-01	5.83E-01	3.03E+49	9.42E+49	1.35E+51	4.83E+51	1.27	4.08E-01
DK_176	5.81E-02	4.90E-01	2.36E+00	1.24E+50	5.98E+50	5.26E+51	3.06E+52	1.26	2.60E-01
DK_2396	4.28E-02	2.35E-01	8.57E-01	8.62E+49	3.15E+50	2.02E+51	8.63E+51	1.48	4.04E-01
DK_2433	1.21E-01	8.28E-02	8.27E-01	2.79E+49	2.79E+50	1.54E+51	2.03E+52	1.1	1.10E-01
DK_2502	2.50E-01	4.87E-01	5.17E+00	3.07E+51	3.26E+52	1.18E+53	1.67E+54	0.84	7.91E-02
DK_2584	3.37E+00	1.37E-01	3.08E+01	1.59E+52	3.57E+54	4.57E+53	1.96E+56	1.35	6.00E-03
DK_b_62	5.64E-02	5.36E-03	2.71E-02	1.90E+48	9.63E+48	5.35E+49	3.29E+50	1.47	2.91E-01
DK_149	8.90E-02	3.77E-01	2.76E+00	2.11E+50	1.54E+51	8.67E+51	8.06E+52	1.35	1.84E-01
DK_2614	4.81E-01	9.05E-02	3.91E+00	3.73E+50	1.61E+52	7.13E+51	4.84E+53	1.56	3.60E-02
DK_2617	7.72E-01	1.35E-01	8.29E+00	1.62E+50	9.96E+51	1.14E+52	1.15E+54	0.84	1.37E-02
DK_2622	1.53E-01	5.93E-04	8.13E-03	2.51E+47	3.45E+48	7.75E+48	1.45E+50	1.2	8.75E-02
DK_2628	2.91E-02	8.32E-01	1.46E+00	2.72E+50	4.76E+50	1.23E+52	2.30E+52	1.08	6.19E-01
DK_2637	2.67E+00	1.11E-04	1.73E-02	8.82E+48	1.37E+51	1.39E+50	3.97E+52	1.17	7.49E-03
DK_2696	8.70E-02	8.67E-02	5.99E-01	1.17E+49	8.11E+49	7.17E+50	6.25E+51	0.84	1.22E-01
DK_2753	5.99E+00	2.73E-02	1.32E+01	4.54E+50	2.19E+53	2.57E+52	2.60E+55	1.08	2.23E-03
DK_2752	6.51E+00	1.53E-02	8.20E+00	2.76E+50	1.48E+53	9.13E+51	1.04E+55	1.1	2.05E-03
DK_2754	4.99E+00	3.28E-02	1.25E+01	2.55E+50	9.73E+52	2.11E+52	1.64E+55	0.81	2.12E-03
DK_2935	2.23E-02	3.65E-01	6.22E-01	5.12E+49	8.74E+49	1.99E+51	3.61E+51	1.25	7.34E-01
DK_2949	6.57E-01	2.00E-02	9.25E-01	8.99E+48	4.16E+50	5.56E+50	4.08E+52	0.42	9.16E-03
DK_2959	2.61E+00	5.11E-02	1.08E+01	5.81E+50	1.23E+53	2.63E+52	1.06E+55	1.23	5.80E-03
DK_3019	3.87E-03	9.91E-01	2.93E-01	5.45E+49	1.61E+49	2.40E+51	6.13E+50	1.42	4.80E+00
DK_3025	1.36E-02	7.62E-01	7.04E-01	2.87E+49	2.65E+49	1.90E+51	1.74E+51	0.91	9.84E-01
DK_3069	4.52E-01	2.44E-02	9.26E-01	3.07E+49	1.16E+51	1.24E+51	7.29E+52	1.12	2.96E-02
DK_3071	1.39E-01	1.10E-01	1.20E+00	1.31E+50	1.43E+51	4.60E+51	6.71E+52	1.36	1.25E-01
DK_759	1.50E-01	1.62E-03	2.15E-02	2.08E+48	2.77E+49	4.41E+49	8.01E+50	1.54	1.16E-01
DK_3094	3.55E+00	3.58E-02	1.01E+01	3.54E+50	9.99E+52	1.26E+52	7.03E+54	1.06	3.76E-03
DK_3095	4.35E-01	9.60E-02	3.04E+00	6.50E+49	2.06E+51	3.14E+51	1.50E+53	0.77	2.43E-02
DK_3174	4.59E-02	2.04E-01	7.44E-01	2.60E+49	9.50E+49	1.24E+51	5.30E+51	1.06	2.91E-01
DK_3226	9.42E-02	2.34E-01	1.76E+00	6.13E+49	4.60E+50	2.37E+51	2.27E+52	1.06	1.42E-01
DK_690	6.75E-01	6.31E-02	3.73E+00	2.68E+50	1.58E+52	6.79E+51	6.54E+53	1.44	2.43E-02
DK_3276	7.38E-02	3.22E-01	1.68E+00	2.66E+50	1.39E+51	1.11E+52	7.06E+52	1.27	2.44E-01
DK_3280	2.23E+00	2.90E-01	3.53E+01	8.95E+52	1.09E+55	2.16E+54	4.67E+56	1.19	9.75E-03
DK_3509	4.04E-01	8.71E-02	1.97E+00	9.78E+49	2.21E+51	4.60E+51	1.51E+53	0.75	3.31E-02
DK_3516	5.56E-02	1.96E-01	8.75E-01	1.70E+49	7.58E+49	8.24E+50	4.40E+51	0.85	1.90E-01
DK_3570	6.00E-01	3.98E-02	2.05E+00	1.04E+50	5.36E+51	4.32E+51	3.57E+53	1.3	2.52E-02
DK_3644	4.08E-01	7.90E-02	2.41E+00	2.76E+50	8.43E+51	8.52E+51	3.92E+53	1.3	4.25E-02
DK_3646	7.51E-02	9.58E-02	5.81E-01	3.14E+49	1.90E+50	6.89E+50	5.19E+51	1.22	2.01E-01
DK_529	8.88E+00	4.20E-02	3.03E+01	3.20E+51	2.31E+54	8.93E+52	1.42E+56	1.41	1.95E-03
DK_3824	5.98E-01	3.98E-02	1.96E+00	6.61E+49	3.26E+51	3.57E+51	2.81E+53	1.1	2.23E-02
DK_3839	1.54E+00	8.19E-02	9.18E+00	1.08E+51	1.21E+53	4.04E+52	7.97E+54	1.26	1.12E-02
DK_3832	9.62E-01	1.24E-01	9.48E+00	7.48E+50	5.73E+52	2.96E+52	3.82E+54	1.31	1.70E-02
DK_3834	8.01E-01	1.12E-01	6.80E+00	2.50E+50	1.52E+52	1.54E+52	1.53E+54	1.01	1.67E-02
DK_3848	3.87E-01	2.64E-02	8.95E-01	6.42E+49	2.18E+51	1.73E+51	8.95E+52	1.44	4.23E-02

DK_3940	6.53E-02	4.98E-01	2.07E+00	2.79E+50	1.16E+51	1.29E+52	6.35E+52	1.1	2.65E-01
DK_3990	6.59E-02	6.14E-02	3.28E-01	2.55E+49	1.36E+50	8.33E+50	5.43E+51	1.33	2.49E-01
DK_4042	1.16E-01	1.17E-01	1.06E+00	8.55E+49	7.70E+50	2.62E+51	3.07E+52	1.27	1.41E-01
DK_4304	4.45E-01	1.02E-01	3.33E+00	1.26E+50	4.12E+51	6.05E+51	3.01E+53	0.98	3.00E-02
DK_4322	3.05E-01	7.33E-02	1.92E+00	9.73E+49	2.55E+51	3.51E+51	1.36E+53	1.3	4.97E-02
DK_4370	6.35E-01	6.33E-02	2.84E+00	7.05E+50	3.16E+52	2.40E+52	1.70E+54	1.34	3.00E-02
DK_383	2.74E-02	4.33E-03	1.07E-02	3.30E+47	8.12E+47	7.53E+48	2.07E+49	1.2	4.87E-01
DK_4516	1.91E-01	3.69E-01	4.64E+00	1.00E+51	1.26E+52	4.20E+52	7.15E+53	1.22	9.73E-02
DK_4513	1.03E+00	2.12E-01	1.13E+01	3.08E+51	1.65E+53	1.29E+53	1.12E+55	0.97	1.81E-02
DK_4595	2.28E-01	1.98E-01	3.05E+00	7.89E+50	1.22E+52	2.08E+52	4.46E+53	1.29	8.37E-02
DK_4856	1.03E+00	2.67E-02	2.31E+00	2.35E+50	2.03E+52	8.53E+51	1.26E+54	1.46	1.69E-02
DK_4858	3.16E-01	9.79E-02	2.36E+00	3.47E+50	8.38E+51	1.33E+52	4.71E+53	1.38	5.70E-02
DK_4877	5.91E-01	5.74E-02	2.86E+00	9.43E+49	4.69E+51	5.31E+51	4.23E+53	1.12	2.26E-02
DK_4897	9.49E-01	5.95E-02	3.98E+00	8.78E+49	5.87E+51	5.65E+51	6.26E+53	0.75	1.12E-02
DK_4918	2.33E-01	3.66E-02	6.60E-01	2.37E+49	4.27E+50	7.60E+50	1.94E+52	1.03	5.74E-02
DK_33	1.67E-02	7.11E-01	9.54E-01	3.31E+49	4.44E+49	1.36E+51	1.90E+51	1.07	7.97E-01
DK_5467	3.15E-04	2.58E-01	3.97E-03	2.26E+47	3.48E+45	7.04E+48	6.57E+46	0.65	4.23E+01
DK_5558	3.09E-01	2.66E-02	6.28E-01	1.28E+49	3.02E+50	5.23E+50	1.80E+52	0.81	3.43E-02
DK_5585	1.50E+01	1.45E-02	1.71E+01	2.44E+51	2.88E+54	8.70E+52	2.40E+56	1.42	1.20E-03
DK_236	3.88E-02	5.59E-01	1.83E+00	3.80E+50	1.24E+51	1.50E+52	5.66E+52	1.61	4.91E-01
DK_226	1.84E-02	1.56E-03	2.53E-03	8.02E+46	1.29E+47	1.59E+48	2.72E+48	1.17	7.24E-01
DK_164	1.90E-01	2.78E-01	3.72E+00	3.61E+49	4.84E+50	2.92E+51	5.33E+52	0.42	3.17E-02
DK_15	1.33E-02	3.22E-01	2.09E-01	2.93E+48	1.90E+48	2.16E+50	1.33E+50	0.29	4.54E-01
DK_5	1.10E-02	4.48E-01	2.86E-01	1.37E+49	8.77E+48	5.28E+50	3.19E+50	0.77	1.21E+00
DK_8	1.27E-02	2.89E-01	2.12E-01	2.51E+48	1.85E+48	1.83E+50	1.30E+50	0.35	4.73E-01
DK_6	1.33E-02	1.40E-01	1.08E-01	2.89E+48	2.22E+48	1.27E+50	9.47E+49	0.61	7.98E-01
DK_3909	1.89E-01	3.25E-02	5.27E-01	4.19E+48	6.80E+49	2.61E+50	5.92E+51	0.52	3.19E-02
DK_42	5.17E-03	1.04E+00	4.05E-01	8.34E+48	3.26E+48	6.14E+50	2.14E+50	0.8	2.05E+00
DK_1340	8.65E-04	1.99E-02	6.37E-04	1.18E+46	3.77E+44	5.58E+47	1.18E+46	0.22	6.96E+00
DK_5550	1.55E-01	2.97E-01	2.66E+00	3.15E+49	2.83E+50	2.54E+51	2.97E+52	0.35	3.88E-02
DK_b_335	5.19E-01	3.32E-02	1.42E+00	2.68E+49	1.15E+51	7.68E+50	5.16E+52	0.87	2.04E-02
DK_977	7.55E-01	8.56E-02	5.46E+00	1.01E+50	6.41E+51	4.90E+51	5.14E+53	0.89	1.40E-02
DK_940	4.80E-01	1.81E-01	6.10E+00	1.35E+50	4.56E+51	4.72E+51	2.43E+53	0.75	2.21E-02
DK_2735	2.44E-01	2.68E-02	5.33E-01	1.02E+49	2.03E+50	4.13E+50	1.17E+52	0.86	4.34E-02
DK_2842	1.01E+00	1.86E-02	1.54E+00	2.92E+49	2.42E+51	1.20E+51	1.68E+53	0.87	1.05E-02
DK_2856	1.99E-01	6.68E-02	8.74E-01	2.07E+49	2.71E+50	9.28E+50	1.65E+52	0.7	5.32E-02
DK_2878	1.81E-02	7.83E-04	9.69E-04	2.20E+46	2.72E+46	5.26E+47	6.68E+47	0.73	5.86E-01
DK_2956	9.01E-02	3.86E-01	1.70E+00	5.41E+49	2.38E+50	2.90E+51	1.53E+52	0.52	1.18E-01
DK_3046	5.30E-01	2.06E-02	9.58E-01	1.70E+49	7.90E+50	4.61E+50	3.39E+52	0.93	2.00E-02
DK_3129	3.18E-03	1.81E+00	3.14E-01	8.96E+48	1.56E+48	5.06E+50	7.12E+49	0.58	3.33E+00
DK_3442	1.66E-01	6.66E-02	8.06E-01	1.72E+49	2.08E+50	7.64E+50	1.25E+52	0.77	6.40E-02
DK_3504	4.47E-02	1.94E-01	5.34E-01	1.35E+49	3.71E+49	6.48E+50	2.01E+51	0.65	2.37E-01
DK_3521	2.09E-01	3.78E-02	6.09E-01	5.40E+48	8.69E+49	3.44E+50	7.73E+51	0.46	2.89E-02
DK_3634	7.39E-03	1.55E-01	5.59E-02	7.84E+47	2.83E+47	5.18E+49	1.65E+49	0.29	8.15E-01
DK_520	6.77E-01	2.24E-02	1.30E+00	1.04E+49	6.04E+50	6.50E+50	6.17E+52	0.52	8.90E-03
DK_3738	1.02E-01	2.34E-01	8.86E-01	3.72E+49	1.41E+50	1.26E+51	5.62E+51	0.39	1.04E-01
DK_420	1.75E-02	3.94E-03	5.41E-03	1.07E+47	1.47E+47	3.10E+48	4.43E+48	0.83	6.06E-01
DK_405	3.71E-03	2.45E-01	6.39E-02	1.41E+48	3.69E+47	4.22E+49	9.38E+48	0.75	2.86E+00
DK_4954	2.59E-01	4.52E-02	8.04E-01	8.01E+48	1.43E+50	5.26E+50	1.32E+52	0.41	2.33E-02
DK_246	9.02E-03	4.66E-01	2.96E-01	2.88E+48	1.83E+48	2.19E+50	1.31E+50	0.42	6.68E-01
DK_1335	1.18E-01	5.55E-02	5.52E-01	4.48E+48	4.46E+49	2.92E+50	3.83E+51	0.51	5.11E-02
DK_195	3.08E-02	2.73E-01	4.45E-01	1.31E+49	2.13E+49	4.30E+50	7.43E+50	0.56	3.45E-01
DK_186	1.15E-01	1.16E-01	1.04E+00	9.11E+48	8.19E+49	6.49E+50	7.59E+51	0.47	5.25E-02
DK_976	1.17E-02	1.13E-01	1.16E-01	2.06E+48	2.11E+48	5.86E+49	6.04E+49	0.93	9.03E-01
DK_2575	9.02E-04	3.71E-02	1.94E-03	2.29E+46	1.20E+45	1.17E+48	4.29E+46	0.35	6.68E+00
DK_151	4.27E-02	2.44E-01	8.89E-01	7.15E+48	2.60E+49	5.35E+50	2.27E+51	0.51	1.41E-01
DK_948	5.17E-01	7.91E-02	3.33E+00	2.80E+49	1.18E+51	2.02E+51	1.34E+53	0.49	1.16E-02
DK_2855	2.42E-01	2.48E-02	3.94E-01	9.33E+48	1.48E+50	2.50E+50	5.54E+51	0.7	4.38E-02
DK_b_808	3.05E-03	2.31E-01	3.27E-02	1.10E+48	1.55E+47	4.82E+49	5.41E+48	0.49	3.47E+00
DK_73	1.69E-01	2.38E-01	2.83E+00	6.26E+49	7.46E+50	3.25E+51	5.21E+52	0.75	6.27E-02
DK_67	4.24E-03	4.57E-01	1.52E-01	1.33E+48	4.41E+47	9.76E+49	2.84E+49	0.47	1.42E+00
DK_5013	1.34E-01	9.04E-02	7.59E-01	8.32E+48	6.98E+49	5.79E+50	6.27E+51	0.38	4.48E-02
DK_277	7.54E-04	9.91E+00	7.47E-02	5.11E+48	3.85E+46	5.08E+50	2.13E+48	0.06	7.99E+00

DK_257	1.26E-03	2.03E-01	2.11E-02	3.96E+47	4.13E+46	1.66E+49	1.32E+48	0.88	8.43E+00
DK_1991	1.56E-02	5.73E-01	4.38E-01	1.39E+49	1.07E+49	7.31E+50	5.41E+50	0.52	6.77E-01
DK_228	3.71E-02	8.36E-02	2.63E-01	4.82E+48	1.52E+49	2.08E+50	7.50E+50	0.9	2.86E-01
DK_2308	1.13E-01	1.26E-01	7.91E-01	2.22E+49	1.40E+50	7.02E+50	5.50E+51	0.59	9.35E-02
DK_1125	1.55E-03	1.14E+00	5.84E-02	2.75E+48	1.41E+47	9.55E+49	3.43E+48	0.35	6.83E+00
DK_175	1.59E-03	4.86E-04	3.76E-05	1.20E+45	9.27E+43	2.45E+46	1.40E+45	0.52	6.68E+00
DK_170	4.22E-04	3.97E-01	1.31E-02	1.15E+47	3.79E+45	7.56E+48	1.66E+47	0.47	1.43E+01
DK_158	1.91E-02	4.01E-01	6.14E-01	1.19E+49	1.82E+49	6.03E+50	9.71E+50	0.85	5.55E-01
DK_3	1.58E-02	2.66E-01	2.44E-01	6.56E+48	6.00E+48	2.10E+50	1.90E+50	0.61	6.70E-01
DK_137	1.82E-02	2.04E-03	3.24E-03	5.76E+46	9.15E+46	1.54E+48	2.59E+48	0.93	5.83E-01
DK_126	5.93E-02	1.24E-01	6.45E-01	5.04E+48	2.62E+49	3.53E+50	2.23E+51	0.53	1.02E-01
DK_b_277	6.29E-03	2.94E-03	1.50E-03	2.88E+46	1.47E+46	7.72E+47	3.65E+47	0.86	1.68E+00
DK_3474	4.90E-03	5.06E-01	1.35E-01	3.86E+48	1.03E+48	1.27E+50	2.91E+49	0.58	2.16E+00
DK_86	2.19E-03	1.30E+00	2.16E-01	1.96E+48	3.25E+47	1.59E+50	2.13E+49	0.46	2.75E+00
DK_546	9.87E-04	3.96E-01	2.26E-02	6.07E+47	3.46E+46	2.73E+49	1.10E+48	0.61	1.07E+01
DK_79	6.53E-03	5.35E-01	1.71E-01	5.44E+48	1.73E+48	2.73E+50	7.58E+49	0.52	1.62E+00
DK_3901	3.42E-02	7.85E-01	5.03E-01	7.46E+49	4.78E+49	2.35E+51	1.43E+51	0.25	3.90E-01
DK_b_526	6.73E-02	4.54E-02	2.17E-01	2.09E+48	9.99E+48	1.30E+50	7.50E+50	0.43	8.94E-02
DK_1544	7.21E+00	2.56E-02	1.44E+01	2.87E+50	1.61E+53	1.33E+52	1.59E+55	0.82	1.47E-03
DK_1763	8.82E-03	1.10E-01	6.19E-02	1.52E+48	8.50E+47	4.26E+49	2.23E+49	0.67	1.20E+00
DK_1833	1.45E-01	2.07E-01	2.11E+00	2.05E+49	2.09E+50	1.58E+51	2.13E+52	0.42	4.17E-02
DK_1473	1.84E+00	9.96E-03	1.39E+00	2.85E+49	3.98E+51	1.11E+51	2.80E+53	0.8	5.76E-03
DK_2115	5.85E-03	3.82E-01	1.29E-01	1.53E+48	5.18E+47	1.12E+50	3.32E+49	0.35	1.03E+00
DK_1238	1.14E-01	3.08E-02	2.95E-01	5.47E+48	5.23E+49	1.46E+50	1.83E+51	0.89	9.29E-02
DK_2141	2.30E+00	2.74E-02	5.53E+00	9.81E+49	1.98E+52	2.91E+51	1.11E+54	0.93	4.61E-03
DK_2168	4.73E-01	2.85E-01	1.08E+01	2.10E+50	7.91E+51	1.16E+52	6.76E+53	0.84	2.24E-02
DK_2190	2.13E-02	6.53E-02	1.14E-01	2.17E+48	3.79E+48	5.92E+49	1.11E+50	0.87	4.98E-01
DK_2307	2.84E-01	1.12E-01	1.91E+00	4.94E+49	8.43E+50	2.39E+51	5.74E+52	0.64	3.73E-02
DK_2350	5.54E+00	2.63E-02	1.24E+01	2.27E+50	1.07E+53	1.04E+52	1.02E+55	0.9	1.91E-03
DK_1115	1.51E+01	1.92E-02	2.45E+01	4.53E+50	5.77E+53	2.08E+52	6.24E+55	0.89	7.01E-04
DK_1000	2.37E-01	7.38E-03	1.43E-01	2.72E+48	5.28E+49	9.42E+49	2.61E+51	0.87	4.48E-02
DK_2533	4.32E-01	6.70E-03	2.43E-01	4.50E+48	1.63E+50	1.06E+50	5.88E+51	0.89	2.45E-02
DK_962	2.28E-01	4.83E-02	8.77E-01	3.06E+49	5.55E+50	7.42E+50	1.91E+52	1.06	5.86E-02
DK_2606	2.59E-03	1.49E+00	2.37E-01	6.00E+48	9.56E+47	2.19E+50	2.80E+49	0.65	4.09E+00
DK_14	8.64E-03	3.06E-01	2.15E-01	4.11E+48	2.89E+48	1.30E+50	8.79E+49	0.86	1.23E+00
DK_12	1.52E-01	4.48E-02	5.53E-01	1.06E+49	1.31E+50	4.47E+50	7.46E+51	0.86	6.98E-02
DK_2	5.40E-02	1.59E-01	6.73E-01	1.34E+49	5.65E+49	4.22E+50	2.12E+51	0.83	1.96E-01
DK_2725	1.88E-03	3.82E-01	5.32E-02	1.11E+48	1.55E+47	5.11E+49	5.62E+48	0.79	5.65E+00
DK_862	4.52E-01	4.68E-02	1.72E+00	1.45E+49	5.34E+50	9.77E+50	5.55E+52	0.49	1.33E-02
DK_2885	1.89E-01	2.79E-02	4.56E-01	8.19E+48	1.34E+50	3.30E+50	7.55E+51	0.92	5.61E-02
DK_2909	3.55E-01	4.44E-02	1.15E+00	2.45E+49	6.35E+50	7.16E+50	2.74E+52	0.77	2.98E-02
DK_3012	2.13E-03	6.95E+00	3.69E-01	2.31E+49	1.23E+48	1.51E+51	5.63E+49	0.26	4.97E+00
DK_3157	1.92E-03	6.23E-01	1.00E-01	8.20E+47	1.32E+47	6.06E+49	7.84E+48	0.5	3.13E+00
DK_719	8.94E-02	1.24E-01	8.11E-01	1.72E+49	1.13E+50	8.06E+50	6.61E+51	0.78	1.19E-01
DK_652	1.82E-02	4.34E-01	6.27E-01	1.22E+49	1.77E+49	4.17E+50	6.31E+50	0.84	5.84E-01
DK_3330	2.01E-03	5.92E-01	8.66E-02	1.85E+48	2.70E+47	5.98E+49	6.96E+48	0.77	5.28E+00
DK_3372	3.06E-04	1.68E+01	5.14E-02	8.00E+48	2.45E+46	5.37E+50	8.20E+47	0.11	3.47E+01
DK_3460	1.09E-01	1.63E-01	1.25E+00	2.76E+49	2.11E+50	8.99E+50	8.78E+51	0.75	9.76E-02
DK_3718	6.23E-03	1.74E-01	7.66E-02	7.45E+47	3.27E+47	4.96E+49	1.97E+49	0.42	9.66E-01
DK_3717	1.13E-02	3.06E-01	1.57E-01	5.40E+48	2.77E+48	1.73E+50	8.21E+49	0.48	9.34E-01
DK_3766	8.83E-03	2.53E-01	1.96E-01	3.48E+48	2.69E+48	1.61E+50	1.21E+50	0.93	1.20E+00
DK_4085	2.11E-03	9.32E-01	8.29E-02	3.06E+48	2.72E+47	1.05E+50	6.98E+48	0.45	5.02E+00
DK_4913	3.16E-01	1.09E-01	3.07E+00	5.34E+49	1.51E+51	1.73E+51	7.29E+52	0.95	3.35E-02
DK_1610	4.24E-02	1.16E-01	3.56E-01	7.64E+48	2.35E+49	3.44E+50	1.21E+51	0.77	2.50E-01
DK_1680	2.77E-02	4.28E-01	5.78E-01	1.84E+49	2.49E+49	6.38E+50	8.94E+50	0.52	3.83E-01
DK_4939	1.02E-01	1.21E-01	8.10E-01	1.92E+49	1.28E+50	8.98E+50	7.56E+51	0.7	1.04E-01
DK_1761	1.41E-01	3.88E-03	4.77E-02	8.48E+47	1.04E+49	2.66E+49	4.43E+50	0.93	7.54E-02
DK_1523	4.31E-01	9.87E-02	2.46E+00	2.91E+49	7.26E+50	2.14E+51	7.86E+52	0.35	1.40E-02
DK_1824	1.30E-01	6.09E-02	6.16E-01	1.24E+49	1.25E+50	5.39E+50	7.19E+51	0.82	8.12E-02
DK_265	8.56E-02	2.64E-01	1.89E+00	3.52E+49	2.51E+50	1.80E+51	1.63E+52	0.88	1.24E-01
DK_260	6.41E-01	4.62E-03	2.50E-01	4.60E+48	2.49E+50	1.05E+50	9.16E+51	0.89	1.65E-02
DK_5559	3.48E-01	9.06E-02	2.14E+00	4.90E+49	1.16E+51	1.56E+51	5.39E+52	0.72	3.05E-02
DK_1305	6.76E-03	2.16E-02	1.15E-02	2.27E+47	1.21E+47	7.77E+48	3.82E+48	0.83	1.57E+00

DK_1256	1.13E-01	3.00E-03	2.86E-02	2.32E+47	2.21E+48	1.06E+49	1.33E+50	0.51	5.33E-02
DK_1232	4.25E-03	1.40E-01	4.49E-02	4.07E+47	1.31E+47	2.59E+49	7.28E+48	0.46	1.42E+00
DK_1231	1.54E-02	3.77E-02	4.81E-02	3.97E+47	5.06E+47	2.28E+49	2.99E+49	0.5	3.91E-01
DK_2171	9.39E+00	6.93E-03	3.58E+00	1.01E+50	5.23E+52	2.70E+51	2.95E+54	0.58	1.13E-03
DK_207	5.94E-02	1.80E-01	7.95E-01	1.67E+49	7.35E+49	8.02E+50	4.23E+51	0.79	1.78E-01
DK_2263	2.28E-01	1.07E-04	2.11E-03	3.80E+46	7.51E+47	7.90E+47	2.24E+49	0.92	4.64E-02
DK_2283	3.81E-01	4.25E-02	1.19E+00	2.52E+49	7.04E+50	7.33E+50	3.06E+52	0.78	2.78E-02
DK_2288	3.04E-03	6.85E-03	1.02E-03	1.43E+46	2.12E+45	6.26E+47	7.40E+46	0.29	1.98E+00
DK_2297	2.99E-01	1.99E-01	4.43E+00	9.28E+49	2.06E+51	4.82E+51	1.55E+53	0.79	3.54E-02
DK_1139	4.86E+00	4.38E-02	1.80E+01	1.46E+50	6.00E+52	1.07E+52	9.09E+54	0.51	1.24E-03
DK_1135	6.61E-02	2.08E-04	9.96E-04	2.14E+46	1.02E+47	3.07E+47	1.77E+48	0.77	1.60E-01
DK_179	2.34E-01	5.20E-03	9.19E-02	8.32E+47	1.47E+49	4.20E+49	1.05E+51	0.46	2.58E-02
DK_171	1.17E-02	2.86E-01	1.93E-01	5.19E+48	3.50E+48	1.65E+50	1.06E+50	0.61	9.09E-01
DK_1037	6.63E-03	4.61E-01	2.74E-01	4.76E+48	2.82E+48	1.57E+50	8.75E+49	0.95	1.60E+00
DK_2458	1.09E-01	7.05E-05	4.46E-04	1.20E+46	7.60E+46	1.54E+47	1.22E+48	0.61	9.69E-02
DK_2534	1.50E-01	1.08E-01	1.14E+00	2.52E+49	2.67E+50	7.90E+50	1.11E+52	0.75	7.05E-02
DK_2572	6.20E-02	6.95E-02	3.16E-01	6.70E+48	3.05E+49	2.88E+50	1.57E+51	0.78	1.71E-01
DK_138	4.02E-03	9.24E-03	3.17E-03	5.79E+46	1.98E+46	1.17E+48	3.53E+47	0.9	2.63E+00
DK_2778	9.86E-01	1.14E-01	2.92E+00	7.69E+49	1.97E+51	5.95E+51	2.26E+53	0.16	6.10E-03
DK_860	1.17E+00	1.76E-02	1.80E+00	3.20E+49	3.27E+51	8.76E+50	1.56E+53	0.93	9.06E-03
DK_2953	5.89E-02	3.61E-01	1.23E+00	3.31E+49	1.13E+50	1.73E+51	6.84E+51	0.61	1.80E-01
DK_2974	7.24E-02	1.57E-04	8.25E-04	1.77E+46	9.29E+46	2.47E+47	1.58E+48	0.77	1.46E-01
DK_783	1.13E-02	2.40E-01	1.14E-01	1.86E+48	8.81E+47	1.31E+50	5.71E+49	0.25	5.34E-01
DK_2996	4.44E-01	1.91E-02	7.55E-01	5.81E+48	2.29E+50	3.52E+50	2.16E+52	0.54	1.36E-02
DK_3035	5.42E-02	5.85E-02	2.50E-01	4.93E+48	2.10E+49	2.07E+50	1.05E+51	0.83	1.96E-01
DK_3067	2.12E-02	4.70E-01	7.83E-01	6.83E+48	1.14E+49	5.38E+50	9.52E+50	0.47	2.84E-01
DK_746	1.53E-01	5.68E-03	7.77E-02	5.95E+47	8.14E+48	2.98E+49	5.59E+50	0.54	3.93E-02
DK_738	3.81E-02	4.62E-02	1.49E-01	2.73E+48	8.80E+48	1.10E+50	4.06E+50	0.9	2.78E-01
DK_3137	3.86E+00	3.75E-03	1.23E+00	9.90E+48	3.24E+51	5.38E+50	3.52E+53	0.51	1.56E-03
DK_3196	5.91E-01	1.09E-01	5.16E+00	1.00E+50	4.75E+51	4.98E+51	3.75E+53	0.85	1.79E-02
DK_3205	8.96E-03	8.00E-01	3.50E-01	1.12E+49	4.88E+48	5.95E+50	2.36E+50	0.52	1.18E+00
DK_687	5.08E-02	2.75E-02	6.83E-02	9.58E+47	2.38E+48	5.55E+49	1.54E+50	0.29	1.18E-01
DK_3269	1.43E-01	3.85E-02	4.48E-01	8.53E+48	9.95E+49	2.36E+50	3.70E+51	0.87	7.43E-02
DK_95	2.77E-01	6.85E-03	1.66E-01	2.95E+48	7.14E+49	1.02E+50	3.62E+51	0.93	3.83E-02
DK_96	8.17E-04	8.32E-01	5.14E-02	1.06E+48	6.53E+46	5.15E+49	2.28E+48	0.8	1.30E+01
DK_3379	8.90E-02	1.01E-01	5.74E-01	6.18E+48	3.50E+49	4.29E+50	2.99E+51	0.38	6.76E-02
DK_b_793	5.25E-03	6.93E-02	2.36E-02	2.49E+47	8.50E+46	1.47E+49	4.42E+48	0.39	1.15E+00
DK_597	5.51E-02	8.69E-04	3.67E-03	7.45E+46	3.15E+47	1.88E+48	9.46E+48	0.81	1.92E-01
DK_592	5.94E-02	6.97E-04	3.72E-03	6.44E+46	3.44E+47	1.59E+48	1.04E+49	0.95	1.79E-01
DK_3593	1.01E-01	2.78E-01	7.02E-01	4.39E+49	1.11E+50	1.52E+51	4.29E+51	0.26	1.05E-01
DK_3740	2.24E-02	3.38E+00	7.57E-01	1.18E+50	2.64E+49	7.75E+51	1.45E+51	0.11	4.74E-01
DK_496	2.31E-03	1.22E-02	2.30E-03	4.39E+46	8.25E+45	8.99E+47	1.38E+47	0.86	4.59E+00
DK_3866	3.47E-01	3.20E-02	8.88E-01	1.73E+49	4.80E+50	7.26E+50	3.00E+52	0.85	3.05E-02
DK_3907	3.54E-01	2.82E-01	5.53E+00	1.55E+50	3.05E+51	8.47E+51	2.38E+53	0.59	2.99E-02
DK_416	1.75E-02	1.40E-02	2.15E-02	3.82E+47	5.85E+47	8.60E+48	1.39E+49	0.93	6.05E-01
DK_4218	4.14E-03	2.16E+00	4.15E-01	1.39E+49	2.68E+48	8.10E+50	1.28E+50	0.49	2.56E+00
DK_58	1.03E-02	7.43E-01	4.41E-01	5.22E+48	3.09E+48	4.21E+50	2.35E+50	0.35	5.87E-01
DK_57	5.41E-04	2.04E+01	1.10E-01	7.57E+48	4.09E+46	8.09E+50	2.34E+48	0.06	1.11E+01
DK_4666	1.89E-02	2.28E-01	3.56E-01	6.71E+48	1.05E+49	3.17E+50	5.23E+50	0.88	5.60E-01
DK_335	8.72E-02	1.50E-03	1.08E-02	2.03E+47	1.47E+48	5.59E+48	5.12E+49	0.88	1.22E-01
DK_4766	5.53E+00	1.42E-06	5.75E-04	5.40E+45	2.18E+48	1.15E+47	9.57E+49	0.44	1.09E-03
DK_4776	7.58E-03	2.90E-01	1.64E-01	3.42E+48	1.93E+48	1.61E+50	8.46E+49	0.79	1.40E+00
DK_4796	5.16E-02	1.24E-01	4.39E-01	4.38E+48	1.55E+49	3.04E+50	1.26E+51	0.41	1.17E-01
DK_304	2.75E-03	3.44E-02	7.84E-03	1.47E+47	3.35E+46	3.43E+48	6.54E+47	0.88	3.86E+00
DK_5044	5.01E-02	3.64E-01	1.22E+00	1.25E+49	4.18E+49	1.47E+51	5.71E+51	0.4	1.20E-01
DK_5315	1.33E-01	7.13E-03	7.44E-02	1.48E+48	1.54E+49	4.98E+49	6.89E+50	0.83	7.97E-02
DK_262	1.66E-03	3.38E-01	4.41E-02	8.75E+47	1.14E+47	2.63E+49	2.69E+48	0.83	6.37E+00
DK_203	1.39E+00	9.95E-02	1.21E+01	2.15E+50	2.61E+52	7.30E+51	1.58E+54	0.93	7.63E-03
DK_178	1.15E-02	6.86E-01	3.31E-01	1.22E+49	5.90E+48	6.47E+50	2.86E+50	0.45	9.25E-01
DK_180	3.38E-02	8.60E-02	1.23E-01	1.99E+48	2.84E+48	1.30E+50	1.94E+50	0.25	1.78E-01
DK_22	1.33E-03	2.16E+00	1.40E-01	4.46E+48	2.89E+47	2.48E+50	1.16E+49	0.52	7.98E+00
DK_19	4.93E-02	2.98E-01	7.17E-01	2.29E+49	5.50E+49	7.76E+50	2.07E+51	0.52	2.15E-01
DK_159	4.56E-01	6.57E-03	2.51E-01	2.05E+48	7.82E+49	1.09E+50	6.46E+51	0.5	1.32E-02

DK_157	4.04E-01	1.48E-01	5.06E+00	9.33E+49	3.19E+51	4.74E+51	2.47E+53	0.89	2.62E-02
DK_143	4.32E-01	6.81E-02	2.18E+00	4.57E+49	1.47E+51	1.42E+51	6.89E+52	0.79	2.45E-02
DK_118	2.97E-01	1.06E-01	2.21E+00	4.88E+49	1.02E+51	2.35E+51	7.09E+52	0.75	3.57E-02
DK_88	9.48E-02	8.37E-02	5.59E-01	1.24E+49	8.25E+49	5.53E+50	4.63E+51	0.75	1.12E-01
DK_84	1.19E-01	3.21E-01	3.36E+00	5.97E+49	6.24E+50	3.17E+51	4.39E+52	0.93	8.88E-02
DK_80	1.37E+00	1.44E-02	1.73E+00	3.07E+49	3.70E+51	8.27E+50	1.77E+53	0.93	7.71E-03
DK_77	3.90E-02	4.57E-05	1.32E-04	1.22E+45	3.53E+45	3.24E+46	1.07E+47	0.45	1.55E-01
DK_40	1.21E-02	4.60E-01	4.22E-01	3.82E+48	3.51E+48	2.94E+50	2.67E+50	0.46	4.96E-01
DK_39	1.21E-02	4.99E-01	4.57E-01	1.68E+49	1.54E+49	4.80E+50	4.35E+50	1.01	1.10E+00
DK_32	1.77E-02	4.01E-01	5.55E-01	1.10E+49	1.53E+49	3.72E+50	5.36E+50	0.83	6.00E-01
DK_24	4.24E-02	1.11E-01	3.69E-01	3.23E+48	1.07E+49	2.20E+50	8.42E+50	0.47	1.42E-01
DK_20	5.78E-03	6.80E-01	1.92E-01	2.69E+48	7.61E+47	2.10E+50	5.11E+49	0.29	1.04E+00
DK_18	1.06E-03	1.76E+00	7.85E-02	1.28E+48	5.69E+46	1.04E+50	3.20E+48	0.25	5.69E+00

Table A.0.23: Derived physical quantities using the shell parameters. Column 2 contains the spatial volume of the shell, $V_{\rm sh}$. The measured particle density, $n_{\rm obs}$, and the upper particle density, $n_{\rm obs,u}$, of each shell are listed in column 3 and 4 respectively. Columns 5 and 6 list the corresponding theoretical total energies ejected from the stars, $E_{\rm tot,w}$ and $E_{\rm w,u}(t)$ respectively (eq. 2.21). The total energies, calculated using eq. 2.7, $E_{\rm c}(t)$ and $E_{\rm c,u}(t)$, are listed in column 7 and 8 respectively. Columns 9 and 10 list the ratio between the results of equation 2.24 for the energy ratio, using the values of $E_{\rm weav}(t)$ and $E_{\rm chev}(t)$, respectively.

1	2	3	4	5	6	7	8	9	10
name:	$\Delta V_{\rm sh}$	$\Delta n_{\rm obs}$	$\Delta n_{\rm obs,u}$	$\Delta E_{\rm w}(t)$	$\Delta E_{\rm w,u}(t)$	$\Delta E_{\rm c}(t)$	$\Delta E_{\rm c,u}(t)$	$\Delta\epsilon_{\rm w}$	$\Delta\epsilon_{\rm w,l}$
unit:	kpc^3	cm^{-3}	cm^{-3}	erg	erg	erg	erg	-	-
DK_1476	5.34E+00	1.17E-02	2.01E+00	7.57E+49	2.81E+52	3.42E+52	1.97E+54	0.73	2.87E-03
DK_2046	9.17E-01	7.84E-02	3.69E+00	2.01E+51	1.73E+53	1.06E+53	4.29E+54	1.34	2.28E-02
DK_1303	7.27E+00	1.62E-02	1.24E+01	1.81E+52	1.83E+55	1.29E+54	9.51E+56	0.9	1.41E-03
DK_1286	2.14E-01	2.87E-01	6.73E-01	4.04E+50	3.50E+51	1.26E+52	7.26E+52	1.36	1.98E-01
DK_1188	1.96E+00	8.92E-02	8.52E+00	2.56E+51	4.27E+53	2.10E+53	1.92E+55	1.27	1.12E-02
DK_1187	2.21E+00	8.85E-02	9.21E+00	3.43E+51	6.48E+53	2.68E+53	2.78E+55	1.33	1.03E-02
DK_1119	3.71E-02	8.05E-01	2.68E-01	2.94E+49	3.77E+49	9.24E+50	1.51E+51	0.74	4.32E-01
DK_857	1.15E-01	5.18E-01	1.78E-01	1.75E+50	5.77E+50	4.27E+51	1.24E+52	1.46	4.42E-01
DK_810	9.79E-02	7.50E-01	2.09E-01	1.85E+50	3.27E+50	3.65E+51	8.25E+51	1.02	4.53E-01
DK_3462	2.94E+00	4.17E-02	1.05E+01	2.55E+51	9.64E+53	3.13E+53	5.03E+55	1.24	4.86E-03
DK_457	7.99E-01	1.36E-01	1.85E+00	1.38E+51	5.52E+52	6.89E+52	1.98E+54	1.14	4.18E-02
DK_1619	3.52E-01	1.14E-01	1.77E+00	1.46E+51	4.42E+52	7.16E+52	1.15E+54	1.58	6.85E-02
DK_1701	3.84E-01	2.61E-01	5.51E-01	8.78E+49	8.26E+50	6.00E+51	3.14E+52	1.02	1.48E-01
DK_1452	1.59E-01	2.22E-01	3.09E+00	3.39E+50	5.56E+51	1.47E+52	2.45E+53	0.81	7.33E-02
DK_1117	4.30E-01	2.14E-01	1.67E+00	1.08E+51	2.20E+52	4.62E+52	6.15E+53	1.37	9.01E-02
DK_960	8.32E-01	3.39E-02	3.09E+00	1.43E+50	1.71E+52	2.68E+52	7.56E+53	1.01	1.19E-02
DK_3275	1.63E+00	2.81E-02	3.74E+00	3.91E+50	7.15E+52	3.36E+52	2.04E+54	0.78	7.08E-03
DK_3297	3.61E-01	1.39E-01	1.39E+00	4.50E+50	1.03E+52	8.34E+51	1.03E+53	1.08	7.22E-02
DK_3295	2.84E-01	1.44E-01	8.79E-01	1.80E+50	2.65E+51	8.63E+51	6.84E+52	1.01	1.01E-01
DK_3296	3.32E-01	1.34E-01	1.10E+00	2.87E+50	5.47E+51	6.50E+51	6.51E+52	1	8.11E-02
DK_3639	1.99E+00	1.32E-02	2.76E+00	1.22E+51	4.12E+53	1.97E+53	1.94E+55	1.21	5.49E-03
DK_b_823	3.08E-02	1.28E-02	8.93E-03	1.37E+48	2.39E+48	1.87E+50	2.47E+50	1.05	4.59E-01
DK_1580	5.09E-01	9.63E-02	1.39E+00	6.85E+50	2.28E+52	3.90E+52	8.60E+53	1.07	4.76E-02
DK_1527	2.29E-01	8.15E-02	3.33E-01	1.07E+50	9.19E+50	5.59E+51	3.57E+52	0.65	1.08E-01
DK_5129	1.60E+00	1.91E-02	1.69E+00	1.17E+51	1.81E+53	8.71E+52	5.03E+54	0.88	9.61E-03
DK_1483	1.75E-02	5.70E-01	1.97E-01	1.87E+49	1.83E+49	5.86E+50	6.86E+50	0.84	6.00E-01
DK_1828	3.33E-01	1.05E-01	4.44E-01	3.97E+49	5.08E+50	3.43E+51	2.32E+52	0.71	8.14E-02
DK_1965	1.25E-02	1.90E-01	7.91E-02	2.07E+49	1.70E+49	7.13E+50	7.15E+50	1.32	1.09E+00
DK_1281	7.36E-03	4.21E-01	5.38E-02	5.56E+48	1.34E+48	1.44E+50	9.38E+49	0.4	7.03E+00
DK_165	6.14E-02	2.51E-01	1.75E-01	7.02E+49	2.32E+50	2.60E+51	7.39E+51	1.2	3.95E-01
DK_928	2.93E-01	2.01E-01	1.08E+00	3.67E+50	5.43E+51	1.74E+52	1.53E+53	1.34	1.21E-01
DK_2819	3.16E-01	2.40E-01	2.36E+00	7.19E+51	1.02E+53	1.19E+53	1.92E+54	1.1	9.52E-02
DK_2820	8.43E-02	7.75E-02	1.54E-01	2.36E+49	1.13E+50	1.90E+51	4.55E+51	1.14	2.86E-01
DK_2873	1.01E-01	1.80E-01	8.78E-01	3.84E+50	2.11E+51	8.41E+51	8.43E+52	0.52	1.28E-01
DK_3145	7.28E-01	3.02E-02	2.72E+00	2.60E+50	3.06E+52	3.70E+52	1.41E+54	0.99	1.26E-02
DK_104	3.35E-02	3.41E-01	1.46E-01	4.17E+49	6.63E+49	1.52E+51	2.23E+51	1.33	6.35E-01
DK_3277	2.40E-01	1.99E-01	1.14E+00	2.45E+50	3.02E+51	1.49E+52	9.64E+52	1.36	1.43E-01

DK_635	2.38E-01	2.45E-01	5.09E-01	9.46E+49	7.22E+50	5.99E+51	2.40E+52	1.26	2.09E-01
DK_4220	1.75E-01	1.04E-01	1.22E+00	3.26E+50	4.84E+51	1.51E+52	1.70E+53	0.87	8.54E-02
DK_1514	1.83E+00	5.46E-02	6.46E+00	7.70E+51	1.96E+54	4.23E+53	8.68E+55	1.31	7.82E-03
DK_1785	4.86E-02	2.21E-01	2.44E-01	1.74E+49	4.22E+49	1.00E+51	2.02E+51	0.8	3.45E-01
DK_1783	2.55E-01	1.81E-01	6.11E-01	1.07E+50	1.15E+51	7.99E+51	3.98E+52	1.35	1.61E-01
DK_1784	7.26E-02	2.42E-01	1.87E-01	8.16E+49	2.24E+50	2.98E+51	6.90E+51	1.14	4.15E-01
DK_5209	1.43E-01	8.85E-02	2.07E-01	5.37E+48	2.08E+49	1.06E+51	3.09E+51	0.35	1.09E-01
DK_1846	4.60E-02	1.08E+00	2.63E-01	1.29E+50	2.78E+50	4.05E+51	4.66E+51	1.97	1.00E+00
DK_5238	6.11E-02	1.85E-01	8.62E-02	4.80E+48	8.64E+48	3.79E+50	6.28E+50	0.59	3.10E-01
DK_1389	1.03E+01	1.87E-02	1.05E+01	1.64E+51	1.41E+54	3.59E+53	8.73E+55	0.94	1.70E-03
DK_2009	2.25E-01	1.10E-04	3.64E-04	2.79E+46	3.08E+47	1.60E+50	4.47E+50	0.86	1.09E-01
DK_1299	6.51E-02	6.43E-01	9.35E-02	1.02E+49	1.05E+49	4.42E+50	5.61E+50	0.71	4.89E-01
DK_1267	4.38E-01	2.48E-02	4.38E-01	2.91E+49	1.29E+51	4.89E+51	8.36E+52	0.68	2.26E-02
DK_1221	1.63E-01	1.00E+00	5.34E-01	2.90E+50	9.22E+50	7.73E+51	1.96E+52	1.71	4.98E-01
DK_930	2.23E-01	8.39E-02	9.52E-01	1.02E+50	1.85E+51	8.74E+51	8.17E+52	0.91	7.28E-02
DK_120	4.48E-02	5.21E-01	2.22E-01	8.23E+49	1.47E+50	2.37E+51	3.93E+51	1.43	6.30E-01
DK_756	1.26E-01	7.33E-01	4.41E-01	3.81E+50	1.41E+51	9.30E+51	3.24E+52	1.51	4.10E-01
DK_b_785	1.73E-01	3.10E-03	2.49E-02	9.32E+48	1.23E+50	3.12E+51	9.86E+51	1.05	1.14E-01
DK_656	8.97E+00	5.90E-02	1.39E+01	1.29E+52	8.28E+54	6.82E+53	2.28E+56	1.2	3.04E-03
DK_3575	3.90E-01	1.99E-01	2.14E+00	3.84E+50	9.99E+51	2.08E+52	4.55E+53	1.03	5.81E-02
DK_3584	3.44E+00	2.34E-02	3.13E+00	1.45E+51	3.92E+53	1.50E+53	2.30E+55	0.81	4.72E-03
DK_562	1.80E+01	2.77E-02	2.00E+01	1.33E+52	1.87E+55	1.91E+54	8.63E+56	1.34	1.42E-03
DK_3668	7.71E-01	2.00E-03	1.06E-01	4.77E+49	3.97E+51	1.73E+52	1.86E+53	0.82	1.54E-02
DK_456	3.06E-02	1.28E-02	3.07E-02	2.28E+48	8.19E+48	5.03E+50	9.36E+50	0.84	2.76E-01
DK_4380	1.53E-01	5.94E-01	4.89E-01	3.29E+50	9.32E+50	7.55E+51	2.30E+52	1.01	3.56E-01
DK_4593	4.44E-01	4.61E-02	8.42E-01	2.55E+50	6.17E+51	2.00E+52	2.39E+53	0.73	4.65E-02
DK_4719	1.80E+00	3.82E-02	9.08E-01	6.99E+50	7.43E+52	6.37E+52	2.60E+54	1.2	1.72E-02
DK_1668	1.34E+01	9.29E-03	1.16E+01	1.92E+51	3.49E+54	5.53E+53	2.29E+56	1.02	8.57E-04
DK_1601	3.20E-02	4.42E-03	1.98E-03	1.25E+47	1.72E+47	8.12E+49	9.72E+49	0.97	5.45E-01
DK_1555	8.51E-03	3.17E-01	4.92E-02	5.92E+48	1.93E+48	1.34E+50	9.61E+49	0.59	5.64E+00
DK_1528	3.49E-01	3.81E-02	4.38E-01	4.01E+49	6.48E+50	4.17E+51	2.77E+52	0.55	5.29E-02
DK_294	1.77E-01	1.30E-04	4.44E-04	2.24E+46	2.48E+47	1.24E+50	3.48E+50	0.71	8.92E-02
DK_1861	9.06E-02	1.48E-01	7.44E-02	9.58E+48	3.17E+49	6.65E+50	1.54E+51	0.82	2.89E-01
DK_1906	8.77E-02	8.76E-02	2.77E-01	3.20E+49	2.26E+50	1.84E+51	9.44E+51	0.73	1.43E-01
DK_1400	1.01E-01	4.71E-01	6.70E-01	2.05E+50	1.04E+51	6.62E+51	4.28E+52	0.91	2.28E-01
DK_1958	6.83E-01	6.85E-02	1.26E+00	2.37E+50	1.01E+52	1.00E+52	1.53E+53	0.99	3.72E-02
DK_5458	1.01E-01	5.08E-01	2.24E-01	3.43E+50	9.49E+50	6.52E+51	2.10E+52	1.2	4.04E-01
DK_1983	8.40E-02	1.75E-01	1.14E-01	2.51E+49	8.46E+49	1.36E+51	3.71E+51	0.87	3.01E-01
DK_1993	6.46E+01	8.74E+00	3.60E+00	1.08E+49	1.54E+51	7.08E+51	2.17E+52	7.8	4.82E-01
DK_1331	5.70E-02	5.57E-02	4.54E-02	5.92E+48	1.74E+49	5.77E+50	9.98E+50	1.06	3.90E-01
DK_2034	7.79E-01	2.68E-02	3.32E-01	6.28E+49	3.38E+51	9.29E+51	1.53E+53	0.98	2.77E-02
DK_2320	2.79E-01	1.09E-01	2.67E-01	2.33E+49	2.82E+50	2.51E+51	1.38E+52	0.9	1.05E-01
DK_2335	4.04E+00	1.23E-02	3.86E+00	2.20E+51	1.30E+54	9.83E+52	2.06E+55	0.86	2.70E-03
DK_2351	9.84E-03	5.59E-01	8.65E-02	3.21E+48	1.17E+48	1.46E+50	9.79E+49	0.69	4.70E+00
DK_2389	2.24E-02	7.66E-01	5.57E-02	3.93E+48	1.59E+48	1.76E+50	1.25E+50	0.93	4.59E+00
DK_2496	6.66E-01	9.99E-02	5.04E+00	3.60E+50	1.66E+52	2.01E+52	1.24E+54	0.38	1.29E-02
DK_2513	9.96E-02	5.99E-02	1.39E-01	1.35E+49	9.50E+49	1.41E+51	4.86E+51	0.85	1.64E-01
DK_1011	5.41E-01	3.20E-02	7.35E-01	2.63E+50	1.08E+52	3.59E+52	3.38E+53	1.37	4.66E-02
DK_2595	2.14E+01	3.15E-03	7.88E+00	5.60E+50	2.11E+54	3.49E+53	1.53E+56	0.91	3.65E-04
DK_2598	2.41E+00	5.14E-02	2.66E+00	2.85E+51	3.43E+53	1.58E+53	1.57E+55	0.79	1.03E-02
DK_2663	1.12E+00	2.86E-02	3.01E+00	1.05E+51	1.55E+53	1.29E+53	6.56E+54	1.18	1.20E-02
DK_919	4.14E-01	9.41E-02	5.63E-01	7.80E+49	1.49E+51	7.44E+51	5.09E+52	1.19	8.66E-02
DK_2740	2.88E-01	5.46E-02	1.29E+00	2.70E+49	8.80E+50	8.22E+51	1.54E+53	0.55	2.10E-02
DK_2779	6.27E-01	8.12E-02	5.67E-01	5.74E+49	1.54E+51	8.09E+51	7.00E+52	1.09	5.80E-02
DK_798	6.19E+00	6.72E-02	9.56E+00	6.46E+51	1.96E+54	5.34E+53	8.20E+55	1.09	5.59E-03
DK_3004	3.84E-01	6.94E-02	6.03E-01	1.92E+50	4.06E+51	1.43E+52	1.27E+53	1.1	7.52E-02
DK_3099	1.17E+00	2.29E-02	1.87E+00	7.40E+50	1.04E+53	8.14E+52	3.59E+54	1.21	1.29E-02
DK_737	3.31E-01	4.03E-02	1.79E+00	5.45E+49	3.18E+51	9.87E+51	1.89E+53	0.79	1.92E-02
DK_3187	4.03E-01	3.80E-02	3.30E-01	7.94E+49	1.99E+51	9.14E+51	6.67E+52	1.17	6.71E-02
DK_609	8.81E-03	7.50E-03	8.78E-04	1.92E+47	8.53E+46	4.52E+49	3.62E+49	1.02	3.76E+00
DK_3489	5.88E-02	1.37E-01	5.25E-01	5.65E+49	2.82E+50	2.94E+51	1.05E+52	0.85	2.19E-01
DK_3722	2.84E-01	1.05E-01	4.07E+00	2.57E+50	1.18E+52	1.85E+52	5.93E+53	0.8	2.64E-02
DK_3745	1.22E-01	1.60E-01	2.53E-01	9.52E+49	6.71E+50	4.73E+51	2.39E+52	1.16	2.14E-01

DK_3833	2.87E-02	5.88E-01	3.00E-01	3.47E+49	4.72E+49	1.21E+51	1.75E+51	1.03	5.74E-01
DK_3894	1.08E+00	7.44E-02	6.48E+00	2.24E+51	3.49E+53	1.30E+53	2.06E+55	1.03	1.03E-02
DK_4385	2.18E-01	4.95E-02	1.24E+00	6.78E+49	2.30E+51	7.85E+51	9.47E+52	0.95	3.98E-02
DK_4456	2.01E-01	9.68E-02	1.42E+00	3.92E+50	8.37E+51	1.97E+52	2.48E+53	1.08	7.43E-02
DK_4735	3.86E+00	4.38E-02	4.16E+00	1.36E+52	3.39E+54	7.71E+53	1.04E+56	1.22	7.28E-03
DK_1602	1.04E-02	6.16E-03	8.18E-04	4.23E+46	2.06E+46	2.16E+49	1.75E+49	0.74	2.31E+00
DK_306	9.26E+00	1.04E-02	1.14E+01	7.10E+50	1.10E+54	2.47E+53	8.06E+55	0.91	8.83E-04
DK_307	2.86E+00	2.27E-02	8.00E+00	1.12E+51	3.62E+53	1.44E+53	2.13E+55	0.63	3.20E-03
DK_b_486	1.97E+00	3.23E-02	1.01E+00	1.17E+50	1.13E+52	1.82E+52	6.53E+53	0.69	1.11E-02
DK_5049	1.80E+00	1.09E-02	1.68E+00	9.48E+50	4.10E+52	3.32E+52	2.23E+54	0.13	4.79E-03
DK_1771	9.23E-02	1.10E-04	8.58E-05	1.86E+46	4.55E+46	7.93E+49	1.35E+50	0.83	3.52E-01
DK_1792	2.74E-01	4.49E-02	3.38E-01	3.70E+49	6.84E+50	4.82E+51	2.87E+52	1.02	7.89E-02
DK_1802	7.02E-02	2.40E-01	2.96E-01	3.20E+49	9.53E+49	1.88E+51	3.50E+51	1.41	4.72E-01
DK_5194	4.01E-01	1.19E-01	3.27E-01	1.36E+50	1.90E+51	7.56E+51	6.53E+52	0.95	9.73E-02
DK_5192	9.31E-01	6.30E-02	1.20E+00	7.82E+50	4.94E+52	6.07E+52	1.93E+54	1.23	2.90E-02
DK_5193	5.21E-01	7.39E-02	4.67E-01	1.85E+50	4.74E+51	1.39E+52	1.94E+53	0.98	5.69E-02
DK_b_449	3.41E+00	6.17E-02	3.98E+00	1.73E+51	3.46E+53	1.81E+53	1.40E+55	1.35	9.97E-03
DK_1879	1.73E+00	4.62E-02	5.22E+00	2.38E+51	4.44E+53	2.34E+53	1.68E+55	1.38	1.07E-02
DK_b_616	1.83E-01	7.82E-03	4.37E-02	3.33E+49	3.33E+50	1.65E+51	4.91E+51	0.94	1.35E-01
DK_1387	1.25E+01	3.25E-01	1.64E+00	2.34E+50	2.57E+52	1.76E+52	7.94E+53	0.8	1.24E-02
DK_1383	2.91E+00	6.22E-02	3.55E+00	1.18E+51	1.88E+53	1.25E+53	7.29E+54	1.27	1.19E-02
DK_5417	2.77E-01	1.88E-01	4.21E+00	3.35E+51	9.44E+52	3.93E+52	1.74E+54	0.71	4.27E-02
DK_5563	9.61E-01	3.50E-04	3.35E-02	7.59E+48	8.62E+50	4.73E+51	3.67E+52	0.75	1.16E-02
DK_5707	1.87E-01	9.83E-02	5.35E-01	4.57E+49	5.45E+50	4.34E+51	2.10E+52	1.13	1.27E-01
DK_b_665	3.72E-03	5.18E-02	2.02E-03	5.05E+47	6.03E+46	1.79E+49	8.53E+48	1.21	7.94E+01
DK_182	6.44E-02	1.60E-01	1.73E-01	1.06E+49	3.35E+49	9.06E+50	1.79E+51	0.97	3.39E-01
DK_2418	9.61E-01	3.48E-02	3.39E-01	4.64E+49	1.74E+51	5.79E+51	8.01E+52	0.65	2.67E-02
DK_1055	2.75E+00	1.17E-01	4.25E+00	3.74E+51	6.04E+53	2.10E+53	2.71E+55	1.25	1.18E-02
DK_2424	4.63E-01	3.65E-02	7.78E-01	7.72E+50	1.46E+52	2.32E+52	6.01E+53	0.38	3.08E-02
DK_2436	4.56E-02	2.77E-01	8.32E-02	4.00E+48	6.01E+48	3.07E+50	4.27E+50	0.72	4.11E-01
DK_b_338	1.25E-01	3.06E-02	1.86E-01	1.62E+49	1.26E+50	2.04E+51	7.13E+51	0.59	1.10E-01
DK_1007	3.20E-02	2.37E-01	2.18E-02	1.34E+49	1.71E+49	7.63E+50	6.99E+50	1.72	1.98E+00
DK_2524	1.87E-02	4.01E-01	5.28E-02	5.06E+48	2.19E+48	2.04E+50	1.66E+50	0.7	3.18E+00
DK_973	2.54E-01	3.64E-03	1.42E-02	1.12E+49	1.54E+50	4.61E+51	1.39E+52	1.5	1.41E-01
DK_2638	1.05E-01	2.24E-01	1.99E-01	4.60E+49	1.93E+50	2.51E+51	7.63E+51	1.07	3.04E-01
DK_146	5.88E-04	6.15E-01	8.12E-03	1.48E+48	2.80E+46	1.63E+49	3.30E+48	0.75	1.92E+03
DK_937	2.39E-01	1.18E-02	1.23E-01	6.99E+48	1.28E+50	2.27E+51	8.66E+51	0.91	6.99E-02
DK_2738	7.25E-01	2.61E-02	1.46E+00	1.10E+51	1.09E+53	9.34E+52	3.25E+54	1.35	2.01E-02
DK_2798	4.59E-02	7.91E-01	8.59E-01	5.89E+50	1.52E+51	9.76E+51	4.16E+52	0.87	3.38E-01
DK_2804	7.88E-01	6.57E-02	5.44E-01	6.32E+49	1.68E+51	8.00E+51	6.94E+52	0.86	4.89E-02
DK_129	5.41E-02	1.44E-01	5.07E-01	3.49E+49	1.99E+50	1.95E+51	7.87E+51	0.87	1.97E-01
DK_3122	2.17E-01	1.96E-01	2.34E-01	1.06E+50	7.03E+50	4.69E+51	2.45E+52	0.94	1.86E-01
DK_712	1.23E+01	9.29E-03	1.14E+01	1.96E+51	3.58E+54	4.98E+53	2.19E+56	1.04	8.68E-04
DK_713	1.24E+01	9.91E-03	1.24E+01	3.09E+51	5.84E+54	6.62E+53	3.41E+56	1.08	8.82E-04
DK_714	1.08E+01	1.09E-02	1.14E+01	4.79E+51	7.96E+54	7.35E+53	4.53E+56	1.06	9.95E-04
DK_3274	3.84E-01	6.00E-04	2.66E-03	3.74E+47	5.64E+48	8.65E+50	2.70E+51	1.15	1.05E-01
DK_3338	5.83E-01	7.21E-02	3.79E-01	1.28E+50	2.77E+51	8.81E+51	1.09E+53	0.79	5.51E-02
DK_3336	1.20E-01	1.94E-01	2.79E-01	3.86E+49	1.81E+50	2.36E+51	7.87E+51	0.88	2.36E-01
DK_3331	6.47E-01	2.08E-02	1.14E+00	3.54E+50	2.68E+52	1.62E+52	4.76E+53	0.71	1.68E-02
DK_b_303	5.62E-01	5.76E-02	3.06E-01	3.29E+49	7.11E+50	3.98E+51	3.39E+52	0.73	5.07E-02
DK_3551	6.94E-01	3.79E-02	1.29E+00	5.83E+50	3.94E+52	5.03E+52	1.43E+54	1.16	2.57E-02
DK_3574	3.45E-01	9.56E-02	9.68E-01	2.50E+50	5.58E+51	1.57E+52	1.55E+53	1.25	7.85E-02
DK_3609	5.69E-01	2.71E-02	1.56E+00	5.43E+50	4.39E+52	4.70E+52	1.55E+54	1	1.94E-02
DK_535	2.23E-02	1.39E+00	2.80E-01	3.41E+49	2.82E+49	1.04E+51	9.74E+50	1.15	9.94E-01
DK_530	2.88E-01	2.64E-01	7.72E-01	1.08E+50	9.92E+50	7.83E+51	3.18E+52	1.52	1.97E-01
DK_3756	1.10E-01	1.53E-01	3.48E-01	1.38E+50	7.83E+50	6.02E+51	2.47E+52	1.07	2.34E-01
DK_b_818	2.71E-01	1.15E-03	4.00E-03	4.27E+47	4.34E+48	3.75E+50	1.04E+51	0.8	1.17E-01
DK_3804	1.29E-01	1.20E-01	6.46E-01	9.43E+49	8.83E+50	5.43E+51	3.91E+52	0.8	1.21E-01
DK_3900	8.09E-02	7.48E-02	1.89E-01	2.24E+49	1.03E+50	1.96E+51	5.12E+51	0.85	2.33E-01
DK_466	1.27E-01	1.81E-03	1.56E-02	1.20E+48	1.58E+49	7.85E+50	2.46E+51	0.79	8.63E-02
DK_70	3.86E-02	1.38E-01	3.56E-01	4.65E+49	1.83E+50	2.17E+51	6.93E+51	0.9	2.75E-01
DK_4223	1.46E+00	2.45E-02	1.99E+00	1.83E+51	2.26E+53	1.21E+53	1.07E+55	0.76	9.62E-03
DK_4236	7.54E-02	4.57E-01	1.61E-01	2.54E+50	4.05E+50	3.14E+51	5.02E+51	1.43	4.99E-01

DK_4318	8.12E-01	4.37E-02	2.08E+00	1.02E+51	8.08E+52	8.23E+52	2.29E+54	1.33	2.42E-02
DK_4341	1.15E+00	3.64E-02	5.09E+00	2.09E+50	4.24E+52	3.38E+52	3.35E+54	0.75	5.38E-03
DK_b_300	1.70E+00	3.19E-02	6.41E-01	6.62E+49	5.25E+51	1.17E+52	2.71E+53	0.77	1.51E-02
DK_4548	2.64E-01	2.15E-01	4.61E-01	1.23E+50	1.09E+51	7.04E+51	3.91E+52	1.07	1.64E-01
DK_48	5.68E-03	3.74E+00	6.90E-02	6.24E+48	7.17E+47	1.43E+50	3.44E+49	1.07	7.81E+01
DK_b_851	6.84E-03	6.02E-02	9.23E-03	1.02E+48	2.49E+47	5.20E+49	3.71E+49	0.55	1.07E+01
DK_4802	1.28E+00	2.53E-02	2.70E+00	3.00E+51	3.99E+53	1.72E+53	1.85E+55	0.77	9.04E-03
DK_4814	1.10E-01	1.62E-01	3.93E-01	5.99E+49	2.63E+50	2.21E+51	1.17E+52	0.49	1.45E-01
DK_1640	3.38E+01	5.77E-03	5.60E+00	4.53E+50	1.00E+54	3.00E+53	5.39E+55	1.16	7.50E-04
DK_1598	6.59E-01	5.97E-02	5.17E-01	1.09E+50	3.24E+51	1.10E+52	1.26E+53	0.96	4.81E-02
DK_b_210	9.57E-03	7.15E-02	5.03E-03	1.92E+47	4.50E+46	3.01E+49	1.87E+49	0.7	1.27E+01
DK_1745	9.43E-01	1.30E-01	1.80E+00	3.74E+51	2.06E+53	1.45E+53	4.99E+54	1.57	3.89E-02
DK_1777	3.36E+01	3.67E-03	1.31E+01	3.81E+51	2.37E+55	1.49E+54	1.69E+57	1.15	2.86E-04
DK_5190	6.76E-02	4.84E-01	2.14E+00	7.85E+50	5.30E+51	6.42E+51	4.94E+52	1.03	2.05E-01
DK_1465	7.12E+00	5.02E-02	2.33E+01	2.24E+52	1.62E+55	1.63E+54	7.64E+56	1.19	2.53E-03
DK_275	9.68E-02	0.00E+00	1.43E-05	8.03E+44	9.13E+45	4.83E+49	1.37E+50	0.88	1.07E-01
DK_5303	2.41E-01	6.09E-02	1.93E+00	1.36E+51	4.83E+52	7.30E+52	1.46E+54	1.13	4.63E-02
DK_1417	8.53E-01	8.90E-04	4.11E-02	3.25E+48	2.40E+50	4.96E+51	2.98E+52	1.09	2.12E-02
DK_5354	3.14E-03	2.02E+00	2.23E-02	1.44E+48	2.56E+46	3.95E+49	9.60E+48	0.17	4.92E+02
DK_5376	1.61E+00	3.25E-02	5.23E+00	3.36E+51	7.97E+53	3.56E+53	2.88E+55	1.45	8.80E-03
DK_2128	7.81E-01	4.10E-01	1.54E+00	2.01E+51	4.36E+52	6.82E+52	9.85E+53	1.65	9.60E-02
DK_2174	9.57E-02	3.49E-01	2.15E+00	4.60E+50	3.42E+51	1.19E+52	1.64E+53	0.61	1.15E-01
DK_2394	1.36E-01	1.09E-01	1.96E-01	1.89E+49	9.79E+49	1.43E+51	4.64E+51	0.68	1.74E-01
DK_2453	2.07E-01	1.17E-01	9.79E-01	2.70E+50	4.67E+51	1.32E+52	1.64E+53	1.06	8.81E-02
DK_168	1.22E-01	1.84E-01	4.29E-01	5.69E+49	4.08E+50	1.95E+51	9.80E+51	0.84	1.68E-01
DK_1013	6.90E-02	1.36E-02	6.53E-02	7.46E+48	5.71E+49	1.19E+51	3.68E+51	0.71	1.28E-01
DK_2639	2.45E-01	8.70E-02	1.38E+00	3.56E+50	6.87E+51	2.08E+52	2.70E+53	0.83	6.50E-02
DK_13	5.65E-03	6.23E-02	3.13E-02	3.91E+48	1.80E+48	1.64E+50	1.55E+50	0.53	2.20E+00
DK_2760	1.30E-02	5.11E-01	7.45E-02	1.02E+49	5.52E+48	2.17E+50	1.79E+50	0.68	1.73E+00
DK_119	6.07E-02	9.01E-02	1.34E-01	1.11E+49	4.49E+49	9.25E+50	2.23E+51	0.87	2.62E-01
DK_797	3.33E-01	4.35E-03	1.98E-02	2.24E+48	2.95E+49	1.80E+51	5.26E+51	1.29	1.28E-01
DK_765	9.60E+00	1.72E-02	2.85E+00	2.23E+50	8.00E+52	6.23E+52	4.40E+54	0.65	2.90E-03
DK_698	1.12E-01	3.73E-03	5.58E-02	3.67E+48	7.72E+49	1.63E+51	6.17E+51	0.93	6.30E-02
DK_3450	6.48E-01	5.56E-02	3.34E-01	3.81E+49	7.22E+50	5.72E+51	3.26E+52	0.83	6.54E-02
DK_616	4.71E-01	8.96E-02	2.20E+00	5.62E+50	2.28E+52	4.54E+52	7.17E+53	1.44	4.84E-02
DK_89	4.21E-02	2.92E-01	3.24E-01	1.51E+49	3.50E+49	9.11E+50	1.54E+51	1.1	4.57E-01
DK_3583	7.60E-02	1.74E-01	7.52E-02	1.22E+49	2.67E+49	4.36E+50	9.25E+50	0.57	2.65E-01
DK_3666	6.28E-02	1.90E-04	3.98E-04	4.87E+46	1.93E+47	1.31E+50	2.53E+50	0.89	2.71E-01
DK_3735	1.67E-02	7.96E-02	4.68E-02	2.98E+48	3.25E+48	2.46E+50	2.77E+50	0.91	6.09E-01
DK_3757	2.86E-01	1.15E-01	1.80E+00	7.33E+50	1.15E+52	2.13E+52	5.43E+53	0.5	4.81E-02
DK_3831	6.58E-01	4.48E-02	4.63E+00	2.69E+50	3.52E+52	3.66E+52	2.00E+54	0.91	1.03E-02
DK_72	8.91E-03	2.67E-01	9.89E-02	4.42E+48	2.76E+48	2.01E+50	1.81E+50	0.65	1.21E+00
DK_3972	1.88E-01	5.42E-01	2.48E-01	3.12E+50	1.29E+51	7.70E+51	3.03E+52	1.3	3.34E-01
DK_69	4.08E-02	1.40E-01	4.31E-01	3.93E+49	1.61E+50	2.36E+51	6.35E+51	0.99	2.88E-01
DK_4113	2.37E-01	1.87E-01	2.40E+00	1.10E+51	2.23E+52	4.91E+52	5.46E+53	1.65	1.02E-01
DK_4128	5.92E+00	5.08E-02	1.71E+01	4.05E+52	2.26E+55	2.36E+54	7.70E+56	1.32	3.52E-03
DK_4179	4.71E-02	8.88E-02	1.30E-01	2.92E+49	6.30E+49	1.21E+51	2.74E+51	0.58	2.70E-01
DK_4307	2.41E-01	4.26E-02	1.18E+00	1.43E+50	5.02E+51	1.09E+52	2.82E+53	0.66	2.89E-02
DK_4336	2.67E-01	3.36E-02	2.66E-01	4.03E+50	5.44E+51	1.21E+52	8.96E+52	0.73	8.00E-02
DK_4648	1.22E+00	2.84E-02	3.76E+00	7.12E+50	1.31E+53	9.92E+52	5.84E+54	1.17	9.45E-03
DK_1622	4.27E+00	2.17E-02	5.11E+00	9.90E+50	3.36E+53	1.47E+53	1.78E+55	0.82	3.83E-03
DK_1611	9.89E-01	1.69E-02	9.87E-01	3.65E+49	3.35E+51	1.09E+52	2.06E+53	0.69	1.11E-02
DK_1672	7.91E-02	1.98E-01	9.16E-02	2.11E+48	6.02E+48	5.20E+50	1.04E+51	0.68	2.51E-01
DK_1673	1.54E-01	1.36E-01	2.94E-01	1.19E+50	1.02E+51	6.10E+51	3.09E+52	1.26	1.93E-01
DK_1600	3.41E-01	5.15E-02	2.26E-01	2.54E+49	4.36E+50	2.94E+51	2.07E+52	0.77	6.66E-02
DK_4995	3.12E-01	4.62E-02	9.76E-01	4.63E+50	1.33E+52	9.44E+51	1.12E+53	0.86	4.99E-02
DK_1779	1.18E+01	3.95E-03	4.06E+00	5.82E+50	9.66E+53	1.30E+53	5.19E+55	0.62	6.28E-04
DK_1489	7.42E+00	8.30E-03	5.18E+00	1.24E+51	9.80E+53	2.01E+53	6.49E+55	0.63	1.28E-03
DK_1813	2.73E-01	5.50E-04	1.29E-03	1.35E+47	1.71E+48	2.80E+50	8.21E+50	0.87	9.91E-02
DK_1474	9.66E-02	3.63E-02	7.75E-02	3.69E+48	1.74E+49	7.68E+50	1.54E+51	1.04	2.59E-01
DK_1462	2.04E+00	8.45E-02	1.28E+00	1.54E+50	9.57E+51	1.40E+52	4.84E+53	0.64	1.61E-02
DK_1420	1.95E+01	8.91E-03	1.37E+01	1.79E+51	4.27E+54	6.69E+53	2.67E+56	1.16	7.14E-04
DK_1912	2.18E+00	2.43E-02	4.21E+00	4.04E+50	6.71E+52	5.42E+52	3.99E+54	0.51	5.09E-03

DK_1401	1.57E-01	2.54E-01	7.80E-01	1.26E+50	9.68E+50	7.31E+51	3.16E+52	1.4	2.22E-01
DK_1940	1.35E-03	5.41E-01	4.60E-03	3.36E+47	1.34E+46	9.11E+48	2.32E+48	0.79	5.03E+02
DK_1399	3.64E-02	3.97E-01	1.45E-01	7.42E+48	8.73E+48	4.33E+50	4.96E+50	1.07	6.68E-01
DK_1395	6.62E-02	1.06E-01	1.90E-01	4.90E+48	1.80E+49	6.75E+50	1.30E+51	0.88	2.68E-01
DK_1943	9.69E-01	1.04E-02	9.88E-01	1.65E+50	1.67E+52	2.91E+52	8.18E+53	0.65	1.03E-02
DK_28	3.09E-03	3.50E-04	9.72E-05	2.01E+46	6.73E+45	1.86E+49	1.43E+49	0.84	6.37E+00
DK_5709	6.42E-01	7.89E-03	5.28E-01	4.34E+49	3.90E+51	1.66E+52	1.75E+53	1.07	1.72E-02
DK_2152	3.67E-01	6.30E-02	4.48E-01	1.11E+49	1.82E+50	2.45E+51	1.05E+52	0.89	7.05E-02
DK_1219	6.14E-02	6.70E-03	3.16E-02	1.17E+48	6.90E+48	5.03E+50	1.18E+51	0.62	1.40E-01
DK_2266	6.54E-01	8.13E-02	6.21E+00	8.17E+50	7.33E+52	5.08E+52	3.95E+54	0.79	1.38E-02
DK_1128	3.57E-02	5.71E-01	7.10E-02	4.70E+48	3.57E+48	2.35E+50	2.17E+50	1	1.07E+00
DK_1031	1.63E+00	1.34E-02	2.24E+00	5.51E+49	1.27E+52	2.49E+52	7.16E+53	0.9	5.27E-03
DK_2542	3.32E+00	2.39E-02	5.64E+00	3.57E+51	1.55E+54	4.14E+53	7.06E+55	1.29	4.50E-03
DK_2544	1.22E-01	1.10E-01	2.35E-01	6.51E+49	4.90E+50	1.74E+51	8.97E+51	0.8	1.60E-01
DK_983	7.55E-02	8.16E-03	4.86E-03	3.21E+47	6.66E+47	1.63E+50	2.40E+50	0.83	3.89E-01
DK_b_735	3.64E-02	3.94E-03	3.62E-03	2.63E+47	2.75E+47	9.14E+49	1.32E+50	0.33	2.79E-01
DK_927	4.55E-02	3.36E-01	1.98E-01	4.75E+49	8.15E+49	1.61E+51	2.98E+51	0.92	4.55E-01
DK_2676	2.29E-01	1.59E-01	2.30E-01	2.17E+49	1.34E+50	1.67E+51	6.20E+51	0.71	1.55E-01
DK_863	1.65E-01	1.26E-01	2.74E-01	9.92E+49	7.86E+50	4.44E+51	3.00E+52	0.83	1.45E-01
DK_855	7.49E-02	7.70E-02	2.64E-01	2.77E+49	2.00E+50	1.88E+51	8.99E+51	0.79	1.50E-01
DK_2871	1.16E-02	4.85E-01	1.75E-01	3.69E+49	9.18E+48	4.70E+50	4.35E+50	0.27	5.35E+00
DK_788	6.92E-02	7.29E-01	1.11E-01	1.86E+49	1.88E+49	6.68E+50	8.49E+50	0.82	5.64E-01
DK_710	9.89E-02	4.96E-02	5.12E-02	3.08E+48	1.41E+49	5.24E+50	1.21E+51	0.69	1.87E-01
DK_709	1.19E-01	3.90E-02	5.67E-02	7.13E+48	3.68E+49	8.36E+50	2.21E+51	0.69	1.76E-01
DK_634	4.75E-03	1.49E-01	3.92E-03	4.68E+47	9.21E+46	4.17E+49	1.83E+49	1.38	1.22E+02
DK_618	1.11E+00	9.07E-02	1.86E+00	8.52E+50	5.30E+52	5.28E+52	2.32E+54	1	2.45E-02
DK_3471	4.18E-01	2.20E-02	1.26E-01	1.21E+49	2.93E+50	2.46E+51	1.41E+52	0.89	5.43E-02
DK_606	4.64E-02	1.94E-01	8.29E-02	3.48E+49	5.48E+49	1.48E+51	2.14E+51	1.22	5.80E-01
DK_3496	2.01E-01	1.07E-01	4.11E-01	6.68E+49	7.55E+50	5.58E+51	2.97E+52	1.14	1.37E-01
DK_3577	4.27E-01	1.64E-02	5.79E-01	6.45E+49	4.03E+51	1.01E+52	2.21E+53	0.79	1.96E-02
DK_576	2.13E-01	7.65E-03	1.44E-01	1.40E+49	4.56E+50	3.23E+51	2.19E+52	0.84	3.88E-02
DK_3761	4.65E-01	8.41E-02	4.11E-01	2.21E+49	3.86E+50	3.18E+51	1.63E+52	1.01	7.91E-02
DK_437	7.42E-03	6.90E-03	6.36E-04	1.13E+47	2.81E+46	3.04E+49	2.04E+49	0.92	1.34E+01
DK_62	2.22E-03	2.18E+00	5.53E-02	5.76E+48	2.03E+47	7.57E+49	1.57E+49	0.33	3.24E+02
DK_388	3.47E-01	1.78E-02	2.25E-01	3.82E+49	1.04E+51	7.94E+51	4.85E+52	1.06	5.70E-02
DK_367	3.02E-01	2.18E-01	9.59E-01	1.37E+50	1.63E+51	9.03E+51	4.71E+52	1.47	1.53E-01
DK_4647	2.53E+00	7.82E-03	2.00E+00	4.40E+50	1.95E+53	1.02E+53	1.05E+55	1.07	3.70E-03
DK_1685	2.60E+01	3.76E-03	1.16E+01	5.45E+50	2.28E+54	4.01E+53	1.29E+56	1.04	3.49E-04
DK_1708	5.88E+00	1.47E-02	7.59E+00	1.57E+51	9.95E+53	2.70E+53	6.06E+55	0.8	2.01E-03
DK_4979	1.72E+00	7.38E-03	1.90E+00	5.42E+50	1.68E+53	1.22E+53	8.59E+54	0.95	4.77E-03
DK_1572	9.20E-02	1.07E-01	1.14E-01	2.14E+49	1.09E+50	1.34E+51	4.19E+51	0.99	2.48E-01
DK_299	2.51E-01	4.13E-02	1.12E+00	1.62E+50	5.92E+51	1.46E+52	1.98E+53	1.07	4.28E-02
DK_1734	6.55E+00	8.39E-02	2.17E+01	4.22E+52	2.04E+55	2.08E+54	7.37E+56	1.28	3.98E-03
DK_1551	1.42E+00	3.63E-02	1.95E+00	1.49E+50	1.52E+52	2.96E+52	6.57E+53	1.16	1.60E-02
DK_5078	3.80E-01	5.43E-02	1.55E+00	1.46E+50	6.57E+51	9.59E+51	1.71E+53	0.91	3.17E-02
DK_5101	1.10E-01	5.26E-02	6.11E-01	1.46E+50	1.60E+51	6.03E+51	6.38E+52	0.55	7.46E-02
DK_1780	8.77E+00	8.11E-03	5.57E+00	1.28E+51	1.42E+54	1.48E+53	6.29E+55	0.62	9.97E-04
DK_1778	2.40E+01	3.57E-03	9.04E+00	1.35E+51	5.66E+54	6.01E+53	4.36E+56	0.96	3.56E-04
DK_1507	2.93E+00	6.38E-03	5.82E-01	4.59E+49	1.11E+52	2.11E+52	5.79E+53	0.9	5.69E-03
DK_5148	6.98E-03	1.27E+00	1.28E-02	1.87E+48	2.36E+47	5.12E+49	1.80E+49	1.05	6.42E+01
DK_1793	1.76E-01	9.20E-04	1.61E-03	1.33E+47	1.04E+48	2.24E+50	5.38E+50	0.9	1.56E-01
DK_1801	6.04E-01	6.88E-02	5.01E-01	4.11E+49	9.86E+50	5.60E+51	3.47E+52	1.17	6.66E-02
DK_5285	4.65E-01	3.50E-02	2.95E-01	1.60E+49	3.57E+50	2.93E+51	2.21E+52	0.59	3.89E-02
DK_5318	1.40E+00	2.17E-02	7.60E-01	1.60E+50	1.75E+52	3.03E+52	8.61E+53	1.09	1.51E-02
DK_1904	2.20E-01	7.22E-03	9.62E-02	5.56E+48	1.55E+50	2.05E+51	1.17E+52	0.72	3.73E-02
DK_1920	1.20E-01	1.16E-01	4.37E-01	1.10E+50	8.82E+50	7.15E+51	2.80E+52	1.35	2.10E-01
DK_1928	1.59E+01	6.91E-03	8.15E+00	8.76E+50	1.68E+54	2.92E+53	9.15E+55	0.99	7.86E-04
DK_b_628	3.24E-01	4.02E-02	2.51E-01	2.14E+49	3.87E+50	2.54E+51	2.39E+52	0.54	4.36E-02
DK_1402	3.91E-02	2.25E-01	9.10E-02	2.86E+48	3.84E+48	2.26E+50	2.77E+50	0.81	4.91E-01
DK_1944	7.02E-01	8.90E-03	4.38E-01	1.76E+50	1.10E+52	1.84E+52	4.16E+53	0.63	1.58E-02
DK_1945	3.92E-01	3.72E-02	1.07E+00	7.11E+49	3.53E+51	8.70E+51	2.64E+53	0.63	1.88E-02
DK_1946	3.87E-01	3.35E-02	9.23E-01	5.74E+49	2.98E+51	7.46E+51	2.04E+53	0.68	1.93E-02
DK_2001	2.37E+00	2.41E-02	6.87E+00	4.87E+51	1.84E+54	2.93E+53	3.14E+55	1.24	5.11E-03

DK_1356	4.93E-01	4.30E-02	2.08E-01	1.28E+49	2.87E+50	2.15E+51	1.63E+52	0.68	4.37E-02
DK_1343	2.73E-02	2.22E-02	6.83E-02	9.06E+47	3.44E+48	3.93E+50	7.49E+50	0.62	1.85E-01
DK_1324	5.19E-01	6.49E-02	2.46E-01	8.12E+49	1.59E+51	6.18E+51	5.82E+52	0.87	6.63E-02
DK_2048	1.56E+00	4.71E-02	3.81E+00	2.18E+51	3.41E+53	1.96E+53	1.40E+55	1.3	1.23E-02
DK_5601	3.25E-01	4.51E-02	3.24E-01	6.55E+49	1.07E+51	5.99E+51	5.00E+52	0.69	6.31E-02
DK_2070	5.17E-03	3.64E+00	1.04E-01	2.90E+49	8.37E+48	7.98E+50	1.85E+50	1.47	5.73E+01
DK_1272	7.34E-01	9.52E-03	1.10E+00	7.38E+49	1.17E+52	2.10E+52	5.96E+53	0.92	8.65E-03
DK_2153	5.91E-01	2.60E-02	3.08E-01	3.74E+49	1.33E+51	6.13E+51	5.09E+52	1	4.15E-02
DK_2179	2.23E-01	6.00E-05	1.80E-04	6.11E+46	5.69E+47	2.80E+50	8.38E+50	0.74	1.13E-01
DK_2247	8.69E-02	2.74E-01	1.03E-01	3.19E+49	9.02E+49	1.47E+51	3.40E+51	1.07	4.01E-01
DK_2271	2.17E+00	1.32E-02	2.60E+00	1.26E+51	3.40E+53	2.69E+53	8.96E+54	1.6	8.10E-03
DK_1118	7.55E-02	1.71E-01	1.71E-01	1.83E+49	5.88E+49	1.32E+51	2.72E+51	1.06	3.62E-01
DK_176	8.76E-02	3.90E-01	1.08E+00	8.16E+49	4.23E+50	3.75E+51	1.40E+52	1.17	2.69E-01
DK_2396	9.45E-02	2.29E-01	2.05E-01	5.38E+49	2.01E+50	2.39E+51	6.05E+51	1.23	3.68E-01
DK_2433	1.69E-01	5.19E-02	1.97E-01	1.54E+49	1.58E+50	2.05E+51	8.22E+51	0.86	1.16E-01
DK_2502	4.45E-01	2.03E-01	1.60E+00	1.84E+51	2.16E+52	4.59E+52	6.03E+53	0.7	8.51E-02
DK_2584	2.25E+00	4.25E-02	7.76E+00	8.73E+51	2.07E+54	5.27E+53	7.78E+55	1.05	6.84E-03
DK_b_62	1.29E-01	5.68E-03	6.29E-03	1.13E+48	5.81E+48	6.00E+50	1.21E+51	1.19	2.82E-01
DK_149	4.51E-02	1.02E-01	4.63E-01	1.18E+50	8.76E+50	5.06E+51	3.30E+52	1.03	1.86E-01
DK_2614	8.61E-01	9.13E-02	2.03E+00	2.60E+50	1.18E+52	2.52E+52	3.13E+53	1.54	4.34E-02
DK_2617	6.16E-01	4.83E-02	1.37E+00	8.39E+49	5.27E+51	1.00E+52	3.76E+53	0.67	1.58E-02
DK_2622	3.06E-01	5.90E-04	2.90E-03	1.52E+47	2.15E+48	4.34E+50	1.30E+51	1.02	9.68E-02
DK_2628	2.99E-02	3.25E-01	4.51E-01	1.83E+50	3.42E+50	4.25E+51	9.66E+51	0.96	4.46E-01
DK_2637	1.32E+01	1.60E-04	4.50E-03	4.79E+48	8.02E+50	2.15E+52	2.02E+53	0.91	8.54E-03
DK_2696	1.21E-01	5.45E-02	1.75E-01	6.57E+48	4.77E+49	1.07E+51	3.22E+51	0.72	1.30E-01
DK_2753	4.67E+00	9.48E-03	1.92E+00	2.33E+50	1.14E+53	6.06E+52	7.85E+54	0.79	2.51E-03
DK_2752	5.16E+00	5.67E-03	1.38E+00	1.43E+50	7.84E+52	4.90E+52	4.43E+54	0.81	2.31E-03
DK_2754	3.81E+00	1.06E-02	1.85E+00	1.31E+50	5.08E+52	3.85E+52	4.45E+54	0.64	2.46E-03
DK_2935	6.27E-02	3.95E-01	1.01E-01	3.14E+49	5.44E+49	1.12E+51	1.94E+51	1.01	4.90E-01
DK_2949	3.65E-01	4.87E-03	1.51E-01	4.62E+48	2.20E+50	2.93E+51	2.71E+52	0.54	1.40E-02
DK_2959	1.34E+00	1.53E-02	2.24E+00	3.08E+50	6.69E+52	5.40E+52	3.74E+54	0.92	6.56E-03
DK_3019	1.37E-02	1.38E+00	9.15E-02	5.33E+49	1.61E+49	2.47E+50	1.37E+50	1.47	1.15E+01
DK_3025	2.74E-02	5.49E-01	1.69E-01	1.68E+49	1.62E+49	5.96E+50	7.44E+50	0.73	5.47E-01
DK_3069	3.58E-01	1.48E-02	4.31E-01	1.96E+49	8.00E+50	6.06E+51	3.77E+52	1.03	3.49E-02
DK_3071	2.13E-01	6.81E-02	1.72E-01	7.26E+49	8.05E+50	5.13E+51	2.94E+52	1.03	1.30E-01
DK_759	3.40E-01	1.85E-03	1.01E-02	1.42E+48	1.98E+49	1.69E+51	5.02E+51	1.47	1.32E-01
DK_3094	1.61E+00	1.37E-02	3.31E+00	2.00E+50	5.98E+52	4.77E+52	2.99E+54	0.86	4.35E-03
DK_3095	3.33E-01	3.19E-02	5.95E-01	3.40E+49	1.11E+51	4.47E+51	6.41E+52	0.62	2.78E-02
DK_3174	4.31E-02	8.24E-02	1.16E-01	1.41E+49	5.23E+49	8.84E+50	2.40E+51	0.8	2.60E-01
DK_3226	1.21E-01	1.34E-01	4.46E-01	3.40E+49	2.65E+50	2.22E+51	1.08E+52	0.84	1.46E-01
DK_690	3.68E-01	3.27E-02	1.51E+00	1.66E+50	1.03E+52	2.31E+52	3.50E+53	1.27	2.84E-02
DK_3276	1.30E-01	2.28E-01	6.26E-01	1.70E+50	9.61E+50	7.67E+51	2.95E+52	1.13	2.48E-01
DK_3280	3.54E+00	1.28E-01	4.76E+00	5.49E+52	6.80E+54	1.01E+54	1.70E+56	0.95	1.09E-02
DK_3509	4.83E-01	3.07E-02	3.10E-01	5.03E+49	1.17E+51	4.95E+51	5.71E+52	0.55	3.60E-02
DK_3516	4.21E-02	7.00E-02	1.61E-01	9.07E+48	4.14E+49	7.42E+50	2.26E+51	0.69	1.87E-01
DK_3570	4.97E-01	2.33E-02	8.56E-01	6.46E+49	3.53E+51	1.43E+52	1.45E+53	1.16	2.95E-02
DK_3644	5.08E-01	3.91E-02	4.14E-01	1.48E+50	4.63E+51	1.38E+52	1.75E+53	0.97	4.68E-02
DK_3646	2.47E-01	1.34E-01	2.54E-01	2.00E+49	1.31E+50	1.95E+51	5.21E+51	1.11	2.13E-01
DK_529	5.18E+00	1.29E-02	5.74E+00	1.68E+51	1.24E+54	2.70E+53	6.63E+55	1.05	2.21E-03
DK_3824	6.79E-01	2.07E-02	4.21E-01	3.53E+49	1.79E+51	7.64E+51	9.30E+52	0.84	2.50E-02
DK_3839	2.19E+00	4.59E-02	2.15E+00	5.80E+50	6.79E+52	6.50E+52	3.08E+54	0.96	1.27E-02
DK_3832	4.50E-01	3.51E-02	1.98E+00	4.00E+50	3.16E+52	3.63E+52	1.50E+54	0.99	1.92E-02
DK_3834	3.73E-01	3.06E-02	1.46E+00	1.32E+50	8.31E+51	1.54E+52	4.68E+53	0.76	1.87E-02
DK_3848	5.43E-01	1.85E-02	2.67E-01	3.71E+49	1.30E+51	8.47E+51	5.36E+52	1.17	4.77E-02
DK_3940	8.42E-01	2.05E+00	5.53E-01	1.66E+50	7.30E+50	5.78E+51	2.47E+52	0.9	2.50E-01
DK_3990	1.29E-01	5.08E-02	7.78E-02	1.48E+49	8.16E+49	1.76E+51	4.27E+51	1.06	2.44E-01
DK_4042	1.67E-01	6.88E-02	1.97E-01	4.74E+49	4.37E+50	3.55E+51	1.63E+52	0.98	1.46E-01
DK_4304	2.26E-01	3.77E-02	1.12E+00	7.09E+49	2.50E+51	8.89E+51	1.13E+53	0.8	3.41E-02
DK_4322	3.59E-01	4.45E-02	5.80E-01	5.59E+49	1.52E+51	7.59E+51	6.19E+52	1.06	5.57E-02
DK_4370	3.23E-01	1.54E-02	5.21E-01	3.86E+50	1.78E+52	3.79E+52	6.26E+53	1.02	3.34E-02
DK_383	6.38E-02	5.07E-03	4.85E-03	2.23E+47	5.74E+47	1.56E+50	2.33E+50	1.13	4.32E-01
DK_4516	2.20E-01	1.70E-01	1.44E+00	5.94E+50	8.03E+51	2.41E+52	2.61E+53	1.02	1.06E-01
DK_4513	7.77E+00	4.20E-01	2.24E+00	1.63E+51	9.18E+52	8.05E+52	3.95E+54	0.73	2.03E-02

DK_4595	2.92E-01	1.06E-01	1.09E+00	4.84E+50	8.14E+51	2.46E+52	2.17E+53	1.11	9.31E-02
DK_4856	6.53E-01	9.46E-03	4.97E-01	1.27E+50	1.13E+52	2.85E+52	4.77E+53	1.12	1.90E-02
DK_4858	2.44E-01	3.42E-02	4.56E-01	1.89E+50	4.70E+51	5.41E+51	5.85E+52	0.83	5.64E-02
DK_4877	5.22E-01	3.02E-02	9.75E-01	5.47E+49	2.86E+51	1.07E+52	1.38E+53	0.93	2.59E-02
DK_4897	4.29E-01	1.31E-02	6.80E-01	4.53E+49	3.12E+51	8.38E+51	2.09E+53	0.59	1.29E-02
DK_4918	3.02E-01	2.12E-02	1.90E-01	1.32E+49	2.50E+50	2.66E+51	1.24E+52	0.82	6.33E-02
DK_33	1.85E-02	4.51E-01	4.17E-01	2.17E+49	3.13E+49	8.08E+50	1.15E+51	0.99	5.56E-01
DK_5467	1.31E-03	2.65E-01	1.10E-03	1.13E+47	3.71E+45	5.09E+48	1.24E+48	0.77	2.71E+03
DK_5558	2.68E-01	1.40E-02	2.57E-01	7.59E+48	1.96E+50	2.53E+51	1.24E+52	0.74	4.06E-02
DK_5585	5.82E+00	5.08E-03	5.31E+00	1.36E+51	1.70E+54	5.09E+53	8.45E+55	1.14	1.39E-03
DK_236	1.23E-01	7.55E-01	3.41E-01	2.68E+50	8.86E+50	6.84E+51	2.18E+52	1.42	4.29E-01
DK_226	3.18E-02	1.48E-03	1.26E-03	5.64E+46	9.64E+46	7.05E+49	9.01E+49	1.15	5.70E-01
DK_164	1.15E-01	7.82E-02	7.60E-01	1.89E+49	2.63E+50	2.75E+51	2.99E+52	0.54	4.73E-02
DK_15	7.61E-03	7.75E-02	6.47E-02	1.58E+48	1.15E+48	1.81E+50	2.07E+50	0.39	5.95E-01
DK_5	5.67E-03	1.23E-01	8.86E-02	8.22E+48	5.70E+48	3.02E+50	3.19E+50	0.64	9.80E-01
DK_8	6.31E-03	7.86E-02	6.58E-02	1.38E+48	1.12E+48	1.78E+50	2.00E+50	0.46	5.90E-01
DK_6	1.86E-02	6.56E-02	3.40E-02	1.64E+48	1.39E+48	1.53E+50	1.73E+50	0.53	5.73E-01
DK_3909	3.35E-01	2.84E-02	2.00E-01	2.51E+48	4.29E+49	1.49E+51	5.78E+51	0.7	4.89E-02
DK_42	5.88E-03	4.96E-01	8.75E-02	4.91E+48	1.98E+48	1.95E+50	1.22E+50	0.68	3.43E+00
DK_1340	1.16E-03	5.76E-03	1.98E-04	7.36E+45	2.60E+44	2.97E+48	1.12E+48	0.3	2.10E+02
DK_5550	6.72E-02	6.01E-02	5.72E-01	1.63E+49	1.55E+50	2.12E+51	1.71E+52	0.45	5.72E-02
DK_b_335	1.00E+00	2.68E-02	1.88E-01	1.38E+49	5.98E+50	2.75E+51	3.10E+52	0.69	2.33E-02
DK_977	3.43E-01	4.20E-02	2.25E+00	6.14E+49	4.17E+51	1.08E+52	2.17E+53	0.83	1.69E-02
DK_940	4.26E-01	7.20E-02	1.66E+00	7.25E+49	2.61E+51	6.51E+51	1.35E+53	0.62	2.56E-02
DK_2735	2.12E-01	1.21E-02	1.41E-01	5.59E+48	1.16E+50	1.71E+51	7.78E+51	0.72	4.95E-02
DK_2842	1.13E+00	9.14E-03	2.63E-01	1.52E+49	1.28E+51	5.41E+51	7.64E+52	0.69	1.21E-02
DK_2856	1.48E-01	2.24E-02	2.37E-01	1.11E+49	1.56E+50	1.86E+51	9.08E+51	0.58	5.96E-02
DK_2878	3.23E-02	5.00E-04	1.84E-04	1.20E+46	1.53E+46	2.25E+49	2.88E+49	0.59	3.73E-01
DK_2956	9.05E-02	1.03E-01	2.91E-01	2.80E+49	1.28E+50	1.31E+51	6.83E+51	0.41	1.15E-01
DK_3046	4.08E-01	8.20E-03	1.81E-01	9.00E+48	4.25E+50	2.76E+51	2.28E+52	0.75	2.30E-02
DK_3129	6.87E-03	1.11E+00	7.47E-02	5.41E+48	9.89E+47	1.32E+50	5.97E+49	0.5	1.60E+01
DK_3442	2.53E-01	3.87E-02	1.43E-01	8.97E+48	1.12E+50	1.35E+51	6.52E+51	0.62	7.02E-02
DK_3504	4.40E-02	6.56E-02	1.01E-01	7.15E+48	2.04E+49	5.24E+50	1.23E+51	0.52	2.08E-01
DK_3521	3.58E-01	2.61E-02	1.22E-01	2.84E+48	4.71E+49	1.30E+51	6.06E+51	0.6	4.33E-02
DK_3634	1.06E-02	6.06E-02	1.52E-02	4.28E+47	1.69E+47	6.77E+49	5.99E+49	0.38	1.74E+00
DK_520	5.04E-01	1.28E-02	5.52E-01	6.42E+48	3.96E+50	5.06E+51	4.31E+52	0.71	1.40E-02
DK_3738	4.62E-02	3.20E-02	2.02E-01	1.92E+49	7.88E+49	1.03E+51	3.97E+51	0.32	9.95E-02
DK_420	4.06E-02	3.72E-03	1.31E-03	6.03E+46	8.59E+46	4.85E+49	6.10E+49	0.7	4.12E-01
DK_405	6.19E-03	1.58E-01	1.85E-02	8.70E+47	2.40E+47	4.88E+49	3.17E+49	0.66	8.29E+00
DK_4954	3.45E-01	2.24E-02	1.70E-01	4.19E+48	7.78E+49	1.71E+51	9.51E+51	0.53	3.50E-02
DK_246	6.23E-03	1.54E-01	7.30E-02	1.59E+48	1.06E+48	1.62E+50	1.54E+50	0.55	8.77E-01
DK_1335	7.74E-02	2.36E-02	1.63E-01	2.52E+48	2.61E+49	1.02E+51	3.42E+51	0.67	7.62E-02
DK_195	2.23E-02	6.46E-02	9.10E-02	6.95E+48	1.19E+49	3.57E+50	6.68E+50	0.45	2.49E-01
DK_186	6.53E-02	4.85E-02	3.63E-01	5.22E+48	5.02E+49	1.40E+51	5.48E+51	0.63	7.85E-02
DK_976	2.25E-02	1.14E-01	5.80E-02	1.43E+48	1.56E+48	1.56E+50	1.67E+50	0.95	6.76E-01
DK_2575	1.17E-03	1.64E-02	6.05E-04	1.46E+46	8.21E+44	4.78E+48	1.83E+48	0.47	1.22E+02
DK_151	4.77E-02	1.57E-01	3.45E-01	4.33E+48	1.67E+49	7.54E+50	1.77E+51	0.7	1.99E-01
DK_948	2.62E-01	4.07E-02	1.48E+00	1.73E+49	7.92E+50	6.38E+51	7.83E+52	0.68	1.83E-02
DK_2855	1.57E-01	9.06E-03	1.37E-01	5.17E+48	9.10E+49	1.50E+51	6.14E+51	0.6	5.04E-02
DK_b_808	6.57E-03	1.23E-01	1.02E-02	6.68E+47	1.04E+47	3.71E+49	2.27E+49	0.44	2.11E+01
DK_73	8.02E-02	9.02E-02	1.06E+00	3.57E+49	4.69E+50	3.15E+51	2.31E+52	0.66	7.14E-02
DK_67	7.99E-03	3.61E-01	4.15E-02	7.73E+47	2.68E+47	8.04E+49	5.19E+49	0.62	3.31E+00
DK_5013	2.14E-01	5.03E-02	2.35E-01	4.49E+48	4.13E+49	1.29E+51	4.95E+51	0.49	6.65E-02
DK_277	1.55E-03	1.09E+00	2.34E-02	3.20E+48	2.69E+46	2.77E+49	6.65E+48	0.08	1.05E+03
DK_257	3.77E-03	2.60E-01	6.11E-03	2.77E+47	2.97E+46	1.76E+49	7.33E+48	0.83	7.26E+01
DK_1991	1.48E-02	1.65E-01	1.19E-01	7.65E+48	6.38E+48	3.05E+50	3.96E+50	0.43	4.77E-01
DK_228	5.32E-02	5.89E-02	8.48E-02	2.82E+48	9.27E+48	4.23E+50	7.69E+50	0.79	2.70E-01
DK_2308	1.06E-01	3.99E-02	2.01E-01	1.17E+49	7.94E+49	1.09E+51	4.11E+51	0.48	9.80E-02
DK_1125	2.44E-03	3.14E-01	1.27E-02	1.77E+48	9.53E+46	2.72E+49	1.10E+49	0.31	1.26E+02
DK_175	1.40E-03	1.30E-04	1.04E-05	7.80E+44	6.45E+43	1.51E+48	7.27E+47	0.47	7.98E+01
DK_170	7.55E-04	3.28E-01	5.60E-03	8.64E+46	3.03E+45	7.80E+48	2.02E+48	0.68	4.18E+02
DK_158	2.23E-02	2.44E-01	2.29E-01	7.23E+48	1.18E+49	4.49E+50	6.58E+50	0.77	4.23E-01
DK_3	7.39E-03	7.14E-02	7.56E-02	3.68E+48	3.70E+48	2.15E+50	2.69E+50	0.53	4.39E-01

DK_137	3.10E-02	1.70E-03	1.07E-03	3.47E+46	5.72E+46	4.60E+49	5.86E+49	0.83	4.41E-01
DK_126	1.42E-01	1.48E-01	3.23E-01	3.38E+48	1.87E+49	8.75E+50	2.13E+51	0.75	1.51E-01
DK_b_277	7.45E-03	1.76E-03	5.08E-04	1.79E+46	9.61E+45	1.73E+49	1.44E+49	0.78	1.96E+00
DK_3474	8.50E-03	2.54E-01	3.22E-02	2.25E+48	6.37E+47	7.73E+49	5.45E+49	0.49	6.07E+00
DK_86	4.24E-03	9.91E-01	4.70E-02	1.15E+48	1.96E+47	7.90E+49	2.87E+49	0.6	1.42E+01
DK_546	9.08E-04	1.40E-01	7.02E-03	4.28E+47	2.60E+46	1.63E+49	6.02E+48	0.59	1.78E+02
DK_79	4.58E-03	1.39E-01	5.29E-02	3.14E+48	1.11E+48	1.24E+50	1.01E+50	0.45	3.63E+00
DK_3901	3.64E-02	9.81E-02	1.56E-01	4.01E+49	2.95E+49	6.82E+50	1.31E+51	0.2	3.15E-01
DK_b_526	1.13E-01	2.91E-02	5.55E-02	1.13E+48	5.67E+48	4.61E+50	1.07E+51	0.55	1.27E-01
DK_1544	3.59E+00	9.38E-03	4.45E+00	1.59E+50	9.49E+52	5.94E+52	6.49E+54	0.7	1.75E-03
DK_1763	7.29E-03	3.55E-02	1.42E-02	8.58E+47	5.04E+47	7.36E+49	7.03E+49	0.56	1.20E+00
DK_1833	1.08E-01	7.72E-02	6.09E-01	1.11E+49	1.21E+50	2.04E+51	1.28E+52	0.55	6.22E-02
DK_1473	1.00E+00	4.46E-03	5.62E-01	1.67E+49	2.56E+51	1.08E+52	1.43E+53	0.73	6.98E-03
DK_2115	6.80E-03	1.42E-01	2.79E-02	8.39E+47	2.99E+47	7.98E+49	6.18E+49	0.45	2.35E+00
DK_1238	7.22E-02	1.76E-02	1.37E-01	3.50E+48	3.60E+49	9.29E+50	2.65E+51	0.86	1.07E-01
DK_2141	6.88E+00	3.62E-02	8.15E-01	5.07E+49	1.03E+52	1.28E+52	6.10E+53	0.73	5.34E-03
DK_2168	5.47E-01	1.83E-01	4.65E+00	1.28E+50	5.25E+51	1.12E+52	2.78E+53	0.79	2.70E-02
DK_2190	3.41E-02	4.81E-02	3.55E-02	1.27E+48	2.32E+48	1.86E+50	2.57E+50	0.76	3.87E-01
DK_2307	2.17E-01	3.53E-02	5.34E-01	2.63E+49	4.87E+50	3.25E+51	2.63E+52	0.53	4.24E-02
DK_2350	4.11E+00	9.99E-03	2.43E+00	1.19E+50	5.74E+52	3.93E+52	4.17E+54	0.72	2.23E-03
DK_1115	6.87E+00	1.01E-02	1.09E+01	2.83E+50	3.86E+53	1.37E+53	2.54E+55	0.85	8.62E-04
DK_1000	2.26E-01	3.35E-03	3.14E-02	1.46E+48	2.91E+49	9.16E+50	3.44E+51	0.71	5.06E-02
DK_2533	2.44E-01	3.75E-03	1.13E-01	2.87E+48	1.12E+50	2.01E+51	9.62E+51	0.86	2.98E-02
DK_962	1.67E-01	2.05E-02	2.62E-01	1.72E+49	3.28E+50	2.73E+51	1.38E+52	0.85	6.48E-02
DK_2606	5.24E-03	9.54E-01	4.53E-02	3.68E+48	6.04E+47	8.64E+49	3.43E+49	0.56	2.17E+01
DK_14	1.02E-02	2.06E-01	9.60E-02	2.70E+48	2.04E+48	1.64E+50	1.53E+50	0.84	1.02E+00
DK_12	6.39E-02	2.24E-02	2.46E-01	6.59E+48	8.82E+49	1.58E+51	5.58E+51	0.82	8.13E-02
DK_2	2.22E-02	5.07E-02	1.83E-01	7.43E+48	3.29E+49	6.65E+50	1.71E+51	0.7	1.95E-01
DK_2725	7.81E-03	5.97E-01	1.21E-02	7.20E+47	1.03E+47	3.20E+49	1.48E+49	0.7	3.51E+01
DK_862	3.83E-01	2.51E-02	6.74E-01	8.60E+48	3.40E+50	4.25E+51	3.57E+52	0.66	2.07E-02
DK_2885	2.61E-01	1.97E-02	1.54E-01	4.78E+48	8.15E+49	1.50E+51	5.75E+51	0.81	6.44E-02
DK_2909	6.05E-01	3.00E-02	3.28E-01	1.34E+49	3.68E+50	2.72E+51	1.86E+52	0.65	3.44E-02
DK_3012	2.98E-03	1.39E+00	1.14E-01	1.43E+49	8.45E+47	1.49E+50	4.68E+49	0.24	8.86E+01
DK_3157	4.58E-03	6.98E-01	4.68E-02	5.66E+47	9.73E+46	5.17E+49	2.33E+49	0.72	1.68E+01
DK_719	2.41E-01	1.30E-01	2.97E-01	9.92E+48	7.09E+49	1.23E+51	3.96E+51	0.69	1.28E-01
DK_652	3.31E-02	3.60E-01	2.44E-01	7.50E+48	1.16E+49	4.00E+50	5.70E+50	0.78	4.39E-01
DK_3330	6.77E-03	7.34E-01	1.46E-02	1.16E+48	1.74E+47	3.62E+49	1.55E+49	0.67	3.10E+01
DK_3372	3.63E-04	1.21E+00	1.61E-02	6.78E+48	2.21E+46	1.93E+49	2.50E+48	0.11	1.13E+04
DK_3460	1.27E-01	7.68E-02	3.08E-01	1.48E+49	1.19E+50	1.28E+51	5.73E+51	0.61	1.04E-01
DK_3718	6.88E-03	8.38E-02	2.37E-02	4.29E+47	2.02E+47	7.36E+49	6.02E+49	0.56	1.69E+00
DK_3717	1.22E-02	8.19E-02	2.98E-02	2.95E+48	1.59E+48	1.20E+50	1.29E+50	0.39	1.05E+00
DK_3766	2.75E-02	3.74E-01	9.81E-02	2.44E+48	2.00E+48	1.86E+50	1.76E+50	0.95	9.64E-01
DK_4085	2.69E-03	2.96E-01	2.58E-02	1.93E+48	1.88E+47	4.27E+49	2.02E+49	0.4	5.16E+01
DK_4913	2.22E-01	6.08E-02	1.23E+00	3.30E+49	9.71E+50	4.35E+51	4.29E+52	0.88	3.98E-02
DK_1610	6.14E-02	7.39E-02	1.37E-01	4.48E+48	1.51E+49	5.59E+50	1.10E+51	0.69	2.40E-01
DK_1680	1.70E-02	1.05E-01	1.79E-01	1.00E+49	1.51E+49	4.44E+50	7.91E+50	0.44	2.68E-01
DK_4939	7.75E-02	3.62E-02	1.59E-01	1.01E+49	7.01E+49	1.04E+51	4.02E+51	0.56	1.09E-01
DK_1761	7.31E-02	1.23E-03	9.35E-03	4.54E+47	5.68E+48	4.03E+50	1.18E+51	0.75	8.31E-02
DK_1523	2.42E-01	2.79E-02	7.61E-01	1.55E+49	4.28E+50	4.34E+51	4.67E+52	0.46	2.14E-02
DK_1824	2.50E-01	4.93E-02	2.01E-01	7.01E+48	7.55E+49	1.33E+51	4.71E+51	0.71	9.05E-02
DK_265	1.21E-01	1.91E-01	7.28E-01	2.12E+49	1.61E+50	1.79E+51	7.70E+51	0.81	1.36E-01
DK_260	4.36E-01	1.99E-03	7.37E-02	2.58E+48	1.45E+50	2.18E+51	1.25E+52	0.76	1.94E-02
DK_5559	2.54E-01	3.17E-02	6.00E-01	2.64E+49	6.69E+50	3.45E+51	3.24E+52	0.6	3.50E-02
DK_1305	1.68E-02	2.19E-02	3.12E-03	1.35E+47	7.47E+46	3.75E+49	3.22E+49	0.72	1.70E+00
DK_1256	8.04E-02	1.63E-03	1.18E-02	1.42E+47	1.44E+48	3.45E+50	9.14E+50	0.69	8.07E-02
DK_1232	6.22E-03	8.26E-02	9.71E-03	2.30E+47	7.63E+46	4.03E+49	2.81E+49	0.59	3.42E+00
DK_1231	1.50E-02	1.92E-02	1.39E-02	2.26E+47	3.01E+47	1.03E+50	1.23E+50	0.66	4.73E-01
DK_2171	5.42E+00	1.40E-03	6.40E-01	5.16E+49	2.78E+52	2.86E+52	1.65E+54	0.46	1.32E-03
DK_207	4.22E-02	5.75E-02	1.51E-01	8.86E+48	4.03E+49	7.43E+50	2.25E+51	0.63	1.75E-01
DK_2263	3.36E-01	7.00E-05	4.37E-04	2.03E+46	4.10E+47	1.62E+50	5.70E+50	0.75	5.24E-02
DK_2283	2.05E-01	1.60E-02	4.00E-01	1.41E+49	4.27E+50	3.08E+51	2.11E+52	0.67	3.25E-02
DK_2288	3.72E-03	2.36E-03	2.80E-04	8.12E+45	1.31E+45	7.63E+48	4.76E+48	0.39	1.16E+01
DK_2297	1.44E-01	7.21E-02	1.45E+00	5.19E+49	1.24E+51	5.13E+51	6.58E+52	0.68	4.10E-02

DK_1139	2.98E+00	1.98E-02	6.07E+00	8.38E+49	3.62E+52	4.68E+52	4.94E+54	0.68	1.93E-03
DK_1135	1.19E-01	1.40E-04	1.87E-04	1.13E+46	5.59E+46	4.63E+49	9.94E+49	0.62	1.60E-01
DK_179	9.69E-02	2.22E-03	3.72E-02	4.89E+47	9.50E+48	8.70E+50	3.13E+51	0.62	3.97E-02
DK_171	8.60E-03	9.01E-02	5.99E-02	2.95E+48	2.18E+48	1.62E+50	1.74E+50	0.53	7.35E-01
DK_1037	1.54E-02	4.87E-01	4.42E-02	2.73E+48	1.64E+48	1.20E+50	9.38E+49	0.79	1.45E+00
DK_2458	8.34E-02	2.00E-05	1.11E-04	6.34E+45	4.30E+46	5.20E+49	1.36E+50	0.5	1.02E-01
DK_2534	1.05E-01	3.87E-02	3.29E-01	1.37E+49	1.56E+50	1.59E+51	7.58E+51	0.63	7.81E-02
DK_2572	1.05E-01	4.78E-02	9.79E-02	3.76E+48	1.83E+49	6.19E+50	1.43E+51	0.67	1.73E-01
DK_138	8.76E-03	8.95E-03	8.06E-04	3.57E+46	1.25E+46	1.39E+49	9.72E+48	0.79	5.31E+00
DK_2778	1.38E+00	2.53E-02	1.09E+00	3.92E+49	1.23E+51	8.48E+51	1.33E+53	0.21	9.43E-03
DK_860	6.54E-01	9.15E-03	7.28E-01	1.96E+49	2.11E+51	8.02E+51	1.00E+53	0.86	1.10E-02
DK_2953	5.40E-02	1.12E-01	2.65E-01	1.75E+49	6.29E+49	9.60E+50	3.30E+51	0.5	1.68E-01
DK_2974	1.30E-01	1.10E-04	2.35E-04	9.77E+45	5.44E+46	5.41E+49	1.20E+50	0.65	1.51E-01
DK_783	4.48E-02	2.04E-01	3.05E-02	9.91E+47	5.17E+47	1.18E+50	1.25E+50	0.33	8.66E-01
DK_2996	2.21E-01	5.70E-03	1.33E-01	3.05E+48	1.22E+50	2.17E+51	1.53E+52	0.69	2.07E-02
DK_3035	1.12E-01	4.83E-02	3.58E-02	2.59E+48	1.12E+49	3.77E+50	8.56E+50	0.66	1.89E-01
DK_3067	4.03E-02	4.05E-01	3.32E-01	4.18E+48	7.59E+48	5.01E+50	7.97E+50	0.65	3.66E-01
DK_746	1.95E-01	4.35E-03	3.42E-02	3.80E+47	5.45E+48	6.42E+50	1.94E+51	0.75	6.06E-02
DK_738	7.48E-02	4.06E-02	3.97E-02	1.54E+48	5.13E+48	3.15E+50	5.61E+50	0.76	2.60E-01
DK_3137	1.93E+00	1.06E-03	2.14E-01	5.16E+48	1.72E+51	1.04E+52	2.22E+53	0.65	2.40E-03
DK_3196	2.67E-01	4.66E-02	1.93E+00	5.85E+49	2.97E+51	8.71E+51	1.58E+53	0.76	2.13E-02
DK_3205	1.08E-02	2.56E-01	6.90E-02	6.19E+48	2.84E+48	1.88E+50	1.77E+50	0.43	1.68E+00
DK_687	2.20E-02	5.53E-03	1.86E-02	5.03E+47	1.37E+48	2.48E+50	4.84E+50	0.38	1.57E-01
DK_3269	4.62E-01	5.41E-02	1.99E-01	5.32E+48	6.71E+49	1.24E+51	4.11E+51	0.82	8.63E-02
DK_95	1.32E-01	3.60E-03	7.03E-02	1.84E+48	4.70E+49	1.40E+51	5.50E+51	0.87	4.56E-02
DK_96	1.51E-03	6.69E-01	2.09E-02	8.10E+47	5.30E+46	2.57E+49	7.68E+48	0.83	1.97E+02
DK_3379	5.55E-02	3.45E-02	1.93E-01	3.39E+48	2.13E+49	9.17E+50	2.71E+51	0.51	9.84E-02
DK_b_793	9.39E-03	4.40E-02	7.32E-03	1.43E+47	5.27E+46	4.03E+49	3.11E+49	0.52	2.60E+00
DK_597	4.85E-02	3.90E-04	1.08E-03	4.18E+46	1.87E+47	9.39E+49	1.87E+50	0.69	1.92E-01
DK_592	1.08E-01	5.90E-04	6.26E-04	3.44E+46	1.86E+47	7.85E+49	1.62E+50	0.77	1.80E-01
DK_3593	6.01E-02	2.65E-02	1.33E-01	2.25E+49	6.02E+49	8.60E+50	3.16E+51	0.21	8.94E-02
DK_3740	1.59E-02	1.81E-01	2.35E-01	6.21E+49	1.61E+49	5.12E+50	8.59E+50	0.09	1.67E+00
DK_496	5.58E-03	1.34E-02	1.03E-03	3.11E+46	6.23E+45	1.08E+49	6.00E+48	0.87	2.01E+01
DK_3866	5.29E-01	2.24E-02	2.97E-01	9.86E+48	2.90E+50	2.89E+51	1.70E+52	0.74	3.56E-02
DK_3907	2.12E-01	6.26E-02	1.16E+00	8.03E+49	1.66E+51	5.31E+51	9.84E+52	0.47	3.38E-02
DK_416	2.22E-02	1.03E-02	9.11E-03	2.47E+47	3.97E+47	9.45E+49	1.19E+50	0.89	4.75E-01
DK_4218	8.90E-03	1.11E+00	8.95E-02	8.13E+48	1.65E+48	1.74E+50	9.03E+49	0.42	1.08E+01
DK_58	9.22E-03	2.59E-01	1.37E-01	2.89E+48	1.89E+48	2.33E+50	2.37E+50	0.46	8.09E-01
DK_57	1.10E-03	2.18E+00	2.77E-02	4.94E+48	2.86E+46	3.67E+49	5.12E+48	0.08	2.05E+03
DK_4666	4.47E-02	2.25E-01	5.44E-02	3.64E+48	5.77E+48	2.47E+50	3.62E+50	0.71	3.90E-01
DK_335	7.02E-01	5.06E-03	5.24E-03	1.32E+47	1.03E+48	2.37E+50	5.65E+50	0.86	1.38E-01
DK_4766	9.42E+00	0.00E+00	1.62E-04	2.91E+45	1.25E+48	7.47E+50	9.38E+51	0.57	1.69E-03
DK_4776	2.00E-02	2.88E-01	2.59E-02	1.93E+48	1.11E+48	1.04E+50	9.11E+49	0.65	1.37E+00
DK_4796	1.49E-01	1.27E-01	1.34E-01	2.41E+48	9.20E+48	5.62E+50	1.26E+51	0.54	1.63E-01
DK_304	6.71E-03	3.75E-02	2.93E-03	9.90E+46	2.36E+46	1.84E+49	1.10E+49	0.84	1.33E+01
DK_5044	5.13E-02	1.58E-01	3.78E-01	6.84E+48	2.49E+49	9.95E+50	2.90E+51	0.53	1.66E-01
DK_5315	7.90E-02	2.17E-03	1.46E-02	7.82E+47	8.39E+48	4.65E+50	1.35E+51	0.67	8.68E-02
DK_262	4.85E-03	4.07E-01	1.65E-02	6.10E+47	8.41E+46	2.87E+49	1.31E+49	0.81	4.26E+01
DK_203	9.36E-01	6.38E-02	6.05E+00	1.43E+50	1.85E+52	2.11E+52	8.66E+53	0.93	9.48E-03
DK_178	8.75E-03	1.44E-01	8.18E-02	6.72E+48	3.51E+48	2.18E+50	2.36E+50	0.37	1.15E+00
DK_180	1.74E-02	1.48E-02	3.02E-02	1.04E+48	1.61E+48	2.33E+50	3.93E+50	0.33	2.17E-01
DK_22	1.43E-03	7.09E-01	4.35E-02	2.98E+48	2.09E+47	5.88E+49	1.76E+49	0.48	1.15E+02
DK_19	2.08E-02	5.95E-02	1.95E-01	1.22E+49	3.21E+49	6.49E+50	1.63E+51	0.43	1.85E-01
DK_159	2.39E-01	1.96E-03	4.74E-02	1.08E+48	4.20E+49	1.46E+51	7.63E+51	0.65	2.01E-02
DK_157	2.10E-01	8.32E-02	2.38E+00	5.98E+49	2.20E+51	7.49E+51	1.05E+53	0.87	3.18E-02
DK_143	1.96E-01	2.84E-02	8.64E-01	2.66E+49	9.39E+50	4.57E+51	4.24E+52	0.71	2.92E-02
DK_118	1.82E-01	3.85E-02	7.12E-01	2.70E+49	6.12E+50	3.76E+51	3.21E+52	0.64	4.12E-02
DK_88	4.07E-02	3.12E-02	2.09E-01	7.08E+48	5.21E+49	1.10E+51	3.28E+51	0.66	1.22E-01
DK_84	6.49E-02	1.25E-01	9.12E-01	3.35E+49	3.60E+50	2.53E+51	1.88E+52	0.78	9.80E-02
DK_80	5.65E-01	5.26E-03	4.88E-01	1.72E+49	2.13E+51	7.56E+51	1.10E+53	0.79	9.09E-03
DK_77	2.20E-02	2.00E-05	4.34E-05	6.88E+44	2.14E+45	1.85E+49	3.20E+49	0.59	2.11E-01
DK_40	1.10E-02	2.10E-01	1.31E-01	2.18E+48	2.13E+48	2.45E+50	2.75E+50	0.6	5.94E-01
DK_39	1.13E-02	2.65E-01	1.85E-01	1.08E+49	1.07E+49	4.06E+50	4.53E+50	0.91	7.01E-01

DK_32	9.26E-03	1.38E-01	1.51E-01	6.29E+48	9.10E+48	3.29E+50	4.67E+50	0.71	4.15E-01
DK_24	1.92E-02	5.19E-02	1.57E-01	1.96E+48	7.10E+48	5.26E+50	1.03E+51	0.65	2.00E-01
DK_20	4.11E-03	1.66E-01	5.23E-02	1.48E+48	4.57E+47	1.06E+50	8.01E+49	0.38	2.92E+00
DK_18	1.50E-03	6.06E-01	2.45E-02	7.86E+47	3.86E+46	3.16E+49	9.65E+48	0.34	1.22E+02

Table A.0.24: Uncertainties of the values of table A.0.23. The columns are arranged in the same order. The name of the respective shell is given in column 1. Column 2 contains the uncertainties of the shell volume ΔV_{sh}. Column 3 and 4 list the uncertainties of the particle density Δn_{obs} and the upper particle density $\Delta n_{\mathrm{obs,u}}$. Columns 5 and 6 contain the uncertainties of the theoretical total energies ejected from the stars, $\Delta E_{\mathrm{w}}(t)$ and $\Delta E_{\mathrm{w,u}}(t)$. Columns 7 and 8 list uncertainties of the total energies for single point explosions approximation $\Delta E_{\mathrm{c}}(t)$ and $\Delta E_{\mathrm{c,u}}(t)$ respectively. The columns 9 and 10 contain the energy ratios $\Delta\epsilon_{\mathrm{w}}$ and $\Delta\epsilon_{\mathrm{w,l}}$ respectively. For more information see section 5.4.

APPENDIX B

Figures

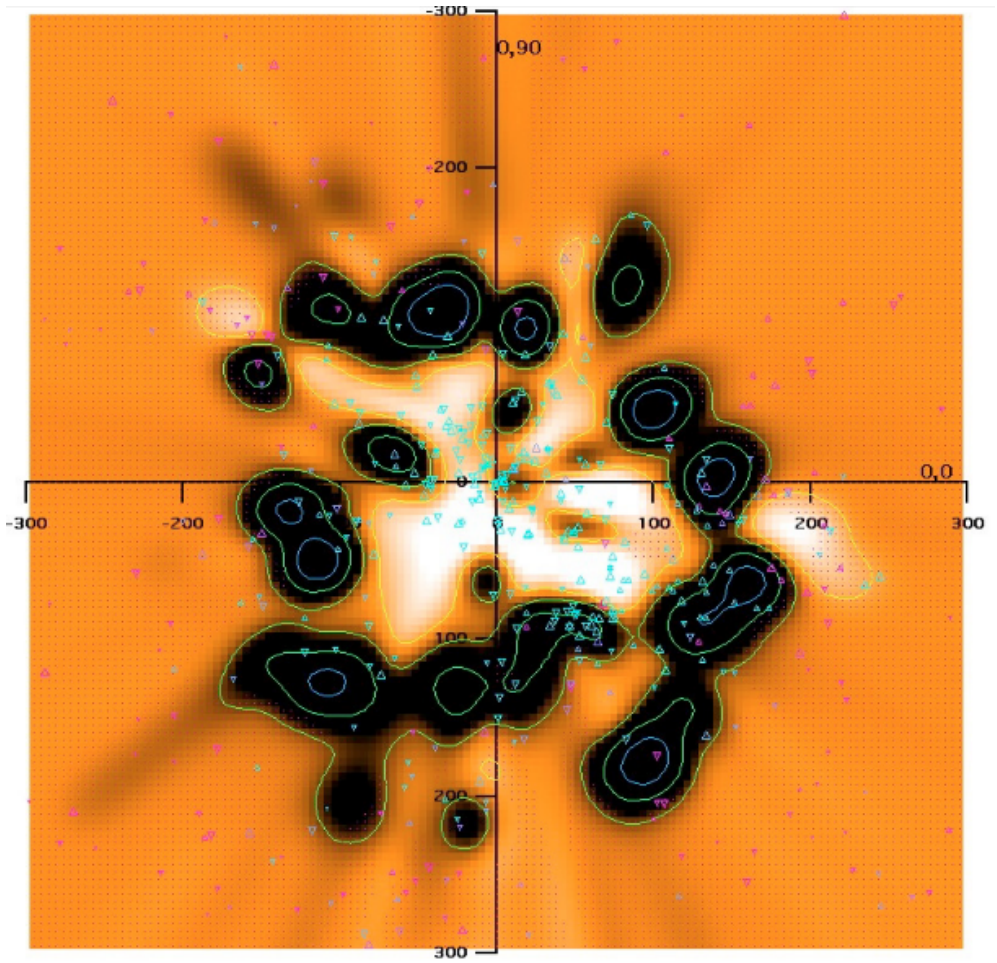

Figure B.0.1: Galactic plane view of the ISM revealed by the interstellar Ca II absorption (figure from Welsh et al. (2010)). The position of th Sun is 0,0 and the ISM is traced to distances up to 300 pc.

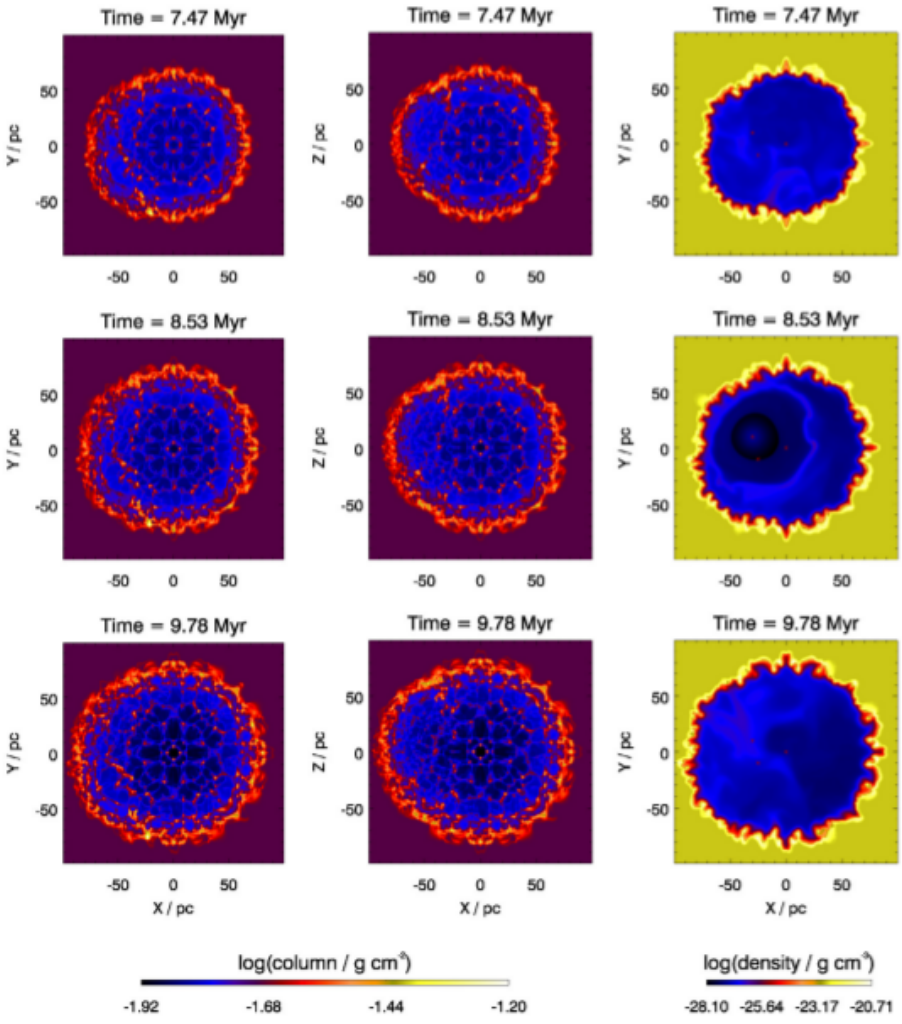

Figure B.0.2: Continuation of figure 2.6 (figure adopted from Krause et al. (2013)).

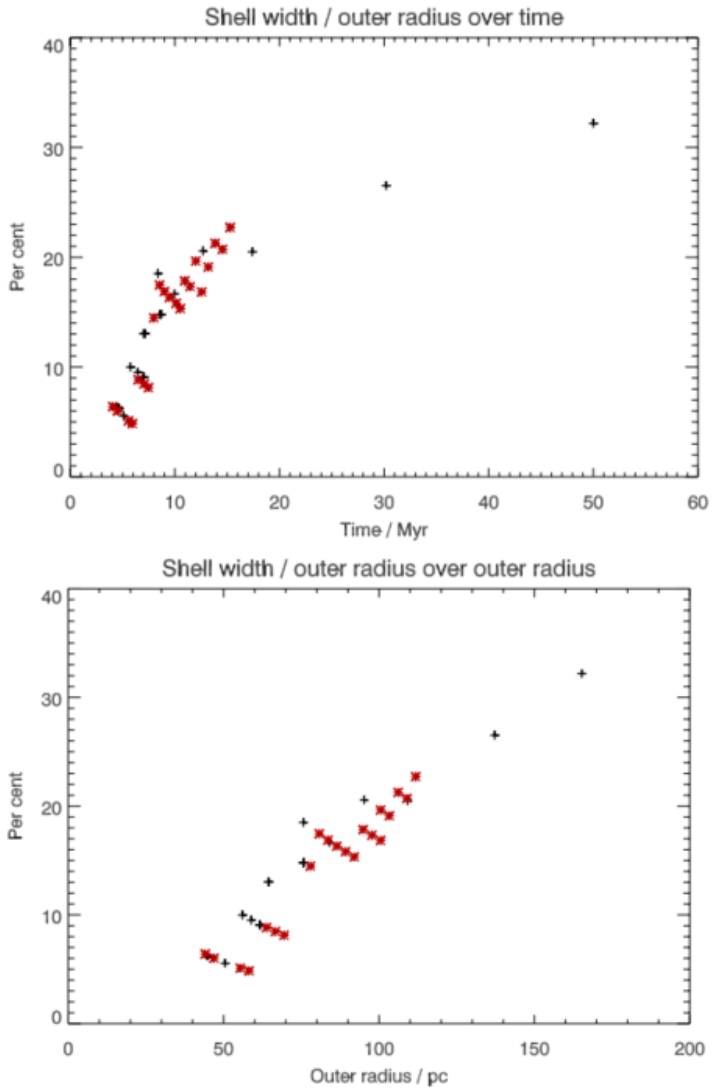

Figure B.0.3: Illustration of the evolution of shell thickness with time in the top panel and shell thickness vs. outer radius in the lower panel. Black plusses are for lower resolution runs than the resulting red crosses. This is described in more detail in Krause et al. (2013), where the figure is adopted from.

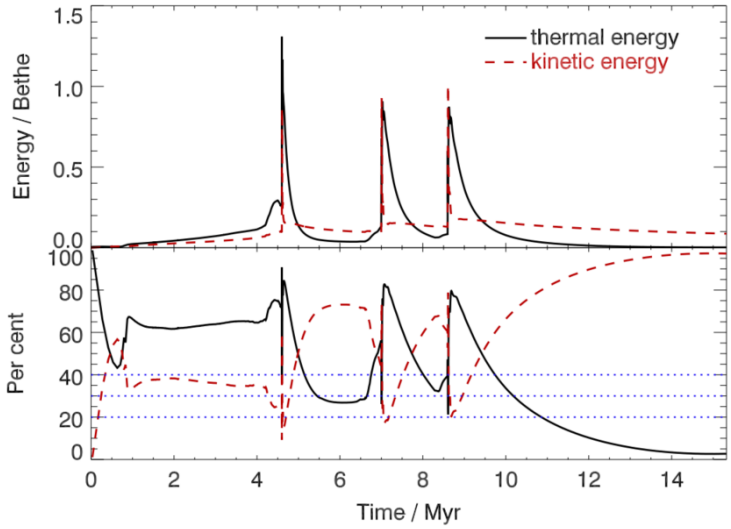

Figure B.0.4: Energy evolution for a 3D hydrodynamical simulation of the ISM around three massive stars. Top: time evolution of the kinetic (red dashed) and thermal energy (black solid). Bottom: corresponding fractions of the total energy. The blue dotted lines mark interesting values for the kinetic energy fraction derived in the thin-shell approximation, namely, the lower limit (20%), the case of a constant luminosity wind (30%) and the case of the isolated adiabatic supernova (40%). Description and figure adopted from Krause & Diehl (2014).

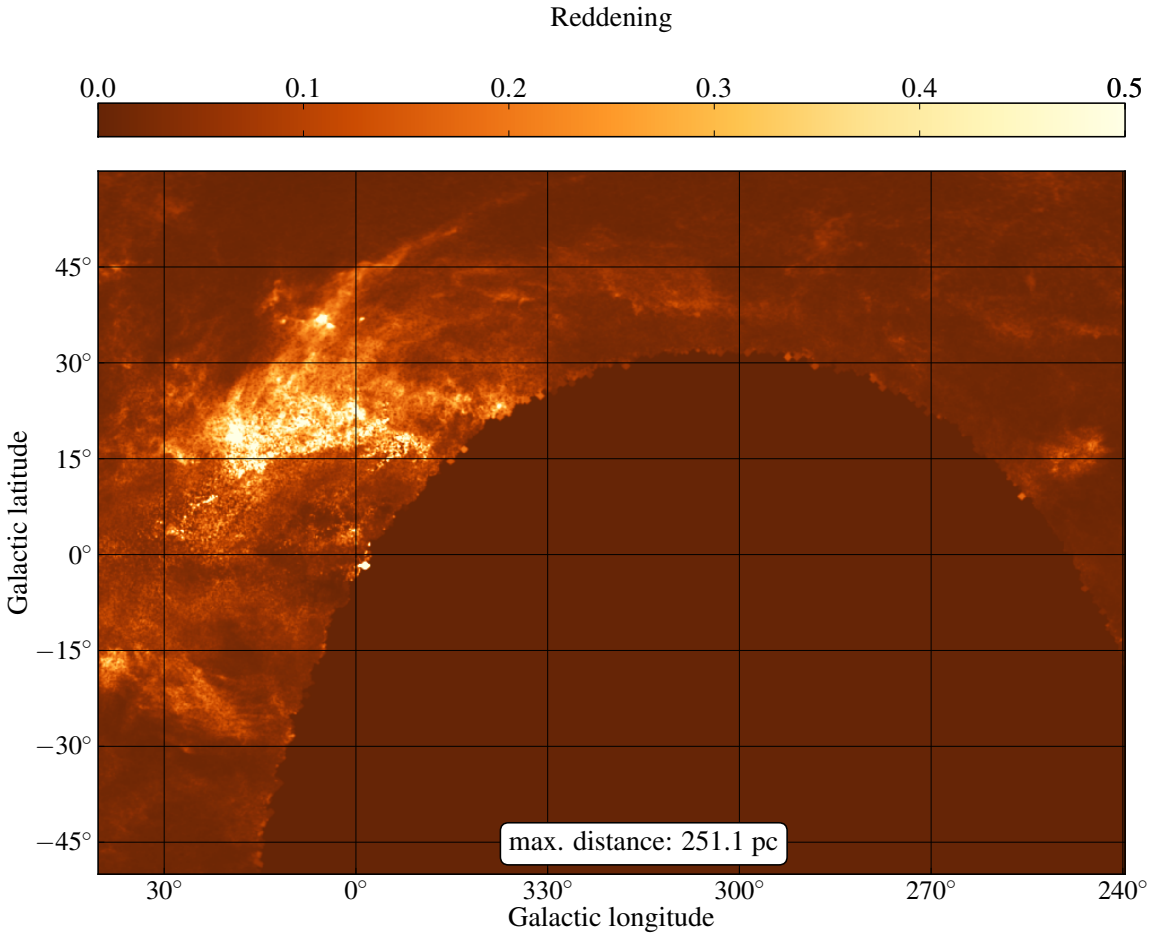

Figure B.0.5: Integrated interstellar reddening map induced by dust of the ISM around Sco-Cen to a distance of 251 pc. The colorbar denotes the reddening in magnitudes. For large parts of this image, no data were available as can be seen in the semi elliptical region of 0 reddening ranging from 240° to 15° in longitude. The data from which this plot was derived stem from Green et al. (2015).

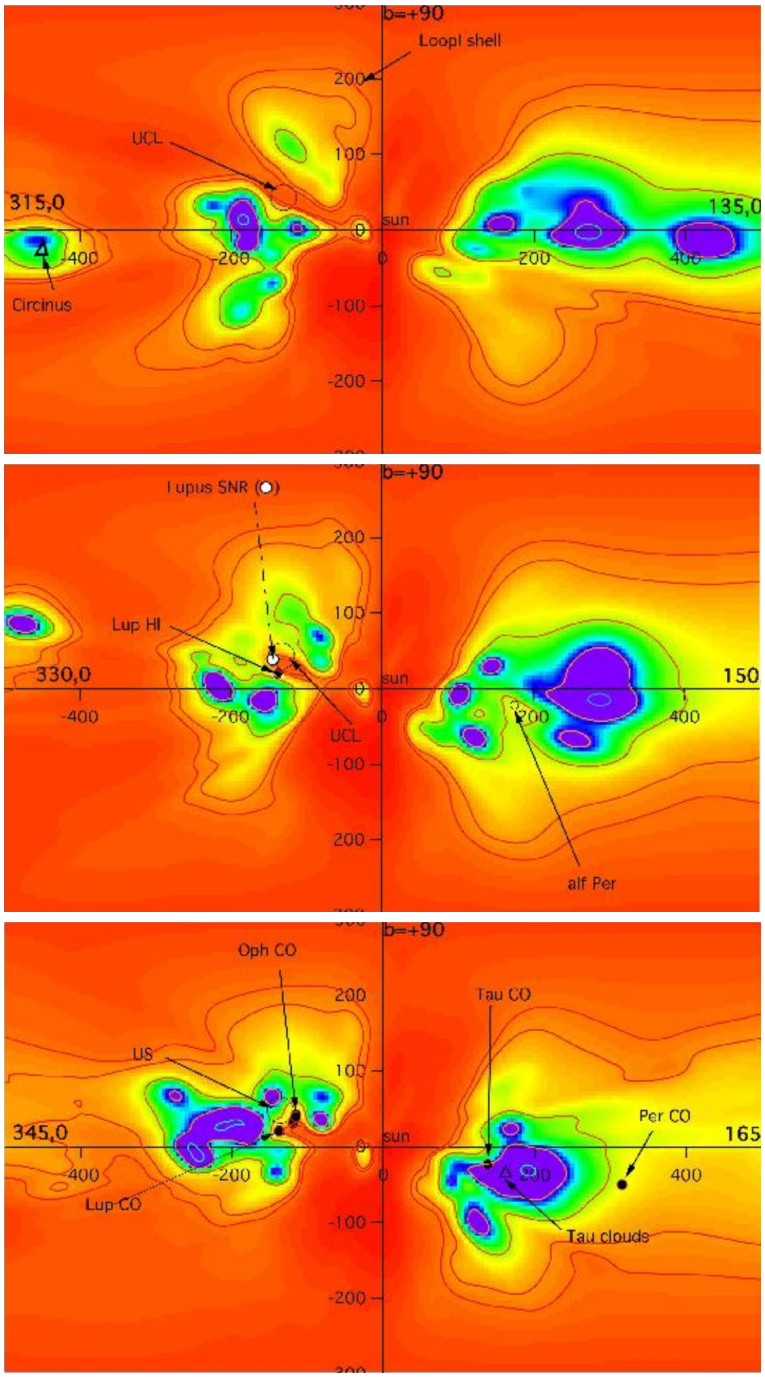

Figure B.0.6: Three vertical plane cuts showing the opacity distribution along the longitudes ($l = 315^\circ, 330^\circ, 345^\circ$) and the anti direction ($l = 135^\circ,\ 150^\circ,\ 165^\circ$). The north pole direction ($b = 90^\circ$) is at the top of each sub-image and the Sun is located at the respective center, i.e. (0,0). Regions from the literature are marked and labeled. The colormap is the same as in figure 2.3 in section 2. Figure extracted from figure 7 in Lallement et al. (2014).

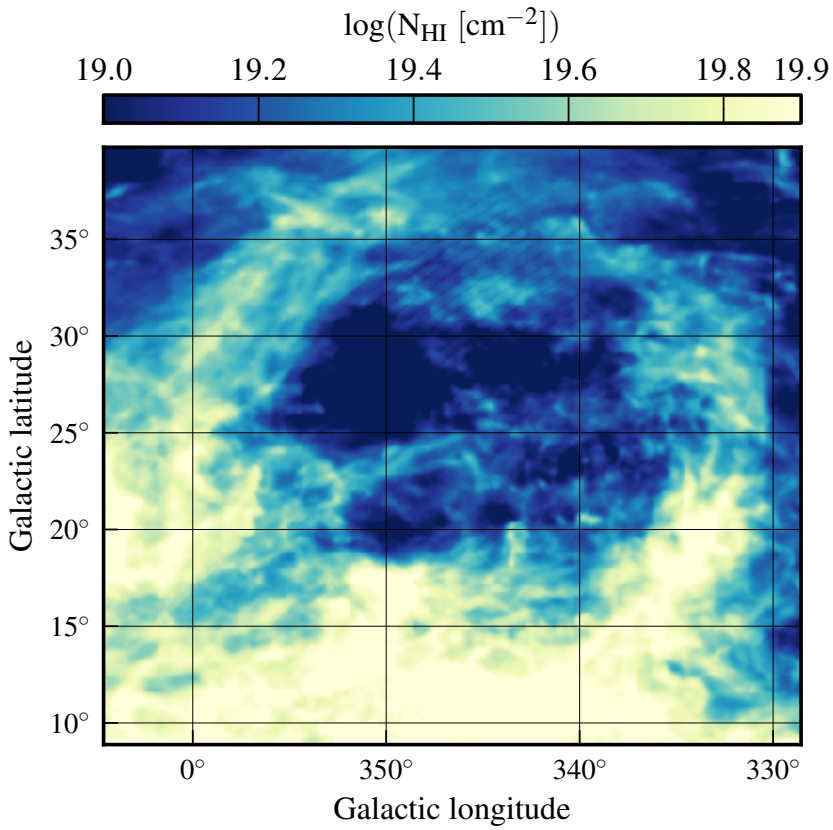

Figure B.0.7: H I channelmap of the region around the USco stellar subgroup of Sco-Cen from the second data release of the GASS Kalberla et al. (2010). The colorbar shows the logarithm of the H I column density. RFI effects are remaining in the region l = (340–350)°, b = (30–35)°.

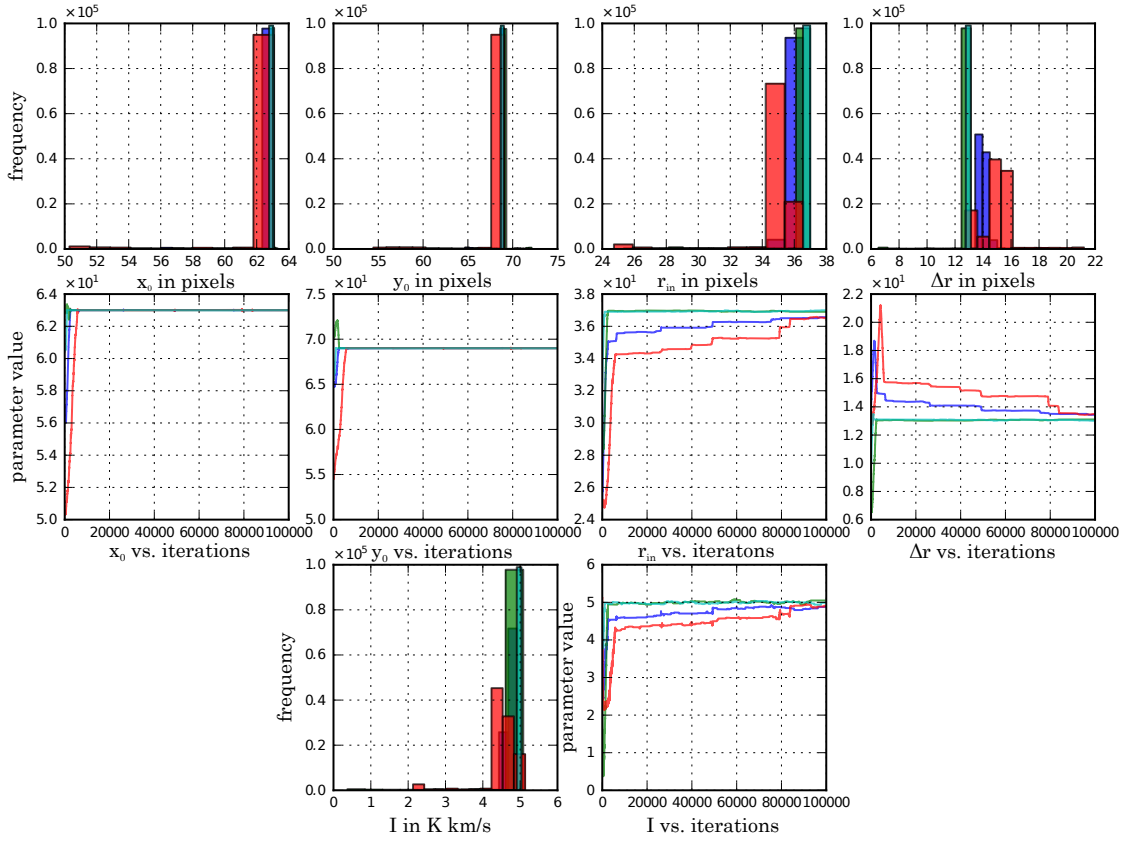

Figure B.0.8: Similar plot arrangement to figure 4.11 but for four fits of a ring to a test dataset of a ring with uniformly randomly drawn noise between 0–1 K km/s. Five sub-plots show the drawn results from the posterior distributions in histograms for each parameter and five additional sub-plots showing the progression of the parameter during the fit iteration.

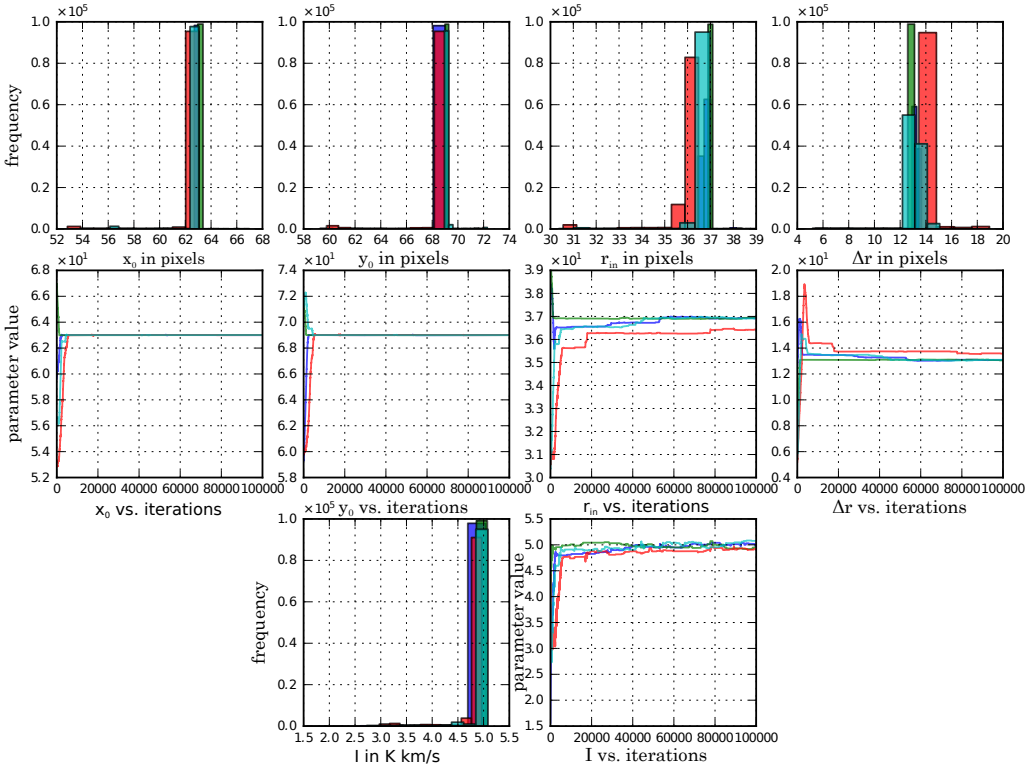

Figure B.0.9: Similar plot arrangement compared to figure 4.11 but for four fits of a ring to a test dataset of a ring with uniformly randomly drawn noise between 0–3 K km/s. Five sub-plots show the drawn results from the posterior distributions in histograms for each parameter and five additional sub-plots showing the progression of the parameter during the fit iteration. For a more detailed description of the sub-plots see fig 4.11.

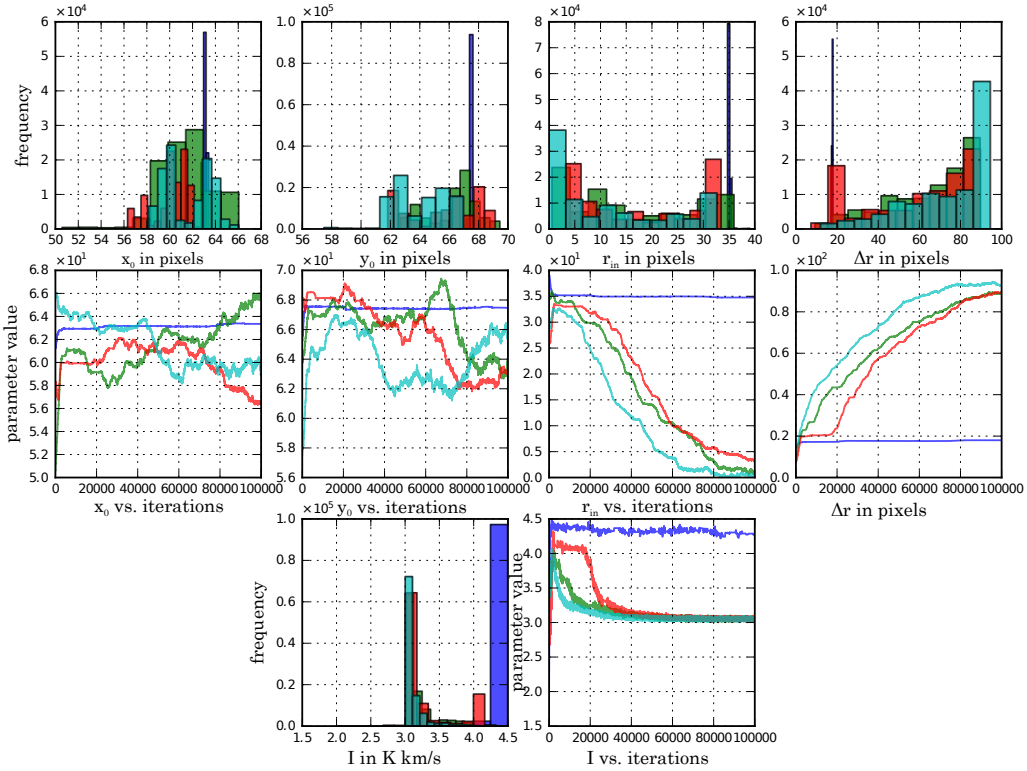

Figure B.0.10: Similar plot arrangement to figure 4.11 but for four fits of a ring to a test dataset of a ring with uniformly randomly drawn noise between 0–5 K km/s. Five sub-plots show the drawn results from the posterior distributions in histograms for each parameter and five additional sub-plots showing the progression of the parameter during the fit iteration.

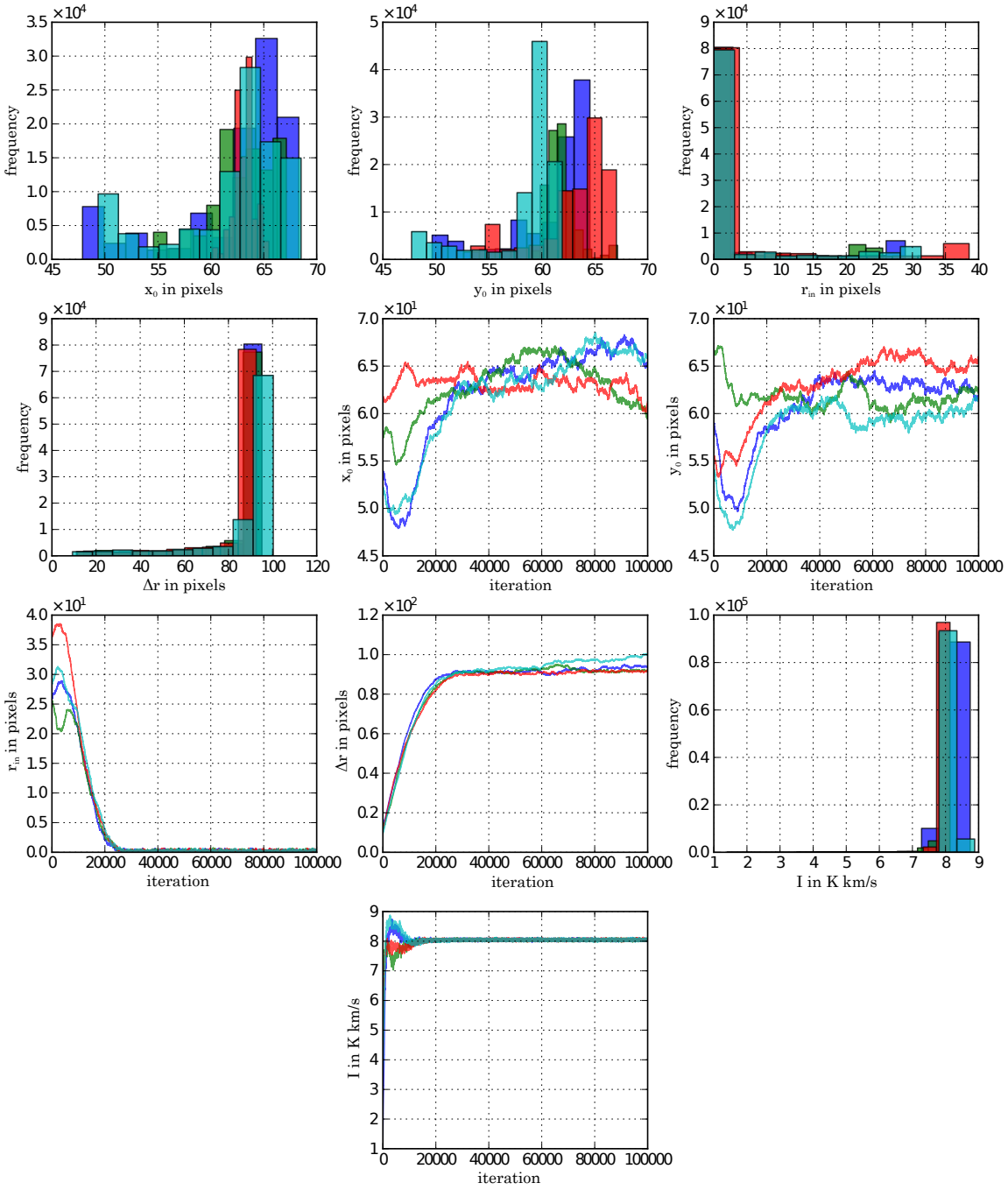

Figure B.0.11: Fit of a ring to a test dataset containing a shell in a realistic H I environment taken from the GASS. Counting the plots from the top left to the bottom right, in plots 1–4 as well as plot 9, the sampled distribution of each parameter is shown for four MCMC runs, with different start parameters. Plots 5, 6, 7, 8 and 10 show the parameter progression of these runs. .

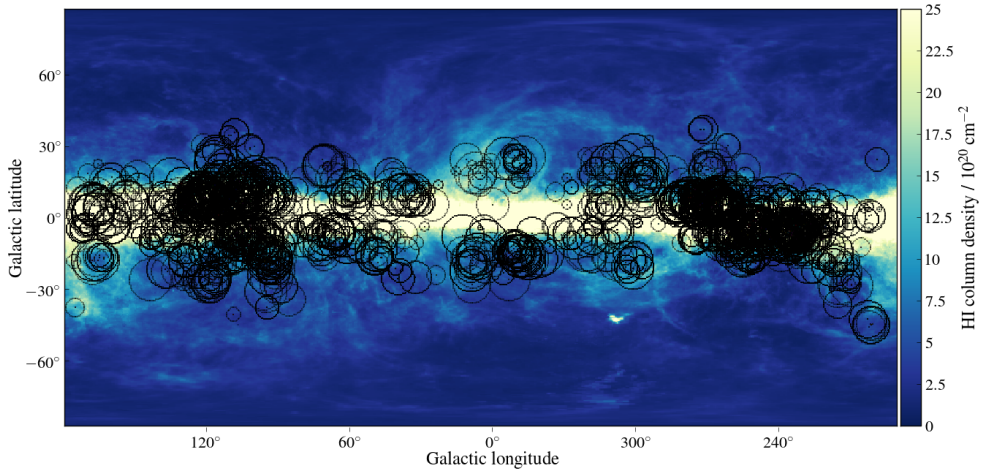

Figure B.0.12: Testresults of SAGHIS applied to the H I data of the LAB survey in full velocity, and angular range. The black circles denote the maximum radius of the shells and the background image shows the logarithm of the Hi column densities for velocities near 0 km/s.

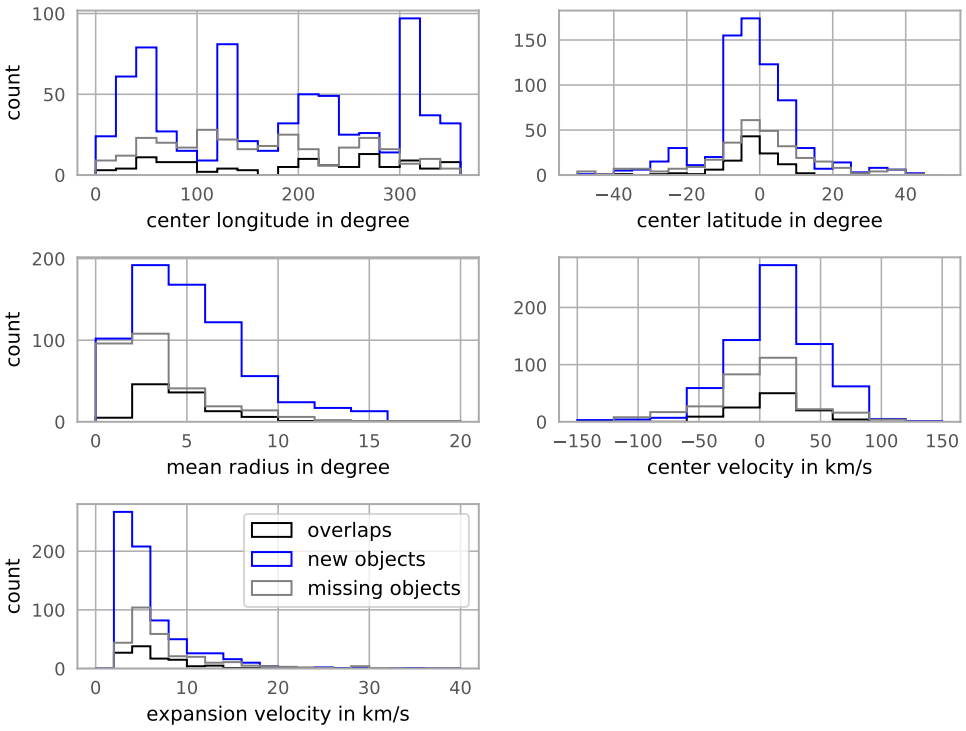

Figure B.0.13: Distributions of new– (blue), overlapping– (black) and missing (grey-dashed) shells when comparing to the catalogs MCG2002, EP2013 and S2015. In each of the five panels separate distributions of the shell parameters are plotted.

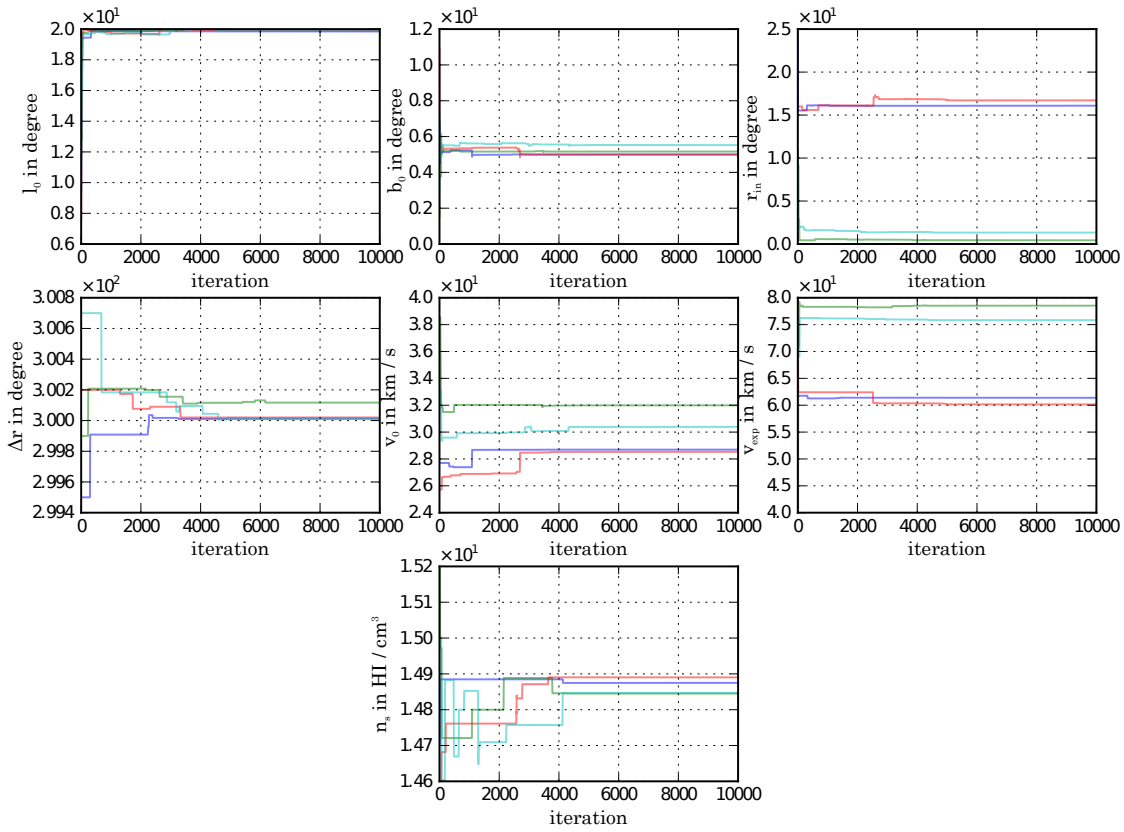

Figure B.0.14: Parameter progression during the MCMC fit of the EHSS-model to the H I test data with background emission. Each plot shows the progression of one parameter during the MCMC fit process for four runs. For each run, the start parameters were drawn randomly for a given range.

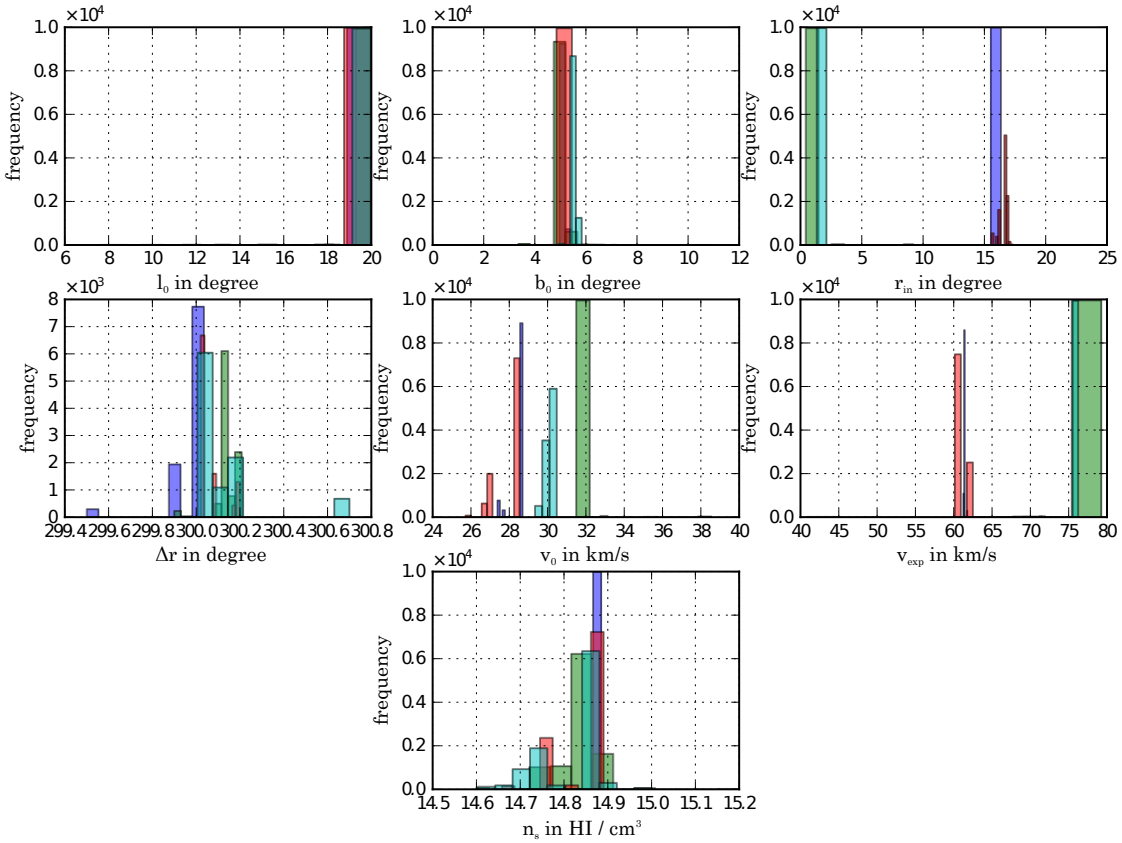

Figure B.0.15: Fit of the EHSS-model to a test dataset containing a shell in a realistic H I environment taken from the GASS. Each of the 7 plots show the sampled distributions from four runs of the MCMC algorithm for one start parameter that is randomly drawn for each of the four runs.

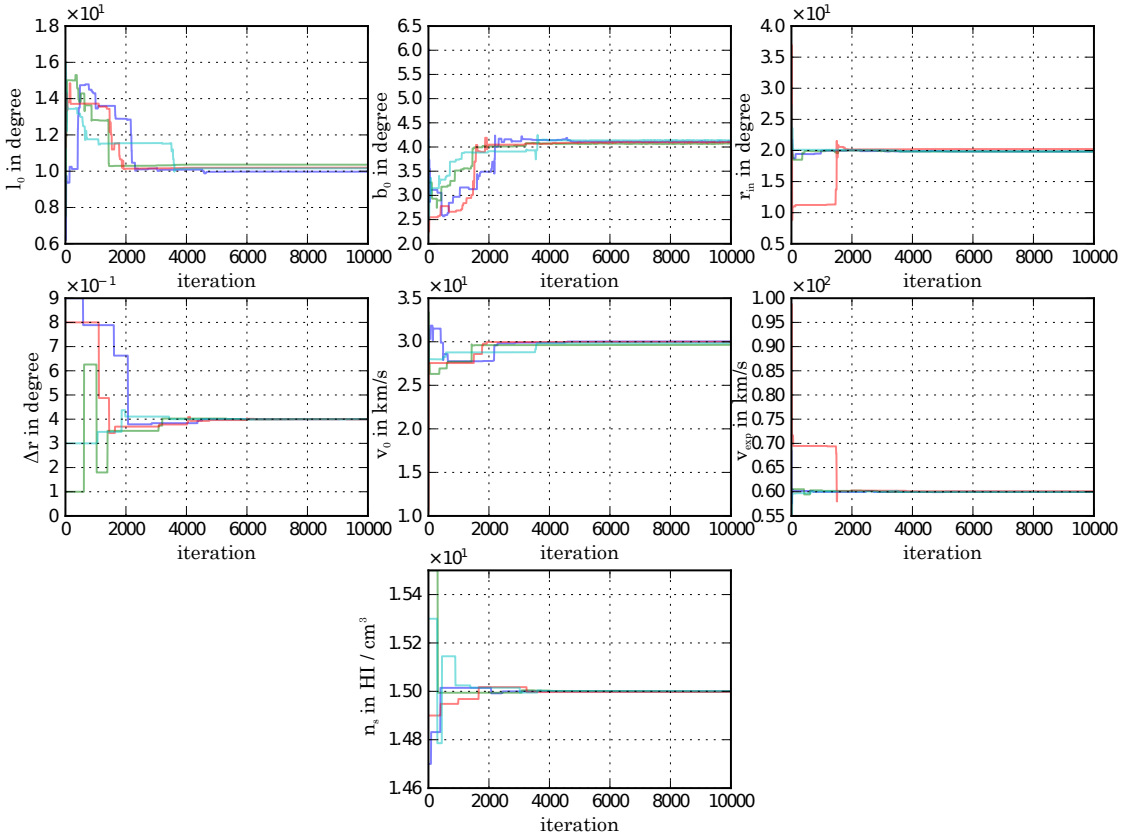

Figure B.0.16: Parameter progression for four runs of the fit of the EHSS-model to H I test data using the MCMC algorithm. Each plot shows the progression of one parameter for the four runs. The start parameters were drawn randomly in a small range (sec. 4.3.4) around the optimal values.

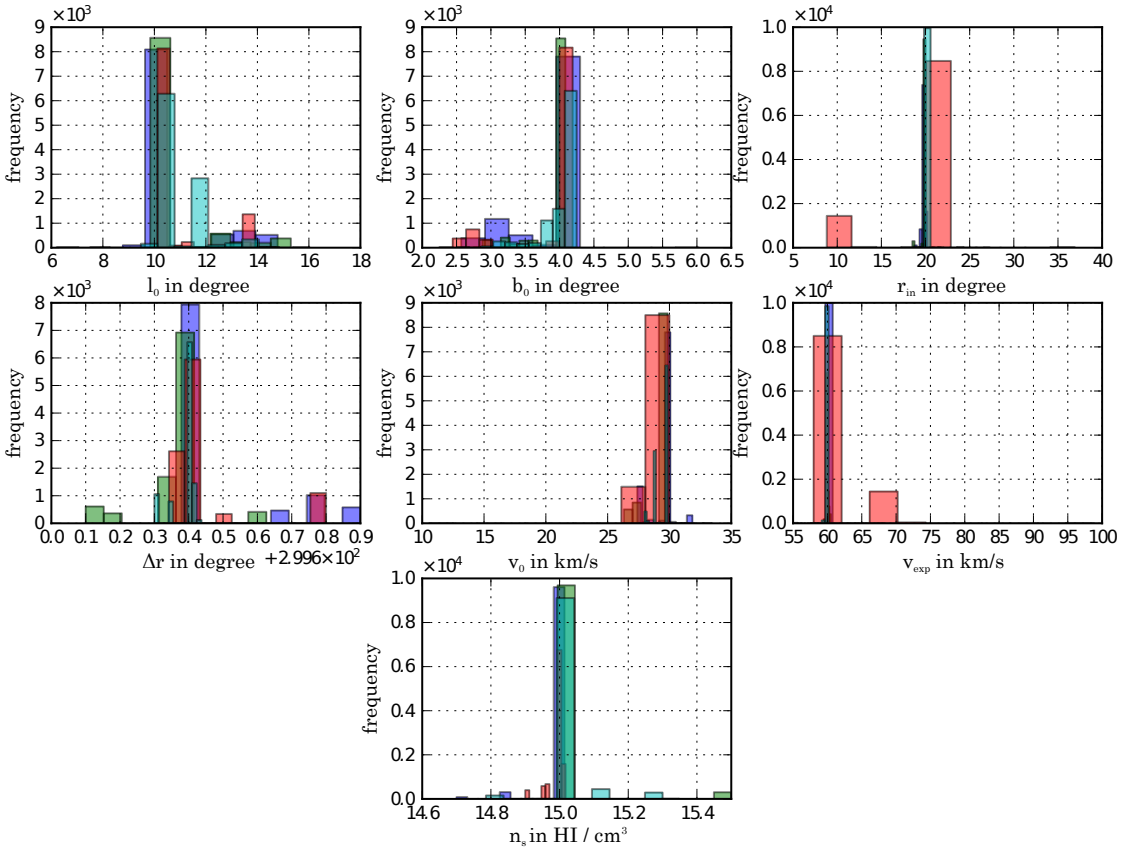

Figure B.0.17: Similar plot to figure 4.15. The EHSS-model is fitted to a pure shell without background but start parameters are drawn randomly in a smaller range (sec. 4.3.4) around the optimal minimum.

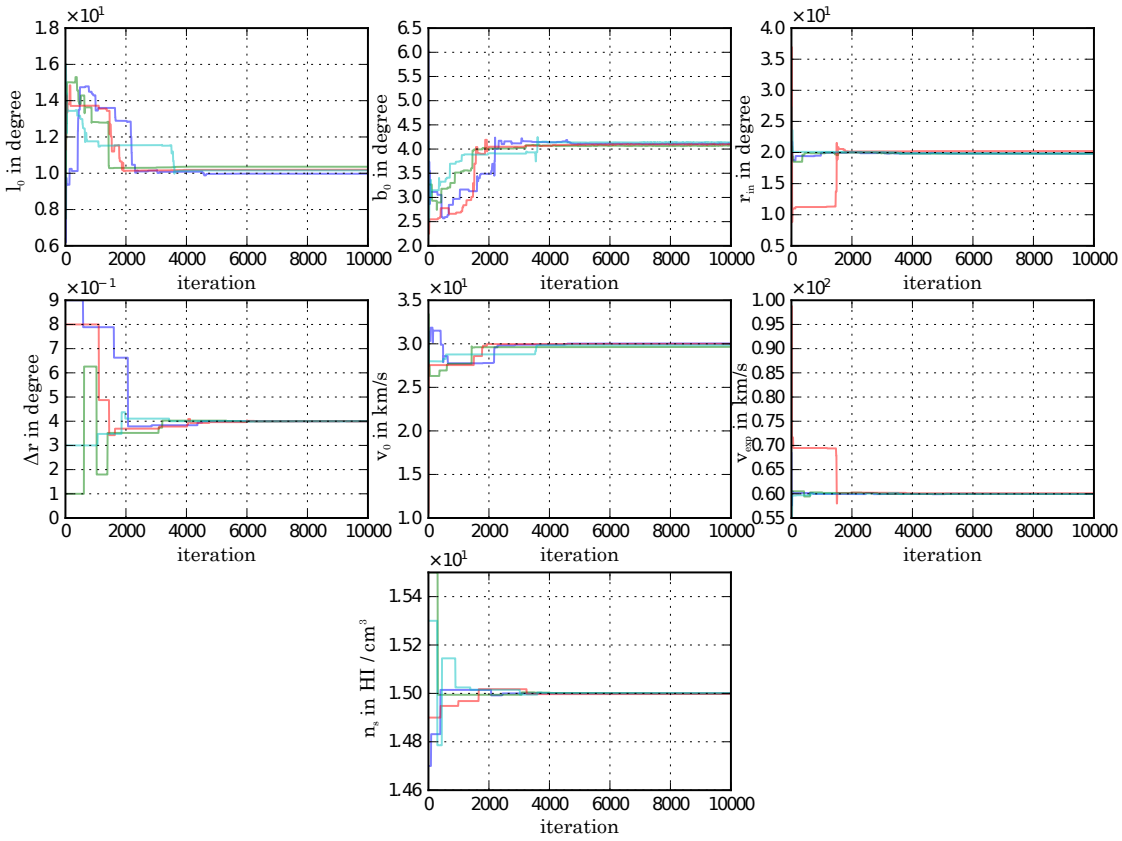

Figure B.0.18: Similar plots to figure 4.14, showing the progression of each parameter of the MCMC fit of the EHSS-model to a test dataset containing a ring without any background H I emission. The progression of four runs is shown for each of the 7 parameters. The start parameters for each run are drawn in a smaller range around the minimum.

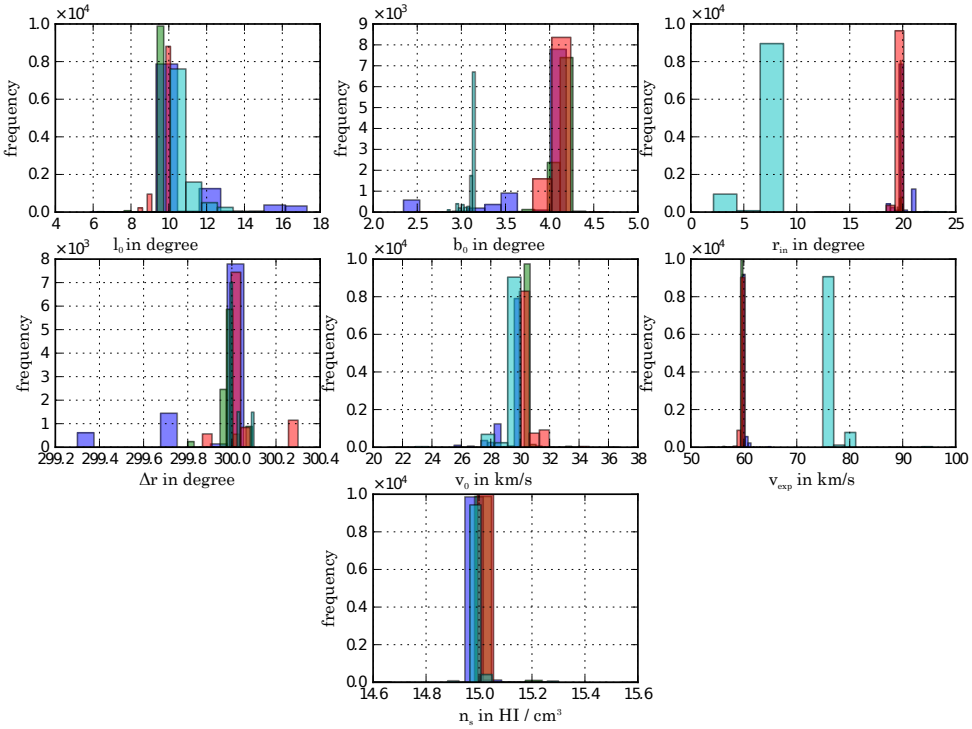

Figure B.0.19: Sampled parameter distributions of the fit of the EHSS-model to a shell in a random noise background for 4 different runs with randomly drawn start parameters each.

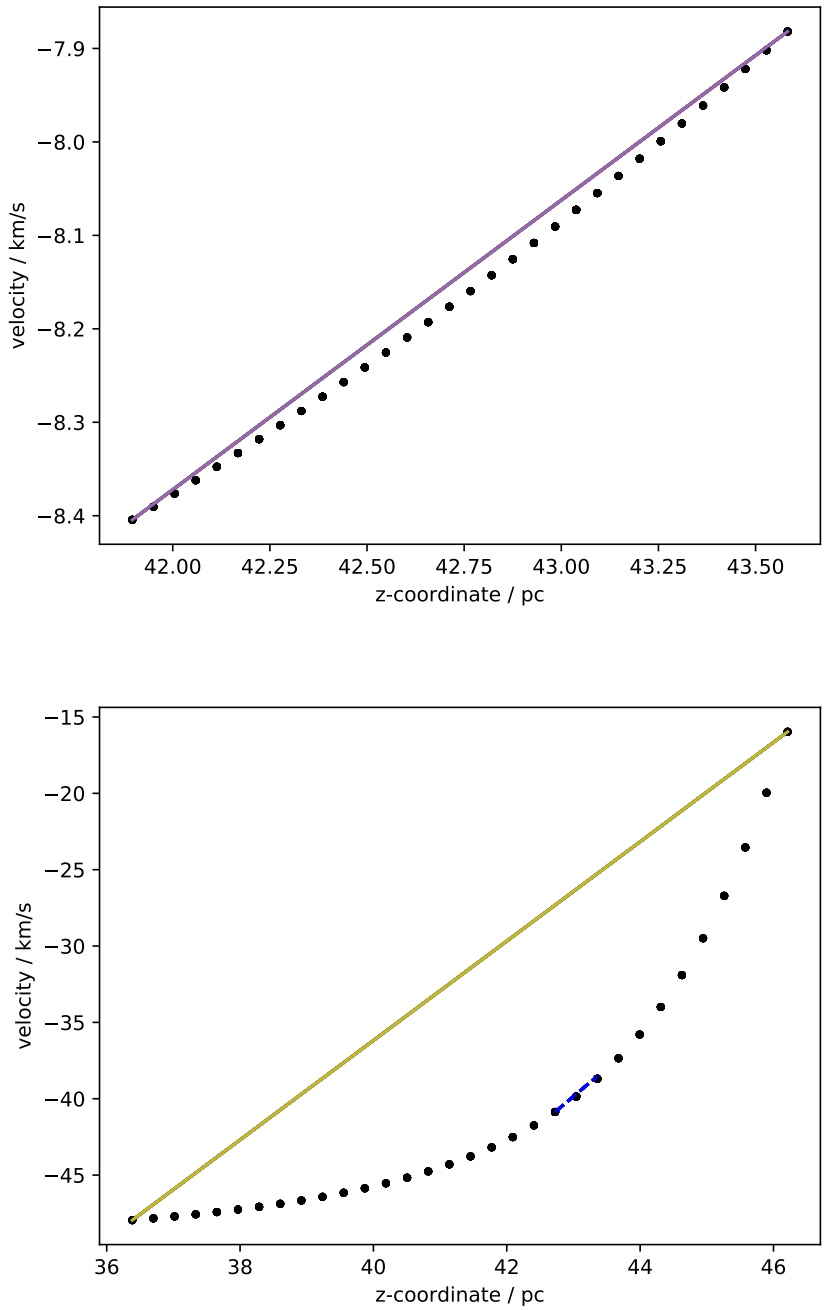

Figure B.0.20: Two plots showing linear approximations for observed velocity components between two points of known velocity (black dots). The blue and yellow line show the connection between the two outermost points in the respective panel. The blue dashed line between three points near z-coordinate 43–44 in the bottom panel marks the interpolation between the points.

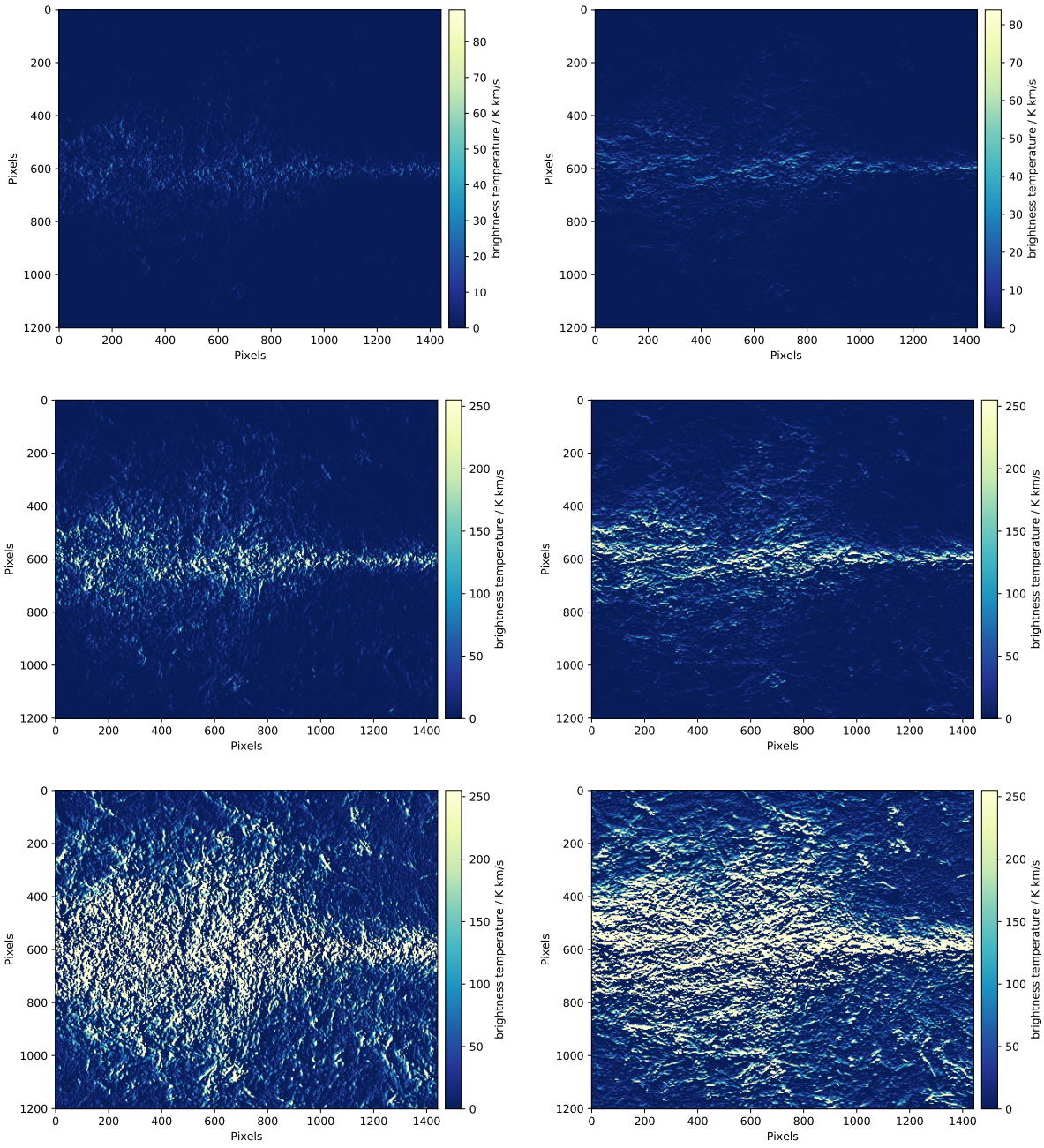

Figure B.0.21: Results of the application of the Sobel operator on H I data from the HI4PI survey for three different kernel sizes of 3, 5 and 7.

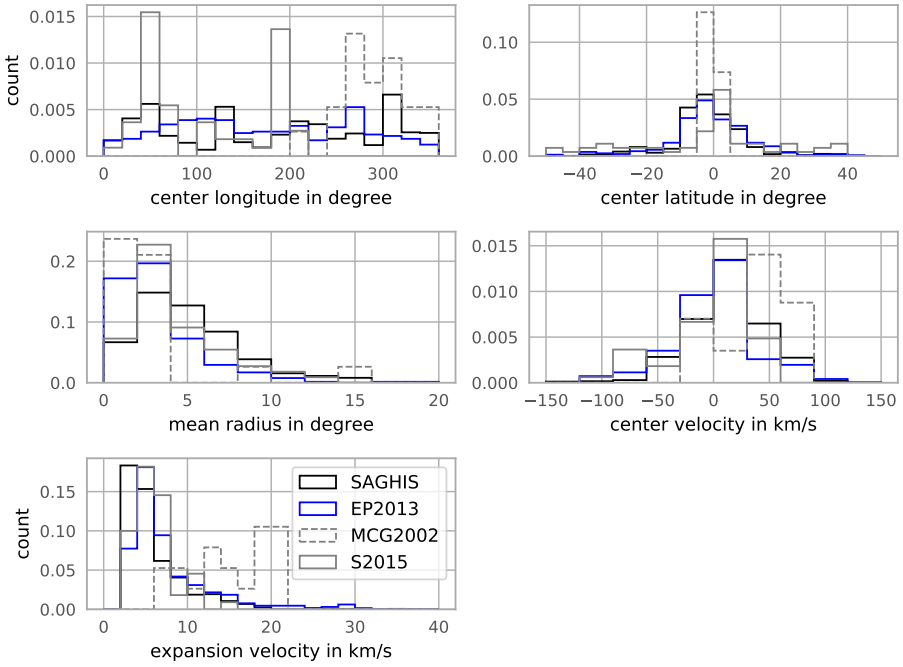

Figure B.0.22: Similar plots as shown in figure 5.4 but the distributions are normalized to 1. The black line marks the shells of this catalog, the blue line represents the list of reference shells of the literature and the dashed grey line marks the high quality shells of this thesis. For more information see section 5.2.1.

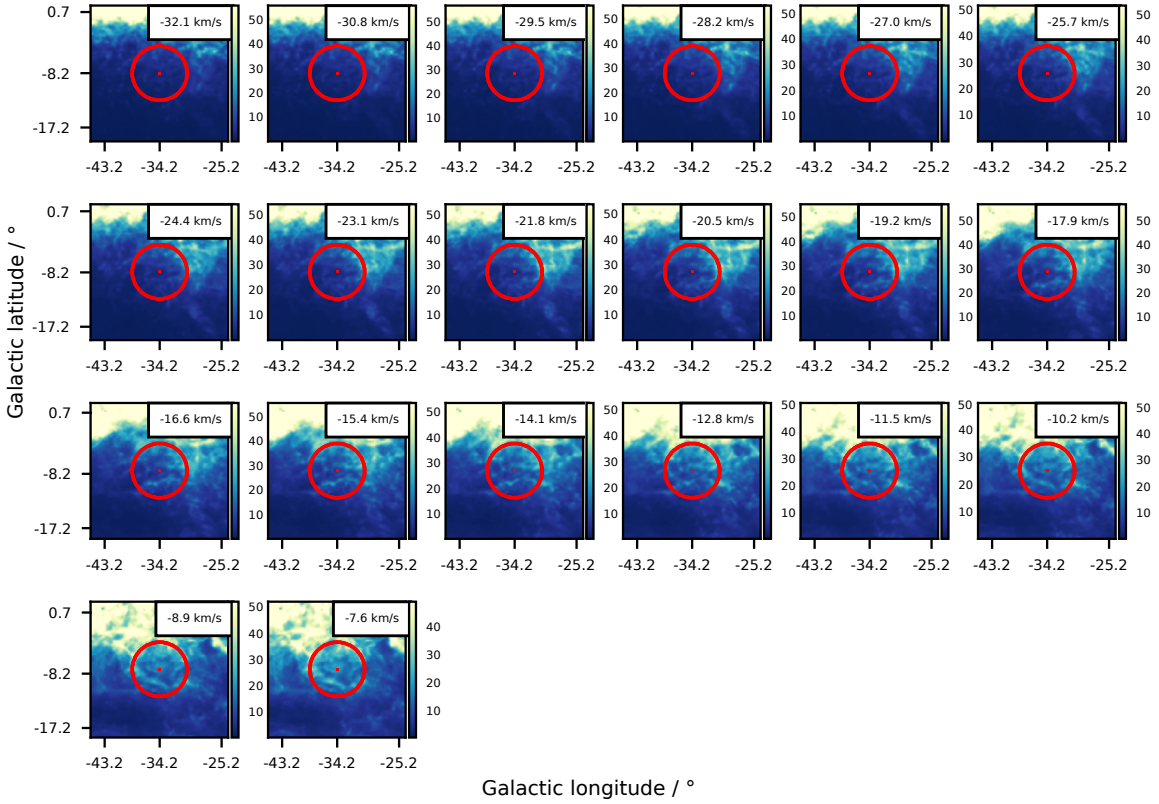

Figure B.0.23: Plot of the velocity spectrum through the center coordinates of catalog shell DK_1286. The x-axis marks the channel number and the y-axis shows the brightness temperature in units of K km/s. The vertical dashed lines mark the lower- and upper channel limits, where the shell is detected by SAGHIS. The red dots mark the intensity maxima near these regions and the black dot marks the intensity minium detected automatically (sec. 4.6.3)

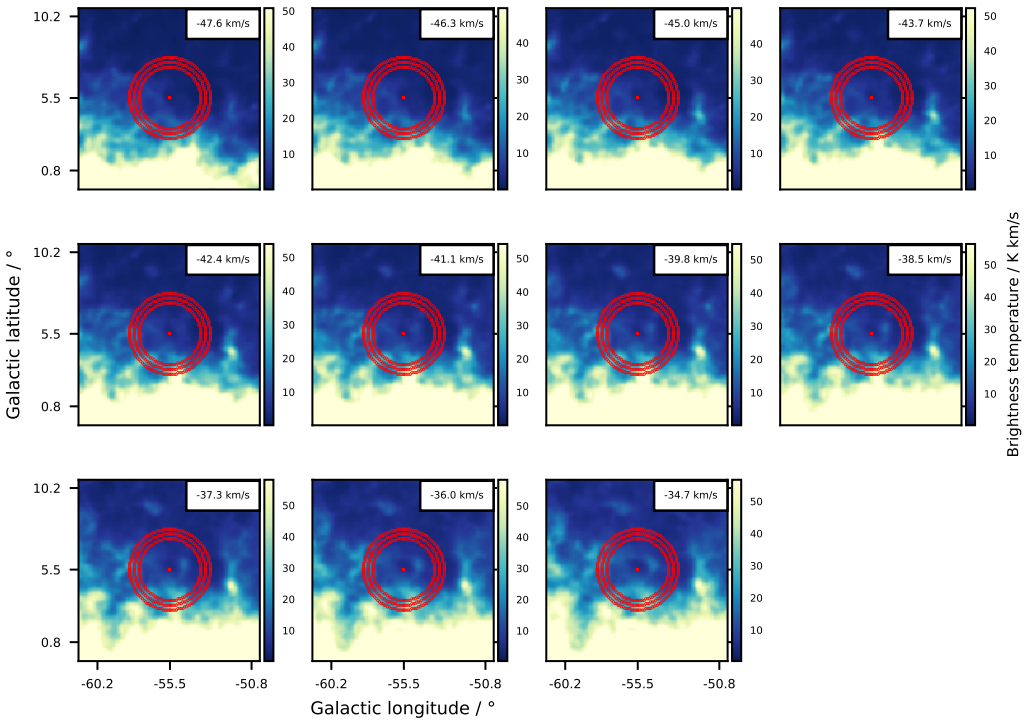

Figure B.0.24: Plots of the shell DK-166 for each channel where its features were detected using SAGHIS on top of the surrounding region of the HI4PI data. The red circles mark the minimum- , mean- and maximum radius of the shell R_{min}, R_{mean} and R_{max} respectively.

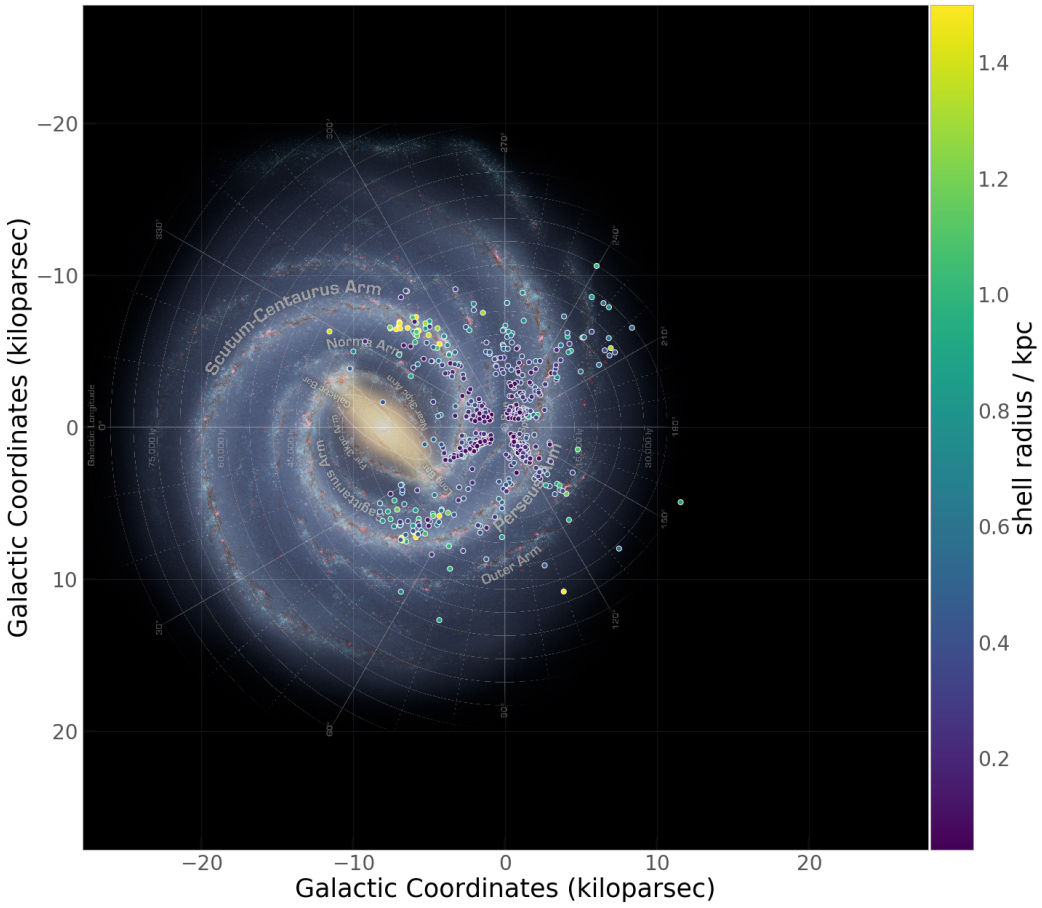

Figure B.0.25: Plot of the catalog shells in galactocentric coordinate system. Each shell is color-coded by its size in kpc according to the colorbar. The background image contains the galacic center and the spiral arms to provide a comparison of the positions of the objects to the large MW structures. The center of the image is the position of the Sun and the plot shows a region of −20 kpc to +20 kpc around the Sun. For more information see section 5.3. Background figure credits https://pypi.org/project/mw-plot (status 01.12.2020).

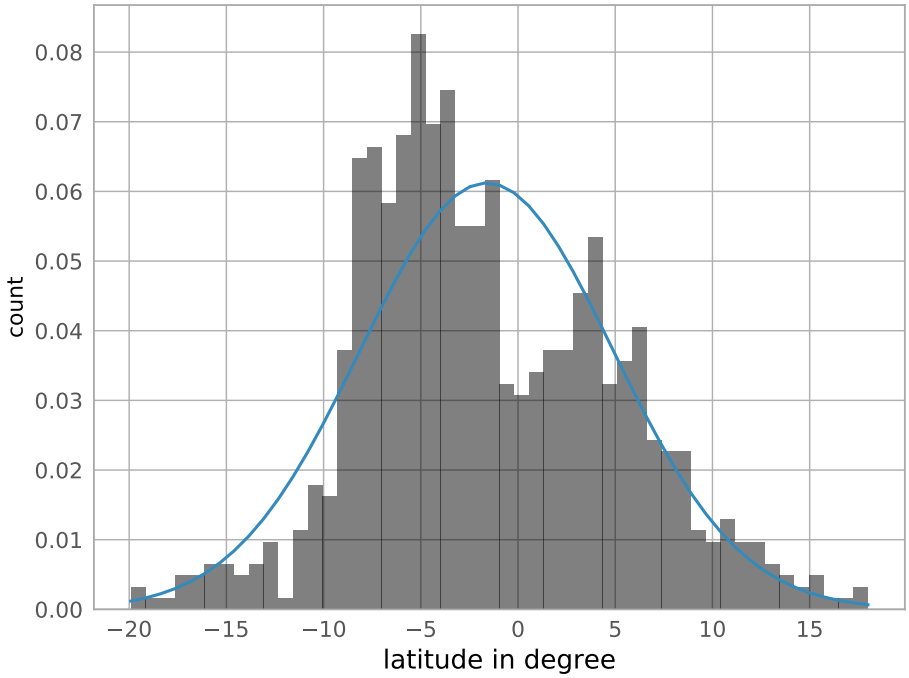

Figure B.0.26: Distribution of shells with center latitudes lower than $b_0 = 20^\circ$. The blue line denotes a fitted Gaussian distribution. The FWHM of the distribution is 6.5° and the outer tails of the gaussian are represented by the shell distribution.

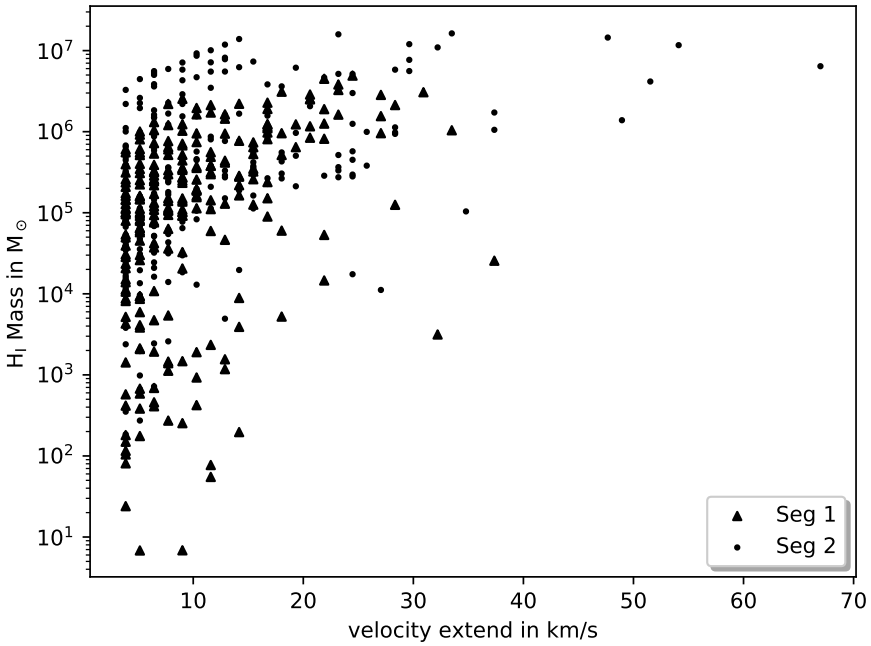

Figure B.0.27: Plot showing the results of the mass calculation of the shells. The resulting mass (log-scale) is plotted against the expansion velocity. For more information see text in section 5.3.1

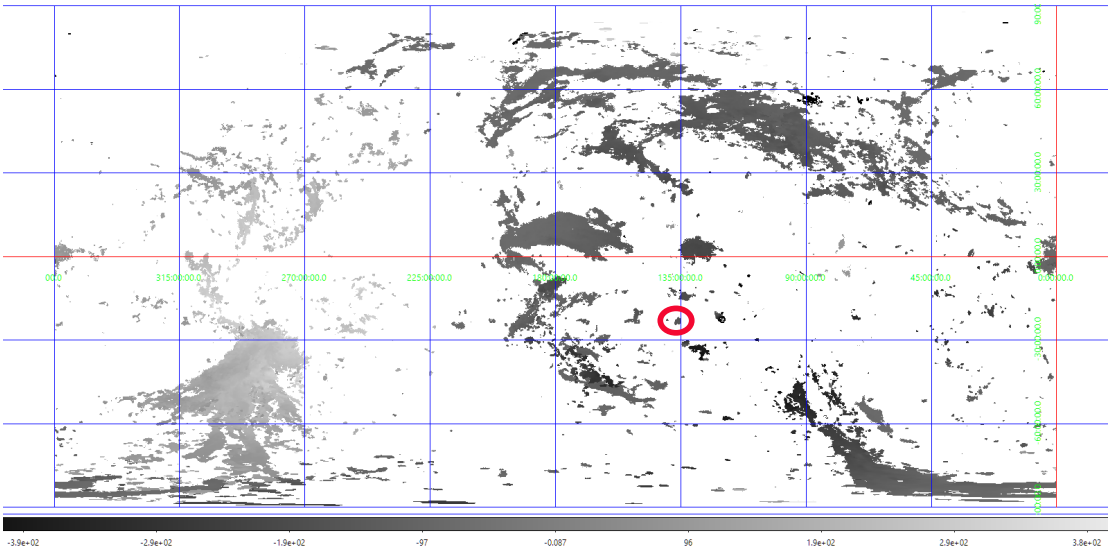

Figure B.0.28: All-sky map containing positions of high-velocity clouds. The intensity is color coded. The high-velocity cloud, which is related to the H I shell DK_102 is marked by a red circle. Fits-data from Westmeier (2018). Screenshot of a visualization in the tool DS-9 (Joye & Mandel 2003).

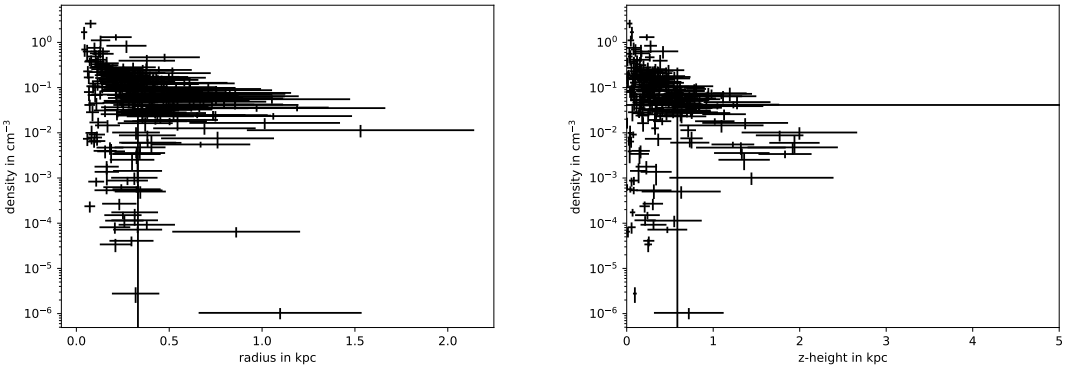

Figure B.0.29: Plots of the calculated initial density, n_0, against the maximum shell radius, R_{max} in the left panel and n_0 vs. the z-height of the center coordinate of the shell in the right panel for the shells of Seg 1. For more information see text.

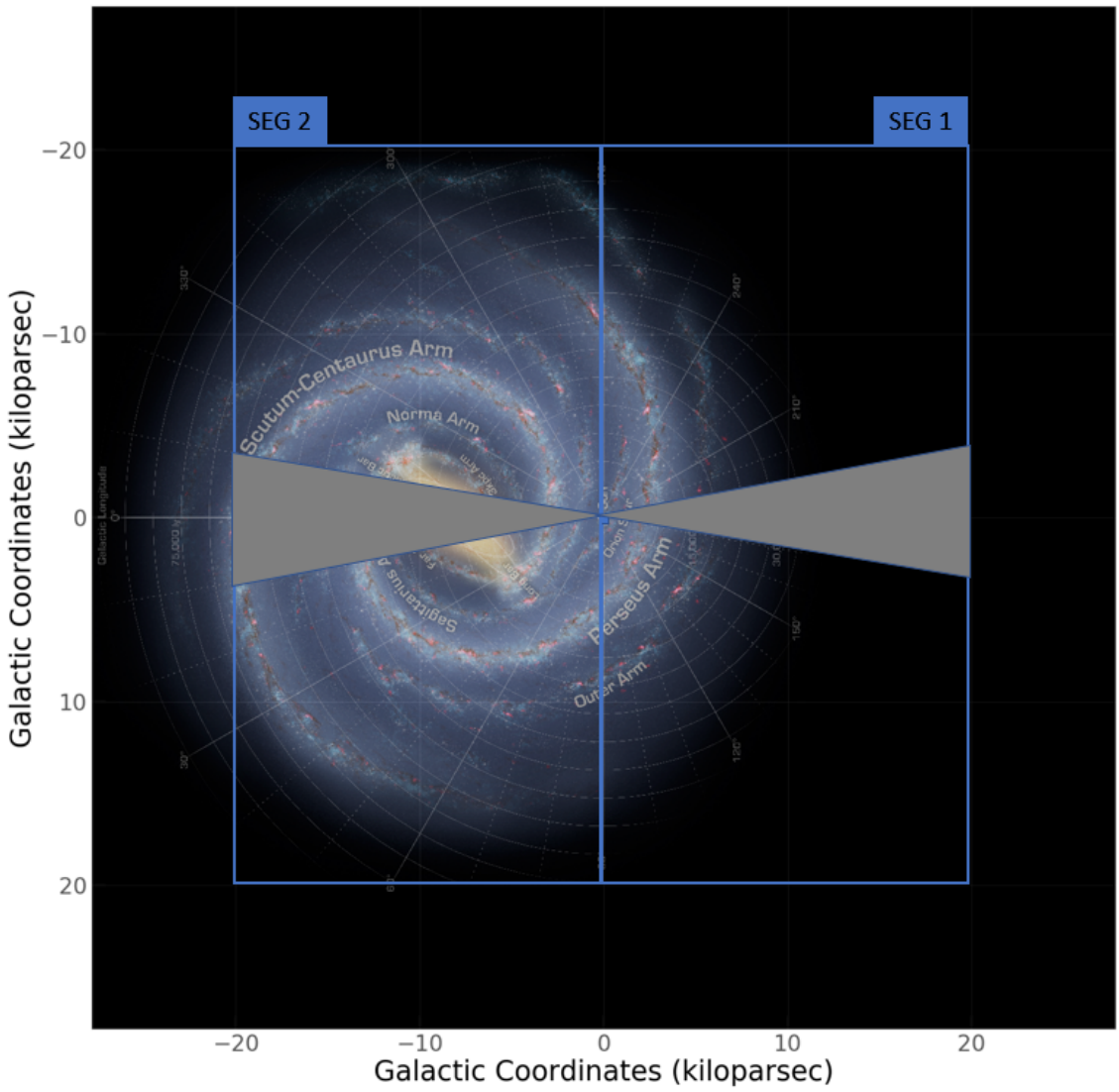

Figure B.0.30: Plot showing the regions of Seg 1 and Seg 2 marked by two blue rectangles. The regions, where the kinematic distance calculation is not applicable are marked by the grey triangles. The background image contains the galactic center and the spiral arms to provide a comparison of the positions of the objects relative to the galactic spiral arms. The location of the Sun lies at the center coordinates (0,0) kpc of the plot. A version of this plot containing the color coded size of the shells instead of the radial velocity, can be found in figure B.0.25 in the appendix. Background figure credits https://pypi.org/project/mw-plot (status 01.12.2020).

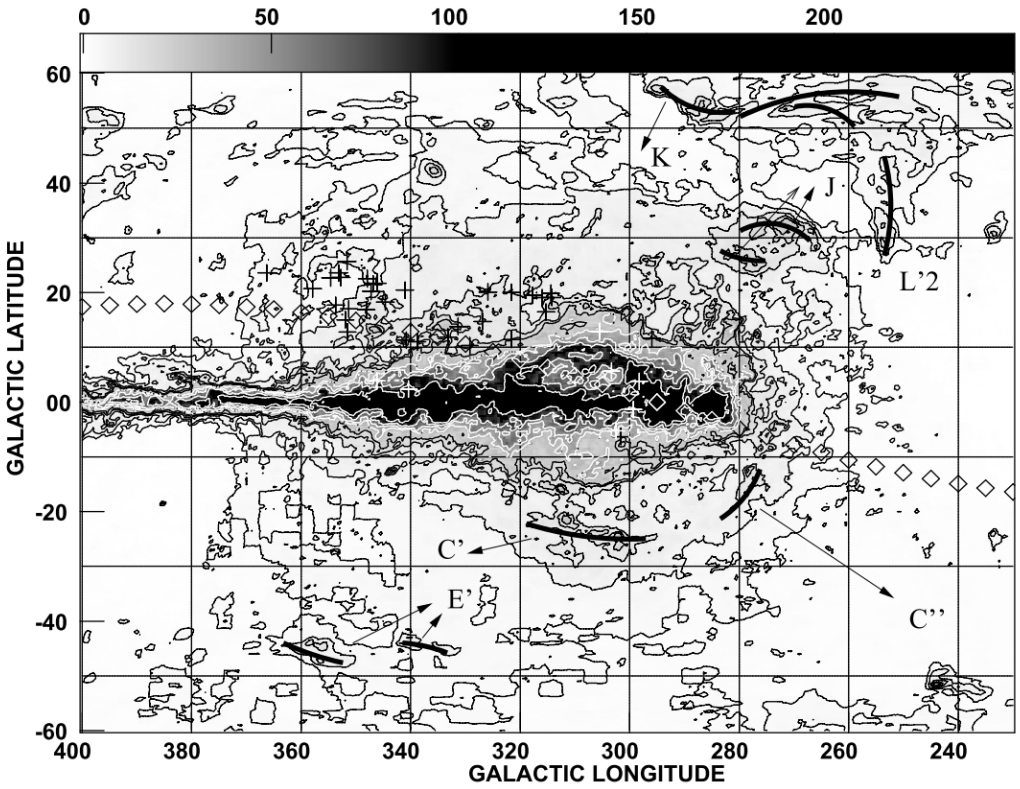

Figure B.0.31: Gray-scale map ranging from 0 to 100 K for integrated H I emission over the range of $V = -41.2$ to -20.6 km/s. The contours are at $2.45 \cdot (1, 2, 4, 6, 8, 14, 20, 30$ and $45)$. The selected branches that are indicated schematically are marked by letters. The crosses mark the stars of spectral type OB2.5 belonging to Sco-Cen (de Bruijne (1999)). The diamonds indicate the plane of the Gould Belt (see section 2.2.2). Figure from Poeppel et al. (2010) figure 1 therein.

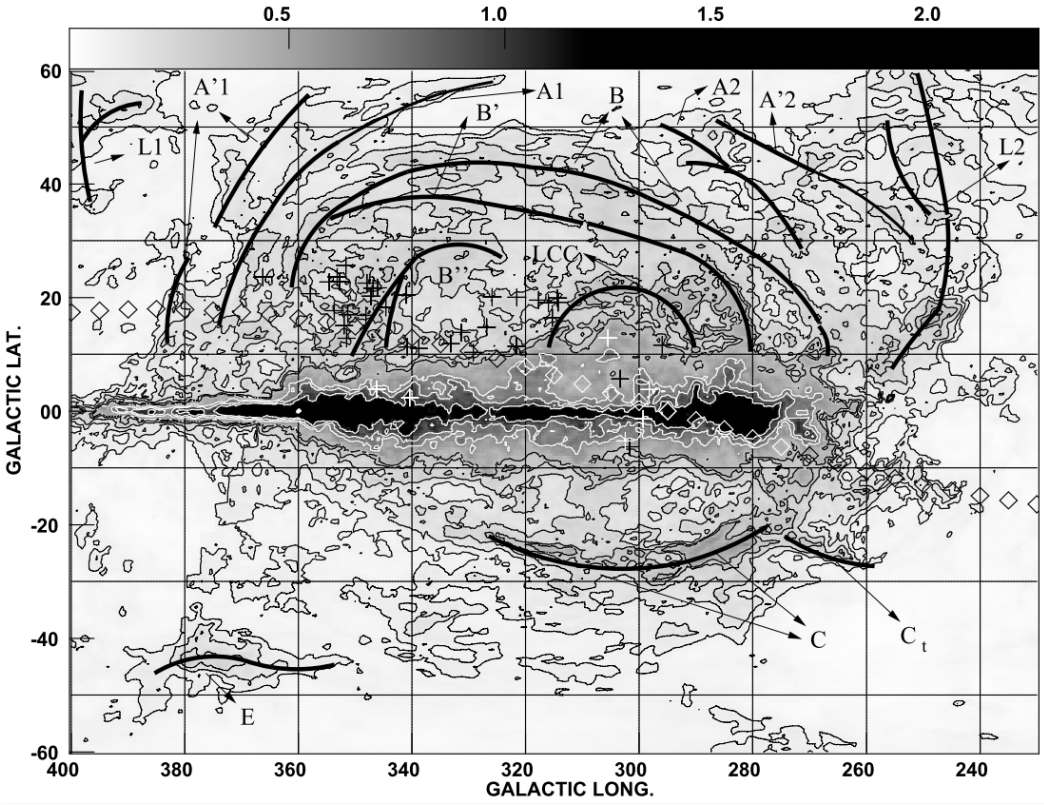

Figure B.0.32: Gray-scale map ranging from 0 to 1200 K for H I with channels integrated over $V = -19.6$ to -1.0 km/s. The contours are at $22.3 \cdot (4, 6, 9, 13, 16, 28, 36$ and $48)$. The selected branches are indicated schematically. The crosse mark the stars of spectral type OB2.5 belonging to Sco-Cen (de Bruijne (1999)). The diamonds indicate the plane of the Gould Belt (see section 2.2.2). Figure from Poeppel et al. (2010) figure 2 therein.

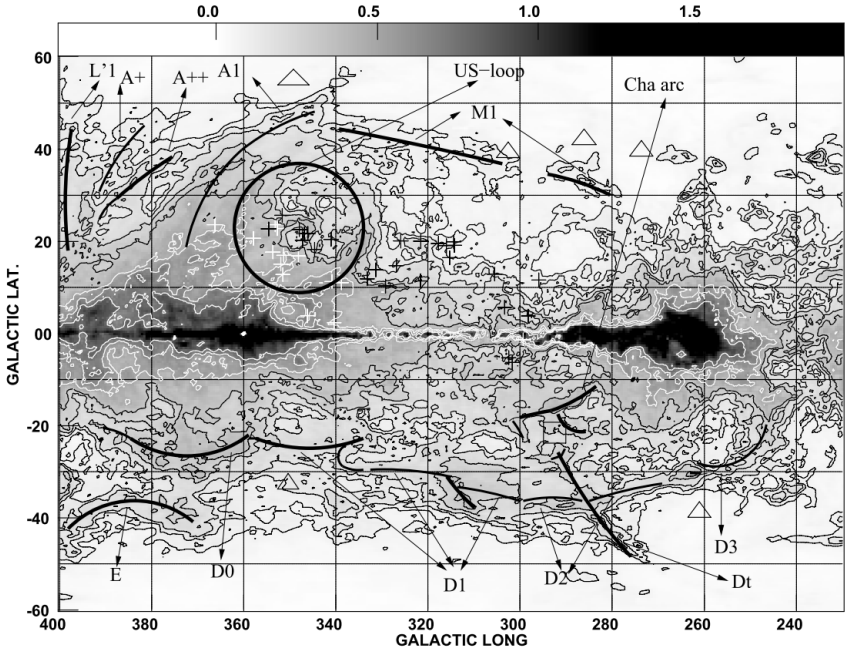

Figure B.0.33: Gray-scale map ranging from 0 to 1200 K with channels integrated over $V = 0.0$ km/s to +15.5 km/s. The contours are at $19.5 \cdot (4, 6, 8, 12, 16, 25, 32$ and $40)$. The selected branches are indicated schematically. The crosses mark the stars of spectral type OB2.5 belonging to Sco-Cen (de Bruijne (1999)). The open triangles indicate the six sight lines sampled by Mamajek et al. (2000). Figure from Poeppel et al. (2010), figure 3 therein.

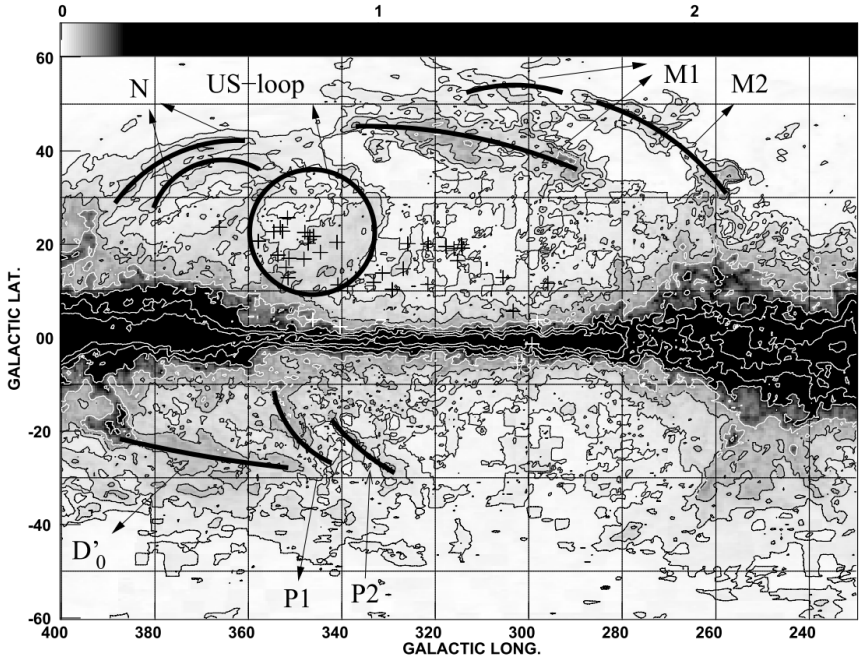

Figure B.0.34: Gray-scale map ranging from 0 to 200 K with channels integrated over $V = +16.5$ to $+40$ km/s. The contours are at $25.1 \cdot (0.5, 1, 2, 4, 8, 16$ and $32)$. The selected branches are indicated schematically. The crosses mark the stars of spectral type OB2.5. Figure from Poeppel et al. (2010), figure 4 therein.

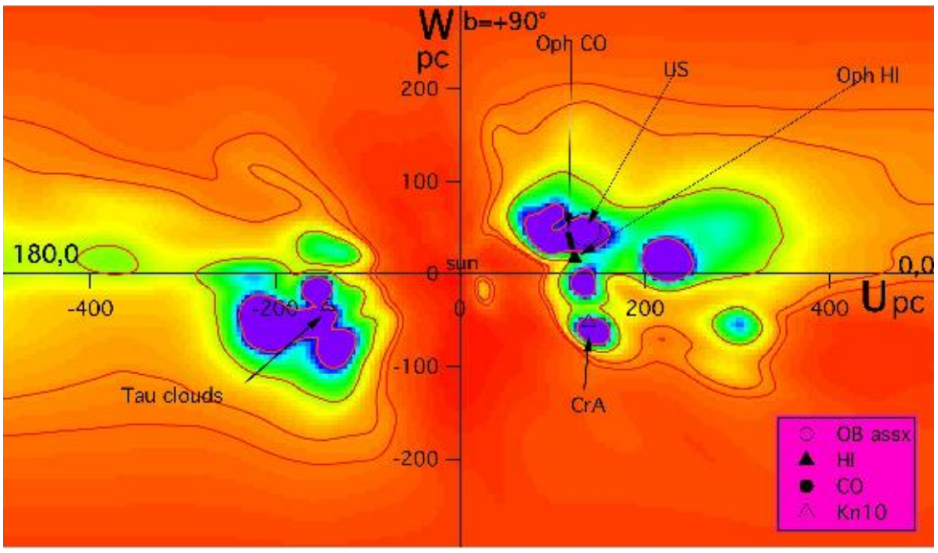

Figure B.0.35: Vertical plane cut showing the opacity distribution in the direction of the center ($l = 0^\circ$) and anticenter ($l = 180^\circ$). The northpole direction ($b = 90^\circ$) is at the top. The Sun is located in the center at (0,0). Regions from the literature are marked and labelled. The colormap is the same as in figure 2.3 in section 2. Figure extracted from figure 7 in Lallement et al. (2014)

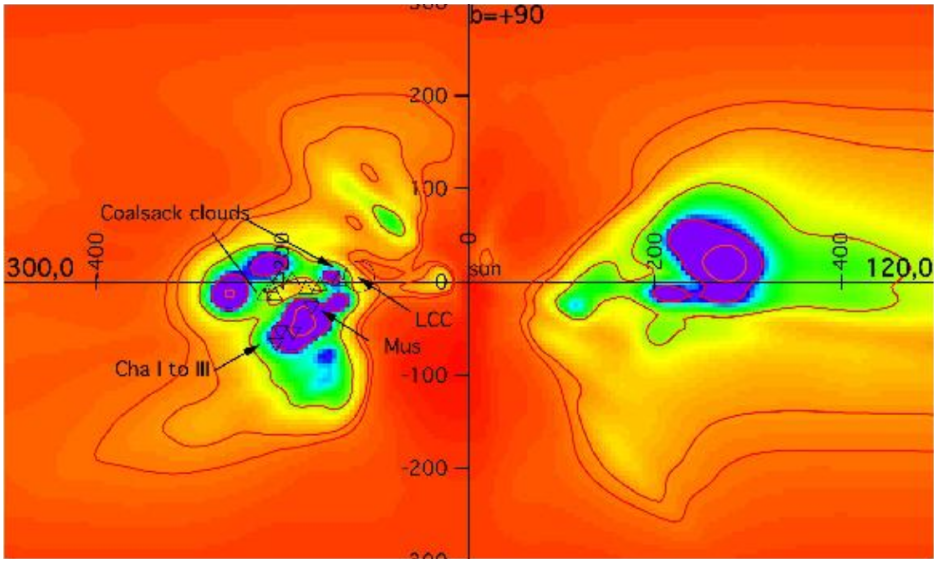

Figure B.0.36: Vertical plane cut in the direction $l = 120^\circ$ and the counter direction $l = 300^\circ$ showing the opacity distribution. The northpole direction ($b = 90^\circ$) is at the top. The Sun is located in the center at (0,0). Regions from the literature are marked and labelled. The colormap is the same as in figure 2.3 in section 2. Figure extracted from figure 6 in Lallement et al. (2014).

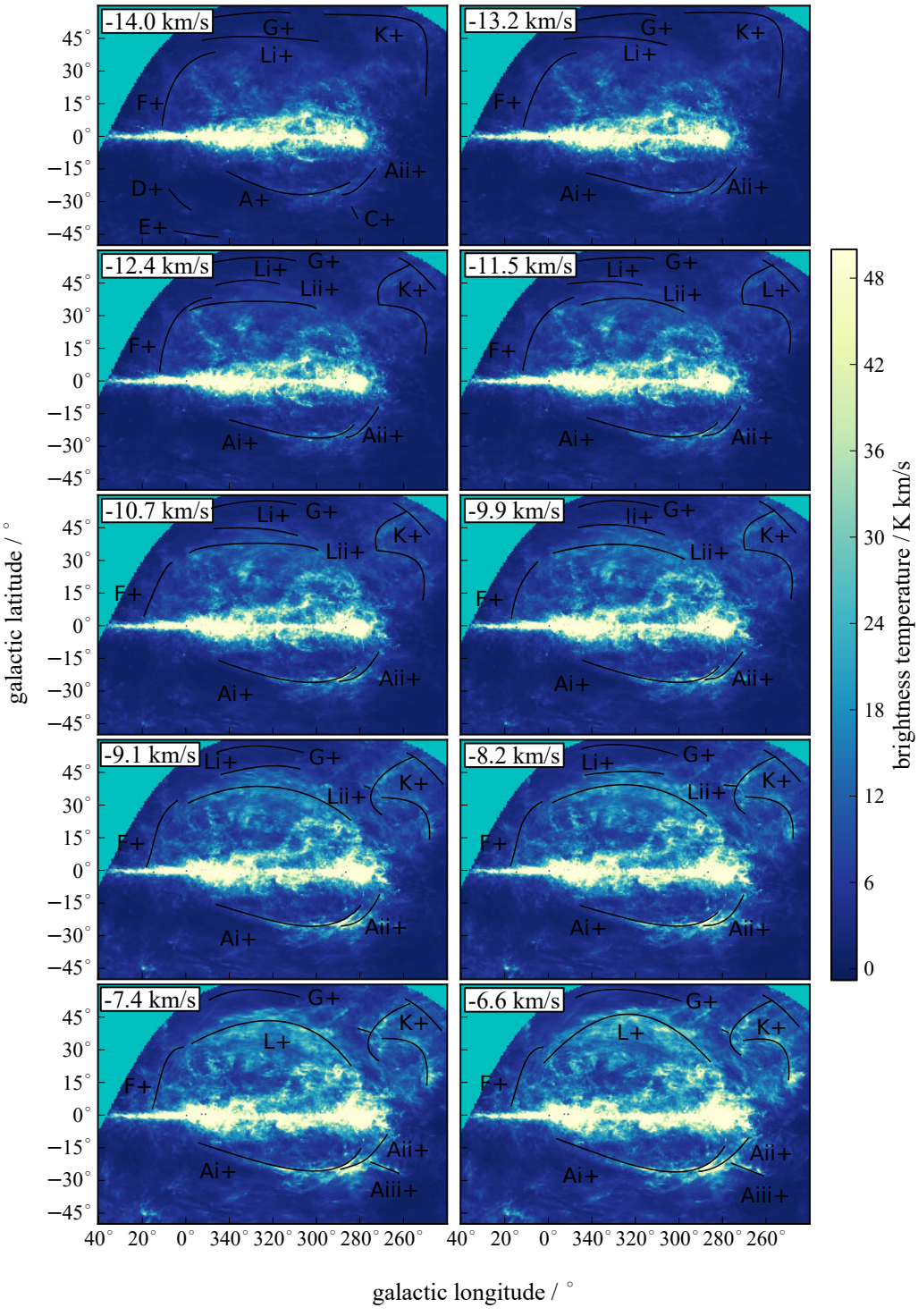

Figure B.0.37: Channelmaps from −14.0 km/s to −6.6 km/s denoting the arcs and features that spread over multiple velocity channels

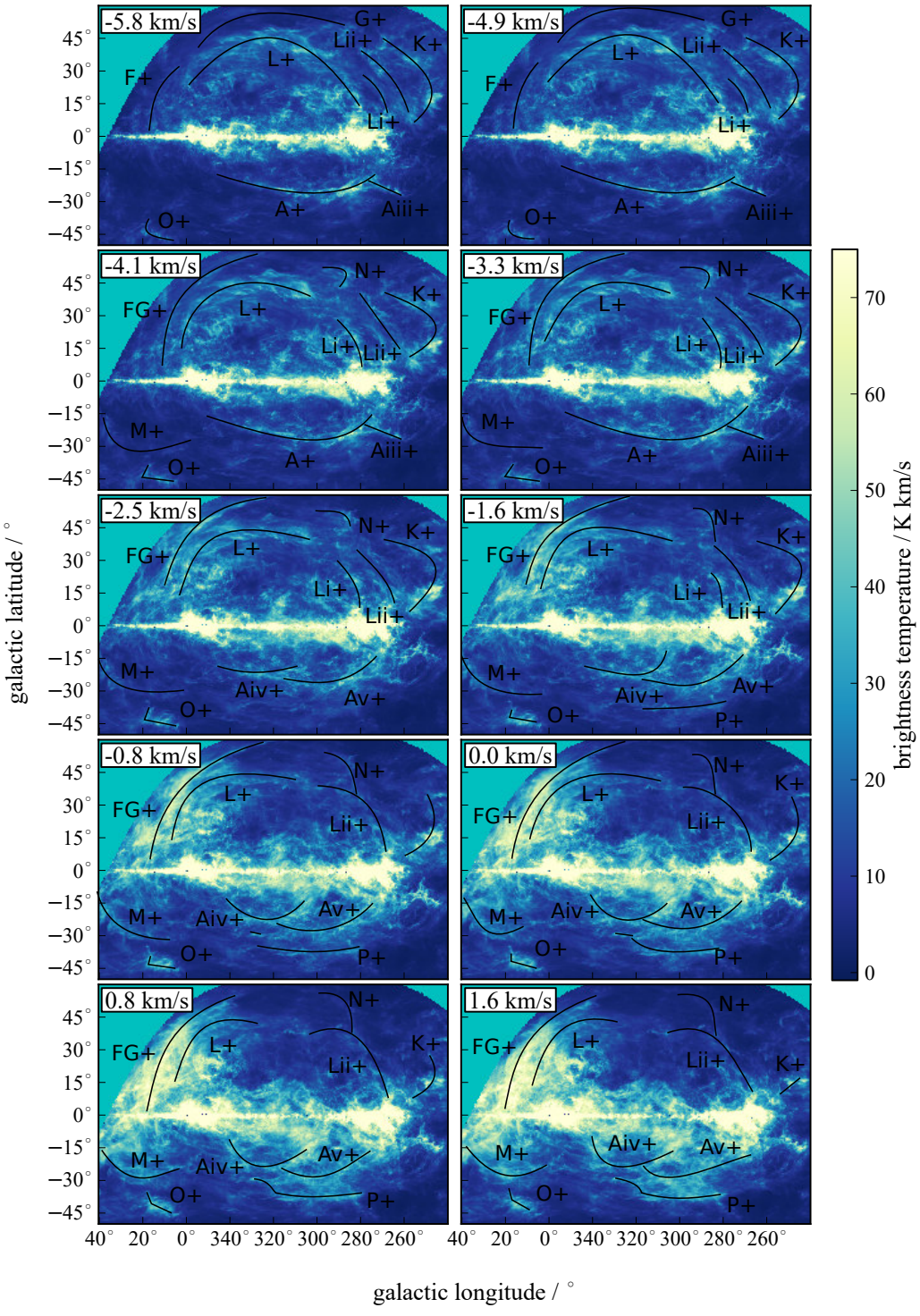

Figure B.0.38: channelmaps from −5.8 km/s to +1.6 km/s denoting the arcs and features that spread over multiple velocity channels

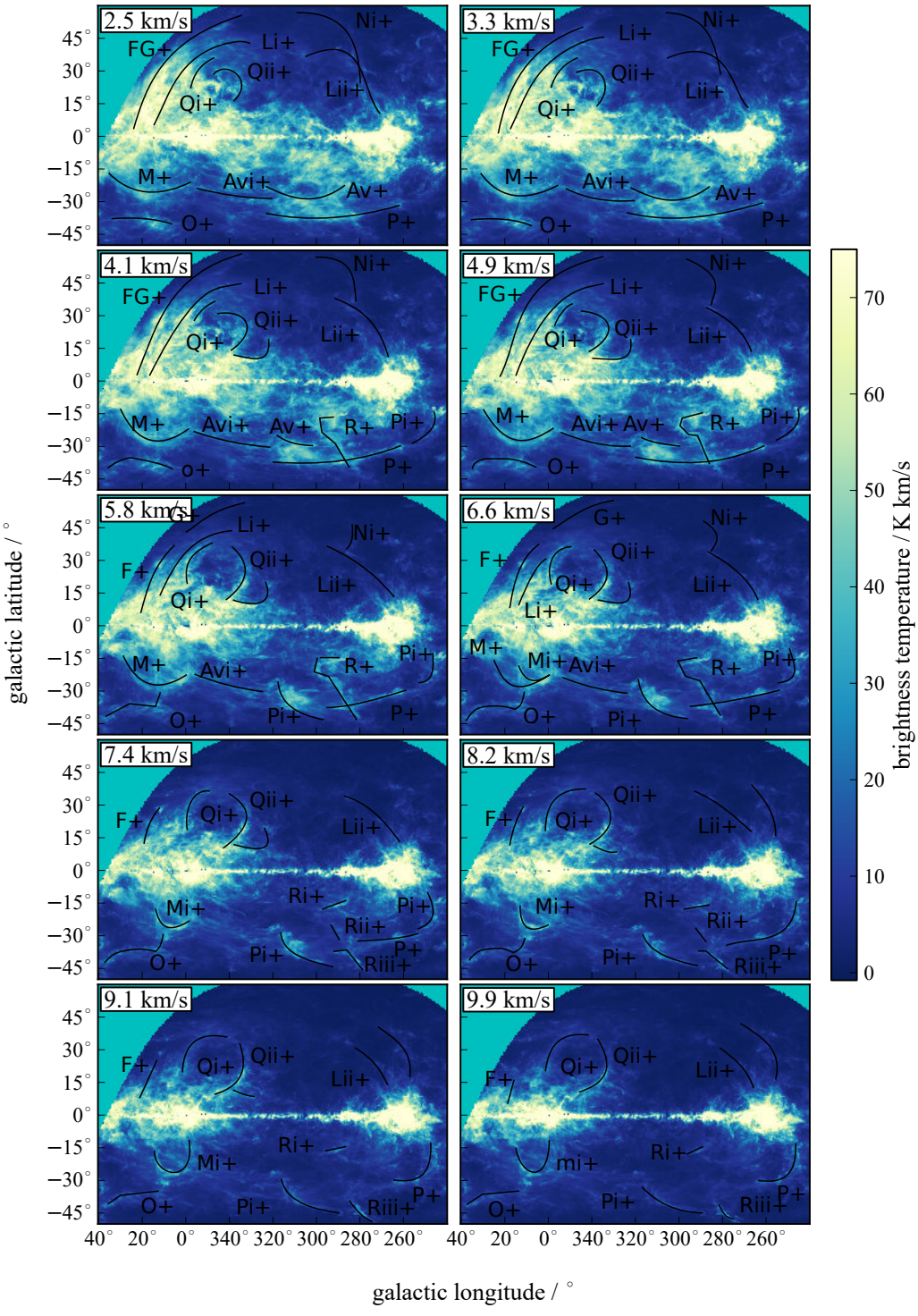

Figure B.0.39: Channelmaps from +2.5 km/s to +9.9 km/s denoting the arcs and features that spread over multiple velocity channels

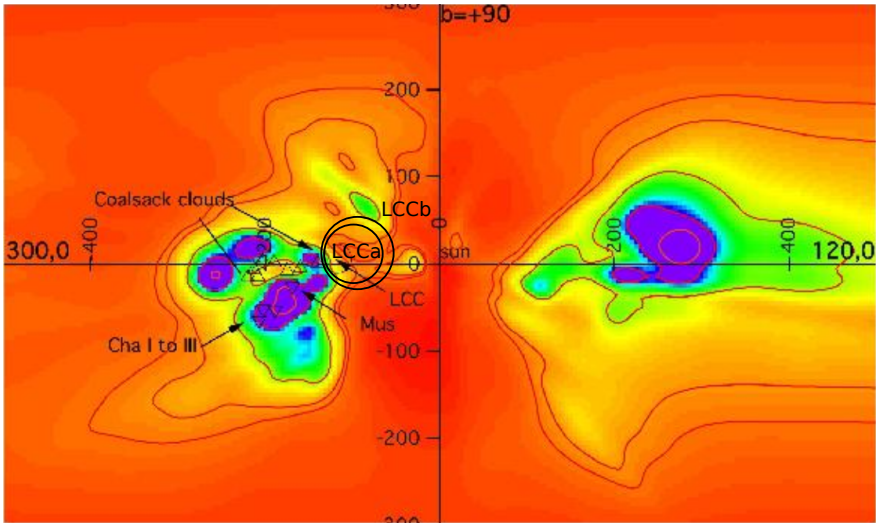

Figure B.0.40: Vertical plane cut in the direction $l = 300^\circ$ and the counter direction $l = 120^\circ$ showing the opacity distribution. The galactic northpole direction ($b = 90^\circ$) is at the top. The Sun is located in the center at (0,0). The two black rings surrounding the opacity minima marked as LCCa and LCCb denote the cavity around the LCC-loop. For more information see section 6.2.4.

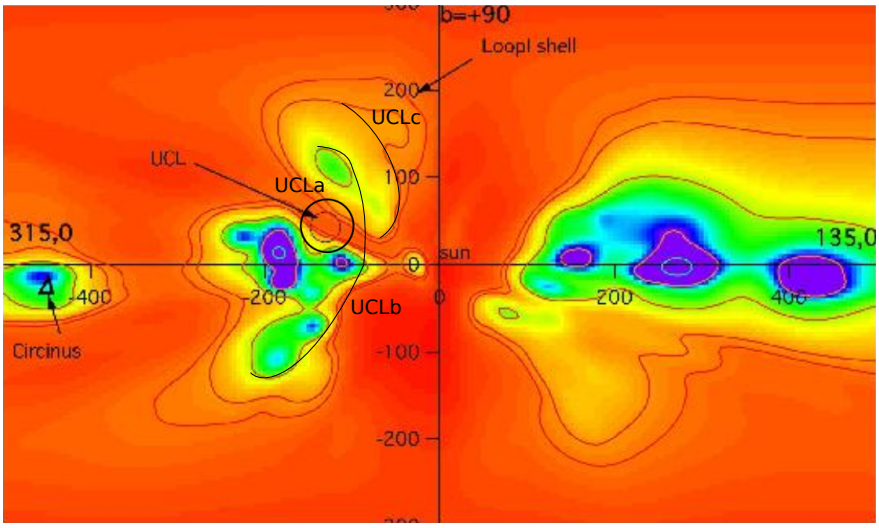

Figure B.0.41: Vertical plane cut of interstellar extinction induced by dust in the longitude direction ($l = 315^\circ$) and the counter direction ($l = 135^\circ$) showing the opacity distribution. The northpole direction ($b = 90^\circ$) is at the top. The Sun is located in the center at (0,0). The black circle marked with UCLa denotes the center of the part of the cavity around the location of the UCL with the lowest density. The black arcs denoted with UCLb and UCLc mark the spread of the high opacity regions in this map for comparison with the angular spread in the H I maps. For more information see section 6.2.4.

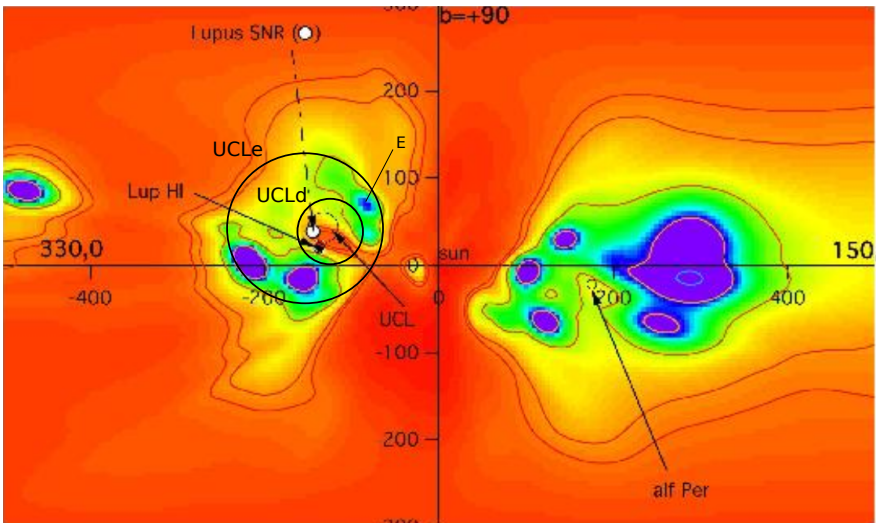

Figure B.0.42: Vertical plane cut of interstellar extinction induced by dust in the direction $l = 330^\circ$ and the counter direction $l = 150^\circ$, showing the opacity distribution. The northpole direction ($b = 90^\circ$) is at the top. The Sun is located in the center at (0,0). The cavity (marked as UCLd) and the estimated shell (marked as UCLe) surrounding the UCL subgroup are denoted as black circles. For more information see section 6.2.4.

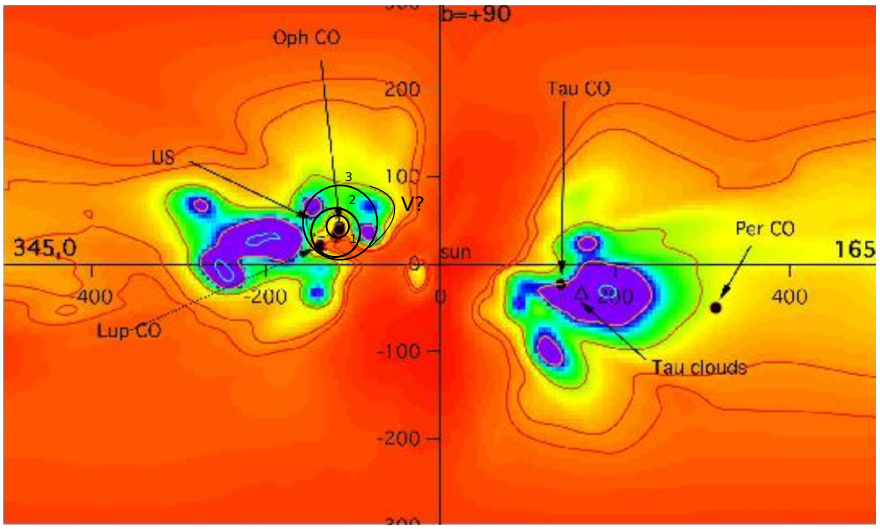

Figure B.0.43: Vertical plane cut of interstellar extinction induced by dust in the longitude directions $l = 345^\circ$ and $l = 165^\circ$, showing the opacity distribution. The northpole direction ($b = 90^\circ$) is at the top. The Sun is located in the center at (0,0). The three circles marked with 1,2 and 3 from small to large represent the estimation of the USco-tunnel, the USco loop‘s cavity and the Usco-shell respectively. For more information see section 6.2.4.

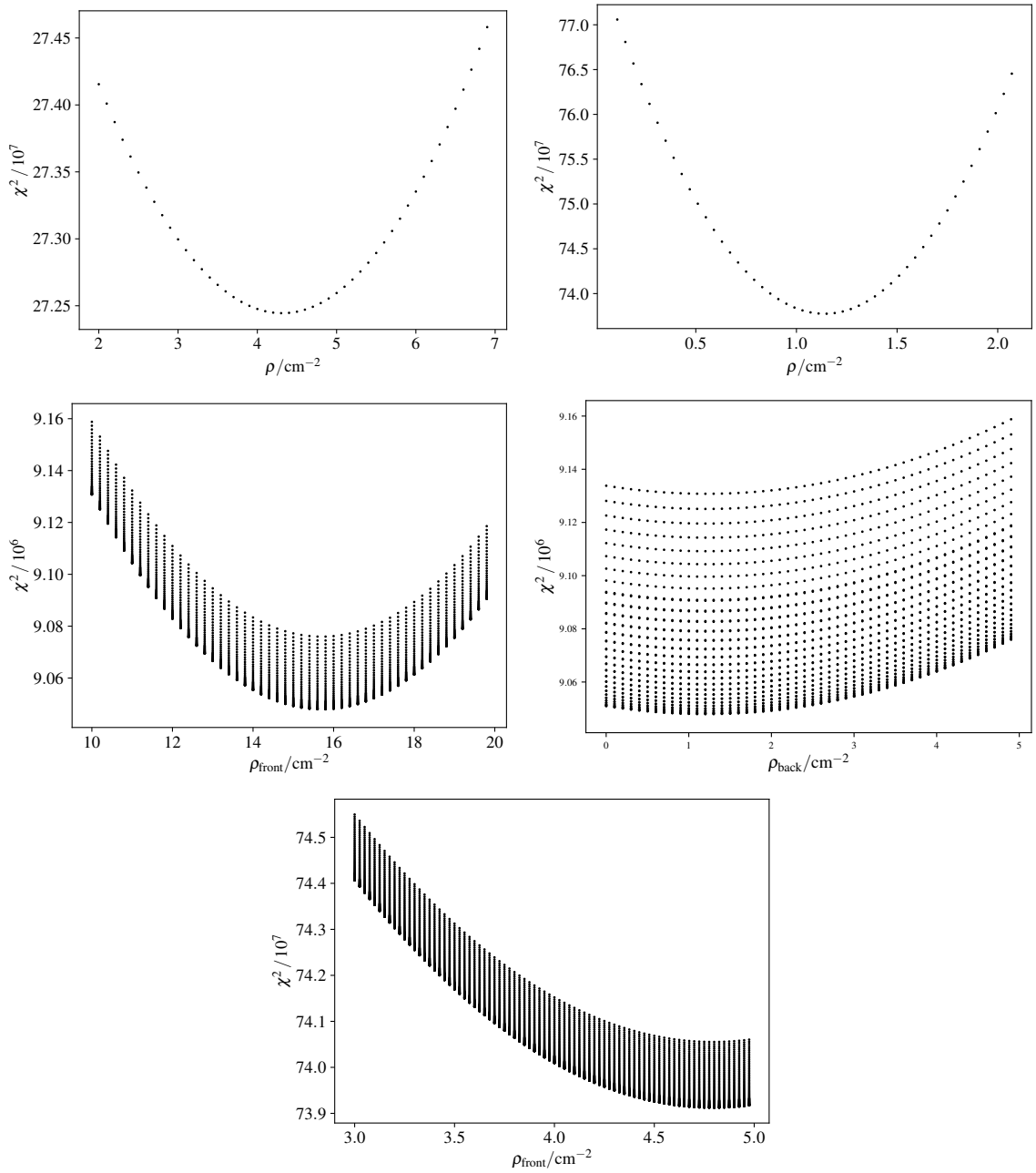

Figure B.0.44: Plots showing χ^2 vs. fit parameter for the fit of the EHSS-model to the GASS data in the region of Sco-Cen. In the top left panel, the density of the LCC-loop is varied while all other parameters are fixed. On the top right hand side, the same is done for the USco-shell. The center left hand plot and the center right hand plot show the variation of the front density of the USco-tunnel ρ_{fornt} and the density of the back ρ_{back} respectively. The variation of the front density of the USco-loop is shown in the lower panel. For a description of the fit process see section 6.3.1.

APPENDIX C

Additional Derivations and explanations

Here, the derivation of the hydrogen column density $N_{\mathrm{H\,I}}$ from the emission coefficients is presented. Using the emission coefficient A_{10} (see eq. 2.1), the statistical weight equation

$$\frac{N_1}{N_0} \equiv \frac{g1}{g2} \exp\left(-\frac{h\nu_{10}}{kT_s}\right), \tag{C.1}$$

and by using the approximation $\frac{h\nu_{10}}{kT_s} \ll 1$, which yields $\frac{N1}{N0} \approx \frac{g_1}{g_0} = 3$, this leads to the number of neutral hydrogen atoms per cm^3 of $n_{\mathrm{H}} = N_0 + N_1 \approx 4N_0$. Using this, the opacity coefficient of the 21 cm line is:

$$\begin{aligned}
\kappa_\nu &= \frac{c^2}{8\pi\nu_{10}^2}\frac{g_1}{g_0}N_0 A_{10}\left[1 - \exp\left(-\frac{h\nu_{10}}{kT_s}\right)\right]\phi(\nu) && \text{(C.2)}\\
&\approx \frac{3c^2}{32\pi}\frac{A_{10}N_{\mathrm{H}}}{\nu_{10}}\frac{h}{kT_{\mathrm{s}}}\phi(\nu)\\
&\approx 5.47\cdot 10^{-19}\cdot n_{\mathrm{H\,I}}\,[\mathrm{cm}^{-3}]\cdot\frac{1}{T_{\mathrm{s}}}[\mathrm{K}]\cdot\phi(\nu)\left[\frac{\mathrm{s}}{\mathrm{km}}\right]\cdot \mathrm{d}s[\mathrm{cm}] && \text{(C.3)}
\end{aligned}$$

where T_{s} is the spin temperature. Since ν can be translated into a velocity v

$$\begin{aligned}
\frac{v}{c} &= \frac{\nu_{10} - \nu}{\nu_{10}} && \text{(C.4)}\\
\Rightarrow v &= c\cdot\frac{\nu_{10} - \nu}{\nu_{10}}. && \text{(C.5)}
\end{aligned}$$

$\phi(\nu)$ can be translated into $\phi(v)$:

$$\begin{aligned}
\phi(\nu)\,\mathrm{d}\nu &= \phi(v)\,\mathrm{d}v && \text{(C.6)}\\
\Rightarrow \phi(\nu) &= \phi(v)\cdot\frac{\mathrm{d}v}{\mathrm{d}\nu} && \text{(C.7)}\\
&= \phi(v)\cdot -\frac{c}{\nu_{10}} && \text{(C.8)}
\end{aligned}$$

with $\mathrm{d}\tau_\nu = \mathrm{d}\kappa_\nu \mathrm{d}s$ and by inserting it into equation C.3 this finally yields

$$\mathrm{d}\tau(v) = 5.47 \cdot 10^{-19} \cdot n_{\mathrm{H\,I}}\,[\mathrm{cm}^{-3}] \cdot \frac{1}{T_\mathrm{s}}[K] \cdot \phi(v) \left[\frac{\mathrm{s}}{\mathrm{km}}\right] \cdot \mathrm{d}s\,[\mathrm{cm}] \tag{C.9}$$

With the definition of the column density (see eq. 2.2) and the addition of a velocity dependence

$$N_{\mathrm{H\,I}}(v) = \int_0^{s_0} n_{\mathrm{H\,I}}(s, v)\mathrm{d}s \tag{C.10}$$

equation C.9 can be rearranged to

$$N_{\mathrm{H\,I}} = 1.823 \cdot 10^{18} \cdot T_\mathrm{s} \cdot \int \tau(v)\mathrm{d}v. \tag{C.11}$$

T_b is related to T_s as

$$T_b(v) = T_s \cdot (1 - \exp(-\tau(v)))\,, \tag{C.12}$$

which simplifies to

$$T_b(v) = \tau(v) \cdot T_s \tag{C.13}$$

in the case of $\tau(v) \ll 1$. If this is inserted into equation C.11, the relation of equation 3.17 is derived. This derivation was added since the resulting equation 3.17 is relevant for the main measurements made in this work. The derivation was adopted from http://www.cv.nrao.edu/course/astr534/HILine.html, (date 01.12.2018). The relations used can all be found in physics literature, e.g. Demtröeder (2005).

C.1 Data reduction steps for EBHIS and GASS

Here, some additional data reduction steps of the EBHIS and GASS are explained, which are not necessary to understand the analyses done in this work and hence were not included in the sections 3.1 and 3.2 but still are the most important techniques that led to the the high data quality and should find some place in this work.

Effelsberg Bonn H I survey– Data reduction

The described reduction methods described here were developed or used in the works of Winkel et al. (2010a) and Winkel et al. (2016) to produce the data used in this work.

Radio frequency interferences Disturbances produced by external sources that affects an electrical circuit by electromagnetic induction, -coupling or -conduction is called radio-frequency interference (RFI).

Near-constant narrow-band spikes typically affect one or two spectral channels and they are detected using coincidence flagging. This is possible because the 7 feed with 2 polarizations each, measure the same RFI environment 14 times independently. This filters out the interference produced by devices on earth. The signal is flagged when it is present in more than one feed at once. This is because all feeds point to different locations and should not get a signal from the same astronomical source simultaneously. For large sources, with extensions over larger areas, this assumption does not hold. Thus the signal is examined in time-frequency plots and it is checked if it matches typical RFI appearances. Just for the innermost part of the Galaxy emissions, all frequencies add up and this method cannot be applied. Narrow-band RFI are detected by averaging each sub-scan of an observation in time. Large scale components in the spectral maps are removed because RFI events take place in a maximum range of three spectral channels. The channels are flagged if they exceed a lower threshold in multiple different feeds simultaneously (Winkel et al. 2016).

The **Intermittent broad-band events** typically affect 100-1000 channels. They are corrected with the same methods as the near-constant narrow-band spikes. A three-point median filter is applied to the data in the time domain, which filters the persistent signals out. Then for the spectral dimension, the data are smoothed using a Gaussian filter. The parameters of the filter are that of typical shape of broad-band events. Then a combination of thresholds of all the 7 feeds are used to determine if the channel should be flagged or not.

Extremely strong RFI are caused by the L3 mode of a GPS satellite system. The L3 mode is extremely bright and it lies at about 1381 MHz, which is close to the non shifted H I emission at 1420 MHz. The root mean square (RMS) in this channel ±1 MHz is compared to the RMS in neighboring frequencies. If the difference in RMS is larger than a factor of two, the next channels in a distance 10 MHz are flagged in both directions. If the data are affected by Intermittent broad-band events and GPS interference they are flagged in advance. But GPS interference usually does not account for radial velocities with $\left|v_{\mathrm{LSR}}\right| \leq 600$ km/s and since the velocity range needed for this work is even much lower ($\left|v_{\mathrm{LSR}}\right| \leq 150$ km/s) it is not discussed any further. For more information see Winkel et al. (2016), section 3.1.1 therein.

The temperature of the noise diode The temperature of the noise diode T_{cal} was obtained by two methods. An absorber was placed around the seven feeds for an RFI-free measurement of all noise

diodes. With this, the frequency-dependence of the temperature of the diodes could be tracked. The absolute calibration temperature value of the noise diodes was determined by observing the International Astronomical Union standard source S7 at zero velocity (Winkel et al. 2010a).

The system temperature In section 3.1.1, the system temperature T_{sys} was introduced. A T_{sys} based weighting system made it possible to improve the final RMS level by 1-2%. In order to do this, the average H I profile per scan and beam was computed. This value was used as the T_{sys} input value for the weighting. This simplification only holds when T_{sys} does not vary too much during one sub-scan. But the resulting effects are of higher orders because the temperature gradient is the same in each feed. The system temperature changes between each run when the diodes are turned off and on and it also varies for the different feeds. The incoming stray radiation produced by the geometrics of the Effelsberg telescope or external sources that have to be eliminated are described in the following.

Side lobes The local maxima (lobes) of the field radiation pattern that is caused by the geometry of the telescope and its components is shown in figure C.1.1. The side lobes have to be filtered out so that the only remaining signal is that of the main lobe. The side lobes are divided into near side lobes that are defined to be in a radial distance of $\leq 4^\circ$ to the main beam and the far side lobes with radial distances $> 4^\circ$.

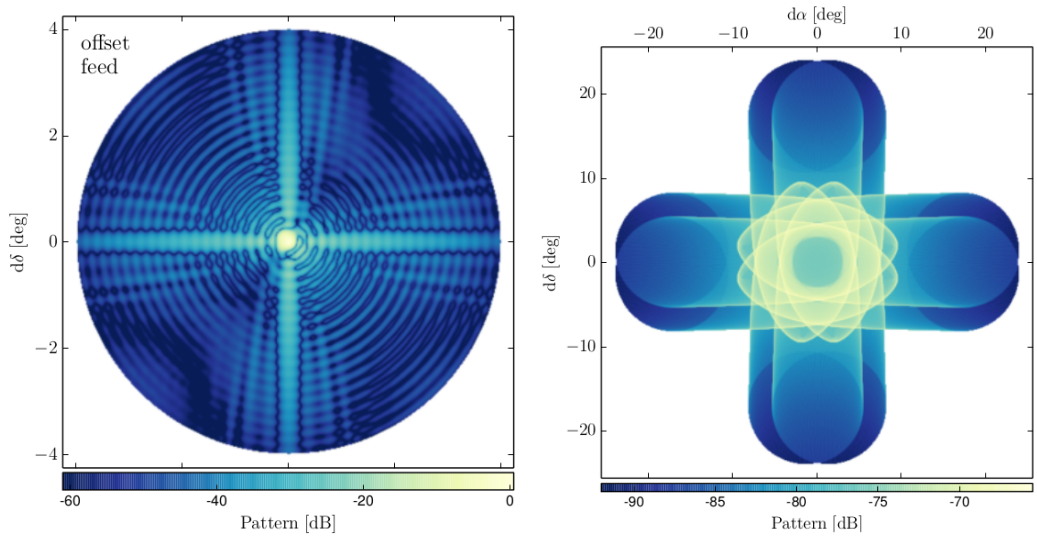

Figure C.1.1: Synthetic antenna patterns within a radius of 4° for an offset beam with a coma lobe at a position angle of 60° (left hand side). On the right hand side, side lopes caused by reflections of spherical waves from the feed at the support legs of the telescope are shown. Credits: Winkel et al. (2016).

As shown in equation 3.5 from section 3.1.1, the brightness temperature depends on the antenna pattern. Since the receiver is rotating during observation, the resulting function is time dependent. Hence the pattern for the near side lobes was determined in 4° rotation steps in a similar detection method as described in Kalberla et al. (2010). For the 7 offset feet 18 antenna diagrams are needed by taking advantage of the array symmetries. On a grid containing 2160 cells in cylindrical coordinates for the inner 4° circle of the antenna, the mean of the modeled side-lobe intensities is taken for the

correction algorithm. The size of one cell is $5^\circ \times 0.125^\circ$ to cover the range from the first minimum to 4° in radial direction (Winkel et al. 2016).

The far side lobes were determined using a ray-tracing model because they are in general difficult to measure (e.g. Higgs (1967)). Unlike for near side-lobes, just a single far side-lobe diagram is sufficient for all receivers. The following side lobes are considered (Kalberla et al. 1980; Winkel et al. 2016):

- cones caused by the reflections of plane waves from the primary mirror at the support legs of the feed
- at the edge of the main reflector spillover leads to radiation which depends on the taper of the primary feeds
- spherical waves from the feed are reflected at the support legs.
- the roof of a cabin containing a secondary focus causes reflections that are offset 40° of the main axis. The reflections of the roof also cause secondary reflections that originally come from the feeds.

The side lobes can be seen in figure C.1.1 on the right hand side. The effect of the four legs can be seen there as an eightfold symmetry. The side lobes caused directly by the roof were determined using the geometry of the roof. Some secondary reflections described above were determined by ray-tracing. The radial side lobe levels from the spillover lobes of the cones were modeled by multiple Gaussian functions (2° FWHM). The other components were adopted from Kalberla et al. (1980). For more information about the correction algorithm and the far side lobes see Kalberla & Haud (2015) and Winkel et al. (2016).

Galactic Allsky survey– Data reduction

The produced data of the GASS underlaid several reduction steps, which are described in the following. A bandpass correction was applied, using a GASS modified version of the *Livedata* software, which was initially produced for HIPASS McClure-Griffiths et al. (2009).

Stray radiation Similar effects as the ones described for the Effelsberg telescope lead to stray radiation. The feed legs and reflections from the spillover regions lead to strong stray radiation effects. The algorithm developed for the Effelsberg telescope and improved for the LAB survey was modified for multi-beam systems. Again equation 3.5 had to be solved and the antenna response P for each of the 13 feeds had to be solved.

Side lobes For the 13 beams three cases are important. The middle feed, a feed of the inner circle and one of the outer circle (see e.g. fig C.1.2). To determine the aperture function, the feed response pattern, shadowing by the focus cabin and the feed support legs as well as the telescopes geometry in general are measured if possible and modelled additionally. Three feed support legs led to an six-fold symmetry for which 5 individual patterns for each feed-ring were calculated. The symmetry and the antenna response can be seen in figure C.1.2 in the top panel. The inner 6° of the antenna pattern was modeled on a grid of 468 cells in cylindrical coordinates.

To consider for the far side lobes, the estimation on the stray-cones, produced by reflections of the support legs, were done based on estimates from the aperture blocking by the feed legs (Kalberla et al.

2010). The spillover from the rim of the telescope was estimated from the edge taper of the receiver feed. Also reflections from the ground had to be corrected. Hence the ground around the telescope was surveyed to map the reflections from low grass and soil by Kalberla et al. (2010).

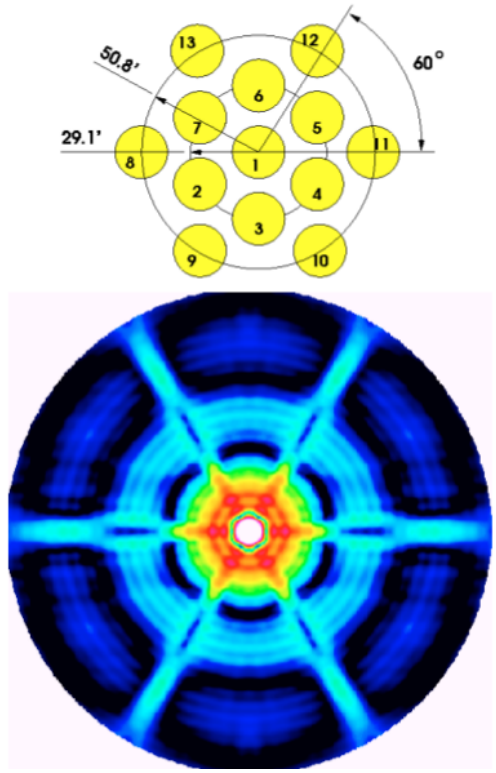

Figure C.1.2: The feed configuration for the receiver (top) and the antenna patterns within a radius of 6° for beam 1 (bottom). The display is restricted to levels between −20 dB (white) to −50 dB (black). Figure from Kalberla et al. (2010)

Baseline fitting The LAB survey data were used to estimate initial parameters for the baseline fit of the GASS. The LAB profile was smoothed to a spectral resolution of 5 km/s and the resulting channel maps where the brightness temperature is smaller than 0.9 K were used as emission free baseline regions. This method is good for diffuse H I emission regions but not for small scale features such as emission from other galaxies. The success of to recovering small scale structures afterwards was limited to a $3\,\sigma$ level by the RMS noise of 0.4 K for the 5 s integration time. A new method was used afterwards to improve the baseline fits. The nearest profile of the HEALPix data, with channels $T_{\rm GASS} < 3\sigma_{\rm RMS}$ was used for emission free-baseline regions. At positions of external galaxies, parameters from the HIPASS bright galaxy catalog were included (Koribalski et al. 2004).

Radio frequency interference Narrow-line interference was flagged using livedata. It is approximately constant over longer periods of time. If a profile has more than 30 flagged channels, it is discarded. After the basic data reduction, when the profiles are corrected for stray radiation and baseline fits are done, the flagged channels are replaced by the interpolated LAB data (Kalberla et al. 2010). This has

to be done for 0.1% of the data. Additionally 0.5% of the spectral channels were discarded (Kalberla 2011) plus 1.5% of the telescope dumps resulting in the 3rd data release[1] (Kalberla & Haud 2015).

[1] A dump is an individual telescope record.

C.2 Mass calculation from the literature

The exact equation that was used by Poeppel et al. (2010) for their mass calculation, where the change of pixel size with latitude was not considered and the mean latitude $\overline{b}$ of a feature was used is shown in the following. The resulting masses estimated from center distances, radii and velocity extent of the H I shells are summarized in table A.0.4 (de Geus 1992; Poeppel et al. 2010). On the left hand side of this table in column3, the masses (M_{comp}) were computed for four different velocity ranges (see column 1). The mass was determined by approximating the shells by rectangles in $l - b$ (Poeppel et al. 2010), add the mass determined from each pixel and integrate over all contributing velocities. The used equation is

$$M = 11.45 \cdot 10^{-7} \cos \overline{b} \cdot (\overline{d} + 0.5\overline{\Delta} d)^2 \cdot \sum T_b \cdot S \tag{C.14}$$

where $S = 0.25^{\circ} \times 0.25^{\circ}$ is the estimated pixel area (Pixel size of the LAB dataset), d is the distance, T_b is the brightness temperature and $\cos b$ is the correction factor for the galactic latitude for a cartesian projection (see section 3.3.1 for an introduction to projections).

C.3 Sphere-line intersection

The intersection of a line with a sphere, which is used in section 4.2, is calculated here. By substituting $G_i = u \cdot \vec{P}_i$ into $R_{1/2} = (x - x_0)^2 + (y - y_0)^2 + (z - z_0)^2$

$$\begin{aligned} \Rightarrow 0 =& (ux_{2,i} - x_0)^2 + (uy_{2,i} - y_1)^2 + (uz_{2,i} - z_0)^2 - R_1/2 \\ =& (ux_0)^2 + x_0^2 - 2ux_{2,i}x_0 + (uy_0)^2 + y_0^2 - 2uy_{2,i}y_0 + (uz_{2,i})^2 + z_0^2 - 2uz_{2,i}z_0 - R_1/2 \\ =& u^2 \cdot \left(x_{2,i} + y_{2,i} + z_{2,i}\right)^2 + u \cdot \left(2(x_{2,i}y_0 + y_{2,i}y_0 + z_{2,i}z_0)\right) + (x_0^2 + y_0^2 + z_0^2 - R_1/2) \\ =& u^2 \cdot a + u \cdot b + c \end{aligned} \tag{C.15}$$

This is a standard quadratic equation that can be solved and leads to eq. 4.22.

C.4 Description of the Levenberg-Marquardt-Algorithm

Given a non linear function $F : R^m \rightarrow R^n$, where $m \leq n$ and an approximating starting value x_0. The function f is now linearised by the Taylor approximation of first order, which is $f'(x) = f(x_0) + \nabla f(x_0)^T (x - x_0)$ where $\nabla f(x_0)^T$ is the Jacobian-Matrix J. Since f should be minimized, this leads to the least-squares problem, which yields the Gaussian-Newtonian iteration step, when deriving the gradient and zeroing it:

$$x^{k+1} = x^k - \alpha^k \left((J|_{x^k})^T J|_{x^k} \right)^{-1} (J|_{x^k})^T f(x^k) \tag{C.16}$$

where x^k is the point where the Jacobean-matrix is evaluated and $\alpha^k \geq 0$ is the step width. Since the convergence of this method can be arbitrary slow, depending on the starting value x_0, equation C.16 is expanded by:

$$x^{k+1} = x^k - \alpha^k \left((J|_{x^k})^T J|_{x^k} + D^k \right)^{-1} (J|_{x^k})^T f(x^k) \tag{C.17}$$

where the new summand D is the diagonal matrix, which is chosen in a way so that the sum of $(J|_{x^k})^T J|_{x^k}$ and d^k is positive. If $D = \beta^k$ I, where $\beta \leq 0$, then this is the Levenberg-Marquardt-Algorithm. This version is more robust to start parameters that are more far away from the optimum than the Gaussian-Newtonian algorithm.

Bibliography

Allen, P. R., Trilling, D. E., Koerner, D. W., & Reid, I. N. 2003, ApJ, 595, 1222

Alves, J., Zucker, C., Goodman, A. A., et al. 2020, Nature, 578, 237

Bagetakos, I., Brinks, E., Walter, F., et al. 2010, The Astronomical Journal, 141, 23

Barrado y Navascués, D., Stauffer, J. R., Song, I., & Caillault, J.-P. 1999, ApJ, 520, L123

Bartoe, J. D. F., Brueckner, G. E., Nicolas, K. R., et al. 1979, MNRAS, 187, 463

Baumgartner, V. & Breitschwerdt, D. 2013, A&A, 557, A140

Belfort, P. & Crovisier, J. 1984, A&A, 136, 368

Bell, A. R. 1978a, MNRAS, 182, 147

Bell, A. R. 1978b, Monthly Notices of the Royal Astronomical Society, 182, 443

Berghöfer, T. W. & Breitschwerdt, D. 2002, A&A, 390, 299

Berkhuijsen, E. M., Haslam, C. G. T., & Salter, C. J. 1971, A&A, 14, 252

Bingham, R. G. 1967, MNRAS, 137, 157

Blaauw, A. 1964a, ARA&A, 2, 213

Blaauw, A. 1964b, in IAU Symposium, Vol. 20, The Galaxy and the Magellanic Clouds, ed. F. J. Kerr, 50

Blaauw, A. 1991, in NATO Advanced Science Institutes (ASI) Series C, Vol. 342, NATO Advanced Science Institutes (ASI) Series C, ed. C. J. Lada & N. D. Kylafis, 125

Blandford, R. D. & Ostriker, J. P. 1978, ApJ, 221, L29

Bobylev, V. V. 2014, Astrophysics, 57, 583

Bobylev, V. V. 2016, Astronomy Letters, 42, 544

Bohlin, R. C. 1975, ApJ, 200, 402

Bolatto, A. D., Wolfire, M., & Leroy, A. K. 2013, Annual Review of Astronomy and Astrophysics, 51, 207–268

Bonnell, I. A., Bate, M. R., & Zinnecker, H. 1998, MNRAS, 298, 93

Bonnell, I. A., Vine, S. G., & Bate, M. R. 2004, MNRAS, 349, 735

Bouy, H. & Alves, J. 2015, A&A, 584, A26

Brand, J. & Blitz, L. 1993, A&A, 275, 67

Braun, R. 2012, ApJ, 749, 87

Braun, R. & Burton, W. B. 1999, A&A, 341, 437

Breitschwerdt, D. & de Avillez, M. A. 2006, A&A, 452, L1

Breitschwerdt, D., de Avillez, M. A., Feige, J., & Dettbarn, C. 2012, Astronomische Nachrichten, 333, 486

Brinks, E. & Bajaja, E. 1986, A&A, 169, 14

Burkhart, B., Lazarian, A., Goodman, A., & Rosolowsky, E. 2013, ApJ, 770, 141

Callaway, M. B., Savage, B. D., Benjamin, R. A., Haffner, L. M., & Tufte, S. L. 2000, The Astrophysical Journal, 532, 943

Canny, J. 1986, IEEE Transactions on Pattern Analysis and Machine Intelligence, PAMI-8, 679

Cappa de Nicolau, C. E. & Poeppel, W. G. L. 1986, A&A, 164, 274

Cappellaro, E. & Turatto, M. 2001, in Astrophysics and Space Science Library, Vol. 264, The Influence of Binaries on Stellar Population Studies, ed. D. Vanbeveren, 199

Carruthers, G. R. 1970, ApJ, 161, L81

Cash, W., Charles, P., Bowyer, S., et al. 1980, ApJ, 238, L71

Castor, J. I., Abbott, D. C., & Klein, R. I. 1975, ApJ, 195, 157

Cha, A. N., Sembach, K. R., & Danks, A. C. 1999, ApJ, 515, L25

Chambers, K. C., Magnier, E. A., Metcalfe, N., et al. 2016, ArXiv e-prints

Chanot, A. & Sivan, J. P. 1983, A&A, 121, 19

Chevalier, R. A. 1974, ApJ, 188, 501

Churchwell, E., Povich, M. S., Allen, D., et al. 2006, ApJ, 649, 759

Comeron, F. & Torra, J. 1994, A&A, 281, 35

Cox, D. P. & Reynolds, R. J. 1987, ARA&A, 25, 303

Cox, D. P. & Smith, B. W. 1974, ApJ, 189, L105

Cox, D. P. & Snowden, S. L. 1986, Advances in Space Research, 6, 97

Crowther, P. A. 2007, ARA&A, 45, 177

Daigle, A., Joncas, G., & Parizeau, M. 2007, The Astrophysical Journal, 661, 285

Dame, T. M., Hartmann, D., & Thaddeus, P. 2001, ApJ, 547, 792

Dame, T. M., Ungerechts, H., Cohen, R. S., et al. 1987, ApJ, 322, 706

Davelaar, J., Bleeker, J. A. M., & Deerenberg, A. J. M. 1980, A&A, 92, 231

Davis, B. L., Berrier, J. C., Shields, D. W., et al. 2012, The Astrophysical Journal Supplement Series, 199, 33

de Avillez, M. A. 2000, MNRAS, 315, 479

de Avillez, M. A. & Breitschwerdt, D. 2005, A&A, 436, 585

de Blok, W. J. G. & Walter, F. 2000, ApJ, 537, L95

de Bruijne, J. H. J. 1999, MNRAS, 310, 585

de Geus, E. J. 1992, A&A, 262, 258

de Geus, E. J., Bronfman, L., & Thaddeus, P. 1990, A&A, 231, 137

de Geus, E. J. & Burton, W. B. 1991, A&A, 246, 559

de Geus, E. J., de Zeeuw, P. T., & Lub, J. 1989, A&A, 216, 44

de Grijs, R. & Peletier, R. F. 1997, A&A, 320, L21

De Loore, C., De Greve, J. P., & Lamers, H. J. G. L. M. 1977, A&A, 61, 251

de Zeeuw, P. T., Hoogerwerf, R., de Bruijne, J. H. J., Brown, A. G. A., & Blaauw, A. 1999, AJ, 117, 354

Demtröeder, W. 2005, Experimentalphysik 3, 2. circulation (Springer-Verlag Berlin Heidelberg New York: Springer-Verlag), 157–175

Deul, E. R. & den Hartog, R. H. 1990, A&A, 229, 362

Dickey, J. M., Hanson, M. M., & Helou, G. 1990, ApJ, 352, 522

Dickey, J. M., Terzian, Y., & Salpeter, E. E. 1978, ApJS, 36, 77

Dosovitskiy, A., Beyer, L., Kolesnikov, A., et al. 2020, CoRR, abs/2010.11929

Draine, B. T. 2011, Physics of the Interstellar and Intergalactic Medium (Princeton: Princeton University Press)

Dubner, G. & Giacani, E. 2015, The Astronomy and Astrophysics Review, 23

Dubner, G., Giacani, E., Cappa de Nicolau, C., & Reynoso, E. 1992, A&AS, 96, 505

Dubner, G. M., Green, A. J., Goss, W. M., Bock, D. C.-J., & Giacani, E. 1998, AJ, 116, 813

Duda, R. O. & Hart, P. E. 1972, Commun. ACM, 15, 11

Duley, W. W. & Williams, D. A. 1981, MNRAS, 196, 269

Dynkin, E. B. 1989, The Annals of Probability, 17, 822

Dzib, S., Loinard, L., Mioduszewski, A. J., et al. 2010, ApJ, 718, 610

Egger, R. J. & Aschenbach, B. 1995, A&A, 294, L25

Ehlerová, S. & Palouš, J. 2005, A&A, 437, 101

Ehlerová, S. & Palouš, J. 2013, A&A, 550, A23

Eiroa, C., Djupvik, A. A., & Casali, M. M. 2008, The Serpens Molecular Cloud, ed. B. Reipurth, 693

Eldridge, J. J., Fraser, M., Smartt, S. J., Maund, J. R., & Crockett, R. M. 2013, MNRAS, 436, 774

Elmegreen, B. G. 1999, ApJ, 527, 266

Elmegreen, B. G. 2011, in EAS Publications Series, Vol. 51, EAS Publications Series, ed. C. Charbonnel & T. Montmerle, 19–30

Ewen, H. I. & Purcell, E. M. 1951, Nature, 168, 356

Feldmann, R., Gnedin, N. Y., & Kravtsov, A. V. 2012, ApJ, 747, 124

Ferrara, A. & Tolstoy, E. 2000, MNRAS, 313, 291

Ferrière, K. M. 2001, Reviews of Modern Physics, 73, 1031

Fich, M., Blitz, L., & Stark, A. A. 1989, ApJ, 342, 272

Field, G. B., Goldsmith, D. W., & Habing, H. J. 1969, ApJ, 155, L149

Flewelling, H. A., Magnier, E. A., Chambers, K. C., et al. 2016, ArXiv e-prints

Freyer, T., Hensler, G., & Yorke, H. W. 2003, The Astrophysical Journal, 594, 888

Freyer, T., Hensler, G., & Yorke, H. W. 2006, ApJ, 638, 262

Frisch, P. C. 1995, Space Sci. Rev., 72, 499

Gaczkowski, B., Preibisch, T., Stanke, T., et al. 2015, A&A, 584, A36

Gaczkowski, B., Roccatagliata, V., Flaischlen, S., et al. 2017, A&A, 608, A102

Gaensler, B. M., Madsen, G. J., Chatterjee, S., & Mao, S. A. 2008, PASA, 25, 184

Gaia Collaboration, Brown, A. G. A., Vallenari, A., et al. 2018, A&A, 616, A1

Gaia Collaboration, Brown, A. G. A., Vallenari, A., et al. 2016, A&A, 595, A2

Gesztelyi, R., Zsuga, J., Kemeny-Beke, A., et al. 2012, Archive for History of Exact Sciences, 66, 427

Gilmore, G. 2004, Science, 304, 1915

Gilra, D. P. 1972, in NASA Special Publication, Vol. 310, Scientific results from the orbiting astronomical observatory (OAO-2), ed. A. D. Code, 295

Goldsmith, D. W., Habing, H. J., & Field, G. B. 1969, ApJ, 158, 173

Goldstein, Samuel J., J. 1972, ApJ, 173, 285

Gooch, R. 1995, in Astronomical Society of the Pacific Conference Series, Vol. 77, Astronomical Data Analysis Software and Systems IV, ed. R. A. Shaw, H. E. Payne, & J. J. E. Hayes, 144

Gottlieb, D. M. & Upson, Walter L., I. 1969, ApJ, 157, 611

Green, D. & Gull, S. 1984, Nature, 312, 527

Green, D. A. 1988, Ap&SS, 148, 3

Green, D. A. 1991, Publications of the Astronomical Society of the Pacific, 103, 209

Green, D. A. 2004a, Bulletin of the Astronomical Society of India, 32, 335

Green, D. A. 2004b, Bulletin of the Astronomical Society of India, 32, 335

Green, D. A. 2009, Bulletin of the Astronomical Society of India, 37, 45

Green, D. A. 2013, Proceedings of the International Astronomical Union, 9, 188

Green, D. A. 2014, Bulletin of the Astronomical Society of India, 42, 47

Green, D. A. 2019, Journal of Astrophysics and Astronomy, 40, 36

Green, G. M., Schlafly, E. F., Finkbeiner, D. P., et al. 2015, ApJ, 810, 25

Grenier, I. A. 2000, A&A, 364, L93

Griffiths, D. J. 1982, American Journal of Physics, 50, 698

Griv, E., Jiang, I.-G., & Hou, L.-G. 2017, The Astrophysical Journal, 844, 118

Gruendl, R. A., Chu, Y.-H., Dunne, B. C., & Points, S. D. 2000, AJ, 120, 2670

Gum, C. S. 1951, The Observatory, 71, 159

Gupta, S., Nath, B. B., Sharma, P., & Shchekinov, Y. 2016, MNRAS, 462, 4532

Habets, G. M. H. J. & Heintze, J. R. W. 1981, A&AS, 46, 193

Hachisuka, K., Brunthaler, A., Menten, K. M., et al. 2009, ApJ, 696, 1981

Hammer, S., Vogel, F., Kaul, M., & Levin, I. 2009, Tellus Series B Chemical and Physical Meteorology B, 61, 547

Hastings, W. K. 1970, Biometrika, 57, 97

Haud, U. & Kalberla, P. M. W. 2007, A&A, 466, 555

Heiles, C. 1979, ApJ, 229, 533

Heiles, C. 1984, ApJS, 55, 585

Heiles, C. & Troland, T. H. 2003, ApJ, 586, 1067

Heithausen, A., Brüns, C., Kerp, J., & Weiss, A. 2001, in ESA Special Publication, Vol. 460, The Promise of the Herschel Space Observatory, ed. G. L. Pilbratt, J. Cernicharo, A. M. Heras, T. Prusti, & R. Harris, 431

Henderson, A. P., Jackson, P. D., & Kerr, F. J. 1982, ApJ, 263, 116

Herczeg, G. J. & Hillenbrand, L. A. 2015, ApJ, 808, 23

HI4PI Collaboration, Ben Bekhti, N., Flöer, L., et al. 2016, A&A, 594, A116

Higgs, L. A. 1967, Bulletin of the Astronomical Institutes of the Netherlands Supplement Series, 2, 59

Hill, A. 1910, J Physiol (Lond), 40, 4

Hindman, J. V. 1967, Australian Journal of Physics, 20, 147

Hobbs, L. M. 1974, ApJ, 191, 381

Hobbs, L. M. 1978, ApJ, 222, 491

Hollenbach, D. & Salpeter, E. E. 1971, ApJ, 163, 155

Hoogerwerf, R., de Bruijne, J. H. J., & de Zeeuw, P. T. 2001, A&A, 365, 49

Hou, L. G. & Han, J. L. 2014, A&A, 569, A125

Hough, P. V. C. 1959, Conf. Proc., C590914, 554

Iwamoto, K. & Kunugise, T. 2006, AIP Conference Proceedings, 847, 406

Janka, H.-T. 2012, Annual Review of Nuclear and Particle Science, 62, 407

Jaskot, A. E., Strickland, D. K., Oey, M. S., Chu, Y. H., & García-Segura, G. 2011, ApJ, 729, 28

Jenkins, E. B. & Savage, B. D. 1974, ApJ, 187, 243

Jordan, C., Brueckner, G. E., Bartoe, J. D. F., Sandlin, G. D., & van Hoosier, M. E. 1977, Nature, 270, 326

Joye, W. A. & Mandel, E. 2003, in Astronomical Society of the Pacific Conference Series, Vol. 295, Astronomical Data Analysis Software and Systems XII, ed. H. E. Payne, R. I. Jedrzejewski, & R. N. Hook, 489

Kafatos, M., Sofia, S., Gull, T., & Bruhweiler, F. 1980, ApJ, 242, 294

Kalberla, P. M. W. 2003, The Astrophysical Journal, 588, 805

Kalberla, P. M. W. 2011, ArXiv e-prints

Kalberla, P. M. W., Burton, W. B., Hartmann, D., et al. 2005, A&A, 440, 775

Kalberla, P. M. W. & Haud, U. 2015, A&A, 578, A78

Kalberla, P. M. W. & Kerp, J. 2009, ARA&A, 47, 27

Kalberla, P. M. W., McClure-Griffiths, N. M., Pisano, D. J., et al. 2010, A&A, 521, A17

Kalberla, P. M. W., Mebold, U., & Reich, W. 1980, A&A, 82, 275

Kalberla, P. M. W., Dedes, L., Kerp, J., & Haud, U. 2007, A&A, 469, 511

Kasen, D., Woosley, S. E., & Heger, A. 2011, ApJ, 734, 102

Kastner, J. H., Zuckerman, B., Weintraub, D. A., & Forveille, T. 1997, Science, 277, 67

Kennicutt, R. C. & Evans, N. J. 2012, Annual Review of Astronomy and Astrophysics, 50, 531–608

Kerp, J. 2009, in Panoramic Radio Astronomy: Wide-field 1-2 GHz Research on Galaxy Evolution

Kim, C.-G., Ostriker, E. C., & Raileanu, R. 2016, The Astrophysical Journal, 834, 25

Kippenhahn, R. & Weigert, A. 1990, Stellar Structure and Evolution (Springer-Verlag Berlin Heidelberg, Germany: Springer-Verlag), 208–209,280

Knacke, R. F. & Thomson, R. K. 1973, PASP, 85, 341

Knapp, G. R., Young, K., Lee, E., & Jorissen, A. 1998, ApJS, 117, 209

Kompaneets, A. S. 1960, Soviet Physics Doklady, 5, 46

Koo, B.-C., Kim, C.-G., Park, S., & Ostriker, E. C. 2020, ApJ, 905, 35

Koribalski, B. S., Staveley-Smith, L., Kilborn, V. A., et al. 2004, AJ, 128, 16

Krause, M., Diehl, R., Böhringer, H., Freyberg, M., & Lubos, D. 2014, A&A, 566, A94

Krause, M., Fierlinger, K., Diehl, R., et al. 2013, A&A, 550, A49

Krause, M. G. H., Burkert, A., Diehl, R., et al. 2018, Astronomy & Astrophysics, 619, A120

Krause, M. G. H. & Diehl, R. 2014, ApJ, 794, L21

Krause, M. G. H., Diehl, R., Bagetakos, Y., et al. 2015, Astronomy & Astrophysics, 578, A113

Kroupa, P. 2002, Science, 295, 82–91

Kroupa, P., Tout, C. A., & Gilmore, G. 1993, MNRAS, 262, 545

Kroupa, P. & Weidner, C. 2003, ApJ, 598, 1076

Kroupa, P., Weidner, C., Pflamm-Altenburg, J., et al. 2013, The Stellar and Sub-Stellar Initial Mass Function of Simple and Composite Populations, ed. T. D. Oswalt & G. Gilmore, 115

Krumholz, M. R. & Burkhart, B. 2016, MNRAS, 458, 1671

Krumholz, M. R. & McKee, C. F. 2008, Nature, 451, 1082

Kulkarni, S. R. & Heiles, C. 1987, Interstellar Processes, ed. D. Hollenbach & D. H.A.Thronson, Jr. (Reidel, p.87

Lada, C. J. & Lada, E. A. 2003, ARA&A, 41, 57

Lallement, R., Snowden, S., Kuntz, K. D., et al. 2016, A&A, 595, A131

Lallement, R., Vergely, J. L., Babusiaux, C., & Cox, N. L. J. 2022, A&A, 661, A147

Lallement, R., Vergely, J.-L., Valette, B., et al. 2014, A&A, 561, A91

Lallement, R., Welsh, B. Y., Vergely, J. L., Crifo, F., & Sfeir, D. 2003, A&A, 411, 447

Lamers, H. J. G. L. M. & Cassinelli, J. P. 1999, Introduction to Stellar Winds (Cambridge University Press)

Langer, N. 2012, ARA&A, 50, 107

Lee, S. U., Yoon Chung, S., & Park, R. H. 1990, Computer Vision, Graphics, and Image Processing, 52, 171

Lenz, D., Kerp, J., Floer, L., et al. 2014, Astronomy & Astrophysics, 573, A83

Lesh, J. R. 1968, ApJS, 17, 371

Levenberg, K. 1944, Quarterly of Applied Mathematics, 2, 164

Levine, E. S., Blitz, L., Heiles, C., & Weinberg, M. 2008, in Mapping the Galaxy and Nearby Galaxies, ed. K. Wada & F. Combes (New York, NY: Springer New York), 85–90

Li, G.-X. & Chen, B.-Q. 2022, MNRAS, 517, L102

Lindblad, P. O. 1967, Bull. Astron. Inst. Netherlands, 19, 34

Lindegren, L., Lammers, U., Bastian, U., et al. 2016, A&A, 595, A4

Liu, W., Chiao, M., Collier, M. R., et al. 2016, The Astrophysical Journal, 834, 33

Liu, Z., Mao, H., Wu, C., et al. 2022, CoRR, abs/2201.03545

Lockman, F. J. 1984, ApJ, 283, 90

Loinard, L. 2013, in IAU Symposium, Vol. 289, Advancing the Physics of Cosmic Distances, ed. R. de Grijs, 36–43

Maciejewski, W. & Cox, D. P. 1999, ApJ, 511, 792

Maciejewski, W., Murphy, E. M., Lockman, F. J., & Savage, B. D. 1996, ApJ, 469, 238

Mackey, J., Gvaramadze, V. V., Mohamed, S., & Langer, N. 2015, A&A, 573, A10

Madrid, J. P., Hurley, J. R., & Sippel, A. C. 2012, ApJ, 756, 167

Maíz-Apellániz, J. 2001, The Astrophysical Journal, 560, L83

Maíz-Apellániz, J. 2001a, ApJ, 560, L83

Maíz-Apellániz, J. 2001b, ApJ, 560, L83

Mamajek, E. E., Lawson, W. A., & Feigelson, E. D. 2000, ApJ, 544, 356

Mamajek, E. E., Meyer, M. R., & Liebert, J. 2002, AJ, 124, 1670

Marquardt, D. W. 1963, Journal of the Society for Industrial and Applied Mathematics, 11, 431

Mason, B. D., Hartkopf, W. I., Gies, D. R., Henry, T. J., & Helsel, J. W. 2009, AJ, 137, 3358

Massey, P. 1999, in Bulletin of the American Astronomical Society, Vol. 31, American Astronomical Society Meeting Abstracts, 1462

Mattsson, L. & Höfner, S. 2011, Astronomy & Astrophysics, 533, A42

McClure-Griffiths, N. M., Dickey, J. M., Gaensler, B. M., & Green, A. J. 2002, j, 578, 176

McClure-Griffiths, N. M., Pisano, D. J., Calabretta, M. R., et al. 2009, ApJS, 181, 398

McCray, R. & Kafatos, M. 1987, ApJ, 317, 190

McGehee, P. M. 2008, Star Formation and Molecular Clouds at High Galactic Latitude

Metropolis, N., Rosenbluth, A. W., Rosenbluth, M. N., Teller, A. H., & Teller, E. 1953, J. Chem. Phys., 21, 1087

Michaut, C., Cavet, C., Bouquet, S. E., Roy, F., & Nguyen, H. C. 2012, ApJ, 759, 78

Miller, G. E. & Scalo, J. M. 1979, ApJS, 41, 513

Minière, J., Bouquet, S. E., Michaut, C., Sanz, J., & Mancini, M. 2018, A&A, 617, A133

Moeckel, N. & Clarke, C. J. 2011, MNRAS, 410, 2799

Moffet, A. T. 1975, in Galaxies and the Universe, ed. A. Sandage, M. Sandage, & J. Kristian, 211

Morton, D. C. 1991, ApJS, 77, 119

Morton, D. C. 1992, ApJS, 81, 883

Morton, D. C., Drake, J. F., Jenkins, E. B., et al. 1973, ApJ, 181, L103

Nan, R., Li, D., Jin, C., et al. 2011, International Journal of Modern Physics D, 20, 989–1024

Ochsendorf, B. B., Brown, A. G. A., Bally, J., & Tielens, A. G. G. M. 2015, The Astrophysical Journal, 808, 111

Oey, M. S. & Clarke, C. J. 1997, Monthly Notices of the Royal Astronomical Society, 289, 570–588

Ofir, N., Galun, M., Alpert, S., et al. 2017, On Detection of Faint Edges in Noisy Images

Olano, C. A. 1982, A&A, 112, 195

Ortega, V. G., Jilinski, E., de la Reza, R., & Bazzanella, B. 2009, AJ, 137, 3922

Ortiz-León, G. N., Loinard, L., Kounkel, M. A., et al. 2017, ApJ, 834, 141

Otsu, N. 1979, IEEE Transactions on Systems, Man, and Cybernetics, 9, 62

Paladini, R., Umana, G., Veneziani, M., et al. 2012, The Astrophysical Journal, 760, 149

Palouš, J. & Ehlerová, S. 2014, ArXiv e-prints

Parmanabhan, T. 2001, Theoretical Astrophysics- volume II: Stars and Stellar Systems (The Edingburgh Building, Cambridge CB2 2RU,UK: Cambridge University Press), 216–222

Patil, A., Huard, D., & Fonnesbeck, C. 2010, Journal of Statistical Software, 35, 1

Pecaut, M. J., Mamajek, E. E., & Bubar, E. J. 2012, ApJ, 746, 154

Peek, J. E. G. & Heiles, C. 2008, ArXiv e-prints

Perrot, C. A. & Grenier, I. A. 2003, A&A, 404, 519

Perryman, M. A. C., de Boer, K. S., Gilmore, G., et al. 2001, A&A, 369, 339

Perryman, M. A. C., Lindegren, L., Kovalevsky, J., et al. 1997, A&A, 323, L49

Peters, T., Banerjee, R., Klessen, R. S., & Mac Low, M.-M. 2011, ApJ, 729, 72

Pittard, J. M. 2013, MNRAS, 435, 3600

Pittard, J. M. 2022, MNRAS, 515, 1815

Poeppel, W., Bajaja, E., Arnal, E., & Morras, R. 2010, http://dx.doi.org/10.1051/0004-6361/200811290, 512

Poppel, W., Marronetti, P., & Benaglia, P. 1996, in Revista Mexicana de Astronomia y Astrofisica Conference Series, Vol. 4, Revista Mexicana de Astronomia y Astrofisica Conference Series, ed. E. Falco, J. A. Fernandez, & R. F. Ferrero, 121

Pöppel, W. G. L. 2001, in Astronomical Society of the Pacific Conference Series, Vol. 243, From Darkness to Light: Origin and Evolution of Young Stellar Clusters, ed. T. Montmerle & P. André, 667

Predehl, P., Sunyaev, R. A., Becker, W., et al. 2020, Nature, 588, 227–231

Preibisch, T., Brown, A. G. A., Bridges, T., Guenther, E., & Zinnecker, H. 2002, AJ, 124, 404

Preibisch, T. & Mamajek, E. 2008, The Nearest OB Association: Scorpius-Centaurus (Sco OB2), ed. B. Reipurth, 235

Preibisch, T. & Zinnecker, H. 2001, in Astronomical Society of the Pacific Conference Series, Vol. 243, From Darkness to Light: Origin and Evolution of Young Stellar Clusters, ed. T. Montmerle & P. André, 791

Press, W. H., Teukolsky, S. A., Vetterling, W. T., & Flannery, B. P. 2007, Numerical Recipes 3rd Edition: The Art of Scientific Computing, 3rd edn. (USA: Cambridge University Press)

Prestage, R. M., Constantikes, K. T., Hunter, T. R., et al. 2009, IEEE Proceedings, 97, 1382

Puls, J., Vink, J. S., & Najarro, F. 2008, A&A Rev., 16, 209

Puspitarini, L. & Lallement, R. 2012, A&A, 545, A21

Rand, R. J. & Stone, J. M. 1996, AJ, 111, 190

Reis, W., Corradi, W., de Avillez, M. A., & Santos, F. P. 2011, ApJ, 734, 8

Reis, W. & Corradi, W. J. B. 2008, A&A, 486, 471

Reynolds, S. P. 2008, ARA&A, 46, 89

Reynoso, E. M. & Dubner, G. M. 1997, A&AS, 123

Richter, P., Wakker, B. P., Savage, B. D., & Sembach, K. R. 2003, ApJ, 586, 230

Rodgers-Lee, D., Krause, M. G. H., Dale, J., & Diehl, R. 2019, Monthly Notices of the Royal Astronomical Society, 490, 1894

Rogerson, J. B., York, D. G., Drake, J. F., et al. 1973, ApJ, 181, L110

Roman-Duval, J., Jackson, J. M., Heyer, M., et al. 2009, ApJ, 699, 1153

Ronneberger, O., Fischer, P., & Brox, T. 2015, CoRR, abs/1505.04597

Rownd, B. K., Dickey, J. M., & Helou, G. 1994, AJ, 108, 1638

Sallmen, S. M., Korpela, E. J., Bellehumeur, B., et al. 2015, AJ, 149, 189

Sallmen, S. M., Korpela, E. J., & Yamashita, H. 2008, ApJ, 681, 1310

Salpeter, E. E. 1955, ApJ, 121, 161

Santillan, A., Franco, J., Martos, M., & Kim, J. 1999, The Astrophysical Journal, 515, 657

Santos, F. P., Corradi, W., & Reis, W. 2011, ApJ, 728, 104

Sarkar, K. C., Jiang, F., Bournaud, F., et al. 2019, Monthly Notices of the Royal Astronomical Society, 488, 4753

Savage, B. D., Sembach, K. R., Jenkins, E. B., et al. 2000, ApJ, 538, L27

Scalo, J. M. 1986a, in Luminous Stars and Associations in Galaxies, ed. C. W. H. De Loore, A. J. Willis, & P. Laskarides, Vol. 116, 451–466

Scalo, J. M. 1986b, Fund. Cosmic Phys., 11, 1

Schlafly, E. F., Green, G., Finkbeiner, D. P., et al. 2014, ApJ, 789, 15

Schultz, G. V. & Wiemer, W. 1975, A&A, 43, 133

Scoville, N. Z. & Sanders, D. 1987, Interstellar Processes, ed. D. Hollenbach & D. H.A.Thronson, Jr. (Reidel, 21

Sedov, L. I. 1958, Reviews of Modern Physics, 30, 1077

Seigar, M. S. & James, P. A. 1998, MNRAS, 299, 685

Sfeir, D. M., Lallement, R., Crifo, F., & Welsh, B. Y. 1999, A&A, 346, 785

Shannon, C. E. 1949, Proc. Institute of Radio Engineers, 37, 10

Shapiro, P. & Field, G. 1976, ApJ, 205, 762

Sharp, D. 1984, Physica D: Nonlinear Phenomena, 12, 3

Shetty, R., Glover, S. C., Dullemond, C. P., & Klessen, R. S. 2011, MNRAS, 412, 1686

Silaj, J., Jones, C. E., Sigut, T. A. A., & Tycner, C. 2014, ApJ, 795, 82

Silich, S., Tenorio-Tagle, G., & Añorve-Zeferino, G. A. 2005, ApJ, 635, 1116

Skrutskie, M. F., Cutri, R. M., Stiening, R., et al. 2006, AJ, 131, 1163

Slesnick, C. L. 2007, PASP, 119, 1205

Smartt, S. J. 2009, ARA&A, 47, 63

Snow, T. P. & McCall, B. J. 2006, ARA&A, 44, 367

Sobel, I. 2014, Presentation at Stanford A.I. Project 1968

Sofue, Y. 2015, MNRAS, 447, 3824

Soler, J. D., Miville-Deschênes, M. A., Molinari, S., et al. 2022, A&A, 662, A96

Sparke, L. & Gallagher, J. 2007, Galaxies in the Universe: An Introduction (Cambridge University Press)

Stephenson, F. & Green, D. 2002, 5

Straižys, V., Černis, K., & Bartašiūte, S. 1996, Baltic Astronomy, 5, 125

Suad, L. A., Caiafa, C. F., Arnal, E. M., & Cichowolski, S. 2014, A&A, 564, A116

Suad, L. A., Caiafa, C. F., Cichowolski, S., & Arnal, E. M. 2019, A&A, 624, A43

Sushch, I., Hnatyk, B., & Neronov, A. 2011, A&A, 525, A154

Sutherland, R. S., Bicknell, G. V., & Dopita, M. A. 2003, ApJ, 591, 238

Tan, M. & Le, Q. V. 2019, CoRR, abs/1905.11946

Tan, M. & Le, Q. V. 2021, CoRR, abs/2104.00298

Taylor, G. 1950a, Royal Society of London Proceedings Series A, 201, 159

Taylor, G. 1950b, Royal Society of London Proceedings Series A, 201, 175

Tenorio-Tagle, G. & Bodenheimer, P. 1988, Annual Review of Astronomy and Astrophysics, 26, 145

Tenorio-Tagle, G., Silich, S., & Muñoz-Tuñón, C. 2003, ApJ, 597, 279

Thilker, D. 1999, in Interstellar Turbulence, ed. J. Franco & A. Carraminana, 104

Thilker, D. A., Braun, R. J., & Walterbos, R. A. M. 1998, Astronomy and Astrophysics, 332, 429

Tielens, A. G. G. M. & Allamandola, L. J. 1987, in Astrophysics and Space Science Library, Vol. 134, Interstellar Processes, ed. D. J. Hollenbach & H. A. Thronson, Jr., 397–469

Townsley, L. K., Broos, P. S., Garmire, G. P., et al. 2014, ApJS, 213, 1

Tremblin, P., Anderson, L. D., Didelon, P., et al. 2014, A&A, 568, A4

Trumpler, R. J. 1930, Lick Observatory Bulletin, 420, 154

Turatto, M. 2003, Classification of Supernovae, ed. K. W. Weiler (Berlin, Heidelberg: Springer Berlin Heidelberg), 21–36

Umbaugh, S. E. 2017, Digital Image Processing and Analysis, ed. S. Umbaugh (Springer), 897

Urquhart, J. S., Figura, C. C., Moore, T. J. T., et al. 2013, Monthly Notices of the Royal Astronomical Society, 437, 1791

van de Hulst, H. C. 1945, Ned. tijd. natuurkunde 11, 210 (cit. on p. 3)

van der Kruit, P. C. & Shostak, G. S. 1984, A&A, 134, 258

Van Marle, A. J., Meliani, Z., & Marcowith, A. 2015

van Marle, A. J., Meliani, Z., & Marcowith, A. 2012, A&A, 541, L8

van Woerden, H., Takakubo, K., & Braes, L. L. E. 1962, Bull. Astron. Inst. Netherlands, 16, 321

Veilleux, S., Cecil, G., & Bland-Hawthorn, J. 2005, ARA&A, 43, 769

Vergely, J.-L., Freire Ferrero, R., Siebert, A., & Valette, B. 2001, A&A, 366, 1016

Vishniac, E. T. 1983, ApJ, 274, 152

Vishniac, E. T. & Ryu, D. 1989, ApJ, 337, 917

Vitrichenko, E. A., Nadyozhin, D. K., & Razinkova, T. L. 2007, Astronomy Letters, 33, 251

Voss, R., Diehl, R., Hartmann, D. H., et al. 2009, A&A, 504, 531

Walter, F., Brinks, E., de Blok, W. J. G., et al. 2008, The Astronomical Journal, 136, 2563

Weaver, H. 1979, in IAU Symposium, Vol. 84, The Large-Scale Characteristics of the Galaxy, ed. W. B. Burton, 295–298

Weaver, R., McCray, R., Castor, J., Shapiro, P., & Moore, R. 1977, ApJ, 218, 377

Webb, R. A., Zuckerman, B., Platais, I., et al. 1999, ApJ, 512, L63

Weidner, C. & Kroupa, P. 2005a, in Astrophysics and Space Science Library, Vol. 327, The Initial Mass Function 50 Years Later, ed. E. Corbelli, F. Palla, & H. Zinnecker, 193

Weidner, C. & Kroupa, P. 2005b, Astronomische Nachrichten, 326, 605

Wells, D. C., Greisen, E. W., & Harten, R. H. 1981, A&AS, 44, 363

Welsh, B. Y., Lallement, R., Vergely, J.-L., & Raimond, S. 2010, A&A, 510, A54

Westerlund, B. E. & Mathewson, D. S. 1966, MNRAS, 131, 371

Westmeier, T. 2018, MNRAS, 474, 289

Wilson, T. L., Rohlfs, K., & Huttemeister, S. 2012, Tools of Radio Astronomy, 5th edition

Winkel, B., Kalberla, P. M. W., Kerp, J., & Flöer, L. 2010a, ApJS, 188, 488

Winkel, B., Kerp, J., Flöer, L., et al. 2016, A&A, 585, A41

Winkel, B., Kerp, J., Kalberla, P. M. W., & Ben Bekhti, N. 2010b, in Astronomical Society of the Pacific Conference Series, Vol. 438, Astronomical Society of the Pacific Conference Series, ed. R. Kothes, T. L. Landecker, & A. G. Willis, 381

Woermann, B., Gaylard, M. J., & Otrupcek, R. 2001, MNRAS, 325, 1213

Wolfire, M. G., Hollenbach, D., McKee, C. F., Tielens, A. G. G. M., & Bakes, E. L. O. 1995, ApJ, 443, 152

Wolleben, M. 2007, ApJ, 664, 349

Woolf, N. J. & Ney, E. P. 1969, ApJ, 155, L181

Xu, Y., Reid, M. J., Zheng, X. W., & Menten, K. M. 2006, Science, 311, 54

Ye, W., Xia, Y., & Wang, Q. 2011, Journal of Computational Information Systems, 75, 1516

York, D. G. 1974, ApJ, 193, L127

Zucker, C., Goodman, A., Alves, J., et al. 2021, The Astrophysical Journal, 919, 35

Zucker, C., Goodman, A. A., Alves, J., et al. 2022, Nature, 601, 334

Zuckerman, B., Song, I., Bessell, M. S., & Webb, R. A. 2001, ApJ, 562, L87